



Sergio Chapela López. TESE DE DOUTORAMENTO 2020
Modelado y simulación CFD de mecanismos de ensuciamiento y
deposición de partículas en combustión de biomasa

Universida de Vigo

Universida de Vigo

Universida de Vigo

TESE DE DOUTORAMENTO

*Modelado y simulación CFD de mecanismos de
ensuciamiento y deposición de partículas en
combustión de biomasa*

Sergio Chapela López

2020



Universidade de Vigo

Escola Internacional de Doutoramento

Sergio Chapela López

TESE DE DOUTORAMENTO

Modelado y simulación CFD de mecanismos de ensuciamiento y deposición de partículas en combustión de biomasa.

Dirixida polos doutores:

Jacobo Porteiro Fresco

José Luis Míguez Tabarés

Ano: 2020





Agradecimientos

En primer lugar, me gustaría agradecer a mis directores de tesis, Jacobo y José Luis, por haberme dado la oportunidad de formar parte de este grupo de investigación y realizar en él mi tesis doctoral.

Agradecer también a mis compañeros del Grupo de Tecnología Energética que me acogieron con los brazos abiertos y apoyaron durante la realización de la tesis.

Quisiera agradecer a mi familia su apoyo a lo largo de estos años y su enseñanza en los valores del trabajo y el esfuerzo continuo. Esta tesis doctoral es la culminación de muchos años aplicándolos.

Finalmente, a Bea, por su comprensión y apoyo a lo largo de estos años.

PD: Agradecer también a todos los procesadores que pasaron por mis manos, los supervivientes por fin podrán descansar y ser jubilados.

Resumen

En la actualidad, la sociedad está cada vez más concienciada de la inviabilidad de sustentar todo su desarrollo en modelos energéticos basados en energías fósiles. En las últimas décadas, diversos programas y directivas han fomentado la transición hacia energías renovables. Esta transición no es sencilla, se necesitan cambios sustanciales en todos los sectores, desde los modelos industriales hasta la sociedad en sí misma.

La biomasa se presenta como la energía renovable más viable a corto plazo por varios motivos. Es la única energía renovable con contenido en carbono, lo que la aproxima a los combustibles fósiles. Entre sus ventajas se encuentran la similitud en las cadenas de suministro e incluso de gran parte de los sistemas de combustión, reduciendo la inversión necesaria para su empleo. De hecho, se presenta a menudo como el combustible clave para la transición energética.

Sin embargo, su empleo entraña grandes retos que deben ser solventados para acelerar su implantación. En la combustión de biomasa se dan grandes emisiones de materia particulada, especialmente en granulometrías finas, que contaminan el aire y el suelo del entorno cercano, pudiendo desencadenar en enfermedades cardiovasculares. Dentro del sistema, los compuestos presentes en la ceniza pueden resultar perjudiciales para el propio sistema, dando lugar al rápido crecimiento de depósitos y sinterizados, los cuales empeoran su rendimiento y pueden derivar en graves problemas de corrosión.

Al igual que ocurre con los combustibles fósiles donde existen diferentes calidades, especialmente en el carbón, sucede con la biomasa. Esta energía renovable cuenta con una enorme heterogeneidad que se deriva de la propia definición realizada por la Directiva 2009/28/CE del Parlamento Europeo y del Consejo de 23 de abril de 2009 relativa al fomento del uso de energía procedente de fuentes renovables [1]: *“la fracción biodegradable de los productos, desechos y residuos de origen biológico procedentes de actividades agrarias (incluidas las sustancias de origen vegetal y de origen animal), de la silvicultura y de las industrias conexas, incluidas la pesca y la acuicultura, así como la fracción biodegradable de los residuos industriales y municipales”*. Dependiendo de su origen, el combustible variará pues en sus propiedades físicas, térmicas y químicas.

El autoconsumo en la industria de sus propios residuos para aprovechamiento energético es cada vez más habitual, pues puede aportar grandes beneficios a través de ahorro en energía y en costes de retirada de residuos. La sociedad también genera gran cantidad de biomasa en forma de residuo sólido urbano y residuos agrícolas que pueden ser aprovechados energéticamente. Es en este tipo de biomásas donde se puede obtener el mayor beneficio.

Este tipo de biomásas son de baja calidad, pues presentan altos contenidos de cenizas y bajos poderes caloríficos. A su vez estas cenizas son ricas en álcalis, cloro y azufre, por lo que agravan los fenómenos de deposición y corrosión dentro del sistema. Este trabajo busca contribuir al despliegue de los sistemas de combustión de biomasa de forma más factible y eficaz. Para ello, a lo largo del tomo se abordarán los aspectos que se mencionan a continuación.

Se realizará un profundo estado del arte en búsqueda de todos los mecanismos involucrados en la creación de estos depósitos de materia no deseada. Para cada uno de ellos se evaluará su relevancia en sistemas de combustión de biomasa y su nivel de incertidumbre al analizar los datos experimentales que se obtengan bien de la bibliografía como de ensayos experimentales en las instalaciones de la Universidad. Aquellos mecanismos relevantes en esta aplicación y cuyos efectos sobre la deposición resultan claros serán modelados numéricamente a través de diferentes aproximaciones. Aunque este trabajo se enfoque primordialmente en las superficies susceptibles de deposición de materia no deseada que han sido objeto de estudio experimental, requiere del adecuado modelado de la fase gaseosa a lo largo del sistema, y por tanto de la combustión en sí.

Aunque no se trata del objetivo principal de este trabajo, el primer paso es lograr una representación adecuada de la combustión, para lo cual será fundamental investigar en la interacción entre la turbulencia y la química en las regiones cercanas al lecho donde el campo gaseoso se ve alterado por su presencia. Se propondrá una modificación del modelado matemático existente en la bibliografía basada para este trabajo en datos experimentales. No obstante, se propondrá también una línea de desarrollo futuro que implique la variabilidad espacio-temporal de la morfología y composición del lecho.

Una vez representada adecuadamente la combustión y, con ella, la evolución de la temperatura del gas de combustión, su velocidad y la concentración de especies gaseosas, se procederá al modelado de los fenómenos de ensuciamiento en combustión de biomasa, objetivo principal de esta tesis.

Para ello, con la información recabada del estado del arte se procederá a la creación de un modelo de ensuciamiento en un marco Lagrangiano, el cual aportará no solo la tasa de deposición de materia no deseada, sino también una estimación del perfil del depósito. Este modelo se validará contra los datos experimentales obtenidos en la planta piloto del Grupo de Tecnología Energética, GTE #1, para un amplio abanico de puntos de operación, logrando resultados adecuados.

Con estos resultados adecuados, se avanza hacia la creación de un modelo de ensuciamiento válido para sistemas de combustión de biomasa comerciales. En éstos, los fenómenos inducidos en el lecho por el sistema de alimentación requieren de adaptaciones del algoritmo general, el cual también se optimiza para un menor coste computacional. Para su validación, se escogen dos sistemas muy distintos a la planta piloto GTE#1 empleada hasta ahora, lo que reforzará la validación del modelo de ensuciamiento. En ellos, los resultados obtenidos muestran gran coherencia con los datos experimentales.

El desarrollo del modelo continúa con el estudio del efecto que tiene esta materia depositada sobre las superficies de trabajo de los sistemas. El efecto directo es la reducción de la transmisión de calor al circuito del agua. Para ello se modelará e implementará la conductividad térmica del depósito en función de su espesor, porosidad y nivel de sinterizado. Para obtener unos resultados más completos se realiza la simulación de la nueva caldera del grupo con este modelo, la cual se modelará con la camisa de agua incluida, suponiendo un importante coste computacional.

Mientras esta simulación es ejecutada, se realiza un estudio de las fortalezas y debilidades del modelo de ensuciamiento empleado hasta el momento. La principal debilidad está en el descenso en rendimiento computacional en entornos altamente paralelos. Tras analizar las tendencias actuales en el desarrollo de la arquitectura de procesadores y el auge de los cálculos en la nube, donde emplean entornos altamente paralelos, se decide crear un nuevo modelo completamente Euleriano. Esta aproximación trabaja de forma mucho más favorable que la Lagrangiana en este tipo de entornos.

Para su desarrollo será necesario migrar todo el código de combustión Euleriano a un entorno multifásico, de forma que puedan realizarse el cálculo simultaneo de varias fases Eulerianas. Tras su migración, se validan sus resultados y se migra la formulación Lagrangiana del modelo de ensuciamiento a una formulación euleriana. Los resultados del nuevo modelo totalmente Euleriano son comparados con el anterior modelo Euler-Lagrange y con los resultados experimentales. Su rendimiento computacional también es analizado.

Durante la realización de este trabajo se estableció un objetivo secundario, la creación de una plataforma de colaboración internacional. Para ello, primero se creó un único modelo de combustión de biomasa en lecho fijo independiente del sistema de alimentación. Después, se procedió al diseño de una potente interfaz gráfica de usuario embebida en el software que simplifica el aprendizaje y el empleo de este modelo de combustión por expertos externos. De esta forma, el modelo es accesible por aquellos expertos que deseen emplear el modelo y aportar su experiencia en el modelado de fenómenos particulares de la combustión sin la necesidad de comprender al detalle todo el modelo.

Esta plataforma de colaboración ha sido probada y puesta a punto gracias a la colaboración con diversos centros de prestigio de Europa y América, las cuales han sido importantes para el desarrollo de este trabajo.

Finalmente, se mostrarán numerosas líneas futuras de desarrollo englobadas en tres campos: el modelado de lecho, el modelado de la deposición y la implementación de ambos mediante las nuevas tecnologías. Se espera que estas líneas puedan ser abordadas en el futuro próximo y, así, seguir contribuyendo a la expansión de la biomasa y, con ello, la expansión de las energías renovables a corto y medio plazo.

Palabras clave: CFD, biomasa, combustión, ensuciamiento, *fouling*, *slagging*, vapores inorgánicos, Euler-Lagrange, Euler-Euler.

Índice de contenido

RESUMEN	I
ÍNDICE DE CONTENIDO	V
ÍNDICE DE FIGURAS	VII
ÍNDICE DE TABLAS	IX
NOMENCLATURA	XI
ORGANIZACIÓN DE LA TESIS	1
OBJETIVOS Y ALCANCE DE LA TESIS	5
INTRODUCCIÓN	7
1.1 EL COMBUSTIBLE	7
1.2 MARCO LEGAL	9
1.3 USO DE LA BIOMASA	15
PROBLEMÁTICA DE LA COMBUSTIÓN DE BIOMASA	17
2.1 EMISIONES DE GASES	18
2.2 EMISIÓN DE MATERIA PARTICULADA	20
2.3 DEPOSICIÓN DE MATERIA NO DESEADA	25
2.4 SOLUCIONES	43
DINÁMICA DE FLUIDOS COMPUTACIONAL	49
3.1 FUNDAMENTOS DE LAS TÉCNICAS CFD	50
SISTEMAS EXPERIMENTALES	61
4.1 PLANTA PILOTO GTE #1	62
4.2 KWB MULTIFIRE™ 60	63
4.3 VAPORMATRA CANTINA™	65
4.4 FERROLI SUN MIKRO P7™	66
4.5 ESTUFA DEL IST-LISBOA, PORTUGAL	67
4.6 GASIFICADOR EN LOTES DE LA UNIVERSIDAD DE ANTIOQUIA, COLOMBIA	69
CREACIÓN DE INTERFAZ DE USUARIO	71
5.1 MOTIVACIÓN	71

5.2	ANTECEDENTES	72
5.3	RESULTADO	72
	MODELADO DE LA COMBUSTIÓN	75
6.1	ANTECEDENTES	75
6.2	MODELO GENERAL	76
6.3	VALIDACIÓN DEL MODELO	82
	MODELO DE ENSUCIAMIENTO EULER-LAGRANGE	87
7.1	INTRODUCCIÓN	87
7.2	MODELADO Y ALGORITMIA	88
7.3	MEJORA, OPTIMIZACIÓN Y VALIDACIÓN FRENTE A SISTEMAS [...]	91
7.4	MODELADO DE PROPIEDADES TÉRMICAS	93
	NUEVO MODELO DE ENSUCIAMIENTO EULER-EULER	95
8.1	INTRODUCCIÓN	95
8.2	MODELADO Y ALGORITMIA	96
	COHERENCIA Y UNIDAD DE LAS PUBLICACIONES	111
	CONCLUSIONES	113
	LÍNEAS FUTURAS	117
11.1	MODELADO DE LECHO	117
11.2	MODELADO DE DEPÓSITO	118
11.3	IMPLEMENTACIÓN DE MODELO	119
	ANEXO A.	139
	TRABAJOS PUBLICADOS ENGLOBADOS EN ESTA TESIS DOCTORAL	
	ANEXO B.	
	TRABAJOS ENVIADOS A REVISTA Y PENDIENTES DEL PROCESO DE REVISIÓN POR PARES	
	ANEXO C.	
	OTROS TRABAJOS DEL AUTOR	
	ANEXO D.	
	EJEMPLO DE CÓDIGO PERTENECIENTE A LA INTERFAZ GRÁFICA DE USUARIO	
	ANEXO E.	
	IMÁGENES DE LA INTERFAZ GRÁFICA DE USUARIO PARA UN CASO CONCRETO	

Índice de figuras

<i>Figura 1. Evolución del trabajo realizado.</i>	2
<i>Figura 2. Clasificación de las fuentes de biomasa.</i>	8
<i>Figura 3. Biomasa proveniente de la industria maderera.</i>	9
<i>Figura 4. Representación gráfica del uso de energías renovables.</i>	11
<i>Figura 5. Consumo interno bruto de energías englobadas dentro de la biomasa en la Unión Europea. Comparación de 2017 con posibles escenarios para el año 2050 (en MTEP) [8].</i>	12
<i>Figura 6. Cadena de suministro de biomasa.</i>	15
<i>Figura 7. Diversidad de propiedades térmicas y físicas de la biomasa. Adaptado de la referencia [14].</i>	18
<i>Figura 8. Procesos de craqueo y oxidación del nitrógeno a lo largo de la conversión térmica del combustible [22].</i>	20
<i>Figura 9. Tendencias en las emisiones de PM_{2.5} de diferentes fuentes [23].</i>	21
<i>Figura 10. Representación de los principales mecanismos involucrados en la formación de partículas [45].</i>	23
<i>Figura 11. Ejemplos de diferentes estructuras encontradas en materia particulada recolectada [34].</i>	24
<i>Figura 12. Mecanismos involucrados en la formación de depósitos.</i>	27
<i>Figura 13. Resumen de los mecanismos involucrados en la deposición [76].</i>	30
<i>Figura 14. Evolución de la tasa de deposición isotérmica con el tiempo de relajación de partícula [77].</i>	31
<i>Figura 15. Resultados de la Ecuación 4 según los coeficientes empleados de la Tabla 6.</i>	32
<i>Figura 16. Escenario de rebote irregular bajo la consideración de tres impactos [85].</i>	33
<i>Figura 17. Representación de las capas presentes en el crecimiento del depósito y la evolución de su temperatura superficial [42].</i>	34
<i>Figura 18. Porcentaje de fracción fundida presente en la partícula según su temperatura [67, 112].</i>	36

<i>Figure 19. Etapas de la erosión causada por la rodadura e impacto [122].</i>	37
<i>Figura 20. Representación del fenómeno conocido como turbulent bursts [125].</i>	38
<i>Figura 21. Representación de las distintas temperaturas encontradas en el estudio de la fusión de cenizas [129].</i>	40
<i>Figura 22. Observación de las temperaturas características de fusión de tres biomasa distintas sometidas a diferentes temperaturas [128].</i>	41
<i>Figura 23. Depósitos formados en los superheater de una planta de combustión de biomasa [42].</i>	43
<i>Figura 24. Impacto de los métodos de lavado en la cantidad de compuestos inorgánicos presentes en la biomasa [156].</i>	46
<i>Figura 25. Impacto de los métodos de lavado en la temperatura de fusión de las cenizas de varios tipos de biomasa [157].</i>	46
<i>Figura 26. Materia no deseada adherida al sistema de refrigeración del lecho [151].</i>	47
<i>Figura 27. Ilustración del criterio de calidad skewness [178].</i>	51
<i>Figura 28. Ilustración del criterio de calidad ortogonal quality [178].</i>	51
<i>Figura 29. Ilustración de la definición de aspect ratio [178].</i>	52
<i>Figura 30. Tipos de celdas de dos y tres dimensiones [179].</i>	52
<i>Figura 31. Terminología específica de las mallas [179].</i>	53
<i>Figura 32. Jerarquía de la estructura de datos de un entorno monofásico.</i>	59
<i>Figura 33. Diseño CAD tridimensional de esta planta piloto GTE#1 y esquema.</i>	62
<i>Figura 34. Detalle de la rejilla, tornillo de alimentación y distribuidor de aire secundario.</i>	63
<i>Figura 35. Esquema interno de la caldera KWB Multifire™ 60.</i>	64
<i>Figura 36. Sondas de deposición en forma de anillo y nomenclatura empleada [182].</i>	65
<i>Figura 37. Diseño CAD tridimensional y esquema de la estufa [182].</i>	65
<i>Figura 38. Diseño CAD tridimensional, sección de la caldera y detalle de la parrilla.</i>	67
<i>Figura 39. Esquema visual de la localización de las infiltraciones de aire [183].</i>	68
<i>Figura 40. Esquema visual de la localización de las sondas [183].</i>	68
<i>Figura 41. Esquema de la instalación del gasificador y sus sistemas periféricos [184].</i>	69
<i>Figura 42. Algoritmo del modelo de ensuciamiento de Euler-Lagrange [45].</i>	89
<i>Figura 43. Modificación del algoritmo del modelo de ensuciamiento de Euler-Lagrange [182].</i>	92
<i>Figura 44. Estructura de dominios en entornos multifásicos [224].</i>	98
<i>Figura 45. Jerarquía de la estructura de datos para un entorno multifásico.</i>	98
<i>Figura 46. Algoritmo de distribución de la tasa de elutriación.</i>	101
<i>Figura 47. Algoritmo de reducción de fase granular.</i>	108

Índice de tablas

<i>Tabla 1. Contribución de energías renovables en la UE28.</i>	10
<i>Tabla 2. Toneladas de residuos per cápita y país.</i>	14
<i>Tabla 3. Nivel de emisiones de materia particulada en relación con la potencia del sistema y su contenido en carbón orgánico [9].</i>	24
<i>Tabla 4. Índices de fouling y slagging.</i>	25
<i>Tabla 5. Compuestos de temperatura de fusión alta vs baja.</i>	26
<i>Tabla 6. Coeficientes de eficiencia de impacto</i>	32
<i>Tabla 7. Capas del depósito presente en un sistema de combustión de paja [42].</i>	39
<i>Tabla 8. Reacciones heterogéneas del carbón y sus cinéticas [2, 190, 191].</i>	79
<i>Tabla 9. Reacciones homogéneas y sus cinéticas.</i>	81

Nomenclatura

a, b, c	Coefficientes de eficiencia de impacto	(-)
A, B	Constantes de Magnussen	(-)
A*	Constante A de Magnussen modificada	(-)
A, \vec{A}	Magnitud de área. Vector de área	(m ²)
Av	Relación Área-Volumen	(m ⁻¹)
Cc	Coefficiente de Stokes-Cunningham	(-)
C _D	Coefficiente adimensional de arrastre o <i>drag</i>	(-)
C _P	Calor específico	(J kg ⁻¹ K ⁻¹)
d	Diámetro	(m)
D	Difusión	(m ² s ⁻¹)
E	Energía total por unidad de masa	(J kg ⁻¹)
\vec{F}	Aceleración debida a fuerzas adicionales	(N)
\vec{F}_l	Vector de fuerza externa	(N)
$\vec{F}_{lift,l}$	Vector de fuerza de sustentación	(N)
$\vec{F}_{wl,l}$	Vector de fuerza de lubricación de pared	(N)
$\vec{F}_{vm,l}$	Vector de fuerza de masa virtual	(N)
$\vec{F}_{td,l}$	Vector de fuerza de dispersión turbulenta	(N)
\vec{f}_m	Vector de fuerza másica	(N)
\vec{g}	Gravedad	(m s ⁻²)
G _{k,q}	Producción de energía cinética de turbulencia	(J m ⁻¹)
h	Coefficiente de transmisión de calor. Entalpía	(W m ⁻² K ⁻¹), (J kg ⁻¹)
I	Intensidad de irradiación	(W m ⁻² sr ⁻¹)
\vec{I}	Matriz identidad	(-)
\vec{j}	Difusión másica	(kg m ⁻² s ⁻¹)
\vec{K}	Coefficientes de intercambio de momento	(kg m s ⁻¹)
k _B	Constante de Boltzman	(J K ⁻¹)
k	Conductividad térmica	(W m ⁻¹ K ⁻¹)
k _e	Coefficiente de erosión	(-)
k _q	Energía cinética por unidad de masa de fase continua	(J kg ⁻¹)
LH	Calor latente	(J kg ⁻¹)

M	Peso molar	(kg kmol ⁻¹)
m	Masa	(kg)
\dot{m}_{ij}	Transferencia de masa de la fase i a la fase j	(kg s ⁻¹)
n	Índice refractivo	(-)
p	Presión del fluido	(Pa)
Prob _{particle}	Probabilidad de adhesión debido a la presencia de fase derretida en la partícula.	(-)
Prob _{wall}	Probabilidad de adhesión debido a la presencia de fase derretida en la pared.	(-)
q _h	Flujo de calor por unidad de masa	(W kg ⁻¹ m ⁻²)
Q	Intensidad de intercambio de calor	(W)
\vec{r}	Vector posición	(m)
R	Tasa de reacción	(mol m ⁻³ s ⁻¹)
R _{diff}	Deposición debida a la difusión	(kg m ⁻³ s ⁻¹)
R _{turb}	Deposición debida al impacto turbulento	(kg/m ⁻³ s ⁻¹)
R _{therm}	Deposición debida a la termoforesis	(kg/m ⁻³ s ⁻¹)
R _g	Constante universal de los gases	(J mol ⁻¹ K ⁻¹)
R _K	Relación de conductividades térmicas	(-)
R _d	Factor de reducción	(-)
\vec{s}	Vector dirección	(m)
T	Temperatura	(K)
T ₀	Temperatura de solidus	(°C)
T ₁₅	Temperatura de adhesión	(°C)
T ₇₀	Temperatura de flujo	(°C)
T ₁₀₀	Temperatura de derretimiento completo	(°C)
TSP	Probabilidad total de adhesión	(-)
\vec{u}, \vec{v}	Velocidad	(m s ⁻¹)
\vec{U}	Velocidad media	(m s ⁻¹)
t	Tiempo	(s)
$\overline{v_{ij}}$	Velocidad relativa entre la fase i y la fase j	(m s ⁻¹)
V	Volumen	(m ⁻³)
x	Posición de partícula	(m)
Y	Fracción másica	(-)

Símbolos griegos

α	Absorción	(m ⁻¹)
δ_{ij}	Función Delta de Kronecker	(-)
ε	Emisividad. Fracción sólida	(-)
ε_q	Tasa de disipación turbulenta de la fase continua	(m ² s ⁻³)
μ	Viscosidad dinámica	(Pa s)
μ_t	Viscosidad turbulenta	(Pa s)
λ_i	Viscosidad granular	(Pa s)
σ	Constante de Stefan-Boltzmann.	(W m ⁻² K ⁻⁴)

σ_i	Fracción volumétrica de la fase i	(-)
$\overline{\tau}$	Tensor de esfuerzos viscosos	(Pa)
τ_p	Tiempo de relajación de la partícula	(s)
τ_j	Tiempo de relajación de la fase granular j	(s)
τ_w	Esfuerzo cortante en la pared	(Pa)
Γ	Coefficiente de difusión. Espesor de depósito	(m ² s ⁻¹), (m)
θ_r	Temperatura de radiación	(K)
ρ	Densidad	(kg m ⁻³)
φ	Ratio CO/CO ₂ . Ángulo de fricción	(-), (rad)
ϕ	Variable genérica	
ϕ_j	Diámetro de la fase granular	(m)
ν	Viscosidad cinemática	(m ² s ⁻¹)
ω	Tasa de generación o consumo de densidad del lecho	(kg m ⁻³ s ⁻¹)
$\Upsilon(Stk)$	Eficiencia de impacto	(-)
Ω	Ángulo sólido	(sr)

Subíndices

ash,sol	Ceniza sólida
ash,vol	Ceniza volátil
C	Carbón
char	<i>Char</i>
dev	Devolatilización
eff	Efectiva
eq	Equivalente
g	Gas
glob	Global
moist	Humedad
i	i-ésima densidad de lecho, reacción, reactivo, fase Euleriana (granular o continua)
i,j	De la fase i a la fase j
j	j-ésimo producto de la reacción. Fase Euleriana granular
j,i	De la fase j a la fase i
m	Masa
wood	Madera
p	Partícula
q	Fase Euleriana continua
s	Sólido
τ	Fricción

Superíndices

conv	Convectivo
n	Paso temporal de partícula
n+1	Siguiente paso temporal de la partícula

g,1 g,2	Cinéticas de gasificación del <i>char</i> 1 y 2
ox	Cinética de oxidación del <i>char</i>
loss	Pérdidas
rad	Radiación
reac	Reacción
T	Turbulento
V, ”	Volumétrico
Y	Función de suavizado

Acrónimos y abreviaturas

AFC	<i>Ash Fusion Characteristics.</i>
AFT	<i>Ash Fusion Temperatures</i>
AMS	<i>Aerosol Mass Spectrometer</i>
ASTM	<i>American Society for Testing and Materials</i>
BC	<i>Black Carbon</i>
CAD	<i>Computer Aided Design</i>
CCD	<i>Central Composite Design</i>
CFD	<i>Computational Fluid Dynamics</i>
CMS	<i>Capsicum Stalk</i>
CNS	<i>Cotton Stalk</i>
COC	<i>Condensable Organic Compounds</i>
CPU	<i>Central Processing Unit</i>
DIN	<i>Deutsches Institut für Normung</i>
DLPI	<i>Dekati Low Pressure Impactor</i>
DMA	<i>Dynamic Mechanical Analysis</i>
DPM	<i>Discrete Phase Model</i>
EDM	<i>Eddy Dissipation Model</i>
EDS/EDX	<i>Energy-dispersive X-ray spectroscopy</i>
ESP	<i>Electrostatic Precipitator</i>
EU28	<i>Member States of the European Union</i>
FEM	<i>Finite Element Method</i>
FGR/ IFGR	<i>Flue Gas Recirculation / Internal Flue Gas Recirculation</i>
FR-ED	<i>Finite Rate – Eddy Dissipation</i>
FT	<i>Fluidization Temperature</i>
FVM	<i>Finite Volume Method</i>
GPGPU	<i>General-Purpose Computing on Graphics Processing Units</i>
GPU	<i>Graphics Processing Unit</i>
GUI	<i>Graphical User Interface</i>
HRTEM	<i>High Resolution Transmission electron microscopy</i>
HT	<i>Hemispherical Temperature</i>
IBA	<i>Ion Beam Analysis</i>
IDT	<i>Initial Deformation Temperature</i>
IEA	<i>International Energy Agency</i>
IRENA	<i>International Renewable Energy Agency</i>

IST	<i>Instituto Superior Técnico</i>
LHS	<i>Latin Hypercube Sampling</i>
Mtoe	<i>Million Tonnes of Oil Equivalent</i>
MUSCL	<i>Monotone Upstream-Centered Schemes for Conservation Laws</i>
MSW	<i>Municipal Solid Waste</i>
OC	<i>Organic Carbon</i>
OFA	<i>Over-Fire Air</i>
OPC	<i>Optical Plankton Counter</i>
PIC	<i>Products of Incomplete Combustion</i>
PM	<i>Particulate Matter</i>
QUICK	<i>Quadratic Upstream Interpolation for Convective Kinematics</i>
RED	<i>Renewable Energy Directive</i>
SEM	<i>Scanning electron microscopy</i>
SIMPLE	<i>Semi-Implicit Method for Pressure-Linked Equations</i>
SMPS	<i>Scanning Mobility Particle Sizer</i>
ST	<i>Softening Temperature</i>
TEM	<i>Transmission Electron Microscopy</i>
TPS	<i>Thermophoretic Sampling</i>
UDF	<i>User Defined Function</i>
UDS	<i>User Defined Scalar</i>
VOC	<i>Volatile Organic Compound</i>
VOF	<i>Volume of Fluid</i>
WTS	<i>Wheat Stalk</i>
XPS	<i>X-ray photoelectron spectroscopy</i>

Dimensionless Numbers

Kn	Número de Knudsen
Nu	Número de Nusselt
Pr	Número de Prandtl
Re	Número de Reynolds
Sc	Número de Schmidt
Stk	Número de Stokes

Organización de la tesis

La tesis que se expondrá a lo largo de este tomo se ha realizado por compendio de artículos bajo la normativa RD 99/2011 en el programa de doctorado [V04D034V06] “Programa de Doutoramento en Eficiencia Enerxética e Sustentabilidade en Enxeñaría e Arquitectura”. Además de los artículos que dan base a esta tesis también se adjuntarán en los anexos del tomo el trabajo adicional realizado que, si bien no conduce directamente a la resolución de los objetivos planteados, sí permite crear una buena base de desarrollo para lograr resolver estos objetivos y otros muchos en el futuro próximo.

Se comenzará con un breve análisis del escenario energético global y el papel que juegan las energías renovables, en concreto la biomasa, en el mismo. Se abordarán los motivos y fenómenos implicados por los que la implantación de la biomasa no progresa de forma más veloz. Una vez se plantee el contexto en el que se desarrolla este trabajo, se explicarán la metodología de trabajo y la motivación para la creación de un modelo de biomasa generalista junto con una interfaz gráfica para su manejo.

Tras esta presentación, se procederá a explicar la motivación del ajuste del modelo de combustión de biomasa en lecho fijo que da origen al primer artículo de la tesis. Después, se abordará la creación de un primer modelado numérico del fenómeno de fouling y se analizará su respuesta para varios parámetros en la planta piloto GTE#1, que resultará en un segundo artículo.

Dado que se obtienen resultados adecuados, se procederá a optimizar y mejorar dicho algoritmo y se empleará para calcular el fenómeno de fouling en dos calderas domésticas distintas, constituyendo un tercer artículo. Este modelo se continúa desarrollando, añadiendo más posibilidades. Más concretamente se añade el efecto que tiene la capa de fouling adherida a las superficies de trabajo y su importancia en la transmisión de calor en calderas de biomasa. Esto será objeto de un cuarto artículo, actualmente en proceso de revisión por pares.

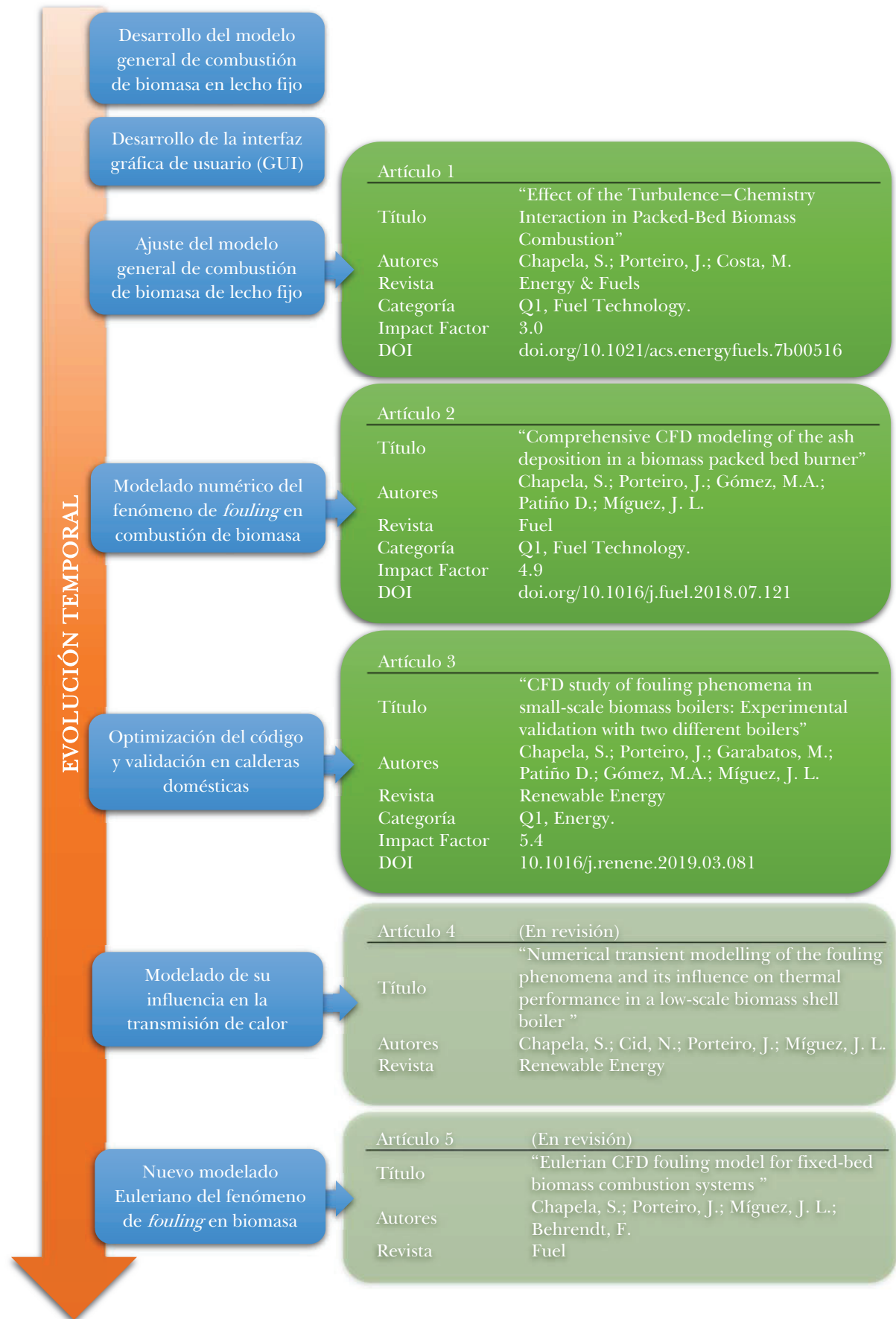


Figura 1. Evolución del trabajo realizado.

Llegados a este punto, se decide analizar el problema desde otra perspectiva. El modelado numérico propuesto hasta entonces aporta buenos resultados y aporta la posibilidad de seguir siendo mejorado con nuevas características. Sin embargo, a pesar de la continua optimización del código, el coste computacional es cada vez mayor y crece con cada nueva característica. Este hecho aleja al modelo de su finalidad última, el usuario, la industria.

Con la experiencia adquirida tras múltiples colaboraciones con entidades externas se concluye que, antes de profundizar más en el modelado numérico, es necesario adaptarse a las necesidades y recursos de este usuario final. Para que se puedan considerar las herramientas CFD (*Computational Fluid Dynamics*) como viables por las empresas, su coste en tiempo e inversión debe ser inferior al coste que tendría construir y realizar directamente el ensayo deseado. Por ello, sin abandonar la línea del modelado empleado hasta la actualidad, se decide construir desde cero un nuevo modelado multifásico de combustión de biomasa y un nuevo modelado de fouling bajo una nueva aproximación, la cual permite realizar los cálculos de forma más veloz y sencilla con unas necesidades de hardware inferiores. Este nuevo modelado se presenta en un quinto artículo, actualmente enviado y en proceso de revisión por pares. En la Figura 1, se muestra de forma resumida y esquemática la evolución de esta tesis y la ubicación temporal de los artículos que la componen.

Adicionalmente, durante la realización de este trabajo conducente a tesis, se ha trabajado en las siguientes publicaciones, ubicadas en el Otros trabajos del autor, relacionadas con la combustión de biomasa para mejorar el comportamiento del modelo de combustión de biomasa en lecho fijo del Grupo de Tecnología Energética de la Universidad de Vigo, mejoras de las que en el futuro se beneficiará el modelo CFD de fouling abordado:

Título	“An Eulerian model for the simulation of the thermal conversion of a single large biomass particle ”
Autores	Gómez, M. A.; Porteiro, J.; Chapela, S.; Míguez, J. L.
Revista	Fuel
Categoría	Q1, Fuel Technology.
Impact Factor	4.9
DOI	doi.org/10.1016/j.fuel.2018.02.063
Título	“Numerical analysis of wood biomass packing factor in a fixed-bed gasification process”
Autores	González, W.A.; Pérez, J.F.; Chapela, S.; Porteiro, J.
Revista	Renewable Energy
Categoría	Q1, Energy.
Impact Factor	5.4
DOI	doi.org/10.1016/j.renene.2018.01.057

Título	“Steady CFD combustion modeling for biomass boilers: An application to the study of the exhaust gas recirculation performance ”
Autores	Gómez, M. A.; Martín, R.; Chapela, S.; Porteiro, J.
Revista	Energy Conversion and Management
Categoría	Q1, Renewable Energy, Sustainability and the Environment.
Impact Factor	7.87
DOI	https://doi.org/10.1016/j.enconman.2018.10.052

Título	“Improving Bed Movement Physics in Biomass Computational Fluid Dynamics Combustion Simulations ”
Autores	Varela, L.G.; Bermúdez, C.Á.; Chapela, S.; Porteiro, J.; Tabarés, J.L.M.
Revista	Chemical Engineering and Technology
Categoría	Q2, Industrial and Manufacturing Engineering.
Impact Factor	0.42
DOI	https://doi.org/10.1002/ceat.201800674

Título	“Three-dimensional CFD simulation of a large-scale grate-fired biomass furnace”
Autores	Bermúdez, C.A.; Porteiro, J.; Varela, L.G., Chapela, S.; Patiño, D.
Revista	Fuel Processing Technology
Categoría	Q1, Fuel Technology.
Impact Factor	4.5
DOI	doi.org/10.1016/j.fuproc.2019.106219

Título	“CFD-based coupled multi phase modeling of biochar production using a large-scale pyrolysis plant”
Autores	Khodaei, H.; Varela, L.G.; Chapela, S.; Porteiro, J.; Nikrityuk, P.; Olson, C.
Revista	Applied Energy
Estado	En revisión

Objetivos y alcance de la tesis

El objetivo principal de esta tesis es el desarrollo de un modelo numérico mediante técnicas CFD para la predicción y estudio del fenómeno de *fouling* en sistemas de combustión de biomasa en lecho fijo. Para ello, será necesario un profundo estado del arte, tanto de los mecanismos involucrados, como de su relevancia en el caso de combustión de biomasa.

Para la validación experimental de los resultados del modelo de fouling se emplearán las instalaciones con las que cuenta el Grupo de Tecnología Energética. Se buscará emplear diversas morfologías de instalaciones para asegurar la flexibilidad del modelo. Por ello, se trabajará tanto con la planta piloto GTE #1 como con calderas domésticas acuotubulares y piro-tubulares.

Para lograr el objetivo principal serán necesario lograr diversos hitos u objetivos secundarios, entre los que se destacan los siguientes:

- Será necesario partir de una base o modelo de combustión de biomasa adecuado que nos proporcione los campos de concentración de especies químicas, velocidades y temperaturas para el modelo de fouling a desarrollar.
- Este modelo deberá ser lo más generalista posible, de forma que se pueda aplicar a cualquier tipo de sistema de combustión de biomasa en lecho fijo, independiente de su morfología o sistema de alimentación.
- Identificar la estrategia a seguir en el desarrollo del modelo de fouling, el equilibrio entre precisión y velocidad de cálculo y su desarrollo como extensión del modelo general.
- Identificar los precursores habituales en las instalaciones experimentales del grupo.
- Integrar estos precursores en el modelo de combustión de biomasa generalista.
- Estudio de la respuesta de estos precursores a diferentes parámetros de operación.
- Definir el modelado adecuado para la elutriación de materia particulada desde el lecho.

- Estudio del comportamiento del modelado de elutriación en diversas morfologías de lecho.
- Definir el modelado adecuado del transporte de materia particulada a lo largo del dominio de cálculo y su interacción con el gas de combustión.
- Análisis del comportamiento dinámico de la materia particulada en suspensión en el entorno cercano de las superficies.
- Definir las propiedades físicas del contacto de esta materia particulada con las superficies de trabajo.
- Estudio de la interacción de la materia particulada con los precursores modelados.
- Analizar en profundidad los resultados experimentales para identificar la estructura de la capa depositada sobre la superficie de trabajo.
- Comparativa y ajuste del modelado numérico con los resultados experimentales.
- Modelado numérico de las consecuencias inmediatas de la deposición de materia particulada sobre las superficies de trabajo.
- Validación experimental del modelado numérico ajustado.
- Diseño y desarrollo del algoritmo para la generación del perfil de deposición sobre las superficies de trabajo.
- Comparativa de este perfil con los resultados experimentales.
- Optimización continua de los algoritmos desarrollados.
- Creación de una plataforma de colaboración internacional para agrupar esfuerzos en el desarrollo de un modelo numérico de combustión de biomasa que contribuya a la expansión de este tipo de combustibles.

Capítulo 1

Introducción

1.1 El combustible

Se define como biomasa, de forma general, como todo tipo de sustancia orgánica cuyo origen esté próximo en el tiempo y sea debido a un proceso biológico. Según la Directiva 2009/28/CE del Parlamento Europeo y del Consejo de 23 de abril de 2009 relativa al fomento del uso de energía procedente de fuentes renovables [1], se define como biomasa a “*la fracción biodegradable de los productos, desechos y residuos de origen biológico procedentes de actividades agrarias (incluidas las sustancias de origen vegetal y de origen animal), de la silvicultura y de las industrias conexas, incluidas la pesca y la acuicultura, así como la fracción biodegradable de los residuos industriales y municipales*”

Como se puede ver, la biomasa se incluye dentro de las Directivas para el fomento del uso de energías renovables. El motivo es lo que se conoce como ciclo cerrado del carbono. Pese a la emisión de gases contaminantes a la atmósfera, esencialmente dióxido de carbono, este combustible puede ser considerado como renovable, pues el contenido en carbono de estas emisiones ha sido previamente extraído de la misma atmósfera a la que se emiten [2, 3].

La biomasa se encuentra ampliamente distribuida en el entorno en múltiples formas y con distintas propiedades termoquímicas. En la Figura 2, se muestran posibles fuentes de biomasa agrupadas según su origen. En esta tesis, se trabajará esencialmente con biomasa de origen vegetal, por estar sus propiedades mejor clasificadas, pero sin perder el foco en el resto de tipos de biomasa ya que no deben dejarse a un lado si se quieren lograr los objetivos marcados por la Directiva 2009/28/CE.

Durante las últimas décadas, la sociedad ha comenzado a preocuparse cada vez más por el medioambiente que le rodea. La amenaza del cambio climático y el continuo incremento del precio de los combustibles fósiles y su repercusión indirecta

en el precio de otros productos han provocado que la sociedad promueva toda aquella tecnología e industria que emplee energías renovables.

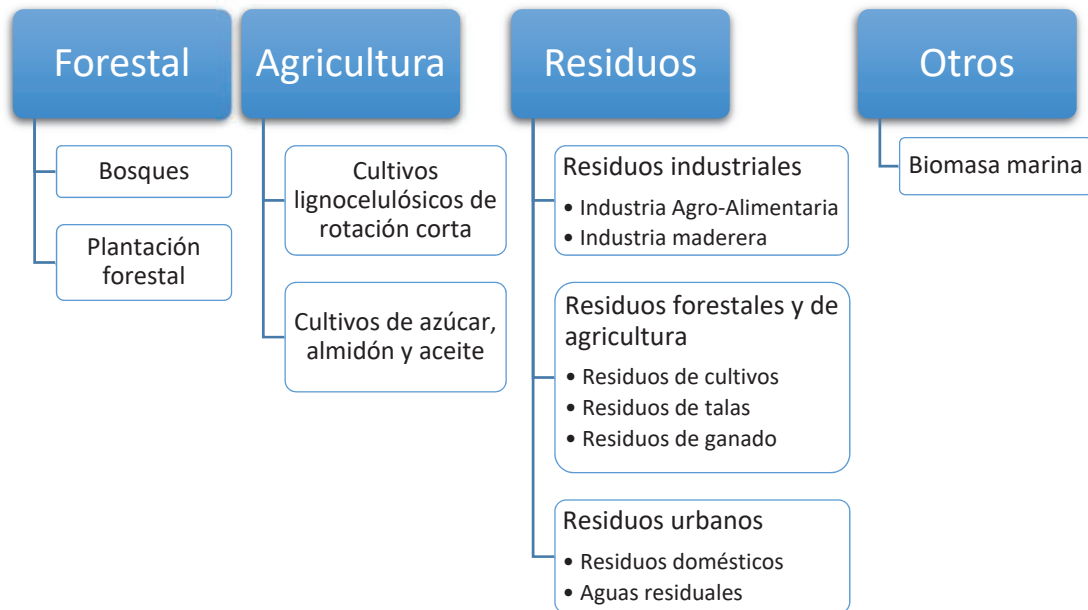


Figura 2. Clasificación de las fuentes de biomasa.

La gran mayoría de las energías renovables (hidráulica, eólica, solar fotovoltaica o térmica, geotérmica, mareomotriz, etc.) presentan la ventaja de no emitir gases de efecto invernadero a la atmósfera como sí lo hacen aquellas energías obtenidas a partir de la combustión. Si bien, estas tecnologías a menudo presentan inconvenientes variados que frenan su desarrollo e implantación. Sus requisitos de espacio, impacto medioambiental e inversión económica frecuentemente desaconsejan su empleo.

Sin embargo, la biomasa logra unir ambos mundos actuales, con sus ventajas e inconvenientes. De entre todos los tipos de energías renovables, la biomasa es la única fuente que presenta contenido en carbono disponible para su empleo en sistemas de combustión basados en combustibles fósiles [4]. Su empleo directo en combustión o su transformación en otro tipo de combustible (biogás, biocombustibles, etc.) para posterior combustión no difiere en gran medida de las tecnologías actuales basadas en combustibles fósiles. Esto permite que pueda ser considerado como un combustible de transición [5, 6]. De esta forma, la industria puede abandonar el uso de combustibles fósiles sin la construcción de una nueva instalación desde los cimientos. A menudo una leve adaptación de la planta permite el cambio de combustible obteniendo un rendimiento aceptable. El tipo de mercado y cadena de suministro también presenta similitudes, lo que aporta confianza al usuario de dicha energía.

Este tipo de combustible también presenta otras ventajas además de la ya mencionada, entre las que destacan su alta disponibilidad en el entorno cercano y la posibilidad de emplear los propios residuos de la producción de una industria para

satisfacer su demanda interna. De esta forma se reduce la cantidad de residuos a retirar y tratar al tiempo que se reduce su demanda. Esto ocurre habitualmente en industrias madereras pues el propio residuo (serrín, astillas, etc.) ya tiene buenas propiedades para ser quemado. Un ejemplo del mismo se puede ver en la Figura 3.



Figura 3. Biomasa proveniente de la industria maderera.

1.2 Marco legal

La Unión Europea, a través de la Directiva 2009/28/CE y la posterior revisión 2018/2001/EU, conocidas como *RED* por sus siglas en inglés (*Renewable Energy Directive*) se ha impuesto el objetivo de una cuota de energías renovables del 20% para el año 2020 y el objetivo de que un 10(%) de los combustibles para el transporte deben tener origen en fuentes renovables.

En su revisión 2018/2001/EU establece un objetivo del 32% para el 2030, con una posible revisión al alza en 2023, permitiendo a los países integrantes establecerse objetivos más severos si así lo desean. Parece pues clara la intención de fomentar el empleo de este tipo de energías renovables e instan a los estados miembros a no dejar de lado las la contribución que la eficiencia energética puede aportar en su artículo 19 de la Directiva 2009/28/CE [1], “ [...] *Cada Estado miembro debe determinar, al evaluar sus previsiones de consumo final bruto de energía en su plan de acción nacional en materia de energías renovables, la contribución que la eficiencia energética y el ahorro energético puedan aportar para alcanzar sus objetivos nacionales. Los Estados miembros deben tener en cuenta la combinación óptima de tecnologías de eficiencia energética con energías procedentes de fuentes renovables.*”

Tabla 1. Contribución de energías renovables en la UE28.

(%) Energías Renovables	2004	2010	2011	2012	2013	2014	2015	2016	2017	2018	2020 Objetivo	Diferencia
EU28	8.5	13.2	13.4	14.7	15.4	16.2	16.7	17.0	17.5	18.0	20.0	-2.0
Alemania [DE]	6.2	11.7	12.5	13.6	13.8	14.4	14.9	14.9	15.5	16.4	18.0	-1.6
Austria [AT]	22.6	31.2	31.6	32.7	32.8	33.7	33.5	33.4	33.1	33.4	34.0	-0.6
Bélgica [BE]	1.9	5.6	6.3	7.2	7.5	8.0	8.0	8.7	9.1	9.4	13.0	-3.6
Bulgaria [BG]	9.2	14.0	14.2	16.0	18.9	18.0	18.2	18.8	18.7	20.5	16.0	4.5
Chipre [CY]	3.1	6.2	6.3	7.1	8.5	9.2	9.9	9.9	10.5	13.9	13.0	0.9
Croacia [HR]	23.4	25.1	25.4	26.8	28.0	27.8	29.0	28.3	27.3	28.0	20.0	8.0
Dinamarca [DK]	14.8	21.9	23.4	25.5	27.2	29.4	31.0	32.3	35.4	36.7	30.0	6.7
Eslovaquia [SK]	6.4	9.1	10.3	10.5	10.1	11.7	12.9	12.0	11.5	11.9	14.0	-2.1
Eslovenia [SI]	16.1	20.4	20.3	20.8	22.4	21.5	21.9	21.3	21.0	21.1	25.0	-3.9
España [ES]	8.3	13.8	13.2	14.3	15.3	16.1	16.2	17.4	17.6	17.4	20.0	-2.6
Estonia [EE]	18.4	24.6	25.4	25.5	25.3	26.2	28.2	28.5	29.1	29.9	25.0	4.9
Finlandia [FI]	29.2	32.4	32.8	34.4	36.7	38.8	39.3	39.0	40.9	41.2	38.0	3.2
Francia [FR]	9.5	12.7	11.0	13.4	14.0	14.6	15.0	15.7	16.0	16.6	23.0	-6.4
Grecia [EL]	7.2	10.1	11.2	13.7	15.3	15.7	15.7	15.4	17.0	18.0	18.0	0.0
Hungría [HU]	4.4	12.7	14.0	15.5	16.2	14.6	14.4	14.3	13.5	12.5	13.0	-0.5
Irlanda [IE]	2.4	5.7	6.6	7.1	7.6	8.6	9.1	9.3	10.6	11.1	16.0	-4.9
Italia [IT]	6.3	13.0	12.9	15.4	16.7	17.1	17.5	17.4	18.3	17.8	17.0	0.8
Kosovo¹ [XK]	20.5	18.2	17.6	18.6	18.6	19.5	18.5	24.5	23.1	24.9	25.0	-0.1
Letonia [LV]	32.8	30.4	33.5	35.7	37.0	38.6	37.5	37.1	39.0	40.3	40.0	0.3
Lituania [LT]	17.2	19.6	19.9	21.4	22.7	23.6	25.8	25.6	26.0	24.4	23.0	1.4
Luxemburgo [LU]	0.9	2.9	2.9	3.1	3.5	4.5	5.0	5.4	6.3	9.1	11.0	-1.9
Macedonia² [MK]	15.7	16.5	16.4	18.1	18.5	19.6	19.5	18.0	19.6	18.1	23.0	-4.9
Malta [MT]	0.1	1.0	1.8	2.9	3.7	4.7	5.1	6.2	7.3	8.0	10.0	-2.0
Noruega [NO]	58.5	61.3	65.0	65.5	66.7	69.2	69.1	70.2	71.5	72.8	67.5	5.3
Países Bajos [NL]	2.0	3.9	4.5	4.7	4.7	5.4	5.7	5.8	6.5	7.4	14.0	-6.6
Polonia [PL]	6.9	9.3	10.3	10.9	11.4	11.5	11.7	11.3	10.9	11.2	15.0	-3.8
Portugal [PT]	19.2	24.2	24.6	24.6	25.7	29.5	30.5	30.9	30.6	30.3	31.0	-0.7
Reino Unido [UK]	0.9	3.8	4.3	4.4	5.5	6.7	8.4	9.0	9.8	11.0	15.0	-4.0
Rep. Checa [CZ]	6.8	10.5	10.9	12.8	13.9	15.1	15.1	14.9	14.8	15.1	13.0	2.1
Rumanía [RO]	16.8	22.8	21.2	22.8	23.9	24.8	24.8	25.0	24.5	23.9	24.0	-0.1
Serbia [RS]	12.7	19.8	19.1	20.8	21.1	22.9	22.0	21.1	20.3	20.4	27.0	-6.6
Suecia [SE]	38.7	47.0	48.2	50.2	50.8	51.9	53.0	53.4	54.2	54.6	49.0	5.6

¹ Bajo la resolución de las Naciones Unidas UN SCR 1244/99² República de Macedonia del Norte

Dentro de esta incentivación de las energías renovables, el potencial de la biomasa es promocionado, recordando a los países en su Artículo 24 que: “*Para explotar plenamente el potencial de la biomasa, la Comunidad y los Estados miembros deben fomentar una mayor movilización de las reservas madereras existentes y el desarrollo de nuevos sistemas de silvicultura*”.

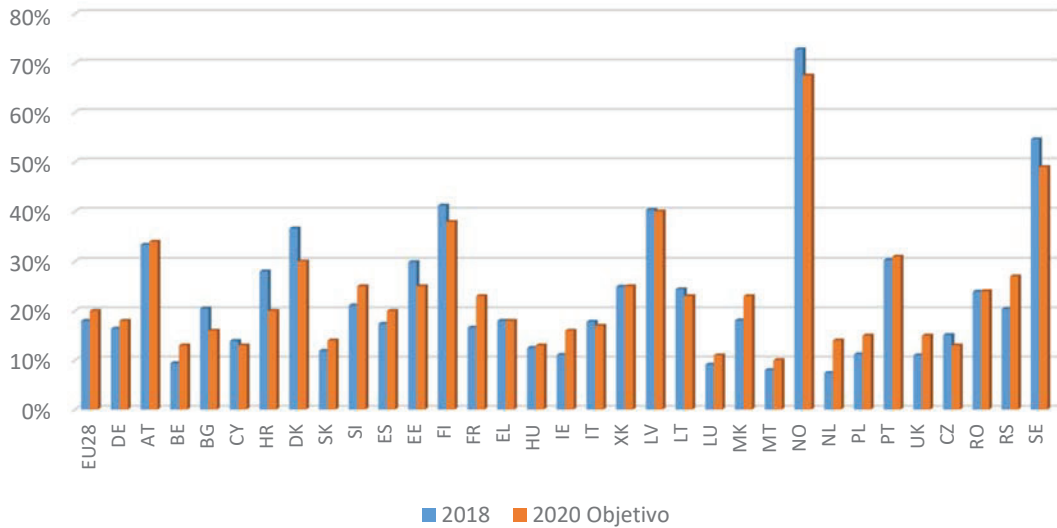


Figura 4. Representación gráfica del uso de energías renovables.

Sin embargo, incentivar en exceso el empleo de la biomasa puede derivar en un mal uso de los recursos disponibles con graves consecuencias indirectas. Se ha comprobado que este tipo de incentivo puede dar lugar al cambio indirecto¹ de uso de la tierra reduciendo la disponibilidad de superficie destinada a uso agrícola. Esto provoca el incremento del precio de los alimentos, aumenta la presión ejercida sobre la tierra y da lugar a la expansión de las tierras agrícolas en tierras con elevada biodiversidad o con elevadas reservas de carbono provocando un aumento de las de gases de efecto invernadero [7].

La Directiva 2009/28/CE no abordó este hecho, y por ello en su revisión del 2018, estableció en el Artículo 81 Párrafo 2 que: “[...] es conveniente limitar, de forma general, la producción de biocarburantes, biolíquidos y combustibles de biomasa producidos a partir de cultivos destinados a la alimentación humana o animal promovidos en la presente Directiva y, además, exigir a los Estados miembros que fijen un límite específico y decreciente para los biocarburantes, biolíquidos y combustibles de biomasa producidos a partir de productos destinados a la alimentación humana o animal respecto de los cuales se haya observado una expansión significativa de la superficie de producción en tierras con elevadas reservas de carbono. Deben quedar exentos del referido límite específico decreciente aquellos biocarburantes, biolíquidos y combustibles de biomasa con bajo riesgo de cambio indirecto en el uso de la tierra.”

Sin embargo, en la Unión Europea, hasta un 15.8(%) de la tierra que podría ser empleada para los cultivos energéticos está abandonada o no usada, mientras que en España asciende al 25(%) [8]. Por tanto, aún existe margen para incrementar la

¹ Art. 81 directiva 2018/2001/EU: “El cambio indirecto del uso de la tierra se produce cuando los cultivos destinados a la producción de biocarburantes, biolíquidos y combustibles de biomasa sustituye a la producción tradicional de cultivos para alimentos y piensos.”

aportación de la biomasa a la cuota de energías renovables sin poner en riesgo el uso de la tierra.

En base a informes de distintas agencias como IEA (*International Energy Agency*), IRENA (*International Renewable Energy Agency*) o *Bioenergy Europe* se puede concluir que el 24(%) del consumo total de energía en 2017 en la Unión Europea puede ser soportado por biomasa en 2050 y, con escenarios favorables, la cifra podría ser del 43(%). De hecho, se espera que dos tercios del crecimiento en el empleo térmico de fuentes renovables serán originados por la Unión Europea junto con los Estados Unidos, China e India [9].

En la Figura 5, se muestran comparativamente la aportación de las distintas biomazas en 2017 y en el escenario más desfavorable y más favorable en 2050. En ella, se puede observar que se espera un fuerte incremento en el uso de biomasa proveniente de la agricultura o los residuos, no así con la biomasa forestal. Esto es debido a que la gestión forestal tiene un gran impacto en este empleo. Gran parte de la superficie forestal pertenece a propietarios o conjuntos de propietarios menores y realizar una gestión efectiva de esta superficie forestal no es sencilla al no estar incentivada económicamente de forma adecuada. A menudo, su cuidado y gestión se debe más a normativas antiincendios que a sus posibles beneficios económicos.

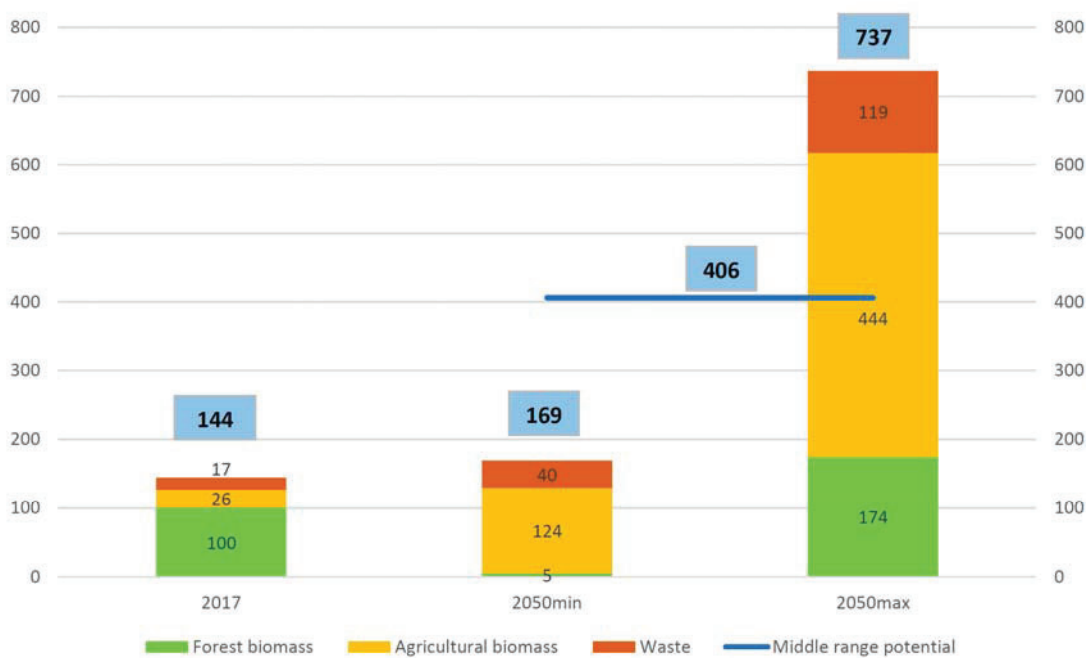


Figura 5. Consumo interno bruto de energías englobadas dentro de la biomasa en la Unión Europea. Comparación de 2017 con posibles escenarios para el año 2050 (en MTEP) [8].

Los paisajes forestales pueden proporcionar un secuestro de carbono significativo gracias al fuerte crecimiento del bosque. Sin embargo, la tasa de secuestro de carbono disminuye a medida que el bosque se acerca a la madurez. La gestión forestal sostenible, para producir madera para bioenergía y otros productos, por ejemplo,

puede generar beneficios climáticos durante múltiples ciclos de aprovechamiento y regeneración de bosques [10].

En cuanto al crecimiento en la aportación de la biomasa proveniente de residuos, sólo en la Unión Europea en 2015, se generaron más de 240 megatoneladas de residuo sólido urbano (en adelante MSW por sus siglas en inglés, *Municipal Solid Waste*). De estas 240 toneladas, tras ser tratadas, aproximadamente un tercio se recicló, un tercio se incineró recuperando energía y un tercio se depositó en vertederos.

Si observamos los mismos datos en España, comprobamos que hasta un 55(%) del residuo sólido urbano fue depositado en vertederos. Del restante 45(%), se incineró recuperando energía en el proceso el 26(%), se recicló el 37.5(%) y se sometió a digestión y compostaje un 36.5(%) [11]. De hecho, en el conjunto de la Unión Europea, España junto con Francia e Italia son los países que envían más MSW al vertedero, perdiendo una excelente oportunidad para incrementar la tasa de reciclado y en último caso, incrementar la tasa de producción energética [8].

El empleo de los residuos tanto industriales como urbanos se encuentra actualmente en el foco de atención. Esto se debe a que es un recurso con gran disponibilidad ya que es inherente a la actividad humana. En la Tabla 2, se muestran los datos en toneladas per cápita y país de residuos según los últimos datos (Eurostat, 13 junio 2019).

La entrada de la Directiva 2008/98/CE del Parlamento Europeo y del Consejo [12] sobre los residuos logró reducir la generación de residuos en gran parte de la Unión Europea. Sin embargo, en la media europea, puede observarse que ésta tiene una suave tendencia al alza. Esta directiva establece, en su Artículo 4 Disposición 1, la siguiente jerarquía para estos residuos:

1. Prevención de su generación.
2. Preparación para la reutilización.
3. Reciclado.
4. Otro tipo de valorización. Por ejemplo, la valorización energética.
5. Eliminación.

Es decir, incentiva convenientemente la reutilización y reciclado de los residuos y, de no ser posible, el empleo de estos recursos como recurso energético antes que su depósito en vertederos.

Tabla 2. Toneladas de residuos per cápita y país.

	2004	2006	2008	2010	2012	2014	2016
EU28	5.161	5.162	4.842	4.872	4.923	4.936	4.968
Alemania [DE]	4.412	4.416	4.540	4.446	4.576	4.785	4.858
Austria [AT]	6.488	6.565	6.767	5.596	5.699	6.537	7.008
Bélgica [BE]	5.068	5.627	4.540	5.630	4.847	5.171	5.573
Bulgaria [BG]	26.050	21.429	22.375	22.635	22.072	24.872	16.907
Chipre [CY]	3.079	1.663	2.343	2.859	2.165	2.316	2.892
Croacia [HR]	1.673	1.258	968	735	789	879	1.265
Dinamarca [DK]	2.329	2.704	2.759	2.923	2.989	3.687	3.663
Eslovaquia [SK]	1.986	2.699	2.133	1.741	1.558	1.636	1.953
Eslovenia [SI]	2.890	3.008	2.493	2.922	2.210	2.273	2.661
España [ES]	3.743	3.625	3.248	2.953	2.535	2.378	2.774
Estonia [EE]	15.310	14.058	14.647	14.270	16.627	16.587	18.451
Finlandia [FI]	13.333	13.711	15.394	19.454	16.961	17.572	22.359
Francia [FR]	4.743	4.923	5.376	5.478	5.268	4.893	4.848
Grecia [EL]	3.044	4.657	6.197	6.333	6.549	6.404	6.715
Hungría [HU]	2.440	2.213	1.688	1.674	1.644	1.688	1.624
Irlanda [IE]	6.019	6.926	5.012	4.344	2.764	3.256	3.207
Italia [IT]	2.424	2.666	3.047	2.676	2.594	2.597	2.705
Kosovo ¹ [XK]	-	-	-	-	646	574	1.607
Letonia [LV]	556	838	687	714	1.135	1.315	1.292
Lituania [LT]	2.076	1.945	1.980	1.801	1.901	2.114	2.317
Luxemburgo [LU]	18.153	17.728	19.630	20.597	15.816	12.713	17.405
Macedonia del Norte [MK]	-	-	666	1.133	4.111	1.058	688
Malta [MT]	7.840	7.060	5.057	3.264	3.467	3.831	4.316
Noruega [NO]	1.623	2.127	2.157	1.929	2.136	2.066	2.127
Países Bajos [NL]	5.678	6.067	6.242	7.291	7.233	7.848	8.281
Polonia [PL]	3.601	4.028	3.645	4.171	4.266	4.714	4.793
Portugal [PT]	2.796	3.322	1.599	1.290	1.271	1.381	1.427
Reino Unido [UK]	4.981	4.785	4.566	3.853	3.794	4.076	4.226
República Checa [CZ]	2.871	2.417	2.448	2.268	2.205	2.223	2.402
Rumanía [RO]	17.215	16.248	9.209	9.949	12.432	8.871	9.012
Serbia [RS]	-	-	-	4.610	7.640	6.890	6.937
Suecia [SE]	10.203	10.459	9.346	12.545	16.420	17.226	14.272

¹ Bajo la resolución de las Naciones Unidas UN SCR 1244/99

1.3 Uso de la biomasa

Al igual que existen diversos orígenes de biomasa, existen múltiples procesos para tratarla y múltiples formas de suministrarla tratada, cada una adecuada para según qué biomasa constituya la materia prima. Sin embargo, a la hora de consumirla se pueden agrupar en tres usos distintos: Generación de electricidad, generación de calor, ambos simultáneamente o cogeneración y para su empleo en transporte. Existen usos como la generación de materia prima para la construcción a través de residuos, pero su empleo es menor en la actualidad. La Figura 6 muestra un resumen de la secuencia de pasos seguida por el combustible, desde su origen a su uso final.

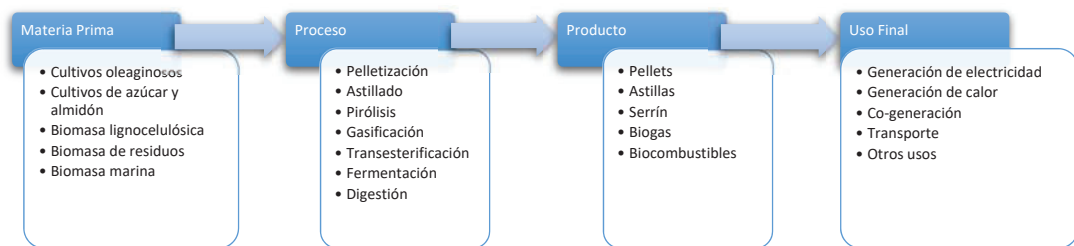


Figura 6. Cadena de suministro de biomasa.

Cabe destacar que la Directiva 2009/28/CE en su Artículo 13.6, establece que los Estados miembros de la Unión Europea fomentarán aquellas tecnologías de conversión que permitan realizar el proceso con una eficiencia de al menos el 85(%) para aplicaciones residenciales y comerciales, donde se espera que la biomasa empleada haya sido convenientemente tratada, y de al menos el 70(%) para aplicaciones industriales. De no garantizar estos mínimos de eficiencia, podría darse el caso de estar emitiendo más gases de efecto invernadero que su proceso equivalente con combustibles fósiles.

No obstante, también establece con el fin de minimizar la carga administrativa, que los criterios de sostenibilidad y reducción de emisiones de gases de efecto invernadero solo se apliquen a instalaciones para la generación de electricidad, calefacción y refrigeración con una potencia térmica nominal igual o superior a los 20 (MW) en el caso de los combustibles sólidos derivados de la biomasa, o igual o superior a los 2 (MW) en el caso de los combustibles gaseosos derivados de biomasa [7].

Este límite para reducir la carga administrativa puede originar que, en aquellas regiones del sur de Europa donde el clima es más benévolo y el *district heating* no es común, la norma pueda ser ineficaz pues esté extendido el uso de sistemas domésticos o a pequeña escala por debajo de esa potencia.

La calefacción o generación de calor es el destino principal de la bioenergía moderna². La provisión de calor a procesos industriales supuso el 63(%) del total de energía térmica proveniente de la bioenergía moderna, seguido del 34(%) para el sector residencial y comercial y del 3(%) para el sector de la agricultura. La biomasa y los combustibles provenientes de residuos son adecuados para lograr la temperatura, presión y cantidad de calor y vapor requeridos por muchos procesos industriales [10, 13] y su empleo en la industria está muy ligado a aquellos sectores que producen residuos de biomasa en su actividad, como la industria papelera.

En el sector residencial, se ha comprobado que la calefacción mediante biomasa es un contribuyente clave en aquellos Estados de la Unión Europea que logran los objetivos de cuota de energía renovables. Especialmente en aquellos países como Suecia o Finlandia [9], en los que el *district heating* y la cogeneración están extendidos, pues permiten el empleo de biomasa y residuos de forma más sencilla al no ser calderas domésticas.

No obstante, la Unión Europea es, con mucho, el mayor consumidor de sistemas de calefacción domésticos y representa el 46(%) del consumo global de bioenergía en el sector residencial y comercial. En el periodo de 2018-2023, se espera que este tipo de consumo crezca un 8(%) globalmente, crecimiento que es menor que el 16(%) alcanzado en los anteriores 6 años. Solamente en el sector residencial, la Unión Europea representa una proporción aun mayor, el 54(%), con Francia, Alemania e Italia suponiendo el 44(%) [9].

Estos sistemas de calefacción domésticos son potencialmente dañinos debido a la permisividad de la normativa mencionada previamente y a su ubicación, cercana a la población que demanda esta calefacción. Se convierten en emisores de grandes cantidades de materia particulada en granulometrías finas, especialmente dañinas para la salud cardiorrespiratoria. Además, la cantidad de compuestos orgánicos volátiles emitidos a la atmósfera, que también resultan nocivos para la salud, puede llegar a ser relevante en instalaciones con poco o ningún sistema de control.

El estudio en detalle de su diseño y la inclusión de medidas anticontaminación activas y pasivas se ven habitualmente muy limitados por motivos económico ya que ambos encarecerían severamente el producto final con las tecnologías actuales. Por ello, el desarrollo y empleo de herramientas CFD puede permitir mejorar estos sistemas suponiendo un bajo coste en el desarrollo del producto, lo que redundaría en una mejor calidad del aire del entorno cercano a la población que se sentiría incentivada a renovar sus sistemas de combustión.

A lo largo del siguiente capítulo, se abordarán los fenómenos perjudiciales que se dan lugar en la combustión de biomasa, tanto externos al sistema como la emisión de gases contaminantes o materia particulada, como fenómenos internos que afectan al rendimiento y viabilidad de estos sistemas.

² Es decir, excluyendo el uso no eficiente de los recursos locales de biomasa por parte de los hogares de bajos ingresos.

Capítulo 2

Problemática de la combustión de biomasa

La combustión de biomasa sólida entraña múltiples retos o problemas que deben ser solventados para garantizar el despliegue de forma eficiente de este tipo de energía renovable. Estos retos se pueden englobar en tres campos: emisión de gases contaminantes, emisión de materia particulada y deposición de materia no deseada.

En lo que concierne a la salud humana, el control de los dos primeros campos es fundamental, pues es consecuencia directa. No obstante, la deposición de materia no deseada sobre las superficies del sistema (fenómenos de *fouling* y *slagging*) afectan a la salud indirectamente. Al reducir la eficiencia térmica del sistema, es necesario quemar más combustible para lograr la transmisión de calor requerida. A mayores, el efecto que tienen estos dos fenómenos, que se explicarán posteriormente, sobre el sistema de combustión ocasionan un empeoramiento de las condiciones de combustión dando lugar a un peor desempeño.

Antes de abordar cada uno de los campos, cabe destacar una de las razones principales por las que estos inconvenientes resultan retos de cara al desarrollo, la heterogeneidad del combustible definido como biomasa. Tal y como definía la Directiva 2009/28/CE, “*la fracción biodegradable de los productos, desechos y residuos de origen biológico procedentes de actividades agrarias (incluidas las sustancias de origen vegetal y de origen animal), de la silvicultura y de las industrias conexas, incluidas la pesca y la acuicultura, así como la fracción biodegradable de los residuos industriales y municipales*”, se denota la amplitud de combustibles que pueden ser englobados.

Esta heterogeneidad se da tanto en propiedades físicas como termoquímicas. El mismo combustible sólido puede ser presentado, por ejemplo, en múltiples formatos físicos como serrín, astilla, pellet, briqueta o tronco. Al mismo tiempo, su origen y los

tratamientos a los que se haya sometido previos a su empleo también modifican sus propiedades termoquímicas. En la Figura 7, se ejemplifica esta diversidad de propiedades. Cabe destacar, que este mismo nivel de diversidad también se da en composiciones químicas de los distintos combustibles.

Lograr desarrollar un sistema que pueda trabajar eficientemente con diversas partidas del mismo combustible o directamente con combustibles diversos constituye un reto que debe ser abordado con inmediatez. El siguiente paso es lograr emplear con fiabilidad combustibles con bajo tratamiento previo y de baja calidad, pues es ahí donde la biomasa resulta económicamente muy viable, como se puede ver en los informes mostrados en el apartado anterior, donde el residuo sólido urbano y los residuos industriales se presentan como futuros motores de esta energía renovable.

Combustible	Poder calorífico neto, as received (kWh/kg)	Poder calorífico neto, seco, (kWh/kg)	Densidad de energía aparente (kg/m ³)	Densidad aparente (kg/m ³)	Contenido de Humedad, as received (%)	Contenido de ceniza, seco (%)
Serrín	▼ 1.7	▲ 5.3	▼ 0.6	▲ 300	▼ 52.5	▼ 0.5
Corteza de abedul	▲ 2.6	▲ 6.1	▼ 0.8	▲ 350	▼ 50.0	▲ 2.0
Corteza de conifera	▼ 1.9	▲ 5.4	▼ 0.6	▲ 300	▼ 57.5	▲ 2.0
Virutas de contrachapado	▲ 4.7	▲ 5.3	▼ 1.0	▼ 250	▲ 10.0	▼ 0.6
Pellets de madera	▲ 4.8	▲ 5.3	▲ 3.0	▲ 600	▲ 7.5	▼ 0.4
Steam Wood chips	▲ 2.5	▲ 5.4	▼ 0.8	▲ 300	▼ 47.5	▲ 1.3
Lof wood (oven-ready)	▲ 3.9	▲ 5.2	▲ 1.7	▼ 280	▲ 22.5	-
Astillas de restos de poda	▼ 2.1	▲ 5.4	▼ 0.8	▲ 325	▼ 55.0	▲ 2.0
Astillas de tala	▲ 2.4	▲ 5.4	▼ 0.8	▲ 300	▼ 50.0	▲ 1.5
Reed canary grass (cosechado en primavera)	▲ 4.2	▼ 5.0	▼ 0.4	▼ 70	▲ 14.0	▲ 5.5
Reed canary grass (cosechado en otoño)	▲ 3.4	▼ 4.8	▼ 0.3	▼ 80	▲ 25.0	▲ 6.1
Grano	▲ 4.3	▼ 4.8	▲ 2.6	▲ 600	▲ 11.0	▲ 2.0
Paja triturada	▲ 4.0	▼ 4.8	▼ 0.4	▼ 80	▲ 16.0	▲ 5.0
Miscanthus triturado	▲ 4.0	▲ 5.0	▲ 2.0	▼ 125	▲ 14.0	▲ 2.8
Pellets de paja	▲ 4.4	▼ 4.8	▲ 2.6	▲ 600	▲ 9.0	▲ 5.0
Orujo de aceituna	▼ 2.1	▲ 5.1	▲ 1.6	▲ 850	▼ 62.5	▲ 4.5
Orujo de oliva	▲ 4.5	▲ 5.1	▲ 2.8	▲ 625	▲ 10.0	▲ 4.5

Figura 7. Diversidad de propiedades térmicas y físicas de la biomasa. Adaptado de la referencia [14].

2.1 Emisiones de gases

La combustión de biomasa sólida emite múltiples contaminantes que afectan a la salud pública. Este hecho es especialmente relevante en el empleo de biomasa para calefacción en el sector residencial, que como se mencionó es un contribuyente clave para lograr los objetivos impuestos [9], tanto en sistemas de calefacción doméstica como *district heating* por múltiples razones. Este último tipo de sistemas se sitúan en entornos urbanos, con gran densidad de población en el entorno cercano que puede verse afectada. En el ámbito doméstico, el empleo de sistemas de control de emisiones existentes, como catalizadores y precipitadores electrostáticos, supone un sobre coste económico no viable [9] para sistemas que den servicio a casas unifamiliares. Además, la actuación de este tipo de medidas secundarias puede verse muy limitada por cómo la combustión está siendo realizada, siendo su desempeño muy pobre si se aleja el punto de funcionamiento del valor nominal.

Las emisiones de contaminantes se ven influenciadas por cómo es operado el sistema, sobre todo en calderas y estufas manuales. En este tipo de sistemas no automáticos, el sistema de alimentación a menudo provoca fuertes variaciones en el punto de operación ya que se suele alimentar grandes cantidades con ciclos muy amplios. Esto da lugar a instantes donde la combustión no se completa por haber un exceso de humedad evaporada, descendiendo la temperatura, instantes de operación adecuada e instantes donde solo queda *char* y ceniza justo antes de volver a realizarse la alimentación. Eso sin contar con la alteración que supone en algunos sistemas la necesidad de abrir una compuerta o la puerta principal para alimentar de nuevo. A mayores, el control que se tiene sobre el suministro de aire y su distribución en etapas, de haberlas, es escaso, sin lazos de control mediante sondas de oxígeno. El procedimiento de arranque seguido a menudo se realiza desestimando las buenas prácticas para evitar emisiones incontroladas.

Los sistemas de calefacción automáticos pueden mantener de forma más sencilla puntos de operación óptimos donde se alcancen combustiones completas o muy cerca de ser completas, siendo capaces de adelantarse a posibles cambios bruscos como los ciclos de alimentación. Este tipo de sistemas logran bajas emisiones de inquemados o PIC (por sus siglas en inglés, *Products of Incomplete Combustion*), dentro de los cuales se engloban los compuestos volátiles orgánicos o VOC (por sus siglas en inglés, *Volatile Organic Compound*) y la materia particulada o PM (*Particulate Matter*).

Pero no solo el punto de operación del sistema es importante, la presencia de un combustible con un estándar de calidad mínima, como la certificación ENplus® para pellets de madera, es esencial si se quieren alcanzar los menores niveles de emisiones. No obstante, como ya se ha adelantado, esta línea de trabajo busca contribuir a lograr la conversión térmica de una mayor variedad de combustibles que la que se incluye en estas certificaciones, y logrando bajas emisiones y alta fiabilidad.

A mayores de los inquemados y compuestos volátiles orgánicos, durante la combustión de biomasa también se emiten NOx. Los precursores de NOx se forman a través de tres rutas diferentes: NO térmico o Zeldovich, NO súbito y NO introducido con el combustible. El primero resulta de la oxidación del nitrógeno atmosférico introducido con el aire suministrado, el segundo se forma a través de la reacción del nitrógeno atmosférico con radicales de hidrocarburos en condiciones subestequiométricas y el tercero se da por la oxidación del nitrógeno proveniente del propio combustible. No obstante, durante la combustión de biomasa las temperaturas de llama alcanzadas son relativamente bajas [15-19], por lo que el mecanismo de formación de NOx térmico es menor en este campo.

Stubenberger et al. [20] y Tu et al. [21] han comprobado para diferentes biomasa que la composición en nitrógeno de los volátiles está íntimamente ligada con el contenido en nitrógeno presente en el combustible de origen. La cantidad de precursores emitidos desde el lecho (NH₃, HCN, HNCO y NO) depende de varios factores además del contenido en nitrógeno del combustible, entre ellos de la temperatura de pirolisis y el exceso de aire. La Figura 8, muestra las rutas seguidas

por el nitrógeno para los otros dos mecanismos a través de procesos de *crackeo* y oxidación a lo largo de la conversión térmica del combustible.

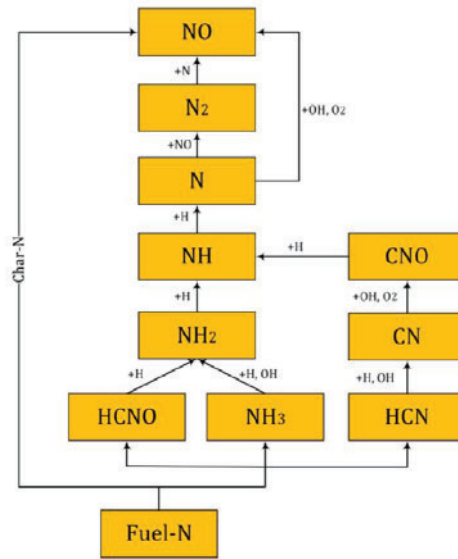


Figura 8. Procesos de craqueo y oxidación del nitrógeno a lo largo de la conversión térmica del combustible [22].

En las zonas con exceso de aire, NO es el principal compuesto basado en nitrógeno que se encuentra. Por el contrario, NH₃ es el principal compuesto que se puede encontrar en régimen subestequiométrico. En el caso de calderas domésticas, la atmósfera puede ser esencialmente oxidante en el entorno cercano al lecho, por lo que se puede generar cantidades relevantes de NO proveniente de la oxidación del combustible. Es importante el empleo de sistemas de combustión por etapas como el *air staging*, donde se mantiene al lecho en condiciones subestequiométricas y posteriormente se completa la combustión con entradas secundarias e incluso terciarias de aire. La presencia de recirculación de gases de combustión o FGR (*Flue Gas Recirculation*) también puede ayudar a controlar la formación de este fenómeno, ya que este defecto de oxígeno provoca mayor presencia de N₂ en vez de NO.

A través de estos métodos se evita la presencia de zonas con exceso de oxígeno cerca del lecho, pues el NO proveniente del combustible puede suponer el 80% de todos los NO_x producidos en el sistema de combustión [21].

2.2 Emisión de materia particulada

Durante cualquier proceso de combustión no ideal o teórico, ocurre la emisión de inquemados que pueden derivar en la presencia de materia particulada a la salida del sistema. Esta materia particulada o PM (por sus siglas en inglés, *Particulate Matter*) entraña diversos problemas según su composición y propiedades físicas como su diámetro. Este tipo de emisiones ha sido objeto de estudio en profundidad para

los combustibles fósiles, en gran medida motivados y demandados por una sociedad que ve como las grandes urbes han comenzado a adolecer de las conocidas como “boinas” de contaminación y que están derivadas a menudo de los medios de transporte.

Sin embargo, las emisiones de materia particulada por parte de sistemas de biomasa no han sido estudiadas al mismo nivel que las derivadas de combustibles fósiles y es en la última década cuando se ha comenzado a investigar en profundidad sus características y como varían según las condiciones de operación y las propiedades fisicoquímicas del combustible.

Muestra de ello son los preocupantes resultados obtenidos por la Comisión Europea [23] sobre la calidad del aire en la Unión Europea y su evolución en los últimos años. Aunque el empleo de combustibles sólidos en los hogares solo supone el 2.6(%) del consumo total de energía en la Unión Europea, contribuye más del 46(%) al total de emisiones de materia particulada fina (PM_{2.5}), más del triple que el transporte por carretera. A esto, se le suma el hecho que su emisión se realiza a baja altura, a causa de las chimeneas cortas de los hogares, y a la alta exposición de la población a ellas. En la Figura 9, se muestran las tendencias seguidas por cinco contribuyentes clave en las emisiones de PM_{2.5}. Se aprecia que el sector de transporte sí ha sido sometido a un control exhaustivo de emisiones con normativas más estrictas cada año, lo que ha repercutido en un considerable descenso de sus emisiones provocadas por el motor de combustión. No ocurre así con la materia particulada desprendida de los frenos o las ruedas, ya que sus emisiones son menores y todavía no se encuentran en el foco de atención. Por otro lado, las emisiones dentro de la EU28 con origen los sistemas domésticos de combustión de biomasa han ascendido. Las Directivas [1, 7] se han mostrado ineficaces, en parte por su no aplicación a sistemas de combustión de sólidos con potencia menor a 20 (MW) como se mencionó.

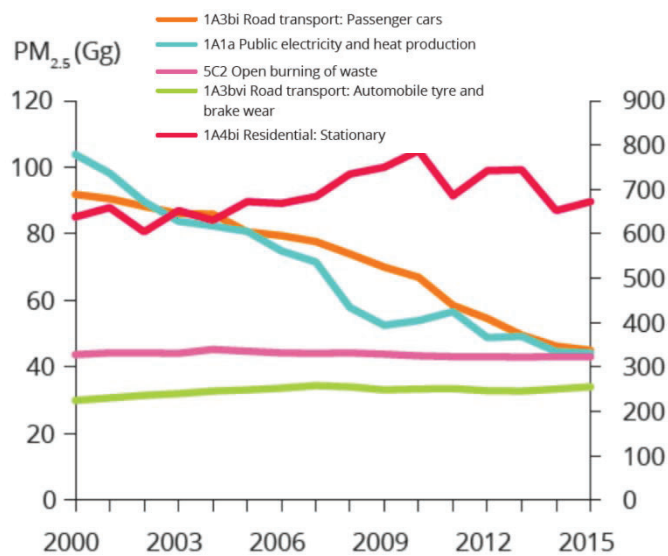


Figura 9. Tendencias en las emisiones de PM_{2.5} de diferentes fuentes [23].

Para estudiar las características morfológicas y químicas de estas emisiones, la comunidad científica se vale de avanzadas técnicas, entre las que destacan:

- TEM (*Transmission electron microscopy*) [24, 25]
- HRTEM (*High Resolution Transmission electron microscopy*) combinado con XPS (*X-ray photoelectron spectroscopy*) e IBA (*Ion Beam Analysis*) [26]
- SEM (*Scanning electron microscopy*) [27, 28]
- EDS/EDX (*Energy-dispersive X-ray spectroscopy*) [24, 29, 30]
- AMS (*Aerosol Mass Spectrometer*) combinado con DMA (*Dynamic Mechanical Analysis*) [31]
- SMPS (*Scanning Mobility Particle Sizer*) [32]
- TPS (*Thermophoretic Sampling*) [33, 34]
- OPC (*Optical Plankton Counter*) [31]
- Análisis gravimétrico [35-37]

Todas estas técnicas y combinaciones de ellas permiten conocer con detalle la morfología y propiedades químicas de partículas individuales o de poblaciones de partículas a través de estudios estadísticos. Estas emisiones de materia particulada por parte de sistemas de combustión de biomasa pueden ser divididas en los siguientes grupos [38, 39]:

- Hollín: Se origina como resultado de una combustión no completa de la biomasa. Se forma a partir de precursores orgánicos en zonas con altas temperaturas y defecto de oxígeno. Esto da lugar a hidrocarburos poliaromáticos que posteriormente se deshidrogenizan formando agrupaciones de partículas esféricas [34]. A este tipo de hollín se le conoce como hollín puro o carbono negro (BC, *Black Carbon*) y lo distinguen del carbono orgánico (OC, *Organic Carbon*), el cual se asocia con hidrógeno, oxígeno o nitrógeno.
- Compuestos Orgánicos Condensables (COC o tar): también se originan por la combustión incompleta. Se liberan en la pirolisis a baja temperatura y en procesos con defecto de oxígeno. Habitualmente están compuestos de hidrocarburos pesados y aparecen recubriendo partículas de hollín o como gotas (*droplets*) gruesas [40].
- Ceniza: minerales o sales inorgánicas presentes en el combustible de partida, como el cloro, potasio, sodio o azufre [41, 42] que son elutriados o evaporados desde el lecho, para salir por la chimenea intactos o tras reaccionar con otros elementos formando aerosoles [43, 44]

En la Figura 10, se muestran de forma visual las múltiples rutas de generación de materia particulada en la combustión de biomasa, desde el lecho hacia la salida del sistema y su evolución a lo largo del campo de temperaturas que ocurre en la llama.

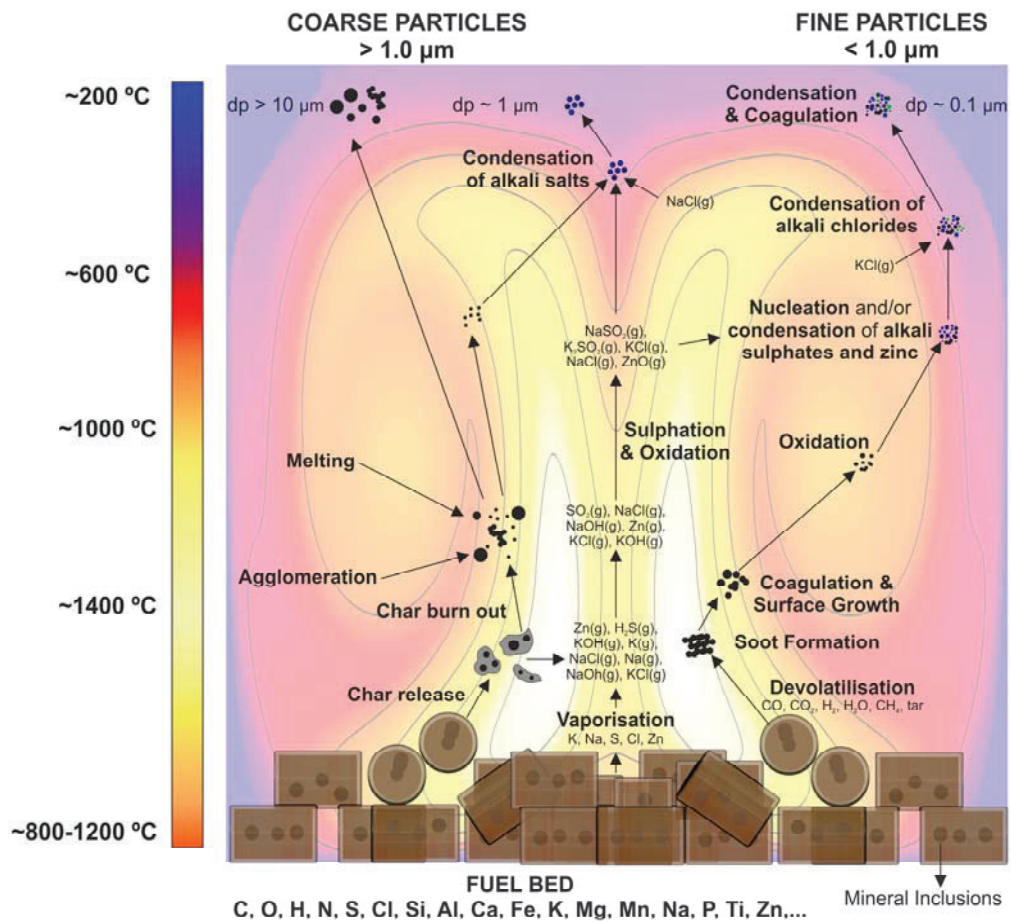


Figura 10. Representación de los principales mecanismos involucrados en la formación de partículas [45].

A pesar de poder ser analizadas en profundidad, una vez generadas y capturadas, a través de las técnicas anteriormente descritas, no pueden ser descritas, modeladas o incluso predichas de forma sencilla. Son multitud los mecanismos y rutas que sufre cada una de ellas en su evolución hacia la salida del sistema y los trabajos publicados son eminentemente experimentales. Desarrollar un modelado preciso y en detalle de todas las interacciones de cada partícula individual o mediante técnicas estadísticas supone un coste computacional no asumible en la actualidad si lo que se desea es obtener resultados en tiempos razonables, que es uno de los pilares del presente trabajo.

La Figura 11, muestra seis micrografías obtenidas en la combustión de biomasa de un sistema en particular [34]. Este trabajo busca caracterizar la morfología y composición de la materia particulada en biomasa mediante la extracción empleando una sonda termoforética (TPS) y combinado con técnicas TEM/SEM, para después analizar su morfología a través de modelos fractales. En estas micrografías se puede ver la gran diversidad de materia particulada, la cual también ha sido reportada por otros autores [46]. En ellas se encuentran aglomeraciones o clústeres de partículas esféricas que pueden ser analizados mediante modelos fractales, pequeñas películas orgánicas o condensados orgánicos e inorgánicos.

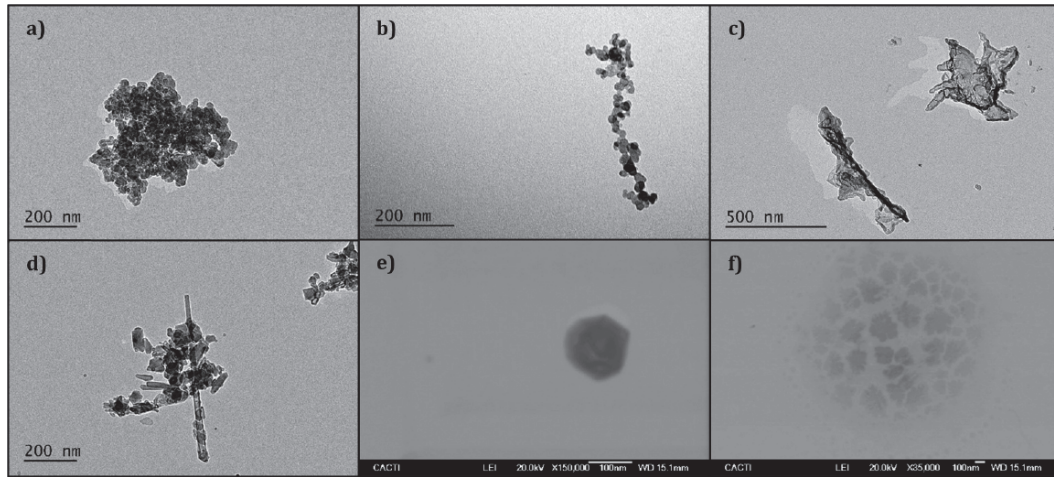


Figura 11. Ejemplos de diferentes estructuras encontradas en materia particulada recolectada [34].

El tipo de sistema también afecta a cómo se realiza la combustión y, por tanto, al nivel de emisiones de materia particulada. En la Tabla 3, se puede ver el nivel de emisiones relativo a la potencia del sistema y su contenido en carbono orgánico. Los sistemas más básicos como las chimeneas abiertas o estufas de leña tradicionales deben ser evitadas en áreas urbanas, especialmente en zonas con baja velocidad de viento debido a sus altísimas emisiones de materia particulada y carbono orgánico, con el riesgo para la salud que conllevan.

Tabla 3. Nivel de emisiones de materia particulada en relación con la potencia del sistema y su contenido en carbón orgánico [9].

	PM (mg/MJ)	Contenido en OC (%)
Chimenea abierta	322 a 1610	40 a 75%
Estufa de leña sencilla	140 a 225	50%
Estufa de leña moderna	46 a 90	20%
Estufa de pellet	3 a 43	10%
Caldera de pellet	3 a 29	5%
Caldera de biomasa sin control de emisiones	28 a 57	3%
Caldera de biomasa con control de emisiones	8 a 15	2%

El efecto que estas emisiones tienen sobre la salud ha sido también objeto de estudio en los últimos años [47, 48]. Especialmente importantes son las granulometrías menores de 2.5 micrómetros o incluso 10 micrómetros, $PM_{2.5}$ y PM_{10} respectivamente. La continua inhalación de materia particulada fina puede causar graves enfermedades cardiopulmonares [39], no solo porque pueden actuar como portadores de sustancias tóxicas y cancerígenas volatilizadas o generadas durante la combustión, sino porque las de menor diámetro (por debajo de 0.1 μm) no son retenidas por los filtros naturales del sistema respiratorio y se acumulan y asimilan en su interior [47, 48].

2.3 Deposición de materia no deseada

Los fenómenos de ensuciamiento y escoriación o como se referirá a ellos en este trabajo *fouling* y *slagging* respectivamente por ser términos más extendidos, son de gran relevancia para el funcionamiento adecuado de los sistemas de conversión térmica de biomasa. Se trata de la generación de depósitos de materia no deseada sobre las superficies del sistema. Las diferencias entre ambos a menudo son tenues en la bibliografía. La principal diferencia entre ambos reside en si estos depósitos están sometidos al calor radiante de la combustión (*slagging*) o si se dan sobre las superficies de intercambio de calor por convección (*fouling*). Si bien, también se usan ambos términos para diferenciar si la materia no deseada es depositada sobre las superficies de la caldera en general (*slagging*) o sobre las superficies de intercambio (*fouling*).

Este tipo de separación de ambos fenómenos tiene sentido en grandes plantas de combustión de biomasa, donde existen diversos sistemas de intercambio de calor, algunos expuestos a la radiación de la llama y otros no. En estos sistemas, el *slagging* se da en las paredes principales de la cámara de combustión y en las primeras etapas de *superheaters* y *reheaters*. Mientras que en el fenómeno del *fouling* tiene lugar del primer paso descendente en adelante, en *reheaters* y economizadores.

Sin embargo, en sistemas de baja potencia, a escala doméstica, la distinción es frecuente realizarla de forma sencilla y directa. Si se trata de la acumulación de materia no deseada en el lecho se denomina *slagging*, si la deposición ocurre en otras regiones del sistema distintas al lecho se le denomina *fouling*.

Habitualmente, estos dos fenómenos se estiman para los sistemas de combustión mediante índices o ratios basados en la composición del combustible. Este tipo de índices o ratios normalmente han sido diseñados para la combustión de carbón, campo para el que existe una bibliografía más extensa, y se adaptan para la combustión de biomasa [49].

La mayoría de estos índices se basan en analizar el contenido en sodio, potasio y fósforo de los combustibles. La composición de las cenizas se expresa en forma de sus óxidos para las correlaciones [50]. En la Tabla 4 se muestran los siguientes índices:

Tabla 4. Índices de fouling y slagging.

Índice	Fórmula	Bajo	Medio	Alto	Severo
Fouling Factor, F	$F = \left(\frac{B}{A}\right) \cdot (\%Na_2O + \%K_2O)$	<0.6		0.6	>40
				-	
Slagging Factor, R _s	$R_s = \left(\frac{B}{A}\right) \cdot S_{dry}$	<0.6	0.6-2.0	40	>2.6
				-	
Slagging Factor, S _R	$S_R = \frac{\%SiO_2}{\%(SiO_2 + MgO + CaO + Fe_2O_3)}$	>72	>72-65	2.0	>65
				-	

Contenido en cloro	$\%Cl_{dry}$	<0.2	>0.5
Álcali, Al (kg/GJ)	$Al = \left(\frac{1}{LHV}\right) \cdot Y_{ash} \cdot (\%Na_2O + \%K_2O)$	0.17 < Al < 0.34 dep. probable Al > 0.34 deposición segura	

Donde los ratios entre componentes con baja temperatura de fusión, B, frente a los componentes con alta temperatura de fusión, A, se calculan de las siguientes formas, dependiendo de la información obtenida acerca de la composición de las cenizas del combustible.

Tabla 5. Compuestos de temperatura de fusión alta vs baja.

Ratio	Fórmula
$\left(\frac{B}{A}\right)$	$\frac{\%(Fe_2O_3 + CaO + MgO + Na_2O + K_2O)}{\%(SiO_2 + Al_2O_3 + TiO_2)}$
$\left(\frac{B}{A}\right) + P$	$\frac{\%(Fe_2O_3 + CaO + MgO + Na_2O + K_2O + P_2O_5)}{\%(SiO_2 + Al_2O_3 + TiO_2)}$
R_b	$\frac{\%(Fe_2O_3 + CaO + MgO + Na_2O + K_2O)}{\%(Fe_2O_3 + CaO + MgO)}$
$\frac{R_b}{\bar{a}}$	$\frac{\%(Fe_2O_3 + CaO + MgO)}{\%(SiO_2 + Al_2O_3)}$

Sin embargo, estos índices solo pueden considerarse como herramienta predictiva del comportamiento de distintos combustibles. Una vez adquirida experiencia con un determinado combustible base sobre un sistema de combustión en concreto, a través de estos índices se puede evaluar si los fenómenos de *fouling* y *slagging* empeorarán o se aliviarán tras cambiar el combustible. No permiten pues predecir el comportamiento de cualquier sistema ante variaciones no solo de combustible, si no de condiciones de operación.

A lo largo de este trabajo, se ha hecho énfasis en el modelado del fenómeno de *fouling* pues para poder modelar el *slagging* es necesario que existan depósitos sobre las superficies del sistema y antes de ello se requiere el modelado preciso de los mecanismos de transporte de esta materia hacia ellas. Una vez el fenómeno de *fouling* se ha modelado de forma razonable, se ha procedido a ir incluyendo en el modelado la generación de sinterizados por fusión total o parcial de los depósitos. Una vez se logren resultados adecuados, será cuando se modele la fusión y el posible movimiento de esta fase fundida, dando lugar al inicio del modelo completo de *slagging*.

Una vez explicadas las diferencias entre ambos fenómenos, se comienza a explicar el fenómeno de la formación de depósitos en combustión de biomasa. Para ello, es importante mencionar que se trata de un fenómeno de gran complejidad pues engloba un gran número de mecanismos que actúan a menudo simultáneamente, y cuando no lo hacen de esta forma el orden en el que aparecen afecta en gran medida al resultado final.

A lo largo del presente capítulo se abordará cada uno de los mecanismos de relevancia implicados en este fenómeno. Se procurará exponerlos de forma “cronológica” según sucede dentro del sistema, si bien como se acaba de mencionar, a menudo ocurren simultáneamente. De esta forma, tras lo explicado en los apartados emisiones de gases y emisiones de PM, se procederá a explicar los mecanismos de la siguiente forma:



Figura 12. Mecanismos involucrados en la formación de depósitos.

Transporte de vapores inorgánicos

La biomasa, además de su composición en carbono, hidrógeno y oxígeno necesarios para la liberación de energía en la combustión, presentan contenidos de otros elementos no deseados o necesarios. Entre estos elementos están el potasio, fósforo, sodio, calcio, cloro o azufre.

Estos elementos se encuentran en la biomasa porque han sido absorbidos durante el proceso normal de generación de dicha biomasa o debido a agentes externos durante su recolección. Por ejemplo, si se habla de biomasa vegetal, durante su crecimiento ha absorbido numerosos minerales de la tierra o del ambiente, como es el caso de la corteza [51-53]. Posteriormente, durante su tala, recolección y tratamiento pueden recibir minerales provenientes del suelo o de las herramientas empleadas.

Durante la combustión de la biomasa estos elementos son liberados, en forma de materia particulada o en forma de vapores, y añadidos al gas de combustión, donde reaccionan de maneras diversas. Los metales alcalinos liberados en forma de materia particulada son esencialmente en la forma M-silicatos o M-aluminosilicatos (siendo M tanto potasio, K, como sodio, Na). Si son liberados en la forma de vapores alcalinos lo hacen en las siguientes formas: $M_{(g)}$, $MCl_{(g)}$, $(MCl)_{2(g)}$, $M_2SO_{4(g)}$ o $MOH_{(g)}$ [54].

Según el contenido en metales alcalinos de la biomasa habrá diversas rutas preferentes de formación. El contenido en cloro es de gran importancia en la

conversión de biomasa pues facilita la liberación de los álcalis [54-56]. En el caso de biomasa herbácea o paja con alto contenido en metales alcalinos y cloro, las principales especies formadas son los cloruros alcalinos. Por el contrario, si el contenido en cloro es bajo, las principales especies son los hidróxidos alcalinos.

Para el potasio, entre 400 [°C] y 1000 [°C], domina la presencia del cloruro potásico, $\text{KCl}_{(g)}$, si el ratio molar entre potasio y cloro es la unidad. Esta presencia se reduce con el descenso en contenido en cloro, es decir con un ratio molar superior a la unidad, dando lugar a $\text{KOH}_{(g)}$. Por el contrario, si hay un exceso de cloro y por tanto el ratio es inferior a la unidad, prácticamente no existe $\text{KOH}_{(g)}$ y el exceso de cloro se libera como $\text{HCl}_{(g)}$.

A lo largo del recorrido del gas de combustión, portando estos vapores, se pueden dar las condiciones adecuadas para la condensación de estos vapores inorgánicos, por ejemplo, al circular por el intercambiador de calor. Cuando estos vapores condensan, pueden depositarse tanto sobre las superficies de trabajo como sobre la materia particulada presente en el gas [57, 58] tras ser transportados hacia las superficies a causa de la fuerza termoforética o la difusión turbulenta [59].

Estos condensados crean una capa pegajosa donde se adhiere la materia particulada, siendo esta capa el precursor fundamental de la deposición de materia no deseada sobre las superficies de trabajo [42, 59-62].

Transporte de materia particulada

La materia particulada suspendida en la corriente gaseosa es transportada a lo largo del dominio bajo la influencia de las siguientes fuerzas y mecanismos, las cuales pueden desembocar si se dan las condiciones necesarias en la deposición de esta sobre la superficie del sistema. Estas fuerzas y mecanismos se encuentran resumidos de forma gráfica en la Figura 13.

Fuerzas de arrastre o Drag

Fuerza que actúa sobre la partícula y que busca en todo momento reducir el deslizamiento entre partícula y fluido. Es expresada como función del coeficiente adimensional de *drag*, C_D . Para partículas por debajo de la micra, se introduce una corrección al deslizamiento, mediante la ley de Stokes-Cunningham.

Fuerzas de sustentación o Lift

Esta fuerza sobre las partículas es debida principalmente a los gradientes de velocidad del fluido. La fuerza de sustentación será de mayor valor a medida que el tamaño de partícula se incrementa. Sin embargo, a menudo es despreciable frente a la fuerza de arrastre.

Fuerza de Saffman

Las partículas en un campo fluido con elevado esfuerzo cortante, como puede ocurrir cerca de una superficie, experimentan una fuerza de elevación perpendicular a la dirección del flujo del campo fluido. Dicha elevación se origina por los efectos inerciales en el fluido viscoso alrededor de esta partícula.

Fuerza de Magnus

También denominado fuerza de sustentación rotacional, se produce cuando una partícula se encuentra rotando dentro de un campo fluido. Esta sustentación está provocada por el diferencial de presiones a lo largo de la superficie de la partícula.

Fuerza de Basset

Junto con la fuerza de Masa Virtual que se explicará a continuación, son fuerzas transitorias debido a la aceleración de la partícula con respecto al fluido en el que se encuentra inmersa. La fuerza de Basset se debe al retraso temporal en el desarrollo de la capa límite frente a la aceleración relativa de la partícula [63]. Esta fuerza es habitualmente despreciada y solo se tiene en cuenta si la aceleración de la partícula es muy elevada [64].

Fuerza de Masa Virtual

Fuerza debida a la inercia inducida por la aceleración de la partícula en el seno del fluido. Cuando la partícula se desplaza debe desplazar a su vez el fluido, al no poder permanecer partícula y fluido en el mismo lugar. Habitualmente se modela como un volumen de fluido desplazándose con la partícula [65]. Solo se considera cuando la densidad de la partícula es muy inferior a la del fluido en el que se desplaza.

Fuerza Termoforética

Las fuerzas termoforéticas que actúan sobre las partículas son debidas a los gradientes de temperatura internos del fluido o de la partícula [58, 66]. Las fuerzas termoforéticas se deben a la diferencia entre las frecuencias de impacto de las moléculas del gas a lo largo de la superficie de la partícula, donde el lado caliente presenta mayores impactos que el lado frío. Este mecanismo se convierte en dominante para partículas del orden de la micra o inferior cuando el gradiente de temperaturas entre el gas de combustión y la superficie es elevado [67].

Fuerza Turboforética

Este mecanismo se debe al gradiente entre velocidades fluctuantes del campo fluido sobre la superficie de la partícula cuando existe turbulencia no homogénea [68, 69]. Cerca de una superficie, la turbulencia es menor, por lo que es menos probable que la partícula se aleje de la superficie que la probabilidad de que se acerque, resultado en una mayor migración de partículas hacia las superficies en entornos turbulentos.

Fuerza Electroforética

Se debe a las fuerzas electrostáticas y a las fuerzas de Van der Waals entre las superficies y las partículas [49, 70, 71]. Son fuerzas débiles que en estos estudios se suelen considerar despreciables.

Difusión Browniana

Se debe al movimiento aleatorio que presentan las partículas suspendidas en un medio fluido debido a las colisiones con las moléculas de éste [72, 73]. Este mecanismo es dominante para las partículas de menor tamaño, esencialmente por debajo de 100 nanómetros, cuando la termoforesis no es relevante [42]

Impacto turbulento

Este mecanismo actúa esencialmente sobre las partículas muy ligeras o pequeñas, cuando estas no presentan inercia suficiente como para atravesar la capa límite de transición e impactar contra la superficie. Si la turbulencia es elevada, estas partículas pueden obtener momento adicional de los remolinos turbulentos y depositarse sobre la superficie [66, 74, 75]. Los depósitos debido a este mecanismo se suelen dar en la parte posterior o sotavento de los intercambiadores de calor, especialmente en zonas de baja temperatura con velocidades de fluido elevadas [57].

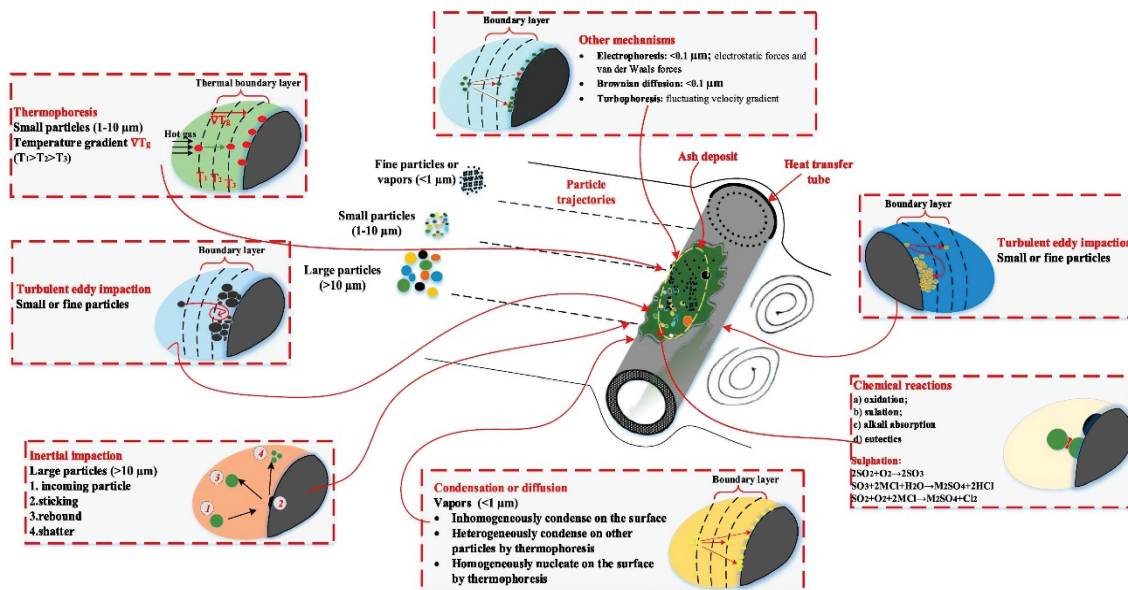


Figura 13. Resumen de los mecanismos involucrados en la deposición [76].

Deposición sobre la superficie

La materia particulada, tras ser elutriada es arrastrada en mayor o menor medida por el gas de combustión, interactuando con su entorno bajo el efecto de los mecanismos expuestos anteriormente. Cuando una partícula circula en el entorno cercano de la superficie, el tiempo de relajación de partícula determina en gran

medida si ésta impactará contra la superficie o será capaz de seguir las líneas de corriente del gas evitando el impacto.

Si ocurre el impacto de la partícula suspendida en el gas contra la superficie, la rugosidad de esta superficie o la presencia de vapores inorgánicos condensados juegan un papel vital en la adhesión de la misma a la superficie. A continuación, se abordarán los mecanismos que pueden derivar en el impacto y adhesión de la partícula a la superficie y los modelados empleados en la bibliografía.

Tiempo de relajación de partícula

El tiempo de relajación de la partícula es un parámetro fundamental en la deposición. Para su determinación se emplea un número de Stokes modificado, donde el tiempo característico de la fase continua es la escala temporal de los remolinos turbulentos cerca de la pared, es decir:

$$Stk = \frac{\tau_p}{\tau_g} \tag{1}$$

Donde el tiempo característico de la fase continua se expresa como:

$$\tau_g = \frac{\nu}{u_{\tau g}^2} \tag{2}$$

De esta forma, el tiempo de relajación de partícula se puede expresar como:

$$\tau_p^+ = \frac{\rho_p d_p^2 \rho_g u_{\tau g}^2}{18\mu} \tag{3}$$

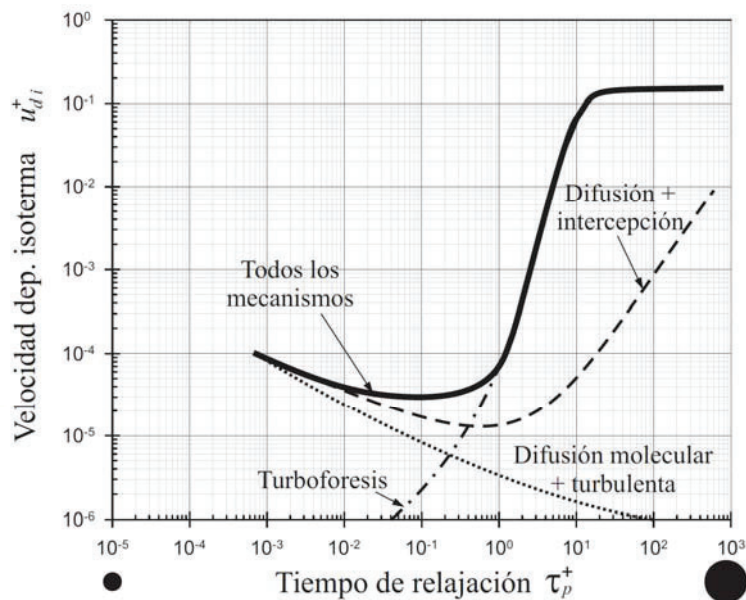


Figura 14. Evolución de la tasa de deposición isotérmica con el tiempo de relajación de partícula [77].

Si el valor del tiempo de relajación de la partícula es inferior a 0.1, las fuerzas de arrastre o *drag* sobre las partículas son dominantes, y la partícula sigue a la fase continua a la perfección. Este régimen se denomina régimen de difusión. Si es superior a 10, la inercia de la partícula es dominante y ésta no sigue a la fase continua, en lo que se conoce como régimen de impacto. Entre ambos, existe una región, de 0.1 a 10, donde las trayectorias de las partículas son afectadas por la fase continua, pero éstas tienden a seguir su propia trayectoria debido a su momento. Este régimen se denomina régimen de inercia y es de gran importancia en el modelado, pues en él una pequeña variación en el diámetro de la partícula supone un cambio brusco de comportamiento de la misma, como se puede ver en la Figura 14.

Numerosos estudios [78-81] se basaron en el número de Stokes para definir la eficiencia de impacto de materia no deseada sobre las superficies a través de la misma formulación, con leves variaciones de las constantes dependiendo de los mecanismos considerados, como la termoforésis por ejemplo [45]. Esta formulación se muestra en la Ecuación (4), la cual arroja los resultados mostrados en la Figura 15 según los coeficientes de la Tabla 6 elegidos.

$$Y(\text{Stk}) \approx (1 + b(\text{Stk} - a)^{-1} - c(\text{Stk} - a)^{-2} + d(\text{Stk} - a)^{-3})^{-1} \quad (4)$$

Tabla 6. Coeficientes de eficiencia de impacto

	a	b	c	d
Israel and Rosner (1983) [78]	0.125	1.25	-0.014	0.00508
Baxter et al. (1990) [80]	0.1425	1.28	0.00215	0.00587
Baxter et al. (1990) [81]	0.1238	1.34	-0.034	0.00289

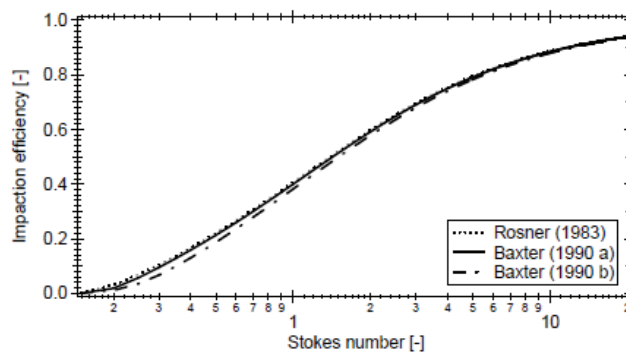


Figura 15. Resultados de la Ecuación (4) según los coeficientes empleados de la Tabla 6. Coeficientes de eficiencia de impacto

Superficie del depósito

Los mecanismos de deposición son seriamente afectados por las propiedades físicas de la superficie del depósito, como su rugosidad o la energía cinética absorbida en los impactos. Si se quiere abordar de forma precisa la predicción de estas dos propiedades, se debe abordar la microestructura de la superficie del depósito. Sin

embargo, la complejidad y la alta incertidumbre han provocado que prácticamente siempre se descarte su modelado. Diferentes investigadores han intentado arrojar luz en este campo a través de distintas aproximaciones. Tassopoulos et al. [82] desarrolló un modelo matemático en el que asumía que las partículas alcanzaban la superficie mediante la superposición de una velocidad promedio y un movimiento estocástico. Al alcanzar la superficie asumía que las partículas se agregaban en un enrejado ortogonal, permitiendo la existencia de porosidad en el depósito. Matsumoto et al. [83] desarrolló un modelo de rebote irregular en dos dimensiones, asumiendo que la rugosidad de la superficie del depósito presentaba una distribución uniforme independiente de la posición de la partícula y modelando el rebote mediante un método de Monte Carlo. Sommerfeld [84] estudió el efecto causado por la rugosidad de la superficie, modelándolo a través de la consideración de una inclinación aleatoria, basada en una distribución gaussiana, relativa de la superficie frente a la partícula. Sin embargo, estos modelos consideran o bien la adhesión perfecta [82] o el rebote irregular de la partícula sobre la superficie [83, 84], pero no consideran la posibilidad de colisiones múltiples de cada partícula con la superficie.

Si se desea modelar adecuadamente el efecto que tiene la rugosidad de la superficie sobre la deposición se debe considerar la posibilidad de múltiples colisiones. Si bien, este fenómeno solo es relevante si el tamaño de la partícula es menor que la longitud característica de la rugosidad. En el caso de que sea su dimensión sea mayor también puede existir el impacto múltiple, pero se puede asumir que sólo uno de ellos gobierna la dinámica del rebote [85].

En las granulometrías más finas, el modelado existente asume que sólo un máximo de tres impactos puede ocurrir tal como se muestra en la Figura 16. No obstante, debido a la adhesión de la partícula a la superficie, se suele rebajar el número de impactos a un máximo de dos colisiones. El ángulo de impacto de la última colisión es complejo de determinar y se asume una distribución estadística en función de la forma de la partícula, sus propiedades y la microestructura de la superficie del depósito [76].

Para predecir de forma adecuada la eficiencia de impacto sobre la superficie, en un estudio CFD que emplee las ecuaciones RANS (*Reynolds-Averaged Navier-Stokes*), es necesario resolver correctamente el flujo en la capa límite, lo que supone el empleo de mallas finas con altos requisitos computacionales.

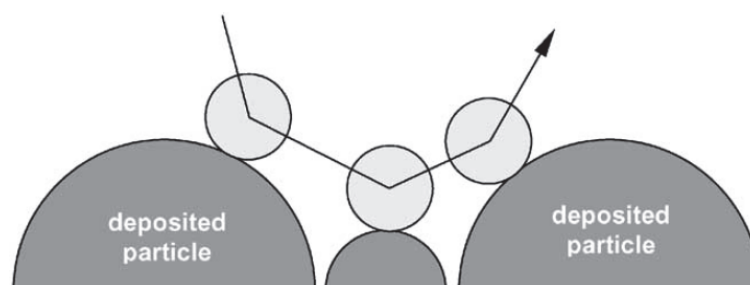


Figura 16. Escenario de rebote irregular bajo la consideración de tres impactos [85].

Modelos de adhesión

Que las partículas terminen finalmente adheridas o no a la superficie depende de varios hechos. Como ya se ha mencionado, la presencia de vapores inorgánicos condensados sobre la superficie aumenta enormemente la adhesión de la materia particulada a la superficie. Estos vapores inorgánicos continúan condensando sobre el depósito ya adherido, formando múltiples capas que aíslan a la superficie fría del gas de combustión, ver Figura 17. Esto provoca que en la superficie más externa hacia el gas de combustión se alcancen temperaturas elevadas que puedan dar lugar a la sinterización de la materia particulada adherida. A medida que el gradiente térmico entre el gas de combustión y la superficie externa del depósito se reduce, debido al efecto aislante de éste, la condensación disminuye.

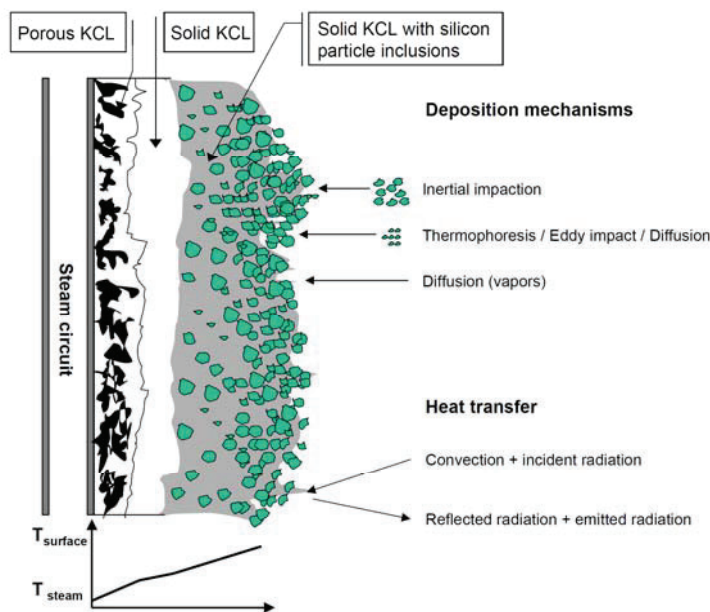


Figura 17. Representación de las capas presentes en el crecimiento del depósito y la evolución de su temperatura superficial [42].

La adherencia de las partículas es función de la energía cinética, la viscosidad y el grado de fusión de las partículas, determinando en cada caso la propensión de las partículas a quedar adheridas a la superficie o rebotar [86-88]. De forma general, se emplean tres teorías diferentes para evaluar si una partícula se adhiere o rebota de una superficie, que se pueden resumir brevemente en: modelo basado en velocidades críticas, modelo basado en viscosidad y modelo basado en fracción fundida [89].

El modelo de velocidades críticas se basa en que todas las partículas de un determinado diámetro quedan adheridas si la velocidad normal de impacto está por debajo de una velocidad crítica determinada mediante experimentos. Si la velocidad normal es superior, se establece que las partículas conservan tras el impacto suficiente energía cinética para rebotar y alejarse de la superficie [79, 90-93].

Este modelo puede ser empleado en casos a baja temperatura. En casos a alta temperatura se debe trabajar con el modelo basado en viscosidades críticas o el modelo basado en fracción fundida.

El modelo basado en viscosidades críticas [94] es aplicable a cenizas muy viscosas, habitualmente aquellas con alto contenido en silicio. En este modelo, se asume que la probabilidad de adhesión de la partícula a la superficie es función del área de contacto desarrollada durante el impacto, a causa de la deformación de la partícula, y la disipación de energía cinética que conlleva. Esta área de impacto desarrollada es inversamente proporcional a la viscosidad de la partícula y se asume que por debajo de una viscosidad crítica la adhesión es segura. El valor de viscosidad crítica ha sido objeto de numerosos trabajos [89, 94-100], centrados en la combustión de carbón, donde valores de diferentes órdenes de magnitud han sido obtenidos, desde 8 (Pa·s) [94] a 10^8 (Pa·s) [98], estando la mayor parte de los valores en el orden 10^5 (Pa·s) [101-106]. La determinación de la viscosidad es muy compleja debida a la multitud de variables involucradas que no pueden ser resueltas únicamente mediante técnicas experimentales [107].

El último modelo y el cual es empleado en este trabajo, es el modelo basado en fracción derretida [42], este modelo se ha aplicado a la combustión de distintos combustibles obteniendo resultados adecuados [108-110]. Backman et al. [111] definió cuatro temperaturas características basándose en curvas de derretimiento teóricas, que se muestran en la Figura 18, y que son las siguientes:

1. T_0 : denominada temperatura de *solidus*, a partir de la cual comienza a aparecer fase derretida
2. T_{15} : denominada temperatura de adhesión. Se asume que se requiere aproximadamente el 15% de fase fundida para que las partículas sean adhesivas.
3. T_{70} : denominada temperatura de flujo, donde la partícula se encuentra fundida en gran medida.
4. T_{100} : temperatura de fusión completa.

Con estas temperaturas se estiman el nivel de fusión del depósito existente y de la partícula en el momento de la colisión. Con estos niveles se calculan las probabilidades de adhesión por ambas partes. Si la fracción derretida es inferior a 0.1, su probabilidad de adhesión por su parte es nula, si es superior a 0.7, la probabilidad de adhesión es total. Entre ambos valores, se asume una relación lineal.

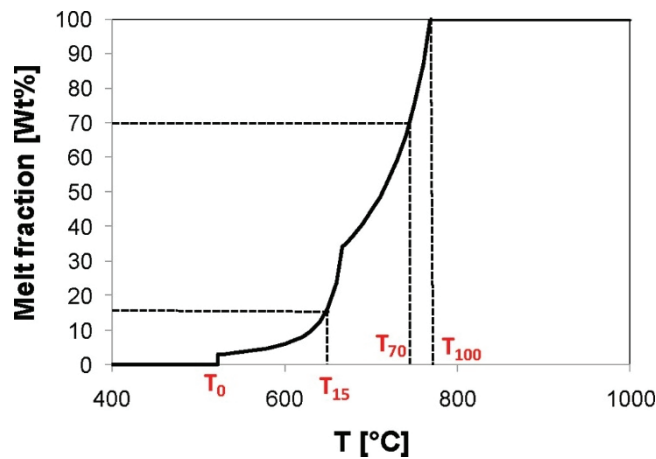


Figura 18. Porcentaje de fracción fundida presente en la partícula según su temperatura [67, 112].

Walsh et al. [94] propuso una expresión, basada en probabilidades, por la que un grupo de partículas con probabilidades de adhesión, $Prob_{particle}$, pueden ser modeladas como si contuviesen una fracción másica, $Prob_{particle}$, de partículas con probabilidad de adhesión total y una fracción másica, $1 - Prob_{particle}$, de partículas con probabilidad de adhesión nula. Adicionalmente, consideró no solo la probabilidad de adhesión por parte de las partículas, sino también por parte de la superficie, $Prob_{wall}$, y el efecto de la erosión a través del último término de la siguiente expresión:

$$TSP = Prob_{particle} + Prob_{wall} (1 - Prob_{particle}) - k_e (1 - Prob_{particle})(1 - prob_{wall}) \quad (5)$$

Sedimentación o silting

Ocurre cuando la gravedad es el principal mecanismo para la formación de un determinado depósito. La cantidad y ritmo de acumulación sobre una superficie es función de múltiples parámetros como el tamaño de las partículas o las características fluidodinámicas del sistema.

Erosión

Los depósitos, y especialmente la superficie exterior de los mismos, está sometida a los fenómenos de erosión causados tanto por el gas de combustión como por otros mecanismos físicos y químicos, tanto propios del depósito como debidos a consecuencias externas, como por ejemplo los ciclos de operación, los cuales pueden crear tensiones térmicas en el depósito que lo resquebrajen.

Son varios los mecanismos de erosión que provocan que la tasa de crecimiento del depósito no sea lineal ni exponencial, si no asintótica. Al comienzo los fenómenos de ensuciamiento superan a los de erosión dando lugar a la mayor tasa de ensuciamiento posible. Posteriormente estos mecanismos se equilibran dando lugar a este valor asintótico.

Fricción del fluido o scrubbing

Considerado el mecanismo principal de erosión. Cuando un depósito crece modifica las características del flujo cercano. Esto provoca que, por ejemplo, a causa de reducciones de sección de paso la velocidad del gas de combustión se incremente, y, con ello, el esfuerzo cortante sobre el depósito. Numerosos estudios [113-118] muestran la relación directa que existe entre el espesor de depósito y el esfuerzo cortante local, alcanzando los mayores espesores en aquellas zonas donde la fricción del fluido es baja.

Gravedad

La gravedad también puede hacer mella en el depósito provocando un fallo estructural [118] en el depósito y que se desprenda cuando el espesor es superior a la resistencia mecánica del mismo.

Impacto y rodadura

El incremento en el espesor del depósito supone un incremento en la sección normal expuesta al gas y, por tanto, a las partículas suspendidas en él. El impacto de estas, además de contribuir al depósito en el caso de que se adhieran, también puede erosionar la superficie.

Por otra parte, la rodadura de partículas sobre la superficie del depósito también contribuye a la erosión cuando la longitud característica de la rugosidad es superior al tamaño de la partícula. Este fenómeno ha sido estudiado por diversos autores [119-121] y se divide en tres etapas [122]:

1. Inicio de la rodadura de la partícula sobre la superficie.
2. Rodadura, durante la cual oscilan las fuerzas de interacción entre partícula y capa depositada, pero sin alcanzar condiciones de reentrada al flujo de gas.
3. Situación de impacto en el que la energía dinámica del impacto supera a las fuerzas de adhesión.

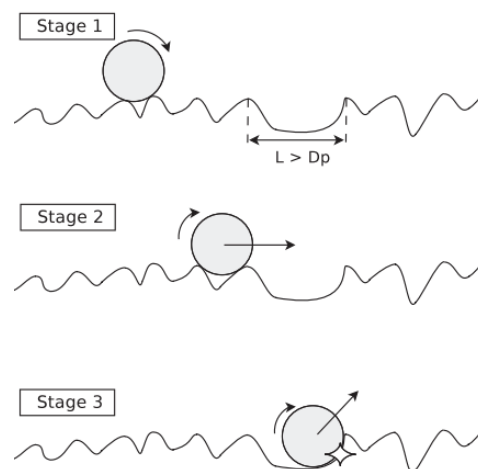


Figure 19. Etapas de la erosión causada por la rodadura e impacto [122].

Turbulencia

La naturaleza turbulenta del fluido también es un mecanismo importante en la erosión [123, 124]. Pequeños remolinos turbulentos en la vecindad de la superficie originan pequeñas erosiones que dañan la superficie del depósito. Una representación de este fenómeno, conocido como *turbulent bursts*, puede verse en la Figura 20.

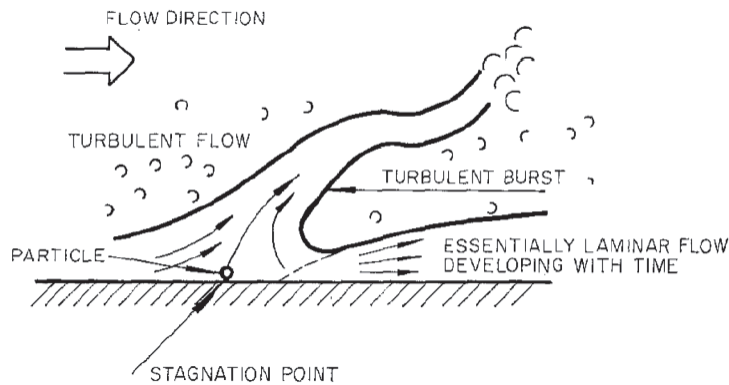


Figura 20. Representación del fenómeno conocido como *turbulent bursts* [125].

Envejecimiento

Una vez el depósito se ha formado y soporta a lo largo del tiempo las condiciones internas del sistema de combustión de biomasa, evoluciona modificando sus propiedades físicas y químicas debido a diversos mecanismos entre los que se destacan las reacciones químicas, la sinterización y la fusión.

Reacciones químicas

Las reacciones químicas son en su mayoría heterogéneas entre el depósito y el gas de combustión, rara vez ocurren de forma interna en el depósito. Las reacciones químicas más importantes relacionadas con la deposición de materia no deseada son de oxidación, sulfatación, absorción de álcalis y eutécticas [49, 58].

Estas reacciones químicas, como la incorporación de especies alcalinas en silicio, la combustión de carbono residual, la formación y descomposición de carbonatos y la sulfatación de especies alcalinas son de gran relevancia para la formación de depósitos de cenizas [126]. Las principales especies sulfatantes son aquellos compuestos que contienen metales alcalinos, potasio y sodio en forma de hidróxidos [58]. Las especies alcalinas, al ser absorbidas por el silicio, disminuyen la temperatura de fusión de éste al formar silicatos. La transformación del silicio en silicatos, que es mucho más lenta si se compara con la reacción de sulfatación, puede provocar cambios importantes en las propiedades del depósito de cenizas y la sinterización [57].

En general, el campo químico en los depósitos de combustión de biomasa podría ser objeto de varias tesis doctorales por su amplitud y complejidad. Se torna necesaria una mayor profundidad en el estudio de todos los mecanismos químicos que intervienen en los fenómenos de *fouling* y *slagging* para poder abordar de forma fiable su modelado, y por ello su modelado queda fuera del presente trabajo.

Sinterización

La materia no deseada acumulada sobre las superficies da lugar a un depósito poroso donde se integran también los vapores inorgánicos adherentes que son precursores de cada capa depositada. Esto provoca una peor transferencia de calor hacia la superficie, aislándola térmicamente. En la Tabla 7, se muestran un ejemplo de las distintas capas de depósito formadas sobre una superficie de un *superheater* de una central de combustión de paja ordenadas desde el interior hacia el lado gas de combustión.

Tabla 7. Capas del depósito presente en un sistema de combustión de paja [42].

Capa	Descripción	Espesor (μm)
1	Capa fina formada por Fe/Cr-óxido	40-80
2	Capa fina formada por K_2SO_4 y Fe_xO_y	40-100
3	Capa gruesa porosa formada por KCl	200-2000
4	Capa gruesa formada por KCl	300-1500
5	Capa gruesa formada por KCl con incrustaciones	400-2000
6	Capa porosa de partículas sinterizadas	200-5000

Las dos primeras capas se pueden despreciar de cara a la transmisión de calor por ser finas. La diferencia entre las capas 3 y 4 muestra el punto de transición entre la zona que alcanza la temperatura de fusión del KCl y la que no. Debido a esta fusión, la capa de KCl comienza a capturar partículas, lo cual muestra que el modelo de fracción derretida puede tener validez. La capa más externa se trata de partículas capturadas que se sinterizan debido a estar expuestas al gas de combustión y aisladas térmicamente del interior.

Debido a este aislamiento y sinterización, se forman depósitos masivos y compactos que no pueden ser retirados de forma sencilla ni combatidos mediante procedimientos de *soot blowing* periódicos. Esta sinterización modifica las propiedades del depósito y es necesario tenerla en cuenta para el adecuado modelado de la transmisión de calor.

Fusión

Al disminuir la transmisión de calor asciende la temperatura de las capas externas del depósito. A través de las reacciones químicas heterogéneas entre el depósito y los componentes del gas de combustión, se forman compuestos con una temperatura de fusión inferior a la que tenían los compuestos que se depositaron inicialmente. Ambos fenómenos dan lugar a la formación de compuestos parcial o totalmente fundidos

que sufren un desplazamiento proporcional a su viscosidad bajo la acción de la gravedad y, en mucha menor medida, la acción del gas de combustión.

La presencia de fase fundida en los depósitos está íntimamente ligada a las características de fusión de la ceniza, AFC (por sus siglas en inglés, *Ash Fusion Characteristics*), del combustible como es lógico. La manera más habitual de determinarlas es a través de las temperaturas de fusión de cenizas o AFT (*Ash Fusion Temperatures*), que engloban [127-129]:

- Temperatura de deformación inicial, IDT (*Initial Deformation Temperature*)
- Temperatura de ablandamiento, ST (*Softening Temperature*)
- Temperatura de hemiesfera, HT (*Hemispherical Temperature*)
- Temperatura de fluidización, FT (*Fluidization Temperature*)

La Figura 21, muestra de forma esquemática la definición gráfica de cada temperatura según la norma seguida, ASTM (*American Society for Testing and Materials*) o DIN.

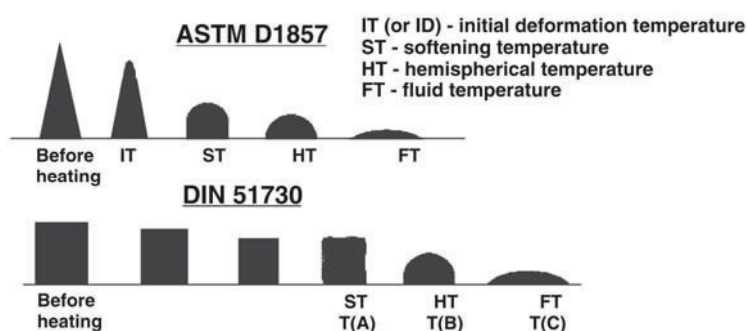


Figura 21. Representación de las distintas temperaturas encontradas en el estudio de la fusión de cenizas [129].

La representación real de estas temperaturas se puede ver en la siguiente Figura 22 para tres tipos de biomasa distintos, con ensayos a distintas temperaturas. En esta figura se puede observar que cenizas de biomazas similares, aunque distinta materia prima, presentan temperaturas de fusión distintas. Las siglas representan los siguientes combustibles sólidos: CMS *Capsicum Stalk* o tallo de pimienta, CNS *Cotton Stalk* o tallo de algodón y WTS *Wheat Stalk* o tallo de trigo.

Se observa en esta Figura 22, además del distinto comportamiento entre distintas biomazas, que la temperatura a la que se someten las cenizas modifican las temperaturas IDT, ST y HT especialmente. Si la temperatura a la que se somete se incrementa, la temperatura inicial de deformación aumenta en gran medida en todas las biomazas. Sin embargo, las restantes temperaturas presentan comportamientos dispares, lo que muestra que distintas proporciones de elementos en la composición

de las cenizas varían significativamente el comportamiento de la fusión, al igual que la temperatura a la que estén sometidos.

Aunque el método es efectivo para caracterizar la respuesta de las cenizas del combustible, presenta multitud de inconvenientes, entre los que se pueden mencionar la selección de una temperatura representativa, el soporte de la muestra o incluso selección del estándar a seguir, y es que el procedimiento seguido para el ensayo tiene efectos no despreciables en los resultados [130].

T /°C	Sample	IDT	ST	HT	FT
400					
	20	1111	1220	1238	1249
600					
	20	1134	1221	1228	1241
815					
	20	1154	1202	1224	1241
Difference	0	+43	-19	-14	-8

a. CMS

T /°C	Sample	IDT	ST	HT	FT
400					
	20	591	1124	1285	1315
600					
	20	631	1160	1309	1342
815					
	20	927	1159	1301	1335
Difference	0	+236	+36	+24	+27

b. CNS

T /°C	Sample	IDT	ST	HT	FT
400					
	20	707	861	1165	1192
600					
	20	730	862	1154	1189
815					
	20	996	1083	1151	1185
Difference	0	+289	+245	-14	-7

c. WTS

Figura 22. Observación de las temperaturas características de fusión de tres biomosas distintas sometidas a diferentes temperaturas [128].

La composición de las cenizas también es un factor clave en la fusibilidad de éstas. Cuanto mayor sea el contenido de las cenizas en metales alcalinos y cloro, menor será la temperatura de fusión de las cenizas y más probabilidades de que aparezca este fenómeno [131]. Por el contrario, el contenido en metales alcalinotérreos, como el calcio o el magnesio, incrementan la temperatura de fusión y causan menores problemas [132, 133] y presentan la ventaja de formar compuestos con temperaturas de fusión elevadas, como silicatos de calcio, que inhiben la formación de compuestos más problemáticos como eutécticos $\text{SiO}_2\text{-K}_2\text{O}$ que tienen temperaturas de fusión de 550 (°C) [134]

Consecuencias de la deposición de materia

Los fenómenos de *fouling* y *slagging* sobre los sistemas de conversión térmica de biomasa causan graves perjuicios sobre la eficiencia térmica del sistema, su fiabilidad y su rentabilidad económica. Sin embargo, la solución a estos fenómenos no es directa en absoluto, pues existen multitud de variables que provocan que los remedios encontrados para un sistema determinado en un punto de operación determinado con un combustible en concreto, sean inefectivos al variar cualquiera de ellos. Y es que, como se mostró en la Figura 7, la heterogeneidad de la biomasa redonda en grandes diferencias en propiedades físicas, químicas y térmicas entre combustibles, incluso entre partidas del mismo combustible [135-137].

El crecimiento de depósitos de materia no deseada sobre las superficies de transferencia de calor provoca un descenso en la transferencia de calor, perdiendo eficiencia e incrementando la temperatura del gas de combustión aguas abajo, lo que puede acarrear el desplazamiento de la condensación de vapores inorgánicos y los problemas que acarrea hacia nuevas zonas. Este descenso en la transmisión de calor provoca a su vez que, si se desea mantener una consigna fija de transferencia de calor, se incremente el caudal de combustible y el caudal de aire suministrados para lograrlo. Esto deriva en un nuevo incremento de temperatura global del sistema, empeorando la situación, y conlleva problemas adicionales como la generación de una mayor fase fundida o parcialmente fundida en los depósitos y mayores emisiones de gases y materia particulada.

Esta fase parcial o totalmente fundida en los depósitos hace que éstos sean muy complicados de retirar mediante técnicas que no supongan paradas regulares de la operación del sistema de combustión por mantenimiento. Aun así, su retirada es costosa siendo aconsejable en algunos casos la sustitución de las superficies afectadas por resultar más sencillo.

Como se abordó en este capítulo, el rápido crecimiento de depósitos en combustión de biomasa está ligado a las altas concentraciones de cloro y metales alcalinos como potasio o sodio presentes en el combustible de partida. Estos depósitos se formaban por capas donde las primeras estaban formadas por vapores inorgánicos actuando como precursores. Estos vapores inorgánicos están formados

por compuestos como el azufre o el cloro, lo que deriva en problemas de corrosión sobre las superficies [138-140].

La acumulación de materia no deseada sobre las superficies de trabajo provoca un volumen cada vez mayor de depósito y con ello una mayor superficie expuesta al gas y a los impactos de materia particulada. Este fenómeno continúa hasta que se equilibran los mecanismos de deposición y erosión. Sin embargo, la reducción de sección útil para el gas de combustión provoca una pérdida de presión mayor en el sistema. En casos extremos de *fouling* y *slagging* severos se puede dar el bloqueo de secciones completas, especialmente en haces tubulares densamente poblados. Esto se debe a varios motivos, el más directo es que se necesita un menor espesor de depósito para que el adherido en una superficie se llegue a unir al depósito adherido a otra superficie formando un puente. Esta menor altura de depósito hace que su estabilidad estructural no se vea comprometida antes de la unión con el depósito vecino. En haces tubulares afectados por calor radiante, como los *superheaters*, es frecuente ver depósitos verticales que han sido parcialmente fundidos y, en su descenso por efecto de la gravedad, unen tubos consecutivos o forman estructuras en forma de estalactitas.



Figura 23. Depósitos formados en los superheater de una planta de combustión de biomasa [42].

2.4 Soluciones

Las consecuencias de estos fenómenos: *fouling*, *slagging*, emisión de gases contaminantes y emisión de PM, sobre los sistemas de biomasa están frenando su desarrollo e implantación en el mercado. Numerosas técnicas se han probado para aliviar estos problemas, pero ninguna de ellas se ha mostrado infalible o, al menos, con un rango de aplicación lo suficientemente amplio. Estas técnicas se pueden agrupar de la siguiente forma:

- Modificación de la combustión: *smouldering combustion* con sólidos inertes [141-144].
- Modificación del suministro de comburente: *air-staging* [37, 145-148], FGR [21, 149-151] y *oxy-fuel combustion* [152-155].
- Modificación del combustible: pretratamiento [156-158] y aditivos [127, 134, 159-165].
- Modificación del diseño: Refrigeración de lecho [151, 166-169], espuma cerámica [170], filtros de mangas, filtros electrostáticos [171-174] y depuradores húmedos (*wet scrubbers*) [175].

Cómo se realice la combustión de la biomasa afecta a todos estos fenómenos. Si se introduce todo el oxígeno necesario, más su exceso para asegurar combustión completa, empleando aire atmosférico por el primario, se obtendrían velocidades y temperaturas elevadas en el lecho. Esto provocaría la elutriación de una gran cantidad de materia inorgánica al disponer de *drag* suficiente. Se alcanzarían temperaturas elevadas en el lecho, que darían lugar a posibles fusiones parciales de la ceniza, aglomerándose, y a una alta liberación de vapores inorgánicos, por lo que se empeorarían los fenómenos de *fouling* y *slagging*.

Una forma de evitar esto es modificando la forma de realizar tanto la combustión como el aporte de comburente. Diversos autores [141-144] han investigado sobre la posibilidad de realizar la combustión de forma más lenta, mezclando la biomasa con sólidos inertes, de forma que las reacciones estén limitadas por una menor difusión del oxígeno a través de lecho a causa de la presencia de estos sólidos. Con este proceso se consigue reducir la temperatura del lecho y evitar la evaporación de compuestos inorgánicos, pero como contrapartida requiere de mayor superficie de parrilla y la gestión y manejo de estos sólidos inertes. Aun así, su efecto sobre las emisiones de materia particulada y sobre los fenómenos de *fouling* y *slagging* no han sido todavía estudiados en profundidad.

Sí está estudiado y extendido el suministro por etapas del comburente o *air-staging* [37, 145-148]. Se trata de un sistema en el que se crea con el aire primario un entorno subestequiométrico en el lecho y se termina la combustión de los volátiles gracias al aire secundario y, en sistemas de mayor tamaño, al aire terciario. De esta forma, las velocidades y temperaturas alcanzadas en el lecho son menores. Diversos autores afirman que con esta estrategia de suministro de aire se reducen las emisiones de gases y de PM. Nuutinen et al. [147] muestra que las emisiones de materia particulada, sobre todo las más finas (PM₁), se reducen entre un 14 y un 58(%) en estufas. Las emisiones de metano entre un 74 y 91(%) y las de monóxido de carbono entre un 26 y 81(%). Por su parte, Khodaei et al. [145, 148] afirma reducciones de hasta nueve veces menos emisiones de materia particulada y hasta un 50(%) menos de monóxido de carbono con este sistema en una planta piloto.

Un nuevo campo de estudio en combustión de biomasa es la modificación de la composición del comburente. Dos vertientes se distinguen aquí, la recirculación de gases de chimenea (FGR) y el empleo de *oxyfuel combustion*.

La recirculación de gases externa es una técnica habitual en el sector de automoción y se estudia implementar sistemas similares en combustión de biomasa a escala doméstica [150, 151]. En sistemas de combustión de biomasa a gran escala se investiga la recirculación de gases interna, o IFGR, que se consigue modificando los inyectores del aire secundario o *over-fire air* (OFA) y reduciendo su número para que los restantes introduzcan aire con mayor momento y se obligue a recircular parte de los gases de combustión [21, 149].

En ambos casos, se han encontrado evidencias de una mayor eficiencia térmica en el sistema al implementar FGR o IFGR, especialmente con valores bajos de exceso de oxígeno, y de reducción de emisiones de NOx. Sin embargo, no hay evidencias de reducción de otro tipo de emisiones gaseosas. Pérez-Orozco et al. [151] encontró en su quemador experimental que las emisiones de materia particulada se reducían hasta un 65(%) con escasa formación de depósito en los intercambiadores de calor cuando se realizaba recirculación de gases de combustión, pero no se han encontrado estudios al respecto cuando se aplica a sistemas a gran escala.

La técnica de *oxy-fuel combustion* trata de realizar la combustión suministrando como comburente una proporción determinada de O₂ y CO₂, el cual sustituye al nitrógeno atmosférico. Esta técnica ha sido frecuentemente estudiada en co-combustión con carbón [152-155]. Mediante ella se consiguen descensos importantes en las emisiones de monóxido de carbono, siempre y cuando el contenido en oxígeno de esta mezcla sea superior al 25(%) en volumen. Contenidos menores, aproximados al oxígeno atmosférico, dan lugar a un descenso en la temperatura de combustión e incluso la extinción de la llama, debido al mayor calor específico de la molécula triatómica del dióxido de carbono en comparación con el nitrógeno [155]. Las emisiones de NOx disminuyen con la concentración de oxígeno en el aporte de comburente.

En cuanto a los fenómenos de *foulingy slagging* se encuentran resultados dispares entre sistemas de diferentes escalas de potencia [152]. Esto se debe a que, si el contenido en oxígeno es superior al atmosférico, se requiere menor caudal total, por lo que las velocidades dentro del sistema son menores, dando lugar a una menor deposición por impacto inercial. Sin embargo, esta menor velocidad fomenta una menor energía cinética de las partículas, por lo que la adhesión provocada por los vapores inorgánicos aumenta.

Si las modificaciones en la forma de realizar la combustión o las modificaciones en el comburente suministrado no logran los resultados deseados por un combustible de muy baja calidad con alto contenido en minerales, existen técnicas para mejorar su aptitud. Se trata del lavado previo del combustible y la inclusión de aditivos.

El lavado previo se realiza habitualmente con agua a temperaturas ambiente o moderadas, 30-90 (°C), durante periodos de varias horas, la cantidad varía según la técnica usada y el combustible [156-158]. Este pretratamiento era habitual realizarlo en biomasa proveniente de agricultura, por su alto contenido en metales alcalinos. Sin embargo, dados los buenos resultados y la voluntad de continuar mejorando los resultados para biomasa lignocelulósicas, se ha decidido estudiar esta técnica también en este tipo de biomasa [157, 158].

Como se puede ver en la Figura 24, con este pretratamiento se logran importantes reducciones en el contenido de compuestos perjudiciales como el cloro o el potasio. Esto tiene un impacto directo en la tendencia al *fouling* y *slagging* de los combustibles tratados, reduciéndose en gran medida ambos fenómenos gracias al incremento en la temperatura de fusión de la ceniza en todos ellos, Figura 25.

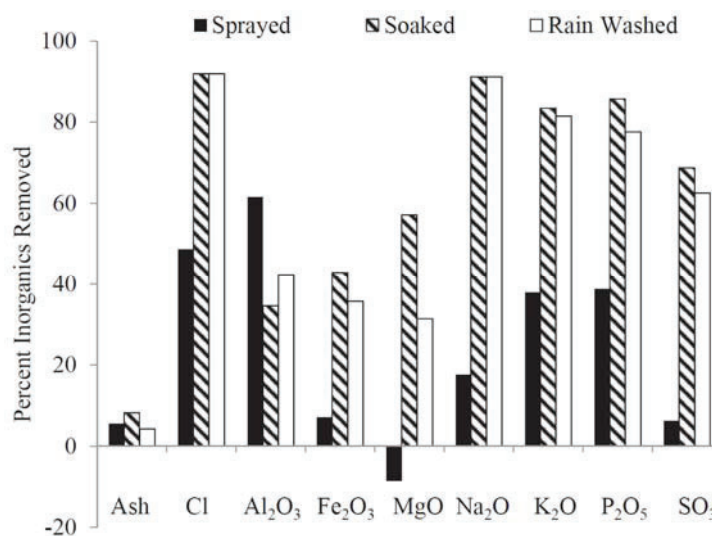


Figura 24. Impacto de los métodos de lavado en la cantidad de compuestos inorgánicos presentes en la biomasa [156].

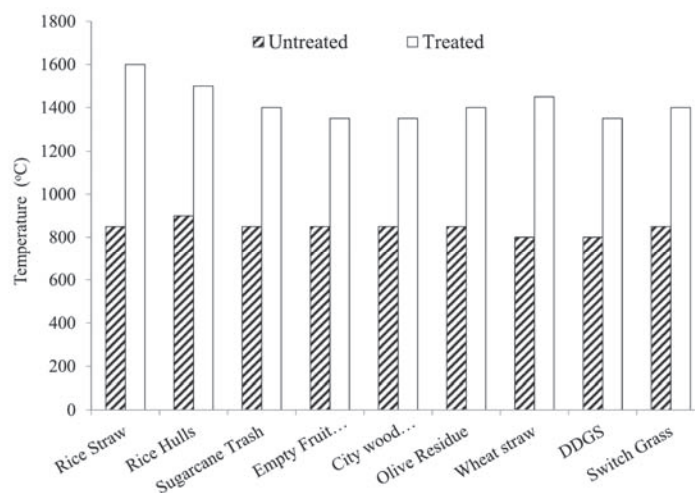


Figura 25. Impacto de los métodos de lavado en la temperatura de fusión de las cenizas de varios tipos de biomasa [157].

Como contrapartida, esta técnica requiere de un gran volumen de agua, que después retendrá los compuestos eliminados del combustible, por lo que surge el problema de su tratamiento para evitar contaminación de ríos y acuíferos cercanos. Incrementando la temperatura se logran los mismos resultados con menor volumen de agua, pero éste sigue siendo importante.

Otra forma de reducir los fenómenos de *fouling* y *slagging* es la aditivación del combustible [127, 134, 159-165]. Con estos aditivos se busca realizar las siguientes tareas: incrementar la temperatura de fusión de la ceniza, reaccionar de forma más veloz formando compuestos menos problemáticos o realizar adsorción de compuestos problemáticos como el KCl. Ejemplos de estos aditivos son la cal (CaO), calcita (CaCO₃), caolinita (Al₂(OH)₄Si₂O₅) o las zeolitas. Estos compuestos están formados por elementos químicos que, como se explicó, incrementan el punto de fusión de la ceniza o capturan los álcalis presentes.

Finalmente, si la modificación de la combustión, el aporte de comburente o el combustible no surten efecto, se torna necesaria la incorporación de sistemas externos como la refrigeración de lecho, la incorporación de espumas cerámicas o los filtros de partículas.

La refrigeración de lecho ha sido estudiada por varios autores [151, 166-169] con distintos niveles de refrigeración, desde 0.5 (kW) [166, 167] hasta superiores a 3 (kW) [151] de potencia de refrigeración. La menor temperatura del lecho da lugar a una gran condensación de vapores inorgánicos sobre la refrigeración del propio lecho, quedando gran parte de la materia particulada adherida a él, por lo que no es emitida por chimenea [151, 167], si bien no representa una solución viable como se puede ver en la Figura 26. En cuanto a emisiones, Gehrig et al. [166] encontró una menor emisión de monóxido de carbono, mientras que los óxidos de nitrógeno se mantuvieron y percibió un incremento en la formación de HCl y SO₂.



Figura 26. Materia no deseada adherida al sistema de refrigeración del lecho [151].

Si sólo se pretende lograr una reducción de emisiones de materia particulada, al menos como efecto inmediato, existen varias aproximaciones: Empleo de espumas cerámicas en la chimenea, filtros electrostáticos, filtros de mangas, ciclones y depuradores húmedos o *wet scrubbers*.

Los ciclones en chimenea solo poseen un buen rango de retención para la materia particulada de mayores dimensiones y no para $PM_{2.5}$ o menores, donde la biomasa presenta uno de los picos de emisión. Los filtros de mangas son una buena opción para cualquier proceso que emita materia particulada al ambiente, sea del tipo que sea. Su rendimiento es bueno si está bien seleccionado, pero los filtros electrostáticos o ESP (*ElectroStatic Precipitator*) presentan rendimientos superiores para los tamaños de partículas donde la biomasa emite más y se está comenzando a desarrollar su posible implementación en sistemas domésticos [171-174].

Finalmente, se ha comenzado a investigar en el empleo de módulos con espumas cerámicas en calderas de biomasa como medida para combatir las emisiones de materia particulada de forma económica y sencilla de implementar [170] e incluso el desarrollo de *wet scrubbers* optimizados para el empleo en calderas domésticas de combustión de biomasa [175].

Capítulo 3

Dinámica de fluidos computacional

El trabajo aquí expuesto se desarrolla enteramente de forma numérica mediante técnicas y herramientas de Dinámica de Fluidos Computacional (CFD), recayendo las necesarias validaciones experimentales en la bibliografía existente y en el trabajo desarrollado por los miembros del Grupo de Tecnología Energética de la Universidad de Vigo.

La Dinámica de Fluidos Computacional es una rama de la mecánica de fluidos constituida por un conjunto de técnicas y procedimientos numéricos para la resolución de problemas complejos de fluidos a través de la simulación por ordenador. Estas técnicas y procedimientos generan unos resultados muy realistas sin incurrir en grandes costes ligados a la metodología experimental, sobre todo cuando son realizados por personal especializado y con recursos de cálculo adecuados. Además, permiten hallar el comportamiento del fluido estudiado bajo condiciones extremas o anómalas sin poner en riesgo la integridad del sistema estudiado o sus operarios.

En este trabajo, el software CFD empleado será ANSYS-Fluent® en sus distintas versiones a lo largo del desarrollo del mismo (v15.0.7, v16.1, v17.1, v18.2 y v19.2) debido a la amplia experiencia en su manejo, si bien posteriormente se estudiará la viabilidad de portar este trabajo a software libre como OpenFOAM [176] para que pueda ser evolucionado por colaboradores externos que no tengan acceso al software de pago de ANSYS.

Las simulaciones CFD constan de un procedimiento secuencial a seguir que se puede resumir en los siguientes pasos:

1. Estudio previo de la simulación a realizar: sistema, condiciones de contorno, etc.
2. Levantamiento CAD del dominio a simular: Se procede a desarrollar el modelo con herramientas CAD lo más fidedigno a la realidad posible.

3. Limpieza de CAD: eliminación de detalles no necesarios para el estudio.
4. Discretización superficial de la geometría.
5. Discretización volumétrica de la geometría.
6. Configuración de la simulación CFD.
7. Simulación CFD del sistema.
8. Comprobación preliminar de los resultados obtenidos.
9. Análisis de sensibilidad de malla.
10. Postprocesado.

3.1. Fundamentos de las técnicas CFD

En este trabajo se empleará esencialmente la especificación Euleriana para el campo gaseoso y el lecho. Para la materia particulada se empleará en un inicio la especificación Lagrangiana y posteriormente la Euleriana.

En esta rama de la mecánica de fluidos se trabaja bajo la hipótesis del medio continuo, por la que se considera que el fluido es un continuo a lo largo del espacio que ocupa sin presentar discontinuidades asociadas a su estructura molecular. En un flujo continuo las variables de campo como la densidad, la presión o la temperatura son, por tanto, variables continuas.

Estas variables continuas pueden ser representadas mediante una serie de valores discretos en un número finito de puntos, lo cual se denomina discretización. De esta manera, las ecuaciones integrales continuas de gobierno son discretizadas y aproximadas en función de los valores para esos puntos finitos. Al resolverlas, se obtienen los valores de las variables de campo en esos puntos discretos. Los métodos de discretización más habituales son:

- Método de diferencias finitas: Primer método empleado para la resolución numéricas de ecuaciones diferenciales mediante el desarrollo de Taylor para discretizar las derivadas de éstas. No es aplicable a geometrías que no sean sencillas.
- Método de elementos finitos o FEM: Desarrollado por Courant y ampliado por Turner et al. [177] a mitad del siglo pasado, fue desarrollado esencialmente para cálculos mecánicos y estructurales. En este método se discretiza el dominio mediante varios tipos de elementos: unidimensionales (vigas), bidimensionales (triangulares y cuadrados) y tridimensionales (tetraedros y hexaedros). Aunque habitualmente se emplean triángulos y tetraedros en aquellos casos que no se pueda reducir el caso a elementos unidimensionales. El tamaño de todos estos elementos se puede reducir tanto como la precisión o el usuario demande, pudiendo captar detalles de geometrías complejas, pero da lugar a un número muy elevado de elementos

a resolver, que junto con una base matemática muy rígida hace que el coste computacional sea elevado.

- Método de volúmenes finitos o FVM: Este método discretiza las ecuaciones diferenciales y las integra en cada uno de los volúmenes finitos de control del dominio. La solución obtenida por el sistema satisface las ecuaciones conservación independientemente del tamaño de la malla. Este método también puede ser aplicado a geometrías complejas y es el método más empleado en esta rama de mecánica de fluidos.

La malla empleada en el método de volúmenes finitos debe cumplir ciertos requisitos para asegurar la adecuada resolución de las ecuaciones y la precisión buscada. Estos requisitos habitualmente se miden con tres parámetros: *skewness*, *orthogonal quality* y *aspect ratio*.

El *skewness* se define como la diferencia entre la forma de la celda y la forma de una celda equilátera de volumen igual. Su valor debe ser lo menor posible, aunque los avances en los modelos han logrado que alcancen la convergencia con valores de *skewness* muy alto, hasta 0.95. Si bien puede requerir de ajustes en la simulación que ralentizan su convergencia.

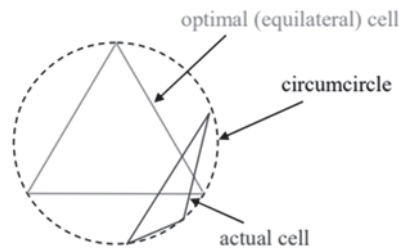


Figura 27. Ilustración del criterio de calidad *skewness* [178].

El parámetro *orthogonal quality* se calcula a través del *skewness* de la celda, el vector desde el centroide de la misma y cada una de sus caras, el vector área de cada cara y el vector entre el centroide y el centroide de cada una de sus vecinas. Este valor debe ser lo más alto posible y nunca inferior a 0.01.

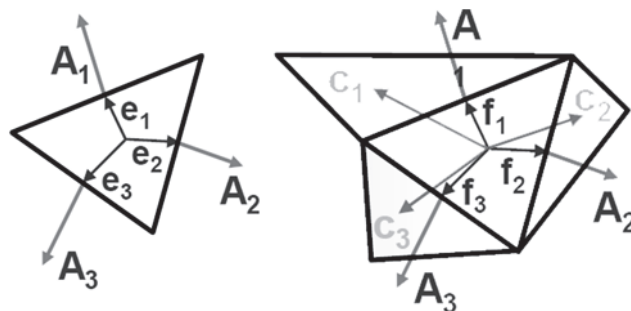


Figura 28. Ilustración del criterio de calidad *orthogonal quality* [178].

El *aspect ratio* es una medida del estiramiento de la celda. En simulaciones con flujos de gran anisotropía, las relaciones de aspecto extremas pueden producir resultados precisos con menos celdas. Como norma, es mejor evitar cambios bruscos en el *aspect ratio* en regiones donde el campo continuo exhibe grandes cambios o fuertes gradientes.

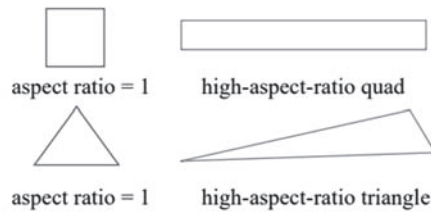


Figura 29. Ilustración de la definición de *aspect ratio* [178].

La continua evolución de los métodos de resolución matemáticos por parte de los desarrolladores ha logrado aliviar estos requerimientos, logrando alcanzar la solución con discretizaciones que anteriormente ocasionarían la no convergencia o incluso la divergencia de la solución. Gracias a estos avances en la matemática subyacente se pueden realizar mallas no homogéneas en tamaño ni forma, facilitando el estudio de geometrías de gran complejidad.

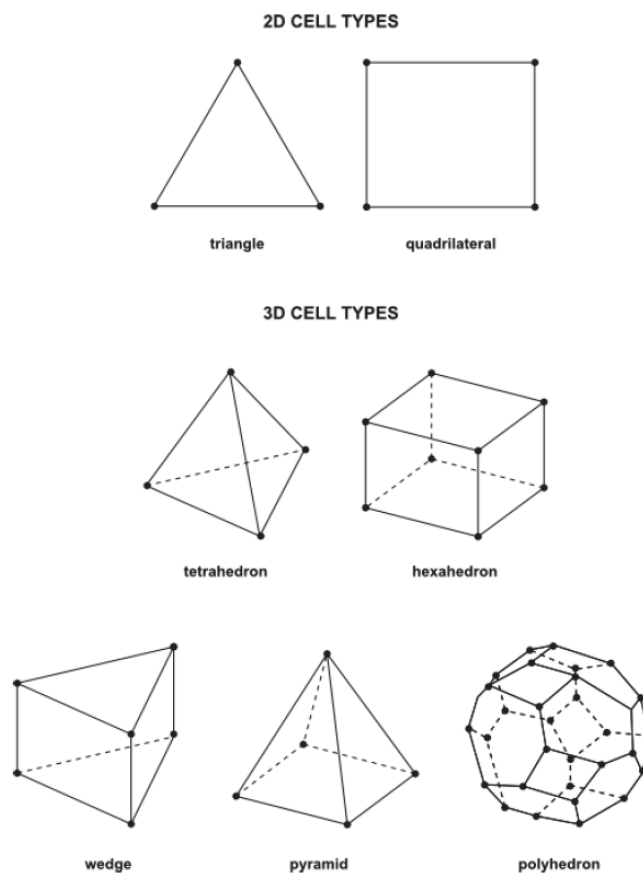


Figura 30. Tipos de celdas de dos y tres dimensiones [179].

Existe una terminología específica para denominar los distintos elementos que conforman las mallas. Los volúmenes de control de dos o tres dimensiones se denominan celdas o *cells*. Las superficies que delimitan estos volúmenes son las caras o *faces* y se apoyan en los vértices o *nodes*. La unión de dos caras da lugar a las aristas o *edges* y, finalmente, el centroide de la celda o *cell center*.

La agrupación de celdas da lugar a una *cell-zone* y la agrupación de caras da lugar a lo que se conoce como *boundary* si es una frontera o *interior* si están formadas por las caras interiores de las celdas de una *cell-zone*.

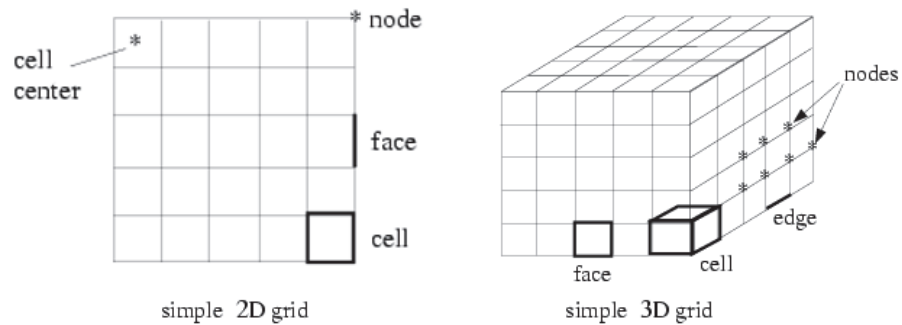


Figura 31. Terminología específica de las mallas [179].

Para realizar la discretización del dominio por lo general se recomienda emplear el menor tamaño posible de celda, normalmente limitado por los recursos computacionales de los que se disponga. Sin embargo, estos pueden no ser suficientes o el tiempo de cálculo demasiado largo, por lo que cuando se discretiza hay que tener en mente el comportamiento de todas las variables a lo largo del dominio, procurando reducir el número de celdas en aquellas regiones donde los gradientes sean menores.

Esto ha de realizarse con cautela, ya que de utilizar un tamaño de celdas muy grande ocasionará que las variables serán promediadas en volúmenes demasiado grandes, dando lugar a soluciones erróneas o incluso la no convergencia. Una buena praxis en el estudio CFD es realizar estudios de independencia de malla para asegurarse de que la discretización empleada no altera la solución lograda.

Tras realizar la discretización del dominio, es turno de la discretización de las ecuaciones que gobiernan el comportamiento de los fluidos. Estas ecuaciones se resumen en los principios de conservación, es decir, conservación de masa, conservación de la cantidad de movimiento y conservación de energía. Estos principios se pueden describir en forma diferencial o integral.

La conservación de las propiedades de un fluido dentro de un volumen de control se puede expresar como un balance de varios procesos que, considerando una variable genérica ϕ de una magnitud intensiva en un volumen de control, se puede dividir en cuatro partes:

1. Tasa de cambio de ϕ en el volumen de control con respecto al tiempo.
2. Tasa neta de incremento de ϕ debido al flujo convectivo en el volumen de control.
3. Tasa neta de incremento de ϕ debido al flujo difusivo en el volumen de control.
4. Tasa neta creación de ϕ en el volumen de control.

El término convectivo se debe al movimiento de las partículas de fluido, las cuales pueden atravesar las fronteras del volumen de control transportando consigo una masa, una energía y una cantidad de movimiento. El término difusivo se debe al movimiento molecular considerando el fluido en reposo. Si se realiza el balance de estos cuatro procesos se obtiene la ecuación general de conservación para la variable ϕ :

$$\int \frac{\partial(\rho\phi)}{\partial t} dV + \oint \rho\phi\vec{v}d\vec{A} = \oint \Gamma_\phi\nabla\phi d\vec{A} + \int S_\phi^V dV \quad (6)$$

siendo ρ la densidad, \vec{v} la velocidad, \vec{A} el vector de área de la superficie de control, Γ_ϕ el coeficiente de difusión, S_ϕ^V el término fuente de ϕ y $\nabla\phi$ el gradiente de la magnitud ϕ . Si se sustituyen los términos, ϕ y S_ϕ^V de la ecuación de conservación se obtienen las tres ecuaciones fundamentales del comportamiento de un fluido, conservación de la masa, de la cantidad de movimiento y de la energía.

La primera de ellas, en esencia expresa que la variación de masa en un volumen cerrado es igual a la masa que entra o sale a través de su superficie de control. En forma integral se puede escribir:

$$\int \frac{\partial\rho}{\partial t} dV + \oint \rho\vec{v}d\vec{A} = 0 \quad (7)$$

donde ρ la densidad del fluido, V el volumen encerrado por cada superficie de control, \vec{v} la velocidad del fluido y \vec{A} el vector normal a cada superficie que delimita el volumen de control.

La ecuación de conservación de la cantidad de movimiento indica que el incremento de la cantidad de movimiento es igual a la suma de las fuerzas que actúan sobre el sistema:

$$\int \frac{\partial(\rho\vec{v})}{\partial t} dV + \oint \rho\vec{v}\vec{v} d\vec{A} = \int \rho\vec{f}_m dV - \oint p\vec{I}d\vec{A} + \oint \vec{\tau}' d\vec{A} \quad (8)$$

donde \vec{f}_m las fuerzas másicas, p la presión del fluido, \vec{I} la matriz identidad y $\vec{\tau}'$ el tensor de esfuerzos viscosos.

La ecuación de conservación de la energía indica que el incremento de energía de un elemento es igual a la energía transferida a ese elemento más su trabajo realizado, es decir:

$$\int \frac{\partial \rho E}{\partial t} dV + \oint \rho E \vec{v} d\vec{A} = \oint k \Delta T d\vec{A} + \int (\rho \vec{f}_m \vec{v} + q_h) dV - \oint p \vec{v} d\vec{A} + \oint (\vec{\tau} \cdot \vec{v}) d\vec{A} \quad (9)$$

siendo E la energía total por unidad de masa del fluido (suma de la energía interna específica y de la energía cinética específica), k la conductividad térmica molecular, o conductividad térmica laminar, del fluido, T la temperatura del fluido y q_h el flujo de calor por unidad de masa de una fuente de calor situada dentro del volumen de control.

En simulaciones CFD como las que se abordarán en este trabajo, estas ecuaciones deben ser discretizadas además en el tiempo, ya que serán simulaciones transitorias. La discretización temporal implica la integración de cada término de las ecuaciones en un intervalo de tiempo Δt específico, que representa la duración temporal o tamaño de cada uno de los pasos de cálculo, denominados *time-step*.

La evolución temporal de una variable ϕ viene dada por la expresión genérica:

$$\frac{\partial \phi}{\partial t} = F(\phi) \quad (10)$$

donde la función F incorpora la discretización espacial.

Para solucionar las ecuaciones de fluidos mediante el método de volúmenes finitos existen varios algoritmos o *solvers*. Habitualmente se habla del *pressure-based solver* y *density-based solver*. En ambos, el campo de velocidades del fluido de trabajo se obtendrá a través de las ecuaciones de cantidad de movimiento. En el *pressure-based solver*, el campo de presiones se obtiene mediante las ecuaciones de continuidad y cantidad de movimiento. En el *density-based solver*, es la densidad la que se obtiene a través de la ecuación de continuidad y la presión se obtiene mediante la ecuación de estado.

El empleo del *pressure-based solver* es habitual la resolución de problemas de flujos incompresibles a baja velocidad, mientras que el *density-based solver* es habitual para sistemas donde se alcanzan velocidad de al menos 0.3 (Mach) y los efectos de compresibilidad se tornan relevantes. En este trabajo no se estima que se den velocidades como éstas ni será necesario tener en cuenta los efectos de compresibilidad, por lo que el modelo se desarrollará y validará para *pressure-based solver* [180].

Para realizar el acoplamiento de presión y velocidad, se empleará el algoritmo SIMPLE (acrónimo de *Semi-Implicit Method for Pressure-Linked Equations*). El algoritmo original, basado en el método predictor-corrector, fue propuesto por Patankar y Spalding [181]. Sustituye la ecuación de corrección de flujo en la ecuación

de continuidad discretizada, para así obtener una ecuación de corrección de la presión en el dominio discretizado.

Los valores discretos obtenidos tras la solución en cada iteración y volumen de control de las ecuaciones de gobierno son almacenados en los centroides de las celdas. Sin embargo, los términos convectivos requieren de estos valores en los centroides de las caras, por lo que deben ser calculados en base a los valores de los centroides de las celdas que comparten cada cara mediante una interpolación. Existen diferentes esquemas de interpolación, entre los que se destacan los siguientes:

1. *First order Upwind*: En este esquema no se tiene en cuenta la variación de la variable dentro de la celda, por lo que el valor de una cara es igual al valor del centroide aguas arriba.
2. *Second order Upwind*: Al contrario del anterior, se realizan aproximaciones mediante un método de reconstrucción multidimensional basado en el desarrollo en series de Taylor.
3. *Power-Law*: Los valores de cada variable en las caras de la celda son evaluados a partir de la solución exacta de una ecuación diferencial unidimensional de tipo convección-difusión.
4. *QUICK (Quadratic Upstream Interpolation for Convective Kinematics)*: Es un modelo de orden superior al *Second order Upwind*, en el que realiza una interpolación ponderando entre éste e interpolación central. Aporta una mayor precisión, pero se emplea en mallas estructuradas alineadas con el flujo, por lo que no será de utilidad en este trabajo.
5. *MUSCL (Monotone Upstream-Centered Schemes for Convection Laws)*: Esquema de tercer orden, similar al *QUICK*, pero aplicable a mallas arbitrarias. Permite reducir la difusión numérica, pero no contiene actualmente ningún tipo de limitador de gradientes, por lo que puede producir *undershoots* y *overshoots* cuando el campo fluido presenta discontinuidades como ondas de choque.

En las simulaciones realizadas en esta tesis, se comenzará con un esquema de interpolación de primer orden, y se finalizará la convergencia de la solución con un esquema de interpolación de segundo orden para alcanzar una mayor precisión.

Hasta ahora se ha abordado la discretización de las ecuaciones de gobierno en el marco Euleriano, el cual será utilizado para la fase gas, el lecho y, en el Nuevo modelo de ensuciamiento Euler-Euler, la materia particulada. La materia particulada en el inicio se desarrollará sobre el marco Lagrangiano, a través de la aproximación Euler-Lagrange del software ANSYS-Fluent® mediante el modelo DPM o *Discrete Phase Model*.

En este modelo la fase dispersa se resuelve mediante el seguimiento de un gran número de partículas, que el usuario puede controlar. La fase dispersa puede

intercambiar momento, masa y energía con la fase continua. En este trabajo se considerará la fase como diluida, por lo que se despreciarán las interacciones entre partículas ya que el volumen de la fase sólida es despreciable frente al de la fase continua.

La trayectoria de cada partícula se predice integrando el balance de fuerzas sobre ella. Este balance de fuerzas se puede expresar como:

$$\frac{d\vec{u}_p}{dt} = \frac{\vec{u} - \vec{u}_p}{\tau_p} + \frac{\vec{g}(\rho_p - \rho)}{\rho_p} + \vec{F} \quad (11)$$

Donde \vec{F} es una aceleración adicional provocada por una fuerza de las descritas en el apartado del Capítulo 2, Transporte de materia particulada, $\frac{\vec{u} - \vec{u}_p}{\tau_p}$ fuerza de arrastre o *drag* por masa de partícula, τ_p el tiempo de relajación de la partícula y la pareja ρ_p y ρ son las densidades de la partícula y del fluido respectivamente [180].

La integración de la ecuación del movimiento de la partícula se resuelve integrando por pasos a lo largo de pasos temporales discretos. Si se engloba el término $\frac{\vec{g}(\rho_p - \rho)}{\rho_p} + \vec{F}$ dentro de \vec{a} , es decir todas las aceleraciones salvo la fuerza de arrastre o *drag*, la ecuación puede ser resuelta para u , τ_p constantes a través de la integración analítica.

La velocidad y posición del siguiente paso de la trayectoria de una partícula, x_p^{n+1} y u_p^{n+1} , se pueden expresar como:

$$x_p^{n+1} = x_p^n + \Delta t(u^n + \alpha\tau_p) + \tau_p \left(1 - e^{-\frac{\Delta t}{\tau_p}}\right) (u_p^n - u^n - \alpha\tau_p) \quad (12)$$

$$u_p^{n+1} = u^n + e^{-\frac{\Delta t}{\tau_p}}(u_p^n - u^n) - \alpha\tau_p(e^{-\frac{\Delta t}{\tau_p}} - 1) \quad (13)$$

Sin embargo, aunque el método analítico es eficiente, puede llegar a ser impreciso cuando las partículas no están en equilibrio hidrodinámico con la fase continua. Por ello, se empleará un sistema automático que alternará entre una discretización numérica implícita de Euler cuando se requiere de estabilidad numérica, y un esquema de orden superior empleando discretización trapezoidal cuando esta es estable. De esta forma la nueva posición de la partícula siempre se calcula mediante la discretización trapezoidal:

$$x_p^{n+1} = x_p^n + \frac{1}{2}\Delta t(u_p^n + u_p^{n+1}) \quad (14)$$

Donde la velocidad en el siguiente punto de la trayectoria para la partícula p , u_p^{n+1} , se expresa como:

$$u_p^{n+1} = \frac{u_p^n \left(1 - \frac{1}{2} \frac{\Delta t}{\tau_p}\right) + \frac{\Delta t}{\tau_p} \left(u^n + \frac{1}{2} \Delta t u_p^n \cdot \nabla u^n\right) + \Delta t \alpha^n}{1 + \frac{1}{2} \frac{\Delta t}{\tau_p}} \quad (15)$$

La ecuación de energía para la partícula puede expresarse de la siguiente forma si se desprecian los gradientes internos de temperatura, es decir, se asume la hipótesis de *Thermally Thin* y la variación de su temperatura entre pasos temporales es pequeña:

$$m_p c_p \frac{dT_p}{dt} = A_p [-(h + \varepsilon_p \sigma T_p^3) T_p + (h T_\infty + \varepsilon_p \sigma \theta_r^4)] \quad (16)$$

Es importante mencionar el hecho de que la temperatura de la partícula debe variar lentamente para que esta ecuación pueda emplearse, pues en el presente trabajo las partículas viajarán por dominios donde suceden combustiones e intercambios de calor, con cambios de temperatura moderadamente rápidos [180]. Por ello, será necesario emplear pasos temporales para las partículas pequeños, lo que implica un mayor coste computacional.

Si se integra la Ecuación (16) para un *time step* t se obtiene:

$$T_p(t + \Delta t) = \frac{h T_\infty + \varepsilon_p \sigma \theta_r^4}{h + \varepsilon_p \sigma T_p^3(t)} + \left[T_p(t) - \frac{h T_\infty + \varepsilon_p \sigma \theta_r^4}{h + \varepsilon_p \sigma T_p^3(t)} \right] e^{-\left[\frac{A_p (h + \varepsilon_p \sigma T_p^3(t))}{m_p c_p} \right] \Delta t} \quad (17)$$

Implementación del modelo

Las herramientas CFD han sido desarrolladas para, entre otras cosas, la simulación de procesos termoquímicos en fase gaseosa. El desarrollo de procesos termoquímicos que implique reacciones heterogéneas y dinámica de sólidos no ha obtenido los mismos avances, siendo esencialmente parte del modelado *Discrete Phase Model* mencionado previamente.

Sin embargo, el software empleado sí incluye la posibilidad de embeber algoritmia externa, desarrollada por los usuarios, para alterar el funcionamiento del software a voluntad de los mismos y adecuarlo a sus necesidades. Para ello, se emplean las denominadas UDF (*User Defined Function*) que se encuentran escritas en lenguaje C++, ampliamente extendido en la ingeniería de software.

Desde ellas se puede alterar gran parte del funcionamiento de este software una vez se aprenden y entienden las estructuras de datos internas del software. Para lograrlo es necesario entender el flujo de datos entre nodos y *host*, y cómo se acceden, modifican o crean las capas de datos almacenadas en los centroides, caras y nodos de la malla en cada iteración.

Para ello, el software incorpora un manual donde se establecen las principales macros que permiten leer y definir estos datos. Si bien, para la realización de este

trabajo, ha sido necesario explorar minuciosamente a mano las librerías base del software que contienen funciones y macros, las cuales no están pensadas para ser leídas ni ejecutadas por personal no implicado en el desarrollo del mismo. Esto ha dado lugar a numerosas ocasiones donde se ha tenido que ejecutar casos básicos, calculables de forma manual, para comprobar el funcionamiento de funciones o el hallazgo de funciones obsoletas en nuevas versiones, lo que se conoce como *deprecated code*.

Las funciones más empleadas a lo largo del código tienen que ver con la jerarquía establecida en la malla, para llegar de un valor de una variable determinada en un elemento en concreto es necesario recorrer jerárquicamente el árbol, mediante lo que se conoce como punteros de acceso a memoria, y saber si esa variable existe en ese punto o no, de lo contrario el software se vuelve inestable y se termina. En la Figura 32, se muestra la jerarquía de un caso típico sencillo:

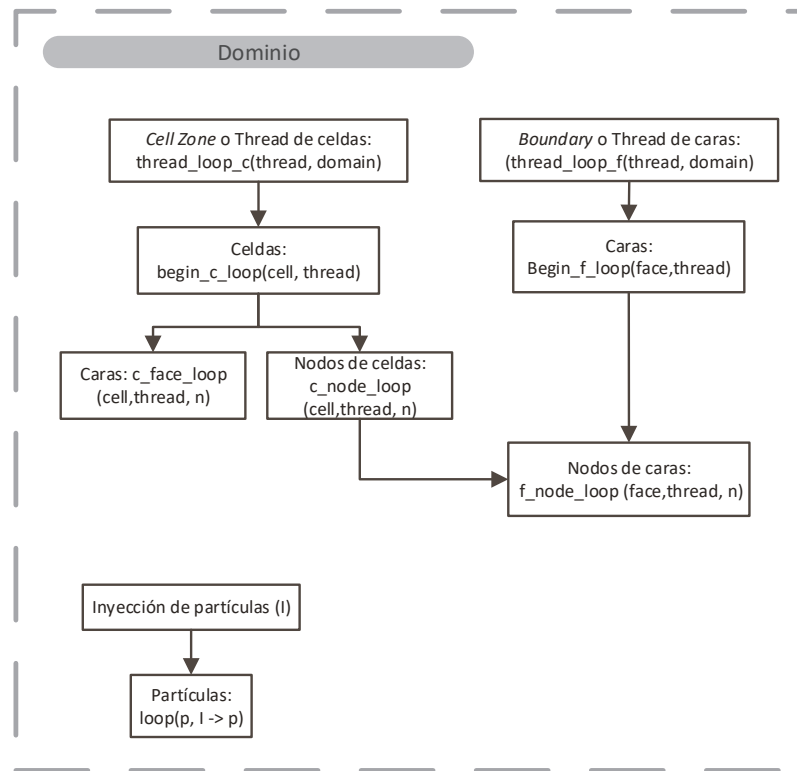


Figura 32. Jerarquía de la estructura de datos de un entorno monofásico.

De esta forma, si se requiere acceder al valor que tiene una cara en concreto almacenado en una celda de una *cell zone*, se deberá recorrer todo el árbol jerárquico hasta llegar a ella. Existen pequeños atajos que permiten, por ejemplo, no realizar un bucle de *threads* de celdas conociendo su ID, pero deben ser evitados si se quiere realizar un código generalista que se adapte sólo a cualquier sistema de combustión. De esta forma será necesario una intensiva labor de diferenciación y exclusión para agilizar las búsquedas dentro de la estructura de datos, por ejemplo, sabiendo si *thread* al que pertenece la celda es siempre fluida o sólida se puede evitar recorrer aquellos que de partida ya no cumplen la condición.

Capítulo 4

Sistemas experimentales

A lo largo del trabajo se emplearon múltiples sistemas de combustión, pues todos estos engloban un amplio abanico de posibilidades que ponen a prueba el comportamiento del modelo.

Entre ellos se encuentran plantas piloto debidamente instrumentalizadas y controladas, vitales para la puesta a punto del modelo, y sistemas domésticos, que permiten aproximarse al escenario habitual de operación de los sistemas de combustión de biomasa.

Este conjunto de sistemas de combustión abarca una variedad de sistemas de alimentación (inferior, lateral y superior), importantes para comprobar y validar el comportamiento del modelo ante fenómenos del lecho derivados de la alimentación. En cuanto a morfología del sistema, se cuenta con sistemas acuatubulares y también pirotubulares. Finalmente, gracias a las colaboraciones promovidas se ha logrado probar el modelo en sistemas de combustión propiedad del grupo y sistemas externos de otras universidades y empresas, de forma que se eviten sesgos producidos por procedimientos o sistemas de medición.

A continuación, se expondrán brevemente los sistemas empleados a lo largo de esta tesis:

- Planta piloto GTE #1.
- KWB Multifire™ 60 (kW)
- Vapormatra Cantina™
- Ferroli Sun Mikro P7™
- Estufa del IST-Lisboa, Portugal
- Gasificador en lotes de la Universidad de Antioquia, Colombia

4.1. Planta piloto GTE #1

Se trata de una planta experimental diseñada de forma modular con una potencia de hasta 15 (kW) construida en acero inoxidable 310 sin aislamiento externo. Su sección de cámara de combustión es cuadrada de 120 (mm) de lado y la altura global del sistema 1500 (mm). La parrilla presenta inclinación positiva respecto a la entrada de los pellets y está formada por 120 orificios de 4 (mm). Los pellets se alimentan a la parrilla por medio de un tornillo sinfín inclinado que lleva a éstos desde la tolva, la cual es pesada continuamente, y los alimenta por el lateral. Sobre este lecho se encuentra una cámara de combustión y posteriormente el distribuidor del aire secundario con 44 agujeros igualmente distribuidos de 4.4 (mm). Entre el aire secundario y la chimenea se introduce el módulo de deposición refrigerado.

Consta pues de los siguientes módulos desde la parte inferior a la superior:

1. Plénium de aire primario
2. Parrilla y lecho
3. Cámara de combustión
4. Distribuidor del aire secundario
5. Módulo de deposición refrigerado
6. Chimenea

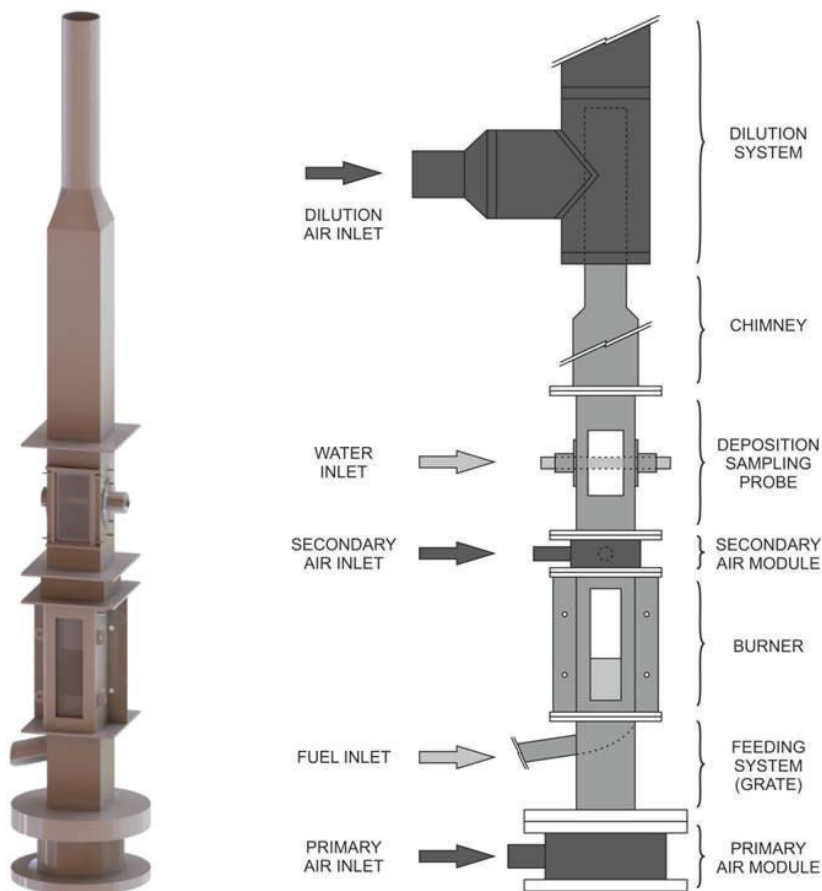


Figura 33. Diseño CAD tridimensional de esta planta piloto GTE#1 y esquema.

Es un sistema completamente monitorizado que permite la variación individual de los caudales de aire suministrados por el primario y por el secundario mediante ventiladores individuales, los cuales son ventiladores centrífugos con motores de frecuencia variable (Schneider Electric Altivar 31) controlados a través de un PID Omron E5CK. Para medir el flujo de aire por cada ventilador, el sistema tiene también dos caudalímetros Van Putten Instruments VPF.R200.100.

El tubo de deposición es refrigerado por agua en circuito cerrado y sus tuberías de conexión de entrada y salida tienen termopares para el cálculo de la potencia transferida al circuito. La disipación final es hacia el ambiente, y se puede ajustar para mantener constante la temperatura de entrada. El tubo puede ser fácilmente desmontado sin inducir vibraciones o impactos que hagan desprenderse la materia depositada sobre él que no esté adherida. De esta forma puede ser analizada tanto la masa no adherida como la adherida y la geometría del depósito.

En la salida del sistema se encuentra un sistema de dilución hacia un impactador de baja presión Dekati DLPI de 13 escalas y un analizador de gas Servomex, tras ser este gas preparado en un acondicionador JCC L-112401.

En la Figura 33 se muestra el diseño CAD tridimensional de esta planta piloto y un esquema explicativo del mismo.

4.2. KWB Multifire™ 60

Se trata de una caldera doméstica de 60 (kW) de potencia nominal del fabricante austriaco KWB. Cuenta con un buen control del punto de operación, aunque con menos grado de precisión que la planta piloto GTE#1. El combustible es alimentado a través de un tornillo a la parrilla desde la parte inferior de la misma, Figura 34. Cuando es alimentado a esta parrilla desde la parte inferior, asciende formando un pequeño volcán de pellets, que avanzan desde el interior del cono hacia el exterior secándose debido a la radiación de la combustión para quemarse a continuación con el aire primario suministrado a través de los agujeros ubicados en anillos concéntricos. Los restos no quemados caen por gravedad por el exterior hacia el cenicero. Esta parrilla cuenta también con un control de nivel para garantizar una combustión adecuada.

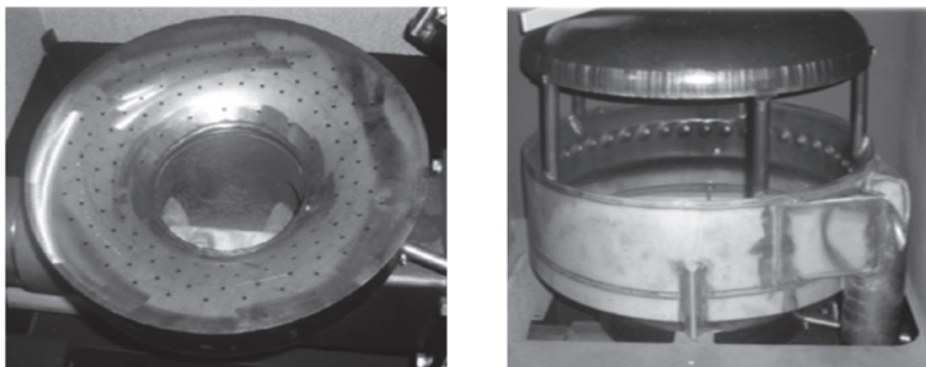


Figura 34. Detalle de la rejilla, tornillo de alimentación y distribuidor de aire secundario.

Sobre el lecho se encuentra un anillo de aire secundario soportado sobre pilares con orificios equiespaciados y orientados en oblicuo, tanto en el sentido axial como vertical, de forma que se genera una beneficiosa turbulencia que favorece el mezclado de los reactivos con el oxígeno, completando la combustión. Esta combustión es confinada gracias a una cúpula situada sobre el distribuidor de aire secundario, mejorando de nuevo el mezclado al aumentar el tiempo de residencia del gas de combustión y evitando el impacto de la llama contra las superficies refrigeradas.

Tras la cúpula de confinamiento, quince tubos verticales conducen el gas de combustión intercambiando calor con el circuito de agua. En ellos están ubicados rascadores con doble función, evitar la formación de depósitos sobre las superficies de intercambio al retirarlos periódicamente para que caigan a la cúpula y de ahí se escurran hasta el cenicero, y generar turbulencia para que el gas de combustión intercambie calor de forma más eficiente sin la generación de efecto pared. Tras el intercambiador, se encuentra un colector de salida, donde se ubica el mecanismo de accionamiento de los rascadores y se conduce al exterior.

Se trata pues de un sistema ciertamente bien diseñado que logra buenas prestaciones y bajas emisiones de materia particulada.



Figura 35. Esquema interno de la caldera KWB Multifire™ 60.

Para estudiar la deposición sobre las superficies de trabajo del intercambiador de calor en esta caldera, se accede por la puerta principal de mantenimiento y se colocan al inicio de cada tubo del intercambiador un anillo metálico de 95.6 (mm) de diámetro y 20 (mm) de altura, como se puede observar en la Figura 36.

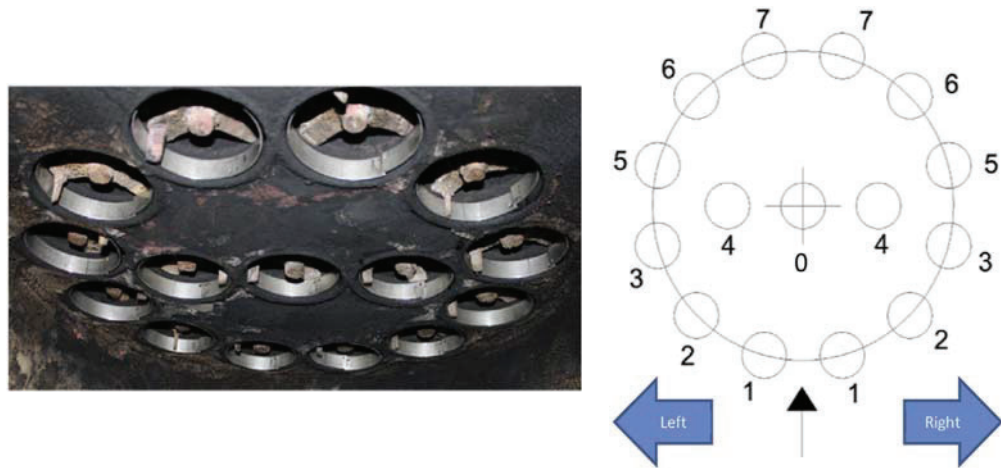


Figura 36. Sondas de deposición en forma de anillo y nomenclatura empleada [182].

4.3. Vapormatra Cantina™

Se trata de una estufa de 24 (kW) de potencia nominal de diseño compacto. Los pellets son alimentados superiormente mediante un acceso inclinado al que llegan los pellets desde la tolva. Tras ser alimentados caen a una parrilla en forma de cesta con múltiples orificios. No presenta *air-staging* más allá del producido por la propia cesta. Tras la combustión, los gases a alta temperatura producidos por esta radian calor hacia la estancia por medio de una ventana a tal efecto y recorren verticalmente un intercambiador tubular de dos pasos, primero de forma ascendente y después descendente antes de salir del sistema con la ayuda del ventilador de extracción. No cuenta con deflectores que impidan el contacto de la llama con los primeros tubos del intercambiador, produciendo mayores emisiones de inquemados. Tampoco cuenta con sistemas que prevengan de la deposición de materia no deseada sobre las superficies.



Figura 37. Diseño CAD tridimensional y esquema de la estufa [182].

Al ser un diseño tan compacto no es viable la colocación de testigos de deposición en todos los tubos del intercambiador, pues al retirarlos se perdería gran cantidad de masa y las medidas no serían fiables. Por ello, solo se colocan testigos en los cinco tubos visibles y accesibles desde la parte superior gracias a la trampilla de acceso que tiene la caldera. En la parte superior de cada uno de los cinco tubos se colocan tres testigos equiespaciados de dimensiones 80 por 35 (mm), por lo que se abarcan 240 (mm) de los 340 (mm) de longitud de cada tubo.

4.4. Ferroli Sun Mikro P7™

Se trata de un sistema doméstico de 25 (kW) de potencia nominal con un diseño sencillo. Este sistema cuenta con un cabezal que realiza la función de quemador de pellets, y un cuerpo metálico, que alberga un gran volumen de agua, construido por módulos. El quemador recibe los pellets a través de una conexión superior curva, a la que se conecta una manguera que conduce los pellets de la tolva anexa tras ser elevados por un tornillo sinfín.

Tras ser conducidos estos pellets por la manguera al quemador, caen por una rampa y un retenedor los ubica al principio de la parrilla evitando que un rebote no esperado los envíe a la cámara de combustión. Esta parrilla está ubicada en una cámara de combustión cilíndrica de pequeñas dimensiones y presenta múltiples ranuras en su parte inferior y orificios a distinta altura en el extremo por el que se alimenta. En este extremo se encuentra también la resistencia que hace la función de ignitor para el arranque del sistema. El aire es alimentado por un único ventilador controlado por una electrónica básica y se distribuye gracias a la parrilla.

La combustión se aboca con un leve ángulo descendente hacia la cámara de combustión principal. En ella no existen deflectores que impidan el impacto de la llama contra la superficie de intercambio. En efecto, toda la cámara de combustión principal, salvo la puerta de acceso donde se ubica el quemador, está refrigerada.

Tras realizar un lazo de mezclado dentro de la cámara de combustión principal, promovido por la leve pendiente negativa mencionada antes, el gas de combustión procede hacia el intercambiador de calor creado por 12 tubos verticales, similares a los de la KWB Multifire™ pero sin rascadores ni turbuladores en ellos.

Tras estos tubos verticales llegan a un colector superior donde se comunican con la chimenea tras sortean un deflector que provoca que los gases de combustión se desplacen hacia el perímetro. En este colector se encuentra también una tapa de acceso.

Todo el sistema, salvo la puerta inferior donde se coloca el quemador y la tapa superior de acceso se encuentra bañado por una camisa de agua, la cual está pobremente aislada del exterior. Esta camisa de agua está formada por tres módulos que se intercomunican entre sí por cuatro cajas de comunicación sencillas, dos en la parte inferior y dos en la parte superior. En este trabajo el sistema se hace trabajar con un salto de temperatura de 5 (°C) entre entrada y salida del agua refrigerante.

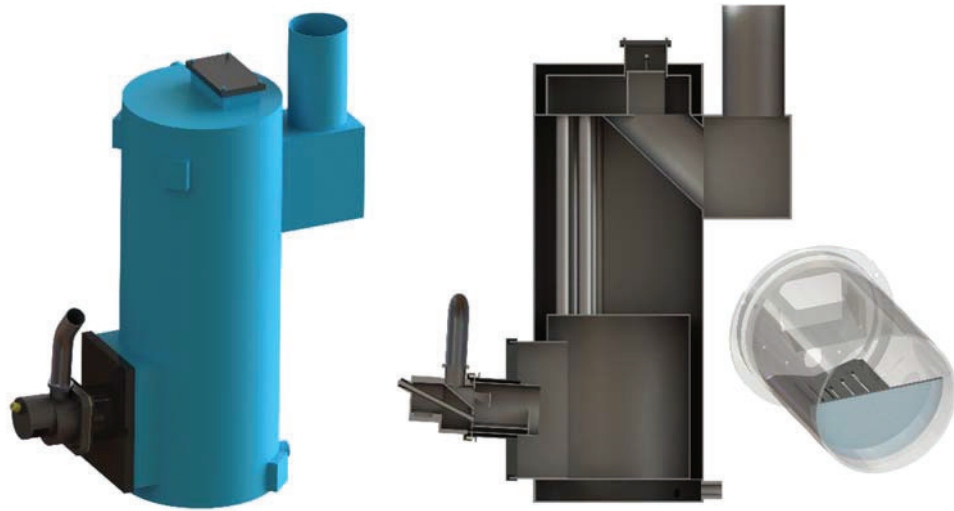


Figura 38. Diseño CAD tridimensional, sección de la caldera y detalle de la parrilla.

4.5. Estufa del IST-Lisboa, Portugal

En la colaboración realizada con el Instituto Superior Técnico de Lisboa, se trabaja con un sistema de combustión ubicado en éste. Se trata de una estufa de pellets doméstica de 22 (kW) profundamente modificada. En este trabajo se empleará con una potencia de 16 (kW) térmicos.

Presenta un sistema de alimentación superior, similar a la Vapormatra Cantina™ ya expuesta. Este sistema introduce los pellets que están previamente alojados en una tolva externa monitorizada, en una cesta hemisférica de 120 (mm) con múltiples perforaciones a distintos niveles.

De esta vez, la cesta cuenta con una caracola exterior que distribuye de forma más acertada el aire generando una entrada de aire primaria por la parte inferior y una suerte de *air-staging* con las ranuras superiores mejorando el mezclado de reactivos. En uno de los laterales de la cesta se encuentra el ignitor.

Se trata de un sistema de tiro forzado por un ventilador, por lo que trabaja a una presión levemente inferior que la atmosférica. Algo común en sistemas domésticos, pero que conlleva grandes dificultades, como la valoración certera de las infiltraciones a lo largo del sistema, especialmente en un sistema tan modificado como éste. En la Figura 39, se muestran la ubicación de las infiltraciones en este sistema.

La parte frontal cuenta con una amplia ventana para permitir la salida de calor radiante hacia la estancia y la visión ornamental de la llama. La parte trasera, los laterales y la parte superior se encuentran refrigerados por una camisa de agua. En esta parte superior se cuenta con dos tubos de intercambio que comunican las camisas

laterales, los cuales están protegidos por un deflector para evitar el contacto de la llama con ellos.

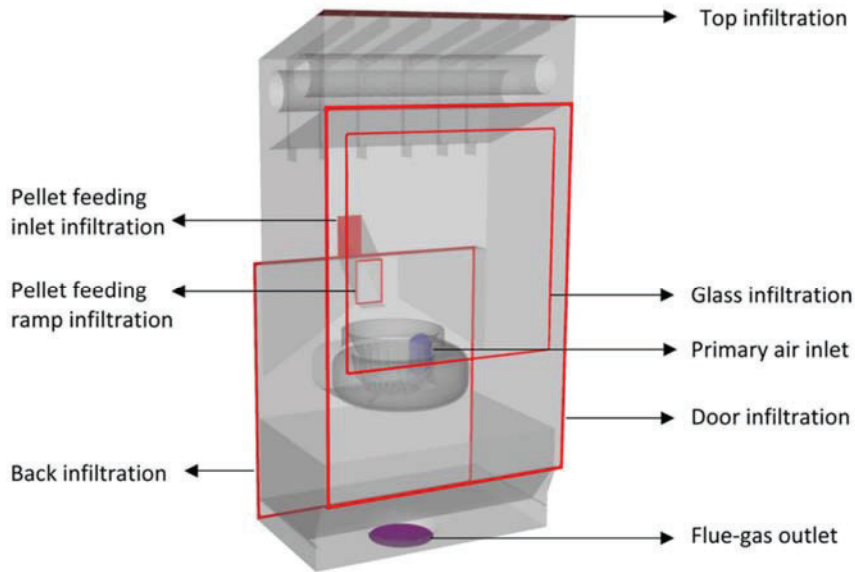


Figura 39. Esquema visual de la localización de las infiltraciones de aire [183].

La cámara de combustión fue modificada para permitir la inserción de sondas a cinco alturas distintas a través del plano medio que cruza al eje vertical de la cesta hemisférica. Estas sondas pueden alcanzar distintas posiciones horizontales, permitiendo registrar la evolución también a lo largo de este plano para cada altura. En cada posición de las que se muestran en la Figura 40, se toman datos de concentraciones de las especies y de la temperatura de gas. Los tiempos de residencia estimados del gas entre el lecho y los puertos 1 a 5, son 28, 56, 88, 115 y 147 (ms) respectivamente.

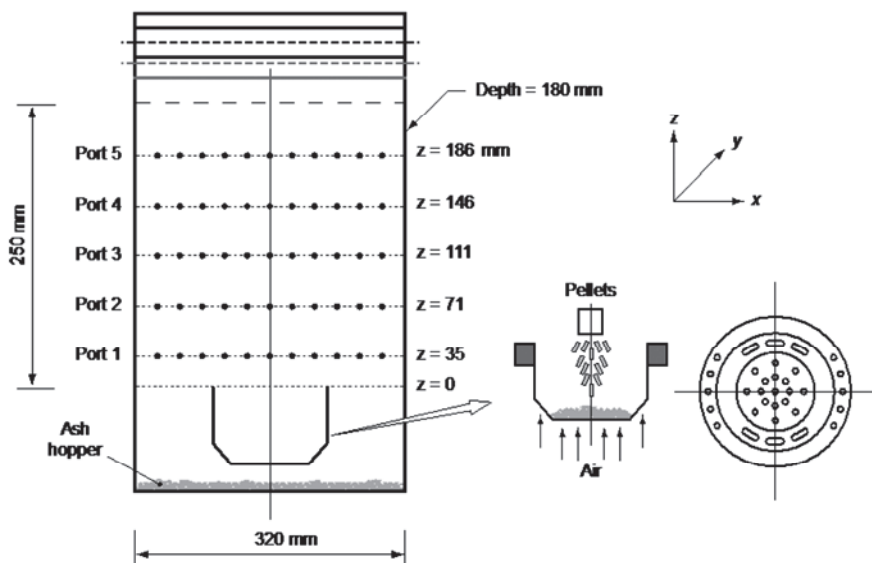


Figura 40. Esquema visual de la localización de las sondas [183].

4.6. Gasificador en lotes de la Universidad de Antioquia, Colombia

Otra de las colaboraciones se realizó mediante la estancia de un alumno de la Universidad de Antioquia, Colombia en el Grupo de Tecnología Energética de la Universidad de Vigo. En esta colaboración se empleó un gasificador autotérmico de lecho fijo para la validación experimental del comportamiento del modelo con biomásas no habituales y su respuesta a la modificación de parámetros como el factor de empaquetamiento.

Su operación es por lotes y funciona a contracorriente, alimentando el agente gasificante desde la parte inferior. Se alimenta y se enciende por la parte superior. Las dimensiones principales del reactor, cuyo sencillo diseño se puede percibir en la Figura 41, son 185 (mm) de diámetro externo, 102 (mm) de diámetro interno, y una altura de lecho de 400 (mm). Para su operación emplea aire como agente gasificante, el cual está controlado mediante un caudalímetro Honeywell AWM500. Este sistema trabaja a presión atmosférica a temperaturas de entre 800 y 1000 (°C).

El gas de síntesis es filtrado y secado en una unidad de acondicionado antes de que su composición sea analizada mediante cromatografía en un Agilent 3000 Micro GC. La evolución temporal del frente de propagación es captada por nueve termopares separados 30 (mm) entre ellos.

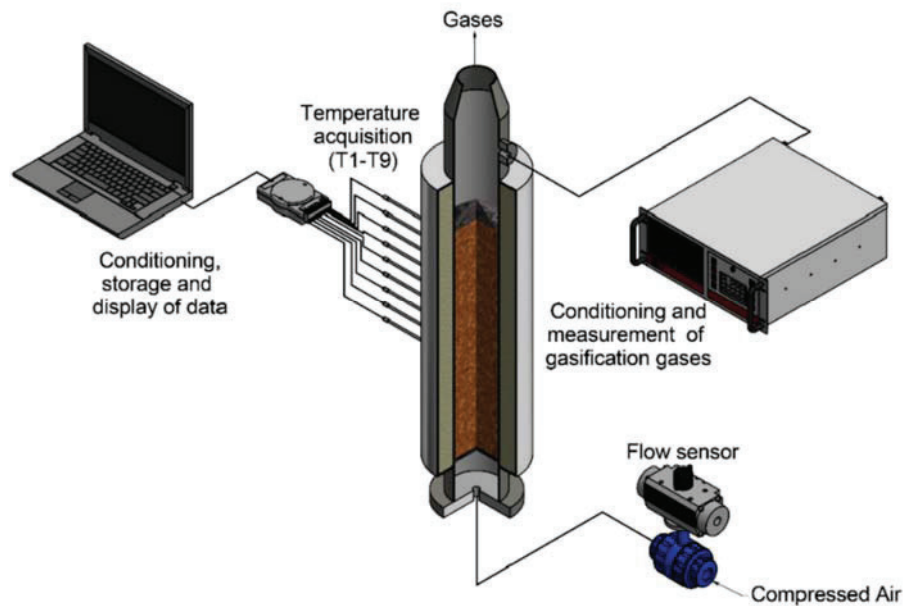


Figura 41. Esquema de la instalación del gasificador y sus sistemas periféricos [184].

Capítulo 5

Creación de interfaz de usuario

5.1 Motivación

Desde el inicio de esta tesis se tuvo una idea clara en la mente. El desarrollo de una plataforma de colaboración internacional en el que expertos y usuarios del modelo pudieran aportar nuevas características e ideas. Para ello se establecieron dos vías de actuación: la compartimentación del modelo y el desarrollo de una interfaz de usuario sencilla e intuitiva.

La compartimentación y refactorización del modelo era vital para el futuro de las colaboraciones. Mediante esta compartimentación, se podría compartir fácilmente partes del modelo a expertos en el campo involucrado en dichas partes. De esta forma, a la hora de mejorar y desarrollar submodelos no requeriría la formación de este experto en el modelo completo, solo conocer las hipótesis de desarrollo del modelo, un conjunto de *inputs* y un conjunto de *outputs*. Por ejemplo, un experto en el campo del modelado de la turbulencia en las microescalas solo necesitaría tener conocimiento de una serie de *inputs* como temperatura, velocidad, vorticidad, etc. y él, con su propuesta de submodelo, devolvería unos *outputs* determinados, como mezclado, transferencia másica o de energía.

Por otra parte, el uso del modelo debe seguir pudiendo ser accesible para este experto si desea comprobar el funcionamiento de su propuesta o, por ejemplo, debe ser accesible para un usuario no experto en ninguno de los campos, pero que desea aportar su experiencia con el modelo. Para ello se comenzó el desarrollo de una interfaz gráfica de usuario o GUI (*Graphic User Interface*) que se embebería en la interfaz de ANSYS-Fluent®.

Las limitaciones de los modelos en el estado de desarrollo en el que se comenzó este trabajo eran las siguientes:

- Dos modelos distintos según sea alimentación por advectiva (tornillo sinfín) o por DPM (alimentación superior por caída).
- Lenta aplicación de cambios en las condiciones de contorno debido a la necesidad de descargar y recompilar el modelo.
- Necesidad de comprender cada submodelo en su totalidad para ejecutar de forma fiable el modelo de combustión demandado.
- Amplia experiencia para configurar el software para ejecutar el modelo de combustión de biomasa de forma correcta.
- Amplia experiencia y tiempo para inicializar la simulación.

5.2 Antecedentes

Para desarrollar esta interfaz era necesario comprender el funcionamiento de la interfaz de ANSYS-Fluent® y su comunicación con el *kernel* o núcleo del software. Cabe mencionar que, en el momento de desarrollar esta interfaz, se trabajaba sobre la versión v15.0.7 del software y en los manuales del mismo no se explicaba la posibilidad de desarrollar interfaces gráficas ni su lenguaje ni macros. Actualmente en los manuales de las versiones v17.0 en adelante, aparecen ejemplos básicos de programación en *Scheme*. No obstante, desde esa versión la interfaz de ANSYS-Fluent® está siendo migrado y remodelado hacia una estética más amigable basada en nuevos lenguajes de programación, aunque internamente sigue trabajando en *Scheme* por el momento.

Tras una extensa búsqueda se logró saber que la interfaz gráfica por aquel entonces se encontraba desarrollada en lenguaje *Scheme*, un dialecto del LISP desarrollado por Guy L. Steele y Gerald Jay Sussman en la década de los setenta. El LISP fue especificado en 1958 por John McCarthy y sus colaboradores en el MIT (*Massachusetts Institute of Technology*). La antigüedad del dialecto generó problemas a la hora de encontrar documentación sobre él a fin de conocer su funcionamiento.

5.3 Resultado

Tras conocer las formalidades del lenguaje, faltaba conocer las macros propias de ANSYS-Fluent® y cómo comunicarse con el software. En esta parte no hubo bibliografía en la que apoyarse ni experiencia externa. Fue necesario un largo periodo de aprendizaje con el método *prueba y error*, investigando como se realizarían tareas de sencillas, como paneles, recorridos y funciones, a tareas más complejas como inyección de código a fichero y a consola del programa. De esta

forma se llegó a las más de 7800 líneas con las que cuenta la interfaz. Una muestra de ellas se puede ver en el ANEXO D.

Hasta la creación de la interfaz gráfica en *Scheme*, los modelos de combustión eran controlados mediante más de un centenar de directivas *#define* y variables globales. Adicionalmente, los parámetros cuya alteración era infrecuente se encontraban escondidos en sus respectivas funciones. Por ello, el modelo requería de una curva de aprendizaje larga y abrupta. La lista de configuración del software para ejecutar un caso de relativa sencillez tomaba en torno a 1 hora y ocupaba tres carillas de forma resumida.

Con la introducción de la interfaz, de la cual se mostrarán capturas a continuación, se lograron grandes avances que se enumeran a continuación:

1. El tiempo de configuración de un caso por parte de un usuario experimentado se redujo a la cuarta parte.
2. Desaparecieron errores de configuración sencillos por fallo humano, como no añadir un término fuente a una variable en un *cell zone* en concreto.
3. Incremento de la fiabilidad de las simulaciones CFD al reducirse la posibilidad de una mala configuración inicial cuyo efecto se hace evidente tras varios días de cálculo.
4. Curva de aprendizaje mucho más corta para usuarios nuevos gracias a la incorporación de una ayuda al propio panel a través del botón “*Model Help*” con explicaciones y consejos.
5. Rapidez en el ajuste de parámetros de las simulaciones en marcha, sin necesidad de recompilar el código.
6. Posibilidad de grabar a un archivo la configuración total del caso para su reutilización en otra simulación o para dar soporte.
7. Posibilidad de generar una librería de combustibles mediante el volcado y lectura de ficheros de combustibles.

La interfaz se desarrolló a lo largo de múltiples versiones gracias a la experiencia adquirida con las colaboraciones externas, las cuales fueron vitales para detectar posibles malfuncionamientos o *bugs* o para detectar aspectos mejorables como, por ejemplo, las definiciones de los campos.

Esta interfaz cuenta con dos modos, usuario básico y usuario avanzado, seleccionable en la parte superior izquierda del panel principal. Después cuatro pestañas dan lugar a las cuatro secciones fundamentales de la configuración:

- *Initial Parameters*: Para especificar detalles básicos de la caldera, el tipo de alimentación y diversos modelos de volátiles.
- *Bed*: En esta sección se muestran datos relacionados con las propiedades físicas del lecho y los controles de la dinámica del lecho

- *Fuel*: Esta sección es compleja y por ello se crean cuatro secciones internas, donde se configuran las propiedades termoquímicas del combustible.
- *Final Steps*: Esta sección pide al usuario información del combustible a emplear, donde estará ubicado el lecho y desde donde se alimentará. Posteriormente realizará la configuración completa del software, informando paso a paso si se ha realizado adecuadamente.

A lo largo de toda la interfaz se proporcionan datos por defecto, extraídos de bibliografía reconocida, en cada campo para evitar la necesidad de escribir valores habituales en cada configuración, reduciendo el tiempo de configuración y posibles errores humanos.

En el Imágenes de la interfaz gráfica de usuario para un caso concreto, se mostrarán capturas de pantalla representativas de la interfaz y su panel de ayuda.

Capítulo 6

Modelado de la combustión

6.1 Antecedentes

Previo la realización de este trabajo conducente a tesis, se recibieron varios modelos de combustión de biomasa en lecho fijo diferenciados esencialmente en el modelado de la alimentación de los pellets. En esencia se podría hablar de dos modelos, modelo de alimentación advectivo y modelo de alimentación superior por DPM, ya que el resto son casos puntuales de éstos como, por ejemplo, el modelo de combustión por lotes sin alimentación. Estos modelos han sido publicados y se pueden consultar en las referencias [185-187].

La primera medida realizada, con la creación de la plataforma de colaboración internacional en mente, fue el desarrollo de un modelo de combustión en lecho fijo general que pudiera trabajar en cualquier tipo de caldera doméstica conocido. Para esto, se procedió al aprendizaje profundo de cada modelo, comprobando que estaban desarrollados bajo las mismas hipótesis y gran parte del código era similar en funcionamiento, solo variaban umbrales, nombres de variables y funciones y otras consideraciones menores.

Por ello, se decidió primero a trasladar las partes iguales del código al modelo general y posteriormente a evaluar las razones existentes para las diferencias entre partes del código que no estaban relacionadas con el sistema de alimentación, principal elemento diferenciante en cuanto a código.

Gran parte de las diferencias se debían a evitar efectos secundarios en sistemas concretos y en el modelado de la alimentación. Para lograr homogeneizar al máximo el código, se realizó una labor de reformulación de esas partes de forma que con un mismo valor el código se readaptase y funcionara correctamente en todos los sistemas conocidos. Finalmente, las partes diferenciantes y exclusivas del sistema de alimentación fueron trasladadas al código general.

Es sobre este modelo general, sobre el que se desarrollará el modelo de fouling Euler-Lagrange. Como se explicará posteriormente en el apartado correspondiente, para el modelo de fouling Euler-Euler se reescribió el modelo desde los cimientos para un entorno multifásico.

6.2 Modelo general

Este modelo general de combustión es, en esencia, el ya publicado en los trabajos [185-187], por lo que en este capítulo se abordará de forma muy resumida su funcionamiento e hipótesis de partida.

El lecho es tratado como un medio poroso variable en forma y propiedades a lo largo del tiempo. Su caracterización se lleva a cabo mediante un conjunto de variables Eulerianas con ecuaciones de transporte asociadas que serán resueltas por el propio software ANSYS-Fluent® simultáneamente con la fase gas. Este conjunto de escalares es introducido mediante las estructuras de datos UDS (*User Defined Scalars*) del propio software y se enumeran a continuación:

1. Fracción sólida de la celda.
2. Entalpía de la fase sólida de la celda.
3. Diámetro esférico equivalente al cubo.
4. Densidad de humedad de la fase sólida presente en la celda.
5. Densidad de madera de la fase sólida presente en la celda.
6. Densidad de char de la fase sólida presente en la celda.
7. Densidad de ceniza sólida de la fase sólida presente en la celda.
8. Densidad de ceniza volátil de la fase sólida presente en la celda.

Como todo modelo numérico, son necesarias hipótesis que controlen y simplifiquen ciertos aspectos de la realidad que no son relevantes para el estudio y que provocarían un mayor esfuerzo computacional. Estas hipótesis deben ser válidas para todo el rango de estudio y el efecto que tienen en la solución debe ser tenido en cuenta a la hora de valorar los resultados obtenidos. Las hipótesis bajo las cuales este modelo de lecho ha sido desarrollado son las siguientes:

- El lecho se modela como un medio poroso variable.
- Este medio poroso es considerado disperso, por lo que se promedian las propiedades del sólido en el volumen de cada celda de cálculo.
- Se asume que las partículas, a efectos de cálculo, son equivalentes a esferas con un parámetro de esfericidad asociado.
- Se asume que no existen gradientes internos de temperatura (hipótesis *Thermally Thin*) ni de composición en la partícula.

- El secado del combustible es controlado térmicamente y ocurre cuando se alcanza una temperatura de 373.15 (K) o superior.
- Se permite un *deslizamiento* de temperatura en el secado, repartiendo la energía que recibe la celda entre el aumento de temperatura y la energía consumida por el secado [185, 188].
- La densidad de la partícula disminuye durante el secado, devolatilización y las reacciones del char. Sin embargo, la fracción sólida sólo disminuye durante el proceso de devolatilización y las reacciones del char, causando la variación de volumen de las partículas.
- La humedad presente en el combustible sólido se considera dispersa, y por tanto no se considera a efectos de volumen de partícula.
- Las especies gaseosas generadas en el interior de la partícula son liberadas instantáneamente a la fase gas a temperatura de referencia y la energía retirada del lecho es introducida como fuente de energía en fase gas.
- La alimentación advectiva de pellets se realiza mediante un flujo continuo de fase sólida.
- La alimentación superior de pellets se realiza mediante trayectorias Lagrangianas durante las cuales se considera que no hay consumo alguno de masa hasta la llegada al lecho.
- En el lecho no se consideran rebotes de los pellets alimentados superiormente, si no que la trayectoria añade sus densidades y energía a la celda de llegada y después se reparte si es necesario por las celdas vecinas.
- Los colapsos locales del lecho están inducidos por el umbral de porosidad local máxima el cual los gobierna.
- Los valores de las celdas de lecho deben ser considerados como valores promediados volumétricamente que representan una región determinada del lecho, y no como partículas individuales contenidas en la celda, pues se pueden alcanzar situaciones en las que las celdas sean más pequeñas que las partículas.

A continuación, se muestran las ecuaciones de gobierno de las variables que caracterizan la fase sólida:

$$\frac{\partial(\varepsilon\rho_p h_s)}{\partial t} + \nabla(\varepsilon \cdot R_d \cdot v_s \cdot \rho_p \cdot h_s) = \nabla(k_{s,eff} \cdot \nabla T_s) + S_{h_s} \quad (18)$$

$$\frac{\partial \varepsilon}{\partial t} + \nabla(\varepsilon \cdot R_d \cdot v_s) = \left(\frac{\dot{\omega}_{wood}'''}{\rho_{wood}^s} + \frac{\dot{\omega}_{G,char}'''}{\rho_{char}^s} - \frac{\dot{\omega}_{C,char}'''}{\rho_{char}^s} \right) \varepsilon \quad (19)$$

$$\frac{\partial d_{eq}^3}{\partial t} + \nabla(\varepsilon \cdot R_d \cdot v_s \cdot d_{eq}^3) = \left(\frac{-\dot{\omega}_{wood}'''}{\rho_{wood}^s} + \frac{\dot{\omega}_{G,char}'''}{\rho_{char}^s} - \frac{\dot{\omega}_{C,char}'''}{\rho_{char}^s} \right) d_{eq}^3 \quad (20)$$

$$\frac{\partial(\varepsilon\rho_{moist})}{\partial t} + \nabla(\varepsilon \cdot R_d \cdot v_s \cdot \rho_{moist}) = -\omega_{moist}''' \cdot \varepsilon \quad (21)$$

$$\frac{\partial(\varepsilon\rho_{wood})}{\partial t} + \nabla(\varepsilon \cdot R_d \cdot v_s \cdot \rho_{wood}) = -\omega'''_{wood} \cdot \varepsilon \quad (22)$$

$$\frac{\partial(\varepsilon\rho_{char})}{\partial t} + \nabla(\varepsilon \cdot R_d \cdot v_s \cdot \rho_{char}) = (\omega'''_{G,char} - \omega'''_{C,char})\varepsilon \quad (23)$$

$$\frac{\partial(\varepsilon\rho_{ash,sol})}{\partial t} + \nabla(\varepsilon \cdot R_d \cdot v_s \cdot \rho_{ash,sol}) = 0 \quad (24)$$

$$\frac{\partial(\varepsilon\rho_{ash,vol})}{\partial t} + \nabla(\varepsilon \cdot R_d \cdot v_s \cdot \rho_{ash,vol}) = -\omega'''_{ash,vol} \cdot \varepsilon \quad (25)$$

$$\rho_p = \rho_{moist} + \rho_{wood} + \rho_{char} + \rho_{ash,sol} + \rho_{ash,vol} \quad (26)$$

Las ecuaciones de transporte incluyen un término transitorio, en su parte izquierda, que representa la variación temporal de cada variable. La temperatura del sólido se deriva de la entalpía del mismo, cuya ecuación de gobierno es la Ecuación (18). Es esta ecuación, el término difusivo modela la conducción entre sólidos mediante una conductividad térmica equivalente. En el resto de ecuaciones, no existe término difusivo por no existir difusión de masa entre ellos. En el lado izquierdo de cada ecuación de gobierno, existen dos términos, el transitorio y el advectivo. Este último solo existe en caso de alimentación advectiva, en él v_s representa el vector de velocidad de la alimentación y el parámetro R_d controla la difusividad no deseada de la fase sólida y se explica en el trabajo de Gómez et al. [187].

En el lado derecho, a excepción del término difusivo en la Ecuación (18) mencionado antes, se encuentran los términos fuente de cada escalar de la fase sólida. Los términos ω'''_i presentes en los términos fuentes de cada ecuación representan los ritmos de generación (subíndice G) y consumo (subíndice C) volumétricos de cada variable y se presentan a continuación:

$$\omega'''_{moist} = \tau \frac{\rho_p C_p}{L_{evap\ moist}} \frac{\partial T_s}{\partial t}, T_s \geq T_{evap} \quad (27)$$

$$\omega'''_{wood} = \rho_{wood} \sum_{i=1}^3 A_i \exp\left(-\frac{E}{RT_s}\right) \quad (28)$$

La devolatilización del combustible orgánico alimentado se divide en volátiles, char y tar. El ritmo de consumo de la madera (Ecuación (28)), se calcula a través de la suma de tres ecuaciones de Arrhenius, las cuales corresponden a cada uno de los tres procesos de conversión la madera. Diversos autores han propuesto cinéticas para estos procesos, la interfaz gráfica ofrece como valores por defecto los valores propuestos por Wagenaar et al. [189].

$$\omega'''_{C,char} = K_{glob}^{ox} A_v [O_2] M_C + K_{glob}^{g,1} A_v [CO_2] M_C + K_{glob}^{og,2} A_v [H_2O] M_C \quad (29)$$

El ritmo de consumo del char se obtiene a través de tres reacciones heterogéneas (oxidación, gasificación con dióxido de carbono y gasificación con vapor de agua) controladas mediante ecuaciones de Arrhenius. En la Tabla 8, se muestran las reacciones heterogéneas y las cinéticas planteadas.

Tabla 8. Reacciones heterogéneas del carbón y sus cinéticas [2, 190, 191].

Reacciones heterogéneas del char	Cinéticas
$C + \varphi O_2 \rightarrow 2(1 - \varphi)CO + (2\varphi - 1)CO_2$	$K^{ox} = 1.715 \cdot T_s \cdot \exp\left(-\frac{9000}{T_s}\right)$
$C + CO_2 \rightarrow 2CO$	$K^{g,1} = 3.42 \cdot T_s \cdot \exp\left(-\frac{1.56 \cdot 10^4}{T_s}\right)$
$C + H_2O \rightarrow CO + H_2$	$K^{g,2} = 5.7114 \cdot T_s \cdot \exp\left(-\frac{1.56 \cdot 10^4}{T_s}\right)$

El parámetro φ reparte los productos resultantes de la oxidación del char entre monóxido y dióxido de carbono. Este parámetro se calcula según la siguiente ecuación [192]:

$$\varphi = \frac{2 + 4.3 \exp\left(\frac{-3390}{T_s}\right)}{2 \left(1 + 4.3 \exp\left(\frac{-3390}{T_s}\right)\right)} \quad (30)$$

Los coeficientes globales de las reacciones heterogéneas, K_{glob}^{ox} , $K_{glob}^{g,1}$ y $K_{glob}^{g,2}$, se expresan a través de las siguientes cinéticas controladas térmicamente y por difusión de los agentes gasificantes en cada caso (oxígeno, dióxido de carbono y vapor de agua) mediante los coeficientes de transferencia de masa (K_m^{ox} , $K_m^{g,1}$ y $K_m^{g,2}$).

$$K_{glob}^{ox} = \frac{1}{\frac{1}{K^{ox}} + \frac{1}{K_m^{ox}}} \quad (31)$$

$$K_{glob}^{g,1} = \frac{1}{\frac{1}{K^{g,1}} + \frac{1}{K_m^{g,1}}} \quad (32)$$

$$K_{glob}^{g,2} = \frac{1}{\frac{1}{K^{g,2}} + \frac{1}{K_m^{g,2}}} \quad (33)$$

El término fuente S_{h_s} de la Ecuación (18) viene dado por la suma de la energía a causa de las reacciones, la energía intercambiada por procesos de convección y radiación con la fase gaseosa y la compensación por la energía asociada a la masa perdida debido a las variaciones de densidades y fracción sólida:

$$S_{h_s} = S_{h_s}^{reac} + S_{h_s}^{conv} + S_{h_s}^{rad} + S_{h_s}^{loss} \quad (34)$$

$$S_s^{reac} = -\dot{\omega}_{moist}''' \varepsilon LH_{moist} - \dot{\omega}_{wood}''' f_{gas} \varepsilon LH_{dev} + \varepsilon k_{s/g} [K_{glob}^{ox} A_V [O_2] M_C [(2\varphi - 1)\Delta H_{CO_2} + 2(1 - \varphi)\Delta H_{CO}] + K_{glob}^{g1} A_V [CO_2] M_C \Delta H_{g,1} + K_{glob}^{g2} A_V [H_2O] M_C \Delta H_{g,2}] \quad (35)$$

$$S_s^{conv} = h A_V (T_g - T_s) \quad (36)$$

$$S_s^{rad} = \int_0^{4\pi} \left[\alpha_s I(\vec{r},) - \frac{\alpha_s n^2 \sigma T_g^4}{\pi} \right] d\Omega \quad (37)$$

$$S_s^{loss} = (\dot{\omega}_{moist}''' + \dot{\omega}_{wood}''' f_{gas} + \dot{\omega}_{char}''') \varepsilon (C_p T_s)^{t-\Delta t} \quad (38)$$

Para realizar la combustión en fase gas se requiere de reactivos y reacciones químicas que resolver para obtener productos y una liberación o consumo de energía. Los diversos softwares CFD, al contrario de lo que ocurre con la combustión de sólidos, sí integran diversos modelos matemáticos para la combustión en fase gas, los cuales se abordarán posteriormente.

En primer lugar, es necesario explicar cómo estos reactivos son introducidos en el dominio. El aire necesario para la combustión, el cual se supone que está compuesto por oxígeno y nitrógeno únicamente (habitual en el modelado de combustión), se introduce de forma sencilla por fronteras específicas del dominio. Se trata pues de lo que se conoce como aire ideal seco, sin humedad. La descomposición térmica de la estructura orgánica de la biomasa da lugar a *tar*, gas y *char*, siendo los dos primeros compuestos volátiles.

Los volátiles que son producto de la descomposición térmica de la materia orgánica que compone la biomasa, son introducidos mediante términos fuente en aquellas celdas que cumplan ciertos requisitos, como tener una temperatura suficiente para descomponerse. La emisión de volátiles fue objeto de diversas consideraciones a lo largo de la evolución de su modelado. Los modelos más básicos contemplan la emisión de una lista reducida de volátiles en proporciones fijas, fruto del ajuste experimental, que conservan el balance de carbonos, oxígenos e hidrógenos. La proporción fija de volátiles independiente de la temperatura a la que se realice da lugar en muchos casos la violación de la ley de conservación de energía. Para solventarlo, Thunmann et al. [192] introdujo un nuevo método del cálculo de los volátiles generados, cuyo concepto es sencillo. En su método resuelve un sistema de ecuaciones que contempla el balance de carbonos, oxígenos, hidrógenos, el balance de energía, y para cerrar el sistema emplea dos ecuaciones de cierre experimentales.

Debido a que en este trabajo solo se considera una lista de especies relativamente corta, *tars* (representados por benceno), hidrocarburos ligeros (representados por metano), hidrógeno, monóxido de carbono, dióxido de carbono y agua, la solución del sistema de ecuaciones puede dar lugar a concentraciones negativas de especies.

Para evitarlo, se introducen estas restricciones en el cálculo y mediante un método iterativo se alcanza una solución que satisfaga las condiciones establecidas con un

error mínimo de energía, el cual será considerado en el modelo de combustión de forma que el balance de energía se mantenga.

$$\begin{bmatrix} Y_{H_2O} \\ Y_{H_2} \\ Y_{CO} \\ Y_{CO_2} \\ Y_{CH_4} \\ Y_{C_6H_6} \end{bmatrix} = \begin{bmatrix} 0 & 0 & 1/M_{CO} & 1/M_{CO_2} & 1/M_{CH_4} & 6/M_{C_6H_6} \\ 1/M_{H_2O} & 1/M_{H_2} & 0 & 0 & 2/M_{CH_4} & 3/M_{C_6H_6} \\ \frac{1}{2}/M_{H_2O} & 0 & \frac{1}{2}/M_{CO} & 1/M_{CO_2} & 0 & 0 \\ \zeta_{H_2O} & \zeta_{H_2} & \zeta_{CO} & \zeta_{CO_2} & \zeta_{CH_4} & \zeta_{C_6H_6} \\ 0 & 0 & 1 & -\Omega_1 & 0 & 0 \\ 0 & 0 & 0 & -\Omega_2 & 1 & 0 \end{bmatrix}^{-1} \cdot \begin{bmatrix} Y_{C,vol}/M_C \\ Y_{H_2,vol}/M_{H_2} \\ Y_{O_2,vol}/M_{O_2} \\ \kappa \\ 0 \\ 0 \end{bmatrix} \quad (39)$$

$$Y_{C,vol} = \frac{Y_{C,wood} - Y_{char} \cdot Y_{C,char}}{Y_{gas} + Y_{tar}} \quad (40)$$

$$Y_{H_2,vol} = \frac{Y_{H_2,wood} - Y_{char} \cdot Y_{H_2,char}}{Y_{gas} + Y_{tar}} \quad (41)$$

$$Y_{O_2,vol} = \frac{Y_{O_2,wood} - Y_{char} \cdot Y_{O_2,char}}{Y_{gas} + Y_{tar}} \quad (42)$$

$$\zeta_i = H_i + \int_{T_{ref}}^{T_{dev}} Cp_i dT \quad (43)$$

$$\kappa = \sum_i Y_i \zeta_i = H_i + \int_{T_{ref}}^{T_{dev}} Cp_i dT \quad (44)$$

Donde Ω_1 y Ω_2 son las ecuaciones experimentales de cierre del sistema de ecuaciones. A continuación, se mostrarán las reacciones homogéneas y las cinéticas empleadas en el modelo que sirve como base de desarrollo para esta tesis doctoral. Se tratan de reacciones de oxidación de benceno, metano, hidrógeno y monóxido de carbono con la ecuación reversible *Water-Gas Shift Reaction* de reformado.

Tabla 9. Reacciones homogéneas y sus cinéticas.

Reacciones homogéneas	Cinéticas
(R.1) $C_6H_6 + \frac{9}{2}O_2 \rightarrow 6CO + 3H_2O$	$R_{R.1} = 1.3496 \cdot 10^9 \cdot \exp\left(-\frac{1.256 \cdot 10^8}{RT}\right) [C_6H_6]^{-0.1} [O_2]^{1.85}$
(R.2) $CH_4 + \frac{3}{2}O_2 \rightarrow CO + 2H_2O$	$R_{R.2} = 5.012 \cdot 10^{11} \cdot \exp\left(-\frac{2 \cdot 10^8}{RT}\right) [CH_4]^{0.7} [O_2]^{0.8}$
(R.3) $H_2 + \frac{1}{2}O_2 \rightarrow H_2O$	$R_{R.3} = 9.87 \cdot 10^8 \cdot \exp\left(-\frac{3.1 \cdot 10^7}{RT}\right) [H_2][O_2]$
(R.4) $CO + \frac{1}{2}O_2 \rightarrow CO_2$	$R_{R.4} = 2.239 \cdot 10^{12} \cdot \exp\left(-\frac{1.702 \cdot 10^8}{RT}\right) [CO][O_2]^{0.25} [H_2O]^{0.5}$
(R.5) $H_2O + CO \rightarrow CO_2 + H_2$	$R_{R.5} = 2.780 \cdot \exp\left(-\frac{1.255 \cdot 10^7}{RT}\right) [H_2O][CO]$
(R.6) $CO_2 + H_2 \rightarrow H_2O + CO$	$R_{R.6} = 93690 \cdot \exp\left(-\frac{4.659 \cdot 10^7}{RT}\right) [CO_2][H_2]$

El software emplea la habitual ecuación de conservación para la resolución local de las fracciones másicas de las especies consideradas. Esta ecuación se expresa de la siguiente forma:

$$\frac{\partial(\rho Y_i)}{\partial t} + \nabla(\rho \vec{v} Y_i) = -\nabla(\vec{J}_i) + R_i + S_i \quad (45)$$

Donde Y_i es la fracción másica de la especie i , R_i es la tasa neta de producción de la especie debido a reacciones químicas, S_i el término fuente de creación o destrucción de esa especie y \vec{J}_i es la difusión de las especies.

Esta difusión de la especie i se puede expresar en la forma:

$$\vec{J}_i = -\left(\rho D_{i,m} + \frac{\mu_t}{Sc_t}\right) \nabla Y_i - D_{T,i} \frac{\nabla T}{T} \quad (46)$$

Donde Sc_t es el número turbulento de Schmidt, $D_{i,m}$ es el coeficiente de difusión másica de la especie y $D_{T,i}$ es el coeficiente de difusión térmica.

Estas especies reaccionarán según el esquema de reacciones químicas y sus cinéticas mostradas en la anterior tabla. Para modelar este fenómeno existen diversos modelos matemáticos que se mostrarán a continuación [180]:

- Uso directo de las cinéticas *finite-rate*: En este método se desprecia el efecto de la turbulencia sobre las reacciones, estando estas gobernadas únicamente por las ecuaciones de Arrhenius. Ideal para llamas laminares, pero impreciso en el caso de combustión turbulenta.
- Eddy-Dissipation Model, EDM: Basado en el trabajo de Magnussen y Hjertager [193], con este modelo se asume que la combustión está gobernada por el mezclado turbulento, despreciando el control cinético mediante ecuaciones de Arrhenius. Presenta un bajo coste computacional pero su precisión se limita al empleo de mecanismos de combustión de uno o dos pasos.
- Finite-Rate-Eddy-Dissipation Model, FR-ED: con este método, se combinan los dos modelos explicados y la tasa de reacción es gobernada por el menor de los dos. Este será el método escogido en este trabajo y, como se explicará a continuación, el potencial foco de ajuste para la captación de fenómenos ligados a la presencia de un lecho poroso.

6.3 Validación del modelo

Para lograr modelar con éxito los fenómenos de *fouling* y *slagging* es necesario obtener un campo gaseoso lo más realista posible en cuanto a distribución de especies, temperaturas y velocidades. Estas variables se encuentran influenciadas en gran medida por cómo se realiza la conversión térmica del combustible sólido en el lecho. Los aspectos fundamentales del modelo general de combustión de biomasa a ajustar y mejorar se engloban en tres líneas:

- Mejora de la geometría del lecho alcanzada durante la combustión.
- Optimización de los polinomios de devolatilización del combustible.
- Mejora en la predicción del mezclado turbulento en fase gaseosa de los reactivos.

La primera línea se abordó de forma interna en el Grupo de Tecnología Energética y será objeto de futuras tesis doctorales [194, 195]. En cuanto a las otras dos, se realizaron en colaboración con instituciones extranjeras.

Para el ajuste del modelo y la optimización del algoritmo que calcula los polinomios de devolatilización en especies gaseosas y las cinéticas consideradas, se realizó una colaboración con la Universidad de Antioquia, Colombia de la que surgió el artículo de González et al. [184] y que se encuentra en el ANEXO C..

Respecto a la mejora en la predicción del mezclado turbulento en fase gaseosa se realizó una colaboración con el Departamento de Ingeniería Mecánica del Instituto Superior Técnico de Lisboa, de la que surgió el artículo “Effect of the Turbulence-Chemistry Interaction in Packed-Bed Biomass Combustion” [183] que se engloba dentro de esta tesis y se adjunta a continuación.

En este artículo, se explica que en la comunidad científica existen numerosos autores que han logrado crear un modelar la combustión de biomasa sólida de formas muy diversas. Por ejemplo:

- Porteiro et al. [196] y Yang et al. [197] plantearon modelos lecho-gas segregados con comunicación a través de la radiación incidente.
- Gómez et al. [198, 199] y Mehrabian et al. [200-202] desarrollaron modelos de combustión de biomasa considerando los gradientes internos de la partícula (hipótesis *Thermally Thick*).
- Hermansson et al. [203] realizó un modelo multipartícula bidimensional que se centra en el *shrinkage* sufrido por el lecho debido a los procesos de alimentación, movimiento y combustión.
- Kurz et al. [204] realizó un modelo Euler-Euler como el empleado en este trabajo a través de una aproximación en un marco multifásico.
- Wiese et al. [205] y Simsek et al. [206] emplearon modelos DEM (*Discrete Element Method*).

Cuando se realizan estos modelados de mayor o menor complejidad, las simulaciones habitualmente se validan contra datos experimentales obtenidos de las emisiones por chimenea o de puntos lejanos al lecho. De esta forma, combustiones realizadas de forma muy distinta, con mayor o menor mezclado, mayor o menor volumen de llama, mayor o menor número de especies intermedias, pueden llegar a superar la validación experimental, pues al medir en regiones lejanas del lecho se diluye el efecto que tiene éste sobre la combustión cercana.

Es en este campo cercano al lecho, donde se pueden dar fenómenos cruciales para la combustión. En esta región, la combustión está fuertemente regida por su mezclado turbulento, pues la temperatura es lo suficientemente elevada como para no suponer un factor limitante. La presencia del lecho ralentiza o promueve este mezclado y en la mayoría de los modelos de combustión de biomasa se resuelve la interacción lecho-gas de forma simplificada, a través de un medio poroso isotrópico y homogéneo, donde se impone una pérdida de carga en base a la Ley de Ergun o la Ley de Darcy.

Esto provoca que se obvie la aparición de fenómenos como el *channeling*, por el que el aire encuentra una ruta preferente sin reaccionar ni mezclarse con los reactivos o la aparición de *gas streaks* por la rápida devolatilización de las partículas.

Sin embargo, al estudiar la combustión de biomasa en lecho fijo mediante técnicas CFD, es habitual emplear para la combustión en fase gaseosa el modelo EDM (*Eddy Dissipation Model*) o su combinación con control térmico FR-ED (*Finite Rate Eddy Dissipation*). Este modelo, desarrollado por Magnussen y Hjertager [193], se desarrolló y validó para combustiones en fase gas con fuerte turbulencia y mecanismos químicos sencillos. Lo cual entra en conflicto con la realidad de la devolatilización de la biomasa, donde pueden existir un número considerable de especies y reacciones intermedias que frenan la reactividad de la combustión, además de los mencionados fenómenos en el lecho.

El *Eddy Dissipation Model* se basa en tres hipótesis:

1. La tasa de combustión es infinitamente rápida.
2. La velocidad de consumo de combustible en llamas de difusión turbulentas está determinada únicamente por la velocidad de mezclado turbulento de los reactivos.
3. La velocidad de reacción es inversamente proporcional a la escala de tiempo de mezcla turbulenta (/).

En base a esas hipótesis, la velocidad de reacción (R) de una reacción genérica, r, con i especies involucradas se expresa como:

$$R_{i,r} = v'_{i,r} \cdot M_{w,i} \cdot A \cdot \rho \cdot \frac{\varepsilon}{\kappa} \cdot \min \left(\frac{Y_s}{v'_{s,r} \cdot M_{w,s}}, B \cdot \frac{\sum_p Y_p}{\sum_j (v''_{j,r} \cdot M_{w,j})} \right) \quad (47)$$

donde los subíndices s y p representan reactivos y productos, respectivamente, Y_s e Y_p representan sus respectivas fracciones de masa, los parámetros $v'_{i,r}$ y $v''_{j,r}$ representan los coeficientes estequiométricos para reactivos y productos, M_w es el peso molecular y las constantes A y B (constantes de Magnussen) corresponden a los parámetros de mezcla para los reactivos y productos, cuyos valores por defecto son $A = 4$ y $B = 0.5$.

En caso de estar combinado con el control cinético por temperatura, FR-ED, se computan las tasas de reacción obtenidas a través de Arrhenius y EDM, escogiendo siempre la menor de ellas.

Como se mencionó, en la región cercana al lecho, la temperatura es suficiente como para que la combustión se encuentre limitada y gobernada por su mezclado turbulento. Por lo tanto, las velocidades de reacción están controladas principalmente por la constante empírica A y la vida media del remolino (τ), como se puede ver en la Ecuación (47).

Autores como Scharler et al. [207] propusieron ajustar el valor de esta constante A propuesta por Magnussen a valores más próximos a la unidad, incluso 0.8, de forma que las reacciones se ralentizaran y las temperaturas alcanzadas en la región cercana fuesen más realistas. Lo cual no resulta coherente pues trata de forma igual la región afectada por el lecho y la región gaseosa abierta.

Por otra parte, Shiehnejadhesar et al. [208, 209] propone un modelo de interacción entre turbulencia y química basado en el número local de Reynolds combinado con un modelo de predicción de los *streaks*. El segundo se basa en la comparación del tiempo de residencia y de mezclado, a través de la comparación con una especie química que hace la función de trazador del mezclado. Aunque logran buenos resultados, se basan en la hipótesis de un lecho de esferas ideal con un flujo no reactivo, por lo que omiten la adición brusca de especies gaseosas dentro del lecho o la variación de la geometría del lecho a lo largo del tiempo.

A menudo, se considera el flujo dentro del lecho como laminar, pero existen evidencias de la aparición de vórtices en el interior del lecho a partir de $Re_d \sim 10$, en concreto, dos tipos de vórtices [210]. El primero, denominado *pseudo-vortex*, generado por el desprendimiento del flujo tras sortear la partícula y el segundo generado dentro del propio poro y denominado *void-vortex*. El segundo tipo puede ser tratado de la forma habitual ya que su longitud de escala es similar al tamaño del poro. Sin embargo, los *pseudo-vortex* pueden potencialmente perturbar el campo gaseoso a mayor distancia, por lo que la continua variación temporal de la geometría del lecho debe ser tomada en cuenta.

Por lo tanto, la conclusión principal de este trabajo es la necesidad de un mejor modelado de los fenómenos turbulentos dentro del lecho y de la interacción turbulencia-química. Estos modelos probablemente reducirán la necesidad de modificar las velocidades de reacción y proporcionarán una mayor precisión en el campo de velocidades del gas por encima del lecho.

Debido a esto, en el artículo mostrado a continuación se adelanta la sustitución de la constante A del modelo EDM por un parámetro A^* . En el futuro, este parámetro A^* no será un valor constante en todo el dominio, sino función de diversas variables que evolucionarán temporalmente y que deberán ser desgranadas. De esta forma, el modelo EDM y sus constantes originales, propuestas y validadas por Magnussen continuarán en vigencia.

La explicación en profundidad de este ajuste del modelo se encuentra en el artículo expuesto en el ANEXO A.1:

Reference

“Chapela, S., J. Porteiro, and M. Costa, *Effect of the Turbulence-Chemistry Interaction in Packed-Bed Biomass Combustion*. *Energy & Fuels*, 2017. 31(9): p. 9967-9982.”

Capítulo 7

Modelo de ensuciamiento Euler-Lagrange

7.1 Introducción

A lo largo de este trabajo se ha expuesto el desarrollo de un modelo de combustión de biomasa general independiente del tipo de alimentación y su posterior ajuste. Se mostró también la generación de la interfaz gráfica de usuario para la creación de una plataforma de colaboración internacional.

Sobre esta base, tras comprobar el adecuado desempeño del modelo de combustión de biomasa en lecho fijo, se comenzó el desarrollo del modelo de ensuciamiento. La primera aproximación se realizó a través del modelo de fase discreta o DPM embebido en ANSYS-Fluent®.

Como se explicó en el Problemática de la combustión de biomasa sobre la problemática que entraña la combustión de biomasa, su alto contenido de cenizas, especialmente en metales alcalinos, como el potasio y el sodio, y la presencia de cloro, causa severos problemas de deposición sobre las superficies de trabajo [42, 146, 211-215]. Weber et al. [216] concluyó que la biomasa genera hasta tres veces más deposición de materia no deseada sobre las superficies de trabajo que el carbón, si se normalizan ambos combustibles respecto a la ceniza introducida para la comparación.

A continuación, durante este capítulo, se expondrán los trabajos realizados durante el desarrollo de este modelo, los cuales han sido objeto de tres artículos, dos de ellos ya publicados y que se incluyen en esta tesis y un tercero que se encuentra en este momento en revisión por parte de una revista Q1 en el campo, el cual se adjuntará en el ANEXO B.1.

7.2 Modelado y algoritmia

Para el modelado de los fenómenos de emisión de materia particulada, vapores inorgánicos y subsecuentes problemas de deposición, se mantuvo en todo momento la idea de encontrar el equilibrio entre esfuerzo computacional y precisión en los resultados.

A lo largo de este trabajo se expuso una variedad de especies gaseosas precursoras de la deposición de materia no deseada. Esta variedad se debe a la heterogeneidad de composición de la biomasa y su ceniza. Para el desarrollo de este modelo, se estudiaron y analizaron los combustibles de uso habitual en el área experimental y se estimó que el principal precursor en estos era el cloruro de potasio, KCl. Debido a que todo desarrollo de modelos CFD debe tener una validación experimental sobre la que sustentarse, se elige emplear sólo este precursor por el momento, dejando la puerta abierta a la inclusión de nuevos precursores e incluso cinéticas de formación.

En el desarrollo del modelo de combustión, la ceniza era dividida en dos escalares, hecho que se aprovechará en este modelado:

- Escalar de ceniza sólida: En este escalar se contendrá la ceniza sólida no volátil, la cual será transportada con el movimiento del lecho.
- Escalar de ceniza volátil: En este escalar se contiene la ceniza sólida volátil, la cual es transportada con el movimiento del lecho y puede ser consumida y añadida a la fase gas.

Con el modelo de ensuciamiento propuesto en este capítulo, el escalar de ceniza sólida puede ser consumido mediante elutriación desde el lecho y convertirse en trayectorias Lagrangianas que viajan a lo largo del dominio interactuando con éste y con el gas de combustión.

Por otro lado, el escalar de ceniza volátil será el empleado para introducir la presencia del precursor en el lecho. Durante la combustión de la biomasa, este precursor se consumirá incorporándose a la fase gaseosa, para después condensar sobre las superficies o ser evaporado desde ellas.

Una vez convergida la simulación de la combustión de biomasa y condensación de vapores inorgánicas se procede al cálculo de las trayectorias Lagrangianas que derivarán en el cálculo de la deposición de materia no deseada sobre las superficies.

Para ello, el algoritmo realizará una búsqueda de las celdas de la frontera del lecho donde exista suficiente *drag* como para elutriar partículas de cada granulometría propuesta, ahorrando esfuerzo computacional al no generar trayectorias que no tendrían suficiente momento como para viajar con la fase gaseosa.

Para cada trayectoria, se hará empleo de procedimientos de seguimiento estocástico para evitar la naturaleza determinista de este tipo de trayectorias

Lagrangianas. En el viaje de cada una de las trayectorias, interactúan con el gas y sufren el efecto de las fuerzas expuestas en el Transporte de materia particulada, salvo las fuerzas de masa virtual, Basset y Magnus, debido a la gran diferencia existente entre las densidades de las fases, tal como propone Crowe [63].

En los casos en los que la partícula impacta sobre una superficie donde existe capa de precursor se calcula su probabilidad de adhesión a la misma. De resultar depositada, se almacenan sus propiedades físicas, acumulando la masa sobre cada celda superficial.

Una vez elutriadas todas las granulometrías deseadas, los datos de la deposición sobre la superficie son tratados mediante diversos algoritmos que proporcionan una estimación del perfil del depósito obtenido.

El esquema del algoritmo se muestra a continuación en la Figura 42:

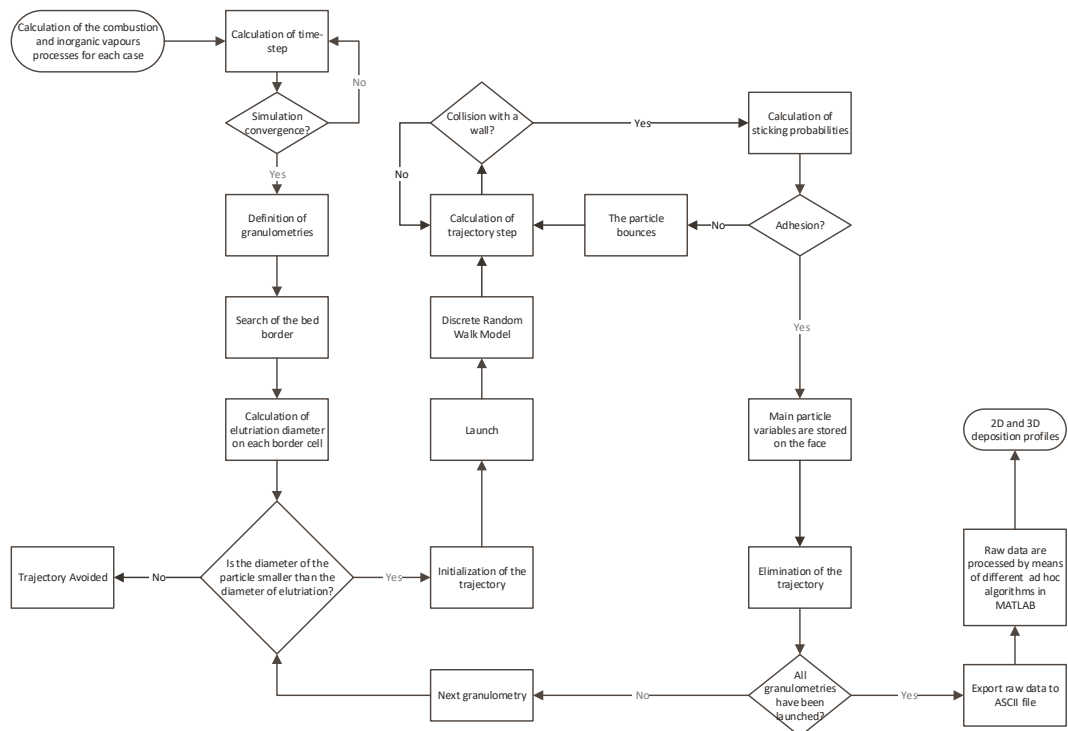


Figura 42. Algoritmo del modelo de ensuciamiento de Euler-Lagrange [45].

Se empleará por el momento la implementación realizada por el propio software para el modelado del movimiento Browniano, la fuerza de Saffman o *lift* y la fuerza termoforética. El movimiento Browniano se puede modelar como una fuerza cuyas componentes son modeladas como un proceso de ruido blanco Gaussiano con intensidad espectral, S_{ij}^n , dada por [180, 217-219]:

$$S_{ij}^n = S_0 \delta_{ij} \tag{48}$$

Donde δ_{ij} es la función delta de Kronecker y S_0 es igual a:

$$S_0 = \frac{216 \nu k_B T_{abs_g}}{\pi^2 \rho_g d_p^5 \left(\frac{\rho_p}{\rho_g}\right)^2 C_c} \quad (49)$$

La sustentación de Saffman se modela a través de una fuerza en la (11), y se calcula a través de la generalización realizada por Li y Ahmadi [217] de la expresión propuesta por Saffman [220]:

$$\overrightarrow{F_{saffman}} = \frac{5.188\sqrt{\nu} \rho_{gas} d_{ij} (\vec{u} - \vec{u}_p)}{\rho_p d_p^4 \sqrt{d_{lk} d_{kl}}} \quad (50)$$

La fuerza termoforética se implementa mediante la expresión propuesta por Talbot [221], que es válida:

$$\overrightarrow{F_{therm}} = \frac{6\pi d_p \mu^2 1.17(R_K + 2.18Kn) \nabla T}{\rho_g (1 + 3.42Kn)(1 + 2R_K + 4.36Kn) m_p T_{local_g}} \quad (51)$$

Donde K es el ratio entre la conductividad del gas basándose en la energía translacional únicamente y la conductividad de la partícula [180]:

$$R_K = \frac{k_g}{k_p} = \frac{15}{4} \frac{\mu R_g}{k_p} \quad (52)$$

En el trabajo que se adjunta en el ANEXO A.2 se presenta el resto del modelado en mayor detalle y su puesta a punto gracias a los datos experimentales que se tienen sobre la deposición.

Para comprobar su adecuado funcionamiento, se procede a realizar un diseño de experimentos CCD (*Central Composite Design*) [222] basado en la técnica LHS (*Latin Hypercube Sampling*) [223] en el que se evalúa el comportamiento del modelo de ensuciamiento ante la variación de la temperatura del agua de refrigeración, reparto de aire primario/secundario y caudal total de aire.

Para permitir la comparación directa entre casos del diseño de experimentos, se procede a elutriar en cada caso granulometrías que se corresponden con tiempos de relajación de partícula fijos que cubren los tres regímenes de deposición (difusión, inercia e impacto).

Finalmente se generan los perfiles de deposición en cada una de las 33 simulaciones y se comparan con los datos experimentales, mostrando un comportamiento adecuado.

Reference

“Chapela, S., et al., Comprehensive CFD modeling of the ash deposition in a biomass packed bed burner. *Fuel*, 2018. 234: p. 1099-1122.”

7.3 Mejora, optimización y validación frente a sistemas comerciales

Tras comprobar el funcionamiento del modelo se estima que su comportamiento es adecuado bajo las condiciones de la planta piloto GTE#1, por lo que se continúa evolucionando. El siguiente paso es adecuar el modelo a su empleo en sistemas domésticos comerciales.

Para ello, se eligen dos sistemas comerciales que difieren en varios aspectos entre ellos y a su vez con la planta piloto, por lo que servirán para comprobar la flexibilidad del modelado realizado. Estos sistemas son la KWB Multifire™ y la Vapormatra Cantina™.

La KWB Multifire™ es una caldera pirotubular, con turbuladores en el intercambiador, por lo que el entorno de deposición es muy diferente a la planta piloto GTE#1. Además, su sistema de alimentación es por ciclos ON/OFF, especialmente a media carga, donde la extensión del lecho y la ubicación de la frontera varía significativamente de un instante a otro.

La Vapormatra Cantina™ es una estufa acuotubular, similar a la planta piloto GTE#1, pero a diferencia de ésta presenta un haz tubular relativamente poblado sometiendo al gas de combustión a un giro de 180° y su sistema de alimentación es superior por caída, distinto a la planta piloto GTE#1. Este sistema crea fuertes variaciones en las propiedades de la frontera.

En estos sistemas se comprueba que el procedimiento de seguimiento estocástico empleado con anterioridad no resulta suficiente para capturar las alteraciones en el flujo de gas causadas por las alimentaciones de los modelos. Por lo que se requiere de la ejecución del modelo, sin este seguimiento estocástico, durante una ventana temporal suficiente como para ser representativa del funcionamiento de los sistemas.

Debido al alto coste computacional que esto supone, se dedican esfuerzos a la optimización del modelo y del algoritmo, el cual se muestra en la Figura 43. Los resultados obtenidos son prometedores y muestran grandes similitudes tanto en la respuesta transitoria de la combustión como en los resultados de la deposición al compararlos con los datos experimentales.

Los detalles de este trabajo se pueden consultar en el siguiente artículo, el cual se encuentra adjuntado en el ANEXO A.3:

Reference

“Chapela, S., et al., CFD study of fouling phenomena in small-scale biomass boilers: Experimental validation with two different boilers. *Renewable Energy*, 2019. 140: p. 552-562.”

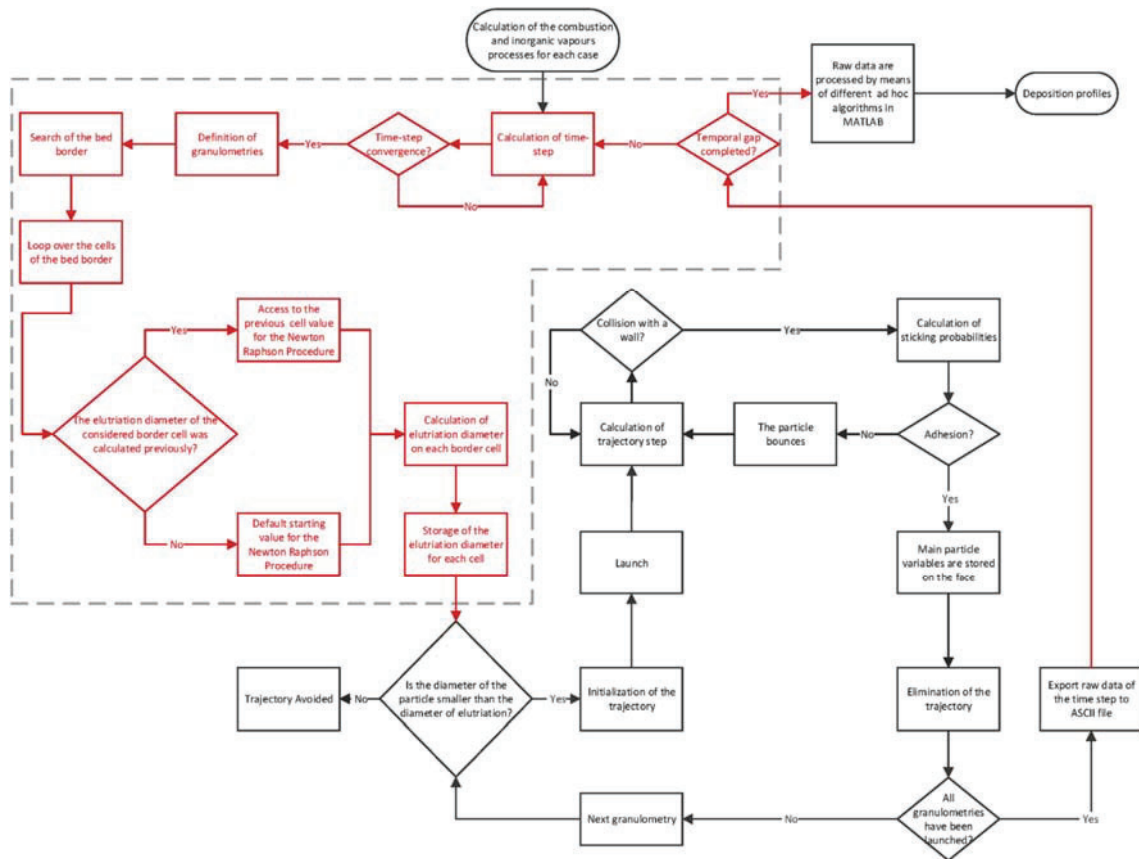


Figura 43. Modificación del algoritmo del modelo de ensuciamiento de Euler-Lagrange [182].

7.4 Modelado de propiedades térmicas

Una vez comprobado el buen comportamiento del modelo ajustado de combustión de biomasa en lecho fijo y el modelo de ensuciamiento Euler-Lagrange trabajando simultáneamente y que su coste computacional es asumible, se decide modelar el efecto que tiene el depósito sobre la transferencia de calor hacia el circuito de agua. Para ello será necesario modelar la porosidad, fracción derretida y su conductividad térmica equivalente, que será función de su tortuosidad, del depósito.

Es decir, es necesario añadir al modelo los siguientes cálculos en cada paso temporal y sobre cada celda superficial:

1. Masa de vapor inorgánico condensada
2. Masa de materia particulada adherida
3. Cálculo de la fracción de depósito derretida
4. Cálculo de la porosidad del depósito resultante
5. Cálculo del espesor de depósito en cada celda
6. Cálculo de la tortuosidad del depósito
7. Cálculo de la conductividad equivalente del depósito

Con estos resultados, se calcula la altura de la celda sólida adyacente a la cara sobre la que se adhiere depósito y, en cada paso temporal, se calcula una conductividad térmica equivalente. Posteriormente, se actualizan las propiedades locales de la celda sólida con la nueva conductividad térmica, reduciendo su transmisión de calor.

El modelo se desarrolla para que funcione sobre cualquier tipo de malla con espesor sólido declarado, adaptándose sin necesidad de intervención por parte del usuario. Para comprobar su funcionamiento, se ejecuta sobre una nueva caldera del Grupo de Tecnología Energética, la Ferroli Sun Mikro P7™.

Habitualmente en la simulación de sistemas de combustión de biomasa, se ahorra esfuerzo computacional obviando el modelado de la camisa de agua e imponiendo un coeficiente de convección estimado a una temperatura promedio del sistema. Esto puede inducir efectos secundarios y desviaciones en los resultados de transmisión de calor, especialmente en el modelado del ensuciamiento en calderas como la estudiada. En esta caldera, el pobre diseño de la cámara de combustión y la camisa de agua malgasta superficie de intercambio y de lugar a una deposición poco homogénea.

El artículo donde se explica en detalle esta evolución del modelo se encuentra en el ANEXO B.1, y actualmente está enviado a revista internacional donde se encuentra en estado de revisión por pares.

Reference

“Numerical transient modelling of the fouling phenomena and its influence on thermal performance in a low-scale biomass shell boiler. Chapela, S.; Cid, N.; Porteiro, J.; Míguez, J. L. Renewable Energy (en revisión)”

Capítulo 8

Nuevo modelo de ensuciamiento Euler-Euler

8.1 Introducción

Durante la evolución de la tesis se trabajó sobre un modelo de combustión Euleriano al que se le embebió un modelo de cálculo de ensuciamiento mediante una aproximación Euler-Lagrange. Este modelo sufrió múltiples evoluciones que lo optimizaron y mejoraron su respuesta. Tras alcanzar un desarrollo tal que cualquier optimización tendría un impacto leve de rendimiento y empeoraría otro ámbito desproporcionadamente, se continuó añadiéndole características, como el cálculo de propiedades térmicas expuesto.

Esto provoca que futuras evoluciones se realicen en base a la adición de características al modelo, por lo que su coste computacional probablemente sea cada vez mayor y se comience a alejar del objetivo inicial, un modelo de ensuciamiento eficaz y práctico para usuarios y empresas.

Además, se constató durante las simulaciones la pobre paralelización del modelado DPM proporcionado por el software, todo lo contrario del marco Euleriano. Para la realización de simulaciones en entornos multinúcleo (habitual en cualquier ordenador actual), el software divide la malla en tantas particiones como núcleos se disponga, con números aproximadamente iguales de celdas entre ellos de forma que las fronteras entre particiones sean lo menos extensas posible. Al ejecutar un lanzamiento de trayectorias DPM, éstas viajan interactuando con la fase continua a lo largo del dominio particionado. Por ello, la carga de trabajo se realiza en aquellos núcleos que corresponden a particiones que tienen trayectorias DPM que calcular, quedando los restantes núcleos a la espera de que finalicen.

En entornos con pocos núcleos, como estaciones de trabajo de 8 núcleos, lo habitual es que la mayor parte del tiempo existan trayectorias en todas las

particiones, pero el sector informático está evolucionando hacia procesadores con mayor número de núcleos físicos y no en que cada uno de éstos sea más veloz.

Los servicios de cálculo en la nube es una de las nuevas tendencias en auge. Permite alquilar potencia de cálculo bajo demanda sin tener que preocuparse de inversiones ni mantenimientos. En este tipo de sistemas, se trabaja en entornos altamente paralelos, encontrándose la simulación no solo en el mismo procesador, a veces incluso entre diversos servidores. Si se quiere lograr un modelo veloz y útil para la industria, no se deben escatimar esfuerzos en la paralelización del código.

Por ello, se alcanzó el momento de desarrollo en el que resulta oportuno comenzar desde cero con una nueva base, beneficiándose de todo lo aprendido hasta ahora. No obstante, no se considera que el modelo de ensuciamiento Euler-Lagrange esté obsoleto, si no que se decide abrir una nueva línea de investigación en paralelo bajo unas nuevas hipótesis.

8.2 Modelado y algoritmia

El nuevo modelado se realiza en un marco totalmente Euleriano, dada la idoneidad de esta aproximación a las granulometrías más pequeñas de la emisión de materia particulada. Como se recuerda, en las emisiones de materia particulada características de la combustión de biomasa existen dos picos, uno de ellos más predominante, que se sitúa por debajo de la micra, por lo que esta aproximación resulta idónea.

Para abordarlo será necesario migrar hacia un entorno multifásico, lo cual abre un nuevo mundo de posibilidades, modelos y elecciones a tomar. El primer paso es escoger cuál de los modelos propuestos se adecúa al problema planteado. Existen tres tipos de modelos [180]:

- *VOF* o *Volume Of Fluid*: modelo habitual para la simulación de dos fases inmiscibles donde se realiza un seguimiento de la superficie frontera o interfaz entre ambas fases sobre una malla fija. En el modelo VOF, las fases comparten un único conjunto de ecuaciones de momento, y se sigue la fracción de volumen de cada uno de los fluidos en cada celda computacional.

Las aplicaciones de este modelo incluyen flujos estratificados, llenados, salpicaduras, movimiento de grandes burbujas en un líquido, cálculo del desprendimiento de un chorro, etc.

- *Mixture Model*: diseñado para la simulación de dos o más fases, fluidas o granulares. Las fases se tratan como medios continuos interpenetrantes. El *Mixture Model* resuelve la ecuación de momento de la mezcla y prescribe velocidades relativas para describir las fases dispersas. Las aplicaciones del modelo de mezcla incluyen flujos con una carga pequeña de partículas, flujos burbujeantes, sedimentación y separadores ciclónicos. Este modelo también

permite la ausencia de velocidades relativas para las fases dispersas y de esa forma modelar un flujo multifásico homogéneo.

- *Eulerian Model*: es el modelo más complejo de los integrados en el software, ya que resuelve un conjunto de ecuaciones de momento, continuidad y energía por cada fase. El acoplamiento se logra a través de los coeficientes de intercambio de presión e interfase.

La manera en que se gestiona este acoplamiento depende del tipo de fases involucradas. Los flujos granulares (fluido-sólido) son manejados de manera diferente a los flujos no granulares (fluido-fluido). Para flujos granulares, las propiedades se obtienen de la aplicación de la teoría cinética. El transporte de momento entre las fases también depende del tipo de mezcla que se está modelando. Las aplicaciones de este modelo multifásico incluyen columnas de burbujas, suspensión de partículas y lechos fluidizados.

Siguiendo las sugerencias de la bibliografía, para el transporte neumático recomiendan el *Mixture Model* o el *Eulerian Model* si el flujo es granular. Para casos con sedimentación recomiendan el *Eulerian Model*. Si hay una amplia distribución de tamaño de las fases dispersas y las partículas más grandes no se separan del flujo de la fase primaria, el *Mixture Model* puede ser preferible por ser menos costoso computacionalmente. Sin embargo, si las fases dispersas se concentran solo en partes del dominio, se debe usar el modelo Euleriano en su lugar.

En resumen, en el caso que atañe al modelado de ensuciamiento en combustión de biomasa, el *Eulerian Model* es recomendado y será el escogido finalmente. Sin embargo, se hacen pruebas también con el *Mixture Model* por su menor coste computacional, pero se encuentran resultados con gran difusión, sin respuestas inerciales apreciables en las granulometrías de mayor tamaño y problemas en la respuesta ante sedimentación. Por lo que finalmente se descarta.

En este nuevo entorno del software, existen nuevos niveles de jerarquía de datos. La estructura aguas abajo es similar, pero ahora para cada fase existirá un dominio y sus estructuras de datos estarán conectadas por niveles entre sí y a su vez con un nuevo nivel llamado *superdomain*. Es decir, el *superdomain* es el dominio de la mezcla y superposición de todos los dominios o *domains*. Cada fase es adscrita a un *domain* distinto, y a su vez se crean *domains* adicionales denominados *interaction domains* donde se da lugar las interacciones entre pares de *domains*.

Una posible representación gráfica de esto se puede ver en la Figura 44, extraída del manual del software [224], donde se observa la superposición de los dominios y la concordancia entre las estructuras de datos de ellos.

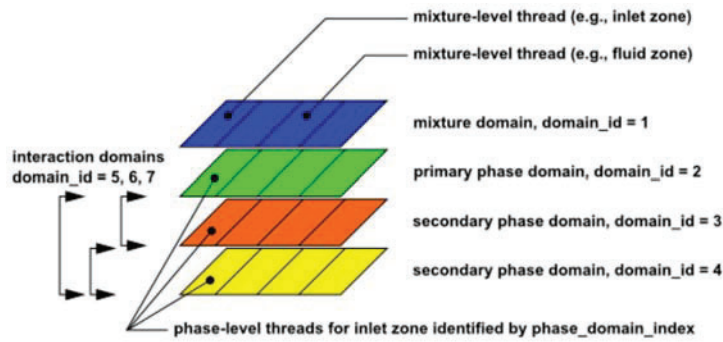


Figura 44. Estructura de dominios en entornos multifásicos [224] .

En base a lo expuesto, se procede a actualizar la jerarquía de datos expuesta en la Figura 32 en el Dinámica de fluidos computacional para entornos monofásicos, resultando la siguiente representación gráfica:

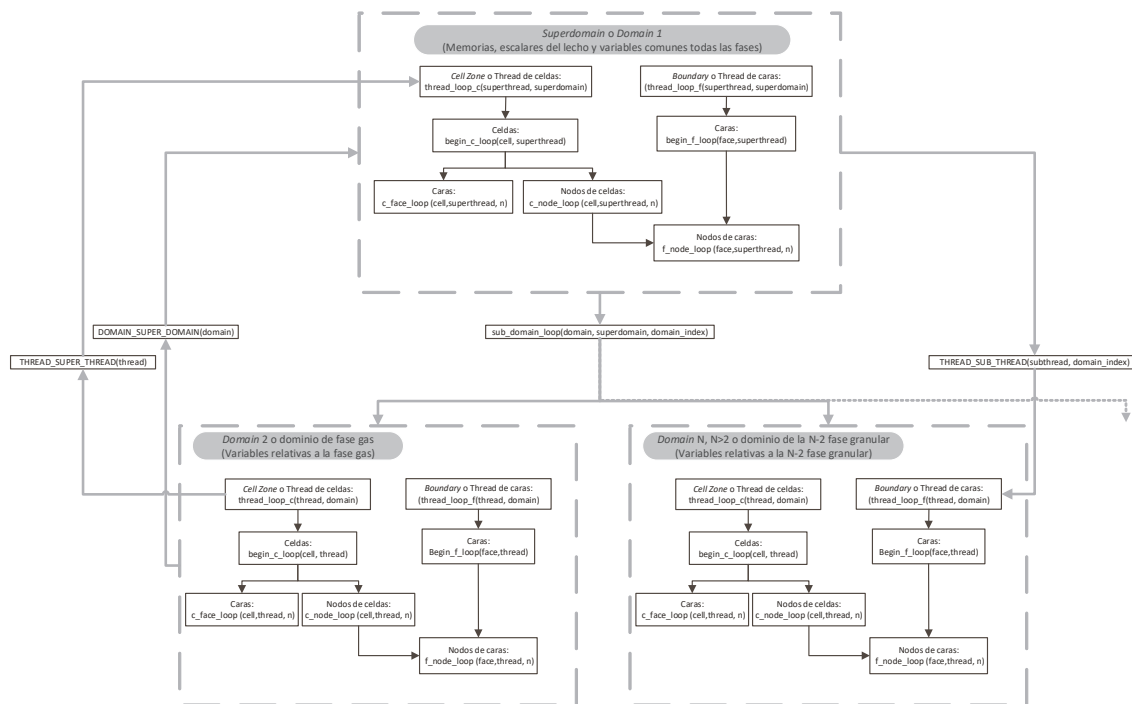


Figura 45. Jerarquía de la estructura de datos para un entorno multifásico.

Es decir, si en una celda se quiere realizar una operación que requiere de una variable global a todas las fases (como la presión), una memoria, un escalar del lecho, la concentración de una especie química del gas y la temperatura de una fase granular y grabar el resultado en otra fase granular distinta, se necesitarían por ejemplo los siguientes pasos:

1. Situarse en el *superdomain*.
2. Recorrer los *superthreads* del *superdomain* hasta la *cellzone* que contiene esa celda.
3. Recorrerlo y situarse en la celda.

4. Acceder al valor de la presión, la memoria y el escalar del lecho para esa celda.
5. Traslarse a la copia de la celda en el *thread* equivalente de la fase primaria, es decir, al *domain 2* o *subthread 0*.
6. Acceder al valor de la concentración de la especie química del gas.
7. Traslarse a la copia de la celda en el *thread* equivalente de la fase granular, es decir, *domain n* ($n > 2$) o *subthread m* ($m > 0$), donde ($m = n - 2$).
8. Acceder al valor de la temperatura de la fase granular.
9. Realizar la operación deseada con los *inputs*.
10. Traslarse a la copia de la celda en el *thread* equivalente de la otra fase granular, es decir, *domain p* ($p > 2$) o *subthread q* ($q > 0$), donde ($p = q - 2$), p n y q m .
11. Grabar o modificar el valor de la variable.

Como se puede ver, una operación que habitualmente se haría con tres punteros (dominio, *thread* y celda) ahora resulta mucho más compleja. Se requiere de una buena capacidad de abstracción para dar resuelto operaciones a menudo básicas.

Debido a esto, se necesitó reescribir el modelo de combustión de biomasa en lecho fijo desde los cimientos de forma que se adaptase a la nueva jerarquía de datos y a un número no conocido de fases y, por tanto, *domains*. Se busca la generalidad en el modelo y no imponer restricciones al usuario desde el inicio.

Tras la creación del nuevo modelo fue necesario volver a validar función a función para comprobar que no se había cometido algún error humano en el proceso. Es importante realizarlo función a función pues errores pequeños pueden pasar desapercibidos y ocultos en el gran volumen de datos de una simulación.

Tras la validación, se procedió a levantar el nuevo modelo de ensuciamiento Euler-Euler. Cabe destacar que se también se debe portar la formulación Lagrangiana empleada en el modelado anterior, al nuevo marco Euleriano.

Vapores inorgánicos y materia particulada

Tras portar con éxito el modelo de combustión de biomasa en lecho fijo a un entorno multifásico, se procede a desarrollar desde cero el modelo de ensuciamiento en este entorno.

El modelado de la evaporación, transporte y condensación de los vapores inorgánicos es el mismo que para el modelo Euler-Lagrange, salvando la nueva jerarquía de datos, ya que se encontraba modelado en formulación Euleriana.

Elutriación

Respecto a la materia particulada se han tenido que reformular los mecanismos de elutriación, transporte y atrapado. Como se mencionó en el apartado anterior, se consideran las fases como continuos interpenetrantes, donde la presión es única y común para todas ellas en cada celda. Cada fase presenta su propio conjunto de ecuaciones de continuidad, momento y energía y se introduce el concepto de fracción volumétrica de la fase tal como se muestra en la Ecuación (53):

$$V_i = \int_V \sigma_i \cdot dV \quad (53)$$

Donde la suma de todas las fracciones volumétricas es igual a la unidad,

$$\sum_{i=1}^n \sigma_i = 1 \quad (54)$$

Al finalizar cada paso temporal, se realiza una búsqueda de las celdas que contienen lecho y conforman una frontera del mismo. Es éstas, se calcula el diámetro de elutriación máximo a través de un balance entre el *drag* presente en la celda y la gravedad, como se explica en el trabajo [45]. Una vez se han localizado las celdas que conforman la frontera del lecho, se distribuye el flujo másico de cada granulometría considerada en función del *drag* presente en cada una, dándole prioridad a aquellas celdas que tienen más *drag*. Sin embargo, en el caso de que la masa a elutriar sea superior a la ceniza presente en la celda, se realiza un nuevo reparto iterativamente teniendo en cuenta las limitaciones de cada celda hasta lograr una solución, tal como se muestra en la Figura 46.

Una vez realizado el reparto y elutriada la fase granular, en forma de incremento de fracción volumétrica, viaja a lo largo del dominio interactuando con el gas de combustión y siendo afectada por los mecanismos expuestos en el Transporte de materia particulada. De nuevo, se desprecian las fuerzas de masa virtual, de Basset y de Magnus debido a la gran diferencia de densidades entre fase gaseosa y fase granular.

Transporte

Para cada fase i , la ecuación de continuidad se expresa como se muestra a continuación:

$$\frac{\partial}{\partial t} (\sigma_i \cdot \rho_i) + \nabla(\sigma_i \cdot \rho_i \cdot \vec{v}_i) = \sum_{i=1}^n (\dot{m}_{ij} - \dot{m}_{ji}) + S_i \quad (55)$$

Donde \dot{m}_{ij} y \dot{m}_{ji} representan la transferencia de masa entre las fases i y j respectivamente. S_i es el término fuente, cuyo valor puede ser positivo o negativo dependiendo si la fase granular es creada por elutriación desde el lecho o atrapada en las superficies del dominio.

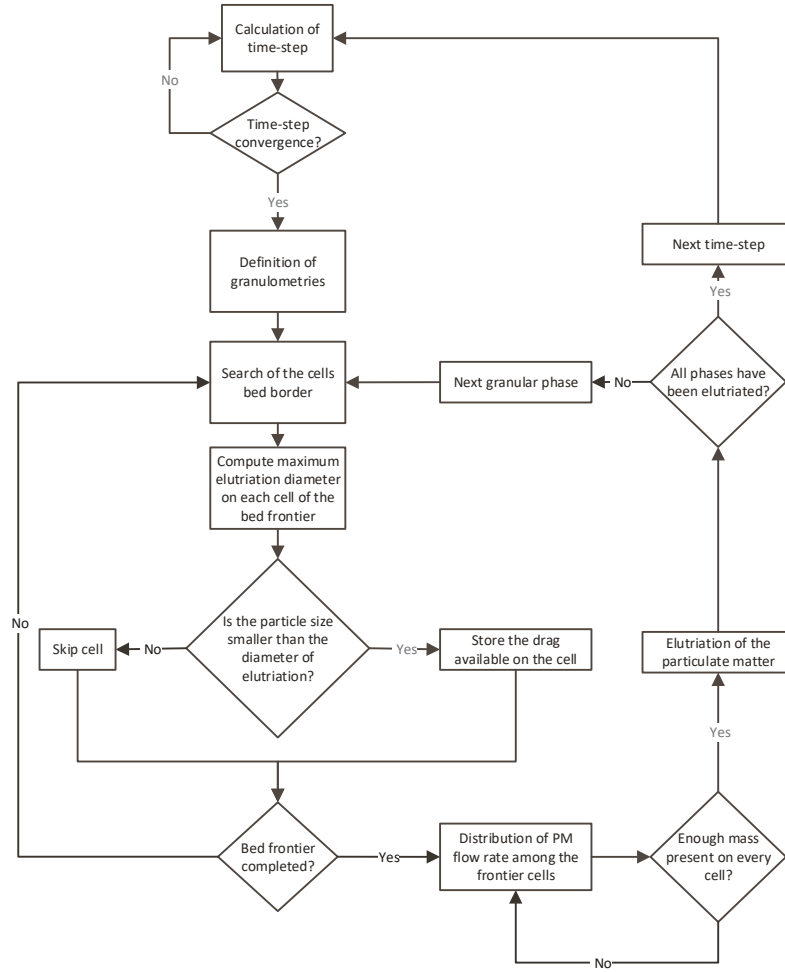


Figura 46. Algoritmo de distribución de la tasa de elutriación.

La ecuación de momento para la fase i puede ser expresada de la siguiente forma:

$$\begin{aligned}
 \frac{\partial}{\partial t}(\sigma_i \rho_i \cdot \bar{v}_i) + \nabla(\sigma_i \rho_i \bar{v}_i \bar{v}_i) \\
 = -\sigma_i \nabla p + \nabla \cdot \bar{\tau}_i + \sigma_i \rho_i \vec{g} \\
 + \sum_{j=1}^n (K_{ij}(\bar{v}_i - \bar{v}_j) + \dot{m}_{ij}\bar{v}_j - \dot{m}_{ji}\bar{v}_i) + (\vec{F}_i + \vec{F}_{lift,i} + \vec{F}_{wl,i} \\
 + \vec{F}_{vm,i} + \vec{F}_{td,i})
 \end{aligned} \quad (56)$$

Donde,

$$\bar{\tau}_i = \sigma_i \mu_i (\nabla \bar{v}_i + \nabla \bar{v}_i^T) + \sigma_i (\lambda_i - 2/3 \mu_i) \nabla \cdot \bar{v}_i \bar{I} \quad (57)$$

Donde μ_i y λ_i son la viscosidad dinámica y granular de la fase i , \vec{F}_i es una fuerza externa, $\vec{F}_{lift,i}$ es la fuerza de sustentación, $\vec{F}_{wl,i}$, la fuerza de lubricación de pared, $\vec{F}_{vm,i}$ la fuerza de masa virtual y $\vec{F}_{td,i}$ es la fuerza de dispersión turbulenta. En esta expresión, \bar{v}_{ij} es la velocidad de la interfase y los términos se desprecian ya que no se considera por el momento transferencia de masa entre fases granulares, por lo que

$\dot{m}_{ij} = 0$. Las ecuaciones de momento de las fases granulares deben ser cerradas con expresiones de los coeficientes de intercambio de momento, $\overline{K_{ij}}$, adecuados.

Estos coeficientes pueden ser escritos de la siguiente forma:

$$K_{ij} = \frac{\sigma_j \rho_j}{\tau_j} F \quad (58)$$

donde τ_j es, de nuevo, el tiempo de relajación de partícula, escrito de la siguiente forma:

$$\tau_j = \frac{\rho_j \phi_j^2}{18 \mu_q} \quad (59)$$

donde el subíndice q representa la fase continua, y el subíndice j cada una de las fases granulares. Por tanto ϕ_j y ρ_j son el diámetro y la densidad de la fase j.

El factor F, en la Ecuación (58), se puede definir de diversas formas dependiendo del modelo empleado. Todas las formas son función de *drag*, C_D , que a su vez es función del número de Reynolds relativo definido como:

$$Re_j = \frac{\rho_q \phi_j |\vec{v}_j - \vec{v}_q|}{\mu_q} \quad (60)$$

Syamlal-O'Brien [225] propuso el cálculo de los coeficientes K_{ij} a través de la función de *drag* derivada por Dalla Valle [226]. Sin embargo, este modelo se basa en mediciones de las velocidades terminales de partículas en lechos fluidizados

Wen y Yu [227] propusieron un modelo que es apropiado para sistemas considerados diluidos, donde el coeficiente de intercambio y la función de *drag* son:

$$K_{jq, Wen\&Yu} = \frac{3}{4} C_D \frac{\sigma_j \sigma_q \rho_q |\vec{v}_j - \vec{v}_q|}{\phi_j} \sigma_q^{-2.65} \quad (61)$$

$$C_D = \frac{24}{\sigma_q Re_j} [1 + 0.15(\sigma_q Re_j)^{0.687}] \quad (62)$$

Sin embargo, este modelo no sirve para el modelado de la sedimentación por gravedad, el cual es uno de los mecanismos que derivan en *fouling*. En situaciones de sedimentación, las fases no pueden considerarse localmente diluidas.

Para solventar este problema, Gidaspow [228] propuso una combinación entre el modelo de Wen y Yu [227] y la conocida ley de Ergun, cambiando entre ambas si la fracción volumétrica de la fase continua, σ_q , es inferior o superior a 0.8. Este modelo se recomienda para casos de lechos fluidizados densos, pero presenta una variación muy brusca en el punto de cambio que puede derivar en inestabilidades en el cálculo.

Para controlar estas inestabilidades, se propuso el modelo Huilin-Gidaspow [229], que añade una función de suavizado para controlar el cambio entre ambas formulaciones, situando este cambio en el valor de la fracción volumétrica de la fase continua igual a 0.2:

$$K_{jq} = \Upsilon K_{jq-Ergun} + (1 - \Upsilon) K_{jq-Wen\&Yu} \quad (63)$$

$$K_{jq-Ergun} = 150 \frac{\sigma_j(1 - \sigma_q)\mu_q}{\sigma_q \phi_j^2} + 1.75 \frac{\rho_q \sigma_j |\vec{v}_j - \vec{v}_q|}{\phi_j} \quad (64)$$

$$\Upsilon = \frac{1}{2} + \frac{\arctan(262.5(\sigma_j - 0.2))}{\pi} \quad (65)$$

En casos de sedimentación o flujo denso con bajo esfuerzo cortante, donde la fracción volumétrica se acerca al límite de empaquetamiento, los esfuerzos se deben principalmente a la fricción entre partículas. Para tener en cuenta este fenómeno, Schaeffer [230], propuso el siguiente modelos:

$$\mu_{friction} = \frac{p_{friction} \sin \varphi}{2\sqrt{I_{2D}}} \quad (66)$$

donde φ es el ángulo de fricción interna, por defecto 30° , I_{2D} es el segundo invariante del tensor de esfuerzos desviatorios y $p_{friction}$ es la presión de fricción definida como [231, 232]:

$$p_{friction} = 0.1\sigma_j \frac{(V\sigma_j - \sigma_{j,min})^2}{(\sigma_{j,max} - \sigma_s)^5} \quad (67)$$

Cabe mencionar, que en este trabajo se desprecian los efectos de compresibilidad en las fases que pueden ocurrir cuando se alcanzan valores límite de empaquetamiento, asumiendo no deformación en los sólidos.

El modelado de la turbulencia de flujos multifásicos es extremadamente complejo, debido al elevado número de términos presentes en las ecuaciones de momento, los cuales se incrementan con el número de fases involucradas. En este trabajo, se empleará el modelo de turbulencia k- habitual en este tipo de trabajos [45, 182, 183].

Una forma de afrontar la turbulencia de flujos multifásicos es emplear el *Mixture Turbulence Model*, donde se emplea un único conjunto de ecuaciones de turbulencia empleando las propiedades de la mezcla de fases, pero sólo es aplicable si las densidades de las fases involucradas son similares, algo que no se puede aplicar en este modelo.

Para este trabajo se debería emplear el *Dispersed Turbulence Model* o el más completo *Per Phase Turbulence Model*, donde se calcula el conjunto de ecuaciones de la turbulencia para cada fase. Sin embargo, el esfuerzo computacional

es muy elevado en el último caso, por lo que se empleará el modelo *Dispersed Turbulence Model*. Con esta decisión, se asume que la turbulencia de las fases granulares se puede representar a través de la turbulencia de la fase gaseosa y del ratio entre el tiempo de relajación de partícula y el tiempo de interacción de la partícula y el *eddy* o remolino. Sin embargo, si se desea, se puede emplear el modelo más completo de turbulencia.

Con el modelado turbulento empleado, *k- Dispersed Turbulence Model*, se añaden términos adicionales a las dos ecuaciones del modelo *k-* monofásico que incluyen la transferencia de momento turbulento.

Las predicciones de las cantidades turbulentas para las fases dispersas *j*, se obtienen mediante la teoría de Tchen de dispersión de partículas discretas en turbulencia homogénea [233]. Las ecuaciones de transporte de la fase continua o gaseosa, *q*, para el modelo *k-* multifásico son:

$$\begin{aligned} \frac{\partial}{\partial t}(\sigma_q \rho_q \cdot k_q) + \nabla \cdot (\sigma_q \rho_q \overline{U}_q k_q) \\ = \nabla \cdot \left(\sigma_q \left(\mu_q \frac{\mu_{t,q}}{\sigma_k} \right) \nabla k_q \right) + \sigma_q G_{k,q} - \sigma_q \rho_q \epsilon_q + \sigma_q \rho_q \Pi_{k,q} \end{aligned} \quad (68)$$

$$\begin{aligned} \frac{\partial}{\partial t}(\sigma_q \rho_q \cdot \epsilon_q) + \nabla \cdot (\sigma_q \rho_q \overline{U}_q \epsilon_q) \\ = \nabla \cdot \left(\sigma_q \left(\mu_q \frac{\mu_{t,q}}{\sigma_\epsilon} \right) \nabla \epsilon_q \right) + \sigma_q \frac{\epsilon_q}{k_q} (C_{1\epsilon} G_{k,q} - C_{2\epsilon} \rho_q \epsilon_q) \\ + \sigma_q \rho_q \Pi_{\epsilon_q} \end{aligned} \quad (69)$$

donde \overline{U}_q es la velocidad media de la fase, $\mu_{t,q}$ es la turbulencia viscosa y Π_{k_q} Π_{ϵ_q} son los términos fuente introducidos para modelar la influencia de las fases dispersas en la fase continua. Sin embargo, para este trabajo se consideran las fases granulares como diluidas, es decir se desprecian sus respectivos efectos en la turbulencia de la fase continua, por lo que ambos términos son nulos.

Para describir la conservación de energía, se resuelve una ecuación de entalpías para cada fase granular, de la forma:

$$\begin{aligned} \frac{\partial}{\partial t}(\sigma_i \rho_i \cdot h_i) + \nabla(\sigma_i \rho_i \overline{u}_i h_i) \\ = \sigma_i \frac{dp_i}{dt} + \overline{\tau}_i \cdot \nabla \overline{u}_i - \nabla \cdot \overline{q}_i + S_i + \sum_{i=1}^n (Q_{ij} + \dot{m}_{ij} h_{ij} - \dot{m}_{ji} h_{ji}) \end{aligned} \quad (70)$$

donde h_i es la entalpía específica para la fase *i*, \overline{q}_i es el flujo de calor y S_i es el término fuente de entalpía. En esta expresión, Q_{ij} es la intensidad de intercambio de calor entre fases y h_{ij} es la entalpía de la interfase. Como es lógico, el intercambio de calor entre fases debe cumplir con las condiciones de equilibrio locales.

La temperatura a la que las partículas impactan contra las superficies de trabajo del sistema es relevante para el modelado del fenómeno de *fouling*. Por ello, se debe

modelar adecuadamente el intercambio de calor entre las fases granulares, j , y continua, q . Se asume que la transmisión volumétrica de calor entre fases, Q_{qj} , es función de la diferencia de temperaturas y el área de la interfaz entre ambas, la cual está definida por unidad de volumen de la siguiente forma:

$$A_j = \frac{6\sigma_j}{\phi_j}(1 - \sigma_j) \quad (71)$$

Para la fase granular j , el área de la interfaz se calcula de forma que ésta se aproxime a cero cuando la fracción volumétrica de la fase, σ_j , se aproxime a la unidad

$$Q_{qj} = h_{qj} A_j (T_q - T_j) \quad (72)$$

donde h_{qj} es el coeficiente de transmisión de calor volumétrica entre la fase continua q y la fase granular j . Este coeficiente se expresa de la siguiente forma:

$$h_{qj} = \frac{K_q Nu_j}{\phi_j} \quad (73)$$

Para flujos granulares, Gunn [234] propuso la siguiente correlación para el número de Nusselt, la cual es aplicable para rangos de porosidad mayores de 0.35 y números de Reynolds relativo hasta 10^5 :

$$Nu_j = (7 - 10\sigma_q + 5 * \sigma_q^2) \left(1 + 0.7 * Re_j^{0.2} Pr^{\frac{1}{3}}\right) + (1.33 - 2.4\sigma_q + 1.2\sigma_q^2) Re_j^{0.7} Pr^{\frac{1}{3}} \quad (74)$$

Donde el número de Prandtl se define como:

$$Pr = \frac{C p_q \mu_q}{K_q} \quad (75)$$

Deposición

El mecanismo de deposición del nuevo modelo trabaja de forma similar al modelado Euler-Lagrange, empleando el *Melt Fraction Modelo* Modelo de Fracción Derretida explicado en el Apartado de Modelos de adhesión del Capítulo 2. De nuevo, se calculan las probabilidades de nuevo en función de la presencia de condensados y la existencia de fracción derretida suficiente como para garantizar la adhesión.

Los mecanismos que actúan sobre las fases granulares, hay que recordar que ya no existen partículas como tal, serán de nuevo:

- Regímenes de transporte
- Impacto Turbulento (*Turbulent Eddy Impaction*)
- Termoforesis

- Turboforesis

En esta ocasión, se debe convertir el modelado lagrangiano de las distintas fuerzas que actúan sobre las partículas a tasas de deposición en función de la presencia de fases granulares en la vecindad de las superficies del dominio.

Al igual que en el modelo anterior, el comportamiento de las fases granulares dentro del sistema será dependiente de su tiempo de relajación, definido como:

$$\tau_j^+ = \frac{\rho_j \phi_j^2 \rho_q u_{\tau q}}{18\mu} \quad (76)$$

Dependiendo del valor de este, se pueden considerar tres regímenes diferenciados que dictarán su comportamiento. No se requiere modelado expreso para este fenómeno pues las propias ecuaciones de momento de las fases dictarán su efecto.

En todos los mecanismos aparecerán los siguientes términos, por lo que se definen a continuación por simplicidad. τ_w es el esfuerzo cortante en la pared, ρ_q la densidad de la fase gaseosa, σ_j la fracción volumétrica de la fase granular j , ρ_j la densidad de la fase granular j , A_f el área de la celda superficial y V_c el volumen de la celda volumétrica adyacente a la cara.

Según el trabajo de Wood [235] and recientemente modificado por Fan y Ahmadi [236], la deposición causada por la difusión puede ser expresada como función del número de Schmidt de la fase granular j , Sc_j :

$$R_{diff} = \sqrt{\left(\frac{\tau_w}{\rho_q}\right)} \left(0.084 * Sc_j^{-\frac{2}{3}}\right) \left(\frac{\sigma_j \rho_j A_f}{V_c}\right) \quad (77)$$

Donde el número de Schmidt se calcula a través de la relación Stokes-Einstein para calcular la difusividad de la partícula D_p :

$$D_p = \frac{k_b T C_c}{3\pi\mu\phi_j} \quad (78)$$

Siendo k_b la constante de Boltzmann, ϕ_j el diámetro de la fase granular j , y C_c el coeficiente de corrección de Cunningham para el cual se ha calculado la distancia libre media del gas a través de la correlación propuesta por Mills [237]:

$$\lambda = v \sqrt{\frac{\pi M}{2R_g T}} \quad (79)$$

Donde v es la viscosidad cinemática y M la masa molecular.

El mecanismo de impacto turbulento resulta relevante para las fases granulares en régimen de inercia, donde un pequeño incremento en su diámetro da lugar a un

fuerte incremento en la deposición. Basado en resultados experimentales, Wood [235] presentó la siguiente expresión:

$$R_{turb} = \sqrt{\left(\frac{\tau_w}{\rho_q}\right)} \left((4.5 \cdot 10^{-4}) \tau_j^{+2}\right) \left(\frac{\sigma_j \rho_j A_f}{V_c}\right) \quad (80)$$

El mecanismo de la termoforesis es de gran relevancia en los intercambiadores de calor de los sistemas de combustión. En particular, en los sistemas domésticos actuales, los cuales cuentan con diseños muy compactos y trabajan con temperaturas de agua caliente sanitaria (ACS), por lo que se alcanzan gradientes de temperatura importantes.

Para las partículas en régimen de difusión hasta un régimen moderadamente inercial, la termoforesis aumenta significativamente la deposición. Las partículas ubicadas en la subcapa viscosa cerca de la superficie son transportadas por la fuerza termoforética hacia la superficie Cha y McCoy [238] propusieron un modelo aplicable para cualquier valor del número de Knudsen que capta adecuadamente el pico de fuerza termoforética que ocurre cuando el diámetro de la partícula es similar a la distancia media libre de las moléculas del gas de combustión [239].

$$F_{Thermophoretic} = \frac{1.15 Kn \left[1 - \exp\left(-\frac{\alpha}{Kn}\right)\right] \sqrt{\left[\frac{4\Theta\omega_1 Kn}{3\pi}\right]} \frac{\nabla T \phi_j^2 k_B}{d_m^2}}{4\sqrt{2} \alpha \left[1 + \frac{\omega_1 Kn}{2}\right]} \quad (81)$$

$$d_m = \sqrt{\frac{5}{16\mu}} \left(\frac{M k_B T_q}{\pi}\right)^{\frac{1}{4}} \quad (82)$$

$$\Theta = 0.25(9\gamma - 5) \left(\frac{c_v}{R}\right) \quad (83)$$

$$\alpha = 0.22 \sqrt{\frac{\left(\frac{\pi \Theta}{6}\right)}{1 + \frac{\omega_1 Kn}{2}}} \quad (84)$$

$$\omega_1 = 0.18 \frac{\left(\frac{36}{\pi}\right)}{\left(\frac{4(2 - S_n + S_t)}{\pi}\right) + S_n} \quad (85)$$

La tasa de deposición debida a la fuerza termoforética se expresa pues como:

$$R_{therm} = \sqrt{\left(\frac{\tau_w}{\rho_q}\right)} \left(\frac{F_{Thermophoretic} \tau_j^+}{m_j}\right) \left(\frac{\sigma_j \rho_j A_f}{V_c}\right) \quad (86)$$

La suma de estas tasas de deposición de cada mecanismo es entonces igual al término fuente de la Ecuación (55).

$$S_i = R_{diff} + R_{turb} + R_{therm} \quad (87)$$

Reducción de fases granulares

A lo largo de este capítulo se ha explicado cómo funciona el nuevo modelo de ensuciamiento Euler-Euler. Mientras se desarrollaba y comprobaba su funcionamiento, se desarrolló a su vez un algoritmo que permite reducir el número de fases granulares a emplear.

El concepto es sencillo, si varias fases de distintos diámetros se van a comportar de forma similar en la región donde se desea estudiar el fenómeno de *fouling*, se reducen a un número discreto de fases menor, con un diámetro ponderado por caudal másico y se elutria el caudal másico acumulado.

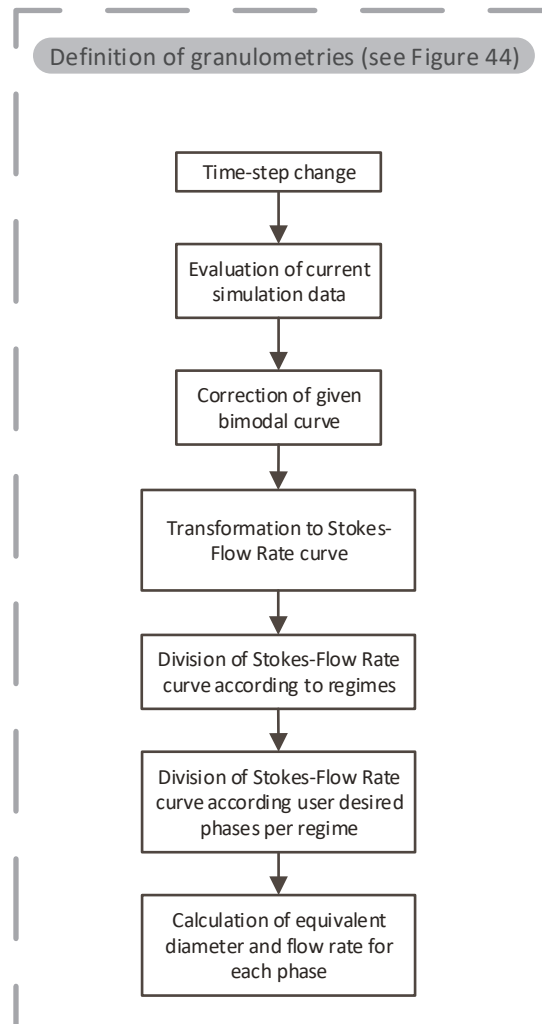


Figura 47. Algoritmo de reducción de fase granular.

Para realizarlo, se realizan los siguientes pasos mostrados en el diagrama de flujo de la Figura 47 y que se explican a continuación:

1. El usuario habrá impuesto un número discreto de fases granulares para modelar cada uno de los tres regímenes de transporte.
2. En el cambio de paso temporal, se analizan automáticamente los datos de interés del flujo en la región donde se quiere analizar y el punto de operación del sistema.
3. Con estos datos, se corrigen la distribución de granulometrías y caudales máscicos de partida que pueden ser tomados, por ejemplo, de una gráfica bimodal conocida del sistema.
4. Se transforman los tamaños de las partículas a su equivalente en número de Stokes modificado con los datos obtenidos de la simulación.
5. Se dividen las granulometrías en regímenes de difusión, inercia e impacto, y a su vez en el número discreto de fases granulares especificado por el usuario.
6. Se calcula el tamaño y caudal de cada nueva fase granular de forma que el caudal máscico se mantenga y el tamaño se calcule por medio de una media ponderada por caudal.
7. Se calcula la simulación con el nuevo set de fases granulares.

De esta forma, se reduce el número de fases a calcular y con ello el coste computacional de la simulación CFD.

Los resultados de todos estos modelos y algoritmos trabajando simultáneamente se pueden comprobar en el artículo enviado, y que se encuentra bajo revisión por pares por parte de la revista, que se adjunta en el ANEXO B.2.

Referencia

“Eulerian CFD fouling model for fixed-bed biomass combustion systems. Chapela, S.; Porteiro, J.; Míguez, J. L.; Behrendt, F. Fuel (en revisión)”

Capítulo 9.

Coherencia y unidad de las publicaciones

En esta sección se exponen los artículos originales publicados y que se engloban en esta tesis, la cual ha sido elaborada bajo la modalidad de compendio de artículos.

El trabajo expuesto en esta tesis ha sido elaborado en el marco de una misma línea de investigación, el modelado numérico de los mecanismos involucrados en el ensuciamiento y deposición de partículas en combustión de biomasa. Para lograr los objetivos ha sido necesaria la validación del modelo de combustión de biomasa en lecho fijo, cuyo planteamiento y resultados han sido objeto de la siguiente publicación:

“Effect of the Turbulence–Chemistry Interaction in Packed-Bed Biomass Combustion. Chapela, S.; Porteiro, J.; Costa, M. *Energy & Fuels*, 2017, 31 (9), 9967-9982. 10.1021/acs.energyfuels.7b00516”

Sobre este modelo de combustión se ha desarrollado el modelo numérico de ensuciamiento Euler-Lagrange, cuyo comportamiento ante la variación de los principales parámetros de operación ha sido validado sobre la planta piloto GTE#1. El planteamiento de este modelo de ensuciamiento y los resultados obtenidos han sido objeto de la publicación:

“Comprehensive CFD modeling of the ash deposition in a biomass packed bed burner. Chapela, S.; Porteiro, J.; Gómez, M.A.; Patiño D.; Míguez, J. L. *Fuel*, 2018, 234, 1099-1122. 10.1016/j.fuel.2018.07.121”

Posteriormente, el modelo de ensuciamiento Euler-Lagrange ha sido optimizado y adecuado para su empleo en sistemas comerciales de combustión de biomasa. La optimización del algoritmo y los resultados logrados en su aplicación a dos sistemas comerciales se han publicado en:

“CFD study of fouling phenomena in small-scale biomass boilers: Experimental validation with two different boilers. Chapela, S.; Porteiro, J.; Garabatos, M.; Patiño D.; Gómez, M.A.; Míguez, J. L. *Renewable Energy*, 2019, 140, 552-562. 10.1016/j.renene.2019.03.081”

Este modelo ha continuado evolucionándose mediante la implementación de nuevas características que han sido descritas en el manuscrito, actualmente en revisión por pares, que puede consultarse en el ANEXO B.1.

“*Numerical transient modelling of the fouling phenomena and its influence on thermal performance in a low-scale biomass shell boiler.* Chapela, S.; Porteiro, J.; Garabatos, M.; Patiño, D.; Gómez, M.A.; Míguez, J.L. *Renewable Energy* (en revisión).”

Durante el cálculo de este último trabajo, se analizó la principal debilidad de este modelo, su coste computacional en entornos paralelos. Se procedió entonces al planteamiento del modelo de ensuciamiento bajo una aproximación Euler-Euler. Los resultados obtenidos con él fueron comparados con los obtenidos por modelo de ensuciamiento Euler-Lagrange, y han sido objeto de otro manuscrito actualmente en revisión por pares. Este trabajo puede consultarse en el ANEXO B.2

“*Eulerian CFD fouling model for fixed-bed biomass combustion systems.* Chapela, S.; Porteiro, J.; Míguez, J. L.; Behrendt, F. *Fuel* (en revisión)”

Capítulo 10

Conclusiones

La sociedad actual está tomando conciencia de la huella ecológica que su modelo energético provoca en el entorno. Debido a ello ha comenzado a investigar y desarrollar nuevos sistemas energéticos basados en el empleo de energías renovables. Dentro de estos sistemas energéticos, la biomasa se presenta como una de las energías renovables más viable a corto plazo por varios motivos. Entre estos motivos se suele resaltar la facilidad de convertir cadenas de suministro de combustible similares e igual sucede con parte de los sistemas de combustión.

Este trabajo busca contribuir al despliegue de los sistemas de combustión de biomasa de forma más factible y eficaz. Busca realizarlo, no de forma individual, sino a través de aportar a la comunidad científica una plataforma de desarrollo donde poder sumar las experiencias y conocimientos de expertos en diversos campos relacionados. Todo esto tratando de no alejarse del usuario final, evitando herramientas con costes computacionales inasumibles.

Por ello, se ha creado una base de desarrollo común con un código de combustión de biomasa independiente del sistema de alimentación, controlado desde una interfaz de usuario gráfica (GUI) creada en el lenguaje de programación *Scheme* para poder ser embebida en la interfaz del software ANSYS-Fluent®.

Esta plataforma se ha puesto a prueba en varias colaboraciones con investigadores de centros de prestigio de otros países con buenos resultados, lo que ha servido para la puesta a punto del modelo de combustión y que ha motivado el primer artículo “*Effect of the Turbulence–Chemistry Interaction in Packed-Bed Biomass Combustion*. Chapela, S.; Porteiro, J.; Costa, M. *Energy & Fuels*, 2017, 31 (9), 9967-9982. 10.1021/acs.energyfuels.7b00516”.

En este primer artículo se abordan los inconvenientes existentes en el modelado de la interacción turbulencia-química ante la presencia de un lecho representado como un medio poroso isotrópico. Mediante esa representación se descartan los

fenómenos de *channeling* y *gas streaks* cuyo efecto es relevante en el campo gaseoso cercano al lecho. Por ello, se procedió a analizar la idoneidad de los modelados numéricos existentes en la bibliografía para abordar estos fenómenos, poniendo de relieve la no existencia en la actualidad de un modelo que tuviera en cuenta la generación de estos fenómenos en un lecho reactivo transitorio. En este trabajo, se planteó una modificación del modelo *Eddy Dissipation Model*, incorporándole un nuevo parámetro A^* .

En una primera aproximación, este parámetro es constante a lo largo del dominio y se encontró que, para el modelo de combustión de biomasa en lecho fijo, valores de A^* entre 2 y 3 son capaces de predecir con mayor precisión los perfiles de temperatura y principales especies gaseosas. Finalmente, en este trabajo se hace hincapié en la necesidad de un modelado donde el parámetro A^* sea función de múltiples parámetros y tenga en cuenta la variación temporal de la morfología del lecho y su reactividad.

Sobre este modelo de combustión se ha desarrollado un modelo de ensuciamiento, basado en una aproximación Euler-Lagrange. El comportamiento de este modelo se ha puesto a prueba en la planta piloto GTE#1, la cual permite controlar el caudal de aire suministrado, el reparto de aire primario y secundario y la temperatura del agua que circula por la sonda de deposición. Se realizó un exhaustivo estudio con la simulación de 33 puntos de operación, obtenidos mediante la variación de estos tres parámetros. Los resultados muestran en la segunda publicación “*Comprehensive CFD modeling of the ash deposition in a biomass packed bed burner*. Chapela, S.; Porteiro, J.; Gómez, M.A.; Patiño D.; Míguez, J. L. *Fuel*, 2018, 234, 1099-1122. 10.1016/j.fuel.2018.07. 121”

Estos resultados numéricos muestran que una menor temperatura del agua conduce a la generación de una mayor cantidad de vapores inorgánicos condensados. Por otro lado, un menor caudal de aire primario reduce la temperatura de lecho y, por tanto, la emisión de estos vapores inorgánicos. Adicionalmente, las velocidades del gas en el lecho son menores, dando lugar a una menor elutriación de materia particulada gruesa y, por consiguiente, una menor tasa de depósito en la parte inferior de la sonda. El incremento de aire primario, bien por un mayor aporte total de aire o por un mayor ratio de aire primario frente a aire secundario, da lugar a una deposición menos homogénea. La desviación causada por la inclinación de la parrilla y la entrada lateral del aire secundario es capturada de forma adecuada por el modelo propuesto.

Los perfiles de deposición obtenidos son más abruptos de lo que cabría esperar debido a la naturaleza determinista de las trayectorias Lagrangianas y a que su cálculo se realiza tras la convergencia de la combustión. El método de cálculo estocástico empleado para tener en cuenta las desviaciones causadas por la turbulencia no resulta suficiente para capturar la variación temporal de las velocidades del campo gaseoso.

Por ello, se procede a realizar el cálculo a lo largo de una ventana temporal tras alcanzar la convergencia de la combustión. De esta forma, el modelo de

ensuciamiento es capaz de capturar más apropiadamente las oscilaciones inherentes de la combustión de biomasa. Con esta decisión, el modelo de ensuciamiento es capaz de capturar también las oscilaciones inducidas por la alimentación discontinua de los sistemas comerciales estudiados. Debido al incremento en coste computacional se realiza un esfuerzo continuo para la optimización del algoritmo, logrando finalmente su viabilidad.

Esta evolución del modelo se emplea sobre dos sistemas de combustión comerciales distintos entre sí y respecto a la planta piloto GTE#1. Estos sistemas son la KWB Multifire™ y la Vapormatra Cantina™. Debido a que no se dispone de datos relativos a la geometría del depósito se analizan las tasas de deposición en cada uno de los testigos colocados en ambos sistemas. Los resultados obtenidos con este modelo son salientables para ambos sistemas domésticos, capturando de forma adecuada la distribución de las tasas de deposición entre los testigos, y han sido objeto de la publicación “*CFD study of fouling phenomena in small-scale biomass boilers: Experimental validation with two different boilers*. Chapela, S.; Porteiro, J.; Garabatos, M.; Patiño D.; Gómez, M.A.; Míguez, J. L. *Renewable Energy*, 2019, 140, 552-562. 10.1016/j.renene.2019.03.081 ”

Tras los buenos resultados obtenidos, se continúa añadiendo características al modelo de ensuciamiento Euler-Lagrange. El primer paso a desarrollar es modelar la reducción en la conductividad térmica causada por la presencia del depósito sobre la superficie. Para ello, se procede a emplear el modelo de ensuciamiento Euler-Lagrange a lo largo de la simulación transitoria de un nuevo sistema de combustión, la caldera Ferroli Sun Mikro P7™.

Para esta simulación, se modela también la camisa de agua de la caldera. De esta forma, se evitan efectos colaterales causados por el empleo de una transferencia de calor mediante una convección impuesta con una temperatura de agua promediada y homogénea en todo el sistema. Los resultados obtenidos muestran la idoneidad de considerar la simulación de la camisa de agua debido al pobre diseño de esta. Al final de cada paso temporal se calcula el espesor de depósito, su nivel de sinterización y la conductividad térmica estimada del mismo.

Con estos datos, se calcula y modifica la conductividad térmica equivalente de la celda sólida adyacente. Esto modificará el comportamiento del modelado de la condensación de vapores inorgánicos y la temperatura de la pared expuesta al gas, modificando la probabilidad de adhesión de más materia particulada.

Los resultados obtenidos muestran un comportamiento adecuado, si bien las exigencias computacionales del modelo no permiten abordar la simulación del suficiente tiempo de operación del sistema. Los resultados experimentales obtenidos, tras un amplio tiempo de operación, muestran un espesor de depósito considerable. Este espesor de depósito, especialmente en la cámara de combustión principal, obliga a ser cautelosos en la comparación directa de los resultados numéricos y experimentales. Este trabajo es objeto de la publicación “*Numerical transient modelling of the fouling phenomena and its influence on thermal performance in a*

low-scale biomass shell boiler. Chapela, S.; Porteiro, J.; Garabatos, M.; Patiño, D.; Gómez, M.A.; Míguez, J.L.”, la cual se encuentra actualmente en proceso de revisión por pares en la revista *Renewable Energy*.

Durante el desarrollo y cálculo de este último trabajo, se analizaron en detalle los puntos débiles del modelo de ensuciamiento Euler-Lagrange, más concretamente su rendimiento de paralelizado, balance del uso de memoria entre núcleos y evolución temporal a lo largo del paso temporal. Su rendimiento de paralelizado y balance de memoria entre núcleos disminuye rápidamente con el incremento de núcleos. La evolución del uso de memoria a lo largo del paso temporal revela un gran desbalance entre el uso medio y la máxima cantidad requerida, fruto de una necesidad de memoria elevada durante periodos puntuales.

Debido a esto, se comienza el desarrollo de un nuevo modelo de ensuciamiento realizado totalmente en un marco Euleriano, el modelo de ensuciamiento Euler-Euler. Para su empleo ha sido necesario migrar el modelo general de combustión de biomasa en lecho fijo por completo a un entorno multifásico, con nuevas estructuras de datos, y validarlo de nuevo. Sobre este modelo multifásico de combustión de biomasa se ha escrito el nuevo modelo de ensuciamiento, el cual ha requerido de la reformulación de los mecanismos que actúan sobre las fases granulares.

Los resultados obtenidos, sobre la planta piloto GTE#1, muestran la bondad de la nueva aproximación en cuanto a su menor coste computacional y a la obtención de perfiles de deposición menos abruptos que con el anterior modelado. Si bien, la formulación de nuevos mecanismos involucrados en el transporte y deposición de materia particulada es mucho más compleja y el modelado de la sedimentación debe ser mejorado.

Los resultados obtenidos con este nuevo modelo, y su comparación con el modelo de ensuciamiento Euler-Lagrange y con los resultados experimentales, han sido objeto de la publicación que se encuentra actualmente en proceso de revisión por pares “*Eulerian CFD fouling model for fixed-bed biomass combustion systems*. Chapela, S.; Porteiro, J.; Míguez, J. L.; Behrendt, F.” en la revista *Fuel*.

Capítulo 11

Líneas futuras

Durante la realización de este trabajo se han detectado diversos campos o líneas de investigación que sería interesante abordar. Estas líneas nuevas, cuyo desarrollo en algunos casos sería propio de nuevas tesis doctorales, se pueden agrupar en tres bloques:

- Modelado de lecho
- Modelado de depósito
- Implementación de modelo

11.1 Modelado de lecho

En este apartado de líneas futuras se engloban todos los aspectos relacionados con modelado de fenómenos de lecho. Se pueden mencionar las siguientes:

- *Thermally Thick Model*: El desarrollo del modelo de combustión general considerando gradientes internos a la partícula (hipótesis *Thermally Thick*) evitará el exceso de temperatura en el campo cercano al lecho derivado de la hipótesis *Thermally Thin*.
- Acoplamiento Turbulencia-Química: Con el primer artículo incluido en esta tesis [183] se mostró la necesidad de un modelado adecuado del acoplamiento turbulencia-química en la cercanía del lecho. Modelado que debía ser capaz de captar los fenómenos (*channeling, gas streak, blow-off*) que alteran el mezclado turbulento en esta región. Este modelado debe tener en cuenta la geometría no estacionaria de un lecho reactivo. Se trata de una línea de desarrollo con un gran potencial y cuyo efecto evitará ajustes experimentales de otros modelos.
- Multidiámetro por celda: Un modelado de lecho Euleriano que permita tener una distribución de diámetros en cada celda en vez de un único diámetro

medio para toda la celda permitirá la posibilidad de un modelado de elutriación más avanzado.

11.2 Modelado de depósito

En el aspecto de modelado de depósito numerosas características pueden ser objeto de líneas futuras, especialmente si no se tiene en cuenta el impacto en coste computacional que éstas pueden provocar:

- Inclusión de más especies precursoras: La inclusión de más precursores permitirá una mayor flexibilidad del modelo en cuanto a tipos de biomasa. Resulta interesante para el modelado del ensuciamiento de sistemas de combustión que empleen residuos agrícolas o urbanos. Si bien, se requieren datos experimentales completos para realizar la validación.
- Cinéticas: La inclusión de más especies precursoras se puede mejorar a través de la introducción de la discretización de los elementos químicos de la ceniza y la incorporación de cinéticas de formación de compuestos precursores. No obstante, el coste computacional sería muy elevado y su validación experimental complicada.
- Movimiento de condensados: Los condensados sobre superficies expuestas al gas de combustión sufren los efectos de las fuerzas gravitatorias y los esfuerzos cortantes del gas. Esto puede derivar en un desplazamiento físico de los mismos a lo largo de la superficie que altere la formación del depósito.
- Modelado del bloqueo volumétrico: En esta línea se han realizado pequeños avances mediante el empleo de malla dinámica. La presencia de depósito geoméricamente modelado permite mejorar el comportamiento a largo plazo de los fenómenos de erosión y deposición por la variación del campo fluido y su esfuerzo cortante en el entorno cercano. También permite no necesitar de modelados matemáticos que modifiquen las propiedades térmicas del material como se propuso en esta tesis, ya que existirá como tal la capa de baja conductividad depositada.
- Movimiento de fase derretida: La capa de materia depositada puede alcanzar su punto de fusión y convertirse en un flujo viscoso bajo la actuación de la gravedad. Esto da lugar a la formación de depósitos con forma de estalactitas en los intercambiadores de calor.
- Erosión: Aunque numerosos autores avalan la no inclusión de los fenómenos de erosión en la combustión de biomasa, sí puede ser interesante considerarlos para la validación de procedimientos tipo *soot blowing*, habituales en sistemas a gran escala.
- Colapso: Ligado a los anteriores fenómenos, la integridad estructural del depósito se puede ver comprometida con su crecimiento, colapsando y dando lugar al traslado de una masa de depósito de una superficie a otra

- Corrosión: Como se mencionó, la presencia de vapores inorgánicos condensados sobre la superficie, especialmente los compuestos de azufre o cloro, pueden derivar en problemas de corrosión. Modelar este fenómeno es de interés para designar mantenimientos preventivos sobre estas superficies.
- Combustión de depósito: La masa depositada puede estar compuesta por restos de carbono que se queman sobre esta nueva superficie, pudiendo incrementar la temperatura local del depósito.
- Ciclos térmicos en el depósito: Habitualmente se estudia sólo el crecimiento continuo del depósito sobre una superficie y cómo evoluciona en un funcionamiento estacionario continuo. Mantener un registro temporal del depósito permitirá modelar los ciclos térmicos que sufre en cambios de operación, los cuales pueden derivar en contracciones y dilataciones que produzcan resquebrajamientos en su estructura.
- Evolución de las partículas: Las partículas en su viaje a lo largo del dominio de cálculo puede sufrir procesos de combustión, coalescencia o rotura. Implementar las variaciones que pueden sufrir las partículas permitirá un modelado más preciso de los depósitos. Estos fenómenos son más sencillos de implementar en el modelado Euler-Lagrange como es lógico por su seguimiento individual de las partículas. En el modelo Euler-Euler se abordará mediante la transferencia de masa entre fases de distintos diámetros.

11.3 Implementación de modelo

Nuevas ideas han surgido fruto de la continua exploración de tendencias en arquitectura informática. Se mostrarán a continuación algunas de ellas:

- Software libre: La implementación de todo el modelo en software libre como OpenFOAM, logrará el acceso al modelo de un mayor número de usuarios, lo cual permitirá su evolución más veloz. Resulta un paso previo fundamental a su ejecución en servicios basados en la nube, pues los precios de las licencias de los softwares privados resultan a menudo prohibitivos.
- Cálculo acelerado por GPGPU (*General-Purpose Computing on Graphics Processing Units*): el cálculo en GPU es una tendencia al alza en el mundo informático, especialmente por sus aplicaciones en *Machine Learning* y *Deep Learning*. Las arquitecturas empleadas en las tarjetas gráficas o GPU permiten resolver ciertas operaciones de forma mucho más veloz que una CPU gracias a su optimización para cálculos en coma flotante, su alto paralelismo y una relación de potencia-precio muy favorable. No obstante, no todos los problemas se resuelven de forma más veloz en la GPU que en la CPU. Su velocidad en coma flotante está muy ligada a su precisión, habitualmente inferior a la empleada por la CPU, y a tareas que sean paralelizables.

Resultaría interesante, aunque complejo, lograr el cálculo de las trayectorias Lagrangianas en la GPU, liberando a la CPU de este proceso. Una GPU media como una NVIDIA Quadro® P4000 posee 1792 núcleos de cómputo, frente a los 8 que posee la CPU de una estación de trabajo media. Las trayectorias Lagrangianas son un caso claro de posible paralelización en GPU, enviando el cálculo de cada partícula a un núcleo al no considerar interacción entre ellas.

En resumen, el modelado de los fenómenos de ensuciamiento en sistemas de combustión de biomasa es un tema de gran interés y donde existe un amplio abanico de posibles líneas de investigación, las cuales se espera poder abordar en el futuro. Se espera que la plataforma de colaboración creada y en general el trabajo mostrado en este tomo sirvan como cimientos para estas futuras líneas de investigación.

Referencias

1. *Directiva 2009/28/CE del Parlamento Europeo y del Consejo de 23 de abril de 2009 relativa al fomento del uso de energía procedente de fuentes renovables y por la que se modifican y se derogan las Directivas 2001/77/CE y 2003/30/CE, in 2009/28/CE.* 2009.
2. Bryden, K.M. and K.W. Ragland, *Numerical modeling of a deep, fixed bed combustor.* Energy & Fuels, 1996. **10**(2): p. 269-275.
3. Demirbas, A., *Potential applications of renewable energy sources, biomass combustion problems in boiler power systems and combustion related environmental issues/Progress in Energy and Combustion Science*, 2005. **31**(2): p. 171-192.
4. Bridgwater, T., *Biomass for energy.* Journal of the Science of Food and Agriculture, 2006. **86**(12): p. 1755-1768.
5. Bunn, D.W., et al., *Analysis of coal conversion to biomass as a transitional technology.* Renewable Energy, 2019. **132**: p. 752-760.
6. Caposciutti, G. and M. Antonelli, *Experimental investigation on air displacement and air excess effect on CO, CO₂ and NO_x emissions of a small size fixed bed biomass boiler.* Renewable Energy, 2018. **116**: p. 795-804.
7. *Directiva (UE) 2018/2001 del Parlamento Europeo y del Consejo de 11 de diciembre de 2018 relativa al fomento del uso de energía procedente de fuentes renovables in DIRECTIVA (UE) 2018/2001.* 2018.
8. Europe, B., *Biomass Supply. Statistical Report*, S. Report, Editor. 2019, Bioenergy Europe.
9. Agency, I.I.E., *Renewables 2018. Analysis and Forecasts to 2023*, in *Market Report Series*, IEA, Editor. 2018.
10. Energy, I.I.A., *Technology Roadmap. Delivering Sustainable Bioenergy*, IEA, Editor. 2018.
11. AEBIOM, *Full Report*, in *AEBIOM Statistical Report*, AEBIOM, Editor. 2017.
12. *Directiva 2008/98/CE del Parlamento Europeo y del Consejo de 19 de noviembre de 2008 sobre los residuos, in 2008/98/CE.* 2008.

13. Europe, B., *Biomass for heat. Statistical Report*, in *Statistical Report*, B. Europe, Editor. 2019.
14. Europe, B., *Pellet. Statistical Report*, B. Europe, Editor. 2019.
15. Elorf, A., et al., *Effect of Swirl Strength on the Flow and Combustion Characteristics of Pulverized Biomass Flames*. *Combustion Science and Technology*, 2019. **191**(4): p. 629-644.
16. Frey, H.H., et al., *Characterization of municipal solid waste combustion in a grate furnace*. *Waste Management*, 2003. **23**(8): p. 689-701.
17. Goerner, K. and T. Klasen, *Modelling, simulation and validation of the solid biomass combustion in different plants*. *Progress in Computational Fluid Dynamics*, 2006. **6**(4-5): p. 225-234.
18. Karim, M.R. and J. Naser, *CFD modelling of combustion and associated emission of wet woody biomass in a 4 MW moving grate boiler*. *Fuel*, 2018. **222**: p. 656-674.
19. Mätzing, H., et al., *Modelling grate combustion of biomass and low rank fuels with CFD application*. *Waste Management*, 2018. **78**: p. 686-697.
20. Stubenberger, G., et al., *Experimental investigation of nitrogen species release from different solid biomass fuels as a basis for release models*. *Fuel*, 2008. **87**(6): p. 793-806.
21. Tu, Y.J., et al., *NO_x reduction in a 40 t/h biomass fired grate boiler using internal flue gas recirculation technology*. *Applied Energy*, 2018. **220**: p. 962-973.
22. Randar, M.H., F. Nasiri, and B. Lee, *A Review of Numerical Modeling and Experimental Analysis of Combustion in Moving Grate Biomass Combustors*. *Energy & Fuels*, 2019. **33**(10): p. 9367-9402.
23. Wolters, R., *EU policy regarding emission reduction from domestic combustion*, E. Commission, Editor. 2018.
24. Torvela, T., et al., *Effect of wood combustion conditions on the morphology of freshly emitted fine particles*. *Atmospheric Environment*, 2014. **87**: p. 65-76.
25. Arora, P. and S. Jain, *Morphological characteristics of particles emitted from combustion of different fuels in improved and traditional cookstoves*. *Journal of Aerosol Science*, 2015. **82**: p. 13-23.
26. Carabali, G., et al., *Morphological and chemical characterization of soot emitted during flaming combustion stage of native-wood species used for cooking process in western Mexico*. *Journal of Aerosol Science*, 2016. **95**: p. 1-14.
27. Gwaze, P., et al., *Comparison of three methods of fractal analysis applied to soot aggregates from wood combustion*. *Journal of Aerosol Science*, 2006. **37**(7): p. 820-838.

28. Chakrabarty, R.K., et al., *Emissions from the laboratory combustion of wildland fuels: Particle morphology and size*. Journal of Geophysical Research-Atmospheres, 2006. **111**(D7).
29. Duo, B., et al., *Individual particle analysis of aerosols collected at Lhasa City in the Tibetan Plateau*. Journal of Environmental Sciences-China, 2015. **29**: p. 165-177.
30. Wagner, J., et al., *Measurement of ambient particulate matter concentrations and particle types near agricultural burns using electron microscopy and passive samplers*. Atmospheric Environment, 2012. **54**: p. 260-271.
31. Schneider, J., et al., *Mass spectrometric analysis and aerodynamic properties of various types of combustion-related aerosol particles*. International Journal of Mass Spectrometry, 2006. **258**(1-3): p. 37-49.
32. Zimmerman, N., et al., *Comparison of three nanoparticle sizing instruments: The influence of particle morphology*. Atmospheric Environment, 2014. **86**: p. 140-147.
33. Vargas, A.M., *Design and Development of a Thermophoretic Soot Sampling System for High-Pressure Laminar Diffusion Flames*, in *Aerospace Engineering*. 2016, University of Toronto: Canada.
34. Patiño, D.;Pérez-Orozco, R.; Porteiro, J.; Lapuerta, M., *Characterization of biomass PM emissions using thermophoretic sampling: Composition and morphological description of the carbonaceous residues*. Journal of Aerosol Science, 2019. **127**: p. 49-62.
35. Febrero, L., et al., *A Comparative Study of Fouling and Bottom Ash from Woody Biomass Combustion in a Fixed-Bed Small-Scale Boiler and Evaluation of the Analytical Techniques Used*. Sustainability, 2015. **7**(5): p. 5819-5837.
36. Regueiro, A., et al., *Experimental study on the fouling behaviour of an underfeed fixed-bed biomass combustor*. Applied Thermal Engineering, 2017. **112**: p. 523-533.
37. Regueiro, A., et al., *Effect of Air Staging Ratios on the Burning Rate and Emissions in an Underfeed Fixed-Bed Biomass Combustor*. Energies, 2016. **9**(11).
38. Nussbaumer, T., *Overview on technologies for biomass combustion and emission levels of particulate matter*. . 2010: Zurich.
39. Nussbaumer, T., *Aerosols from biomass combustion. Technical report on behalf of the IEA Bioenergy Task 32*, in *IEA Bioenergy Task*, IEA, Editor. 2017: VerenumResearch, Zurich, and Lucerne University of Applied Sciences and Arts, Horw, Switzerland. p. 32.
40. Pósfai, M., et al., *Individual aerosol particles from biomass burning in southern Africa: 1. Compositions and size distributions of carbonaceous particles*. 2003. **108**(D13).

41. Vassilev, S.V., et al., *An overview of the organic and inorganic phase composition of biomass*. Fuel, 2012. **94**: p. 1-33.
42. Kaer, S.K., *Numerical investigation of ash deposition in straw-fired boilers-Using CFD as the framework for slagging and fouling predictions*, in *Institute of Energy Technology*. 2001, Aalborg University, Denmark.
43. Wiinikka, H., et al., *High-temperature aerosol formation in wood pellets flames: Spatially resolved measurements*. Combustion and Flame, 2006. **147**(4): p. 278-293.
44. Wiinikka, H., et al., *Influence of fuel ash composition on high temperature aerosol formation in fixed bed combustion of woody biomass pellets*. Fuel, 2007. **86**(1): p. 181-193.
45. Chapela, S., et al., *Comprehensive CFD modeling of the ash deposition in a biomass packed bed burner*. Fuel, 2018. **234**: p. 1099-1122.
46. Wang, G.L., et al., *Evaluation of the combustion behaviour and ash characteristics of biomass waste derived fuels, pine and coal in a drop tube furnace*. Fuel, 2014. **117**: p. 809-824.
47. Asgharian, B., *A model of deposition of hygroscopic particles in the human lung*. Aerosol Science and Technology, 2004. **38**(9): p. 938-947.
48. Broday, D.M. and R. Rosenzweig, *Deposition of fractal-like soot aggregates in the human respiratory tract*. Journal of Aerosol Science, 2011. **42**(6): p. 372-386.
49. Tortosa Masiá, A.A., *Characterisation and prediction of deposits in biomass co-combustion*, in *Process and Energy*. 2010, Technische Universiteit Delft.
50. Pronobis, M., *Evaluation of the influence of biomass co-combustion on boiler furnace slagging by means of fusibility correlations*. Biomass & Bioenergy, 2005. **28**(4): p. 375-383.
51. Lindstrom, E., et al., *Slagging Characteristics during Combustion of Woody Biomass Pellets Made from a Range of Different Forestry Assortments*. Energy & Fuels, 2010. **24**(6): p. 3456-3461.
52. Werkelin, J., et al., *Ash-forming elements in four Scandinavian wood species part 3: Combustion of five spruce samples*. Biomass & Bioenergy, 2011. **35**(1): p. 725-733.
53. Werkelin, J., B.J. Skrifvars, and M. Hupa, *Ash-forming elements in four Scandinavian wood species. Part 1: Summer harvest*. Biomass & Bioenergy, 2005. **29**(6): p. 451-466.
54. Wei, X., U. Schnell, and K.R.G. Hein, *Behaviour of gaseous chlorine and alkali metals during biomass thermal utilisation*. Fuel, 2005. **84**(7): p. 841-848.

55. Blomberg, T., *A thermodynamic study of the gaseous potassium chemistry in the convection sections of biomass fired boilers*. Materials and Corrosion, 2011. **62**(7): p. 635-641.
56. Dayton, D.C. and T.A. Milne, *Laboratory Measurements of Alkali Metal Containing Vapors Released during Biomass Combustion*, in *Applications of Advanced Technology to Ash-Related Problems in Boilers*, L. Baxter and R. DeSollar, Editors. 1996, Springer US: Boston, MA. p. 161-185.
57. Couch, G., *Understanding slagging and fouling in pf combustion*. 1994: IEA Coal Research London.
58. Baxter, L.L., *Ash deposition during biomass and coal combustion: A mechanistic approach*. Biomass and Bioenergy, 1993. **4**(2): p. 85-102.
59. Jensen, P.A.S.B., M.; Wedel, S.; Jappe Frandsen, F.; Wadenbäck, J.; Pedersen, S. T.; DamJohansen, K. , *Characterization and quantification of deposits build up and removal in straw suspension fired boilers*. 2013, Technical University of Denmark.
60. Niu, Y., et al., *Study on Deposits on the Surface, Upstream, and Downstream of Bag Filters in a 12 MW Biomass-Fired Boiler*. Energy & Fuels, 2010. **24**(3): p. 2127-2132.
61. Mu, L., et al., *Elemental Distribution and Mineralogical Composition of Ash Deposits in a Large-Scale Wastewater Incineration Plant: A Case Study*. Industrial & Engineering Chemistry Research, 2012. **51**(25): p. 8684-8694.
62. Hansen, L.A., et al., *Influence of deposit formation on corrosion at a straw-fired boiler*. Fuel Processing Technology, 2000. **64**(1-3): p. 189-209.
63. Crowe, C.T., et al., *Multiphase Flows with Droplets and Particles, 2nd Edition*. Multiphase Flows with Droplets and Particles, 2nd Edition, 2012: p. 1-487.
64. Johnson, R.W., *The handbook of fluid dynamics*. 1998, United States: CRC Press.
65. Roco, M.C., *Particulate two-phase flow*. 1993, Boston: Butterworth-Heinemann.
66. Larry, L.B., *Ash Deposit Formation and Deposit Properties. A Comprehensive Summary of Research Conducted at Sandia's Combustion Research Facility*. 2000: United States.
67. Zhou, H., P.A. Jensen, and F.J. Frandsen, *Dynamic mechanistic model of superheater deposit growth and shedding in a biomass fired grate boiler*. Fuel, 2007. **86**: p. 1519-1533.
68. Sippola, M.R. and W.W. Nazaroff, *Particle deposition from turbulent flow: Review of published research and its applicability to ventilation ducts in commercial buildings*. 2002, Lawrence Berkeley National Lab.(LBNL), Berkeley, CA (United States).

69. Ojaniemi, U., *Modelling particulate fouling in heat exchanger with high solid content liquid suspension*. 2015.
70. Kaufmann, H., et al., *Deposit formation on a single cylinder during combustion of herbaceous biomass*. *Fuel*, 2000. **79**(2): p. 141-151.
71. Raask, E., *Mineral impurities in coal combustion: behavior, problems, and remedial measures*. 1985: Taylor & Francis.
72. Li, A. and G. Ahmadi, *Dispersion and Deposition of Spherical Particles from Point Sources in a Turbulent Channel Flow*. *Aerosol Science and Technology*, 1992. **16**(4): p. 209-226.
73. Ounis, H., G. Ahmadi, and J.B. McLaughlin, *Brownian diffusion of submicrometer particles in the viscous sublayer*. *Journal of Colloid and Interface Science*, 1991. **143**(1): p. 266-277.
74. Li, M., *Eddy Impaction As An Ash Deposition Mechanism: A Theoretical And Experimental Investigation*. 2011, Brigham Young University: Provo, Utah, United States.
75. Im, K.H. and R.K. Ahluwalia, *Turbulent eddy deposition of particles on smooth and rough surfaces*. *Journal of Aerosol Science*, 1989. **20**(4): p. 431-436.
76. Cai, Y., et al., *Modeling of ash formation and deposition processes in coal and biomass fired boilers: A comprehensive review*. *Applied Energy*, 2018. **230**: p. 1447-1544.
77. Guha, A., *Transport and deposition of particles in turbulent and laminar flow*. *Annual Review of Fluid Mechanics*, 2008. **40**: p. 311-341.
78. Israel, R. and D.E. Rosner, *Use of a Generalized Stokes Number to Determine the Aerodynamic Capture Efficiency of Non-Stokesian Particles from a Compressible Gas Flow*. *Aerosol Science and Technology*, 1982. **2**(1): p. 45-51.
79. Rosner, D.E. and P. Tandon, *Rational prediction of inertially induced particle deposition rates for a cylindrical target in a dust-laden stream*. *Chemical Engineering Science*, 1995. **50**(21): p. 3409-3431.
80. Baxter, L.L. *Coal combustion science. Quarterly progress report*. 1990. Livermore, California: Sandia National Laboratories.
81. Baxter, L.L. *The dynamic variation of particle capture efficiency during ash deposition in coal-fired combustors*. in *In Proc. of the Twenty-Third Symposium (International) on Combustion*. 1990.
82. Tassopoulos, M., J.A. Obrien, and D.E. Rosner, *Simulation of Microstructure Mechanism Relationships in Particle Deposition*. *Aiche Journal*, 1989. **35**(6): p. 967-980.
83. Matsumoto, S. and S. Saito, *MONTE CARLO SIMULATION OF HORIZONTAL PNEUMATIC CONVEYING BASED ON THE ROUGH*

- WALL MODEL*. Journal of Chemical Engineering of Japan, 1970. **3**(2): p. 223-230.
84. Sommerfeld, M., *Modelling of particle-wall collisions in confined gas-particle flows*. International Journal of Multiphase Flow, 1992. **18**(6): p. 905-926.
85. Lee, B.E., et al., *Computational study of fouling deposit due to surface-coated particles in coal-fired power utility boilers*. Fuel, 2002. **81**(15): p. 2001-2008.
86. Kær, S.K., L.A. Rosendahl, and L.L. Baxter, *Towards a CFD-based mechanistic deposit formation model for straw-fired boilers*. Fuel, 2006. **85**(5): p. 833-848.
87. Ma, L. and M. Pourkashanian, *A numerical model for predicting biomass particle depositions in a PF furnace*. Proceedings of the ASME Turbo Expo 2006, Vol 2, 2006: p. 333-342.
88. Mueller, C., et al., *Deposition behaviour of molten alkali-rich fly ashes - development of a submodel for CFD applications*. Proceedings of the Combustion Institute, 2005. **30**: p. 2991-2998.
89. Mu, L., L. Zhao, and H. Yin, *Modelling and measurements of the characteristics of ash deposition and distribution in a HRSG of wastewater incineration plant*. Applied Thermal Engineering, 2012. **44**: p. 57-68.
90. Xu, M., et al., *Impaction and Rebound of Particles at Acute Incident Angles*. Aerosol Science and Technology, 1993. **18**(2): p. 143-155.
91. Rosner, D.E., P. Tandon, and A.G. Konstandopoulos, *Local size distributions of particles deposited by inertial impaction on a cylindrical target in dust-laden streams*. Journal of Aerosol Science, 1995. **26**(8): p. 1257-1279.
92. Konstandopoulos, A.G., *Deposit growth dynamics: particle sticking and scattering phenomena*. Powder Technology, 2000. **109**(1-3): p. 262-277.
93. Kostoglou, M. and A.G. Konstandopoulos, *Particulate deposit shape evolution on cylinders in cross-flow at high Stokes numbers*. Journal of Aerosol Science, 2000. **31**(4): p. 427-436.
94. Walsh, P.M., et al., *Deposition of Bituminous Coal Ash on an Isolated Heat-Exchanger Tube - Effects of Coal Properties on Deposit Growth*. Progress in Energy and Combustion Science, 1990. **16**(4): p. 327-346.
95. Erickson, T.A., et al., *Modeling of Fouling and Slagging in Coal-Fired Utility Boilers*. Fuel Processing Technology, 1995. **44**(1-3): p. 155-171.
96. Lee, F.C.C. and F.C. Lockwood, *Modelling ash deposition in pulverized coal-fired applications*. Progress in Energy and Combustion Science, 1999. **25**(2): p. 117-132.
97. Huang, L.Y., et al., *Prediction of ash deposition on superheater tubes from pulverized coal combustion*. Fuel, 1996. **75**(3): p. 271-279.
98. Rushdi, A., et al., *Mechanistic prediction of ash deposition in a pilot-scale test facility*. Fuel, 2005. **84**(10): p. 1246-1258.

99. Senior, C.L. and S. Srinivasachar, *Viscosity of Ash Particles in Combustion Systems for Prediction of Particle Sticking*. Energy & Fuels, 1995. **9**(2): p. 277-283.
100. Brink, A., et al., *A temperature-history based model for the sticking probability of impacting pulverized coal ash particles*. Fuel Processing Technology, 2016. **141**: p. 210-215.
101. Erickson, T.A., et al., *Modelling of fouling and slagging in coal-fired utility boilers*. Fuel Processing Technology, 1995. **44**(1): p. 155-171.
102. Richards, G.H., P.N. Slater, and J.N. Harb, *Simulation of ash deposit growth in a pulverized coal-fired pilot scale reactor*. Energy & Fuels, 1993. **7**(6): p. 774-781.
103. Fan, J.R., et al., *Simulation of ash deposit in a pulverized coal-fired boiler*. Fuel, 2001. **80**(5): p. 645-654.
104. Fang, Q., et al., *Numerical simulations of the slagging characteristics in a down-fired, pulverized-coal boiler furnace*. Fuel Processing Technology, 2010. **91**(1): p. 88-96.
105. Taha, T.J., et al., *CFD modeling of ash deposition for co-combustion of MBM with coal in a tangentially fired utility boiler*. Fuel Processing Technology, 2013. **114**: p. 126-134.
106. Garba, M.U., et al., *Modelling of deposit formation and sintering for the co-combustion of coal with biomass*. Fuel, 2013. **113**: p. 863-872.
107. Kondratiev, A., et al., *Slag viscosity prediction and characterisation : Al_2O_3 - CaO - FeO - SiO_2 and Al_2O_3 - CaO - FeO - MgO - SiO_2 SYSTEMS*. 2006.
108. frandsen, F.J.H., L. A., *Characterization of ashes from biofuels. Final report EFP-95*. 1998, 87-7782. p. 87-7782.
109. Jak, E., *Prediction of coal ash fusion temperatures with the F*A*C*T thermodynamic computer package*. Fuel, 2002. **81**(13): p. 1655-1668.
110. Thompson, D., *Predicted mineral melt formation by BCURA Coal Sample Bank coals: Variation with atmosphere and comparison with reported ash fusion test data*. Fuel, 2010. **89**(8): p. 2062-2071.
111. Backman, R.H., M.; Uppstu, E., *Fouling and corrosion mechanisms in the recovery boiler superheater area*. Tappi J, 1987. **70**(6): p. 123-127.
112. Hupa, M., *Ash-related issues in fluidized-bed combustion of biomasses: recent research highlights*. Energy & Fuels, 2011. **26**(1): p. 4-14.
113. Webb, R.L.N.-H., K., *Principles of Enhanced Heat Transfer*. 2005.
114. Mwaba, M.G., M.R. Golriz, and J. Gu, *A semi-empirical correlation for crystallization fouling on heat exchange surfaces*. Applied Thermal Engineering, 2006. **26**(4): p. 440-447.

115. Kim, N.H. and R.L. Webb, *Particulate Fouling of Water in Tubes Having a 2-Dimensional Roughness Geometry*. International Journal of Heat and Mass Transfer, 1991. **34**(11): p. 2727-2738.
116. Keefer, R.H., J.L. Rider, and L.A. Waldman, *An analytical model for particulate deposition on vertical heat transfer surfaces in a boiling environment*. 1993: United States. p. 16.
117. Bouris, D., et al., *Design of a novel, intensified heat exchanger for reduced fouling rates*. International Journal of Heat and Mass Transfer, 2005. **48**(18): p. 3817-3832.
118. Bohnet, M., *Fouling of heat transfer surfaces*. 1987. **10**(1): p. 113-125.
119. Ziskind, G., M. Fichman, and C. Gutfinger, *Adhesion moment model for estimating particle detachment from a surface*. Journal of Aerosol Science, 1997. **28**(4): p. 623-634.
120. Reeks, M.W. and D. Hall, *Kinetic models for particle resuspension in turbulent flows: theory and measurement*. Journal of Aerosol Science, 2001. **32**(1): p. 1-31.
121. Ibrahim, A.H., P.F. Dunn, and R.M. Brach, *Microparticle detachment from surfaces exposed to turbulent air flow: controlled experiments and modeling*. Journal of Aerosol Science, 2003. **34**(6): p. 765-782.
122. Guingo, M. and J.P. Minier, *A new model for the simulation of particle resuspension by turbulent flows based on a stochastic description of wall roughness and adhesion forces*. Journal of Aerosol Science, 2008. **39**(11): p. 957-973.
123. Corino, E.R. and R.S. Brodkey, *A Visual Investigation of Wall Region in Turbulent Flow*. Journal of Fluid Mechanics, 1969. **37**: p. 1-+.
124. Kline, S.J., et al., *Structure of Turbulent Boundary Layers*. Journal of Fluid Mechanics, 1967. **30**: p. 741-+.
125. Cleaver, J.W. and B. Yates, *Mechanism of detachment of colloidal particles from a flat substrate in a turbulent flow*. Journal of Colloid and Interface Science, 1973. **44**(3): p. 464-474.
126. Miles, J. R.; Baxter, L.L.B., R. W.; Jenkins, B. M.; Oden, L. L., *Alkali deposits found in biomass power plants. A preliminary investigation of their extend and nature*. 1995, National Renewable Energy Laboratory.
127. Niu, Y.Q., H.Z. Tan, and S.E. Hui, *Ash-related issues during biomass combustion: Alkali-induced slagging, silicate melt-induced slagging (ash fusion), agglomeration, corrosion, ash utilization, and related countermeasures*. Progress in Energy and Combustion Science, 2016. **52**: p. 1-61.
128. Niu, Y.Q., et al., *Study on fusion characteristics of biomass ash*. Bioresource Technology, 2010. **101**(23): p. 9373-9381.

129. Weber, R., et al., *On predicting the ash behaviour using Computational Fluid Dynamics*. Fuel Processing Technology, 2013. **105**: p. 113-128.
130. Gray, V.R., *Prediction of ash fusion temperature from ash composition for some New Zealand coals*. Fuel, 1987. **66**(9): p. 1230-1239.
131. Wang, S., et al., *Fusion Characteristic Study on Seaweed Biomass Ash*. Energy & Fuels, 2008. **22**(4): p. 2229-2235.
132. Vamvuka, D. and D. Zografos, *Predicting the behaviour of ash from agricultural wastes during combustion*. Fuel, 2004. **83**(14): p. 2051-2057.
133. Boström, D., et al., *Ash Transformation Chemistry during Combustion of Biomass*. Energy & Fuels, 2012. **26**(1): p. 85-93.
134. Wang, L., M. Becidan, and Ø. Skreiberg, *Sintering Behavior of Agricultural Residues Ashes and Effects of Additives*. Energy & Fuels, 2012. **26**(9): p. 5917-5929.
135. Rezaei, H. and S. Sokhansanj, *Physical and thermal characterization of ground bark and ground wood particles*. Renewable Energy, 2018. **129**: p. 583-590.
136. Singh, Y.D., P. Mahanta, and U. Bora, *Comprehensive characterization of lignocellulosic biomass through proximate, ultimate and compositional analysis for bioenergy production*. Renewable Energy, 2017. **103**: p. 490-500.
137. Dhyani, V. and T. Bhaskar, *A comprehensive review on the pyrolysis of lignocellulosic biomass*. Renewable Energy, 2018. **129**: p. 695-716.
138. Melissari, B., *Ash related problems with igh alkali biomass and its mitigation - Experimental evaluation*, M.I.e. Ingeniería, Editor. 2014, Facultad de Ingeniería, Universidad de Montevideo, Montevideo, Uruguay.
139. Ma, H.T., C.H. Zhou, and L. Wang, *High temperature corrosion of pure Fe, Cr and Fe-Cr binary alloys in O₂ containing trace KCl vapour at 750°C*. Corrosion Science, 2009. **51**(8): p. 1861-1867.
140. Livingston, W.R., *Biomass ash deposition, erosion and corrosion processes. Workshop on ash related issues in biomass combustion. Glasgow: IEA Task 32/Thermalnet Workshop; 2006*. 2006.
141. Gianfelice, G., et al., *Onset and propagation of smouldering in pine bark controlled by addition of inert solids*. Renewable Energy, 2019. **132**: p. 596-614.
142. Stefanelli, G., et al., *Secondary organic aerosol formation from smoldering and flaming combustion of biomass: a box model parametrization based on volatility basis set*. Atmospheric Chemistry and Physics, 2019. **19**(17): p. 11461-11484.
143. Huang, X.Y. and G. Rein, *Thermochemical conversion of biomass in smouldering combustion across scales: The roles of heterogeneous kinetics,*

- oxygen and transport phenomena*. Bioresource Technology, 2016. **207**: p. 409-421.
144. Carvalho, E.R., C.A.G. Veras, and J.A. Carvalho, *Experimental investigation of smouldering in biomass*. Biomass & Bioenergy, 2002. **22**(4): p. 283-294.
145. Khodaei, H., et al., *An experimental study into the effect of air staging distribution and position on emissions in a laboratory scale biomass combustor*. Energy, 2017. **118**: p. 1243-1255.
146. Regueiro, A., et al., *Experimental Study of the Viability of Low-Grade Biofuels in Small-Scale Appliances*. Sustainability, 2017. **9**(10).
147. Nuutinen, K., et al., *Effect of air staging on fine particle, dust and gaseous emissions from masonry heaters*. Biomass and Bioenergy, 2014. **67**: p. 167-178.
148. Khodaei, H., et al., *Air staging strategies in biomass combustion-gaseous and particulate emission reduction potentials*. Fuel Processing Technology, 2017. **157**: p. 29-41.
149. Tu, Y.J., et al., *Experimental and numerical study on the combustion of a 32 MW wood-chip grate boiler with internal flue gas recirculation technology*. Leveraging Energy Technologies and Policy Options for Low Carbon Cities, 2017. **143**: p. 591-598.
150. Gomez, M.A., et al., *Steady CFD combustion modeling for biomass boilers: An application to the study of the exhaust gas recirculation performance*. Energy Conversion and Management, 2019. **179**: p. 91-103.
151. Pérez-Orozco, R.P., D.; Porteiro, J.; Míguez, J. L., *Novel Test Bench for the Active Reduction of Biomass Particulate Matter Emissions*. Sustainability, 2020. **12**.
152. Yang, X., et al., *Understanding the effects of oxyfuel combustion and furnace scale on biomass ash deposition*. Fuel, 2019. **247**: p. 36-46.
153. Fryda, L., et al., *Study on ash deposition under oxyfuel combustion of coal/biomass blends*. Fuel, 2010. **89**(8): p. 1889-1902.
154. Holtmeyer, M.L., B.M. Kumfer, and R.L. Axelbaum, *Effects of biomass particle size during cofiring under air-fired and oxyfuel conditions*. Applied Energy, 2012. **93**: p. 606-613.
155. Sher, F., et al., *Oxy-fuel combustion study of biomass fuels in a 20 kWth fluidized bed combustor*. Fuel, 2018. **215**: p. 778-786.
156. Jenkins, B.M., R.R. Bakker, and J.B. Wei, *On the properties of washed straw*. Biomass and Bioenergy, 1996. **10**(4): p. 177-200.
157. Gudka, B., et al., *A review of the mitigation of deposition and emission problems during biomass combustion through washing pre-treatment*. Journal of the Energy Institute, 2016. **89**(2): p. 159-171.

158. Jenkins, B.M., et al., *Combustion properties of biomass*. Fuel Processing Technology, 1998. **54**(1): p. 17-46.
159. Wang, L., et al., *A Critical Review on Additives to Reduce Ash Related Operation Problems in Biomass Combustion Applications*. Energy Procedia, 2012. **20**: p. 20-29.
160. Tobiasen, L., et al., *Deposit characteristic after injection of additives to a Danish straw-fired suspension boiler*. Fuel Processing Technology, 2007. **88**(11): p. 1108-1117.
161. Niu, Y.Q., et al., *Experimental evaluation of additives and $K_2O-SiO_2-Al_2O_3$ diagrams on high-temperature silicate melt-induced slagging during biomass combustion*. Fuel, 2016. **179**: p. 52-59.
162. Wang, Q., et al., *Influence of phosphorous based additives on ash melting characteristics during combustion of biomass briquette fuel*. Renewable Energy, 2017. **113**: p. 428-437.
163. Steenari, B.-M., et al., *Investigation of Ash Sintering during Combustion of Agricultural Residues and the Effect of Additives*. Energy & Fuels, 2009. **23**(11): p. 5655-5662.
164. Wang, L., et al., *Investigation on Ash Slagging Characteristics During Combustion of Biomass Pellets and Effect of Additives*. Energy & Fuels, 2018. **32**(4): p. 4442-4452.
165. Aho, M., *Reduction of chlorine deposition in FB boilers with aluminium-containing additives*. Fuel, 2001. **80**(13): p. 1943-1951.
166. Gehrig, M., et al., *Implementation of a firebed cooling device and its influence on emissions and combustion parameters at a residential wood pellet boiler*. Applied Energy, 2015. **159**: p. 310-316.
167. Gehrig, M., et al., *Influence of a Direct Firebed Cooling in a Residential Wood Pellet Boiler with an Ash-Rich Fuel on the Combustion Process and Emissions*. Energy & Fuels, 2016. **30**(11): p. 9900-9907.
168. Pettersson, A., F. Niklasson, and F. Moradian, *Reduced bed temperature in a commercial waste to energy boiler - Impact on ash and deposit formation*. Fuel Processing Technology, 2013. **105**: p. 28-36.
169. Jones, F., et al., *Effects of Reduced Bed Temperature in Laboratory- and Full-Scale Fluidized-Bed Boilers: Particle, Deposit, and Ash Chemistry*. Energy & Fuels, 2013. **27**(8): p. 4999-5007.
170. Meloni, E., et al., *Soot abatement from biomass boilers by means of open-cell foams filters*. Renewable Energy, 2019. **131**: p. 745-754.
171. Brunner, T., G. Wuercher, and I. Obernberger, *2-Year field operation monitoring of electrostatic precipitators for residential wood heating systems*. Biomass & Bioenergy, 2018. **111**: p. 278-287.

172. Migliavacca, G., et al., *Reduction of PM Emissions from Biomass Combustion Appliances: Evaluation of Efficiency of Electrostatic Precipitators*. Iconbm: International Conference on Biomass, Pts 1 and 2, 2014. **37**: p. 25-+.
173. Carroll, J. and J. Finnan, *Use of electrostatic precipitators in small-scale biomass furnaces to reduce particulate emissions from a range of feedstocks*. Biosystems Engineering, 2017. **163**: p. 94-102.
174. Berhardt, A., F. Lezsovits, and B. Gross, *Integrated Electrostatic Precipitator for Small-Scaled Biomass Boilers*. Chemical Engineering & Technology, 2017. **40**(2): p. 278-288.
175. Bianchini, A., et al., *Theoretical model and preliminary design of an innovative wet scrubber for the separation of fine particulate matter produced by biomass combustion in small size boilers*. Biomass & Bioenergy, 2018. **116**: p. 60-71.
176. OpenFOAM. *The open source CFD toolbox*. 2020 [cited 2020 Enero 2020]; Available from: <https://www.openfoam.com/>.
177. TURNER, M.J., et al., *Stiffness and Deflection Analysis of Complex Structures*. 1956. **23**(9): p. 805-823.
178. ANSYS, I., *Introduction to ANSYS Meshing*, in *Lecture 7. Mesh Quality & Advanced Topics*. 2015.
179. ANSYS, I., *ANSYS Fluent User's Guide v18.2*. 2017.
180. ANSYS, I., *ANSYS Fluent Theory Guide v18.2*. 2017.
181. Patankar, S.V. and D.B. Spalding, *A calculation procedure for heat, mass and momentum transfer in three-dimensional parabolic flows*. International Journal of Heat and Mass Transfer, 1972. **15**(10): p. 1787-1806.
182. Chapela, S., et al., *CFD study of fouling phenomena in small-scale biomass boilers: Experimental validation with two different boilers*. Renewable Energy, 2019. **140**: p. 552-562.
183. Chapela, S., J. Porteiro, and M. Costa, *Effect of the Turbulence-Chemistry Interaction in Packed-Bed Biomass Combustion*. Energy & Fuels, 2017. **31**(9): p. 9967-9982.
184. Gonzalez, W.A., et al., *Numerical analysis of wood biomass packing factor in a fixed-bed gasification process*. Renewable Energy, 2018. **121**: p. 579-589.
185. Collazo, J., et al., *Numerical simulation of a small-scale biomass boiler*. Energy Conversion and Management, 2012. **64**: p. 87-96.
186. Gomez, M.A., et al., *Numerical simulation of the combustion process of a pellet-drop-feed boiler*. Fuel, 2016. **184**: p. 987-999.
187. Gomez, M.A., et al., *Eulerian CFD modelling for biomass combustion. Transient simulation of an underfeed pellet boiler*. Energy Conversion and Management, 2015. **101**: p. 666-680.

188. Mahmoudi, A.H., F. Hoffmann, and B. Peters, *Application of XDEM as a novel approach to predict drying of a packed bed*. International Journal of Thermal Sciences, 2014. **75**: p. 65-75.
189. Wagenaar, M., W. Prins, and W.P.M. Vanswaaij, *Flash Pyrolysis Kinetics of Pine Wood*. Fuel Processing Technology, 1993. **36**(1-3): p. 291-298.
190. Thunman, H., et al., *Combustion of wood particles—a particle model for eulerian calculations*. Combustion and Flame, 2002. **129**(1): p. 30-46.
191. Hagge, M.J. and K.M. Bryden, *Modeling the impact of shrinkage on the pyrolysis of dry biomass*. Chemical Engineering Science, 2002. **57**(14): p. 2811-2823.
192. Thunman, H., et al., *Composition of volatile gases and thermochemical properties of wood for modeling of fixed or fluidized beds*. Energy & Fuels, 2001. **15**(6): p. 1488-1497.
193. Magnussen, B.F.H., B. H. *On mathematical modeling of turbulent combustion with special emphasis on soot formation and combustion*. in *Symp. Combust.* 1977.
194. Varela, L.G., et al., *Improving Bed Movement Physics in Biomass Computational Fluid Dynamics Combustion Simulations*. Chemical Engineering & Technology, 2019. **42**(12): p. 2556-2564.
195. Bermudez, C.A., et al., *Three-dimensional CFD simulation of a large-scale grate-fired biomass furnace*. Fuel Processing Technology, 2020. **198**.
196. Porteiro, J., et al., *Numerical Modeling of a Biomass Pellet Domestic Boiler*. Energy & Fuels, 2009. **23**(1-2): p. 1067-1075.
197. Yang, Y.B., et al., *Effect of fuel properties on biomass combustion. Part II. Modelling approach - identification of the controlling factors*. Fuel, 2005. **84**(16): p. 2116-2130.
198. Gomez, M.A., et al., *Fast-solving thermally thick model of biomass particles embedded in a CFD code for the simulation of fixed-bed burners*. Energy Conversion and Management, 2015. **105**: p. 30-44.
199. Gomez, M.A., et al., *Dynamic simulation of a biomass domestic boiler under thermally thick considerations*. Energy Conversion and Management, 2017. **140**: p. 260-272.
200. Mehrabian, R., et al., *A CFD model for thermal conversion of thermally thick biomass particles*. Fuel Processing Technology, 2012. **95**: p. 96-108.
201. Mehrabian, R., et al., *Multi-physics modelling of packed bed biomass combustion*. Fuel, 2014. **122**: p. 164-178.
202. Mehrabian, R.S., A.; Scharler, R.; Obernberger, I. *Numerical modelling of biomass grate furnaces with a particle based model*. in *Proceedings of the 10th European Conference on Industrial Furnaces and Boilers*, 2015. Porto, Portugal.

203. Hermansson, S. and H. Thunman, *CFD modelling of bed shrinkage and channelling in fixed-bed combustion*. Combustion and Flame, 2011. **158**(5): p. 988-999.
204. Kurz, D., U. Schnell, and G. Scheffknecht, *Euler-Euler simulation of wood chip combustion on a grate - effect of fuel moisture content and full scale application*. Progress in Computational Fluid Dynamics, 2013. **13**(5): p. 322-332.
205. Wiese, J., et al., *DEM/CFD modeling of the fuel conversion in a pellet stove*. Fuel Processing Technology, 2016. **152**: p. 223-239.
206. Simsek, E., et al., *Numerical simulation of grate firing systems using a coupled CFD/discrete element method (DEM)*. Powder Technology, 2009. **193**(3): p. 266-273.
207. Scharler, R.F., T.; Obernberger, I., *Modification of a Magnussen constant of the Eddy Dissipation model for biomass grate furnaces by means of hot gas in-situ FT-IR absorption spectroscopy*. Progress in Computational Fluid Dynamics, 2003(3): p. 102-111.
208. Shiehnejadhesar, A., et al., *Development of a gas phase combustion model suitable for low and high turbulence conditions*. Fuel, 2014. **126**: p. 177-187.
209. Shiehnejadhesar, A., et al., *Development and validation of CFD models for gas phase reactions in biomass grate furnaces considering gas streak formation above the packed bed*. Fuel Processing Technology, 2015. **139**: p. 142-158.
210. Masuoka, T. and Y. Takatsu, *Turbulence model for flow through porous media*. International Journal of Heat and Mass Transfer, 1996. **39**(13): p. 2803-2809.
211. Verma, V.K., et al., *Evaluation of the performance of a multi-fuel domestic boiler with respect to the existing European standard and quality labels: Part-I*. Biomass and Bioenergy, 2011. **35**(1): p. 80-89.
212. Cardozo, E., et al., *Combustion of agricultural residues: An experimental study for small-scale applications*. Fuel, 2014. **115**: p. 778-787.
213. Öhman, M., et al., *Slagging tendencies of wood pellet ash during combustion in residential pellet burners*. Biomass and Bioenergy, 2004. **27**(6): p. 585-596.
214. Örberg, H., et al., *Combustion and Slagging Behavior of Biomass Pellets Using a Burner Cup Developed for Ash-Rich Fuels*. Energy & Fuels, 2014. **28**(2): p. 1103-1110.
215. Sandberg, J., et al., *Dynamic simulation of fouling in a circulating fluidized biomass-fired boiler*. Applied Energy, 2011. **88**(5): p. 1813-1824.
216. Weber, R., et al., *Combustion of biomass in jet flames*. Proceedings of the Combustion Institute, 2015. **35**(3): p. 2749-2758.

217. Li, A. and G. Ahmadi, *Dispersion and Deposition of Spherical-Particles from Point Sources in a Turbulent Channel Flow*. Aerosol Science and Technology, 1992. **16**(4): p. 209-226.
218. Ounis, H., G. Ahmadi, and J.B. McLaughlin, *Dispersion and Deposition of Brownian Particles from Point Sources in a Simulated Turbulent Channel Flow*. Journal of Colloid and Interface Science, 1991. **147**(1): p. 233-250.
219. Uhlenbeck, G.E. and L.S. Ornstein, *On the theory of the Brownian motion*. Physical Review, 1930. **36**(5): p. 0823-0841.
220. Saffman, P.G., *Lift on a Small Sphere in a Slow Shear Flow*. Journal of Fluid Mechanics, 1965. **22**: p. 385-&.
221. Talbot, L., et al., *Thermophoresis of Particles in a Heated Boundary-Layer*. Journal of Fluid Mechanics, 1980. **101**(Dec): p. 737-758.
222. Dutka, M.D., M.; Løvås, T., *Application of a Central Composite Design for the Study of NOx Emission Performance of a Low NOx Burner*. Energies, 2015. **8**(5): p. 3606-3627.
223. Viana, F., *Things you wanted to know about the Latin hypercube design and were afraid to ask*. 2013.
224. ANSYS, I., *ANSYS Fluent UDF Manual v18.2*. 2017.
225. Syamlal, M.O.B.T., *Computer Simulation of Bubbles in a Fluidized Bed*. AIChE Symp. Series, 1989. **854**: p. 22-31.
226. Dalla Valle, J.M., *Micromeritics*. 1948, London: Pitman.
227. Wen, C.Y.Y., Y. H., *Mechanics of Fluidization*. Chem. Eng. Prog. Symp. Series, 1966. **62**: p. 100-111.
228. Gidaspow, D.B., R.; Ding J. *Hydrodynamics of Circulating Fluidized Beds, Kinetic Theory Approach*. in *7th Engineering Foundation Conference on Fluidization*. 1992.
229. Huilin, L.G., D., *Hydrodynamics of binary fluidization in a riser: CFD simulation using two granular temperatures*". Chemical Engineering Science, 2003. **58**: p. 3777-3792.
230. Schaeffer, D.G., *Instability in the Evolution-Equations Describing Incompressible Antigranulocytes Flow*. Journal of Differential Equations, 1987. **66**(1): p. 19-50.
231. Johnson, P.C. and R. Jackson, *Frictional-Collisional Constitutive Relations for Granular Materials, with Application to Plane Shearing*. Journal of Fluid Mechanics, 1987. **176**: p. 67-93.
232. Ocone, R., S. Sundaresan, and R. Jackson, *Gas-Particle Flow in a Duct of Arbitrary Inclination with Particle-Particle Interactions*. Aiche Journal, 1993. **39**(8): p. 1261-1271.
233. Hinze, J.O., *Turbulence*. McGraw-Hill Publishing Co. 1975, New York.

234. Gunn, D.J., *Transfer of Heat or Mass to Particles in Fixed and Fluidized-Beds*. International Journal of Heat and Mass Transfer, 1978. **21**(4): p. 467-476.
235. Wood, N.B., *The Mass-Transfer of Particles and Acid Vapor to Cooled Surfaces*. Journal of the Institute of Energy, 1981. **54**(419): p. 74-93.
236. Fan, F.G. and G. Ahmadi, *A Sublayer Model for Turbulent Deposition of Particles in Vertical Ducts with Smooth and Rough Surfaces*. Journal of Aerosol Science, 1993. **24**(1): p. 45-64.
237. Mills, A.F., *Heat and Mass Transfer*. 1995.
238. Cha, C.Y. and B.J. McCoy, *Thermal Force on Aerosol-Particles*. Physics of Fluids, 1974. **17**(7): p. 1376-1380.
239. He, C.H. and G. Ahmadi, *Particle deposition with thermophoresis in laminar and turbulent duct flows*. Aerosol Science and Technology, 1998. **29**(6): p. 525-546.

ANEXO A.

Trabajos publicados englobados
en esta tesis doctoral

Effect of the Turbulence–Chemistry Interaction in Packed-Bed Biomass Combustion

S. Chapela, J. Porteiro and M. Costa

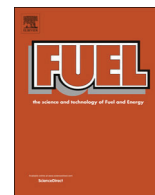
To cite this article: *Energy Fuels* 2017, 31, 9, 9967-9982 Publication Date: August 7, 2017
<https://doi.org/10.1021/acs.energyfuels.7b00516> Copyright © 2017 American Chemical Society

The final authenticated version is available online at:

<https://doi.org/10.1021/acs.energyfuels.7b00516>

Abstract:

Numerous studies in packed-bed biomass combustion modeling have been carried out, with the validation being usually performed against experimental data obtained in regions far from the bed. It is known, however, that in these regions standard modeling has a tendency to overpredict the solid and gas temperatures and the mixing rates of the gaseous species released from the packed-bed. This leads to an underprediction of the unburned hydrocarbon and soot concentrations in these regions, originating incorrect estimates of the pollutant emissions. Due to more and more stringent legislation, the combustion appliances need to improve their designs, for which deeper studies of the near-bed region modeling are necessary. This study seeks to find the main causes for the temperature and gaseous species misprediction in this region. Current biomass combustion models represent the gas–solid interaction by means of a porous medium, impeding the representation of the streaks with nonperfect mixed species that are known to be present. The modeling of gas-phase reactions with the standard eddy dissipation model is not suitable to account for complex chemical mechanisms and the weakened turbulent region created above the bed, despite its computational robustness and cost being highly appreciated. This work presents the first step toward the formulation of a modified Magnussen parameter (A), so the reaction rate resulting will reach a better physical modeling under transient packed-bed conditions, recovering the original value proposed for the Magnussen constant. In this work, the best adjustment was found for $A^* = 2$, instead of $A = 0.6–1$ as proposed previously by other authors, especially in regions far from the packed-bed. As a result of this work, the computational fluid dynamics (CFD) code was able to predict the spatially resolved profiles of temperature and major gas species concentration in the flame region of a domestic boiler with reasonable accuracy.



Full Length Article

Comprehensive CFD modeling of the ash deposition in a biomass packed bed burner

S. Chapela^{a,*}, J. Porteiro^a, M.A. Gómez^b, D. Patiño^a, J.L. Míguez^a^a Industrial Engineering School, University of Vigo, Lagoas-Marcosende s/n, Vigo, Spain^b Defense University Center, Spanish Naval Academy, Spain

ARTICLE INFO

Keywords:

Biomass combustion
Ash deposition
Fouling and slagging
CFD model

ABSTRACT

Ash-related issues such as fouling and slagging are likely the main operational problems of most commercial solid fuel burners. To study this kind of system, a full 3D-transient bed model embedded into the commercial CFD code ANSYS-Fluent was developed to describe the main processes that occur inside the bed. The model employs several sub-models that have been validated in previous studies (e.g., drying, devolatilisation, char reaction, radiation) and were combined with an ash evaporation model that functions in conjunction with a fine-particulate ejection model for predicting typical ash-related problems. In this work, the model is applied to simulate a pilot plant where the deposition of ash on refrigerated tubes is investigated. Several operational points were tested and simulated to assess the capability of the model to explain and predict the experimental fouling rates on the tubes, using which we show the relevance of the bed thickness variation and the primary air flow in the deposition profile. The ash evaporation and fine-particulate ejection models work symbiotically with the existing packed-bed biomass combustion model. The results obtained in this work show that this is a powerful tool for improving the operation of most existing appliances and contributes to the creation of a complex ash-layer deposition model.

1. Introduction

Currently, the use of biomass in residential and industrial thermal processes is increasing worldwide. The main reasons for its increased use include the rise of fossil fuel prices and the fact that biomass is the only carbon-based renewable fuel [1]. Its use in small-scale combustion systems for thermal energy production is an increasing trend and is not far from being cost-efficient when using high-quality fuels (e.g., wood chips and pellets); indeed, it would be enormously profitable if poorer or cheaper fuels could be used instead. However, these fuels present low thermal power output, high ash content and inadequate physical and flow properties [2–6].

The combustion of such biomass fuels, due to their high alkali metal and chlorine contents, causes several operational problems, such as fouling in the heat transfer zones of the systems and slagging [7,8]. Approximately three times more deposit has been observed for biomass fuels than for coal (normalized to the ash introduced with the fuel) [9].

In addition, wood combustion appliances are a major emission source of fine particles and volatile organic compounds. The smallest diameters produce respiratory and cardiovascular diseases, and the largest diameters cause air and soil contamination in the surrounding

areas [10].

The amount and composition of the ash that is released from the bed depend on the fuel ash composition [11] and the optimal combustion conditions. Small-scale boilers that burn wood logs in batch-mode result in higher emissions of products due to incomplete combustion. However, pellet-fired boilers that operate under a continuous feed show lower emissions. At the same time, a good design of the bed, combustion chamber and secondary air can help reduce the emissions of pollutants [12].

Packed-bed biomass combustion facilities typically show a bimodal particle size distribution in the flame region, including a fine mode in the range of 0.05–0.5 μm and a coarse mode in the range of 0.5–100 μm. Far from the flame region, the bimodal distribution usually vanishes, and the distribution is unimodal [13].

Fig. 1 shows that sub-micrometre particles are produced by the vaporization, homogeneous condensation and nucleation of ash elements or from the production of soot, whereas the coarse mode is produced both from mechanical ejection and agglomeration [12,15–17].

The physical phenomena and stages of fouling are summarized as follows [18]:

* Corresponding author.

E-mail address: schapela@uvigo.es (S. Chapela).

Nomenclature

Symbol	Parameter (Units)	Symbol	Parameter (Units)
a,b,c,d	Impaction efficiency coefficients (–)	Stk	Stokes number (–)
C_D	Drag coefficient (–)	t_η	Temporal scale of turbulent eddies near the wall (s)
D_{KCl}	Diffusivity of potassium chloride (m^2/s)	T_{sol}	Temperature of the solid (K)
d_p	Released particle diameter (m)	TSP	Total Sticking Probability (–)
G	Gravity (m/s^2)	$u', v' \text{ and } w'$	Gaussian distributed random velocity fluctuation (m/s)
k	Turbulent kinetic energy (m^2/s^2)	u_τ	Fluid friction velocity (m/s)
k_e	Erosivity of impacting ash particles towards the deposit (–)	<i>Greek symbols</i>	
M	Mass transfer coefficient for spheres (m/s)	Γ	Impaction efficiency (–)
MW_{KCl}	Molecular weight of KCl specie (kg/mol)	ε	Solid fraction (m_{solid}^3/m_{cell}^3)
$Prob_{particle}$	Sticking probability of the particle (–)	ζ	Normally distributed random number (–)
$Prob_{wall}$	Sticking probability of the wall (–)	μ	Dynamic viscosity (Pa s)
P_{vap}	Vapour pressure (Pa)	μ_s	Dynamic viscosity at the temperature of the surface (Pa s)
sa/vol	Surface area to volume ratio of the bed particle (1/m)	ν	Kinematic viscosity (m^2/s)
R_{gas}	Universal constant of gases (J/mol K)	ρ_g	Gas density (kg/m^3)
Re	Reynolds number (–)	ρ_{KCl}	Potassium chloride density (kg/m^3_{cell})
Sc	Schmidt number (–)	ρ_p	Particle density (kg/m^3_{solid})
S_{KCl}	Source term of gaseous potassium chloride ($kg/m^3 s$)	τ_p^+	Particle relaxation time (s)
		ϕ_{el}	Elutriation diameter (m)
		ϕ_{eq}	Equivalent diameter of the average pellet present inside the cell (m)

- Dispersion: This is a basic phenomenon that governs the transport of particles from the core of the duct to the walls. Gas turbulence helps in the process, which tends to homogenise the concentration of particles in the gas.
- Deposition: In this stage, the particle crosses the boundary layer until it contacts the wall. All of the forces acting on the innermost part of the boundary layer are fundamental. Two zones are distinguished: the region away from the wall where dispersion is dominant and the region near the wall where turbulence is attenuated and other forces, such as thermophoresis, become dominant.
- Adhesion: This is a very complicated phenomenon in which many different mechanisms may intervene. Chemical, mechanical and electrostatic forces may be responsible for the adhesion of a particle to the wall, which can be covered by previously deposited material.
- Detachment: The re-entry of the particle to the gas phase.
- Ageing: A stage in which the physicochemical properties of deposition on the walls are modified, resulting in sintering, condensation or partial collapse.

The main mechanisms that act over particles inside the boundary layer (i.e., the viscous and transition sublayer) and affect the transport of particles toward the wall are divided into four groups [19]:

- Fluid dynamics: drag, lift, friction (Saffman), free rotation support (Magnus), turbulent support (Basset) and virtual mass forces.
- Static forces: hydrostatic pressure.
- External forces: gravitational, electromagnetic and electrostatic forces.
- Molecular forces: Brownian motion and thermophoresis.

Previous studies [10,14,20] used thermodynamic balances, based on the minimization of the Gibbs energy, to account for some of the aforementioned processes. These tools work well for ash chemistry but require a large amount of experimental data to have good predictive abilities.

In this work, a full 3D-transient bed model that employs several sub-models for every stage of biomass combustion (all of which have been validated in previous studies) is improved with an ash evaporation and condensation model and a fine-particulate matter ejection model based on the Discrete Phase Model (DPM) of the commercial CFD code ANSYS-Fluent.

Using this full 3D-transient bed model, the ash deposition modelling benefits from the accuracy given by a model that accounts for the geometry of the boiler and transient combustion conditions of the bed.

2. Methodology

2.1. Pilot plant

A pilot plant of 12 (kW) nominal power that was specifically designed to test deposition over cooled surfaces was tested in previous studies [13,21], which have provided the experimental data used in this work.

Primary air enters through the bottom of the plant and reaches an inclined grate (dashed line) through a matrix of holes. This bed is side-fed by a screw. Secondary air enters the combustion chamber through a row of holes that are equally spaced at a distance between 0.35 and 0.45 (m) above the surface of the bed. The deposition sampling probe is a water-cooled pipe that has an outer diameter of 25 (mm) and a thickness of 1 (mm) and is made of stainless steel. It is placed 0.192 (m) above secondary air inlet. In current domestic boilers, it is common for water pipes to be in areas that are very close to the flame due to the considerable reduction of the volume of the combustion chamber owing to the requirement of compactness of the design. The selected position corresponds approximately to the typical distance in domestic boilers.

This facility allows the user to control four parameters: the separate control of the total air flow rate in the primary and secondary inlets, the temperature of water entering the deposition probe and the fuel mass delivered per unit of time. However, to avoid the side effects caused by a partially uncovered grate, the latter is controlled through a bed level controller. If the bed level drops, uncovering part of the gate, it acts over the feeding system to feed extra fuel. Therefore, for this study, deposition has been studied for the remaining three parameters: water temperature, primary-to-secondary air ratio and total air flow rate. The fuel used for this work is summarized in Tables 1 and 2. Although it is not a low-quality fuel, it was chosen because this fuel allows the steady operation of the system for a longer period of time, therefore leading to a much lower uncertainty of the results.

Fig. 2 shows a schematic diagram of this plant and the section of the CAD for the CFD simulations. The CFD model presents the correct orientation of the secondary air inlet because the schematic view is re-oriented for an easier representation.

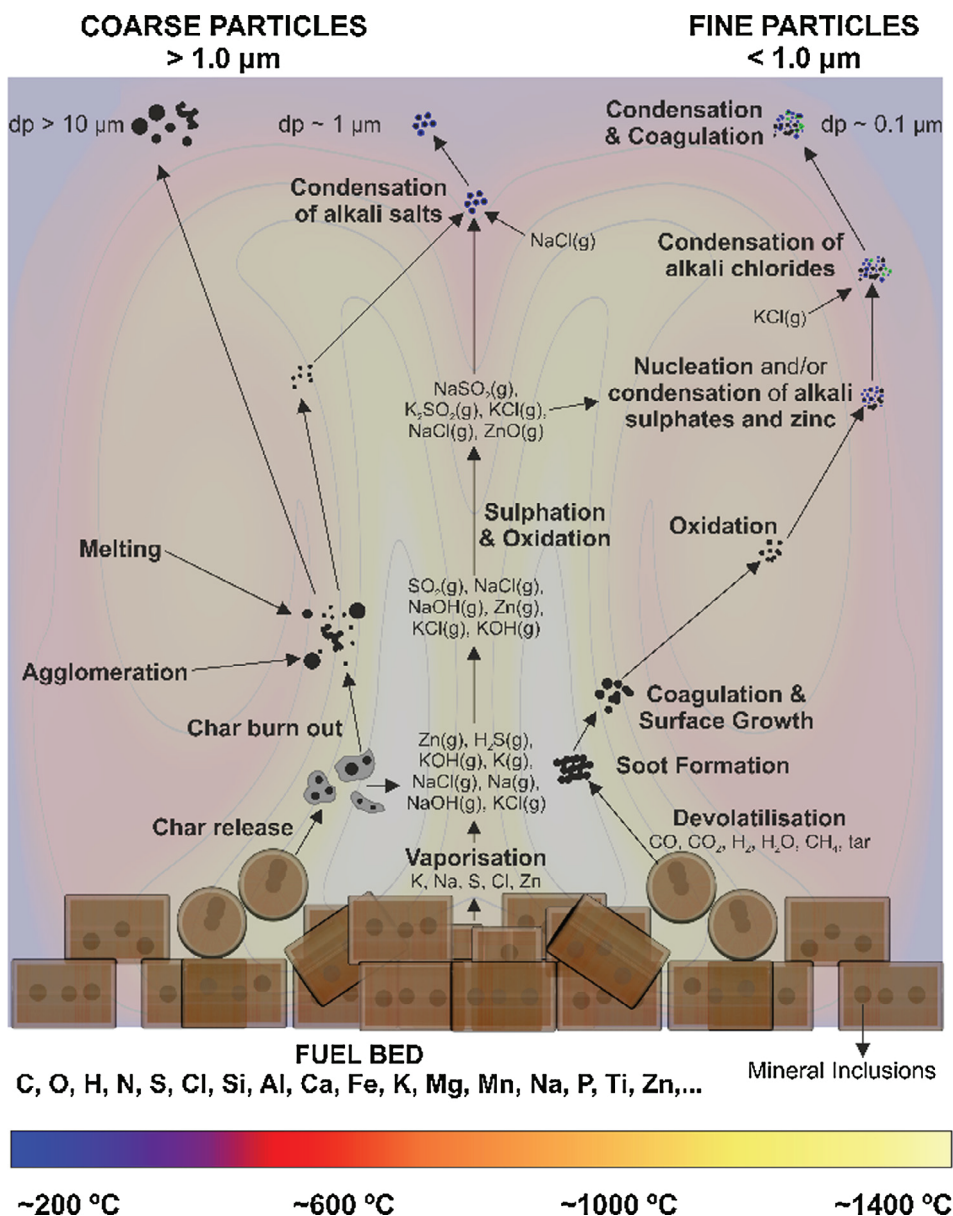


Fig. 1. Representation of the main mechanisms involved in the formation of particulate matter (). adapted from [14]

2.2. Model

2.2.1. Numerical setup

As mentioned previously, the facility has been modelled entirely and discretized with special attention to the pipe surface and surroundings to properly capture the gas flow pattern. This leads to a large number of elements in this area and, thus, to large computational effort. To accomplish the entire set of simulations, an equilibrium between precision and computational effort must be reached, as reaching a

steady-state through a transient simulation can be time-consuming. Several different mesh sizes were tested in the extreme cases of the experimental design, which are presented later, until the variation among the three mesh sizes led to no appreciable differences.

The domain was discretized in 750,000 polyhedrons because this number provides a good accuracy to computational effort ratio in free flow regions. Near the domain walls, the boundary layer was

Table 1 Proximate analysis of the fuel.

	Mass Fraction
Moisture content	0.0850
Volatile content	0.7468
Fixed carbon content	0.1620
Ash content	0.0062

Table 2 Ultimate analysis of the fuel.

	Mass Fraction
C	0.5170
H	0.0670
O	0.4070
N	0.0017
S	0.0001
Cl	0.0005

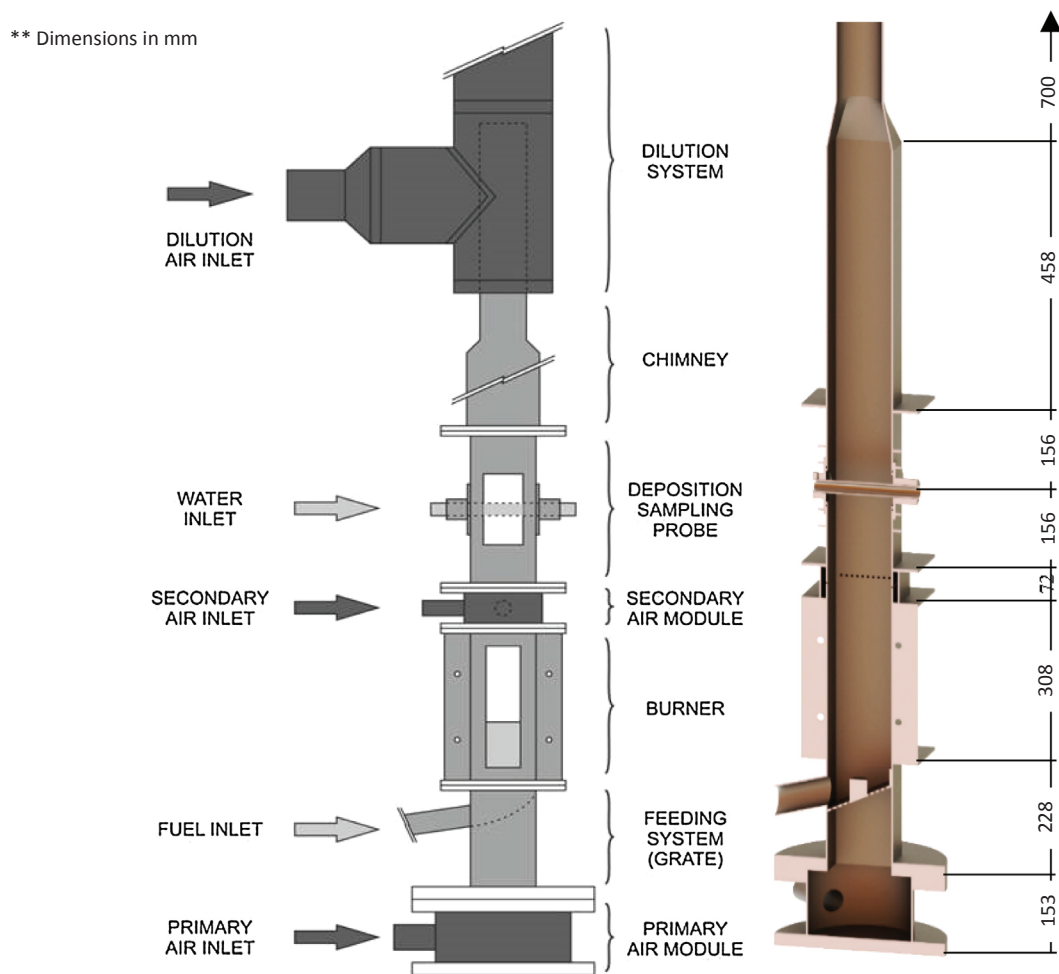


Fig. 2. Schematic and longitudinal section of the CAD used for CFD simulations.

specifically treated to properly capture the flow near the walls, ensuring smooth transition to free flow. It is common to use the value of y^+ to ensure the proper function of the turbulence model. In this case, a value of y^+ equal to 1 is mandatory in the first layer of the boundary layer of the pipe area surfaces. For the rest of the domain, to save computational effort, this requisite was lowered to values ranging from 3 to 10.

The setup constructed for the numerical study uses the Realizable $k-\epsilon$ turbulence model, which is broadly used due to its good accuracy to computational effort ratio, and the Enhanced Wall Treatment model. Combustion in the gas phase is performed using the Finite Rate/Eddy Dissipation algorithm, and the Discrete-Ordinates Model is used for radiation.

2.2.2. Inorganic vapours

Several studies [8,11,20,22] have concluded that the inorganic vapours, which condense over the cold surfaces, play a dominant role in ash deposition during biomass combustion.

Following previous studies, to reduce the otherwise excessive computational effort of tracking each type of particulate matter over time, we release the particulate matter once the system has reached a quasi-steady condition. In addition, the ash composition is the same as that of the bottom ash, and the erosion mechanisms are considered to be negligible compared to deposition due to the high stickiness of the layer of KCl that pre-condensed over the particles and cold surfaces, as proposed by Schulze [23].

However, these studies are based on several hypotheses that this work attempts to circumvent, such as neglecting deposition by inertial impaction, gravitational settling and the consideration of a single

particle size.

The model presented in this work comprises the following steps: evaporation, transport and condensation over the surfaces of KCl vapours, release of particles in the flue gas and adhesion of particles over the adherent surfaces.

Fig. 3 shows the effect of these inorganic vapours on deposition. The condensed phase forms an initial layer that provides high stickiness to which the particulate matter that reaches the surface becomes adhered. Once this mass is adhered, the voids are filled with more condensed inorganic vapours, and a new adherent layer is created.

The proper modelling of evaporation, transport and condensation of these vapours is necessary for good model accuracy. In this work, the KCl is introduced and transported as part of the inorganic ash, which is represented by two user scalars. Afterwards, it is evaporated from the bed, resulting in several source terms. In the energy equation, the evaporation and condensation of the specie is considered. Additionally, two mass source terms and three extra source terms for the user scalars and KCl transport equation are considered for these phenomena. It is worth noting that, as previously stated, not only is the KCl compound responsible for enhancing deposition, but several compounds, including NaCl, NaOH, NaSO₄, K₂SO₄ and KOH, can also enhance deposition. However, at the present state of development for this model, a first approximation using KCl as a tracer for these compounds is used.

The release of KCl is determined using the following expression:

$$S_{KCl} = M\rho_{KCl}esa/vol \quad (1)$$

where M is the mass transfer coefficient for spheres according to the Whitaker correlation, as given by Eq. (2):

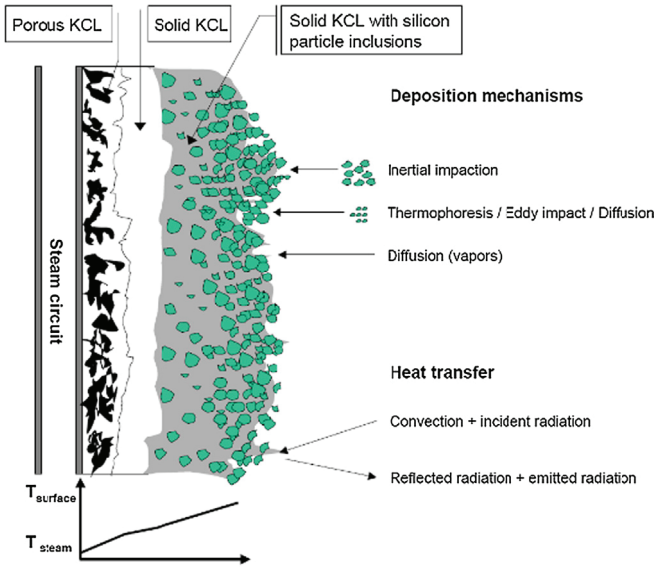


Fig. 3. Illustration of deposit structure on a surface [8].

$$M = (D_{KCl}/\phi_{eq})(2 + 0.4Re_D^{\frac{1}{2}} + 0.66Re_D^{\frac{2}{3}})Sc^{0.4} \left(\frac{\mu}{\mu_s} \right)^{\frac{1}{4}} \quad (2)$$

The calculation of potassium chloride density is based on the vapour pressure using the Stull's correlation for this term. Eq. (3) shows the calculation of this density, and Eq. (4) shows the Stull's correlation for the vapour pressure of KCl as a function of temperature:

$$\rho_{KCl} = \frac{P_{vap} M_{W_{KCl}}}{R_{gas} T_{sol}} \quad (3)$$

$$P_{vap} = 10^{4.78236 - \left(\frac{7440.91}{T_{sol} - 122.709} \right)} 100000 \quad (4)$$

Once the potassium chloride specie is incorporated into the gas that is emitted by the bed, it diffuses and travels through the combustion chamber towards the refrigerated surfaces, where the equilibrium of vapour pressures dictates the concentration at the wall. If the gaseous potassium chloride density is higher than the density dictated by the vapour pressure, condensation is allowed until equilibrium is reached. Otherwise, if it is lower, the previously condensed potassium chloride evaporates.

2.2.3. Particulate matter

The deposition and impaction rates of the particles contained in the continuous phase over the surfaces have been studied for several decades. Numerous studies have addressed [24–27] the variation in particle impaction efficiency using the Stokes number. Most such studies use the same equation (Eq. (5)) to predict the impaction efficiency, with small variations in the coefficients (see Table 3) depending on the consideration of different phenomena such as thermophoresis. The results of this equation for the three sets of coefficients are shown in Fig. 4.

$$\Gamma(Stk) \approx (1 + b(Stk-a)^{-1} - c(Stk-a)^{-2} + d(Stk-a)^{-3})^{-1} \quad (5)$$

Table 3
Impaction efficiency coefficients.

	a	b	c	d
Israel and Rosner (1983) [24]	0.125	1.25	-0.014	0.00508
Baxter et al. (1990) [25]	0.1425	1.28	0.00215	0.00587
Baxter et al. (1990) [26]	0.1238	1.34	-0.034	0.00289

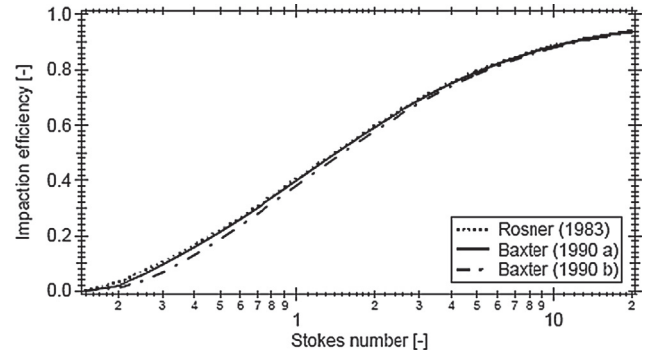


Fig. 4. Results of Eq. (5) depending on coefficients [8].

Although this is an elegant and simple way to predict the impaction efficiency, it is only valid for cases that do not have the complex geometry and the phenomenology involved in biomass appliances.

In the model used in this work, for the release of particulate matter from the bed, we perform a search over all of the cells where the solid fraction exists, and those that belong to the surface of the bed are marked. In these cells, the maximum elutriation diameter is computed by balancing the drag forces exerted by the gases with the gravitational forces, leading to the following expression:

$$\phi_{el} = \frac{3C_D \rho_g \phi_{eq} v^2}{4\rho_p G} \quad (6)$$

This elutriation diameter is calculated using a Newton-Raphson procedure. This iterative procedure is required due to the variation of Reynolds number with particle diameter and, therefore, the variation of the coefficient C_D , which follows a piecewise function, as shown in Eq. (7) [28].

$$\begin{aligned} \text{If } Re \leq 0.01, & \quad C_D = 4.5 + \frac{24}{Re} \\ \text{If } 0.01 < Re \leq 20, & \quad C_D = \frac{24}{Re} (1 + 0.1315 Re^{0.82 - 0.05 \log_{10} Re}) \\ \text{If } 20 < Re \leq 260, & \quad C_D = \frac{24}{Re} (1 + 0.1935 Re^{0.6305}) \\ \text{If } 260 < Re \leq 1500, & \quad C_D = 10^{(1.6435 - 1.1242 \log_{10} Re + 0.1558 (\log_{10} Re)^2)} \\ \text{If } Re > 1500, & \quad C_D = 10^{(-2.4571 + 2.5558 \log_{10} Re - 0.9295 (\log_{10} Re)^2 + 0.1049 \log_{10} Re^3)} \end{aligned} \quad (7)$$

When the diameter of the chosen particle is smaller than the maximum elutriation diameter, an ejection trajectory is created. This is done to avoid the generation of Lagrangian trajectories that will not have the momentum necessary to leave the bed, thus saving computational resources.

It is common to use a modified Stokes number, where the characteristic time of the continuous phase is the temporal scale of turbulent eddies near the wall, as shown in Eq. (8):

$$t_\eta = \frac{\nu}{u_\tau^2} \quad (8)$$

The particle relaxation time is expressed in Eq. (9):

$$\tau_p^+ = \frac{\rho_p d_p^2 \rho_g u_\tau^2}{18\mu} \quad (9)$$

If $\tau_p^+ < 0.1$, the drag forces are so dominant that the dispersed phase follows the continuous phase almost perfectly through every change in direction or velocity. This is called the diffusion regime. If $\tau_p^+ < 10$, the inertia of the particle is dominant, and the continuous phase is incapable of substantially changing the trajectory of the particles. This is called the impaction regime. The inertial regime exists between these regimes, in which the particle trajectories are affected by the flow but also tend to follow their own path due to their meaningful momentum.

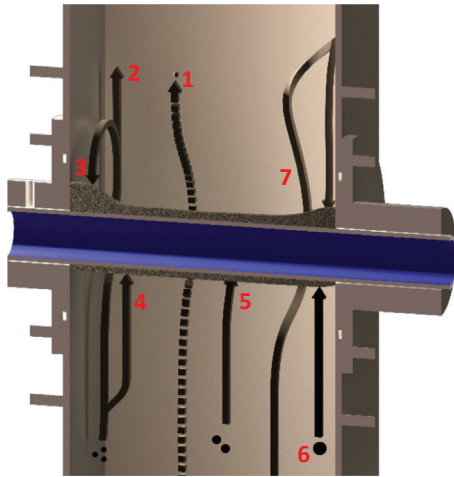


Fig. 5. Illustration of different trajectories for particulate matter.

The diameters considered are chosen based on their particle relaxation time to cover the entire impaction regime and are used to analyse the contribution of each regime to the total deposition.

Due to the great difference between the densities of continuous and dispersed phases, the Basset and Magnus forces and the virtual mass forces are neglected, as proposed by Crowe [29].

The particle is initialized with the conditions of its starting cell. During its travel through the domain, it is heated by the flue gas and the radiation received from the surroundings. Fig. 5 shows the different typical trajectories that may lead to the deposition of a particle on the test-probe of the experimental facility employed in this work. Some particles simply skip the refrigerated tube due to a trajectory that is far from the cold surface (Fig. 5 - case 1). When their trajectories are near the cooled tube, depending on the particle size, they can do the following:

1. Circumvent the cooled pipe and escape through the chimney (case 2).
2. Partially circumvent the cooled pipe but get trapped by its wake, and gravitationally deposit on the leeward side (case 3).
3. Come into contact with and stick to the cooled pipe (cases 4–6).
4. Come into contact with a wall downstream, losing some of their momentum and falling. Some might lay on top of the pipe, and others might fall to the bed (case 7).

Backman et al. [30] originally defined four characteristic temperatures based on theoretical melting curves, which are shown in Fig. 6:

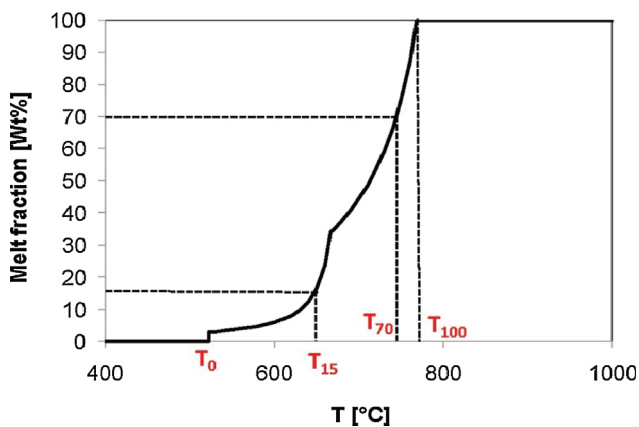


Fig. 6. Mass-weighted percentage of molten fraction of the particle depending on temperature [31,32].

1. T0: also called the solidus temperature; the first molten phase appears.
2. T15: also called the sticky temperature; it is assumed that approximately 15% of the molten phase is required to make the particles sticky.
3. T70: the flow temperature; the particle is heavily molten.
4. T100: temperature of complete melting.

Therefore, if the particle temperature is lower than 900 (K), the probability for the particle to be partially or fully molten is 0. If it is greater than 1200 (K), the probability is 1. For the remaining cases, a linear relationship is assumed.

The existence of a molten phase in the particle does not lead to adhesion in all scenarios. The weight or momentum of the particle can lead to its detachment from the surface. Therefore, a minimum of 10% of the molten fraction is required for it to remain adhered to the surface. Moreover, if the particle is heavily molten, the particle will not detach from the surface.

Similar to the previous procedure, the probability of the particle remaining adhered is 0 if the molten fraction is less than 0.1, and the probability is 1 if the fraction is greater than 0.7. Again, a linear relationship is assumed for the remaining scenarios.

When a particle hits a wall, if the temperature of the wall is less than 600 (K), there is no molten potassium chloride present to act as a glue; hence, the molten fraction is 0. If it is greater than 700 (K), all of the condensed potassium chloride is molten. For the remaining temperatures, a linear relationship is assumed. If the molten fraction of potassium chloride is less than 0.1, the sticking probability is 0; if it is greater than 0.7, the probability is 1. A representation of these sticking propensities is shown in Fig. 7. Walsh et al. [33] proposed the following expression based on the assumption that a group of particles with a given sticking probability, $Prob_{particle}$, can be modelled as if it contained a mass fraction, $Prob_{particle}$, of perfectly sticky particles and a mass fraction, $1-Prob_{particle}$, of non-sticky particles. In addition, Walsh considered not only the stickiness of the impacting particle but also that of the deposit surface itself and the erosion phenomena through the last term of Eq. (10).

$$TSP = Prob_{particle} + Prob_{wall}(1-Prob_{particle}) - k_e(1-Prob_{particle})(1-Prob_{surface}) \tag{10}$$

Because erosion phenomena are not considered in this work, the total sticking probability is calculated as:

$$TSP = Prob_{particle} + Prob_{wall}(1-Prob_{particle}) \tag{11}$$

Due to the deterministic nature of the Lagrangian trajectories caused by the use of a RANS approach for the gas phase, ANSYS-Fluent provides a stochastic tracking approach for predicting the dispersion of particles due to the chaotic nature of turbulence. By integrating the trajectory equations for each particle along its path using the instantaneous fluid velocity and computing the trajectory for a discrete

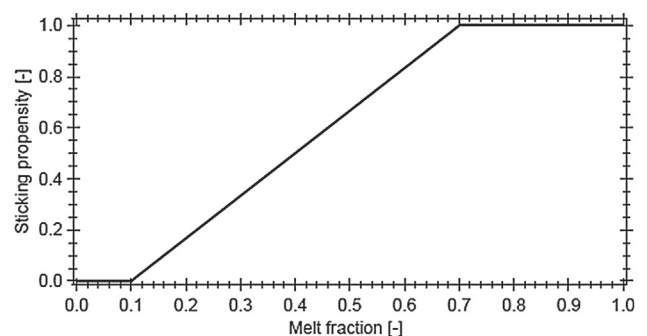


Fig. 7. Representation of the assumed relation between the molten fraction and sticking probability [8].

number of tries, the effects of turbulence effects can be determined. This model is called the Discrete Random Walk (DRW) model. In this model, each turbulent eddy is characterized by a Gaussian distributed random velocity fluctuation (u' , v' and w') and a time scale (τ_e) [34].

The values of u' , v' and w' then obey the following expression:

$$u' = \zeta \sqrt{u'^2} \quad (12)$$

where ζ is a normally distributed random number and the term $\sqrt{u'^2}$ is the local RMS value of the fluctuations in the velocity. Since the k - ϵ turbulence model is used in this work, assuming isotropy, the next expression is reached.

$$\zeta \sqrt{u'^2} = \zeta \sqrt{2k/3} \quad (13)$$

2.2.4. Bed level controller

In this study, experimental runs have been made by using a level controller that controls the fuel feed, ensuring that no grate remains uncovered because an uncovered grate would lead to a large amount of primary air flowing through the final part of the grate, where most of the fuel has been consumed and only ashes would remain, as the fuel inlet is on the opposite side.

In the numerical study, we used the bed modelling already validated in previous studies [35], which have shown good accuracy in terms of bed thickness. In addition, a specific algorithm was programmed to look for the maximum vertical coordinate where the bed exists, thus ensuring a minimum level equal to one pellet in the final part of the grate. Additionally, a damping control is provided to avoid uncontrolled oscillations of the CFD calculation such that convergence is reached more quickly.

2.3. 2D/3D profile algorithms

Fouling is often studied from both the quantitative and geometric perspectives. The latter is relevant because it affects the gas flow pattern, enhancing deposition in some cases, and it affects the efficiency of the boiler. In this work, two different algorithms were developed to analyse the geometry.

Once the trajectories and their respective adhesion probabilities are calculated, deposition profiles are generated using the logarithmic graph of particulate emissions of the facility studied. To do this, the raw data extracted from each simulation are treated with different ad hoc algorithms in MATLAB.

The 2D profile generator sweeps the entire surface and stores both the cylindrical coordinates of the cells along the pipe and the mass adhered for each diameter, accumulating the mass adhered due to each granulometry after weighting their contributions by using the logarithmic curve of particulate emissions of the facility. Once the algorithm has swept the entire surface of the pipe, it calculates the average mass deposited on the cells. Then, the algorithm plots the maximum resulting displacement of the centroid in the normal direction of the face for each angular coordinate in the side profile or the Cartesian coordinate for the front profile. Once these scattered data are plotted, they are ordered by angle, and each datum is joined with its neighbours and smoothed by means of a moving average with a window equal to 10 face values. Finally, the surface wrapped by this profile is coloured.

This type of representation is faster to create and is often used in experimental papers to analyse deposition, as they are created from direct photographs of the object studied. However, the 3D algorithm allows the user to examine the deposition profile more closely. Using the rotate and translate tools, the user can minimize the errors that occur when interpreting two-dimensional profiles when a high value hides other values behind it. However, these profiles are slower to create and are only useful when using software, as they present nearly the same problems when they are printed or attached to paper.

3D representations are also created from the raw data and processed by means of the average mass deposited weighted by the logarithmic curve of the facility. In this case, the algorithm sweeps the surface, and the value of each cell is first smoothed with the direct neighbours with a ratio of 0.5, ensuring the conservation of the mass deposited, and then they are smoothed by nodal interpolation.

Fig. 8 summarizes the procedure followed for the calculation of deposition of particulate matter over the surfaces.

2.4. Design of experiments

To improve the representativeness of the study and reduce the computational effort, a Central Composite Design (CCD) based on a Latin Hypercube Sampling (LHS) technique is used in this work. These strategies have become very popular in experimentation, among others such as orthogonal arrays or Hammersley designs [36] because they can reach the same level of significance with fewer attempts.

The Central Composite Design requires three types of trials: 2k factorial trials, 2k axial trials and 1 nc centre point trials. The value at the centre is used to detect curvature in the response, and the others are used to estimate the response for each dimension and the interactions between each set of dimensions. To assess the rotatability of the design, each factor is divided into five levels: $-\alpha$, -1 , 0 , 1 , and α . When a design is rotatable, it will produce information that predicts the response with the same precision at all points that are equidistant from the origin of the design [37].

Fig. 9 shows the final design. A three-parameter central composite design was used. Fifteen points are necessary, and they are distributed as one central point (central red dot), eight points (blue dots in the cube vertices) as limits of a cube that is centred on the central point, and 6 star points (remaining red dots). Finally, to improve the accuracy, 18 extra attempts were performed (green dots), resulting in a total of 33 complete simulations.

Table 4 shows the codified levels for each dimension of the design of experiments that was used to summarize the entire set of simulations, as shown in Table 5. Runs from 1 to 15 belong to the original CCD, and the remainder are the extra runs.

3. Results

3.1. Combustion

Due to the intrinsic transient nature of the combustion of biomass and of the bed model used in this work, there are inherent fluctuations over time in the results of the simulations, which are generally driven by local oscillations in the bed [38–40]. Therefore, a simulation is considered to have reached its quasi-steady condition when the maximum fluctuation of the variables of interest are less than 5% around its time-averaged value in a 500-second period of time and the slope of its linear regression is near zero (to avoid trends). The variables of interest and maximum permissible slopes are summarized in Table 6.

To reach these values, the required simulation flow time, depending on the case, varies from 9000 to 39,000 s, with an average value of 19,500 s. Fig. 10 shows a comparison between the experimental work and the CFD model. It is apparent that there are similar trends in the evolution of the thermally related variables. It is important to note that it was not possible to perform the experimental test with the highest total air flow due to stability problems in the facility [21].

Moreover, the experimental results in this work were obtained over the course of several months with different fuel batches; therefore, direct comparisons of the results must be made with caution. The same fuel was used for the entire set of experiments, but because there is a large number of experiments, small differences between batches of the same fuel are expected. In addition, the storage of biomass during the tests can have affected its moisture and the experimental uncertainty of the fuel mass consumed due to the bed level controller may explain a

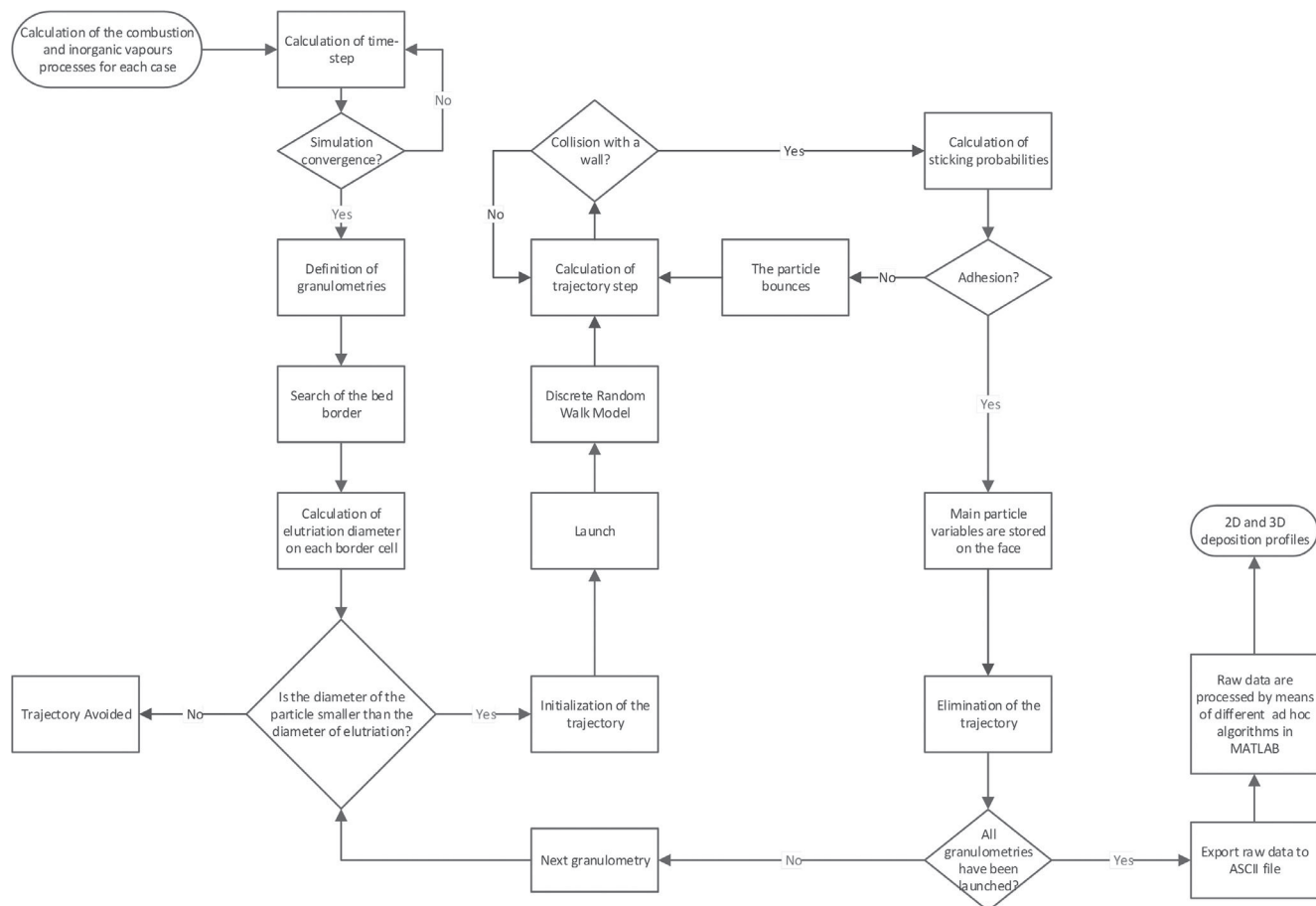


Fig. 8. Flow chart of the procedure followed.

small portion of the difference in the measured thermal power. However, the most probably reason is that, due to the very short travel of the cooling water inside the combustion rig and the very high mass flow rate of the circuit, it is obtained a very small gradient between the inlet and outlet, where the thermocouples are located. This made the precise measurement of thermal power very difficult. As aforementioned, the combustion rig was first designed for 12 (kW) and then a bed level controller to avoid uncovered grate was attached, therefore it is probably that the CFD value is closer to reality that the one reported experimentally but there are no strong evidences to assess this.

The result shown in the third graph for the water temperature once

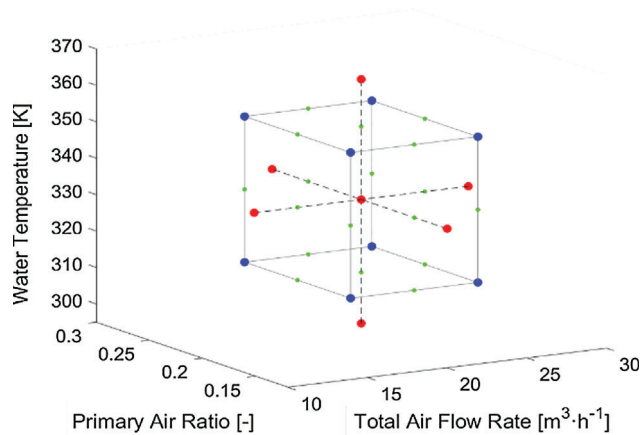


Fig. 9. Final Central Composite Design (CCD) of the field of study for CFD simulations.

heated inside the facility validates the assumption made for CFD calculations when setting a uniform temperature for the water-side wall of the cooled pipe as the high mass flow rate across the pipe led to a negligible variation of the temperature along the pipe. Fig. 11 shows a visual comparison of the flame volume in the pilot plant and its simulation.

3.2. Bed level

As previously mentioned, the bed level is controlled by a specific algorithm, so only small variations of the level inside the interval specified are allowed. Fig. 12 shows the profile reached in the extreme cases of the design of experiments. For cases in which low primary air is introduced due to a low primary-to-secondary air ratio or due to a low total air flow rate, the thickness at the end of the grate is greater than that observed in the opposite cases. In all cases, the bed is wedge-shaped due to the thrust induced by the feed screw and the slope of the grate.

Table 4
Codified levels.

Levels	Temperature (K)	Primary Ratio (-)	Total air flow rate (m ³ /h)
(-α)	299.4	0.116	13.27
(-)	313	0.15	16
(0)	333	0.2	20
(+)	353	0.25	24
(α)	366.8	0.284	26.73

Table 5
List of simulations.

Point	Temperature (K)	Primary Ratio (-)	Total air flow rate (m ³ /h)
1	-α	0	0
2	-	-	-
3	-	-	+
4	-	+	-
5	-	+	+
6	0	-α	0
7	0	0	-α
8	0	0	0
9	0	0	α
10	0	α	0
11	+	-	-
12	+	-	+
13	+	+	-
14	+	+	+
15	α	0	0
16	-	0	0
17	0	-	-
18	0	-	+
19	0	+	-
20	0	+	+
21	+	0	0
22	-	-	0
23	-	0	-
24	-	0	+
25	-	+	0
26	0	-	-
27	0	-	+
28	0	+	-
29	0	+	+
30	+	-	0
31	+	0	-
32	+	0	+
33	+	+	0

3.3. Deposition

Once the biomass combustion simulation is converged, where the potassium chloride is evaporated, transported and condensed over surfaces, twelve diameters are calculated from the modified particle relaxation time for each simulation.

Diameters for $\tau_p^+ = 0.01, 0.02, 0.05, 0.1, 0.2, 0.5, 1, 2, 5, 10, 20,$ and 50 were launched from the packed bed from cells where there was enough drag. One thousand iterations of Random Walk for each diameter were performed. This resulted in 3 to 5 million trajectories for each simulation. Once the trajectories of different diameters were launched for the set of simulations, they were exported from ANSYS-Fluent to an ASCII file and processed by several ad hoc algorithms.

3.3.1. Alkali salt condensation

As previously mentioned, the deposition of alkali salts over cooled surfaces plays a dominant role in the subsequent deposition of particulate matter due to its high stickiness. Fig. 13 shows the influence of the three main control parameters: total air flow rate, primary air ratio and water temperature. The latter is represented by three surfaces, from

Table 6

Maximum permissible slopes for variables of interest.

Variable of interest	Unit	Max. slope
Average wall temperature of cooled probe	K	0.002
Lambda	-	1e-05
Bed mass	kg	2e-05
Heat transfer to cooled probe	W	0.1
Power released	W	0.1
KCl deposition over cooled probe	mg/cm ² /h	2e-04

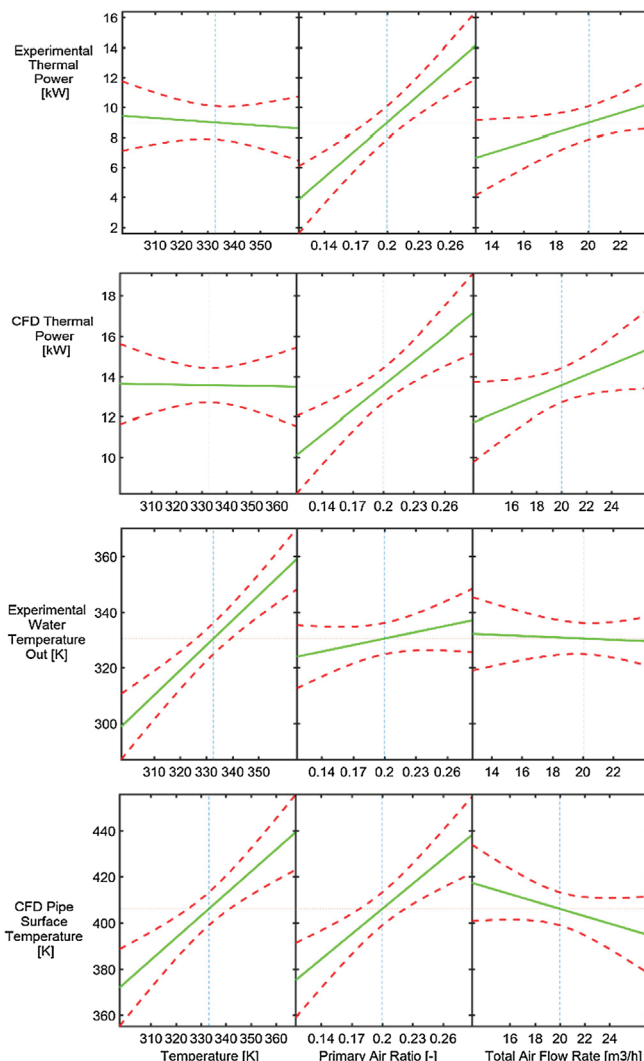


Fig. 10. Comparison of the evolution of the thermal-related results obtained from experimental and CFD runs.

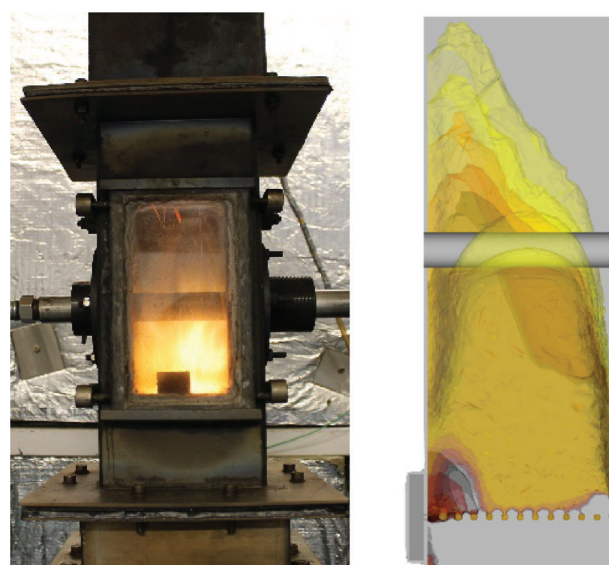


Fig. 11. Visual comparison between experimental and numerical behavior of the facility.

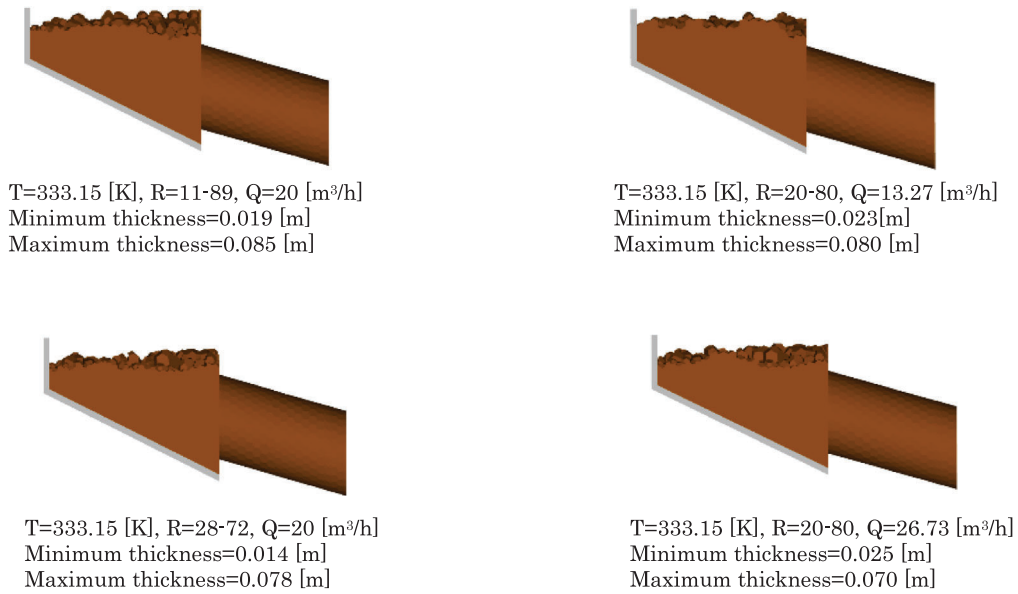


Fig. 12. Effect of each parameter on bed level and shape. Left: primary-to-secondary air ratio. Right: Total air flow rate.

top to bottom, at 40, 60 and 80 °C (313.15, 333.15 and 353.15 K). Therefore, if the water flowing through the pipe is introduced at higher temperatures, the condensation over the pipe surface decreases, which corresponds to what was expected.

In addition, if the primary air ratio increases with the same total air flow rate, a combination of higher bed temperature and lower velocities in the secondary air inlet leads to a higher KCl concentration in the region close to the probe and, thus, to a higher KCl condensation over the surface. Although higher velocities near the pipe could lead to higher heat transfer by convection and an increase in the surface temperature of the pipe, this effect appears to be negligible. The same trend is shown when the total air flow rate increases with the same primary air ratio.

Fig. 14 shows the amount of KCl condensed on the tube, normalized according to the average value of the tube. For simplicity, only the extreme cases of the field of study are shown, which are the minimum

and maximum water temperature, minimum and maximum primary-to-secondary air ratio and minimum and maximum total air flow rate.

It is apparent that, despite having the secondary air completing the combustion relatively close to the refrigerated tube, the almost constant wall temperature imposed by the inner water allows the existence of a condensed phase throughout the tube, preferably toward the side associated with a thinner bed in the region of the detachment of the flow around the tube. Fig. 15 shows the distribution of gaseous KCl present in the flue gas and the temperature of the surface, both of which are relevant parameters to condensation over the pipe. Fig. 16.

In studying the effect of the water temperature, a similar KCl condensation is observed, with a predominance of the case with a lower water temperature. The condensed phase is more abundant on the leeward side of the pipe. The location with a lower condensed phase is placed on the opposite side of the reader, which will slightly affect the deposition of the solid phase.

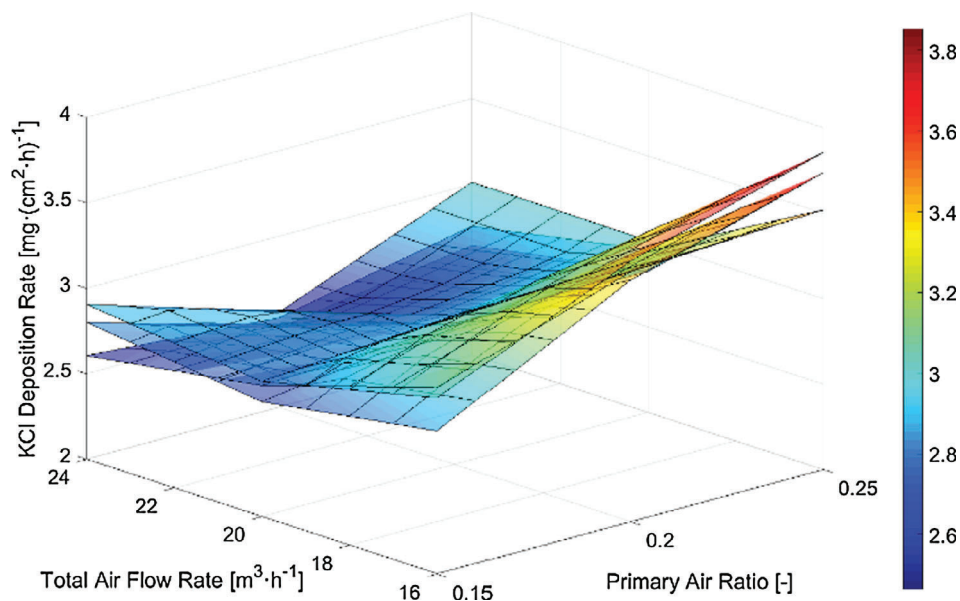


Fig. 13. Deposition of KCl for different water temperatures. From bottom to top, 353.15, 333.15 and 299.15 K.

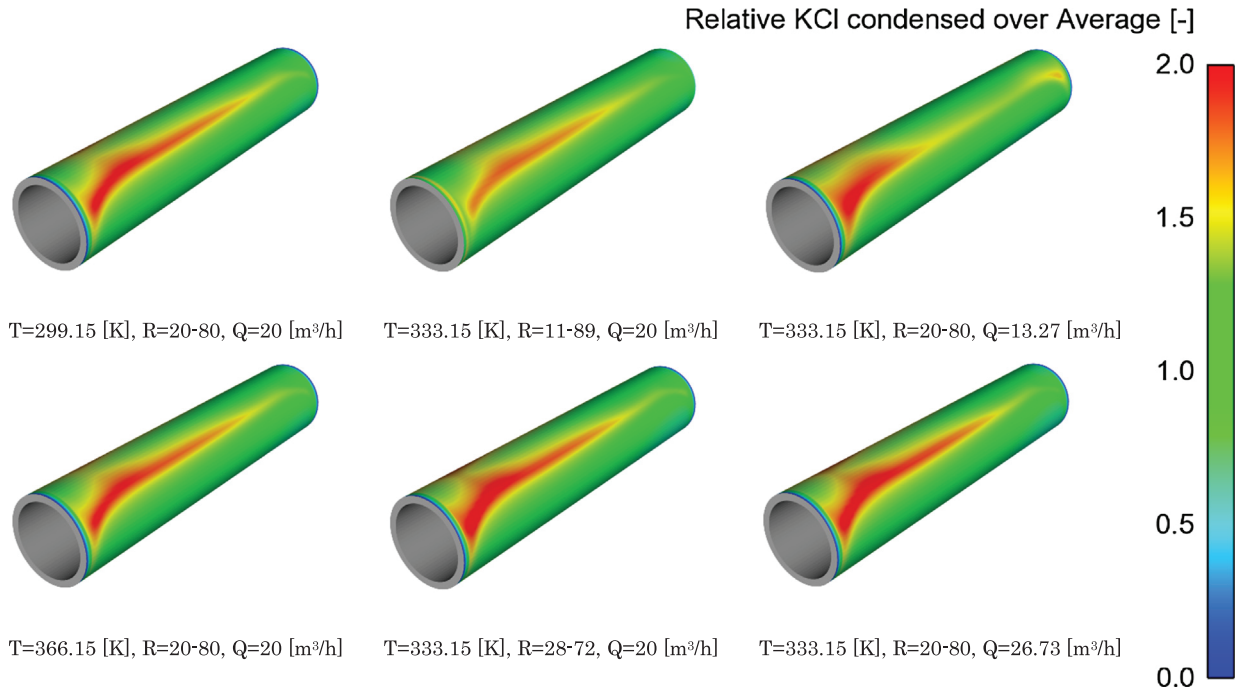


Fig. 14. Effect of the each parameter on the condensed phase over the cooled pipe. Left: Water temperature. Center: Primary-to-secondary air ratio. Right: Total air flow rate.

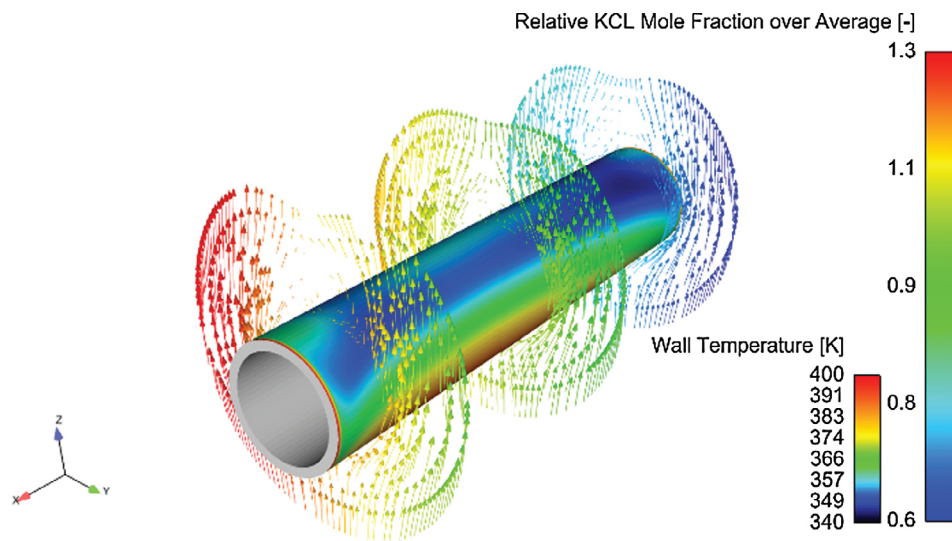


Fig. 15. Example of distribution of gaseous KCl present surrounding the cooled pipe and temperature of the cooled surface for T = 299.15 [K], R = 20–80, Q = 20 [m³/h].

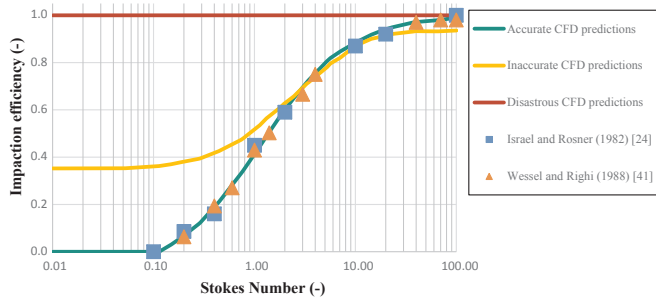


Fig. 16. Representation of different CFD-predictions [22]. (See above-mentioned reference for further information).

Regarding distribution, it is apparent that it is a predominant factor in terms of the homogeneity of the deposition of the condensed phase. The lower primary air achieves a lower bed temperature, so less KCl is evaporated, and it is more diluted with secondary air. In addition, a smaller displacement is generated toward the side with a thinner bed. As the secondary air dilutes the smaller amount of gaseous KCl and increases the turbulence around the tube, the condensation becomes more homogeneous over the pipe.

Fig. 14 shows the effect that the total air flow rate has on the condensed KCl phase for a fixed primary-to-secondary air distribution of 20–80 with a water temperature of 333.15 K. Similar to what occurs with the primary-secondary distribution, a lower total air flow rate causes a lower bed temperature and a lower thermal-power/installation-volume ratio. This results in slightly more homogeneous deposition. The effect of the increased speed at the beginning of the wake is

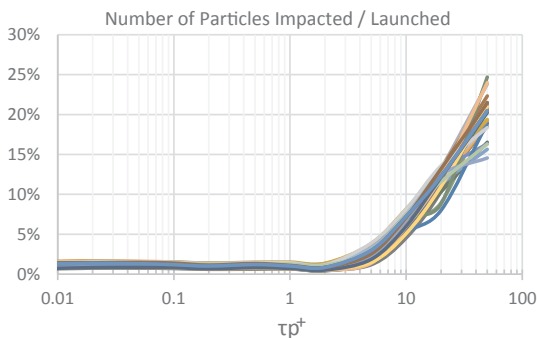


Fig. 17. Fraction of particles launched that remain adhered to the deposit surface.

appreciated, with a greater deposition of KCl as the velocities increase in the surroundings with a higher total air flow rate. The increase in the total air flow rate with the same primary-to-secondary ratio decreases the effect that the bed thickness has on deposition.

In summary, the condensation of KCl is quite homogeneous along the periphery of the pipe with greater deposition on the side of a thinner bed and in the swirls formed at the beginning of the wake. Moreover, the presence of the secondary air completing the combustion and the particular geometry of the installation force the entire batch of particles to cross regions with high temperatures, causing a molten phase to exist, so the calculation of probabilities explained in chapter 2.2 will be favourable for the adhesion of the particles to the tube.

3.3.2. Particulate matter

Previous work conducted by Weber et al. [22] shows the importance of performing the correct modelling of both the Eulerian phase and the Lagrangian phase. If the modelling is not adequate, either by using models that are not advised for the situation or by a poor discretization of the calculation domain, the user can arrive at easily identifiable large-scale errors or at imprecise predictions, which can lead to erroneous conclusions.

Fig. 17 is an equivalent figure obtained from the simulations in this work. As highlighted in previous work [42], the use of the k-epsilon turbulence model, which is used in this paper for its good compromise between computational-effort and precision, can lead to an overall

overestimation of impacts from 1 to 3%, which may be the reason for the bottom performance found at low Stokes regimes.

It is also important to note that the perpendicular section of the tube represents 20.8% of the perpendicular section of the combustion chamber, so the slightly higher values obtained for the coarse particles are due to deposition by gravity after colliding with downstream walls, which can also be affected by the use of the k-epsilon turbulence model.

For analysing the deposition rates based on the regime, Fig. 18 shows the relevance in terms of number of particles adhered for the three different regimes, i.e., diffusion, inertial and impact regimes, from bottom to top. The diffusion and inertial regimes present similar trends along the field of study, and the increase in particle relaxation times leads to a larger contribution of the inertial regime. The trend for impact regime is, logically, completely different. As the total air flow rate or the total primary air increases, larger particles are surrounded by sufficient gas velocity to reach their ejection thresholds.

Fig. 19 shows the contribution of each regime to the mass deposited over the pipe surface. Clearly, the impact regime contributes significantly to the total mass deposition because the average diameter of the particles that reach the pipe in this regime is larger; hence, their mass is greater. The same can be applied between the inertial and diffusion regimes. The latter present the same behaviour as the inertial regime but with a lower contribution.

Using these figures, a quantitative estimate could be made of the deposition on the tube if from bed were thrown all granulometries with of the same mass flow, except those that would not have sufficient momentum to be mechanically ejected. However, this would lead to unrealistic results.

This occurs because, as mentioned, in the combustion of biomass, the diffusion regime prevails in the particulate matter emissions followed by, to a lesser extent, the inertial regime, giving rise to a bimodal particulate matter emissions curve.

For this plant, due to its design, the particulate emission curves of Fig. 20 are obtained, resulting a unimodal distribution with a representative size in the range of 50–100 nm. This distribution is used to weight the contribution of each particle diameter released from the bed, thus giving predominance to the particles in the diffusion regime.

3.3.3. Deposition geometry

As previously mentioned, for this work, different algorithms were developed to estimate the 2- and 3-dimensional profiles after

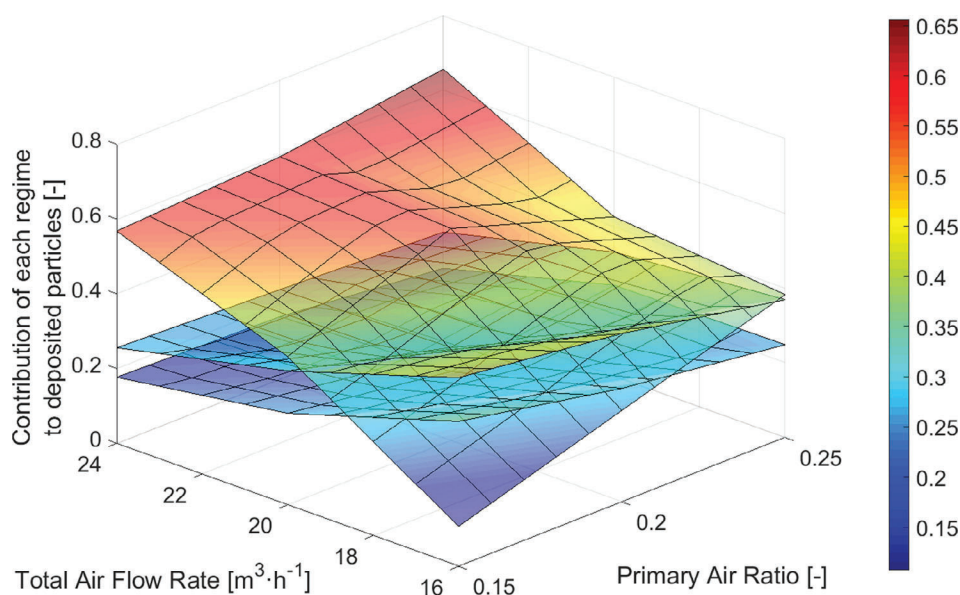


Fig. 18. Contribution of each regime to the total of deposited particles. From bottom to top, diffusion, inertial and impact regimes.

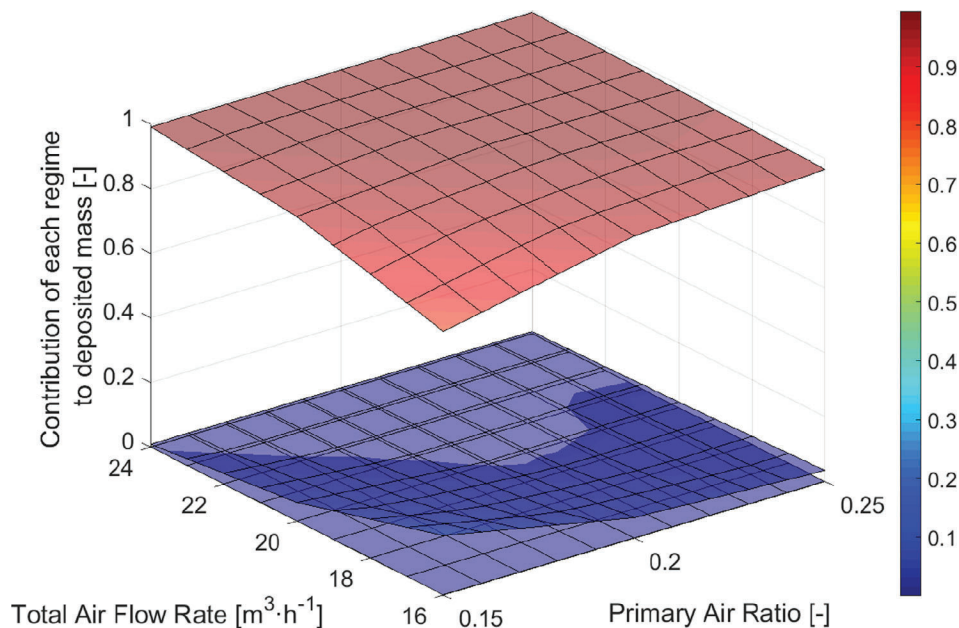


Fig. 19. Contribution of each regime to the total deposited mass. From bottom to top, diffusion, inertial and impact regimes.

calculating the Lagrangian trajectories. These trajectories are clearly affected or unaffected by the gas velocities depending on the particle relaxation times. The non-homogeneous velocities in the plane just above the bed that are caused by the inclined grate are clearly shown in Fig. 21. Although part of its effect fades with the secondary air, the particles are released predominantly from the thinnest bed region due to the lower pressure drop and higher velocities. In the case of particles located in the diffusion regime, this effect vanishes as the secondary air enters, but for the more massive particles, the effect of secondary air is less significant.

After the secondary air, it is apparent that the preferred flow path has partially disappeared but the flow moves to the opposite side of the secondary air inlet due to the alignment of the holes of the secondary distributor with the inlet.

Fig. 22 shows the preferred path of the flow along the facility, and it is apparent that some of the pathlines are trapped in the wake of the cylinder. This flow and loss of momentum due to the collisions of the particles against the walls downstream of the pipe, in a facility with such a high height-to-section ratio, cause significant deposition on the upper side of the tube, as shown in the pictures of both the experimental and numerical profiles.

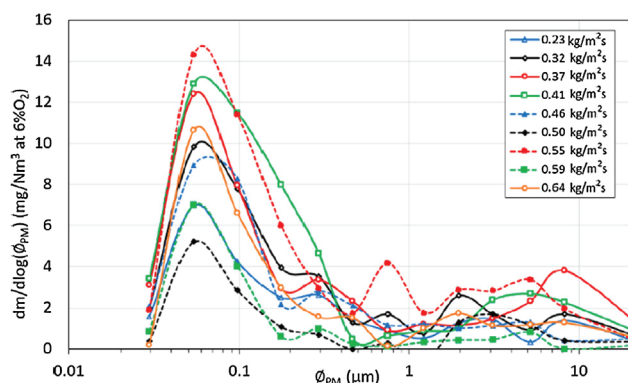


Fig. 20. Experimental data for the diameter distribution of particulate matter [13].

Focusing on the geometry of the normalized deposition on the tube, we studied the effect of each of the three variables considered (water temperature, primary-to-secondary air ratio and total air flow rate). For ease of understanding, pictures of the relevant cases are added to a three-dimensional representation of the complete field of study in Appendix A.

The 2- and 3-dimensional profiles of the deposition of PM on the refrigerated pipe are shown in Figs. 23–25. The deposition is analysed by varying one of the parameters and keeping the other two invariable with the values $-\alpha$, -1 , 0 , 1 , and α , as shown in Table 4.

3.3.3.1. Water temperature. Regarding the effect of water temperature in the facility (Fig. 23), after observing its negligible effect on the condensation of KCl above the pipe’s surface, except for the lower corner at the side of greater bed thickness in Fig. 14, the following results are extracted.

As expected, the water temperature does not substantially affect the combustion or temperature in the bed. There is no appreciable variation in how the flue gas is cooled in the surroundings, so there are no large variations in the flow of flue gas or the radiation toward the bed.

It is important to mention that the creation of fine PM due to flame-quenching is not considered in the deposition calculation. It is assumed that due to the short distance and high turbulence of the area, its contribution to the deposition geometry will be homogeneous throughout the periphery of the tube.

In Fig. 23, two different phenomena can be observed. The first is the increase in deposition on the leeward side of the tube and opposite the inlet of secondary air. The displacement has been previously explained, and the increase in deposition in that zone may be due to the greater condensation of KCl on the tube (Fig. 13).

The second phenomenon is the decrease in deposition of PM on the opposite side of the 3-dimensional profile, which is the area of greater bed thickness on the windward side of the cooled pipe, an area that is directly exposed to radiation of the secondary flame. This phenomenon is related to the lower condensation of KCl in that area.

Therefore, the effect that the water temperature has on the deposition of particulate matter is evident by the condensation of KCl, which acts as an adherent to particles with momentum that does not exceed the adhesion force facilitated by the condensed phase. In general, the smallest particles circulating in the vicinity of the tube will be

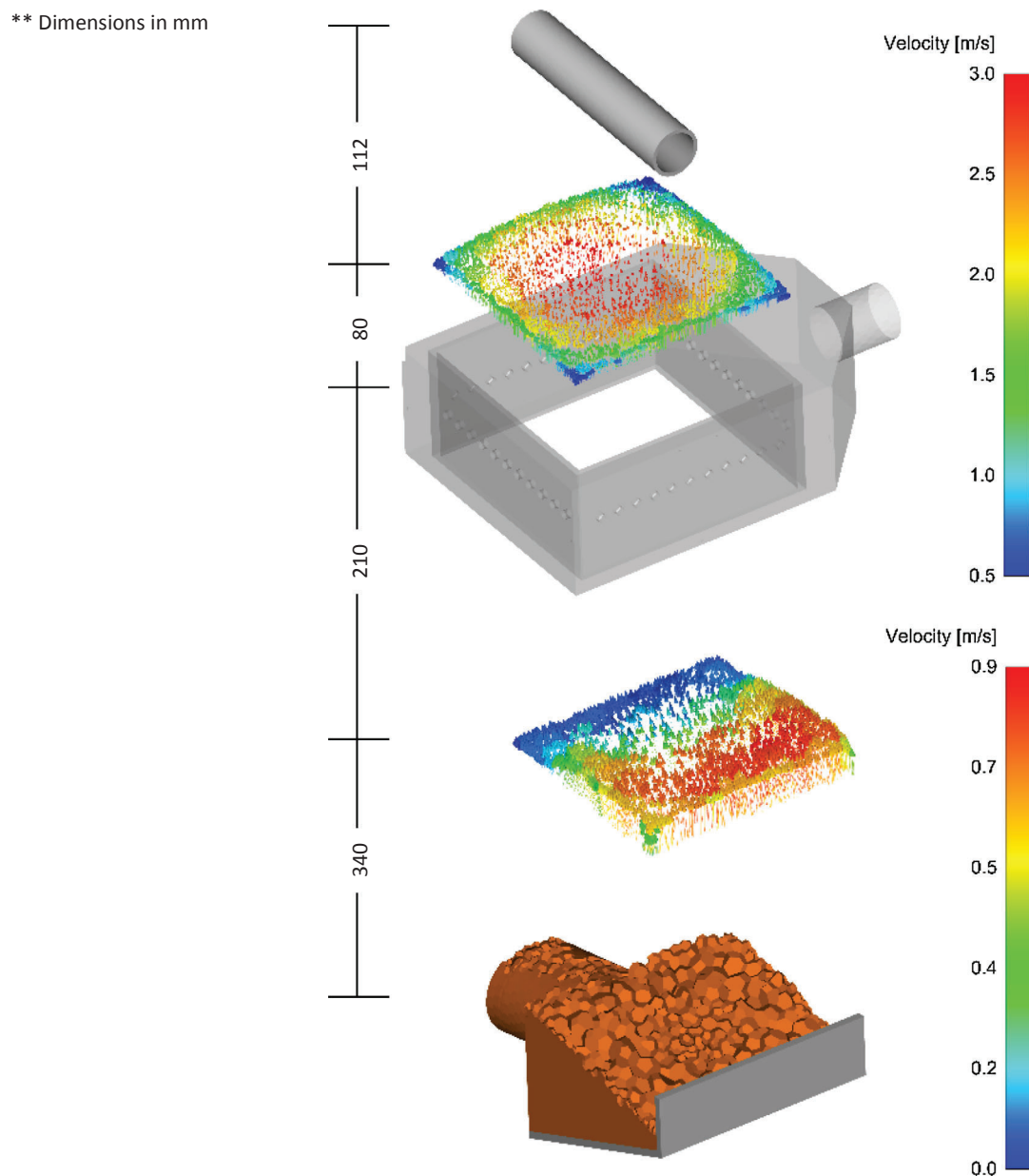


Fig. 21. Experimental data of diameter's distribution of particulate matter.

prone to sticking after they are heated in the combustion zone created by secondary air.

3.3.3.2. Primary-to-secondary air ratio. The deposition of undesirable matter is analysed according to the distribution between primary and secondary airs, maintaining an invariable water temperature of 333.15 (K) and 20 (m³/h). Fig. 24 shows the 2- and 3-dimensional profiles that were obtained.

As shown in Figs. 18 and 19, increasing the primary-to-secondary air ratio for the same total air flow rate results in a higher speed generated by primary air, which causes the existence of a higher number of coarse particles that find a sufficient gas velocity and are released from the bed. High flow rates, even at low primary-to-secondary air ratios, provide a sufficient gas velocity for many coarse particles to suffer mechanical ejection, thus making the adjustment of this parameter less relevant.

Studying the deposition profiles presented in Fig. 24, the following

phenomena are appreciated. On the 2-dimensional profile, it is apparent that at low primary-to-secondary air distributions, deposition is more homogenous along its periphery, with smaller differences between the maximum and minimum thicknesses, resulting relevant the displacement made by the secondary air. This is due to the greater predominance of particles located in the diffusion regime due to the lower gas velocity in the bed and the presence of higher gas velocity in the secondary combustion zone. As the primary-to-secondary air ratio increases, the deposition at the very beginning of the wake decreases.

In the frontal profile, there is a decrease in deposition on the leeward side of the tube on the side where the bed is the thinnest. With lower primary airs flows, the flow becomes more homogeneous in the secondary zone since a more uniform flow is distributed through the holes, which is caused by the increase in magnitude of the pressure drop within them, resulting in deposition centred on the leeward side of the tube. As the distribution of total air flow favours the primary air, the flow in the secondary becomes less centred, and the presence of higher

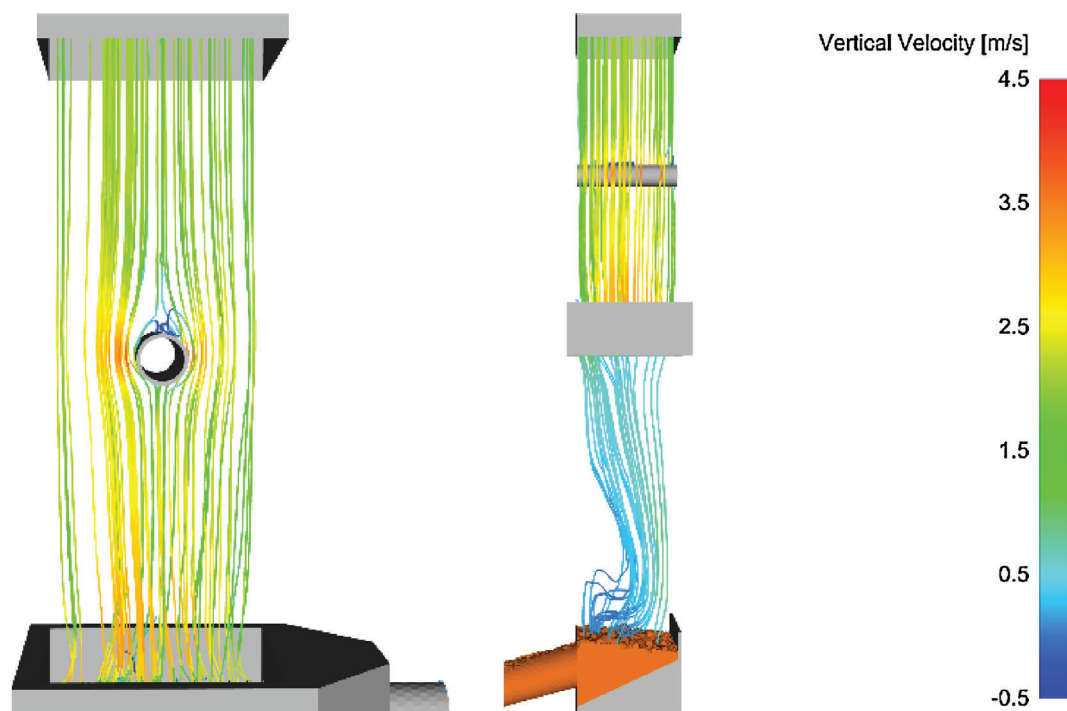


Fig. 22. Distribution of flue gas velocities above the bed and below the cooled pipe.

velocities above the bed on the side of low bed thickness creates enough speed to avoid gravitational settling on that side, favouring deposition on the opposite side.

3.3.3.3. Total air flow rate. The effect of the two parameters above is less relevant than the following parameter (Fig. 25), where the effect of the total air flow rate on the deposition is shown. For this case, both the temperature of 333.15 (K) and a primary-to-secondary air ratio of 20–80 are fixed.

Observing the effect of the flow on the deposition in the 2-dimensional profiles, erroneous conclusions can be reached due to the non-homogeneity of deposition. With low total air flow rates, the deposition over the surface is more homogeneous due to the lower velocities reached. Very few massive particles are released, which decreases the deposition in the windward side of the tube.

The lower velocities also cause a smaller wake, so the speeds downstream of the tube have a greater homogeneity. This decreases the deposition on the leeward side of the cooled pipe because the small particles, despite hitting walls downstream, experience enough gas velocity to continue their trajectories toward the chimney.

3.3.4. Experimental contrast

As previously mentioned, experiments have been performed for deposition in this plant. Figs. 26 and 27 show examples of the deposition profiles on the tube.

In Fig. 26, the 2-dimensional profiles are oriented in the same way that the numerical profiles are shown. Fig. 27 shows a frontal view of the profile and a superior view of the pipe. The front and superior profiles are oriented with the positive slope of the bed's grate from left to right. The side profile is performed from the right side of the pipe, so the secondary air enters from the bottom right corner of this figure. In the superior profile, the air enters from the top of the figure.

In these figures, several phenomena that were observed in the analysis of the numerical profiles are appreciated. In the frontal view, greater deposition is observed on leeward side compared to the

windward side of the pipe. Focusing on windward side, greater deposition is observed on the right compared to the left. This is due to the variation in bed thickness, which causes higher speeds in the right-hand part of the facility. Additionally, it is observed on the leeward side deposition that the displacement of the gas flow toward the right side causes greater deposition on the leeward left side through gravitational settling due to the lower velocities.

In the superior view and the side view, the effect of the secondary air inlet from the upper part or the lower right part of the figure, respectively, is slightly appreciated, displacing deposition toward the opposite side.

It is important to remember that for this work, deposition is calculated in a post-process step. The effect of the distribution of the condensation of alkali salts results in a less significant effect than in reality, and as shown in previous figures, this phenomenon is closely linked to the temperature of the tube. Once deposition is adhered to the tube, a new layer of alkali salts can be condensed on it. However, this deposit increases the section of the tube, and its low conductivity increases the temperature of the deposit-to-gas interface, causing less alkali salt condensation.

In reality, both phenomena cause the water temperature to have a greater effect on the deposit geometry than that calculated numerically. On the leeward side in particular, as observed in Fig. 14, the greatest amount of condensation occurs in this location. In the sequences of images shown in Figs. 29 and 30, photographs of deposition on the tube observed for different angles are shown. The images are placed varying 30° from the lower end (see Fig. 28), where the lowest image is a photo taken from the bottom ($A = 0^\circ$).

The first sequence of images (Fig. 29) shows the effect of the increase in total air flow rate, with flow rates of 14, 20 and 23 m³/h, keeping the water temperature (333.15 K) and primary-to-secondary air ratio (25–75) constant. In this sequence, it is apparent how the deposition, observed from the front, decreases on the side of the smaller bed thickness, as predicted by the numerical model.

The lower sequence (Fig. 30) shows the effect of the primary-to-secondary air ratio in the real world, keeping the water temperature

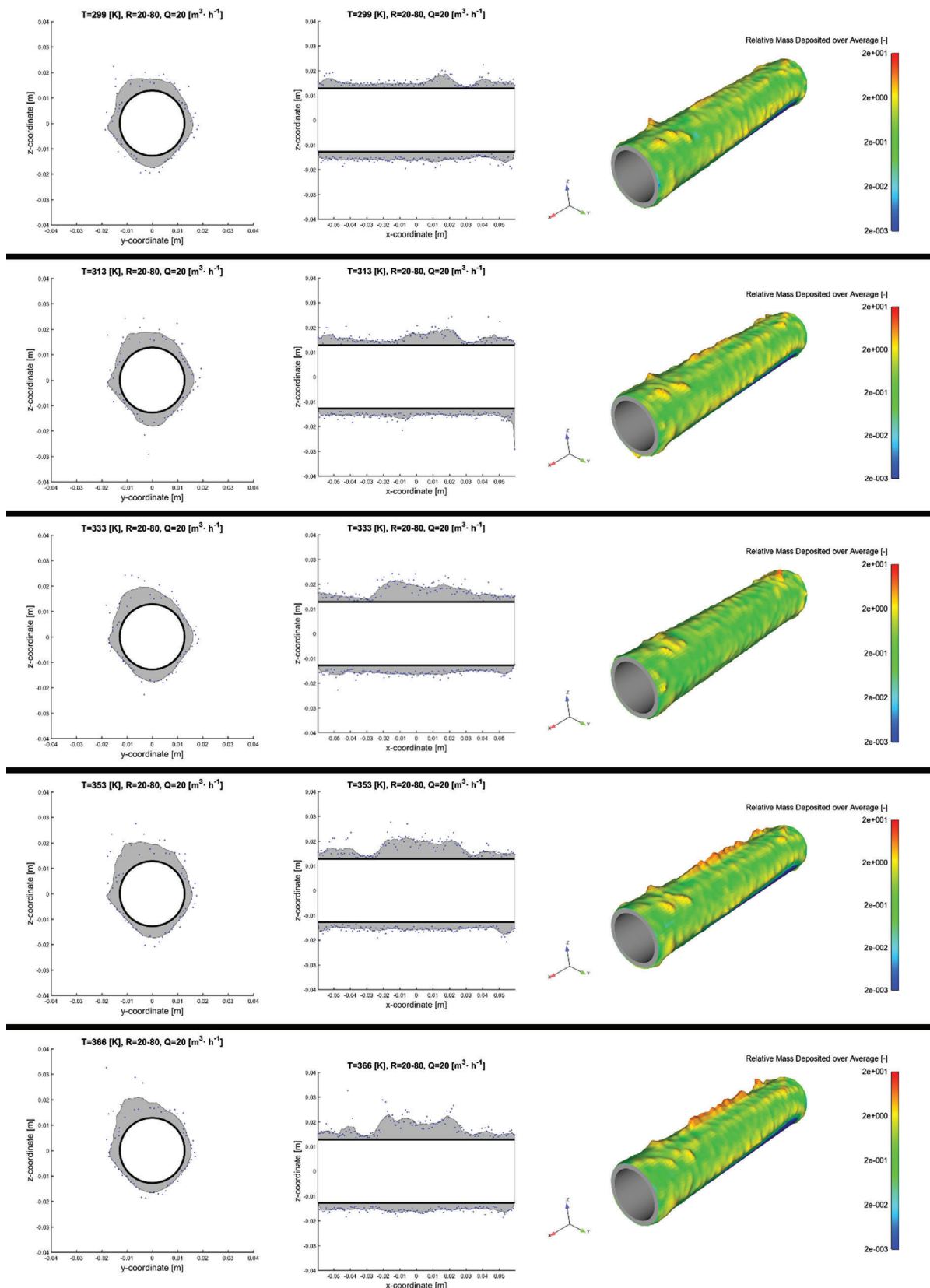


Fig. 23. Estimated profiles for varying water temperature and fixed primary-to-secondary air ratio and total air flow rate.

and total air flow rate constant. The cases shown are runs for primary-to-secondary air ratios of 20–80, 25–75 and 30–70.

As predicted by the numerical model, the deposition in the cases with low primary-to-secondary air ratios is more homogeneous than in

cases with high primary-to-secondary air ratios. Additionally, it is apparent that the deposit is composed of finer particles. As the distribution is more favourable to the primary air, the deposit becomes thicker in both quantity and average particle size, which is a symptom of the

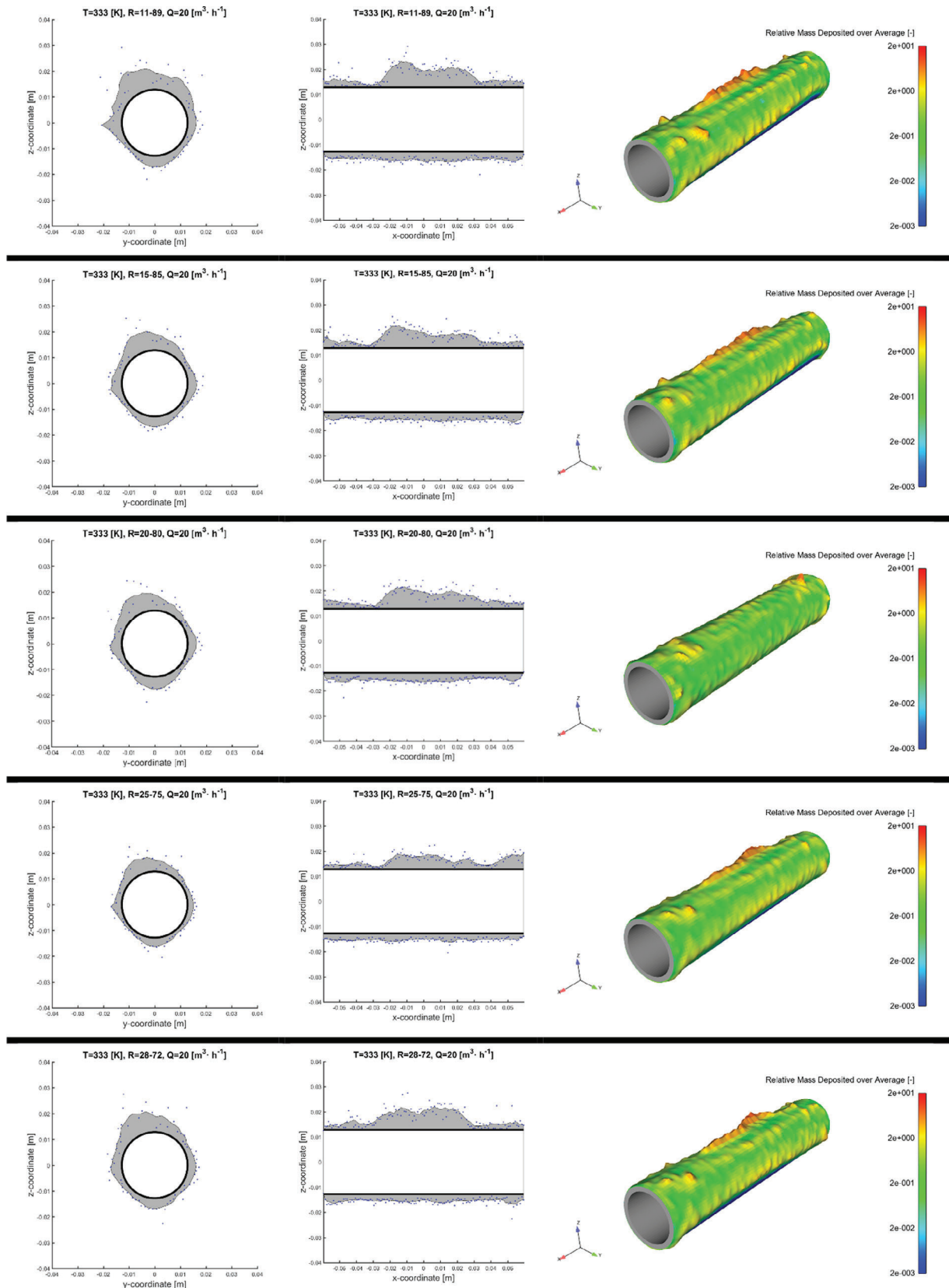


Fig. 24. Estimated profiles varying primary-to-secondary air ratio with a fixed water temperature and total air flow rate.

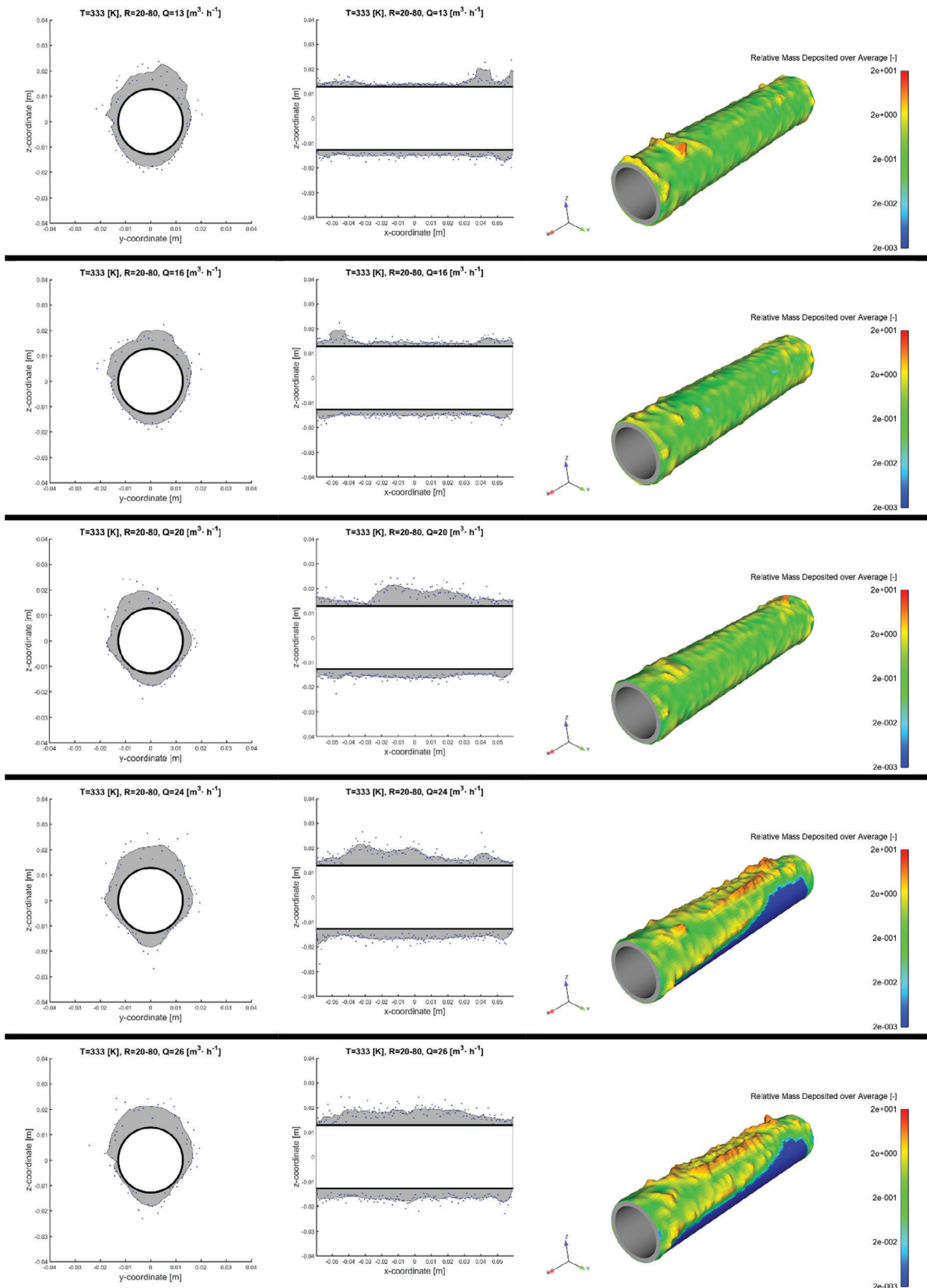


Fig. 25. Estimated profiles with varying total air flow rate and a fixed water temperature and primary-to-secondary air ratio.

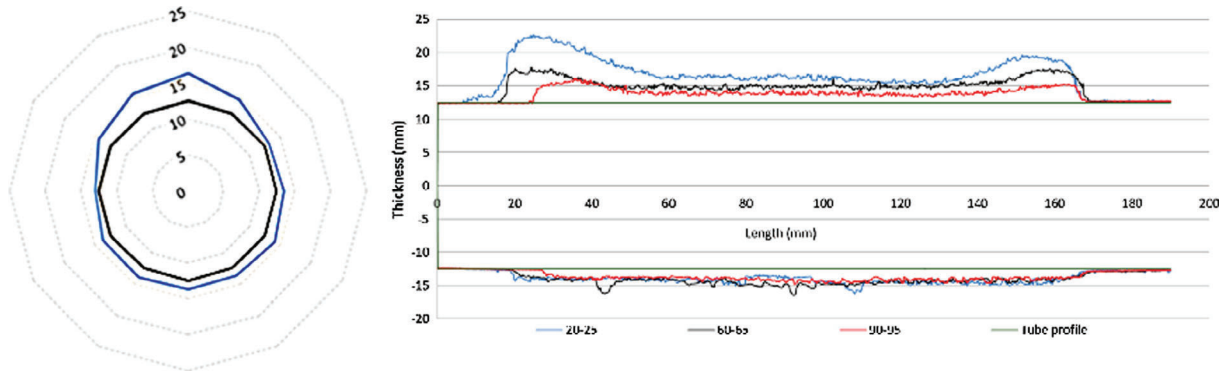


Fig. 26. Side and frontal profile obtained from experimental data for $R = 25\text{--}75$ and $20\text{ m}^3/\text{h}$ [21].

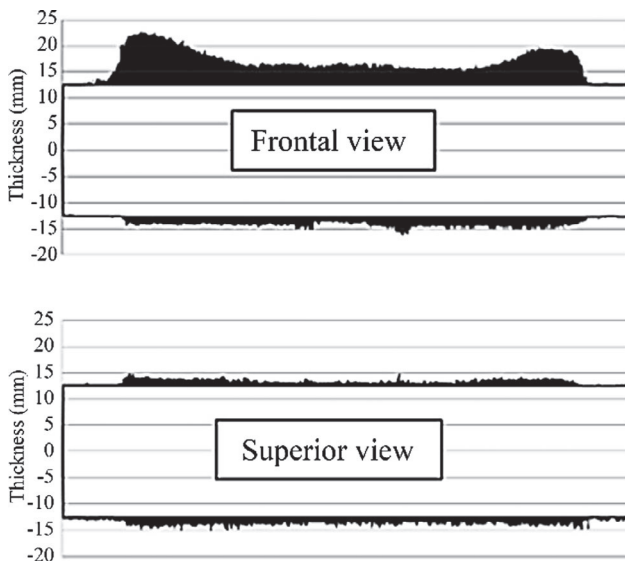


Fig. 27. Frontal and superior view of the profile obtained from experimental data for $R = 25\text{--}75$ and $20\text{ m}^3/\text{h}$ [21].

presence of greater velocities in the bed, which provides enough drag to

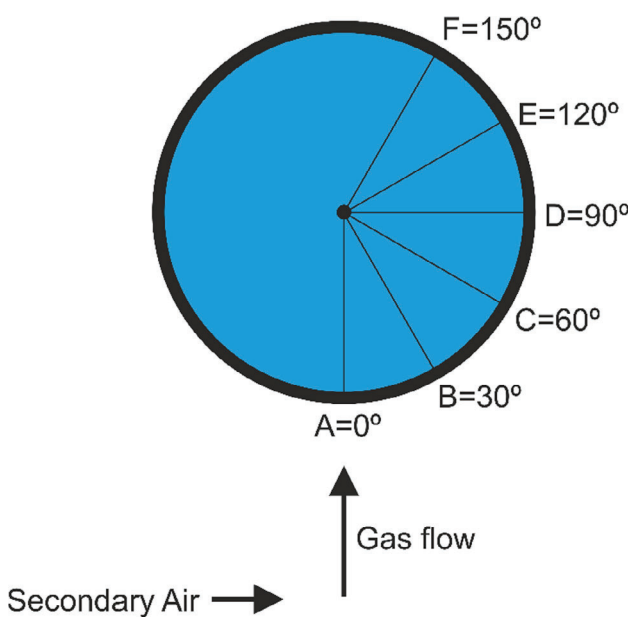


Fig. 28. Schematic representation of the orientation used for the image sequences shown in Figs. 29 and 30.

transport larger particles. It is also noted the increase in the deposit on the leeward side of the tube being, at the same time, displaced towards the side of greater bed thickness. This phenomenon is also predicted by the numerical model because it is caused by the less homogeneous speeds and greater displacement toward the right-hand part of the installation, causing greater gravitational settling in the opposite part where there are lower speeds.

4. Conclusions

The deposition of undesirable matter on surfaces in biomass combustion, entails one of the great difficulties and challenges that exist on its use. The model shows relatively good accuracy for its response to the boundary conditions compared to the available experimental data, closely following trends of the main variables of interest. Therefore, this work presents the first step toward a complex model which will predict these phenomena over time and will help to avoid or minimize it.

The present model shows that lowering the bed temperature and primary air flow leads to a lower deposition rate by means of lower KCl concentration in the flue gas and higher gas temperature in the secondary zone, both of which contribute to lower KCl condensation over the cooled surfaces. Additionally, low primary air velocities lead to the lower ejection of coarse particles, whose contribution to the deposition is considerable. This decrease in the amount of coarse particles ejected from the bed causes a smaller deposit in the windward side of the tube, whereas the greater presence of fine particles causes more homogeneous deposition. The increase in flow rate of the primary air, due to either a greater total flow or an increase in the distribution, causes a decrease in the homogeneity of the deposit. It is observed both in reality and in the model that there is a thicker deposit on the leeward side of the tube that is displaced toward the area with a greater bed thickness. This occurs because the particles that have not impacted the cooled pipe but have bumped against the walls of the facility downstream of the tube lose speed and then fall due to gravity and being displaced towards the area of lower speed. They end up being deposited by gravitational settling.

However, the actual phase of development provides more abrupt profiles than those achieved in reality due to the following. First, releasing particles in a post-process step does not account for the actual oscillation of flue gas flow beyond the fluctuation estimated by the Random-Walk Model, and there is no modification of the thermal properties of the surface. Second, the impact of a particle does not cause a variation in the physical properties of the deposit that is already adhered to the surface. By neglecting the erosion caused by the impact of these particles and the gas, the deposit surface is not properly smoothed.

This phenomenon makes the section perpendicular to the average velocity of the gas smaller, causing a greater impact of coarse particles, and causes variation in the velocities of gas more proximal to the tube, which will modify the trajectories of smaller particles. Because a larger



Fig. 29. Experimental runs increasing total air flow rate.

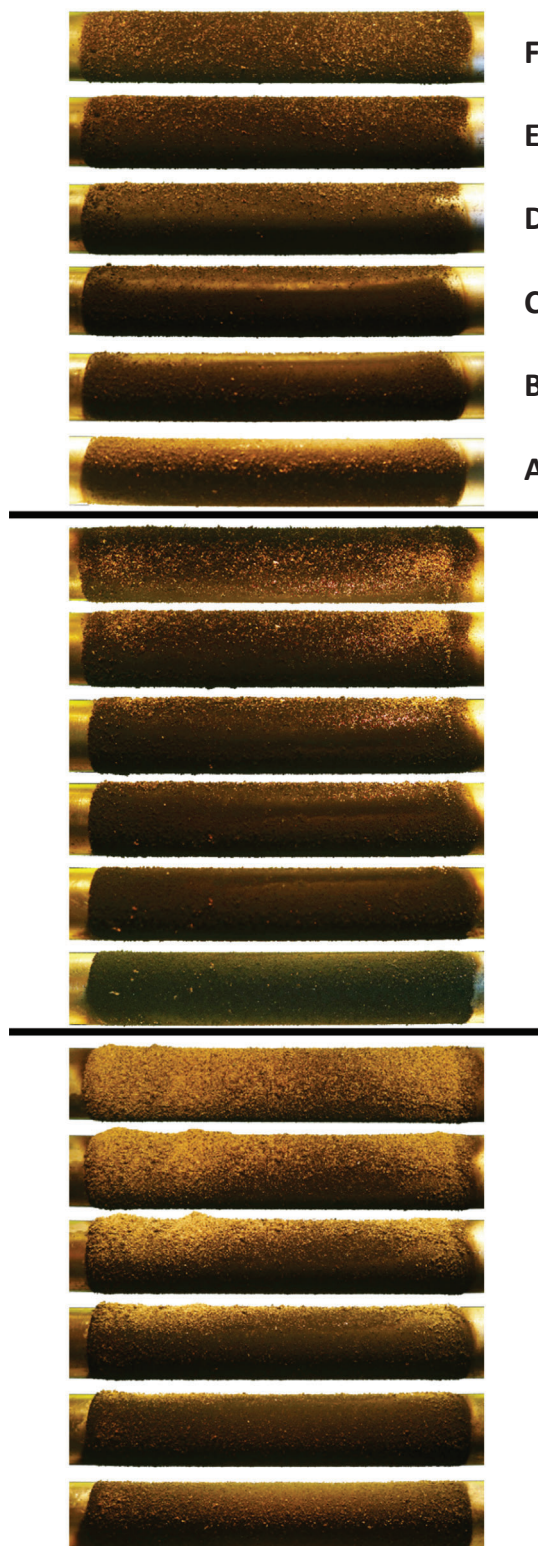


Fig. 30. Experimental runs increasing the primary-to-secondary air ratio.

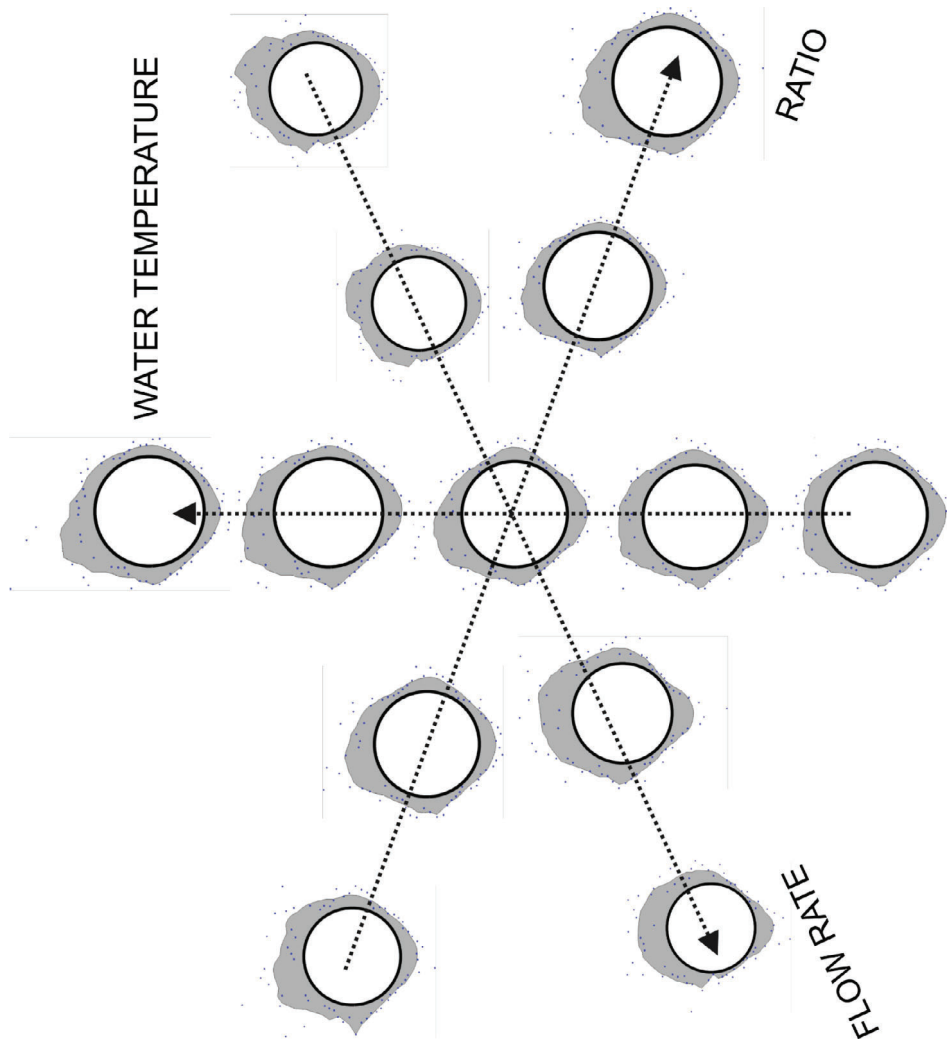
part of the perpendicular section will be occupied, there will be a greater wake and an increment of gravitational settling.

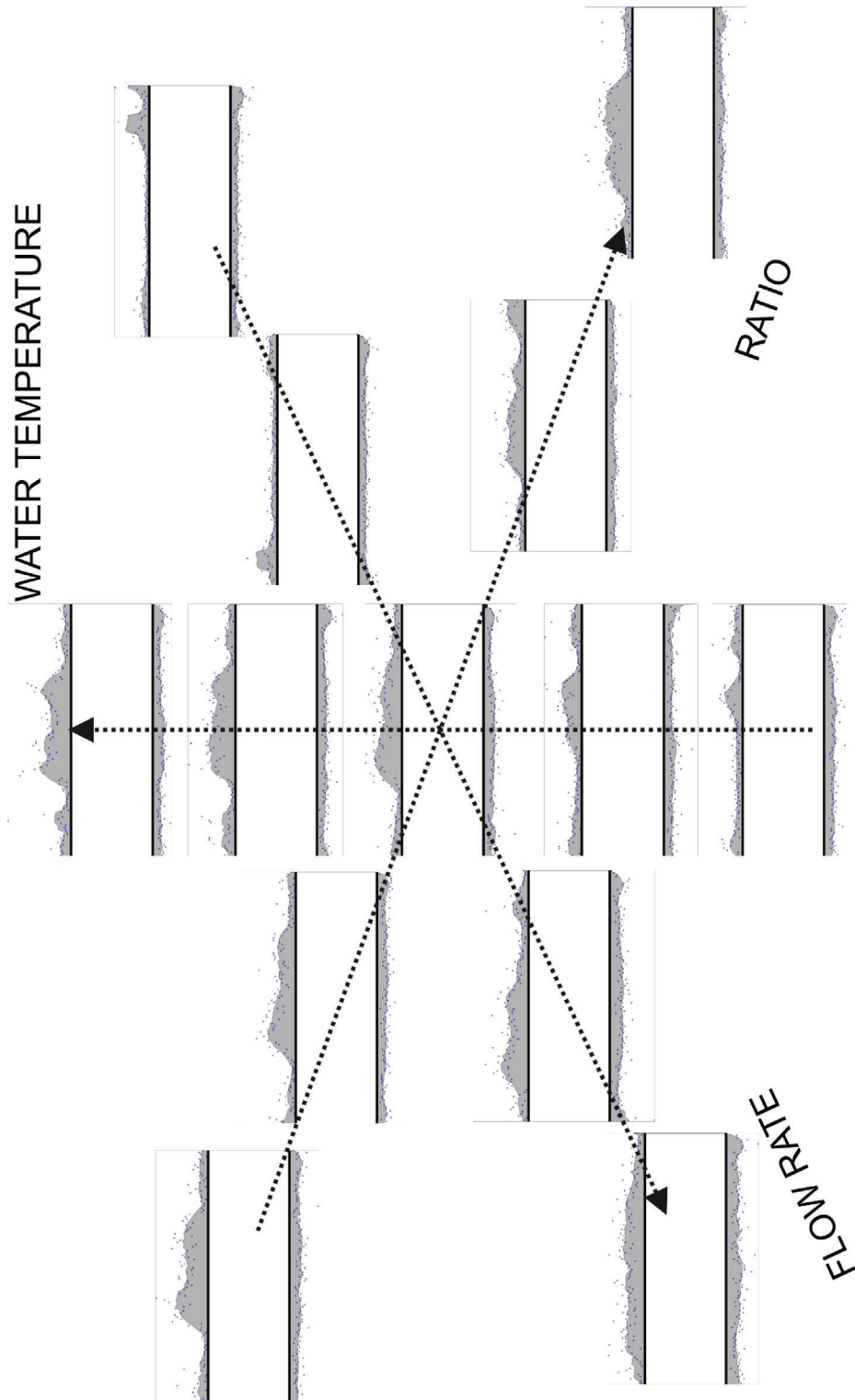
All of these aspects conform the future development lines of the presented model, helping it acquire greater complexity and precision. However, the results obtained show that good qualitative results have already been achieved. This means that it is possible to perform qualitative studies of the designs of biomass combustion facilities, resulting in a design tool to be considered.

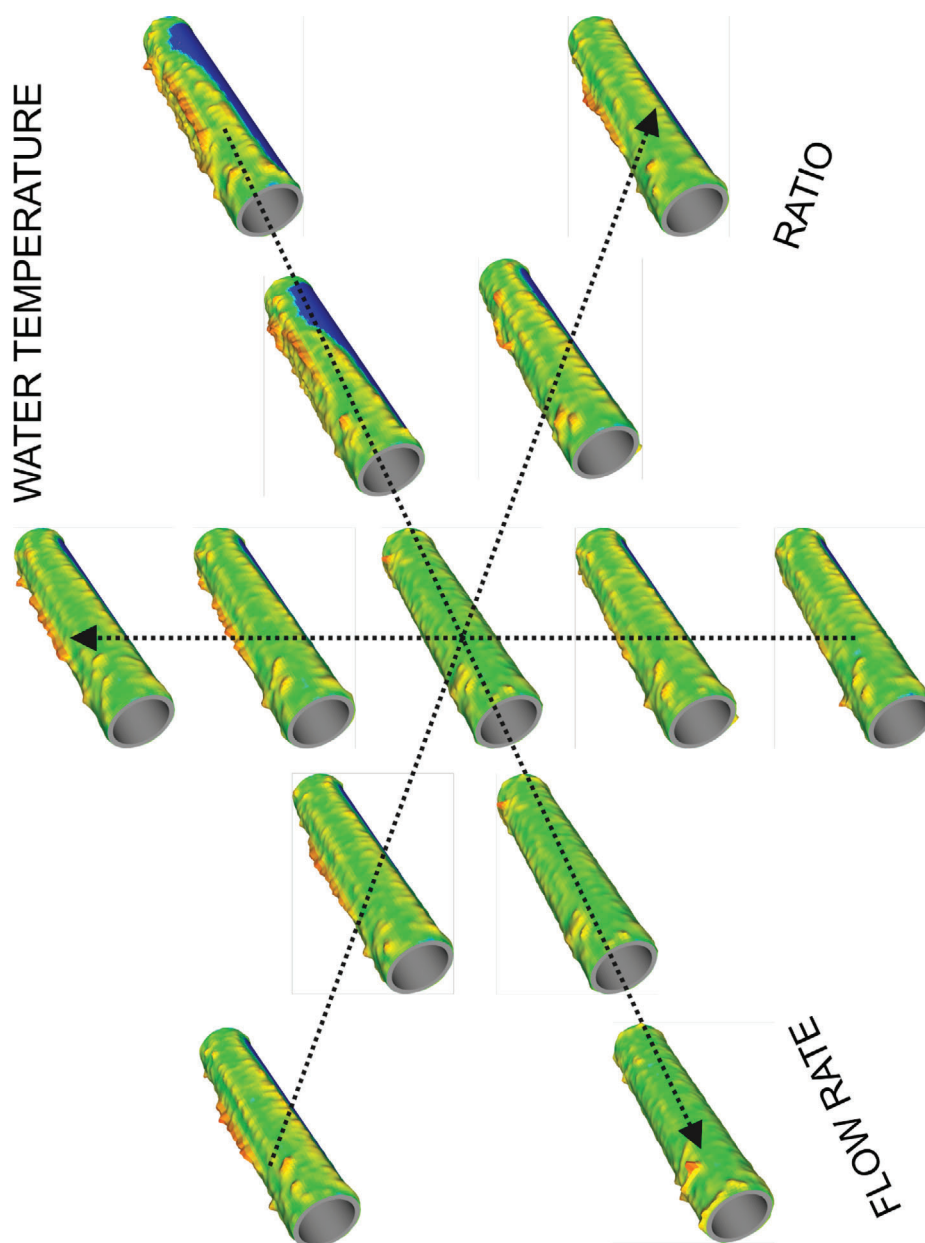
Acknowledgements

This work was financially supported by project ENE2015-67439-R. The work of Sergio Chapela López was supported by grant BES-2016-076785 of the Ministry of Economy, Industry and Competitiveness (Spain).

Appendix



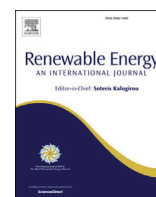




References

- [1] Luque R, Herrero-Davila L, Campelo JM, Clark JH, Hidalgo JM, Luna D, et al. Biofuels: a technological perspective. *Energy Environ Sci* 2008;1:542–64.
- [2] Regueiro A, Jezerská L, Patiño D, Pérez-Orozco R, Nečas J, Židek M. Experimental study of the viability of low-grade biofuels in small-scale appliances. *Sustainability* 2017;9:1823.
- [3] Verma VK, Bram S, Gauthier G, De Ruyck J. Evaluation of the performance of a multi-fuel domestic boiler with respect to the existing european standard and quality labels: Part-1. *Biomass Bioenergy* 2011;35:80–9.
- [4] Cardozo E, Erlich C, Alejo L, Fransson TH. Combustion of agricultural residues: an experimental study for small-scale applications. *Fuel* 2014;115:778–87.
- [5] Öhman M, Boman C, Hedman H, Nordin A, Boström D. Slagging tendencies of wood pellet ash during combustion in residential pellet burners. *Biomass Bioenergy* 2004;27:585–96.
- [6] Örberg H, Jansson S, Kalén G, Thyrel M, Xiong S. Combustion and slagging behavior of biomass pellets using a burner cup developed for ash-rich fuels. *Energy Fuels* 2014;28:1103–10.
- [7] Sandberg J, Fdhila RB, Dhlquist E, Avelin A. Dynamic simulation of fouling in a circulating fluidized biomass-fired boiler. *Appl Energy* 2011;88(5):1813–24.
- [8] Kær SK. Numerical investigation of ash deposition in straw-fired boilers-Using CFD as the framework for slagging and fouling predictions. Ph. D. 2001.
- [9] Weber R, Poyraz Y, Beckmann AM, Brinker S. Combustion of biomass in jet flames. *Proceed Combust Inst* 2014;35:2749–58.
- [10] Sippula O, Hytönen K, Tissari J, Raunemaa T, Jokiniemi J. Effect of wood fuel on the emissions from a top-feed pellet stove. *Energy Fuels* 2007;21:1151–60.
- [11] Wiinikka H, Gebart R, Boman C, Boström D, Öhman M. Influence of fuel ash composition on high temperature aerosol formation in fixed bed combustion of woody biomass pellets. *Fuel* 2007;86(1–2):181–93.
- [12] Buchmayr M, Gruber J, Hargassner M, Hochenauer C. Experimental investigation of the primary combustion zone during staged combustion of wood-chips in a commercial small-scale boiler. *Biomass Bioenergy* 2015;81:356–63.
- [13] Regueiro A, Patiño D, Porteiro J, Granada E, Miguez JL. Effect of air staging ratios on the burning rate and emissions in an underfeed fixed-bed biomass combustor. *Energies* 2016;9:940.
- [14] Wiinikka H, Gebart R, Boman C, Boström D, Nordin A, Böhman M. High temperature aerosol formation and emission minimisation during combustion of wood pellets. *Combust Flame* 2006;147:278–93.
- [15] García-Maraver A, Zamorano M, Fernandes U, Rabaçal M, Costa M. Relationship between fuel quality and gaseous and particulate matter emissions in a domestic pellet-fired boiler. *Fuel* 2014;119:141–52.
- [16] Boman C, Petterson E, Westerholm R, Boström D, Nordin A. Stove Performance and emission characteristics in residential wood log and pellet combustion, part 1: pellet stoves. *Energy Fuels* 2011;25:307–14.
- [17] Valmari T, Lind TM, Field Kauppinen EI. Study on ash behavior during circulating

- fluidized-bed combustion of biomass. 2. Ash deposition and alkali vapor condensation. *Energy Fuels* 1999;13:390–5.
- [18] Bohnet M. Fouling of heat transfer surfaces. *Chem Eng Technol* 1987;10:113–25.
- [19] E. Suarez Modelado y Simulación de la Deposición de Partículas en Flujos Bifásicos Turbulentos Dispersos en Presencia de Gradiente de Temperatura. Aplicación a Enfriadores de Gases de Escape. Ph.D 2010 Spanish) (in spanish).
- [20] Lindberg D, Backman R, Chartrand P, Hupa M. Towards a comprehensive thermodynamic database for ash-forming elements in biomass and waste combustion – Current situation and future developments. *Fuel Process Technol* 2013;105:129–41.
- [21] Regueiro A, Patiño D, Granada E, Porteiro J. Experimental study on the fouling behaviour of an underfeed fixed-bed biomass combustor. *Appl Therm Eng* 2017;112:523–33.
- [22] Weber R, Mancini M, Schaffel-Mancini N, Kupka T. On predicting the ash behaviour using computational fluid dynamics. *Fuel Process Technol* 2013;105:113–28.
- [23] Schulze K, Scharler R, Telian M, Obernberger I. Advanced modelling of deposit formation in biomass furnaces - investigation of mechanisms and comparison with deposit measurements in a small-scale pellet boiler. *Bioenergy* 2020+. Impacts of fuel quality on. *Power Product Environ* 2010.
- [24] Israel R, Rosner DE. Use of a generalized Stokes number to determine the aerodynamic capture efficiency of non-stokesian particles from a compressible gas flow. *Aerosol Sci Technol* 1982;2:45–51.
- [25] Baxter LL. Coal combustion science. Quarterly progress report, Sandia National Laboratories, Livermore, California; 1990.
- [26] Baxter LL. The dynamic variation of particle capture efficiency during ash deposition in coal-fired combustors. In Proc. of the Twenty-Third Symposium (International) on Combustion. The Combustion Institute, 1990.
- [27] Rosner D, Tandon P. Rational prediction of inertially induced particle deposition rates for a cylindrical target in a dust-laden stream. *Chem Eng Sci* 1995;50(21):3409–31.
- [28] Clift R. Bubbles, Drops, and Particles. Academic Press; 1978.
- [29] Michaelides E, Crowe CT, Schwarzkopf JD. *Multiphase Flow Handbook*. 2nd ed. Taylor & Francis; 2006.
- [30] Backman R, Hupa M, Uppstu E. Fouling and corrosion mechanisms in the recovery boiler superheater area. *Tappi J* 1987;70:123–7.
- [31] Hupa M. Ash-Related issues in fluidized-bed combustion of biomasses: recent research highlights. *Energy Fuels* 2011;26:4–14.
- [32] Haosheng Z, Jensen PA, Frandsen FJ. Dynamic mechanistic model of superheater deposit growth and shedding in a biomass fired grate boiler. *Fuel* 2007;86:1519–33.
- [33] Walsh P, Sayre A, Loehden D, Moenroe L, Ber J, Sarofim A. Deposition of bituminous coal ash on an isolated heat exchanger tube: effects of coal properties on deposit growth. *Prog Energy Combust Sci* 1990;16:327–46.
- [34] ANSYS-Fluent. Theory Guide. V17.2.
- [35] Chapela S, Porteiro J, Costa M. Effect of the turbulence-chemistry interaction in packed-bed biomass combustion. *Energy Fuels* 2017;9:9967–82.
- [36] Viana FAC. Things you wanted to know about the Latin hypercube design and were afraid to ask. 10th World Congress on Structural and Multidisciplinary Optimization; 2013.
- [37] Dutka M, Ditaranto M, Løvås T. Application of a Central Composite Design for the Study of NOx Emission Performance of a Low NOx Burner. *Energies* 2015; 8: 8606–3627.
- [38] Gómez MA, Porteiro J, Patiño D, Míguez JL. Eulerian CFD modelling for biomass combustion. Transient simulation of an underfeed pellet boiler. *Energy Convers Manage* 2015;101:666–80.
- [39] Gómez MA, Porteiro J, De la Cuesta D, Patiño D, Míguez JL. Numerical simulation of the combustion process of a pellet-drop-feed boiler. *Fuel* 2016;184:987–99.
- [40] Gómez MA, Porteiro J, De la Cuesta D, Patiño D, Míguez JL. Dynamic simulation of a biomass domestic boiler under thermally thick considerations. *Energy Convers Manage* 2017;140:260–72.
- [41] Wessel RA, Righi J. Generalized correlations for inertial impaction of particles on a circular cylinder. *Aerosol Sci Technol* 1988;9:29–60.
- [42] Weber R, Schaffel-Mancini N, Mancini M, Kupka T. Fly ash deposition modelling: Requirements for accurate predictions of particle impaction on tubes using RANS-based computational fluid dynamics. *Fuel* 2013;108:586–96.



CFD study of fouling phenomena in small-scale biomass boilers: Experimental validation with two different boilers

S. Chapela ^a, J. Porteiro ^{a,*}, M. Garabatos ^a, D. Patiño ^a, M.A. Gómez ^b, J.L. Míguez ^a

^a Industrial Engineering School, University of Vigo, Lagoas-Marcosende s/n, Vigo, Spain

^b Defense University Center, Spanish Naval Academy, Spain

ARTICLE INFO

Article history:

Received 20 December 2018

Received in revised form

21 February 2019

Accepted 14 March 2019

Available online 19 March 2019

Keywords:

Fouling

CFD

Biomass

Combustion

Deposition

ABSTRACT

The use of biomass is growing as it is considered as a renewable energy by a society with increasing ecological awareness. Biomass has the advantage of being easily used in existing installations with non-renewable solid fuels, either as a final fuel or as a transition fuel. However, biomass use presents serious operational problems, such as slagging and fouling, which have slowed its development. This work continues the development of an advanced and flexible fouling model that is embedded in a fixed-bed biomass combustion model developed by the University of Vigo for the commercial code, ANSYS-Fluent. The modifications to the algorithm enable the analysis of commercial water-tube and fire-tube combustion systems, with diverse types of fuel-feeding systems. To validate the model, a numerical study of the combustion and fouling phenomena of two commercial systems that have already been analysed experimentally and published was carried out. The results obtained are in good agreement with the experimental results and demonstrate the accuracy and flexibility of the proposed model. After this validation, future research lines can be opened that consider more complex phenomena.

© 2019 Elsevier Ltd. All rights reserved.

1. Introduction

Society has become increasingly aware of the environment in recent decades. This awareness has been driven by the upward trend in the costs of fossil fuels, not only in their extraction and production but also in their distribution caused by the increased depletion of fossil fuel reservation [1]. This ecological awareness has led to the strong development of many renewable energy sources including biomass. Biomass constitutes one of the immediate focus areas of this evolution. It is an energy source with numerous properties which facilitate the transition to energies such as solar or wind. If implemented properly, the cost of converting an existing facility to use biomass is less than the cost of new construction, and the supply chain and business models do not differ greatly [2,3].

The evolution in the massive use of biomass has developed through several applications. First, on large-scale, it has been used in the transition from the use of coal to carbon-biomass blends whose physical and chemical properties are currently being studied [4,5]. The use of low-quality biomass, such as urban, agricultural

and forestry waste would provide greater profitability to facilities due to its lower cost and high availability. In a search for profitability, there are several studies about fast pyrolysis to convert these low-energy density fuels in intermediate products such as bio-oil [6] and the reuse of the ashes generated in the combustion of this type of low-quality biomass in a way that does not pose health risks [7,8].

On small-scale, there is a growing interest in the use of biomass in Combined Heat and Power (CHP) and Organic Rankine Cycle (ORC) micro-generation systems [3], which benefit from the high availability of biomass in the vicinity of most installations.

Biomass covers a broad variety of very different fuels, both in physical and chemical properties. As presented in works such as [9–11], this kind of fuel often possess high moisture contents, low heating values and chemical compounds that lead to a multitude of problems, such as high emission of PM, fouling or slagging due to the formation of low-temp eutectic compounds. The emission of PM in the submicron range can lead to respiratory diseases in surrounding areas, whereas phenomena such as fouling or slagging are responsible for the loss of efficiency and corrosion of the surfaces of the systems [12,13].

These problems hinder the development and implementation of biomass and therefore are the subject of numerous current studies.

* Corresponding author.

E-mail address: porteiro@uvigo.es (J. Porteiro).

Nomenclature

C_D	Drag coefficient (–)
D	Diffusivity of potassium chloride (m^2/s)
d_p	Released particle diameter (m)
F_D	Drag force (N)
G	Gravity (m/s^2)
M	Mass transfer coefficient for spheres (m/s)
sa/vol	Surface area to volume ratio of the bed particle (1/m)
Re	Reynolds number (–)
Sc	Schmidt number (–)
S	Source term of gaseous potassium chloride ($kg/m^3 s$)

Greek symbols

ε	Solid fraction (m^3_{solid}/m^3_{cell})
λ	Molecular mean free path (m)
μ	Dynamic viscosity (Pa s)
μ_s	Dynamic viscosity at the temperature of the surface (Pa s)
ν	Kinematic viscosity (m^2/s)
ρ_{gas}	Gas density (kg/m^3)
ρ_{KCl}	Potassium chloride density (kg/m^3_{cell})
ρ_p	Particle density (kg/m^3_{solid})
ϕ_{el}	Elutriation diameter (m)
ϕ_{eq}	Equivalent diameter of the average pellet present inside the cell (m)

Multiple solutions that eliminate or at least reduce these effects have been explored. These include direct actions, such as the use of foam filters to trap particulate matter [14], additives that prevent the fusion of the ashes [15–19] and changes in the way the thermal energy is used. Examples of the latter are conversion to Refined Renewable Biomass Fuel (RRBF) [20], smouldering combustion with inert solids [21] or gasification for subsequent combustion of biogas generated.

The work presented in this manuscript improves a CFD tool published in Ref. [22] that allows qualitative prediction of the fouling phenomenon for its use in biomass commercial combustion systems. This tool works in symbiosis with the fixed-bed biomass combustion model of the University of Vigo [23,24] and is embedded and executed on the commercial code ANSYS-Fluent.

2. Materials and methods

As mentioned above, the model modified in this work has been previously published and validated with an experimental burner side-fed continuously with a screw and level controller. In this work, the algorithm was shown to adequately respond to a wide range of boundary conditions of the experimental burner, both in primary-secondary air flow distribution and in total air flow and water temperature.

In the present work, the algorithm was modified to adapt the fouling model to the physical and operational characteristics of the commercial systems studied in the experimental manuscript [25].

2.1. Fouling model

The modelling used is summarized below, and further details can be found in Ref. [22]. The modifications made to the model and the global algorithm in which it is used are also presented.

In several previously published works [13,26,27], the condensation of inorganic vapours on the heat exchange surfaces of combustion systems is suggested as one of the most relevant mechanisms in the deposition of undesired matter. Therefore, in the fouling model used, potassium chloride is released from the bed, acting as a tracer of these inorganic vapours. However, it is not the only inorganic vapour that participates in this phenomenon, but it is the most relevant factor for the biomass used in this work. The source of the release of this inorganic vapour is governed by the following expression:

$$S = M \rho_{KCl} \varepsilon sa/vol \quad (1)$$

where M stands for the Whitaker correlation for the mass transfer coefficient over spheres:

$$M = (D/\phi_{eq}) \left(2 + 0.4Re_D^{1/2} + 0.66Re_D^{2/3} \right) Sc^{0.4} \left(\frac{\mu}{\mu_s} \right)^{1/4} \quad (2)$$

The inorganic vapour, after being released by the bed, travels with the gas phase along the CFD domain. When it is close to walls, the vapour pressure equilibrium is calculated according to the correlation of Stull. The vapour pressure equilibrium dictates how much steam condenses on the surface or evaporates from it.

Once both combustion and inorganic vapour condensation reach convergence in each time step, a search for the frontier cells of the existing bed is performed. On each of the frontier cells, the maximum elutriation diameter is calculated through a Newton-Raphson procedure following this equation:

$$\phi_{el} = \frac{3C_D \rho_{gas} \phi_{eq} v^2}{4\rho_{particle} G} \quad (3)$$

where the C_D coefficient follows the next piecewise function [28]:

If $Re \leq 0.01$

$$C_D = 4.5 + \frac{24}{Re}$$

If $0.01 < Re \leq 20$

$$C_D = \frac{24}{Re} \left(1 + 0.1315Re^{0.82-0.05 \log_{10} Re} \right)$$

If $20 < Re \leq 260$

$$C_D = \frac{24}{Re} \left(1 + 0.1935Re^{0.6305} \right)$$

If $260 < Re \leq 1500$

$$C_D = 10^{(1.6435 - 1.1242 \log_{10} Re + 0.1558 (\log_{10} Re)^2)}$$

If $Re > 1500$

$$C_D = 10^{(-2.4571 + 2.5558 \log_{10} Re - 0.9295 (\log_{10} Re)^2 + 0.1049 (\log_{10} Re)^3)} \quad (4)$$

When the particle diameter is smaller than the diameter of elutriation, a new Lagrangian trajectory is generated. In this way, the model avoids launching trajectories without enough momentum to be ejected from the bed, thus saving computational effort. After being marked for ejection, the particles are assigned the initial conditions of their starting cell, and their trajectory is calculated whilst interacting with the environment.

Fig. 1 shows the different cases of trajectories that can occur and which of them can lead to deposition on the surfaces. In all cases that lead to deposition, a calculation of adhesion probabilities, proposed by Walsh et al. [29] and explained in detail in previous

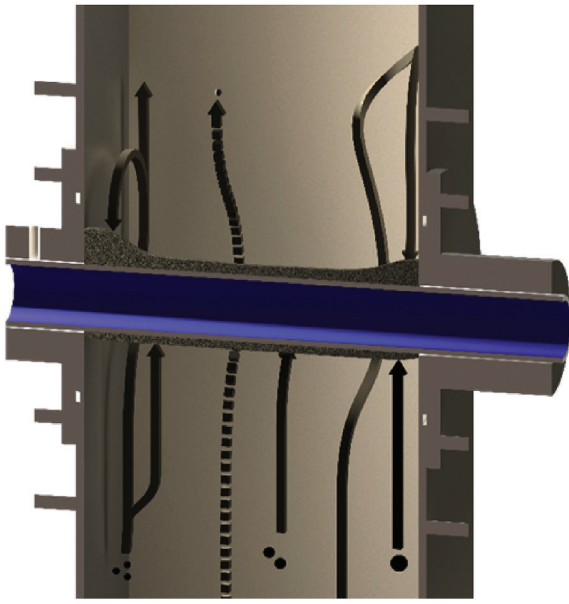


Fig. 1. Illustration of different cases for particulate matter trajectories [22].

work, is used.

Due to the absence of information about the shape of the particles when travelling through the system, the modified Stokes-Cunningham drag law [30,31] will be used, which follows the expression:

$$F_D = \frac{18\mu}{d_p^2 \rho_p C_c} \quad (5)$$

The C_c coefficient corrects the Stokes drag law, and its expression is:

$$C_c = 1 + \frac{2\lambda}{d_p} \left(1.257 + 0.4e^{-\frac{1.1d_p}{2\lambda}} \right) \quad (6)$$

The values of maximum elutriation diameter obtained for each frontier cell in the time step are stored so that in the next time step, when the algorithm is executed, they are used as starting conditions for the Newton-Raphson procedure thus increasing the overall speed of the code.

Due to the deterministic nature of the Lagrangian trajectories caused by using the RANS approach, the Random Walk stochastic approximation model of ANSYS-Fluent was formerly used to predict the dispersion due to turbulence.

However, unlike 5–12 [kW] the experimental burner used in Ref. [22], see Fig. 2, which had a continuous screw feed, a level controller and a complete control of the water, fuel and air supplies allowing to reach a high level of stability, the boilers that are studied in this work do not have this type of feeding and control system.

Therefore, the perturbations in the gas phase caused by the feeding system are much higher than the intrinsic ones derived from the combustion of biomass and considered by the aforementioned stochastic model.

Based on this, several changes are made in the deposition calculation algorithm, which will be detailed below and summarized in the flowchart shown in Fig. 3. The trajectory calculation loop, coloured in black, remains unchanged, but the main loop, coloured in red, is modified. With this modification, once a quasi-steady regime is reached, the trajectories are created at the end

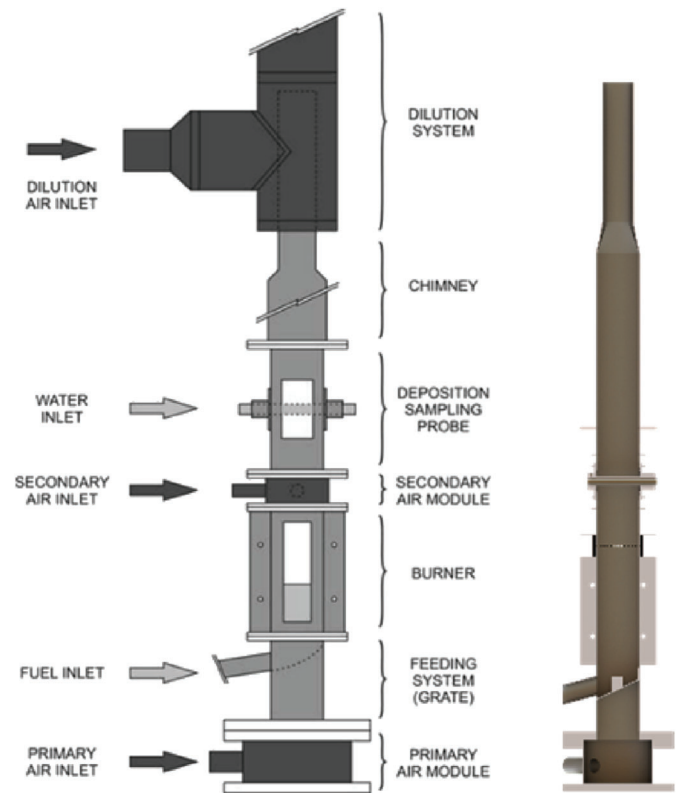


Fig. 2. Schematic and longitudinal section of the system used to validate previous algorithm [22].

of each time step that make up a time period of length equal to a multiple of the main oscillation of the system.

Due to the high computational effort involved in each of these executions, the execution speed of the initial algorithm is increased at the expense of a slightly higher memory consumption. Because the starting algorithm was already optimized, the improvements are small, and it is necessary to penalize resources such as volatile memory to achieve faster execution speed.

Values are stored in those cells that during the time period belong at some point to the bed frontier so that they serve as initialization values and the iterative calculations are closer to convergence.

In each execution of the algorithm, raw data are written to an ASCII file to be processed later through ad hoc algorithms in MATLAB. These algorithms access the ASCII files and reconstruct the fouling profiles in the surfaces of interest.

2.2. Domestic boilers studied

Next, the characteristics of the biomass boilers studied in this work are presented. Both boilers have been studied experimentally in an article by Patiño, D. et al. [25], which is used as the baseline to study and validate the proposed modelling on commercial facilities.

The test boundary conditions reflected in the experimental article have been maintained where it is specified that the water-tube boiler is tested at full load and the fire-tube boiler is tested at partial load (50% load), to achieve a worst-case scenario in terms of combustion quality.

2.2.1. Water-tube boiler. Full load

The general operation of the 24 [kW] water-tube boiler, is shown in Fig. 4. The system is fed from the top through a ramp

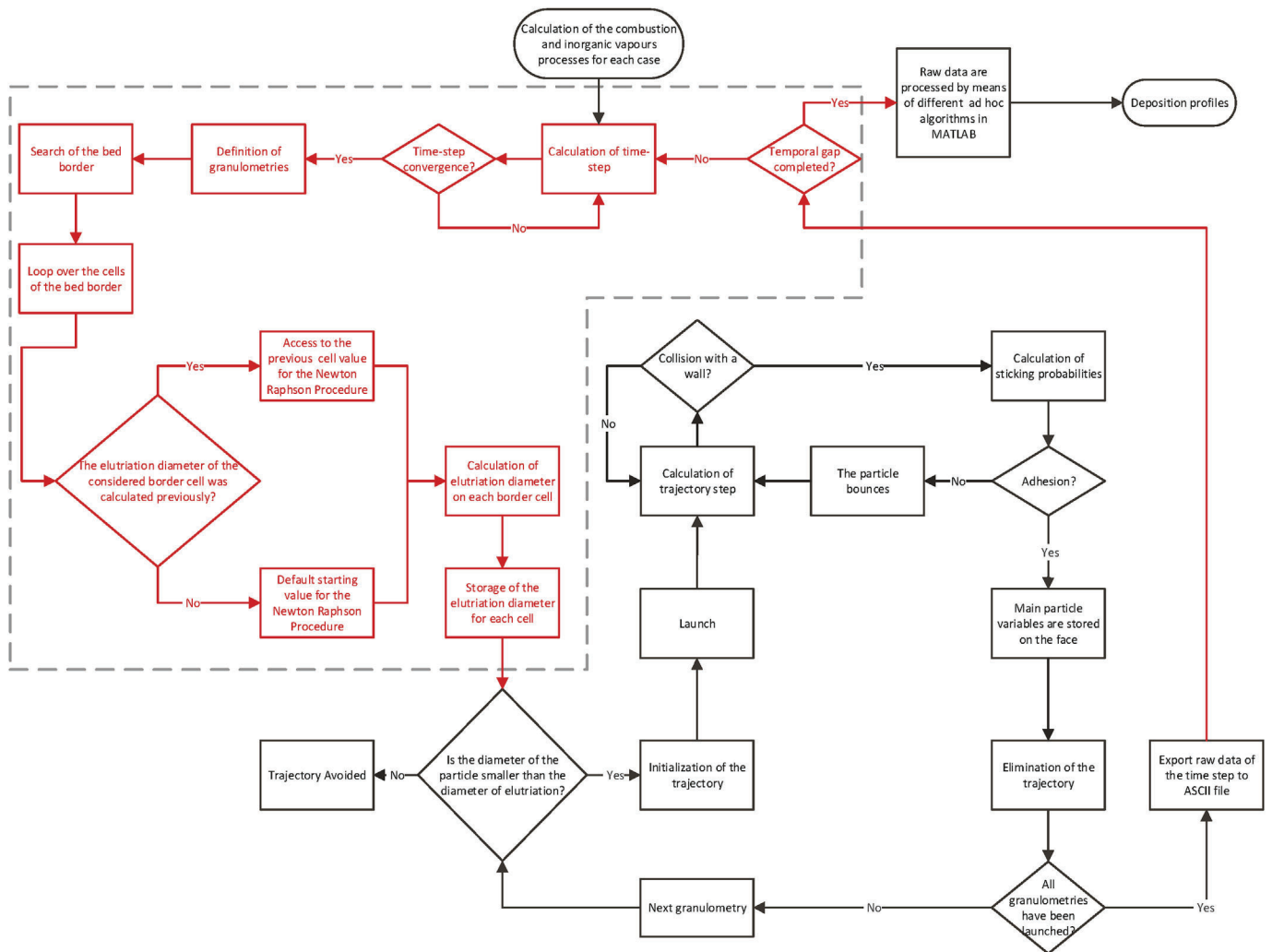


Fig. 3. Modified flowchart of the algorithm of the fouling numerical model.

connected to a screw fed by a hopper. The air is fed by the lower part of the bed grate, and the combustion gases make two passages through the tubular bundle of the heat exchanger before leaving the system through the lower part.

The fuel used in this system is reflected in Table 1 and is taken from the experimental article [25], where it is referred to as Wood Pellet A. To measure the deposition, fifteen sampling probes were placed, 3 per tube, on top of each of the five exchange tubes shown in Fig. 5. The probe dimensions are 80×35 [mm]. With the tubes being 340 [mm] in length, the probes only cover 240 [mm] of the 340 [mm], remaining equally spaced.

2.2.2. Fire-tube boiler. Partial load

In this case, a 60 [kW] nominal power fire-tube boiler is used, unlike the experimental burner. This boiler is fed by screw from the bottom of the bed but is without level control and has a discontinuous feeding system. In this way, the frontier will vary in height and extension according to the level of load and will also do so in each feeding cycle, moving periodically in opposite directions. In Fig. 6, a picture and a schematic of the system are shown.

The left side of Fig. 7 shows that air is fed by a fan through a series of holes located in concentric rings of the conical upper part of the grate. The fuel is fed by the lower central part of this grate. The right side of Fig. 7 shows that the secondary air is introduced by

an elevated ring supported by pillars that, together with a metal dome, confine the flame. This prevents the flame-quenching phenomenon and enhances the gas mixing to achieve better combustion performance.

This heat exchanger consists of fifteen vertical tubes with turbulators through which the flue gas circulates. These turbulators also act periodically as scrapers, eliminating the deposition on the tubes. To measure the deposition, fifteen internal rings with a height of 20 [mm] and an inner diameter of 95.6 [mm] were placed in the lower part of each of these vertical tubes; see Fig. 8, where the nomenclature followed in this manuscript is also shown.

As in the experimental article, it was decided to test the worst-case scenario for the boiler, which is when it works at a partial load of 30 [kW], which is 50 [%] of nominal power. For this boiler, the fuel shown in Table 1, named Wood Pellet B, will be used.

3. Calculation

For the numerical study of both systems, identical configurations have been used for the turbulence, radiation and species models. The turbulent k-epsilon model is used with Enhanced Wall Treatment, which is widely used in previous works of biomass combustion [33,34]. The model used for radiation is the Discrete-Ordinates Model, and for the species transport Finite-Rate/Eddy

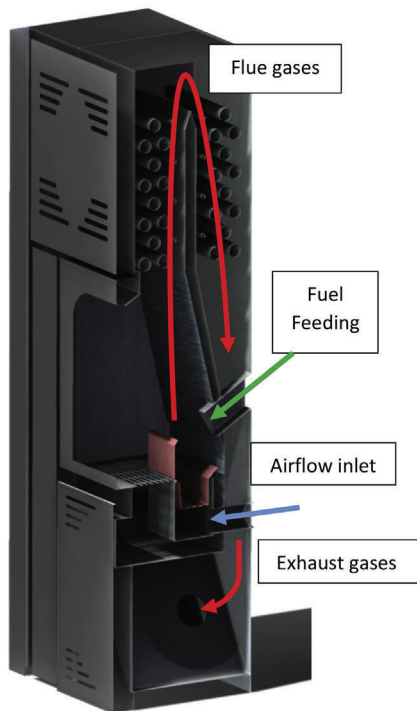


Fig. 4. CAD representation and schematic of the water-tube boiler.

Dissipation will be used.

The combustion of biomass is transitory in nature, as is the bed model used. This causes fluctuations in the variables of interest that make it difficult to consider the simulations as having reached a steady state.

In a previous study [22], it is considered that the simulations have reached a steady state when the fluctuation of the variables of interest is less than 5% of its average value in a time period that is

Table 1
Fuel properties.

	Wood Pellet A	Wood Pellet B
Proximate analysis, wet basis, as received. (%)		
Moisture	7.02	6.85
Volatiles	67.87	68.25
Char	23.36	24.24
Ash	1.75	0.41
Ultimate analysis, dry basis (%)		
C	45.85	47.21
H	6.75	6.19
O	44.96	46.46
N	2.41	0.14
S	<0.30	<0.30



Fig. 5. Location of the 5 tubes where the sampling probes are placed.

representative of the operation of the system and, additionally, when the slope of its linear regression is close to zero. In this work, as mentioned, there are no continuous feeding systems. This adds oscillations of greater magnitude to those inherent to the combustion of biomass as shown in Fig. 12.

Therefore, it will be considered that the system has reached the steady state when the slope of the variables of interest is close to zero and the periodicity and magnitude of the oscillations with greater magnitude is constant.

4. Results and discussion

This chapter will show the results obtained in both combustion systems using the fouling numerical model through the modified algorithm, which is reflected in the flowchart of Fig. 2. These results will be divided into two parts for each system. A first part where the results of the combustion will be shown and a second part where the deposition will be addressed and compared with the experimental results.

As mentioned above, the boilers studied in this work differ in



Fig. 6. Picture and schematic of the fire-tube boiler [32].

operation from the experimental burner and between each other, so they are ideal for validating and improving the applicability of the fouling numerical model. However, the information obtained from the experimental tests does not allow for contrasting between the fouling profiles, but only the normalized fouling rate on each sampling probe. This normalized fouling rate is calculated in the same way in as the experimental article [25], which is defined as the ratio between the individual fouling rate of a sampling probe and the average fouling rate for the whole set of probes. In any case,

the profiles estimated by the numerical model are included in this work to provide a wider perspective of the results.

4.1. Combustion results

The numerical study of the combustion was carried until convergence was reached. Depending on the system, this took from 5400 to 10800 s of flow time simulation, where the systems started from room temperature and evolved continuously until reaching a steady state.

4.1.1. Water-tube boiler. Full load

In the results shown below, the transient nature of the biomass combustion can be appreciated in the fluctuations of lesser magnitude. In addition, top-fed systems, lead to larger oscillations mainly driven by the high gradients present at the bed frontier and more abrupt changes in the shape of this frontier.

Figs. 8 and 9 show results, corresponding to the time period considered as a characteristic of system operation, in this case 600 s. In Fig. 9, the air excess with respect to time shows that the system oscillates between 2.3 and 1.8 [-] with an average value of 1.95 [-].

On the other hand, the heat transfer to the water circuit, in Fig. 10, oscillates between values of 21 and 27 [kW] with an average value of 23.96 [kW], which is the thermal power output declared by the system studied.

4.1.2. Fire-tube boiler. Partial load

As stated, the experimental test was carried out at partial load because it is the worst-case scenario for the system. At partial load, the system delivers 30 [kW] to the water circuit with an excess of air of approximately 2.9 [-] [25].

Figs. 11 and 12 show the results of excess air and thermal power delivered to the water circuit obtained by the fixed-bed biomass combustion model along the time period of 300 s, after reaching a quasi-steady regime. Both cases show oscillations with the feeding cycle having average values of 29.75 [kW] and 2.93 [-], thus indicating adequate agreement to the experimental runs.

4.2. Fouling results

After reaching the quasi-steady regime, the operational characteristic time period of each system is evaluated and defined. As mentioned above, in the case of the water-tube boiler, a time period of 600 s will be studied, while for the fire-tube boiler, the time period will be 300 s.

The main reason for using a longer duration in the water-tube

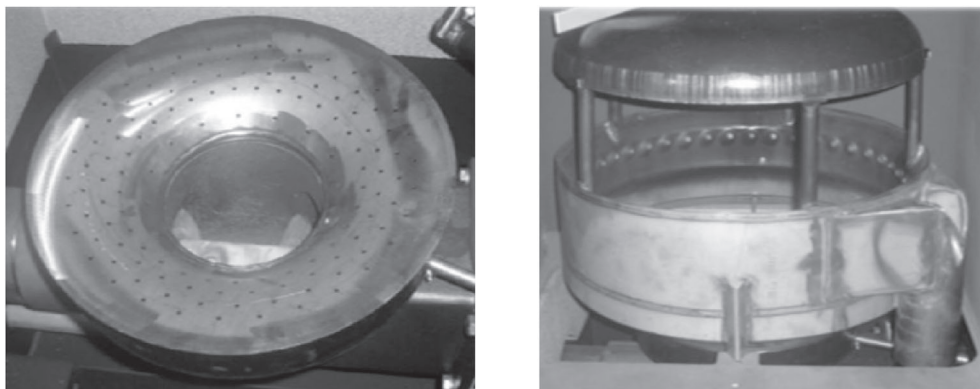


Fig. 7. Left, conical grate with several holes for primary air; right, secondary air circuit and dome.

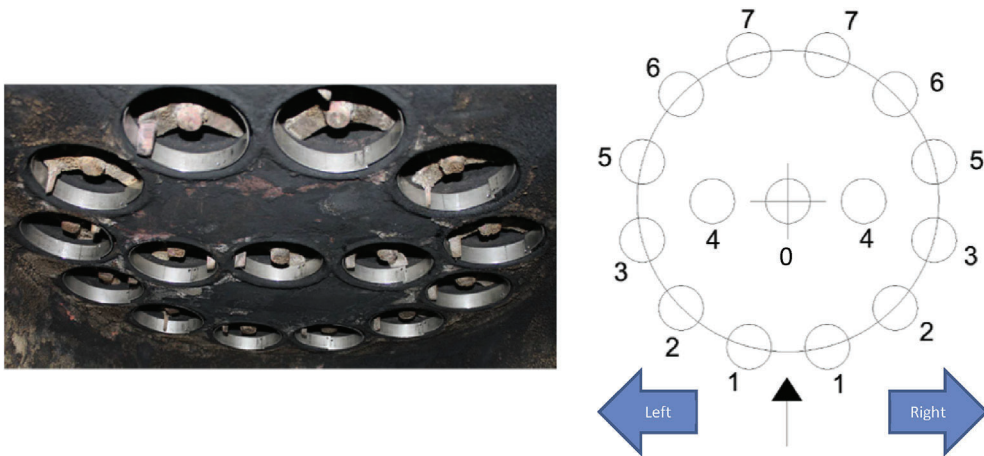


Fig. 8. Location of the sampling probes and nomenclature followed in both the experimental and numerical works.

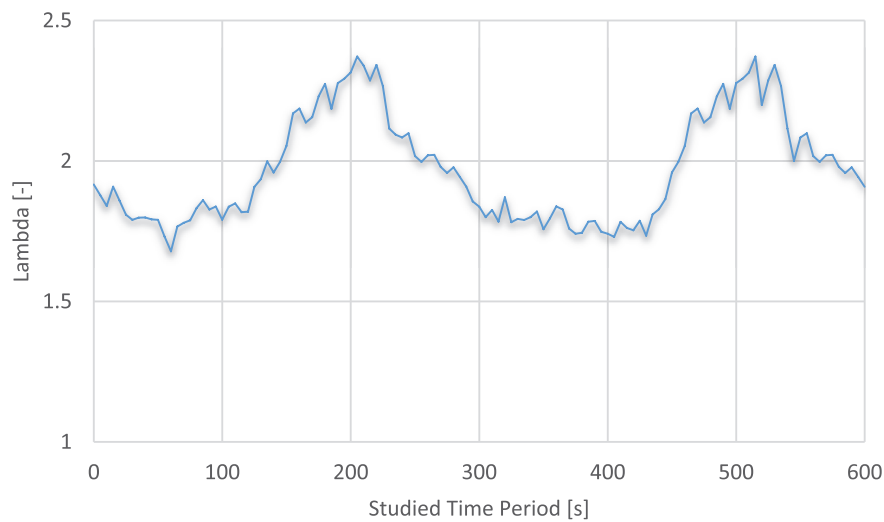


Fig. 9. Air excess along the studied time period of the water-tube boiler working at full load.

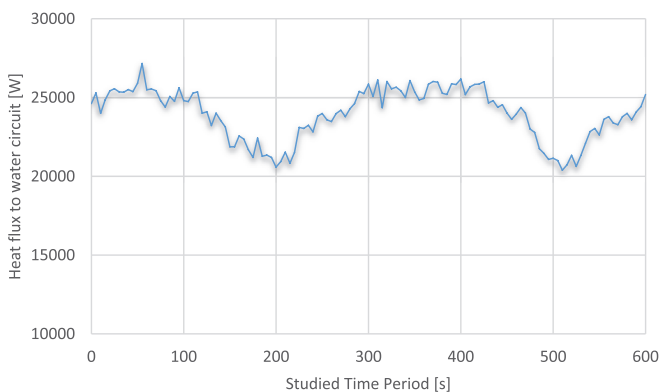


Fig. 10. Heat flux to the water circuit along the studied time period of the water-tube boiler working at full load.

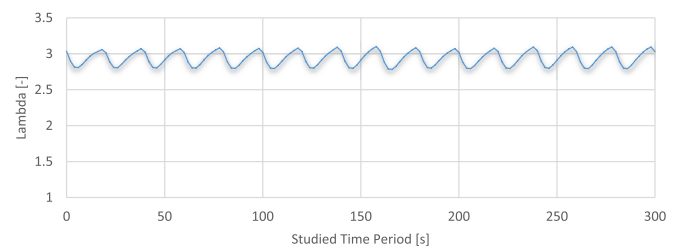


Fig. 11. Air excess along the studied time period of the fire-tube boiler working at partial load.

4.2.1. Water-tube boiler. full load

The results for the fifteen probe samples that were used in the experimental run to analyse fouling phenomena are shown in Fig. 13. It should be noted that due to the scarce information on the shape of the plates and to simplify the geometry calculated, it was decided not to include them in the CAD and mesh. The profiles were calculated using the data of the corresponding cells from the surface of each tube.

An adequate agreement between numerical and experimental data is observed in the results with the model and the proposed

boiler is to enable the calculation of fouling during at least two complete main oscillations. Performing the deposition calculation during even more oscillations would result in non-assumable computational effort.

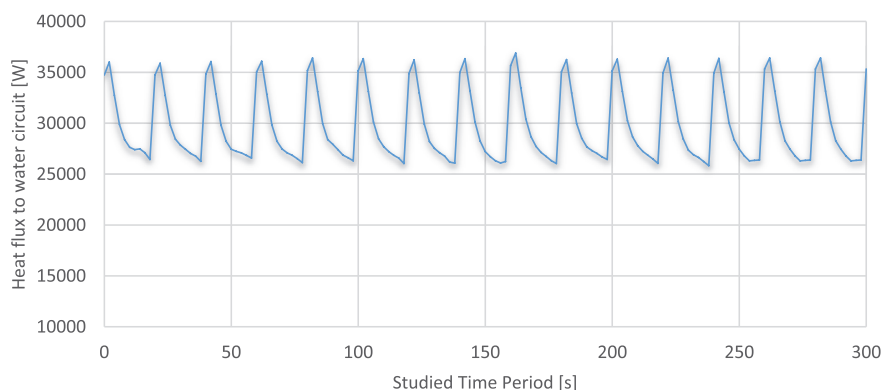


Fig. 12. Heat flux to water circuit along the studied time period of the fire-tube boiler working at partial load.

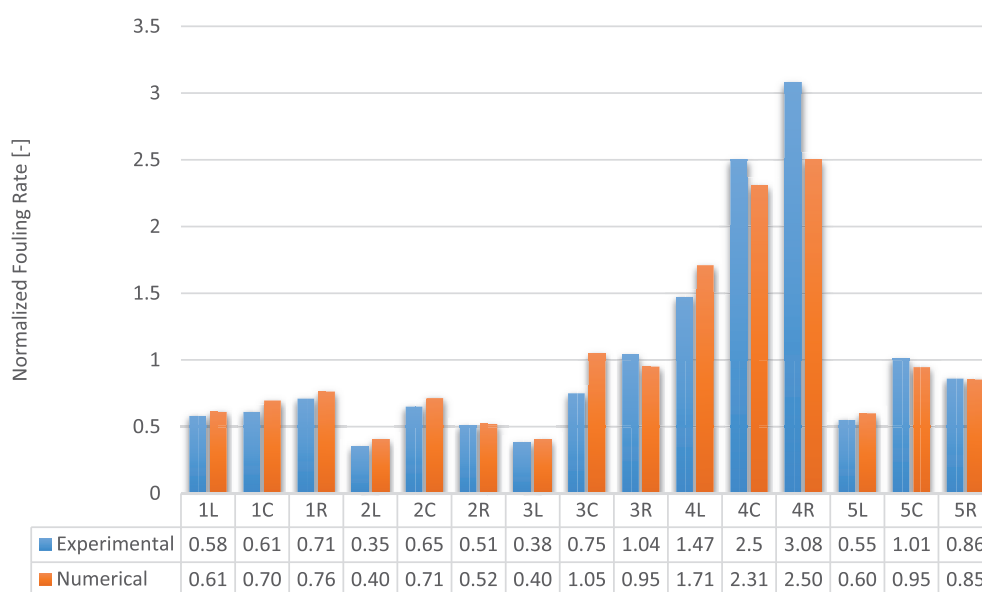


Fig. 13. Comparison of the normalized fouling rate between numerical and experimental tests for the water-tube boiler at full load. See Fig. 5 to check the location of the sampling probes.

algorithm. In the windward cooled tubes (1 and 2), fouling estimations are slightly higher than the values experimentally measured. On the other hand, the leeward cooled tubes (3, 4 and 5) present significantly lower depositions than those measured experimentally; however, the trends are adequately captured.

These phenomena can be due to the non-inclusion of the sampling probes, which would give rise to a larger surface normal to the flow. Additionally, by not modelling the surface increase derived from the deposition of unwanted matter, the gas flows easily through the tubular bundle and, with the flue gas, the less massive particles. In the case of windward tubes, the wake created is lower in the numerical calculation than in the real case. In the leeward tubes, the first to be impacted is tube 4, followed by tube 3, due to the preferred path of the gas in the vicinity of the intermediate deflector.

In Fig. 14, the deposition profile estimated by the algorithm is shown. An agreement with the numerical values is observed, although no experimental deposition profiles of the boiler have been found to contrast them. A side effect of the nodal smoothing used by the algorithm is also observed when obtaining the fouling data from the surface mesh of each cooled tube and not from independent surfaces, as would be the case if the sampling probes

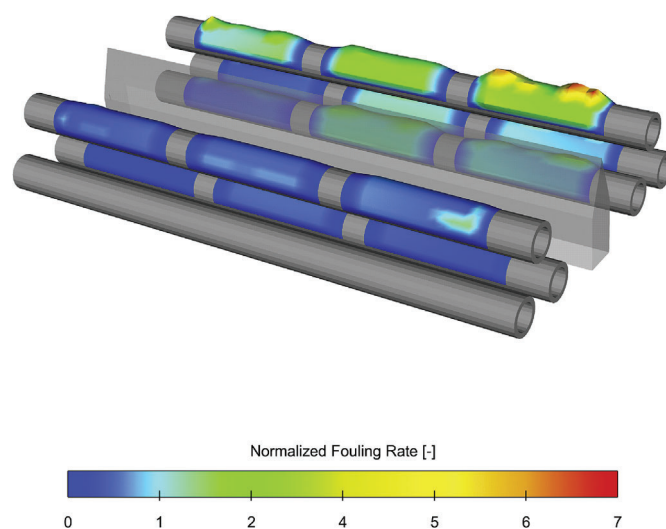


Fig. 14. Fouling profile estimated by the numerical fouling model for the water-tube boiler at full load.

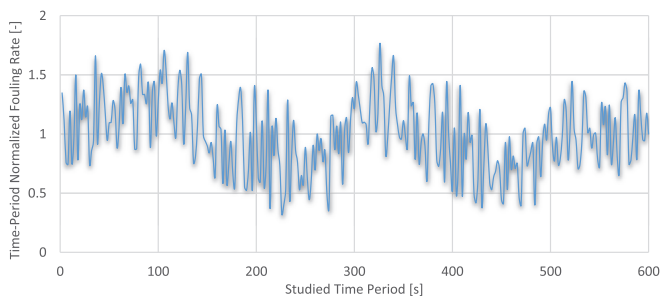


Fig. 15. Evolution of the normalized fouling rate for the water-tube boiler along the studied time period.

were included. This phenomenon is observed on the edges of the estimated profiles with close to zero values.

Fig. 15 shows the evolution of the fouling rate after being normalized within the time period studied. The fouling rate is highly irregular due to the strong perturbations caused by feeding from the top. Compared with Figs. 9 and 10, a slight correlation of the normalized fouling rate with the air excess and thermal power can be noted, especially with the latter. It is noteworthy to remember that the air supplied remains unchanged, so the relationship between both is direct. Hence, the increase in the fouling rate is probably due to an increase in the inorganic vapours released and the greater gas velocities caused by higher temperatures, which also promotes the stickiness of the walls and the particles elutriated.

4.2.2. Fire-tube boiler: partial load

This boiler has a much more complex flow than the water-tube boiler since it is a fire-tube boiler with turbulators. In addition, the boiler has a secondary air ring providing vorticity and a superior dome. Elutriated particles from the bed circulate following the gas to a greater or lesser extent according to their Stokes number, and their path is influenced by the vorticity added by the secondary air. Throughout their trajectory, they can impact against surfaces such as the upper dome, losing momentum and falling due to gravity,

with the possibility of being suspended again by the flow of flue gas. Subsequently, the rings studied are found at the entrance to the exchange tubes, in the vicinity of the turbulators. In this region, properly capturing the movement of the particles would require knowing the geometrical and physical properties of each particle in that region exactly, which is beyond the scope of this work.

The boiler is not symmetrical, although externally it may seem so. The causes of this asymmetry are several details but the most relevant are the following. The combustion chamber has a cylindrical shape with a flat side due to the presence of the access door and the structure on which it rests. The second cause is the air supply circuit. The primary air enters from a side surrounding the bed and is distributed in a simple way through the grate, so a slight asymmetry can be expected. Furthermore, the secondary air is supplied from the same side and distributed in the suspended ring. Again, this causes a certain asymmetry since higher speeds are found in the orifices near the inlet of the secondary air. The sum of these phenomena causes the displacement of the fouling rate towards the rear-left side.

In Fig. 16, the comparison of the values obtained between the experimental tests and the numerical calculation is shown. In this case, the results obtained, although they present an adequate precision and properly capture the trends, do not reach the same level of accuracy as the results for the water-tube boiler.

These results adequately capture the displacement of the fouling rate towards the rear tubes of the system, tubes 5-6-7 on both the left and right sides. However, a larger homogeneity of the fouling is observed in the numerical results that in experimental data when analysing a set of adjacent tubes, such as 1L-2L-3L, 1R-2R-3R, 5L-6L-7L and 5R-6R-7R. The minimum and maximum values do not reach the same levels, and the fouling is distributed within those sets of tubes.

This may be due to the use of the RANS averaged equations with k-epsilon turbulence modelling that overestimates deposition [35] in certain cases. Additionally, it should be considered that in the current model, neither erosion phenomena nor obstruction of passages caused by the deposition are considered.

The profiles estimated by the algorithm in the sampling rings

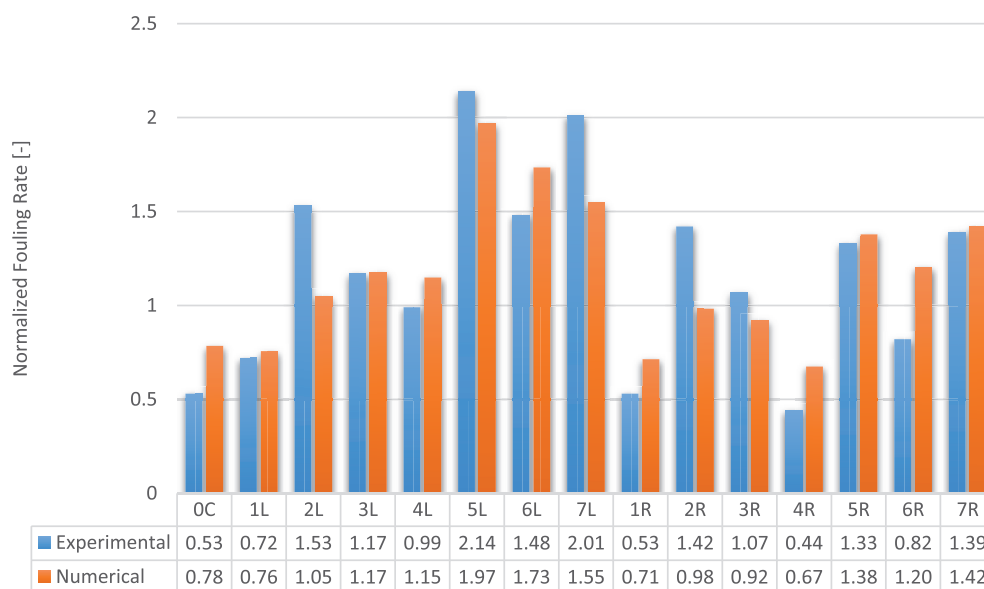


Fig. 16. Comparison of the normalized fouling rate between numerical and experimental tests for the fire-tube boiler at partial load. See Fig. 8 to check the location of the sampling probes.

are shown in Fig. 17. The greatest deposition is located at the entrance of each tube, where the particles must undergo an abrupt change of direction, and the more massive granulometries, with a high Stokes number, do not follow the flue gas flow and impact against the walls.

Fig. 18 shows the evolution of the fouling rate for the fire-tube boiler after its normalization within the time period studied. The evolution of the fouling rate does not have the same type of small random irregularities present in the water-tube boiler, thanks to its bottom-feeding system. However, this non-continuous bottom-feeding system generates larger but cyclical irregularities, accompanying the feeding cycle, necessary to sustain the partial load of the system. As the feeding system introduces the fresh fuel, this fuel fed pushes up the bed column and spreads to outer rings of the grate, leading to a larger bed surface which reacts and is volatilized. As the fuel travels to outer regions of the conical grate finishes its conversion and only char and ashes remains. In addition, the bed thickness is lower in the outer regions, which will promote the PM to be elutriated.

5. Conclusions

In this work, the modification of the fouling numerical model

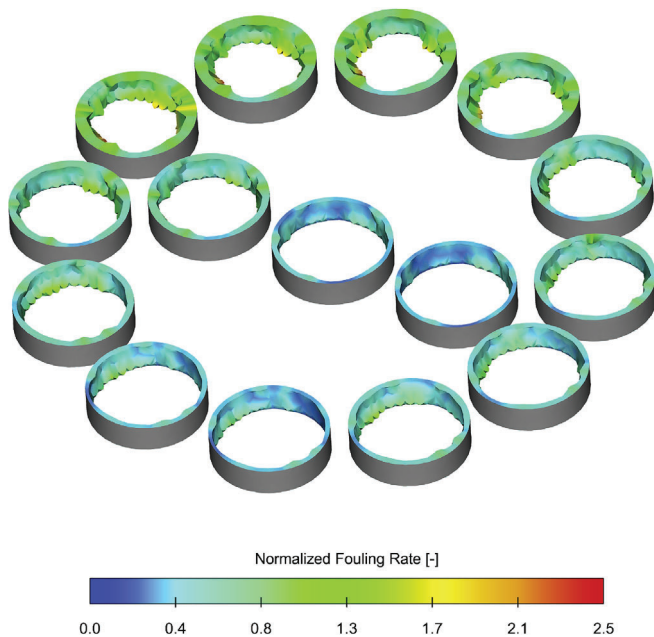


Fig. 17. Fouling profile estimated by the numerical fouling model for the fire-tube boiler at partial load.

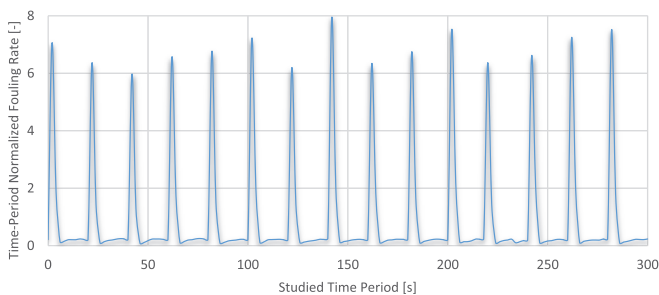


Fig. 18. Evolution of the normalized fouling rate for the fire-tube boiler along the studied time period.

and overall algorithm for the fouling profile prediction is detailed, adapting it to a wider spectrum of commercial systems after the validation of the base modelling carried out in the previous work [22].

The previous model was suitable for biomass combustion systems with great stability of operation. Therefore, once the system reached the quasi-steady regime, the complete fouling algorithm was executed only once, since the fluctuations of the bed and gas fields were minor and their effect on Lagrangian trajectories was consequently small. To capture the inherent dispersion due to local fluctuations always present but not resolved in the model, a stochastic tracking approach was employed that predicted the natural dispersion of the particles. However, commercial domestic systems, operational load management and control systems are quite basic. As shown in the results, this very simple management tend to cause oscillations of greater magnitude than those inherent to a steady, well controlled biomass combustion. Hence, the stochastic dispersion model applied to a ‘frozen’ solution of the algorithm was considered not suitable.

Hence the new approach was to co-simulate the fouling of the boiler with the solution of the whole combustion model. Although this modified fouling model required a deep revision and optimization of its algorithm to improve its computational efficiency to make it feasible to be coupled with the ongoing CFD simulation. In fact, deep changes in the algorithm were made seeking to achieve a compromise between the computational effort of calculating the trajectories in each time step and appropriately capturing the effect of the fluctuations in the solid-phase and gaseous-phase fields over these trajectories.

After making these modifications in both the numerical model and the algorithm, they were validated against previously published experimental articles [25]. In that work, fouling phenomena were analysed in two commercial boilers with large differences in operation compared with that of the experimental burner studied initially. One of the systems is a water-tube top-fed boiler with a heat exchanger consisting of cooled walls and a two-step tube bundle. The other system is a fire-tube bottom-fed boiler with non-continuous feeding with several combustion enhancements, such as a secondary ring, to induce tangential flow and turbulators in the heat exchanger.

With the proposed modelling, the qualitative results achieved are in good agreement with the experimental data. A new milestone has been reached with this modified fouling model, as it can be used in the simulation of commercial domestic systems since it is able to evolve at the same time the combustion does.

Future improvements will include the following: including new fouling precursors, such as sodium compounds, which would allow the fouling model to work with more types of biomass, such as residential solid waste. Another interesting but very complex improvement would be to capture the generation and evolution of each particle along its path through the system, as their physical-chemical properties are being affected by the phenomena of coalescence, oxidation, surface melting or condensation of vapours over its surface.

Finally and crucially, it becomes necessary to increase the parallelism of the Lagrangian calculation of commercial software through use of new technologies such as the highly parallel calculations being assisted by the GPU. In this way, the very high computational cost of the Lagrangian trajectories could be reduced. Also, a full Eulerian fouling model could reduce the high computational cost without the use of highly parallel computing.

All these lines of improvement will be the object of study and subsequent incorporation into the tool proposed in this work. The goal is to develop an advanced fouling model with great flexibility and simple implementation in the commercial software.

Acknowledgements

The authors would like to acknowledge the financial support from the project Biomasa AP, approved by the programme INTER-REG V-A España-Portugal 2014–2020 (POCTEP) and co-financed by the European Regional Development Fund (FEDER) (0015_BIOMASA AP_1_E). The work of Sergio Chapela López was supported by grant BES-2016-076785 of the Ministry of Economy, Industry and Competitiveness (Spain).

References

- [1] Q. Xiong, Y. Yang, F. Xu, Y. Pan, J. Zhang, K. Hong, G. Lorenzini, S. Wang, Overview of computational fluid dynamics simulation of reactor-scale biomass pyrolysis, *ACS Sustain. Chem. Eng.* 5 (2017) 2583–2798.
- [2] D.W. Bunn, J. Redondo-Martin, J.L. Muñoz-Hernandez, P. Diaz-Cachinero, Analysis of coal conversion to biomass as a transitional technology, *Renew. Energy* 132 (2019) 752–760.
- [3] G. Caposciutti, M. Antonelli, Experimental investigation on air displacement and air excess effect on CO, CO₂ and NO_x emissions of a small size fixed bed biomass boiler, *Renew. Energy* 116 (2018) 795–804.
- [4] S. Link, P. Yrjas, L. Hupa, Ash melting behaviour of wheat straw blends with wood and reed, *Renew. Energy* 124 (2018) 11–20.
- [5] U. Kleinhans, C. Wieland, F.J. Frandsen, H. Spliethoff, Ash formation and deposition in coal and biomass fired combustion systems: progress and challenges in the field of ash particle sticking and rebound behaviour, *Prog. Energy Combust. Sci.* 68 (2018) 65–168.
- [6] S. Aramideh, Q. Xiong, S. Kong, R.C. Brown, Numerical simulation of biomass fast pyrolysis in an auger reactor, *Fuel* 156 (2015) 234–242.
- [7] D. Vamvuka, G. Kaniadakis, D. Pentari, G. Alevizos, Z. Papapolikarpou, Comparison of ashes from fixed/fluidized bed combustion of swine sludge and olive-by-products. Properties, environmental impact and potential uses, *Renew. Energy* 112 (2017) 74–83.
- [8] D. Kronenberger, B. Groß, Chemical and physical analysis of different ash fractions from small biomass boilers, *Chem. Eng. Technol.* 41 (2018) 2159–2167.
- [9] V. Dhyani, T. Bhaskar, A comprehensive review on the pyrolysis of lignocellulosic biomass, *Renew. Energy* 129 (2018) 695–716.
- [10] H. Rezaei, S. Sokhansanj, Physical and thermal characterization of ground bark and ground wood particles, *Renew. Energy* 129 (2018) 583–590.
- [11] Y.D. Singh, P. Mahanta, U. Bora, Comprehensive characterization of lignocellulosic biomass through proximate, ultimate and compositional analysis for bioenergy production, *Renew. Energy* 103 (2017) 490–500.
- [12] J. Capablo, J. Salvadó, Estimating heat transfer losses caused by alkali salt deposits in biomass combustion, *Renew. Energy* 105 (2017) 449–457.
- [13] S.K. Kær, Numerical Investigation of Ash Deposition in Straw-Fired Boilers-Using CFD as the Framework for Slagging and Fouling Predictions, 2001. Ph. D.
- [14] E. Meloni, M. Caldera, V. Palma, V. Pignatelli, V. Gerardi, Soot abatement from biomass boilers by means of open-cell foams filters, *Renew. Energy* 131 (2019) 745–754.
- [15] Q. Wang, K. Han, J. Wang, J. Gao, C. Lu, Influence of phosphorous based additives on ash melting characteristics during combustion of biomass briquette fuel, *Renew. Energy* 113 (2017) 428–437.
- [16] L. Wang, J.E. Hustad, Ø. Skreiberg, G. Skjevraak, M. Grønli, A critical review on additives to reduce ash related operation problems in biomass combustion applications, *Energy Proced.* 20 (2012) 20–29.
- [17] M. Aho, Reduction of chlorine deposition in FB boilers with aluminium-containing additives, *Fuel* 80 (13) (2001) 1943–1951.
- [18] L. Tobiasen, R. Skytte, L.S. Pedersen, S.T. Pedersen, M.A. Lindberg, Deposit characteristic after injection of additives to a Danish straw-fired suspension boiler, *Fuel Process. Technol.* 88 (11–12) (2007) 1108–1117.
- [19] B.M. Steenari, A. Lundberg, H. Pettersson, M. Wilewska-Bien, D. Andersson, Investigation of ash sintering during combustion of agricultural residues and the effect of additives, *Energy Fuels* 23 (2009) 5655–5662.
- [20] T. Schulzke, J. Westermeyer, H. Giani, C. Hornsby, Combustion of Refined Renewable biomass Fuel (RRBF) in a bubbling fluidized bed, *Renew. Energy* 124 (2018) 84–94.
- [21] G. Gianfelice, M.D. Zassa, A. Biasin, P. Canu, Onset and propagation of smouldering in pine bark controlled by addition of inert solids, *Renew. Energy* 132 (2019) 596–614.
- [22] S. Chapela, J. Porteiro, M.A. Gómez, D. Patiño, J.L. Míguez, Comprehensive CFD modeling of the ash deposition in a biomass packed bed burner, *Fuel* 234 (2018) 1099–1122.
- [23] M.A. Gómez, J. Porteiro, D. Patiño, J.L. Míguez, Eulerian CFD modelling for biomass combustion. Transient simulation of an underfeed pellet boiler, *Energy Convers. Manag.* 101 (2015) 666–680.
- [24] M.A. Gómez, J. Porteiro, D. De la Cuesta, D. Patiño, J.L. Míguez, Numerical simulation of the combustion process of a pellet-drop-feed boiler, *Fuel* 184 (2016) 987–999.
- [25] D. Patiño, B. Crespo, J. Porteiro, J.L. Míguez, Experimental analysis of fouling rates in two small-scale domestic boilers, *Appl. Therm. Eng.* 100 (2016) 849–860.
- [26] H. Wiinikka, R. Gebart, C. Boman, D. Boström, M. Öhman, Influence of fuel ash composition on high temperature aerosol formation in fixed bed combustion of woody biomass pellets, *Fuel* 86 (1–2) (2007) 181–193.
- [27] D. Lindberg, R. Backman, P. Chartrand, M. Hupa, Towards a comprehensive thermodynamic database for ash-forming elements in biomass and waste combustion – current situation and future developments, *Fuel Process. Technol.* 105 (2013) 129–141.
- [28] R. Clift, *Bubbles, Drops and Particles*, Academic Press, 1978.
- [29] P. Walsh, A. Sayre, D. Loehden, L. Moenroe, J. Ber, A. Sarofim, Deposition of bituminous coal ash on an isolated heat exchanger tube: effects of coal properties on deposit growth, *Prog. Energy Combust. Sci.* 16 (1990) 327–346.
- [30] H. Ounis, A. Goodarz, J.B. McLaughlin, Brownian diffusion of submicrometer particles in the viscous sublayer, *J. Colloid Interface Sci.* 143 (1) (1991) 269–277.
- [31] ANSYS-Fluent. Theory Guide. V18.2.
- [32] Hackgut- und Pelletheizung KWB Multifire 15-100 kW. Technik und Planung. <https://www.pelletshome.com/-/files-index-/files-CompaniesKwbMultifire.pdf> (accessed 5 February 2019).
- [33] A. Rezeau, L.I. Díez, J. royo, M. Dias-Ramírez, Efficient diagnosis of grate-fired biomass boilers by a simplified CFD-based approach, *Fuel Process. Technol.* 171 (2018) 318–329.
- [34] J. Wiese, F. Wissing, D. Höhner, S. Wirtz, V. Scherer, U. Ley, H.M. Behr, DEM/CFD modeling of the fuel conversion in a pellet stove, *Fuel Process. Technol.* 152 (2016) 223–239.
- [35] R. Weber, N. Schaffel-Mancini, M. Mancini, T. Kupka, Fly ash deposition modelling: requirements for accurate predictions of particle impaction on tubes using RANS-based computational fluid dynamics, *Fuel* 108 (2013) 586–596.

ANEXO B.

Trabajos enviados a revista y
pendientes del proceso de revisión
por pares

Numerical transient modelling of the fouling phenomena and its influence on thermal performance in a low-scale biomass shell boiler

Sergio Chapela, Natalia Cid, Jacobo Porteiro, José Luis Míguez

Industrial Engineering School, University of Vigo, Lagoas Marcosende s/n, Vigo, Pontevedra, Spain.

e-mail: schapela@uvigo.es

ABSTRACT

Biomass has been used as a fuel throughout history because of its abundance and the ease of obtaining it from nearby environments. Its use has been increasing in recent decades because it is considered a renewable energy source. However, the heterogeneity of its physical properties and chemical composition can cause major problems that hinder its development. Such problems are mainly slagging phenomena in beds, fouling of the main thermal-exchange surfaces and emission of particulate matter, with the last problem being closely linked to the first two. In the present work, modelling and simulation of combustion in a low-power biomass shell boiler will be approached. At the same time, the phenomena involved in the fouling of the exchange surfaces will be modelled, and their impact on the performance will be calculated. The modelling of the fouling phenomena in this boiler, in conjunction with the EBITCoM (Eulerian Biomass Transient Combustion Model) developed by the Energy Technology Group of the University of Vigo, will produce a detailed view of the problematic areas of the system. From these models, preventive actions can be anticipated to avoid or greatly delay the drop in global efficiency, reducing emissions and the overall operating cost.

Keywords: Fouling; CFD; biomass; combustion; deposition

Symbol	Parameter	Units
F	Weighting factor on porosity correlation	-
$M_{\text{condensed}}$	Mass of inorganic vapours condensed	kg
$M_{\text{PMadhered}}$	Mass of particulate matter adhered	kg
S	Area of the surface cell	m^2
TC_{deposit}	Deposit thermal conductivity	W/m K
TC_{gas}	Gas phase thermal conductivity	W/m K
TC_{solid}	Solid phase thermal conductivity	W/m K
Vol_{liquid}	Molten phase volume	m^3
Vol_{solid}	Solid phase volume	m^3

Greek symbols

$\emptyset_{\text{initial}}$	Initial porosity	-
\emptyset_{layer}	Deposit layer porosity	-
$\rho_{\text{condensed}}$	Inorganic vapour condensed density	kg/m^3
$\rho_{\text{PMadhered}}$	Particulate matter adhered density	kg/m^3
Γ_{deposit}	Thickness of the deposit	m
Γ_{wall}	Thickness of the adjacent solid cell	m

26 **1. Introduction**

27 Biomass has been used as a fuel throughout history because of its abundance and the ease of
28 obtaining it from nearby environments [1, 2]. Its use has increased in the last half of the twentieth
29 century and in the course of the current century. It is mainly being considered as a renewable
30 energy source due to growing ecological consciousness in society and a rising price of fossil fuels
31 [3].

32 Biomass has been used for numerous activities, being its use to endure adverse weather one of
33 the engines of its boom. In early times, its direct combustion in an open hearth provided a source
34 of heat for humans, mainly by radiation and convection of direct gas on the surfaces being heated,
35 although with a very low efficiency. Subsequently, humans proceeded to perform combustion in
36 a closed hearth and exploit the heat transferred by radiation and convection directly and also
37 along the surfaces of flue gas-air exchangers. This improvement allowed increased thermal
38 utilization of the biomass and avoided the emission of particulate matter (PM) and harmful gases
39 into rooms. The desire to increase the thermal performance of systems and, above all, the desire
40 to transport this heat to other rooms gave rise to systems with flue gas-water exchangers. The
41 use of these exchange surfaces involved the inclusion of surfaces that possess strong thermal
42 gradients. These cooled surfaces are where one of the biggest problems entailed by the
43 combustion of biomass, the fouling phenomenon, occurs.

44 This phenomenon causes a very significant loss in performance in the system, as it severely lowers
45 the heat transfer and blocks the free flow of the flue gas within heat exchangers. A dominant
46 factor in this phenomenon is the condensation of inorganic vapours on these surfaces. Previous
47 authors [4-8] concluded that when these inorganic vapours condensed on the surfaces, either on
48 the PM or on the heat exchanger surfaces, the stickiness between both increases, resulting in
49 increased deposition.

50 However, the concept of biomass itself is a problem with no straightforward solution. Biomass
51 represents a large group of fuels, ranging from wood to MSW (Municipal Solid Waste) to
52 agricultural waste or even algae [9]. The variety and range of the physicochemical properties of
53 biomass compared to those of refined fossil fuels, as shown in the works of Dhyani et al.[10],
54 Singh et al.[11] or Rezaei et al.[12], are the reasons that hinder biomass development.

55 The mechanisms to minimize fouling are varied, and some examples include studying the
56 combustion chamber geometry, using air-staged systems, using additives [13-17] or using new
57 combustion procedures, such as smouldering [18] with inert solids or gasification; however, the
58 lack of a fuel-independent solution should be highlighted.

59 In the proposed work, the modelling of deposit thickness and its effect on heat transfer will be
60 addressed simultaneously as the combustion and deposition of undesired matter is simulated in
61 a low-scale domestic biomass shell boiler. This tool will allow us to identify possible actions to
62 reduce the temporary degradation of the overall efficiency of the system.

63

64 **2. Materials and methods**

65 The EBiTCoM (Eulerian Biomass Transient Combustion Model) of the University of Vigo, which is
66 summarized in the works of Gómez et al.[19, 20], will be used to perform this work. In addition,
67 the Euler-Lagrange Fouling Model of the same research group carried out by Chapela et al.[21]
68 and adapted to commercial systems in a later step [22] will be modified and used. Using both

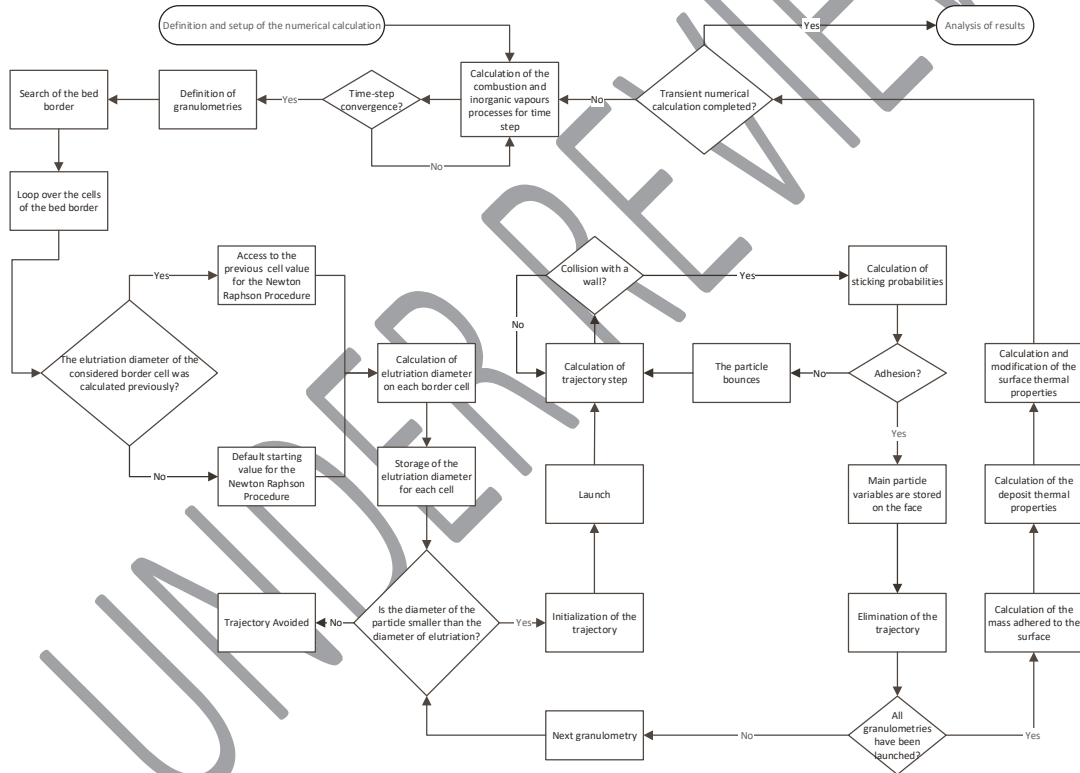
69 models, a modification of the latter model that predicts the transient growth of the deposit and
 70 its influence on heat transfer will be developed and evaluated in this work.

71

72 **a. Fouling model**

73 The fouling model uses the evaporation, transport and condensation of inorganic vapours,
 74 specifically potassium chloride, as tracers of deposition precursors. Subsequently, a Lagrangian
 75 framework for tracking PM throughout the system is used, which results in a rate of mass
 76 adhesion to the surfaces when combined with the first model. Further details are shown in the
 77 works of Chapela et al.[21, 22].

78 After obtaining the rate at which the undesired matter adhered to the walls, the deposit layer
 79 thickness and its physical properties are calculated in this modified algorithm. With these results,
 80 the thermal conductivity of the local surface on which the material has adhered is modified. The
 81 algorithm is shown in the flowchart seen in Figure 1, and the fundamental steps are explained in
 82 increased depth.



83

84

Figure 1. Proposed flowchart for the fouling model algorithm.

85 Once the execution of the main algorithm loop has finished for the current time step, the values
 86 of each cell are analysed, and the rate of mass adhesion is calculated. Porosity of the deposit layer
 87 is a relevant factor due to its direct influence on the deposit thickness and the thermal
 88 conductivity.

89 If the deposit layer consists only of solid particles on a precursor layer of the condensed phase,
 90 its porosity is relatively high. However, as the condensed phase melts with temperature, it
 91 partially fills the voids, resulting in a lower porosity. Richards et al. [23] proposed a correlation
 92 based on a parameter based on the liquid to solid volume ratio that has been adopted in
 93 subsequent studies as performed by Hecken et al. [24] and Wang et al. [25]

$$\phi_{layer} = 1 - \left[(1 - \phi_{initial}) + \frac{Vol_{liquid}}{Vol_{solid}} (1 - \phi_{initial}) \right] \quad (1)$$

94 Once the porosity is calculated, there are several models to determine the thermal conductivities
 95 for a deposit layer, depending on its tortuosity or its anisotropy. Kær [7] combined the models
 96 proposed by Hadley [26] and Hsu et al.[27] and implemented them as a weighting factor on the
 97 correlation proposed by Richards et al.[23]. This weighting factor, F, is shown in Eq. 2 and applied
 98 to Eq. 3 for the calculation of the deposit thermal conductivity.

$$F = \frac{2^{6.5}}{2^{6.5} - 1} \cdot \left(1 - \frac{1}{(1 - \phi_{layer})^{6.5}} \right) \quad (2)$$

$$TC_{deposit} = (1 - F) \cdot TC_{solid} + F \cdot TC_{gas} \quad (3)$$

99 Assuming a density of the adhered mass of 2000 kg/m³ for all granulometries and a density of
 100 1980 kg/m³ for the inorganic precursor vapour layer, the deposit thickness on each surface cell
 101 of the domain studied is calculated as shown in Eq. 4.

$$\Gamma_{deposit} = \frac{\left[\frac{M_{condensed}}{\rho_{condensed}} + \frac{M_{PM_{adher}}}{\rho_{PM_{adhered}}} \right]}{(1 - \phi_{initial}) \cdot S} \quad (4)$$

102 The implementation of this extra thickness caused by the precursor layer and the adhesion of
 103 undesired material is performed by modifying the thermal properties of the solid cell in which the
 104 surface deposit exists. For this, it is necessary to know the thickness of the solid, metallic in this
 105 study, normal to the surface of the volumetric cell.

106 To perform a general model without mesh restrictions, such as requiring a structured mesh or
 107 requiring cells of known shape, queries of both the face centroid coordinates and the solid cell
 108 centroid coordinates are performed. With both results, the solid cell thickness is computed.

109 Once the thickness of this solid cell and the deposit thickness are known, through the thermal to
 110 electrical analogy model, the new thermal conductivity is calculated in Eq. 5.

$$TC_{equivalent} = \frac{\Gamma_{deposit} + \Gamma_{wall}}{\left[\frac{\Gamma_{deposit}}{TC_{deposit}} + \frac{\Gamma_{wall}}{TC_{wall}} \right]} \quad (5)$$

111 With this modified thermal conductivity for each cell, the next time step is calculated, decreasing
 112 the heat transfer to the water circuit. In the present model, erosion phenomena are not taken
 113 into account, as suggested by Schulze et al.[28], and displacement of the condensed phase in the
 114 vertical walls is also not taken into account.

115

116 b. Boiler study

117 Figure 2 shows the shell boiler body used in this work, which was initially designed to be coupled
 118 to a diesel burner; in this work, the shell boiler body has been coupled to a pellet burner. These
 119 pellets come from a hopper located next to the boiler and are top fed by a flexible hose. The
 120 burner consists of a grate that has multiple holes and grooves to distribute the air properly. The

121 air is supplied by a fan, which is controlled by the same electronic control unit that controls the
122 feeding. Finally, the boiler has a modular construction and is largely cooled by a high-volume
123 water chamber.



124

125

Figure 2. 3D model used in the present work.

126 The combustion gases are confined in the main chamber before being conducted through twelve
127 vertical tubes, and then the combustion gases are directed by a deflector to the exterior of the
128 upper water jacket and out of the system as seen Figure 3. The water jacket consists of three
129 modules that are interconnected by four communication boxes, allowing two communication
130 boxes for each pair of modules. The cooling circuit works with a temperature jump of 5 [K].



131

132

Figure 3. Section of the boiler and detail of the grate.

133 The properties of the fuel used in this work are summarized in the following table:

Table 1. Fuel composition and thermal properties

Proximate analysis, wet basis, as received %	
Moisture	6.10
Volatile	69.52
Char	23.90

Ash	0.48
LHV [kJ/kg], wet basis	16739.4

134

135 c. Numerical setup

136 An unstructured mesh composed of 4.5 million polyhedral elements is used, with special
137 refinement on the near-bed region. Usual assumptions on the water circuit, such as water-side
138 convection coefficients and temperatures, will be avoided in favour of modelling the whole water
139 circuit. In this way, the preferential flow routes will be modelled, and the temperatures reached
140 on the wall will be more accurate, although this will have a large impact on the computational
141 cost.

142 In addition to the aforementioned models for bed combustion and the modified fouling model,
143 the turbulence model used is the k- ϵ model with Enhanced Wall Treatment, which is widely used
144 due to its good compromise between precision and computational cost [29-32], although it
145 presents a slight overestimation of the impact rate against the surfaces as stated by Weber et al.
146 [33]. The radiation model used is the Discrete-Ordinates Model, which works well with porous
147 media using the work of Gómez et al. [34], and the species transport model is the Finite-
148 Rate/Eddy-Dissipation Model with the setup proposed by Chapela et al.[35]

149

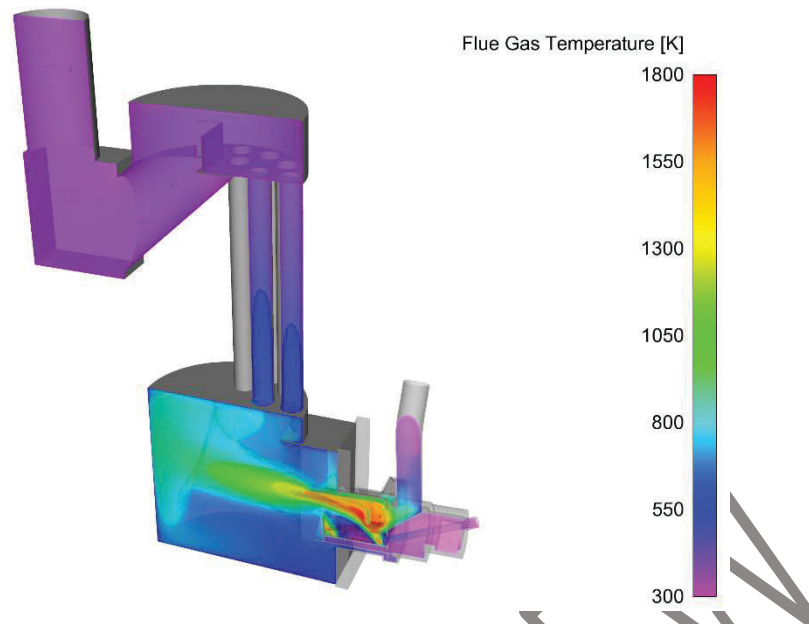
150 3. Results and discussion

151 The first 90 minutes of operation of the boiler was simulated with a cold start with fresh bed and
152 stagnant water. Due to the large thermal inertia of the system with 0.1 m³ of water inside and its
153 large metal body, a first long heating phase is required before the system was close to the
154 stationary regime.

155 After this first transient phase, the average thermal power burned is 25 kW with an air excess of
156 1.5. The thermal power transferred to the water circuit is 15 kW; therefore, the efficiency of the
157 boiler is 60%. In the experimental run, the overall efficiency is as low as 46%; however, this facility
158 has been studying different fuel batches, and the fouling rate has possibly reached asymptotic
159 behaviour.

160 Throughout the simulation, the fouling phenomena have been calculated through the proposed
161 modified model. The results that are shown correspond to the state of the boiler after the first
162 1.5 hours of simulation.

163 Figure 4 shows the flue gas temperature field with the isosurfaces of the values equal to the
164 colormap levels. The boiler design may not be the most suitable for use when coupled to a
165 biomass burner; although the air flow supplied plus the fuel mass burned to give the nominal
166 power is similar, because although the diesel has approximately three times more calorific value,
167 it also has a proportionally superior stoichiometry of air.

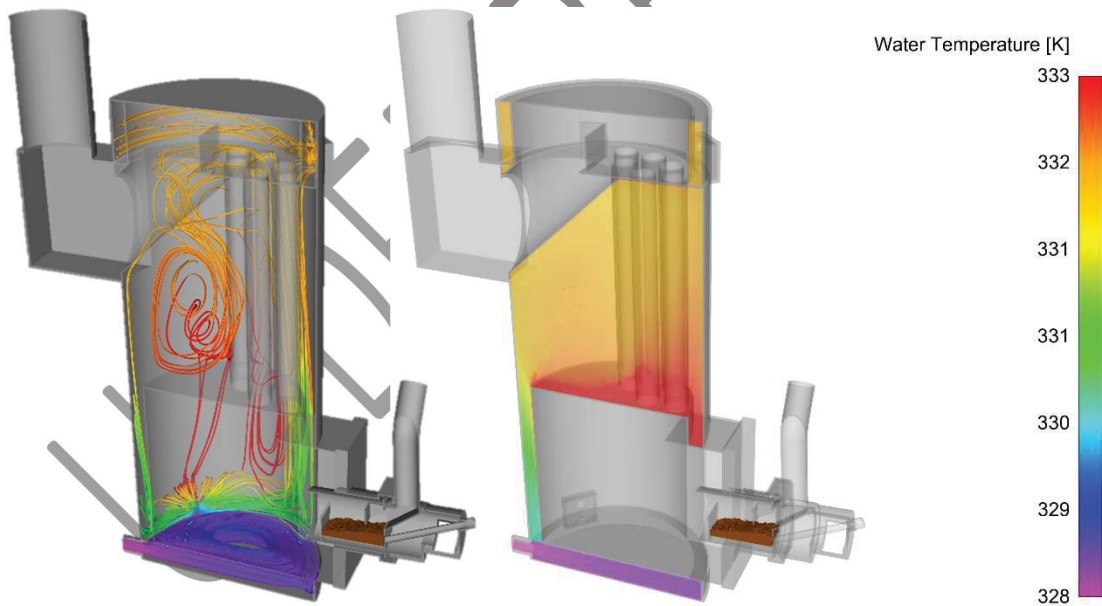


168

169

Figure 4. Flue gas temperature and isosurfaces of the levels shown on the colormap.

170 The burner does not have any combustion enhancement systems, such as air staging or
 171 turbulators, to enhance heat transfer on the vertical pipes. Additionally, the main body of the
 172 boiler does not have a dome or deflector to prevent flame quenching when hitting the
 173 combustion chamber walls, which is almost entirely cooled.



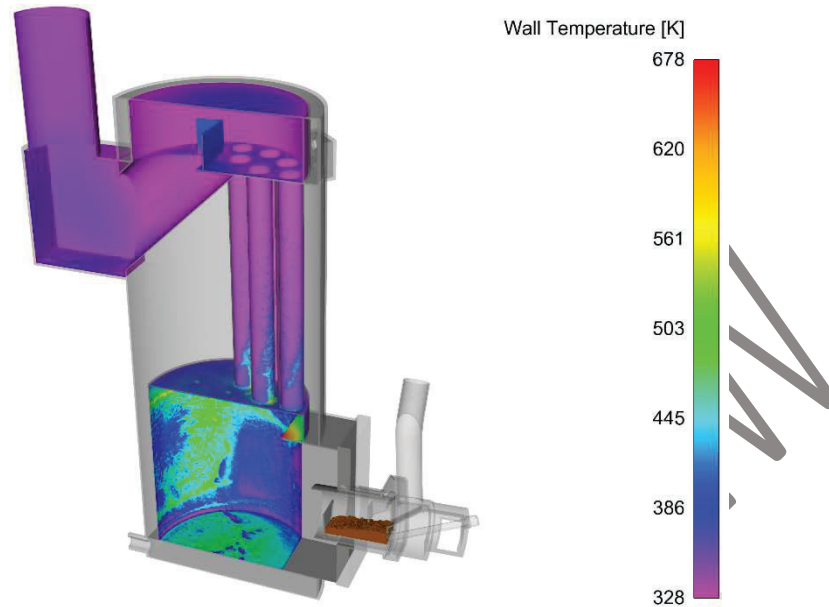
174

175

Figure 5. Left. Water circuit pathlines coloured by temperature. Right. Water temperature field.

176 Figure 5 shows the water temperature evolution along the water circuit, which is built in a
 177 straightforward and modular way with two communicating boxes between each pair of modules.
 178 The simplicity of this circuit seems adequate for a non-continuous operation, working as a hot
 179 water storage volume, where water stratification is reached. This type of system is able to work
 180 efficiently under the usual demand patterns for domestic use due to the fast response of the
 181 diesel burner. In this design, the circuit works under continuous demand while coupled to the
 182 biomass burner, so the design is not the most efficient since improved routes are established
 183 wasting part of the exchange surface.

184 Within the water jacket, local temperatures higher than those shown in the colormap, closer to
185 the boiling point, are reached in the joints of the vertical tubes with the combustion chamber.
186 The low temperatures present on the water-side are also shown on the flue gas-sidewalls, as
187 shown in Figure 6. These low temperatures are a key factor in the condensation of inorganic
188 vapours.



189
190

Figure 6. Temperature of the surfaces on the flue gas side.

191 In the combustion chamber, the highest temperatures, excluding the uncooled surface of the
192 burner, are reached in the lower part and in an annular-shaped region if seen from the burner
193 side.

194 As will be explained, this shape is due to two causes. The first cause is the morphology of the
195 movement of the fluid; when impacting against the front wall, a small low-speed region is
196 generated that diverts the rest of the flue gas. The second cause, which is directly linked to the
197 first cause, is the deposition of PM in the chamber, resulting in a lower thermal conductivity, as
198 will be shown later.

199 Figure 7 shows, on a logarithmic scale, that the inorganic vapours are condensed along the entire
200 system downstream of the bed in a relatively uniform manner; these inorganic vapours are
201 condensing to a greater extent in the upper part of the system, where the gas temperature and
202 the refrigerated walls are already relatively low, than the lower part. On the other hand, in the
203 hottest zones, where the combustion gas impacts at high temperature, the condensation is
204 decreased.

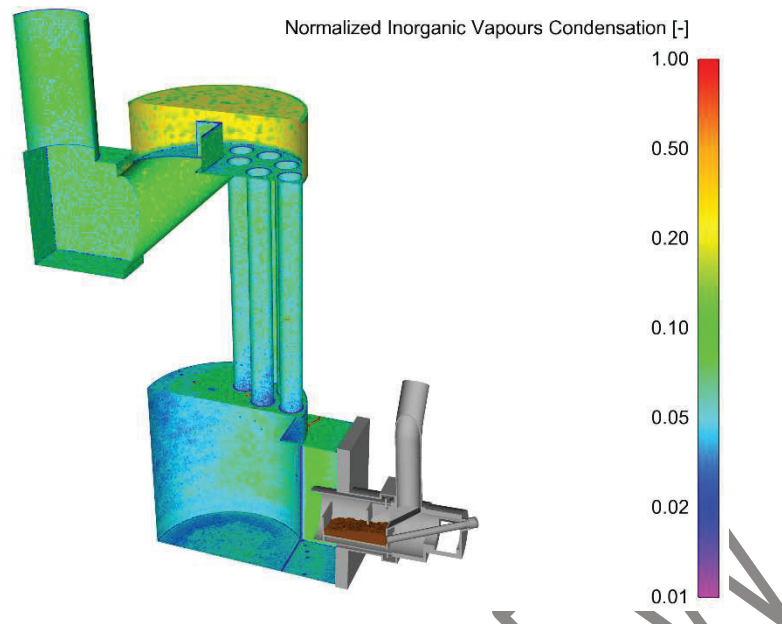


Figure 7. Normalized inorganic vapour condensation over surfaces on a logarithmic scale.

205

206

207 Figure 8, also on a logarithmic scale for easier visualization, shows the normalized distribution of
 208 particulate matter throughout the system. There are clearly three different zones in the flue gas
 209 path, where the particulate matter is deposited by gravity. The first, in the lowest part of the
 210 boiler, shows that particulate matter, especially the most massive, remains in the combustion
 211 chamber in areas of lower speed, such as corners and in the shadow part of the burner. The next
 212 area where gravity sedimentation occurs is in the bottom surface of the upper collector after
 213 circulating the flue gas through the exchange tubes. In this region, the particles are forced to
 214 make sharp turns, losing momentum and, after colliding with the walls, being deposited by
 215 gravity. Finally, an abrupt turn before the exit of the system results in deposition on the bottom
 216 surface.

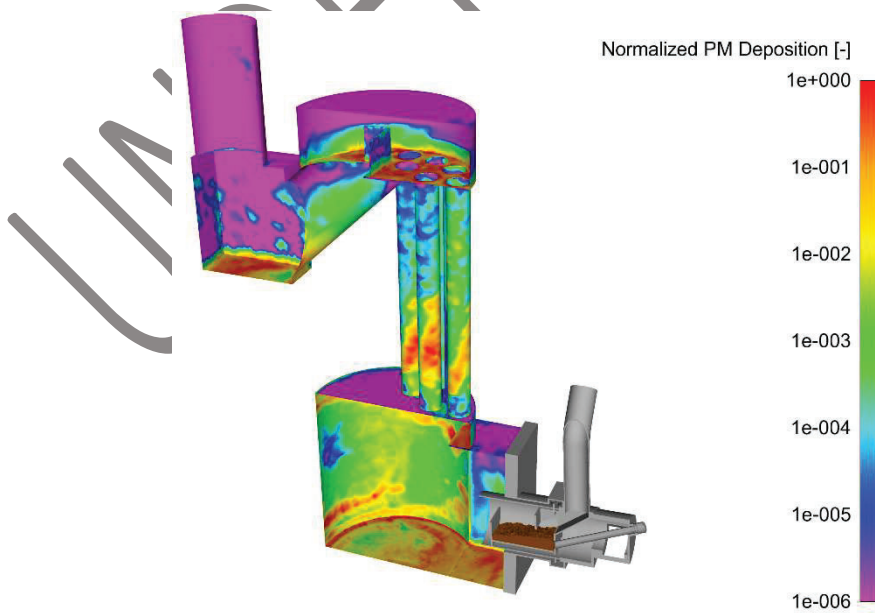


Figure 8. Normalized particulate matter deposition over surfaces on a logarithmic scale.

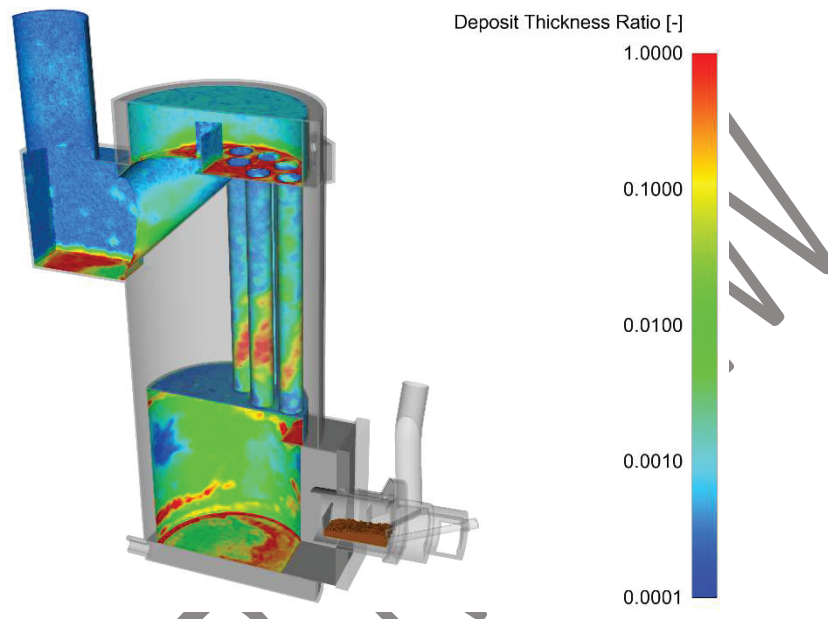
217

218

219 The low-speed region occurs on the opposite surface of the burner. The particles contained in
 220 the flue gas are diverted after the gas before impacting to a greater or lesser extent according to

221 their number of Stokes. This creates a soft annular shape of deposition. Downstream, the
222 deposition on the internal face of the tubes occurs mainly in the first half. Again, due to the abrupt
223 turn of the gas, the most massive particles impact and adhere there. As the gas flow aligns with
224 the pipe, the deposition decreases

225 All of this particulate matter, which has adhered and embedded in a matrix of inorganic vapours
226 that continuously condense while the surface is sufficiently cooled, generates a deposition
227 thickness that is shown in Figure 9. This deposition thickness will be a function of the adhered
228 mass, the presence of condensed phase, and the level of sintering of this layer.



229

230 *Figure 9. Deposit thickness ratio over surfaces, in logarithmic scale.*

231 Figure 9 shows, on a logarithmic scale, the thickness of the deposit layer through the system. It is
232 represented in this way due to the short operation time of the simulated boiler, which would
233 result in low deposit thicknesses with high proportions of the same deposits in the corners of the
234 planes normal to gravity.

235 The homogeneity of the inorganic vapour deposition throughout the system corresponds to a
236 great extent with the figure of adhered particulate matter, noting only differences in the upper
237 part of the system where there is a greater condensation of vapours.

238 Figure 9 can be compared with the images in Figures 10 and 11, which were taken from the
239 experimental plant, which had been run for several days when these photographs were taken.

240 As Figure 10 shows, the annular shape of the fouled matter predicted by the model corresponds
241 adequately with the profile obtained in the experimental run. In addition, the massive deposit on
242 the front door below the burner is appropriately captured. In the top region of the boiler, high
243 levels of deposited masses are found but not at the end of the vertical pipes, which is also shown
244 in the experimental run in Figure 11.

245



246
247
248

Figure 10. Experimental run. Left, fouling on front access door. Right, annular shape of the fouling on the combustion chamber surface.



249
250

Figure 11. Experimental run. Fouling on top surface due to gravitational settling.

251 Once the deposit thickness distribution in the initial stages of the boiler is presented, its influence
252 on the thermal conductivity of the affected areas is shown as seen in Figure 12. As mentioned
253 above, the physical and thermal properties of the cells belonging to the solid body of the boiler
254 are affected and modified by the deposition layer.

255 Figure 12. Thermal conductivity ratio of the surfaces. shows how the thermal conductivity of
256 these cells drops abruptly after 1.5 hours of operation, with an average equivalent thermal
257 conductivity of $4 \text{ W/m} \cdot \text{K}$ on the regions with lower adhered matter rates. The cold start of a clean
258 system is critical for the fouling phenomena due to the vast cooling of the flue gas. After a few
259 hours of use, the deposition rate of particulate matter becomes asymptotic due to the
260 competition of deposition and erosion mechanisms.

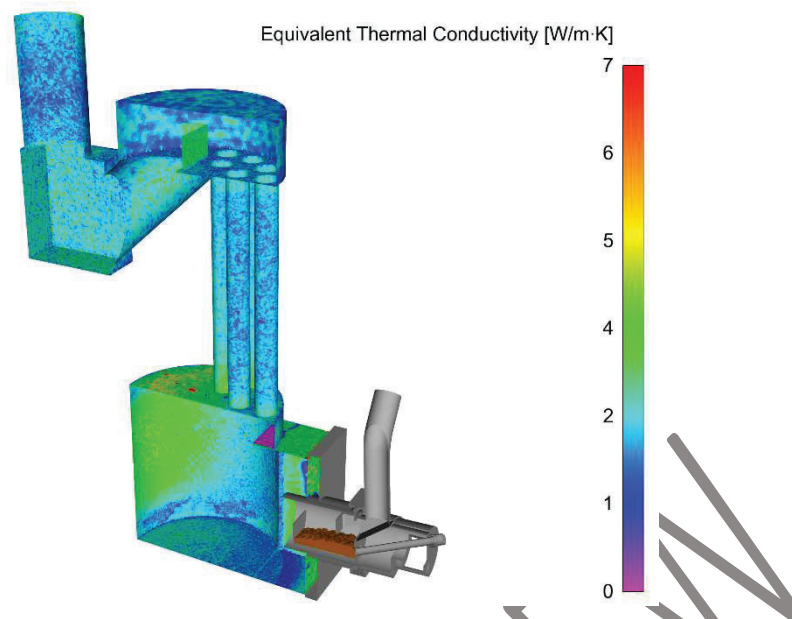


Figure 12. Thermal conductivity ratio of the surfaces.

261

262

263 This low equivalent thermal conductivity causes a very marked decrease in boiler performance
 264 compared to that achieved with a completely clean boiler. Its efficiency after 1.5 hours of
 265 combustion has dropped to 60% in the numerical study and 47% in the experimental run, which
 266 highlights the great impact that the fouling phenomenon has on biomass combustion facilities.

267

268 4. Conclusions

269 The modelling in this manuscript is described to show the direct influence of undesired mass
 270 deposition on the exchange surfaces in a domestic commercial boiler that has been adapted to
 271 use biomass. This modelling is carried out on the basis of the combustion and fouling models
 272 explored in previous works of the authors. The results show an adequate response of the
 273 combustion and fouling models, and the coherent results of the deposit thickness and its
 274 influence on the physical properties of the metal thickness are affected by deposition. The
 275 simulated time gap is short for the time scale in which the study of the fouling phenomena is
 276 usually framed, although the cold start of a clean boiler is important in terms of fouling
 277 phenomena.

278 From the results, the importance of the fouling phenomena on the heat transfer of the affected
 279 surfaces is recognized; the heat exchange performance is lowered to 60%, highlighting the need
 280 for a good burner design to maximize this heat transfer performance over time. Including the
 281 numerical study of the water circuit instead of using temperature and convection coefficient
 282 assumptions increases result accuracy due to the inhomogeneity of the cooling, allowing us to
 283 see how the location of the affected zones temporarily evolves.

284 The body of the boiler presents easy access to the main combustion chamber, but that is not the
 285 case for the set of vertical tubes and chimney. Including the turbulators and scraper systems on
 286 the vertical tubes would be advisable to clean and improve heat transfer. Additionally, a redesign
 287 of the burner and combustion chamber to improve combustion and avoid unwanted phenomena
 288 is advisable.

289 The present work is a breakthrough in the modelling of fouling in biomass, improving present
290 tools and allowing for future development opportunities.

291

292 5. Acknowledgments

293 The authors would like to acknowledge the financial support from the project 'Fouling en
294 Superficies de Transferencia de Calor: Mitigación y/o Regeneración. Programa Estatal de
295 Investigación, Desarrollo e Innovación Orientada a los Retos de la Sociedad, Convocatoria 2017,
296 2018-2020' (ENE2017-87855-R). The work of Sergio Chapela López was supported by grant BES-
297 2016-076785 of the Ministry of Economy, Industry and Competitiveness (Spain). Natalia Cid has
298 been supported by the Xunta de Galicia ("Programa de axudas á etapa predoutoral", Consellería
299 de Educación, Universidade e Formación Profesional).

300

301 REFERENCES

- 302 [1] W.E. Council, Bioenergy in: World Energy Resources 2016, in, Vol. 2018, 2016.
303 [2] J. Islas, F. Manzini, O. Masera, V. Vargas, Chapter Four - Solid Biomass to Heat and Power, in:
304 C. Lago, N. Caldés, Y. Lechón (eds.) The Role of Bioenergy in the Bioeconomy, Academic Press,
305 2019, pp. 145-177.
306 [3] I.E. Agency, World Energy Outlook 2018, in, Vol. 2018, 2018.
307 [4] J. Capablo, J. Salvado, Estimating heat transfer losses caused by alkali salt deposits in biomass
308 combustion, Renewable Energy, 105 (2017) 449-457.
309 [5] H. Wiinikka, R. Gebart, C. Boman, D. Boström, M. Öhman, Influence of fuel ash composition
310 on high temperature aerosol formation in fixed bed combustion of woody biomass pellets, Fuel,
311 86 (2007) 181-193.
312 [6] D. Lindberg, R. Backman, P. Chartrand, M. Hupa, Towards a comprehensive thermodynamic
313 database for ash-forming elements in biomass and waste combustion — Current situation and
314 future developments, Fuel Processing Technology, 105 (2013) 129-141.
315 [7] S.K. Kaer, Numerical investigation of ash deposition in straw-fired boilers-Using CFD as the
316 framework for slagging and fouling predictions, in: Institute of Energy Technology, Aalborg
317 University, Denmark, 2001.
318 [8] J. Sandberg, R.B. Fdhila, E. Dahlquist, A. Avelin, Dynamic simulation of fouling in a circulating
319 fluidized biomass-fired boiler, Applied Energy, 88 (2011) 1813-1824.
320 [9] J. Sánchez, M.D. Curt, N. Robert, J. Fernández, Chapter Two - Biomass Resources, in: C. Lago,
321 N. Caldés, Y. Lechón (eds.) The Role of Bioenergy in the Bioeconomy, Academic Press, 2019, pp.
322 25-111.
323 [10] V. Dhyani, T. Bhaskar, A comprehensive review on the pyrolysis of lignocellulosic biomass,
324 Renewable Energy, 129 (2018) 695-716.
325 [11] Y.D. Singh, P. Mahanta, U. Bora, Comprehensive characterization of lignocellulosic biomass
326 through proximate, ultimate and compositional analysis for bioenergy production, Renewable
327 Energy, 103 (2017) 490-500.
328 [12] H. Rezaei, S. Sokhansanj, Physical and thermal characterization of ground bark and ground
329 wood particles, Renewable Energy, 129 (2018) 583-590.
330 [13] Q. Wang, K. Han, J. Wang, J. Gao, C. Lu, Influence of phosphorous based additives on ash
331 melting characteristics during combustion of biomass briquette fuel, Renewable Energy, 113
332 (2017) 428-437.
333 [14] L. Wang, J.E. Hustad, Ø. Skreiberg, G. Skjevraak, M. Grønli, A Critical Review on Additives to
334 Reduce Ash Related Operation Problems in Biomass Combustion Applications, Energy Procedia,
335 20 (2012) 20-29.

336 [15] M. Aho, Reduction of chlorine deposition in FB boilers with aluminium-containing additives,
337 Fuel, 80 (2001) 1943-1951.

338 [16] L. Tobiasen, R. Skytte, L.S. Pedersen, S.T. Pedersen, M.A. Lindberg, Deposit characteristic
339 after injection of additives to a Danish straw-fired suspension boiler, Fuel Processing Technology,
340 88 (2007) 1108-1117.

341 [17] B.-M. Steenari, A. Lundberg, H. Pettersson, M. Wilewska-Bien, D. Andersson, Investigation of
342 Ash Sintering during Combustion of Agricultural Residues and the Effect of Additives, Energy &
343 Fuels, 23 (2009) 5655-5662.

344 [18] G. Gianfelice, M. Della Zassa, A. Biasin, P. Canu, Onset and propagation of smouldering in
345 pine bark controlled by addition of inert solids, Renewable Energy, 132 (2019) 596-614.

346 [19] M.A. Gomez, J. Porteiro, D. Patiño, J.L. Miguez, Eulerian CFD modelling for biomass
347 combustion. Transient simulation of an underfeed pellet boiler, Energy Conversion and
348 Management, 101 (2015) 666-680.

349 [20] M.A. Gomez, J. Porteiro, D. de la Cuesta, D. Patiño, J.L. Miguez, Numerical simulation of the
350 combustion process of a pellet-drop-feed boiler, Fuel, 184 (2016) 987-999.

351 [21] S. Chapela, J. Porteiro, M.A. Gomez, D. Patiño, J.L. Miguez, Comprehensive CFD modeling of
352 the ash deposition in a biomass packed bed burner, Fuel, 234 (2018) 1099-1122.

353 [22] S. Chapela, J. Porteiro, M. Garabatos, D. Patiño, M.A. Gomez, J.L. Miguez, CFD study of fouling
354 phenomena in small-scale biomass boilers: Experimental validation with two different boilers,
355 Renewable Energy, 140 (2019) 552-562.

356 [23] G.H. Richards, P.N. Slater, J.N. Harb, Simulation of Ash Deposit Growth in a Pulverized Coal-
357 Fired Pilot-Scale Reactor, Energy & Fuels, 7 (1993) 774-781.

358 [24] M.R. Hecken, L.; Renz, U., Numerical simulation of slagging films in the pressurized coal
359 combustion facility Aachen, in: Proceeding of the 4th International Symposium on Coal
360 Combustion, Peking, 1999.

361 [25] H.F. Wang, J.N. Harb, Modeling of ash deposition in large-scale combustion facilities burning
362 pulverized coal, Progress in Energy and Combustion Science, 23 (1997) 267-282.

363 [26] G.R. Hadley, Thermal-Conductivity of Packed Metal Powders, International Journal of Heat
364 and Mass Transfer, 29 (1986) 909-920.

365 [27] C.T. Hsu, P. Cheng, K.W. Wong, Modified Zehner-Schlunder Models for Stagnant Thermal-
366 Conductivity of Porous-Media, International Journal of Heat and Mass Transfer, 37 (1994) 2751-
367 2759.

368 [28] K.S. Schulze, R.; Telian M.; Obernberger, I., Advanced modelling of deposition formation in
369 biomass furnaces - investigation of mechanisms and comparison with deposit measurements in
370 a small-scale pellet boiler, in: Impacts of Fuel Quality on Power Production & Environment,
371 Lapland, Finland, 2010.

372 [29] A. Rezeau, L.I. Díez, J. Royo, M. Díaz-Ramírez, Efficient diagnosis of grate-fired biomass boilers
373 by a simplified CFD-based approach, Fuel Processing Technology, 171 (2018) 318-329.

374 [30] J. Wiese, F. Wissing, D. Hohner, S. Wirtz, V. Scherer, U. Ley, H.M. Behr, DEM/CFD modeling
375 of the fuel conversion in a pellet stove, Fuel Processing Technology, 152 (2016) 223-239.

376 [31] H. Mätzing, H.-J. Gehrmann, H. Seifert, D. Stapf, Modelling grate combustion of biomass and
377 low rank fuels with CFD application, Waste Management, 78 (2018) 686-697.

378 [32] M. Farokhi, M. Birouk, Modeling of the gas-phase combustion of a grate-firing biomass
379 furnace using an extended approach of Eddy Dissipation Concept, Fuel, 227 (2018) 412-423.

380 [33] R. Weber, M. Mancini, N. Schaffel-Mancini, T. Kupka, On predicting the ash behaviour using
381 Computational Fluid Dynamics, Fuel Processing Technology, 105 (2013) 113-128.

382 [34] M.A. Gomez, D. Patiño, R. Comesana, J. Porteiro, M.A.A. Feijoo, J.L. Miguez, CFD simulation
383 of a solar radiation absorber, International Journal of Heat and Mass Transfer, 57 (2013) 231-240.

384 [35] S. Chapela, J. Porteiro, M. Costa, Effect of the Turbulence-Chemistry Interaction in Packed-
385 Bed Biomass Combustion, Energy & Fuels, 31 (2017) 9967-9982.

1 Eulerian CFD fouling model for fixed bed biomass combustion systems

2 Sergio Chapela*, Jacobo Porteiro*, José Luis Míguez* and Frank Behrendt**

3 * Industrial Engineering School, University of Vigo, Lagoas-Marcosende s/n, Vigo, Spain

4 ** Technische Universität Berlin, Institute of Energy Engineering, Chair for Energy Process Engineering and Conversion Technologies for Renewable
5 Energies, Berlin, 10623, Germany

6 E-mail: schapela@uvigo.es

7

8 ABSTRACT

9 Driven by a society that is becoming more aware of the environment over the recent decades, biomass use has
10 increased on both the domestic and industrial scales. In addition, the ease of the use of biomass as a transition
11 fuel in non-renewable solid fuel installations has contributed to this rising trend. Nevertheless, the use of
12 biomass presents serious operational problems, especially in facilities not designed for biomass combustion or
13 in cases of low-quality biomass. To manage these issues, CFD codes have become a powerful tool that provides
14 valuable data on the phenomena involved inside facilities. Previous works of the authors examine the fouling
15 phenomenon through a deeply optimized Euler-Lagrange framework; nevertheless, the computational effort is
16 still high and not suitable for highly parallelised environments. Due to the physical and thermal limitations, the
17 IT industry research on the core density inside each die is evolving faster than that on the individual core
18 performance. Therefore, parallelisation has become of great relevance when coding. This work begins a new
19 line of research on the study of the phenomenon of fouling in biomass combustion systems; however, this study
20 is developed entirely in an Eulerian framework, guaranteeing a greater performance. The new full Eulerian-
21 fouling model is based on the 3D-EBITCOM (3D Eulerian Biomass Transient Combustion Model) from the
22 University of Vigo. The initial results are compared against experimental and previous modelling data obtained
23 in an experimental burner, and they show an overall lower computational effort and better response in most
24 scenarios.

25

26 Keywords: Eulerian, CFD, biomass, fouling, combustion

27

28 1. Introduction

29 During recent decades, society has become aware of the serious consequences of current energy systems with
30 respect to the environment. Because of this awareness, society has begun to investigate, develop and develop
31 alternative systems, more specifically, systems based on the use of biomass. This work has been conducted not
32 only on a domestic scale but also on an industrial scale.

33 This industrial field has seen multiple opportunities in these alternative systems. On the one hand, industrial
34 work often generates waste, and a cost is associated with its removal by external, specialized companies;
35 however, now the waste can be considered an energy source that reduces operating costs if they are well
36 implemented, although this waste does not always produce economic benefits [1, 2]. On the other hand, the
37 use of this type of alternative system often yields commercial benefits or lower taxes, which allows the company
38 to be considered ecological.

39 In addition, the ease of the use of biomass in non-renewable solid fuel installations as a transition fuel has
40 contributed to this rising trend in its use. The use of this type of fuel, either directly or by blending with the
41 original fuel, is viable in the short-term in existing compatible installations [3, 4].

42 Nevertheless, biomass use presents serious operational problems in long-term operations, especially in facilities
43 not designed for biomass combustion, due to the inherently high presence of sulphur, silica and alkaline
44 compound contents, which lead to high levels of sintering and corrosion along the path of the flue gas [5, 6].

45 This problem can be alleviated by the pretreatment of biomass, together with the use of specific additives for
46 the particular type of biomass [7-11] or with alternative combustion techniques, such as smouldering or
47 gasification [12]. However, biomass pretreatment implies that the system must always work with the same type
48 of biomass, which allows little variation in its composition and physical-chemical properties; in addition, the use
49 of alternative combustion techniques implies profound reforms in the existing combustion systems or implies
50 the direct construction of a new system [13]. Therefore, the use of biomass in this sector may not be
51 economically viable through the currently available technology.

52 Thus, it is noted that the success of biomass lies in the use of low-quality biomass and in its use in facilities of
53 other non-renewable solid fuels without causing harmful phenomena to occur inside and outside of the system.
54 The simultaneous achievement of both tasks is not simple. To this end, progress in the development of CFD
55 tools that allow the proper modelling of biomass combustion and of the entire fouling and slagging phenomena
56 is fundamental so that the best performance of biomass combustion is achieved in systems already built without
57 causing damage to them.

58 These CFD tools are known to be computationally very expensive. To run a simulation of a thermochemical
59 system, such as a domestic boiler, correctly and not at extremely simplified conditions, it is necessary to use
60 specialized workstations or HPC (*high performance computing*) servers with great computing power and RAM.
61 The main problem is essentially attributed to the computing power. The evolution over time in the computing
62 power of each core of a processor has decreased. The origin of this stagnation is to be close to reaching the
63 limit of current technology, based on silicon, since transistors are not able to work reliably at a greater number
64 of cycles due to their switching time; in addition, the heat generated by each core is increasing with the density
65 of transistors within the chip.

66 Currently, the main processor manufacturers are focusing their efforts on increasing the computing power in
67 the simplest way, increasing the number of processing units, or cores, within each package. However, this
68 implies an effort on the part of the programmer in the parallelization of those operations that can be
69 parallelized, such as those carried out on a large matrix. Nevertheless, not all operations can be parallelized,
70 and some must be executed serially. For example, the calculation of a single Lagrangian trajectory is eminently
71 in series, since its subsequent state is a consequence of its evolution along the domain in a specific order.

72 In this work, based on studies in recent years about the modelling of combustion of biomass in fixed beds [14-
73 17], we seek to adapt to these new requirements of parallelization. Eulerian treatment has been shown to adapt
74 well to a high-parallel environment. Therefore, a new line of research begins in which, instead of modelling
75 combustion and transport through a Eulerian treatment of inorganic vapours and subsequently modelling the
76 fouling phenomena through a Lagrangian treatment, all phenomena that occur within the system will be treated
77 as combustion in a Eulerian framework.

78

79 2. Materials and methods

80 For the development of this new model, the 3D-EBITCOM (3D Eulerian Biomass Transient Combustion Model)
81 [15-17] has been rewritten from scratch and adapted to a multiphasic Eulerian framework so that the bed is in
82 a phase, the flue gas phase is in other phase, and particulate matter is in additional granular phases.

83 a. Modelling of the multiphasic framework

84 The model is implemented using UDF (*user-defined functions*) with the commercial software ANSYS-Fluent. This
85 model is applied based under the following assumptions. This model is an interpenetrating continuum, where
86 the pressure is unique and is shared by all the phases present on each cell; in addition, the momentum,

87 continuity and energy equations are solved for each phase, and the concept of phasic volume fractions is
88 incorporated as shown in Equation 1.

$$V_i = \int_V \sigma_i \cdot dV \quad (1)$$

89 where,

$$\sum_{i=1}^n \sigma_i = 1 \quad (2)$$

90 For each i^{th} phase, the continuity equation is defined as Equation 3, where \dot{m}_{ij} and \dot{m}_{ji} characterize the mass
91 transfer between phases i and j , respectively. S_i is the source term, which can be positive or negative depending
92 on whether the granular phase is created by elutriation from the bed or if it is trapped on the surfaces of the
93 calculation domain.

$$\frac{\partial}{\partial t} (\sigma_i \cdot \rho_i) + \nabla(\sigma_i \cdot \rho_i \cdot \vec{v}_i) = \sum_{i=1}^n (\dot{m}_{ij} - \dot{m}_{ji}) + S_i \quad (3)$$

94 At the end of each time step, a loop is performed that scans for those cells that act as bed frontiers. In each of
95 these cells, the maximum elutriation diameter is computed through a balance between the drag forces exerted
96 by the gases and the gravitational forces, as explained in previous work [18]. Once the cells where sufficient
97 energy exists to elutriate each particle size are calculated, a distribution of the flow assigned for each particle
98 size is generated according to the available drag, giving priority to the cells with greater drag. However, it may
99 be the case that the first distribution forces the cell to elutriate more ash mass than is available. Therefore, an
100 iterative process is carried out until a valid distribution is reached, as shown in Figure 1.

101

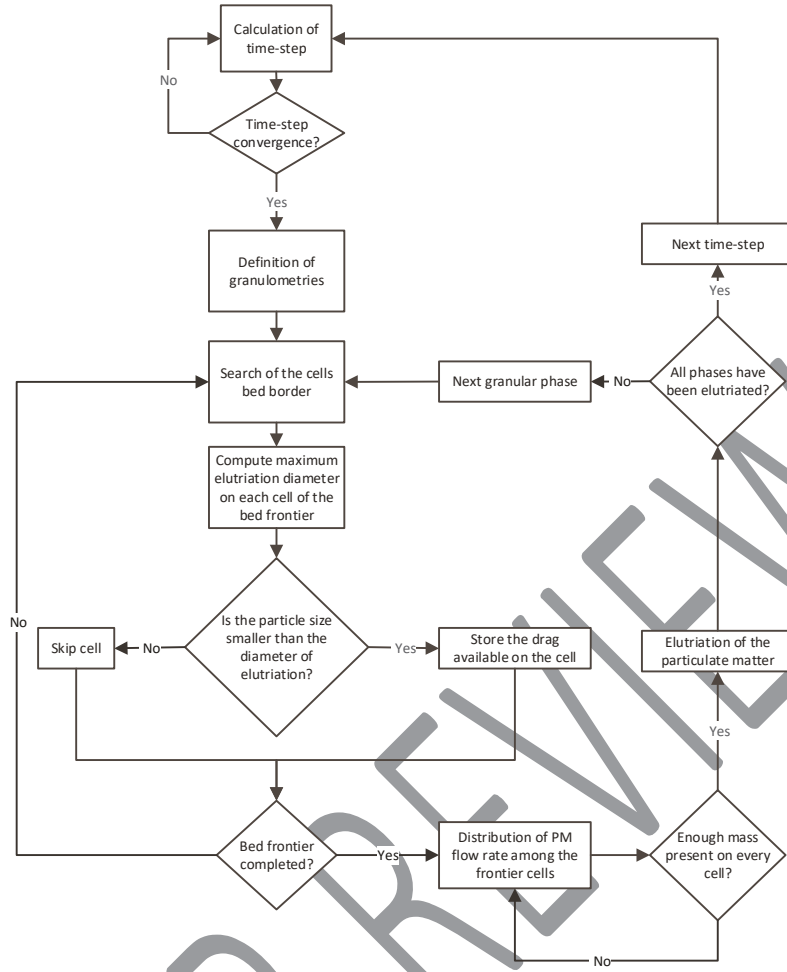


Figure 1. Flowchart of the elutriation distribution algorithm.

102

103

104 Once the corresponding granular phase is elutriated from the bed, it travels along the domain with the flue gas
 105 and undergoes the effect of the negative source terms, which will create the deposition and will be explained
 106 later in section 2.2 called Fouling.

107 The momentum equation for each i^{th} phase is expressed as Equation 4,

$$\begin{aligned}
 \frac{\partial}{\partial t}(\sigma_i \rho_i \bar{v}_i) + \nabla(\sigma_i \rho_i \bar{v}_i \bar{v}_i) \\
 = -\sigma_i \nabla p + \nabla \cdot \bar{\tau}_i + \sigma_i \rho_i \bar{g} \\
 + \sum_{i=1}^n (\bar{K}_{ij}(\bar{v}_i - \bar{v}_j) + \dot{m}_{ij} \bar{v}_j - \dot{m}_{ji} \bar{v}_i) + (\bar{F}_i + \bar{F}_{lift,i} + \bar{F}_{wl,i} + \bar{F}_{vm,i} + \bar{F}_{td,i})
 \end{aligned} \quad (4)$$

108 where,

$$\bar{\tau}_i = \sigma_i \mu_i (\nabla \bar{v}_i + \nabla \bar{v}_i^T) + \sigma_i (\lambda_i - 2/3 \mu_i) \nabla \cdot \bar{v}_i \bar{I} \quad (5)$$

109 where μ_i and λ_i are the shear and bulk viscosities of the i^{th} phase, \bar{F}_i is an external body force, $\bar{F}_{lift,i}$ is a lift
 110 force, $\bar{F}_{vm,i}$ is a virtual mass force, and $\bar{F}_{td,i}$ is a turbulent dispersion force. Here, \bar{v}_{ij} is the interphase velocity,
 111 as $\dot{m}_{ij} = \mathbf{0}$. The momentum balance equation must be closed with appropriate expressions for the momentum
 112 exchange coefficient, \bar{K}_{ij} .

113 As mentioned above, an energy equation is solved for each i^{th} phase. To describe the conservation of energy, a
 114 separate enthalpy equation is solved for each granular phase, as shown in Equation 6.

$$\frac{\partial}{\partial t}(\sigma_i \rho_i \cdot h_i) + \nabla \cdot (\sigma_i \rho_i \bar{u}_i h_i) = \sigma_i \frac{dp_i}{dt} + \bar{\tau}_i \cdot \nabla \bar{u}_i - \nabla \cdot \bar{q}_i + S_i + \sum_{i=1}^n (Q_{ij} + \dot{m}_{ij} h_{ij} - \dot{m}_{ji} h_{ji}) \quad (6)$$

115 where h_i is the i^{th} phase specific enthalpy, \bar{q}_i is the heat flux, and S_i is a source term that includes sources of
 116 enthalpy. Here, Q_{ij} is the intensity of heat exchange between phases, and h_{ij} is the interphase enthalpy. The heat
 117 exchange between phases must comply with the local balance conditions.

118 The modelling of turbulence in multiphase flows is extremely complex, as the number of terms in the
 119 momentum equations increases with the number of phases involved. In the present work, the k- ϵ model is used
 120 as in previous works [18-20]. A way to address this issue is to consider a mixture turbulence model, where using
 121 mixture properties and velocities is sufficient to capture important phenomena, for example, nearly stratified
 122 phenomena, and the density ratio between phases is close to the unit. For the present study, the density ratio
 123 is large; therefore, modelling the turbulence for each phase is required. However, this approach would cause a
 124 substantial computational effort, as this approach will add two additional transport equations for each phase.
 125 In the middle of both methods, the dispersed phase turbulence method exists. With this method, the fluctuating
 126 quantities of the secondary phases can be given in terms of the mean characteristics of the flue gas phase and
 127 the ratio of the particle relaxation time and eddy-particle interaction time. Nevertheless, the model presented
 128 in this work allows the use of a per phase turbulence model if desired.

129 In this way, the turbulent predictions for the continuous phase are obtained using the standard k- ϵ with
 130 additional terms that include the interphase turbulent momentum transfer. The momentum exchange terms
 131 contain the correlation between the instantaneous distribution of the dispersed phases and the turbulent fluid
 132 motion. It is possible to account for the dispersion of the dispersed phases transported by the turbulent fluid
 133 motion.

134 The predictions for turbulence quantities for the dispersed phases, j , are obtained using the Tchen theory of
 135 dispersion of discrete particles by homogeneous turbulence [21]. Turbulent predictions are obtained from the
 136 modified k- ϵ model. The transport equations for the continuous phase, q , are:

$$\frac{\partial}{\partial t}(\sigma_q \rho_q \cdot k_q) + \nabla \cdot (\sigma_q \rho_q \bar{U}_q k_q) = \nabla \cdot \left(\sigma_q \left(\mu_q \frac{\mu_{t,q}}{\sigma_k} \right) \nabla k_q \right) + \sigma_q G_{k,q} - \sigma_q \rho_q \epsilon_q + \sigma_q \rho_q \Pi_{k_q} \quad (7)$$

$$\begin{aligned} \frac{\partial}{\partial t}(\sigma_q \rho_q \cdot \epsilon_q) + \nabla \cdot (\sigma_q \rho_q \bar{U}_q \epsilon_q) \\ = \nabla \cdot \left(\sigma_q \left(\mu_q \frac{\mu_{t,q}}{\sigma_\epsilon} \right) \nabla \epsilon_q \right) + \sigma_q \frac{\epsilon_q}{k_q} (C_{1\epsilon} G_{k,q} - C_{2\epsilon} \rho_q \epsilon_q) + \sigma_q \rho_q \Pi_{\epsilon_q} \end{aligned} \quad (8)$$

137 where \bar{U}_q is the phase-weighted velocity, $\mu_{t,q}$ is the turbulent viscosity and Π_{k_q} Π_{ϵ_q} are source terms that can
 138 be included to model the influence of the dispersed phases on the continuous phase q ; however, as the
 139 secondary phases are considered to be diluted, their influence on the turbulence of the continuous phase is
 140 neglected, and thus, this source terms are null.

141 As shown in Equation 4, the momentum exchange between phases is based on the value of the K_{ij} coefficient.
 142 This coefficient can be written in the form:

$$K_{ij} = \frac{\sigma_j \rho_j}{\tau_j} F \quad (9)$$

143 where τ_j is the particle relaxation time defined as:

$$\tau_j = \frac{\rho_j \phi_j^2}{18 \mu_q} \quad (10)$$

144 where q is the continuous phase, ϕ_j is the diameter of j^{th} and F is a factor defined in several different ways
 145 depending on the exchange-coefficient model used. All definitions of this parameter include a drag function
 146 (C_D) that is based on the relative Reynolds number, defined as:

$$Re_j = \frac{\rho_q \phi_j |\vec{v}_j - \vec{v}_q|}{\mu_q} \quad (11)$$

147 There are several models for the F factor. For example, Syamlal-O'Brien [22] proposed a model with the drag
 148 function derived by Dalla Valle [23]; however, this model is based on measurements of the terminal velocities
 149 of particles in fluidized or settling beds. Wen and Yu [24] proposed a model that is appropriate for dilute systems
 150 where the fluid-solid exchange coefficient and drag function are:

$$K_{jq, \text{Wen\&Yu}} = \frac{3}{4} C_D \frac{\sigma_j \sigma_q \rho_q |\vec{v}_j - \vec{v}_q|}{\phi_j} \sigma_q^{-2.65} \quad (12)$$

$$C_D = \frac{24}{\sigma_q Re_j} [1 + 0.15(\sigma_q Re_j)^{0.687}] \quad (13)$$

151 However, the phenomenon of gravitational settling is one of the fouling mechanisms. In this case, the phases
 152 cannot be considered to be locally diluted. To address this situation, Gidaspow [25] proposed a combination of
 153 the Wen and Yu [24] model and the Ergun equation depending on if the σ_q is lower or higher than 0.8. This
 154 model is recommended for dense fluidized beds but presents a sharp variation in the change value.

155 Lately, the Huilin-Gidaspow model [26] added a smoothing function to switch between the Wen and Yu and
 156 Ergun equations when the solid volume fraction is less than 0.2:

$$K_{jq} = Y K_{jq-\text{Ergun}} + (1 - Y) K_{jq-\text{Wen\&Yu}} \quad (14)$$

$$K_{jq-\text{Ergun}} = 150 \frac{\sigma_j (1 - \sigma_q) \mu_q}{\sigma_q \phi_j^2} + 1.75 \frac{\rho_q \sigma_j |\vec{v}_j - \vec{v}_q|}{\phi_j} \quad (15)$$

$$Y = \frac{1}{2} + \frac{\arctan(262.5(\sigma_j - 0.2))}{\pi} \quad (16)$$

157

158 The temperature at which the particles collide with the boiler surfaces is highly relevant when modelling fouling
 159 phenomena on biomass combustion. The sticking behaviour of the particles is dependent on the temperature,
 160 as they can become partially fused, increasing their stickiness when hitting the surface, as their restitution
 161 coefficient is lower, and the deformed surface is higher. In addition, inorganic vapours present in the flue gas
 162 can condense over the particle surface, also enhancing their stickiness.

163 The volumetric rate of energy transfer between phases, Q_{jq} , is assumed to be a function of the temperature
 164 difference and the interfacial area, which is defined as the interfacial area between two phases per unit of
 165 volume:

$$A_j = \frac{6\sigma_j}{\phi_j} (1 - \sigma_j) \quad (17)$$

166 For the j^{th} -dispersed phase, the interface area is calculated in a form that ensures that the interfacial area
 167 concentration approaches zero as σ_j approaches 1.

$$Q_{jq} = h_{qj} A_j (T_q - T_j) \quad (18)$$

168 where h_{qj} is the volumetric heat transfer coefficient between the gas and j^{th} solid phase. This coefficient is
 169 defined as:

$$h_{qj} = \frac{K_q Nu_j}{\phi_j} \quad (19)$$

170 For granular flows, Gunn[27] proposed the following correlation for the Nusselt number, which is applicable to
 171 a porosity range higher than 0.35 and a Reynolds number of up to 10^5 :

$$Nu_j = (7 - 10\sigma_q + 5 * \sigma_q^2) \left(1 + 0.7 * Re_j^{0.2} Pr^{\frac{1}{3}}\right) + (1.33 - 2.4\sigma_q + 1.2\sigma_q^2) Re_j^{0.7} Pr^{\frac{1}{3}} \quad (20)$$

172 where the Prandtl number is defined as:

$$Pr = \frac{Cp_q \mu_q}{K_q} \quad (21)$$

173 As mentioned above, each secondary phase is defined as a granular dispersed phase. The diameter of each
 174 phase is set to the values obtained by the phase reduction algorithm. The solid compressibility effects due to
 175 the phase reaching its packing limit are neglected, assuming no deformation of the solids.

176 In dense flow at low shear, where the volume fraction for a granular phase is close to the packing limit, the
 177 generation of stress is mainly due to friction between particles. Schaeffer [28] proposed a model to account for
 178 this:

$$\mu_{friction} = \frac{p_{friction} \sin \varphi}{2\sqrt{I_{2D}}} \quad (22)$$

179 where φ is the angle of internal friction, which is set to 30° , I_{2D} is the second invariant of the deviatoric stress
 180 tensor and $p_{friction}$ is the frictional pressure defined as [29, 30]:

$$p_{friction} = 0.1\sigma_j \frac{(V\sigma_j - \sigma_{j,min})^2}{(\sigma_{j,max} - \sigma_s)^5} \quad (23)$$

181

182 b. Fouling model

183 The fouling phenomenon comprises several different mechanisms that result in inorganic vapours being
 184 condensed over surfaces and particulate matter being deposited by gravitational settling or remaining adhered
 185 due to the stickiness of these vapours. This particulate matter travelling with the flue gas reaches the surfaces
 186 of the facility through different mechanisms. The mechanisms considered in this work are the stickiness of the
 187 inorganic vapours, thermophoresis, turbulent impaction and diffusion.

188 The effect of the presence of partially molten inorganic vapours over the cooled surfaces has been studied in
 189 previous works[6, 31, 32], and the numerical modelling carried out was also studied in references [18, 20].

190 As already explained in these studies, the behaviour of the particles inside the facility is dependent on their
 191 particle relaxation times, defined as:

$$\tau_j^+ = \frac{\rho_j \phi_j^2 \rho_q u_q}{18\mu} \quad (24)$$

192 Depending on the value of this relaxation time, three regimes can be differentiated and will change the
 193 behaviour of the particle inside the facility. If the relaxation time is lower than 0.1, the drag forces of the flue
 194 gas are dominant, and the particles closely follow the flow pattern of the gas, which is called the diffusion
 195 regime. If the relaxation time is higher than 10, the inertia of the particle is dominant, and the turbulence and
 196 flow pattern of the flue gas does not alter the movement of the particle; this regime is named the impaction
 197 regime. A third regime exists between both regimes, namely, the inertial regime, where the flue gas affects the
 198 trajectory of the particles, but they also tend to follow their own path due to their momentum.

199 As stated in the work of Wood [33] and recently modified by Fan and Ahmadi[34], the deposition caused by
 200 diffusion can be expressed in terms of the particle Schmidt number:

$$R_{diff} = \sqrt{\left(\frac{\tau_w}{\rho_q}\right)} \left(0.084 * S c_j^{-\frac{2}{3}}\right) \sigma_j \rho_j A_f / V_c \quad (25)$$

201 where A_f is the face area, and V_c is the volume of the cell.

202 The turbulent impaction mechanism becomes relevant for particles in the inertial regime, where a small
203 increase in their diameter leads to a strong increase in deposition. Based on experimental data, Wood [33]
204 presented the following relationship:

$$R_{turb} = \sqrt{\left(\frac{\tau_w}{\rho_q}\right)} ((4.5 \cdot 10^{-4}) \tau_j^{+2}) \sigma_j \rho_j A_f / V_c \quad (26)$$

205 The thermophoresis mechanism is very relevant in any combustion facility whose use is made through the
206 transmission of heat to a low temperature circuit. In particular, in low-scale domestic facilities, as they work
207 with DHW (domestic hot water) temperatures and are designed to be compact, the heat exchanger is close to
208 the flame, leading to high temperature gradients.

209 For smaller particles, up to a moderate inertial regime, thermophoresis significantly enhances deposition. The
210 particles placed in the viscous sub-layer close to the surface are affected by the thermophoretic force,
211 transporting them towards the surface. Cha and McCoy [35] proposed a model that can be applied for all
212 Knudsen numbers and properly captures the peak value of the thermophoretic force, which occurs when the
213 diameter of the particle is almost equal to the mean free path of the flue gas [36].

$$F_{Thermophoretic} = \frac{1.15 Kn \left[1 - \exp\left(-\frac{\alpha}{Kn}\right)\right] \sqrt{\left[\frac{4\Theta\omega_1 Kn}{3\pi}\right]} \frac{\nabla T \phi_j^2 k_B}{d_m^2}}{4\sqrt{2} \alpha \left[1 + \frac{\omega_1 Kn}{2}\right]} \quad (27)$$

$$d_m = \sqrt{\frac{5}{16\mu} \left(\frac{M k_B T_q}{\pi}\right)^{\frac{1}{4}}} \quad (28)$$

$$\Theta = 0.25(9\gamma - 5) \left(\frac{c_v}{R}\right) \quad (29)$$

$$\alpha = 0.22 \frac{\left(\frac{\pi \Theta}{6}\right)}{\sqrt{1 + \frac{\omega_1 Kn}{2}}} \quad (30)$$

$$\omega_1 = 0.18 \frac{\left(\frac{36}{\pi}\right)}{\left(\frac{4(2 - S_n + S_t)}{\pi}\right) + S_n} \quad (31)$$

214 Therefore, this thermophoretic force leads to the following deposition rate expression:

$$R_{therm} = \sqrt{\left(\frac{\tau_w}{\rho_q}\right)} \left(\frac{F_{Thermophoretic} \tau_j^+}{m_j}\right) \sigma_j \rho_j A_f / V_c \quad (32)$$

215 Therefore, the term S_i in Equation 3 is written as:

$$S_i = R_{diff} + R_{turb} + R_{therm} \quad (33)$$

216 Finally, the PM will remain adhered on the surface using the stickiness probabilities model explained in the
217 previous work [18]

218

219

c. Phase reduction algorithm

220 The calculation of a large number of secondary granular phases results in a great computational effort, since
221 each individual phase involves a set of equations and an increase in the number of terms involved in the
222 equations of the turbulence model. This increase in the number of equations also results in a more complex
223 convergence. To reduce these inconveniences, an algorithm to reduce the number of granular secondary
224 phases has been developed and integrated in the present study, as shown in Figure 2.

225 The main objective of this algorithm is to analyse the granulometries and flow rates that the user has
226 introduced, which can be obtained from a usual logarithmic graph of the facility. From the results of the
227 simulation, which is being calculated, the algorithm corrects this logarithmic curve to adjust the mass flow rates
228 to the volumetric flow rate and the oxygen content present in the flue gas. After this step, this curve graph is
229 converted to a Stokes-Mass Flow graph through Equation 24.

230 This curve is divided into three different sections, one for each regime (diffusion, inertial and impact regimes).
231 Each of these regimes will be divided into as many sections as the user has previously specified. Then, a
232 weighted diameter and the resulting flow rate are calculated for each granular phase. In this way, the algorithm
233 is able to assign the granular phase diameters very close to the bimodal characteristic values, and the total PM
234 flow rate is maintained.

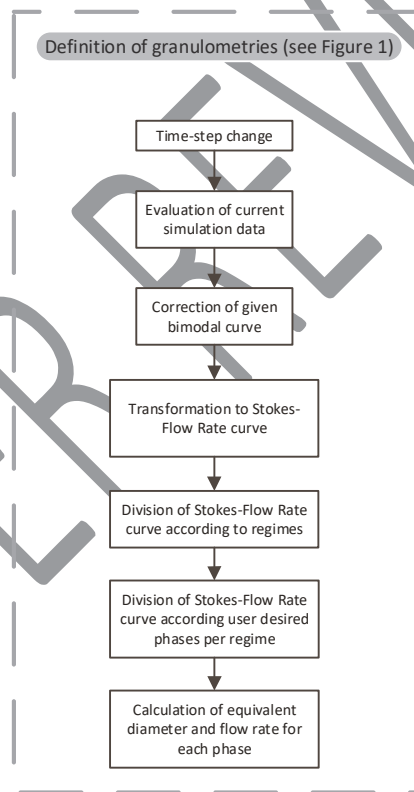


Figure 2. Flowchart of the elutriation distribution algorithm

235

236

d. Facility

237 The same pilot plant from the previous work of the authors [18] will be used to allow a simple and direct
238 comparison of the results. In summary, it is a pilot plant with 12 kW nominal power designed in a modular way.
239 In this pilot plant, an easy-to-remove module was designed to analyse deposition on refrigerated surfaces.

240 This installation allows full control of four key parameters: primary airflow, secondary airflow, fuel flow and
241 cooling water temperature. The primary air is introduced through the lower plenum and passes through the
242 inclined grill through a matrix of holes. This inclined grate is side-fed by means of a screw, and above the bed,

243 the secondary air distributor module and then the deposition module are placed (see Figure 3). Further details
 244 can be found in [18].

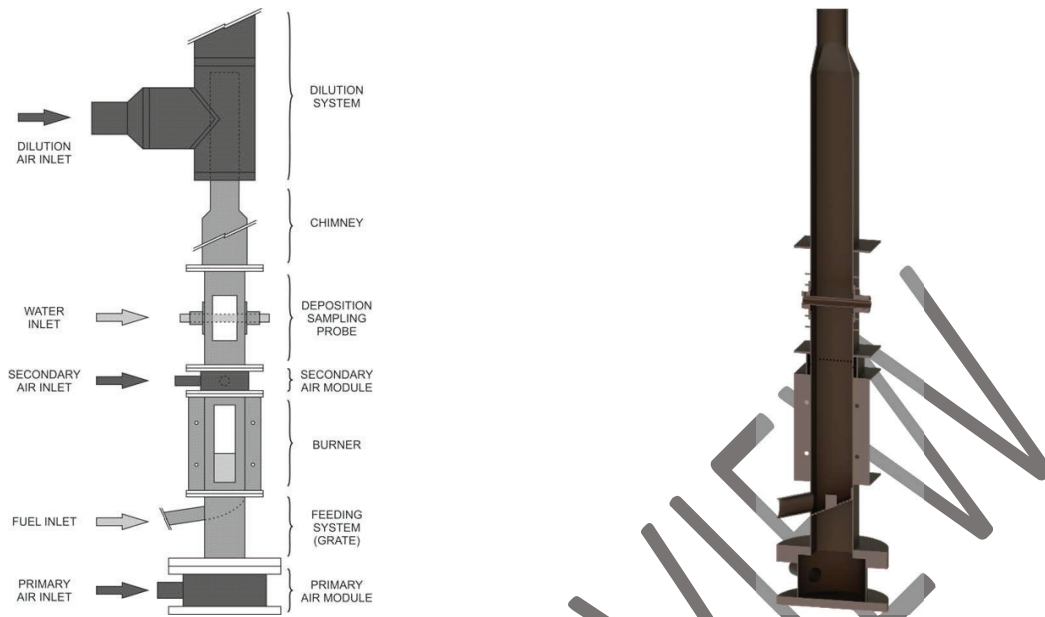


Figure 3. Schematic and CAD of the pilot plant. Note that the secondary air is reoriented in the schematic for easy interpretation.

245

246 To ensure direct comparison, the same fuel will be used as in the previous work [18], which is summarized in
 247 Table 1.

Table 1. Proximate and ultimate analysis of the fuel used.

Proximate analysis of the fuel	Mass Fraction
Moisture content	0.0850
Volatile content	0.7468
Fixed carbon content	0.1620
Ash content	0.0062
Ultimate analysis of the fuel	Mass Fraction
C	0.5170
H	0.0670
O	0.4070
N	0.0017
S	0.0001
Cl	0.0005

248

249 e. Numerical setup

250 CFD simulation is carried out until convergence is reached. However, assessing convergence on biomass
 251 combustion is not straightforward, as there are inherent oscillations driven by the bed due to feeding systems
 252 or particle evolution. As a result, the simulation is considered to have reached their quasi-steady condition when
 253 the maximum fluctuations of the variables of interest are less than 5% near its time-averaged value in a 500-
 254 second period and when the slope of its linear regression is near zero so that trends can be avoided.

255 As mentioned above, the k-ε turbulence model will be used [37, 38]. The species transport model used is the
 256 finite-rate/eddy dissipation model, and the discrete ordinates model will be used for radiation [18-20].

257

258 3. Results and discussion

259 In this work, two phases were chosen in the diffusion regime: three phases in the inertial regime and one phase
 260 in the impact regime. The reason for this division is that due to the geometry of the installation, almost all the
 261 granulometries of which information is available are in the diffusion and inertial regime, with the inertial regime
 262 being the most sensible due to the rapid variation in the fouling phenomena against the increase in its particle
 263 relaxation time. The initial bimodal curve is shown in Figure 4.

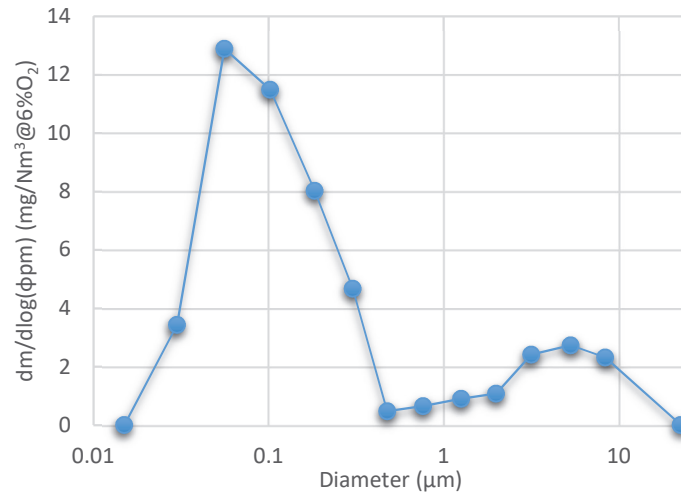


Figure 4. Initial bimodal curve used in this work.

264

265 Table 2 shows the diameters and flow rates representative of each granular phase:

Table 2. Representative diameters and flow rate for each granular phase

Phase Name	Diameter (μm)	Flow rate (mg/Nm³)	τ_j^+
Diffusion Phase 1	0.136	30.790	0.000389
Diffusion Phase 2	1.102	10.908	0.0257
Inertial Phase 1	4.457	5.982	0.421
Inertial Phase 2	8.791	2.444	1.637
Inertial Phase 3	16.48	0.969	5.748
Impact Phase 1	22.154	0.076	10.392

266

267 These granulometries will be used in the present work for the study of fouling in the aforementioned installation
 268 [18], with parameters of 20 m³/h, 20-80 (-) of primary to secondary air distribution and 333.15 K of cooling
 269 water temperature. Due to the entirely new Eulerian fouling treatment, the smoothing algorithm implemented
 270 in the previous Euler-Lagrange approach will not be used on the solution.

271 The behaviour of the particle sizes along the calculation domain will be shown in the following figures. In each
 272 case, a vertical section of the domain will be shown on the left side, and a detail on the distribution in a plane
 273 normal to gravity and the five planes normal to the deposition probe will be shown on the right side. It should
 274 be noted that the reader is located on the secondary air inlet side and above the thinnest part of the bed for
 275 the pictures shown on the right part of the figures.

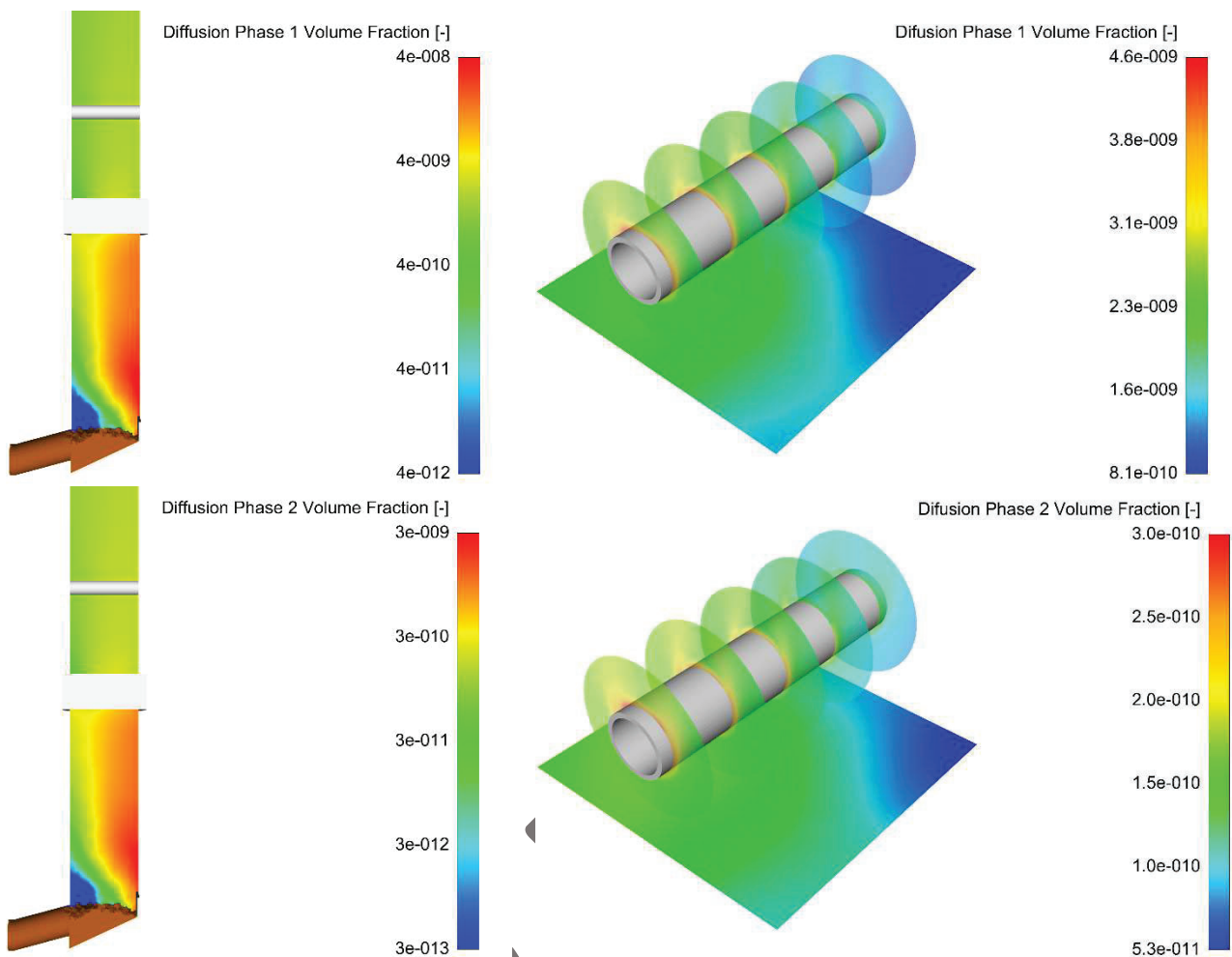


Figure 5. Evolution of representative granular phases of the diffusion regime.

276

277 Figure 5 shows the evolution along the domain and, more specifically near the deposition probe, of the fraction
 278 volume of each of the two granular phases calculated by the algorithm to represent the diffusion regime. It can
 279 be seen that there is a higher level of elutriation of particulate matter in the area of the smaller bed thickness.
 280 This phenomenon is due to two reasons. On the one hand, a smaller bed thickness causes a lower pressure
 281 decrease in that area; thus, more primary air circulates through it, reaching greater speed and, therefore, higher
 282 momentum to generate the necessary drag. On the other hand, this area is the furthest part of the bed from
 283 its inlet, so it is expected that there is a greater proportion of ashes in that area of the bed as most raw material
 284 has been consumed before reaching this area.

285 In the region affected by high-velocity air currents generated by the secondary air, the granular phases are
 286 diluted and homogenized along the vertical path. However, on the right side of Figure 5, several phenomena
 287 can be clearly seen: a displacement caused by both elutriation from the bed, diverted to one side of the
 288 chamber, and another caused by the secondary air inlet. The result is a displacement of the granular phases
 289 towards the corner opposed to both fuel and secondary air inlets.

290 When observing the normal planes to the probe, this displacement caused by bed and secondary air can also
 291 be appreciated, and a greater concentration of each phase around the perimeter of the probe can be seen. As
 292 the Stokes number increases, a more homogeneous distribution in the plane that is normal to gravity and along
 293 the probe is realized, despite the displacement caused by the inclined grate.

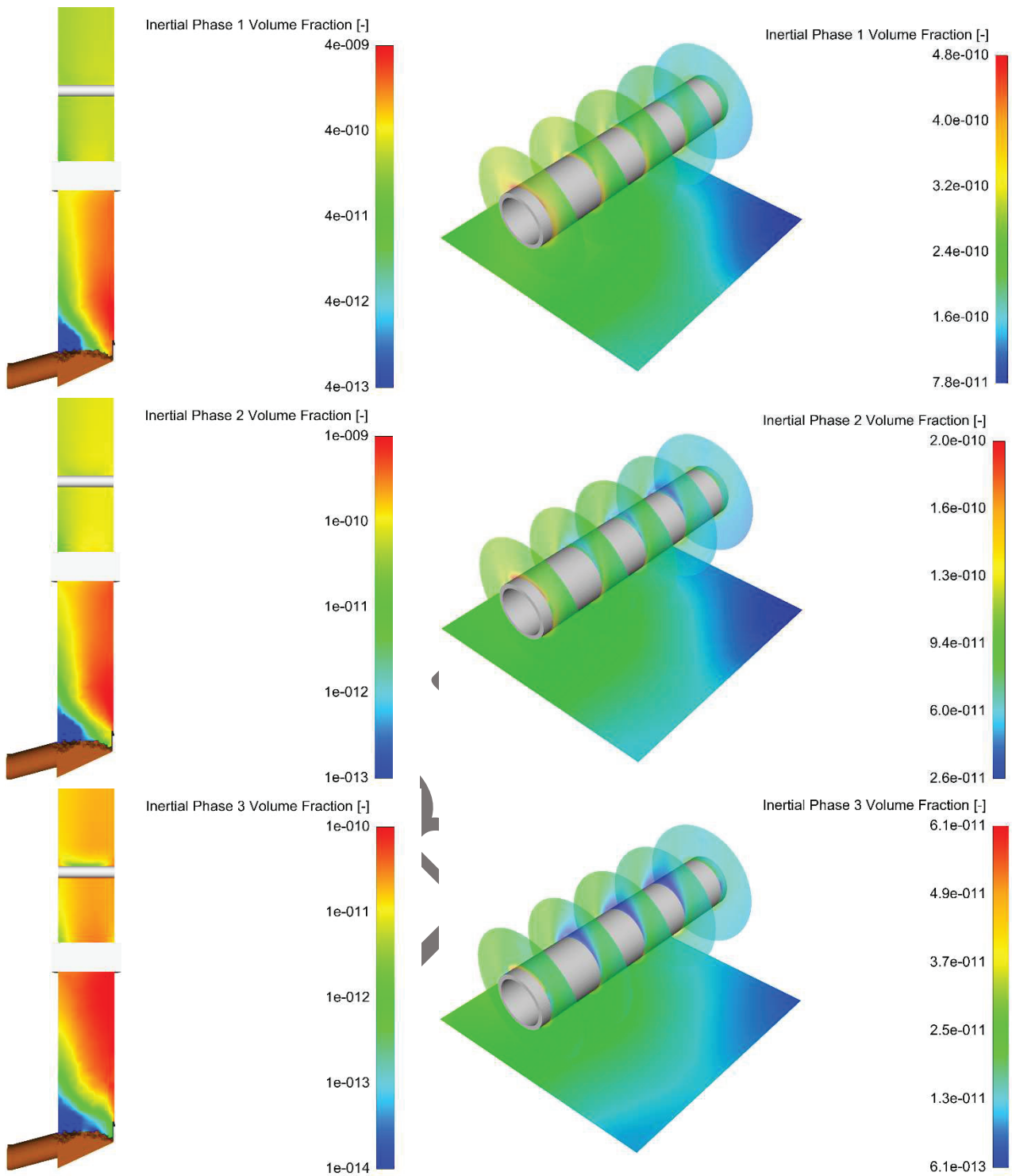


Figure 6. Evolution of representative granular phases of the inertial regime.

294

295 Figure 6 shows the evolution of granulometries in an inertial regime elutriated from the bed. It is in this regime
 296 where there will be the greatest change in the phase's behaviour[6] with a small variation in diameter. The first
 297 phase, with $\tau_j^+ = 0.421$, which is approximately 16 times greater than that of diffusion phase 2, behaves in a
 298 very similar manner.

299 However, for the next phase of the inertial regime, with $\tau_j^+ = 1.637$, which is four times greater than inertial
 300 phase 1, a significant change in behaviour can be seen. The left part of the figure, on the bed region, shows that

301 despite being elutriated from the end of the bed, a small part of the phase deviates, and its greater mass causes
302 a descent by gravitational forces. In this descent, the PM can be reintroduced to the area of greater speed,
303 ascending or becoming trapped in the bed, becoming part of its ash content. The latter phenomenon is more
304 visible in the third phase of the regime, where the area of elutriation is seen, then an area with low
305 concentration of that granular phase, and finally towards the middle of the bed a higher concentration, which
306 corresponds with a small portion of the grate not having holes, see Figure 3 of the facility.

307 On the right side of Figure 6, the environment of the probe for the three phases of the inertial regime is shown.
308 The beginning of an increasingly intense wake can be observed, which is extended throughout the probe.
309 Focusing on the normal planes to the probe that are closest to the reader, it can be seen that the presence of
310 the granular phase around the perimeter starts to focus on its upper and lower part with a marked decrease in
311 the shoulders or onset of the wake. The granular phase starts to impact the lower part of the probe, and in the
312 upper part close to the walls, there is a greater concentration produced by the eddies of the wake being stopped
313 in the vicinity of the wall.

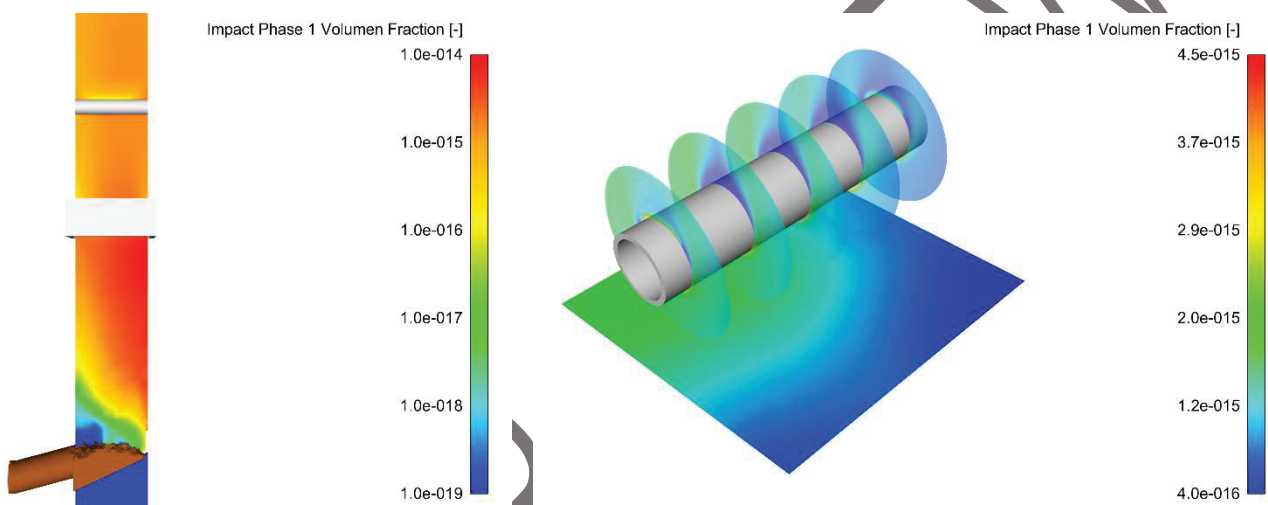


Figure 7. Evolution of representative granular phases of the impact regime.

314

315 Finally, only one phase was selected for the impact regime, since low PM flow was observed in this regime due
316 to the vertical morphology of this installation. In this regime, the phase is elutriated from the thinnest part of
317 the bed and a larger amount, than in previous phases, loses momentum and falls to the bed again. Near the
318 probe, the concentration is low, and the wake becomes relevant in the areas near the sidewalls of the system.

319

320 a. Fouling profile

321 In this section, the resulting fouling profile will be shown for a particular case analysed in the paper [18]; more
322 specifically, the central case of the design of experiments will be performed and will be compared with the
323 profile obtained experimentally and by the previous Euler-Lagrangian model. As already mentioned, the
324 following phenomena are considered in this model: Brownian diffusion, turbophoresis, thermophoresis,
325 presence of condensed inorganic vapours on the surface and the sticking probabilities model. These
326 phenomena are considered to calculate whether the surrounding granular phase adheres on the surface.

327 Unlike the previous Euler-Lagrangian model, the execution of the final smoothing algorithm is not necessary,
328 since the full Eulerian model does not undergo the deterministic nature of the old model, despite its use of
329 stochastic tracking methods, such as the random walk model. This allows future users to run the simulation in
330 a single step without their needed intervention to achieve an adequate deposition profile.

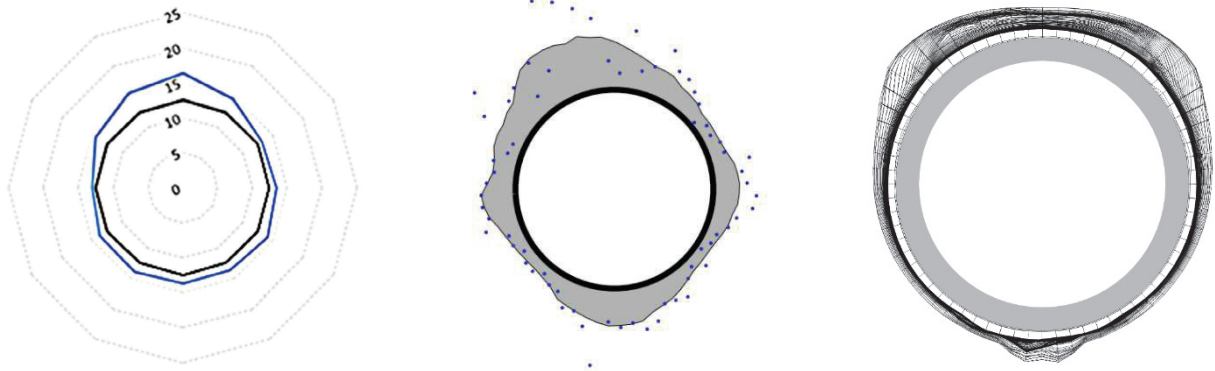


Figure 8. Side profile of the fouling layer. Left, experimental profile. Middle, Euler-Lagrangian model profile. Right, full Eulerian model profile.

331

332 Figure 8 shows the normal section of the fouling profile obtained in each case. The Euler-Lagrange model
 333 responds adequately to the displacement caused by secondary air but overestimates the side fouling and
 334 impaction regimes. On the other side, the full Eulerian model performs better on smaller granulometries,
 335 providing a smoother profile around the deposition probe; however, it underestimates the fouling caused by
 336 gravitational settling on the upper side.

337 On the front profile, Figure 9, we can see a better behaviour with the new model, as there is more deposition
 338 on the sides due to near-wall phenomena than with the previous modelling. However, there is low deposition
 339 on the top centre, but the overall shape of the fouling profile is closer to the experimental shape.

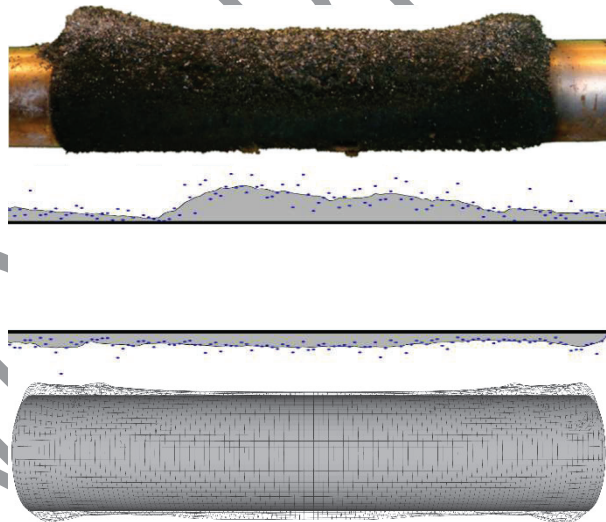


Figure 9. Front profile of the fouling layer. Top, experimental profile. Middle, Euler-Lagrangian model profile. Bottom, full Eulerian model profile.

340

341 Finally, Figure 10 shows the 3D profile generation with the data collected for each model. In the Euler-Lagrange
 342 model, a smoothing algorithm has been employed to reach an adequate profile, but the full-Eulerian approach
 343 profile that reached is shown with no smoothing processing. Between these models, there are similarities that
 344 can be easily observed, such as the presence of some ridges near the sidewalls or the ridges on the shoulders
 345 after the detachment of flow around the probe.

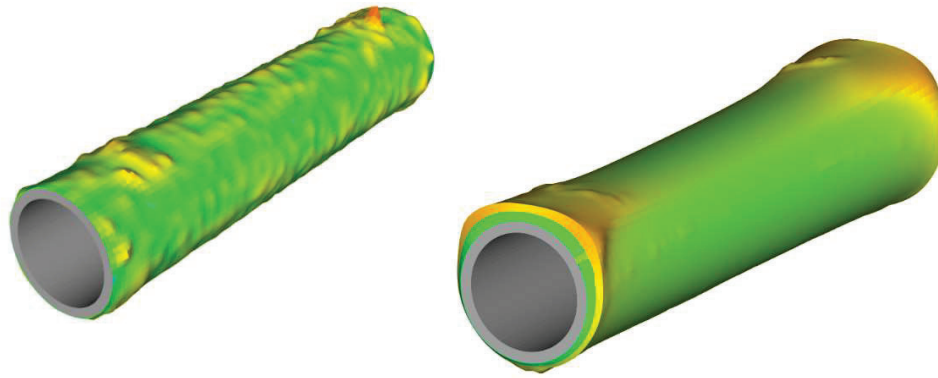


Figure 10. 3D-Profile re-creation of the fouling layer over the deposition probe. Left, previous Euler-Lagrange model [18]. Right, new full Eulerian model.

346

347 This softer profile, without the need for subsequent algorithms, allows a more reliable future model of the
348 section or volume blockage made by the fouling layer by means of a dynamic mesh or re-mesh techniques,
349 since the mesh algorithms will not have to solve complex and abrupt surfaces. This profile will also avoid
350 dependence on erosion mechanisms to achieve smoother profiles.

351

352 b. Computational effort comparison

353 Using the same mesh, combustion and fouling were simulated with both models. The calculation was performed
354 on the same computer with the same configuration and number of cores used, software version, MPI protocol
355 and identical default mesh partitioning system. For the Euler-Lagrange model, the latest version of the code
356 [20] has been executed, which is better optimized than that cited in the paper [18]. In the average CPU time
357 per time step, both the time necessary for the execution of the combustion and the time necessary for the
358 execution of the fouling algorithm are considered, which, in the case of the Euler-Lagrange model, runs
359 sequentially after each time step, as explained in previous works [18, 20]. In the case of the full Eulerian model,
360 both are executed simultaneously.

361 The results obtained show a great reduction in the CPU runtime for each time step. The calculation of each time
362 step takes three and a half times less time with the new model. The average RAM consumption with the new
363 model has doubled, but as previously mentioned for the new model, it almost represents the maximum RAM
364 consumption, which is 20% lower than the maximum necessary for the Euler-Lagrange model.

365 As noted in the full Eulerian model, the average use of RAM is higher because during the calculation of biomass
366 combustion, the fouling calculation is also performed. This fact implies an increase in the number of equations
367 and data layers to be permanently stored in the memory. However, the maximum RAM amount needed is less
368 than that in the Euler-Lagrange model. This reduced RAM requirement is due to the greater amount of data to
369 be stored in the volatile memory only during the segregated execution of the old algorithm, since a very large
370 number of Lagrangian trajectories is needed to adequately represent the fouling layer.

371 Based on this simplified comparison, it can be concluded that the new model is more efficient in terms of
372 computing resources. Although this new model has a higher consumption of average RAM, it takes less time to
373 calculate and has lower RAM requirements. For this reason, this new model involves a smaller hardware
374 investment both in the case of owning a specialized workstation or in the case of renting hardware in a
375 computer centre.

376 Additionally, there is a higher parallelization level inherent to the software itself when working in Eulerian
377 frameworks than when working in Lagrangian frameworks, so it scales-up more easily if it is run on external
378 high-performance computer centres.

379 4. Conclusions

380 In the present work, a new approach to the modelling of fouling in biomass combustion systems has been
381 revealed and explained through a full Eulerian model, in both the combustion and fouling algorithms. In this
382 method, the model is executed simultaneously with combustion, and the interaction between the different
383 granulometries and between these and the flue gas is possible in a bidirectional way.

384 To implement this new fouling model, it has been necessary to port the 3D EBITCOM model of the University
385 of Vigo to a multiphase environment where there is a phase for the bed, a phase for the flue gas and a phase
386 for each particle size considered. This port has been successfully achieved, and an Eulerian fouling model has
387 been created that considers the evaporation-condensation of inorganic vapours, thermophoresis,
388 turbophoresis, Brownian diffusion and sticking probabilities model.

389 In summary, the advantages and disadvantages of the new modelling versus the previous modelling are
390 discussed. On the one hand, the advantages are that the new full Eulerian modelling presents a direct solution
391 to the user without the need to execute sequential algorithms. This new model is more efficient in terms of
392 computational requirements, and its parallelization is direct through the software. This new model also benefits
393 from allowing the interaction between different particle sizes and with the gas and bed. The behaviour of this
394 new model is not as deterministic as with the previous modelling, so smoothing algorithms are not necessary,
395 since the profile itself is already smooth. This will allow the performance of more stable section or volume-
396 blockage and erosion algorithms in the future.

397 However, this new model also has disadvantages. The previous Euler-Lagrange model was allowed to run as an
398 add-on over the 3D EBITCOM model, so it benefits directly from the latest updates in this model. This new
399 model requires continuous adaptation of the improvements done to the multiphase environment. Additionally,
400 the Eulerian approach entails the need for a more complex modelling of all the phenomena involved. Finally,
401 the convergence of multiphase systems is more complex because of the addition of numerous new interaction
402 terms in the equations. Therefore, the size of the time step should not be large to ensure stability of the
403 solution.

404 The initial results are promising and provide new path to erosion and volume blockage algorithms by providing
405 a more stable research base. Although the Euler-Lagrange model achieves favourable results in all simulated
406 systems to date and allows the tracking of each individual particle, this new full Eulerian model allows potential
407 users to perform simple execution types of simulations in highly parallel systems, such as high performance
408 computing centres, which is of great interest in the industrial environment.

409

410 5. Acknowledgements

411 The authors would like to acknowledge the financial support from the project 'Fouling en Superficies de
412 Transferencia de Calor: Mitigación y/o Regeneración. Programa Estatal de Investigación, Desarrollo e
413 Innovación Orientada a los Retos de la Sociedad, Convocatoria 2017, 2018-2020' (ENE2017-87855-R). The work
414 of Sergio Chapela López was supported by grant BES-2016-076785 of the Ministry of Economy, Industry and
415 Competitiveness (Spain).

416

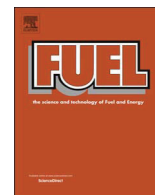
417 References

- 418 [1] G. Caposciutti, M. Antonelli, Experimental investigation on air displacement and air excess effect on CO, CO₂
419 and NO_x emissions of a small size fixed bed biomass boiler, *Renewable Energy*, 116 (2018) 795-804.
- 420 [2] D.W. Bunn, J. Redondo-Martin, J.I. Muñoz-Hernandez, P. Diaz-Cachinero, Analysis of coal conversion to
421 biomass as a transitional technology, *Renewable Energy*, 132 (2019) 752-760.
- 422 [3] S. Link, P. Yrjas, L. Hupa, Ash melting behaviour of wheat straw blends with wood and reed, *Renewable*
423 *Energy*, 124 (2018) 11-20.
- 424 [4] U. Kleinhans, C. Wieland, F.J. Frandsen, H. Spliethoff, Ash formation and deposition in coal and biomass fired
425 combustion systems: Progress and challenges in the field of ash particle sticking and rebound behavior, *Progress*
426 *in Energy and Combustion Science*, 68 (2018) 65-168.
- 427 [5] J. Capablo, J. Salvadó, Estimating heat transfer losses caused by alkali salt deposits in biomass combustion,
428 *Renewable Energy*, 105 (2017) 449-457.
- 429 [6] S.K. Kaer, Numerical investigation of ash deposition in straw-fired boilers-Using CFD as the framework for
430 slagging and fouling predictions, in: Institute of Energy Technology, Aalborg University, Denmark, 2001.
- 431 [7] Q. Wang, K. Han, J. Wang, J. Gao, C. Lu, Influence of phosphorous based additives on ash melting
432 characteristics during combustion of biomass briquette fuel, *Renewable Energy*, 113 (2017) 428-437.
- 433 [8] L. Wang, J.E. Hustad, Ø. Skreiberg, G. Skjevraak, M. Grønli, A Critical Review on Additives to Reduce Ash
434 Related Operation Problems in Biomass Combustion Applications, *Energy Procedia*, 20 (2012) 20-29.
- 435 [9] M. Aho, Reduction of chlorine deposition in FB boilers with aluminium-containing additives, *Fuel*, 80 (2001)
436 1943-1951.
- 437 [10] L. Tobiasen, R. Skytte, L.S. Pedersen, S.T. Pedersen, M.A. Lindberg, Deposit characteristic after injection of
438 additives to a Danish straw-fired suspension boiler, *Fuel Processing Technology*, 88 (2007) 1108-1117.
- 439 [11] B.-M. Steenari, A. Lundberg, H. Pettersson, M. Wilewska-Bien, D. Andersson, Investigation of Ash Sintering
440 during Combustion of Agricultural Residues and the Effect of Additives, *Energy & Fuels*, 23 (2009) 5655-5662.
- 441 [12] G. Gianfelice, M. Della Zassa, A. Biasin, P. Canu, Onset and propagation of smouldering in pine bark
442 controlled by addition of inert solids, *Renewable Energy*, 132 (2019) 596-614.
- 443 [13] K.S. Schulze, R.; Telian M.; Obernberger, I., Advanced modelling of deposition formation in biomass
444 furnaces - investigation of mechanisms and comparison with deposit measurements in a small-scale pellet
445 boiler, in: Impacts of Fuel Quality on Power Production & Environment, Lapland, Finland, 2010.
- 446 [14] M.A. Gomez, J. Porteiro, D. De la Cuesta, D. Patino, J.L. Miguez, Dynamic simulation of a biomass domestic
447 boiler under thermally thick considerations, *Energy Conversion and Management*, 140 (2017) 260-272.
- 448 [15] M.A. Gomez, J. Porteiro, D. de la Cuesta, D. Patino, J.L. Miguez, Numerical simulation of the combustion
449 process of a pellet-drop-feed boiler, *Fuel*, 184 (2016) 987-999.
- 450 [16] M.A. Gomez, J. Porteiro, D. Patino, J.L. Miguez, Eulerian CFD modelling for biomass combustion. Transient
451 simulation of an underfeed pellet boiler, *Energy Conversion and Management*, 101 (2015) 666-680.
- 452 [17] M.A. Gomez, J. Porteiro, D. Patino, J.L. Miguez, CFD modelling of thermal conversion and packed bed
453 compaction in biomass combustion, *Fuel*, 117 (2014) 716-732.
- 454 [18] S. Chapela, J. Porteiro, M.A. Gomez, D. Patino, J.L. Miguez, Comprehensive CFD modeling of the ash
455 deposition in a biomass packed bed burner, *Fuel*, 234 (2018) 1099-1122.
- 456 [19] S. Chapela, J. Porteiro, M. Costa, Effect of the Turbulence-Chemistry Interaction in Packed-Bed Biomass
457 Combustion, *Energy & Fuels*, 31 (2017) 9967-9982.
- 458 [20] S. Chapela, J. Porteiro, M. Garabatos, D. Patino, M.A. Gomez, J.L. Miguez, CFD study of fouling phenomena
459 in small-scale biomass boilers: Experimental validation with two different boilers, *Renewable Energy*, 140 (2019)
460 552-562.
- 461 [21] J.O. Hinze, *Turbulence*, New York, 1975.
- 462 [22] M.O.B.T. Syamlal, Computer Simulation of Bubbles in a Fluidized Bed, *AIChE Symp. Series*, 854 (1989) 22-
463 31.
- 464 [23] J.M. Dalla Valle, *Micromeritics*, Pitman, London, 1948.
- 465 [24] C.Y.Y. Wen, Y. H., *Mechanics of Fluidization*, Chem. Eng. Prog. Symp. Series, 62 (1966) 100-111.
- 466 [25] D.B. Gidaspow, R.; Ding J., *Hydrodynamics of Circulating Fluidized Beds, Kinetic Theory Approach*, in: 7th
467 Engineering Foundation Conference on Fluidization, Vol. Fluidization VII, 1992, pp. 75-82.

- 468 [26] L.G. Huilin, D., Hydrodynamics of binary fluidization in a riser: CFD simulation using two granular
469 temperatures". *Chemical Engineering Science*, 58 (2003) 3777–3792.
- 470 [27] D.J. Gunn, Transfer of Heat or Mass to Particles in Fixed and Fluidized-Beds, *International Journal of Heat*
471 *and Mass Transfer*, 21 (1978) 467-476.
- 472 [28] D.G. Schaeffer, Instability in the Evolution-Equations Describing Incompressible Antigranulocytes Flow,
473 *Journal of Differential Equations*, 66 (1987) 19-50.
- 474 [29] P.C. Johnson, R. Jackson, Frictional-Collisional Constitutive Relations for Granular Materials, with
475 Application to Plane Shearing, *Journal of Fluid Mechanics*, 176 (1987) 67-93.
- 476 [30] R. Ocone, S. Sundaresan, R. Jackson, Gas-Particle Flow in a Duct of Arbitrary Inclination with Particle-Particle
477 Interactions, *Aiche Journal*, 39 (1993) 1261-1271.
- 478 [31] H. Wiinikka, R. Gebart, C. Boman, D. Boström, M. Öhman, Influence of fuel ash composition on high
479 temperature aerosol formation in fixed bed combustion of woody biomass pellets, *Fuel*, 86 (2007) 181-193.
- 480 [32] D. Lindberg, R. Backman, P. Chartrand, M. Hupa, Towards a comprehensive thermodynamic database for
481 ash-forming elements in biomass and waste combustion — Current situation and future developments, *Fuel*
482 *Processing Technology*, 105 (2013) 129-141.
- 483 [33] N.B. Wood, The Mass-Transfer of Particles and Acid Vapor to Cooled Surfaces, *Journal of the Institute of*
484 *Energy*, 54 (1981) 74-93.
- 485 [34] F.G. Fan, G. Ahmadi, A Sublayer Model for Turbulent Deposition of Particles in Vertical Ducts with Smooth
486 and Rough Surfaces, *Journal of Aerosol Science*, 24 (1993) 45-64.
- 487 [35] C.Y. Cha, B.J. Mccoy, Thermal Force on Aerosol-Particles, *Physics of Fluids*, 17 (1974) 1376-1380.
- 488 [36] C.H. He, G. Ahmadi, Particle deposition with thermophoresis in laminar and turbulent duct flows, *Aerosol*
489 *Science and Technology*, 29 (1998) 525-546.
- 490 [37] A. Rezeau, L.I. Díez, J. Royo, M. Díaz-Ramírez, Efficient diagnosis of grate-fired biomass boilers by a
491 simplified CFD-based approach, *Fuel Processing Technology*, 171 (2018) 318-329.
- 492 [38] J. Wiese, F. Wissing, D. Hohner, S. Wirtz, V. Scherer, U. Ley, H.M. Behr, DEM/CFD modeling of the fuel
493 conversion in a pellet stove, *Fuel Processing Technology*, 152 (2016) 223-239.

ANEXO C.

Otros trabajos del autor



Full Length Article

An Eulerian model for the simulation of the thermal conversion of a single large biomass particle

M.A. Gómez^{a,*}, J. Porteiro^b, S. Chapela^b, J.L. Míguez^b

^a Defense University Center, Spanish Naval Academy, Plaza de España s/n, 36900 Marín, Spain

^b Industrial Engineering School, University of Vigo, Lagoas-Marcosende s/n, 36310 Vigo, Spain

ARTICLE INFO

Keywords:

CFD modelling
Biomass particle
Thermal conversion

ABSTRACT

This paper presents a comprehensive model for simulating the combustion of large biomass particles. The model implements a set of Eulerian variables that represent the components of solid biomass in a commercial CFD code. The evolution of these variables represents the thermal conversion of biomass and its interaction with the gas flow. The model consists of several reaction submodels of heat transfer and species diffusion. A wood shrinkage submodel was also proposed, and it acts locally in cells according to calculations of the consumption densities and globally in the particle according to mass and energy movements across the mesh. An experimental reactor, in which a biomass particle was irradiated with a xenon lamp, was modelled to simulate the drying and devolatilization stages under controlled conditions. Two documented experiments were simulated, and the predictions were compared with the experimental results. The temperature evolution of the particle at several depths was analysed, and a qualitative comparison of the particle shrinkage was performed. The comparison yielded reasonably good predictions for temperatures inside the particle and similar trends in log shrinkage despite some uncertainties regarding the biomass composition and experimental conditions.

1. Introduction

The lack of fossil fuel resources in numerous European countries and the growing need for investments in renewable energies have made biomass combustion an important field of research in recent decades. Advances in computational techniques have contributed to the study of different processes in combustion science via modelling and simulation tools that aid in predicting and understanding combustion phenomena. However, these techniques require significant development for application to solid biomass combustion since they cannot simulate the complex conversion, transport and reaction processes in the biphasic medium in a boiler or burner.

The main difficulty is the thermal conversion of solid biomass since CFD techniques are highly efficient at modelling gas combustion. Researchers have proposed a wide variety of strategies to implement submodels for the conversion of solid biomass in CFD codes. Most of these works have focused on beds of small particles or grates of straw. The simplest approach is the zero-dimensional bed [1–5], which uses mass, energy and species balances to predict the species and energy emitted by the bed during the conversion. Another typical strategy is the walking column, a one-dimensional approach commonly used for the simulation of grates of straw [6–9] that models the transient

advance of biomass in a grate through the steady exchange of mass and energy between the bed columns. Some models have achieved a higher level of geometrical discretization and a better resolution for combustion stages using two-dimensional [10] and three-dimensional beds [11–15]. These models have obtained the best results when the internal gradients of particles have been considered, i.e., a thermally thick approach and a separation of the combustion stages inside the particles [16–19]. Integration of discrete element model (DEM) with CFD has contributed to highly detailed models for the simulation of packed beds. Mahmoudi et al. [20] applied this approach to a grate obtaining a good agreement with experimental measurements. Wiese et al. [21] also applied a DEM model in a pellet stove and simulated complex particle shapes for thermally thick biomass particles in a multi particles approach.

Most studies have been performed in packed or fluidized beds of small particles. However, modelling large wood particles is still a challenge due to the need to increase the number of grid points inside the particles. Porteiro et al. [22] used a one-dimensional internal discretization in 25 layers combined with a shrinkage scheme based on an elementary cell analogy that considers the particle shrinkage and growing internal porosity. Babu and Chaurasia [23] calculated the heat transfer inside the particle subgrid with a tri-diagonal matrix algorithm

* Corresponding author.

E-mail address: miguelgr@uvigo.es (M.A. Gómez).

<https://doi.org/10.1016/j.fuel.2018.02.063>

Received 4 November 2017; Received in revised form 18 January 2018; Accepted 8 February 2018

Available online 22 February 2018

0016-2361/ © 2018 Elsevier Ltd. All rights reserved.

Nomenclature			
A_i	Pre-exponential factor (s^{-1})	$\Gamma_{\perp/\parallel}$	Ratio of perpendicular to parallel thermal conductivity (-)
A_{fi}	Area of face i (m^2)	ε	Solid fraction (-)
A_v	Area-volume ratio (m^{-1})	ε_m	Emissivity (-)
C_p	Specific heat ($J \cdot kg^{-1} \cdot K^{-1}$)	η	Permeability (m^2)
C_μ	k- ε model constant	κ	von Karman constant (-)
d	Diameter (m)	μ	Dynamic viscosity ($kg \cdot m^{-1} \cdot s^{-1}$)
Di_i	Diffusivity of the species i in the mixture ($m^2 \cdot s^{-1}$)	ν	Kinematic viscosity ($m^2 \cdot s^{-1}$)
E	Surface constant for the law of the wall (-)	ρ	Density ($kg \cdot m^{-3}$)
E_i	Activation energy ($J \cdot mol^{-1}$)	τ	Fraction of heat received by the particle employed in drying (-)
h	Convection coefficient ($W \cdot m^{-2} \cdot K^{-1}$)	τ_w	Wall shear stress ($kg \cdot m^{-2} \cdot s^{-1}$)
h_s	Solid phase enthalpy ($J \cdot kg^{-1}$)	$\Upsilon_{\perp/\parallel}$	Ratio of perpendicular to parallel permeability (-)
k	Thermal conductivity ($W \cdot m^{-1} \cdot K^{-1}$)	φ	Char oxidation parameter (-)
k_{turb}	Turbulent kinetic energy ($m^2 \cdot s^{-2}$)	$\dot{\omega}_i'''$	Generation or consumption rate of the wood components ($kg \cdot m^{-3} \cdot s^{-1}$)
k_L	Thermal conductivity perpendicular to fibres		
K	Char reaction constants ($m \cdot s^{-1}$)	<i>Subscripts</i>	
k_m	Mass transfer constant ($m \cdot s^{-1}$)	C	Carbon
LH	Latent heat ($J \cdot kg^{-1}$)	c	Consumption
M_i	Molecular weight ($kg \cdot kmol^{-1}$)	col	Collapse
\vec{r}	Position vector (m)	eff	Effective
R	Ideal gas constant ($J \cdot K^{-1} \cdot mol^{-1}$)	DC	Discharging cell
Nu	Nuselt number (-)	g	Gas
Pr	Prandtl number (-)	G	Generation
Sh	Sherwood number (-)	glob	Global
Sc	Schmidt number (-)	int	Internal
S	Source term ($W \cdot m^{-3}$)	lam	Laminar
T	Temperature (K)	moist	Moisture
T^+	Dimensionless temperature for the function of the wall (-)	RC	Receiving cell
t	Time (s)	part	Particle
V	Volume (m^3)	s	Solid
u^+	Law of the wall, dimensionless velocity (-)	turb	Turbulent
v_∞	Gas velocity ($m \cdot s^{-1}$)	wood	Dry wood
\vec{v}_{shr}	Shrinkage direction vector (m)		
X	Volumetric fraction (-)	<i>Superscripts</i>	
Y	Mass fraction (-)	g,1	Gasification reaction with CO_2
y_{node}	Distance from the wall to the node (m)	g,2	Gasification reaction with H_2O
y^+	Dimensionless distance to the wall (-)	ox	Char oxidation
		s	Specific
<i>Greek</i>			
Γ	Tortuosity (-)		

that is based on classical techniques used in numerical heat transfer theory [24]. Lu et al. [25] also discretized biomass particles in several layers and simulated several combustion phenomena, such as drying, rapid pyrolysis, gasification, and char oxidation processes, using a model that is applicable to different geometrical shapes and that considers the surroundings of a particle. This work demonstrates that the commonly used spherical approximations for nonspherical particles are not applicable to large sizes. To reduce the high computational cost, Thunman et al. [26] proposed an Eulerian approach that reduces the number of grid points to a few layers that represent the stages in biomass thermal conversion. This approach has been applied by several authors [16–19] for packed beds; however, all of the studies have focused on relatively small particles. Grønli and Melaaen [27] also used finite volume discretization to model logs of different biomass species and tested the model using an experimental reactor. The authors discretized cylindrical trunks along the main length using a simplified one-dimensional model and produced reasonably good results. Shi et al. [28] used a three-dimensional model to calculate the pyrolysis reactions of biomass particles via finite element techniques. They applied the model to one-centimetre-sized particles; however, the model is

applicable to larger particles. Okeunle et al. [29] also modelled heat transfer and wood pyrolysis reactions inside particles using a finite volume approach. Soria et al. [30] proposed a two-dimensional model for single particles that calculates the thermal conversion of particles considering the heat, mass and species transport inside the particle porous structure. The model results were in good agreement with experiments performed using a solar radiation concentrator.

In this study, a numerical model is implemented in CFD code to simulate large biomass particles. A three-dimensional discretization is applied in the region of solid biomass, and a set of Eulerian variables are defined to model the main parameters of the solid phase. The evolution of these variables defines the state of biomass degradation and the stage of combustion. The gas phase is also calculated in the particle region using a porous formulation. A complete reaction scheme is used to model both the biomass thermal conversion and gas reactions. Heat transfer through the solid phase, the interaction with the gas phase and the diffusion of mass and species through the biomass porous structure are detail. The model also includes a particle shrinkage sub-model that accounts for the contraction suffered by the entire biomass piece during conversion through mass and energy movements across

the grid. This shrinkage only affects the degraded regions of the biomass particle. The model is applied in the geometry used by Grønli and Melaaen [27] in a reactor, and their experimental results for pine wood are used to test the model behaviour. The evolution of internal temperatures and the global shrinkage of the particle in the tests are compared with the model results. In this work, the model is applied to a 2 × 3 cm particle, this is a first step to extend the model to larger particles such as trunks or groups of a few trunks.

2. Model description

2.1. Model assumptions

The modelling used to simulate the biomass combustion is based on the following main assumptions:

- The biomass particle is modelled as a disperse porous medium with local volume-averaged properties.
- The solid biomass is considered a continuous medium, and fissures are neglected.
- Internal pores are considered cylindrical.
- Drying occurs at a constant temperature.
- The devolatilization of dry wood is modelled using a three-step mechanism.
- Char heterogeneous reactions occur from the outer layer of the particle to the core, resulting in a shrinking core regime.

2.2. Solid phase

The modelling of the solid-phase thermal conversion and its interaction with gas inside the particle is based on the implementation of several variables that represent the evolution of the solid biomass. The authors of previous works [11,12] used a set of Eulerian variables to model a packed bed. A similar approach is proposed in this work with different considerations to represent the characteristics of a large piece of biomass. Fig. 1 shows the thermal conversion approach used in this work.

The main scalar variables used to define the solid biomass are shown as follows:

- Enthalpy of the solid (h).
- Local solid fraction (ϵ).
- Local moisture density (ρ_{moist})
- Local dry wood density (ρ_{wood}).
- Local char density (ρ_{char}).
- Local ash density (ρ_{ash}).

Table 1
Equations of the solid phase variables.

Solid phase enthalpy	$\frac{\partial(\epsilon\rho_{part}h_s)}{\partial t} = \nabla(k_{s,eff}\cdot\nabla T_s) + S_{h_s}$	(1)
Solid fraction	$\frac{\partial\epsilon}{\partial t} = \left(\frac{-\dot{\omega}_{wood}^{prime}}{\rho_{wood}^s} + \frac{\dot{\omega}_{G,char}^{prime} - \dot{\omega}_{c,char}^m}{\rho_{char}^s} \right) \epsilon$	(2)
Moisture density	$\frac{\partial(\epsilon\rho_{moist})}{\partial t} = -\dot{\omega}_{moist}^m \epsilon$	(3)
Dry wood density	$\frac{\partial(\epsilon\rho_{wood})}{\partial t} = -\dot{\omega}_{wood}^m \epsilon$	(4)
Char density	$\frac{\partial(\epsilon\rho_{char})}{\partial t} = (\dot{\omega}_{G,char}^m - \dot{\omega}_{c,char}^m) \epsilon$	(5)
Ash density	$\frac{\partial(\epsilon\rho_{ash})}{\partial t} = -\dot{\omega}_{ash}^m \epsilon$	(6)
Total particle density	$\rho_{moist} + \rho_{wood} + \rho_{char} + \rho_{ash} = \rho_{part}$	(7)

The transport equations of the solid-phase variables are shown in Table 1 (Eqs. (1)–(6)), and the relationships between the biomass component densities (i.e., moisture, wood, char and ash) and the total particle density (Eq. (7)) are also shown. In the scalar transport equations (Eqs. (1)–(6)), the first term on the left side denotes a transient term that represents the temporal evolution of each variable. On the right, there is a diffusion term, which is only present in the enthalpy equation, and a source term representing the generation or consumption of each variable.

The source terms in Eqs. (2)–(5) are affected by the consumption or generation of the biomass components ($\dot{\omega}_i^m$). Eqs. (8)–(12) in Table 2 show how these $\dot{\omega}_i^m$ terms are calculated. The drying rate is modelled using an evaporation process when the temperature reaches a value of 373.15 K; however, because part of the cell already dried and wood heating continues while a fraction of the cell is still drying, there is drying and heating overlap. Thus, some of the heat gained by the particle is used for drying, whereas the remainder is provided to the heating process. To account for this effect, the parameter, τ is introduced in Eq. (8) to represent the fraction of heat employed in drying, which in our case was set to 0.5 [11,12,31]. Other different values were tested and no significant differences were observed for the typical heat fluxes found in combustion applications. The differences are compensated only a few kelvins of over- or under-heating and those differences are not noticeable in the range of temperatures that takes place in combustion. In any case, a more detailed drying model would be needed to simulate any accurate drying experiment. Devolatilization is modelled by three Arrhenius reactions for tar, light volatiles and char (Eq. (9)). One of these reactions represents the char generation rate (Eq. (10)). Ash is considered non-reactive; thus, no consumption rate is considered (Eq. (12)).

The devolatilization process is affected by several factors, such as solid temperatures, heating rates and the thicknesses of the particle reaction layers [32,33]. Because biomass combustion occurs at high

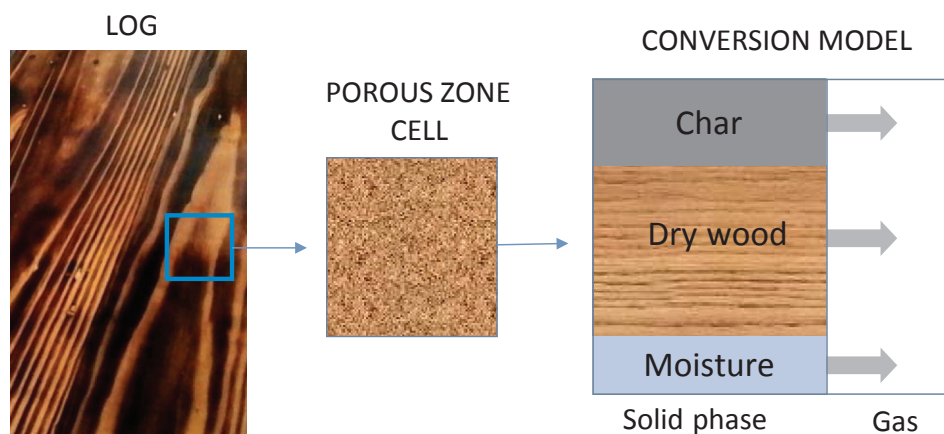


Fig. 1. Schematic of the thermal conversion model.

Table 2
Equations of the solid consumption rates.

Drying rate	$\dot{\omega}_{moist}^m = \tau \frac{\rho_{part} c_p}{LH_{moist}} \frac{\partial T_s}{\partial t}, T_s \geq T_{evap}$	(8)
Devolatilization rate	$\dot{\omega}_{wood}^m = \rho_{wood} \sum_{i=1}^3 A_i \exp\left(-\frac{E_i}{RT_s}\right)$	(9)
Char generation rate	$\dot{\omega}_{G, char}^m = \rho_{wood} A_3 \exp\left(-\frac{E_3}{RT_s}\right)$	(10)
Char consumption rate	$\dot{\omega}_{c, char}^m = K_{glob}^{ox} A_v [O_2] M_C$	(11)
Ash consumption rate	$\dot{\omega}_{ash}^m = 0$	(12)

temperatures and instantaneous reactions are frequent, dry wood consumption is modelled considering flash pyrolysis kinetics [34]. The devolatilization rate shown in Eq. (9) follows the reaction kinetics shown in Table 3. The char consumption rate is modelled as direct char oxidation (R.1) and with two gasification reactions, (R.2) and (R.3), which were used in previous works [11,12,31,35]. However, the parameter, φ , controls the CO/CO₂ ratio (Eq. (13)) during char burning [26], and K_{glob}^{ox} , $K_{glob}^{g,1}$ and $K_{glob}^{g,2}$ control the char reactions with oxygen, carbon dioxide and water vapour, respectively (Eq. (14)). These coefficients take into account both the thermally controlled kinetics and diffusion of reactants. The formulation of the mass transfer coefficients is shown below in the section “Heat and mass transfer”.

$$\varphi = \frac{2 + 4.3 \exp\left(-\frac{3390}{T_s}\right)}{2\left(1 + 4.3 \exp\left(-\frac{3390}{T_s}\right)\right)} \quad (13)$$

$$K_{glob}^{ox} = \frac{1}{\frac{1}{K^{ox}} + \frac{1}{K_m^{ox}}}, K_{glob}^{g,1} = \frac{1}{\frac{1}{K^{g,1}} + \frac{1}{K_m^{g,1}}}, K_{glob}^{g,2} = \frac{1}{\frac{1}{K^{g,2}} + \frac{1}{K_m^{g,2}}} \quad (14)$$

2.3. Gas phase

This section refers to the gas transport both inside and outside the particle. CFD techniques have been extensively used in gas-phase combustion simulations for many different systems [38–44]. Gas dynamics are typically modelled using conservation equations of variables such as pressure, momentum, energy, turbulence, radiation and chemical species. In this work, realizable k- ϵ modelling with enhanced wall treatment for turbulence, Finite-rate/Eddy-dissipation (FR-ED) modelling for the species reactions and the Discrete Ordinate model for radiation transport are used. Gas flow inside the biomass pores is modelled using a dispersed porous media approach with a momentum source (Eq. (15)) based on Darcy’s law, which requires the coefficients of permeability (Eq. (16)). Inertial terms are neglected since low Reynolds numbers are expected inside the pore structure compared with the low permeability found for biomass and char. The permeability is calculated as an average of the wood and char permeabilities. As fibres direction affects to the mass transport across the solid wood, an

Table 3
Kinetics of the solid heterogeneous reactions.

Pyrolysis reactions	Kinetics: $A_i (s^{-1}), E_i (J \cdot mol^{-1})$	Source
Drywood \rightarrow Gas	$A_1 = 111 \cdot 10^9, E_1 = 177 \cdot 10^3$	[32]
Drywood \rightarrow Tar	$A_2 = 9.28 \cdot 10^9, E_2 = 149 \cdot 10^3$	[34]
Drywood \rightarrow Char	$A_3 = 30.5 \cdot 10^9, E_3 = 125 \cdot 10^3$	[34]
Heterogeneous char oxidation	Kinetics	Source
(R.1)	$C + \varphi O_2 \rightarrow 2(1-\varphi)CO + (2\varphi-1)CO_2$	$K^{ox} = 1.715 \cdot T_s \cdot \exp\left(-\frac{9000}{T_s}\right)$ [36,37]
(R.2)	$C + CO_2 \rightarrow 2CO$	$K^{g,1} = 3.42 \cdot T_s \cdot \exp\left(-\frac{1.56 \cdot 10^4}{T_s}\right)$ [36,37]
(R.3)	$C + H_2O \rightarrow CO + H_2$	$K^{g,2} = 5.7114 \cdot T_s \cdot \exp\left(-\frac{1.56 \cdot 10^4}{T_s}\right)$ [36,37]

anisotropic permeability was considered model the fibres preferential directions. The permeability perpendicular to fibres was modelled through a ratio to parallel direction shown in Eq. (17). Several authors found different ratios of permeabilities summarized in [45]. In this work, a ratio of 10^{-4} was consider based in that compilation.

$$S_{mom} = -\frac{\mu}{\eta} v_{\infty} \quad (15)$$

$$\eta = X_{wood} \cdot \eta_{wood} + X_{char} \cdot \eta_{char} \quad (16)$$

$$\eta_{\perp} = \eta \cdot \Gamma_{\perp//} \quad (17)$$

The mass of biomass consumed from the solid phase is introduced in the gas phase equations of mass and species. The gas release is modelled by the gaseous emissions of H₂O from drying, the volatiles species generated during devolatilization composed of light hydrocarbons (represented by CH₄), tars (represented by C₆H₆), CO, CO₂, H₂ and H₂O [46] and CO and CO₂ released in the char oxidation. The method for obtaining the volatile species fractions was previously explained by Gómez et al. [12]. This method searches for a combination of species fractions that minimizes the errors associated with C, H, and O and from the energy balances.

2.4. Heat and mass transfer

Heat and mass transfer is a key factor in the thermal conversion of biomass due to its important influence in the transport equations. In the gas phase, the models are solved using the transport equations of gas flow, species reactions and the radiative transport. These calculations are completely solved by commercial CFD code. Otherwise, the heat and mass transfers must be modelled for the solid phase and the interaction between the two phases. The radiative exchange between the solid phase and the surroundings is solved through the modified Discrete Ordinates model proposed in [47] for packed beds, which gives a good directional accuracy.

The solid enthalpy equation (Eq. (1)) includes some terms and parameters that define the heat transfer. Conduction is determined by the thermal conductivity, $k_{s,eff}$, which considers the conduction through wood fibres and the different components of biomass (moisture, dry wood and char) through a mass weighted average (Eq. (18)). Wood fibres have an important influence on the thermal conductivity since there is a directional preference for heat conduction along the fibres. This was taken into account by introducing the anisotropic thermal conductivity. The transversal conductivity can be reduced with respect to the longitudinal direction through a coefficient ($\Gamma_{\perp//}$), as shown in Eq. (19).

$$k_{s,eff} = Y_{moist} \cdot k_{moist} + Y_{wood} \cdot k_{wood} + Y_{char} \cdot k_{char} \quad (18)$$

$$k_{\perp} = k_{s,eff} \cdot \Gamma_{\perp//} \quad (19)$$

The convective heat exchange is modelled as a source term in both

the solid and gas energy equations. The exchange that occurs in the pores of the biomass internal structure is modelled using the source term shown in Eq. (20). The area/volume ratio of the computing cell is calculated by considering the pores as perfect cylinders along the porous structure (Eq. (21)). The convection coefficient is calculated using the Nusselt dimensionless number (Eq. (22)). The mass transfer follows the heat transfer analogy of the Nusselt and Sherwood dimensionless numbers with the thermal conductivity and mass diffusivity, respectively (Eq. (23)). Considering the low values of the pores diameter and the gas velocities due to the low biomass permeability, the Reynolds number values obtained inside the pores exhibit a laminar flux; therefore, a Nusselt number of 3.66 is used. Regardless, the values of A_v and the pore diameter lead to a high heat exchange that produces a thermal equilibrium between phases. On the particle surface, the convective exchange conditions can be variable. Therefore, the heat transfer is calculated directly without any correlation. In the case of the adjacent cell in the boundary layer with $y^+ < 11.63$, the heat is exchanged through linear conduction with the flow layer. Otherwise, if the adjacent cell is far enough from the wall to be affected by the viscous effects, a wall law is necessary to calculate the heat flux (Eq. (24)). The dimensionless wall distance, considering the kinematic viscosity and shear velocity, is shown in Eq. (25), and we use the threshold value of 11.63, as recommended by Versteeg and Malalasequera [48]. The law of the wall is a function of the temperature distribution (Eq. (26)) and the dimensionless velocity (Eq. (27)) in the near-wall turbulent flow. Eq. (28) is a function of the laminar and turbulent Prandtl numbers, which are necessary to determine the temperature profile, as shown in Eq. (26) [48]. The external mass transfer is also calculated using the analogy with heat transfer. Because different Nusselt correlations can be found for laminar and turbulent regimes in a plate and most are proportional to $Pr^{1/3}$, an equivalent Sherwood number is found using Eq. (29).

$$S_h^{int} = h_{int} A_v (T_g - T_s) \quad (20)$$

$$A_v = \frac{4}{d_{pore}} \frac{\varepsilon}{1-\varepsilon} \quad (21)$$

$$h_{int} = \frac{Nu \cdot k_g}{d_{pore}} \quad (22)$$

$$k_m^i = \frac{Sh \cdot Di_{eff}}{d_{pore}} \quad (23)$$

$$S_h^{ext} = k_{gas} \frac{A_{face}}{y_{node} \nu_{cell}} (T_g - T_s) \text{ if } y^+ \leq 11.63, \quad (24)$$

$$S_h^{ext} = C_p \rho_g C_\mu^{1/4} k_{turb}^{1/2} \frac{(T_g - T_s)}{r^+} \text{ if } y^+ > 11.63$$

$$y^+ = \frac{y_{node}}{\nu} \sqrt{\tau_w} \quad (25)$$

$$T^+ = Pr_{turb} \left(u^+ + P \left(\frac{Pr_{lam}}{Pr_{turb}} \right) \right) \quad (26)$$

$$u^+ = \frac{1}{\kappa} \ln(Ey^+) \quad (27)$$

$$P \left(\frac{Pr_{lam}}{Pr_{turb}} \right) = 9.24 \left[\left(\frac{Pr_{lam}}{Pr_{turb}} \right)^{0.75} - 1 \right] \cdot \left[1 + 0.28 \cdot \exp \left[-0.007 \left(\frac{Pr_{lam}}{Pr_{turb}} \right) \right] \right] \quad (28)$$

$$Sh = Nu \cdot \left(\frac{Sc}{Pr} \right)^{1/3} \quad (29)$$

The species diffusivity inside the porous structure plays a key role in mass transport. The diffusivity of a chemical species across a porous medium can be estimated using the Knudsen diffusivity, as shown in Eq. (30). Thus, both molecular and Knudsen diffusivities are used to calculate the diffusivity across the pores (Eq. (31)) [30]. The effective diffusivity can be obtained by considering the porosity (1-solid fraction) and the tortuosity, Γ , of the pores (Eq. (32)).

$$Di_K = \frac{d_{pore}}{3} \sqrt{\frac{8R}{\pi M_i}} T^{1/2} \quad (30)$$

$$Di_{pore} = \left(\frac{1}{Di_{K,i}} + \frac{1}{Di_{m,i}} \right)^{-1} \quad (31)$$

$$Di_{eff} = \frac{1-\varepsilon}{\Gamma} Di_{pore} \quad (32)$$

2.5. Particle shrinkage

Changes in the size and density in biomass thermal conversion are well-known occurrences, as most experiments have shown. In this respect, the finite volume method presents several limitations when fixed size computing cells are used, which is common. Therefore, modelling the size changes suffered by biomass particles is a challenge. The use of a dynamic mesh can be a solution; however, it is complicated to determine how the local shrinkage of a computing cell affects the surrounding cells and how to move the nodes to adapt to the mesh. Based on mass movements across the mesh, an alternative method is proposed in this section to account for the local shrinkage.

Particle shrinkage is modelled at both cell and multi-cell scales. To account for the cell shrinkage, a specific density is defined for wood and char ($\rho_{wood}^s, \rho_{char}^s$) as the density of a compact particle completely formed by that component. Therefore, the source term of the solid fraction takes into account the relationship between the wood/char consumption/generation and their specific densities as shown in Fig. 2. This formulation implies that Eq. (33) is satisfied. This local process reduces the solid fraction in the cell and increases the porosity.

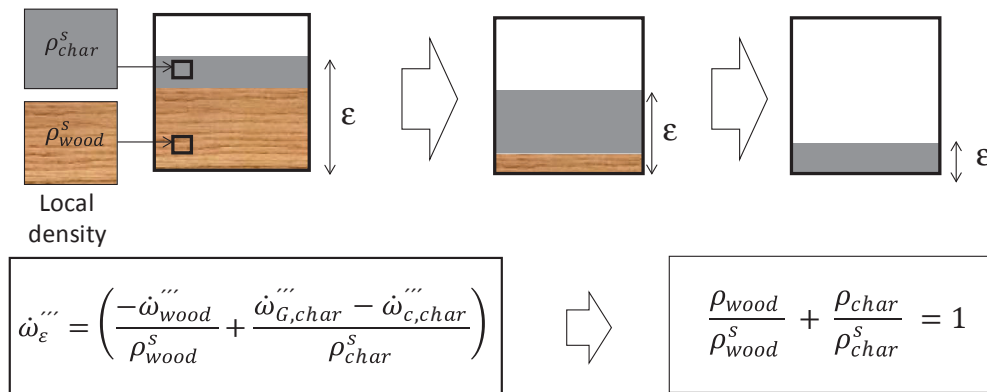


Fig. 2. Schematic of the cell shrinkage model.

$$\left(\frac{\rho_{wood}}{\rho_{wood}^s}\right)^{Y_{wood}} + \left(\frac{\rho_{char}}{\rho_{char}^s}\right)^{Y_{char}} = 1 \tag{33}$$

Based on the local shrinkage results produced for each computing cell, multi-cell shrinkage is modelled to reduce the global size of the particle via mass movements across the cells. To do this, a threshold solid fraction (ϵ_{col}) is defined that decides when a cell collapses and moves its mass in the direction of the mass centre. In this manner, the mass is transferred to the following cells, and these cells are filled up to reach the char solid fraction (ϵ_{char}) value obtained from literature [45]. Thus, a cell that collapses loses mass, and its solid fraction can decrease until it is fully empty ($\epsilon = 0$) or until the neighbouring cells are saturated ($\epsilon = \epsilon_{char}$). A representation of this process is shown in Fig. 3. It shows several cells of the particle whose solid fraction (ϵ) decreases as the cells react. If the solid fraction of a cell decreases below the collapsed solid fraction, the mass is moved in the direction of the vector, \vec{v}_{shr} , which points from the cell centroid to the mass centre (MC) of the particle (Eq. (34)). The mass moved is related to the solid volume of the cell that collapses. The solid volume transferred is the minimum between the volume contained in the discharging cell (DC) and the volume that overflows the receiving cell (RC) scaled by the area of the face that is crossing (A_{fj}) and divided by the total area of the faces since the volume can be discharged through several faces (Eq. (35)). The mass movements occur at the end of each time step, if the collapse condition is fulfilled in any cell. The mass is removed from the discharging cell and added to the receiving cell. To achieve this, the solid phase variables are modified, as shown in Table 4. Eq. (36) shows how the solid fraction is updated. Eq. (37) shows the changes in the densities of the biomass components (moisture, dry wood, char and ashes). Because mass movement implies energy movement, Eq. (38) shows the enthalpy corresponding to the solid volume moved.

$$\vec{v}_{shr} = \vec{v}_{cell} - \vec{v}_{MC} \tag{34}$$

Table 4
Equations of solid-phase variables for the mass movements in the global shrinkage model.

Discharging cell	Receiving cell
$\epsilon_{DC} = \epsilon_{DC} - \frac{\Delta V_s}{V_{DC}}$	$\epsilon_{RC} = \epsilon_{RC} + \frac{\Delta V_s}{V_{RC}}$
$\rho_{iRC} = \frac{\rho_{iRC} \epsilon_{RC} V_{RC} + \Delta V_s \rho_{iDC}}{\epsilon_{RC} V_{RC} + \Delta V_s}$	
$\Delta H_s = \Delta V_s \cdot \rho_{iDC} \int_{T_{ref}}^{T_{DC}} C_p dT$	

$$\Delta V_s(f_j) = \min \left(\epsilon_{DC} \cdot V_{DC} \frac{A_{f_i}}{\sum_i (A_{f_j})}, [\epsilon_{char} - \epsilon_{RC}] V_{RC} \frac{A_{f_j}}{\sum_i (A_{f_j})} \right) \tag{35}$$

2.6. Experimental setup

The models described above were applied to the reactor used by Morten Grønli in his PhD Thesis [45]. In this setup, a pellet that had a 20-mm diameter and a 30-mm depth was irradiated by a xenon lamp. The biomass pellet was located inside a camera where the gas emissions were purged with nitrogen. A data collection system was installed to measure, e.g., the temperatures at different positions along the cylinder depth and the emissions of the main volatile species. A schematic of the reactor is shown in Fig. 4. Several thermocouples were introduced at depths of 1 mm, 4 mm, 8 mm, 12 mm and 24 mm, along the centreline, and another was placed on the surface. In addition, a gas analyser was used to measure the volatile emissions at the gas outlet. All these parameters were recorded during the simulations, and results were analysed to study the model behaviour. Morten Grønli performed several empirical tests with different types of wood and different fibre orientations (longitudinal and radial) for wood logs. In those tests, the pellet was irradiated using two different radiation fluxes: a low

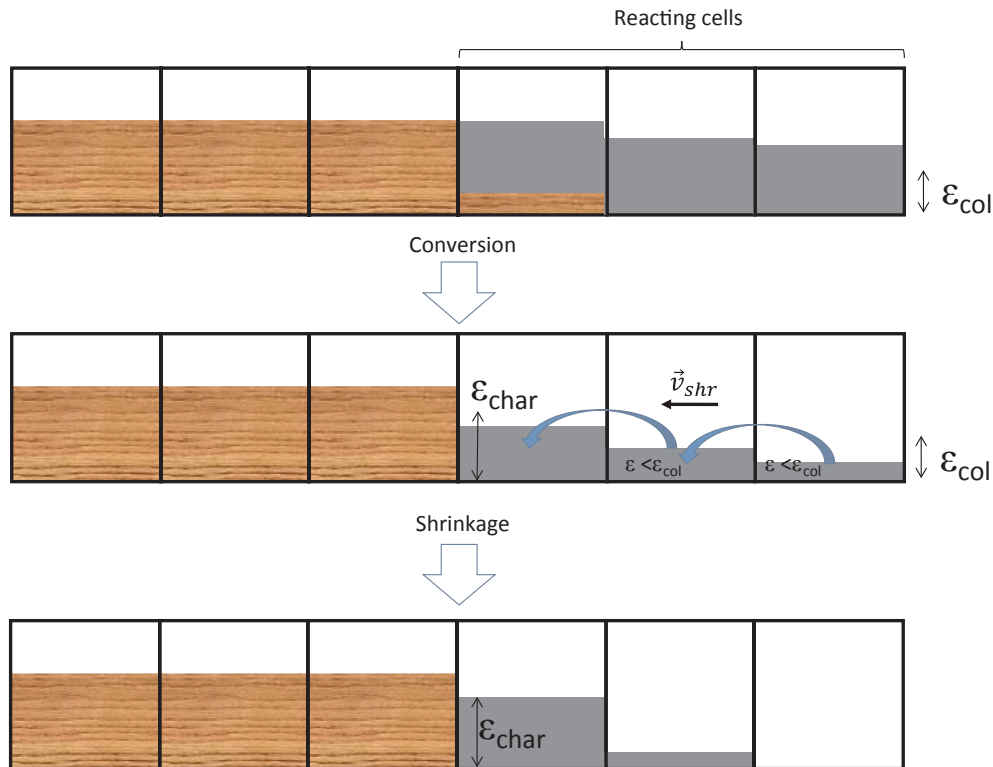


Fig. 3. Representation of the mass movements that occurred in the log to model particle shrinkage at the multi-cell scale.

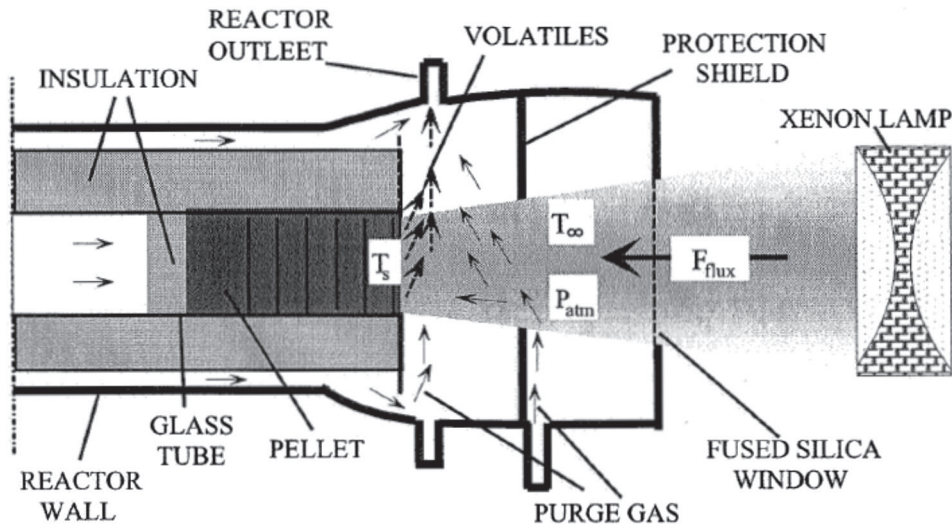


Fig. 4. Schematic diagram of the experimental reactor [45].

intensity flux of 80 kW/m^2 and a high intensity flux of 130 kW/m^2 .

3. Simulation and results

3.1. Simulation conditions

The experiments performed by Grønli [45] used particles of pine wood with fibres orientated in the longitudinal direction. Both low and high radiation fluxes (80 kW/m^2 and 130 kW/m^2 , respectively) were simulated with a total nitrogen mass flux of $8.2 \cdot 10^{-5} \text{ kg/s}$ distributed among several inlets. A time step size of 1 s was used for the simulations.

The experimental reactor was meshed and calculated with a structured mesh for the particle region and a polyhedral mesh in the rest of the reactor. The mesh was formed by approximately $250 \cdot 10^3$ elements, with an edge length of 0.5 mm in the particle region and 1–2 mm in the gas zone. Several meshes were tried. In the reactor gas region, no significant differences were observed with the refinement of the mesh

since no reactions are produced out of the particle region. In the particle region, 1 mm side elements guarantee the mesh independence from a thermal point of view. Nevertheless, 0.5 mm elements were used to obtain a more accurate profile for the shrinkage model. An image of the mesh is shown in Fig. 5. In addition, Table 5 shows some properties and values that were used in the model and Table 6 shows the details of the particle composition.

3.2. Main variable fields

The effect of the incident radiation in the particle can be understood through the contours of the variables of the solid phase. Fig. 6 shows the main variables of the solid phase in the simulation of high radiation (130 kW/m^2) after two minutes of exposure. These variables include the solid phase temperature, the solid fraction and the densities of wood and char in the computational cells. The temperature reached 1120 K at the irradiated surface, and it decreased along the pellet depth. In the heated area, the solid fraction reduced due to the shrinkage produced

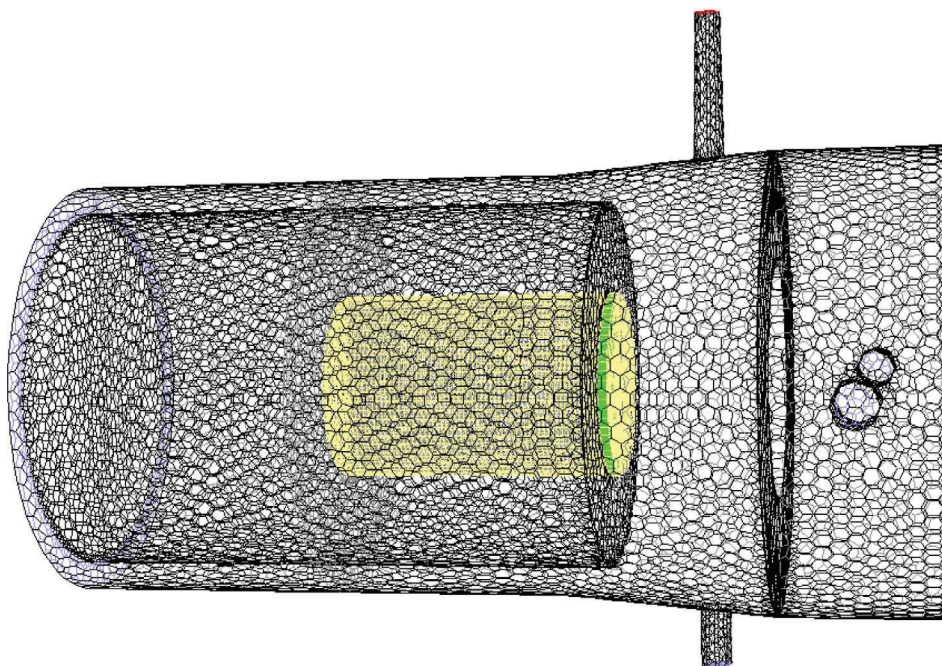


Fig. 5. Image of the mesh.

Table 5
Parameters of the material used in the model.

Parameter	Units	Value	Reference
$\rho\epsilon_0$	kg/m ³	450	[45]
ϵ_m	–	0.85	[45]
ϵ_0	–	0.4	[45]
ϵ_{char}	–	0.25	[45]
ϵ_{col}	–	0.2	Own model
$d_{pore,wood}$	m	$4 \cdot 10^{-5}$	[30]
$d_{pore,char}$	m	$4 \cdot 10^{-4}$	[30]
X_{wood}	m ²	10^{-12}	[49]
X_{char}	m ²	10^{-11}	[49]
k_{wood}	W/(m·K)	0.2	[22]
k_{char}	W/(m·K)	0.1	[22]
k_{moist}	W/(m·K)	0.58	[22]
$\Gamma_{L//I}$	–	0.71	[26]
$\Upsilon_{L//I}$	–	10^{-4}	[45]
$C_{p,moist}$	J/(kg·K)	4180	[22]
$C_{p,wood}$	J/(kg·K)	$-91.2 + 4.4 T_s$	[50]
$C_{p,char}$	J/(kg·K)	$420 + 2.09 T_s - 6.85 \cdot 10^{-4} T_s^2$	[50]

Table 6
Proximate and ultimate analyses of the fuel [45].

Proximate analysis	Values	Ultimate analysis	Values
Ash [wt%]	0.1	C [wt%]	47.4
Fixed carbon [wt%]	13.2	H [wt%]	6.3
Volatile matter [wt%]	86.7	O [wt%]	46.7
HHV [MJ/kg]	19.03	N [wt%]	0.07

during the devolatilization stage, and the wood density was completely consumed. During the same process, char was generated, and its maximum density occurred in this heated area. In the figure, the devolatilization front is visible, and the maximum value for the solid fraction was produced due to the high char generation at low devolatilization temperatures, which produced a swelling effect. This occurs due to the local solid fraction formulation (Eq. (2)). When the ratio of char generation and char specific density is higher than the ratio of dry wood

consumption and dry wood specific density. Thus, a positive source of solid fraction is obtained.

Fig. 7 shows the temperature field in the reactor (gases and insulation) and the concentrations of CO, CO₂ and hydrocarbons in the high-radiation simulation after two minutes of exposure. In the temperature field, we observed a high temperature in the surroundings of the irradiated surface of the particle and the walls of the reactor that were not directly cooled by the nitrogen stream. High concentrations of CO, CO₂ and hydrocarbons were found in the gases leaving the particle, which are products of the devolatilization process.

3.3. Experimental measurements and model results

The experimental reactor was simulated by reproducing the operating conditions in the experimental tests of pine wood [27]. Thermocouples located at different depths were used to record the temperature during the experiments. Figs. 8 and 9 show the temperatures registered by the thermocouples and the experimental data for the particle exposed to high (130 kW/m²) and low (80 kW/m²) radiation fluxes, respectively. Fig. 8 shows aggressive heating of the most superficial thermocouples at the beginning of the experiment but a low heating rate for the deepest thermocouples in the high radiation flux” experiment. The superficial thermocouples (1 mm and 4 mm) reached lower temperatures as the experiment progressed. The remaining thermocouples predicted similar heating trends and temperatures as the experimental data. The model seems to have difficulties heating the particle at high temperatures. This may be due to the specific heat of char, whose adjusted polynomial returns excessively high values at high temperatures. Excessive cooling of the released gases from devolatilization may also cause a decrease in temperature. The surface of pores can be overestimated since in real biomass there are preferred channels for the release of gases. Fig. 9 also shows that the model was not able to reach the highest temperatures shown by the superficial thermocouples for the experimental particle. As shown by the deeper thermocouples, the heating was more gradual than in the experiment at the beginning of the test. Otherwise, the heating became more aggressive at higher temperatures as the particle lost mass during devolatilization. These discrepancies in both tests are reasonable since some biomass

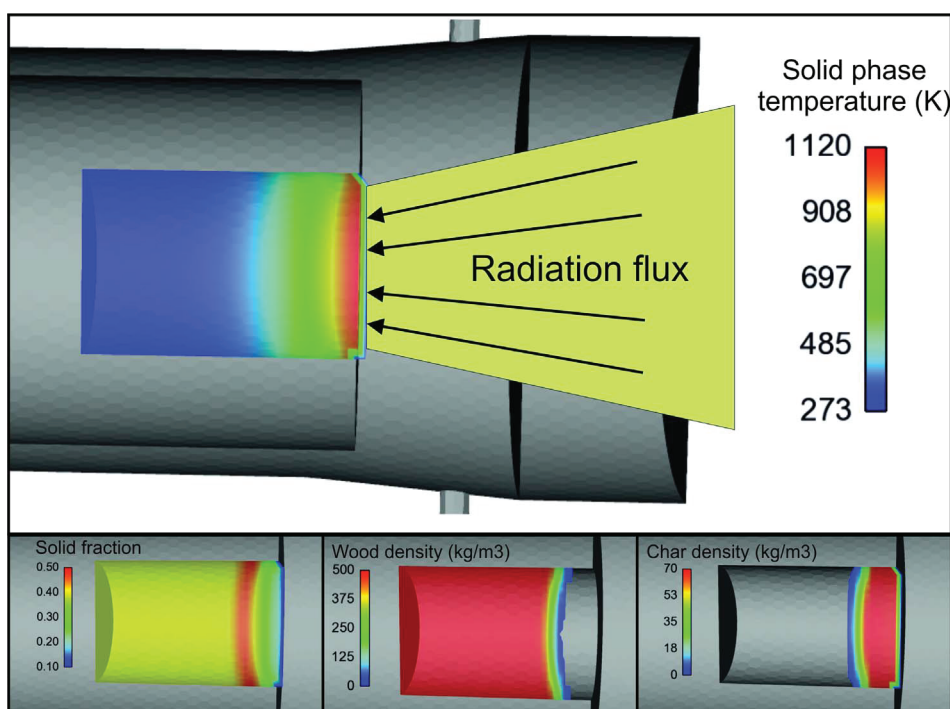


Fig. 6. Main variables of the solid phase after two minutes of radiation exposure.

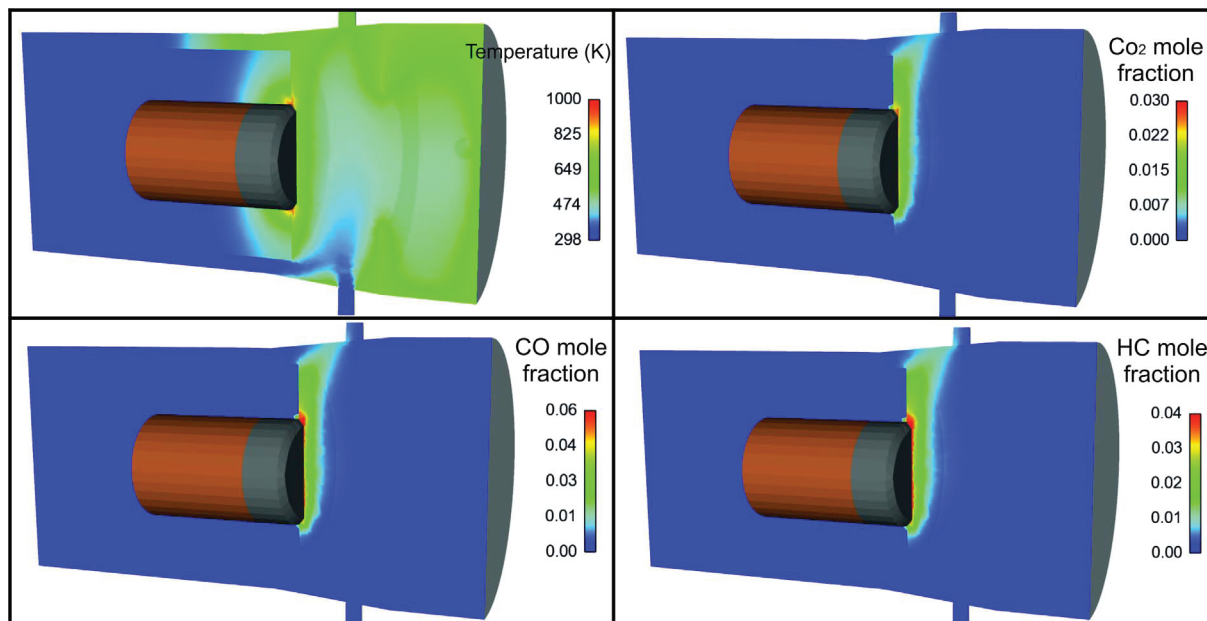


Fig. 7. Main variables in the gas phase after two minutes of radiation exposure.

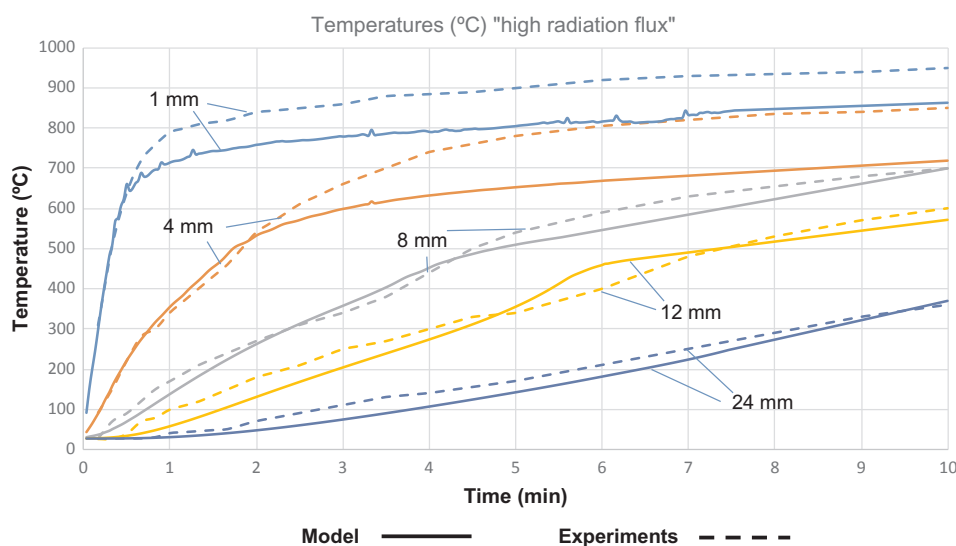


Fig. 8. Comparison of model predictions and experimental temperatures for pine wood irradiated with a high radiation flux.

parameters, such as thermal conductivity and specific heat may not be especially accurate at high temperatures. In the one hand, thermal conductivity is modelled as a function of the local density and biomass composition. However, it is not a function of temperature. On the other hand, specific heat is a function of composition and temperature, but these polynomial functions may not be especially accurate at high temperatures. The consideration of isotropic mass transfer inside the particle could affect to these discrepancies too. A consequence of this is the fact that the model underpredicts the evolution of the superficial thermocouples which are the ones that reach the highest temperatures. The predictions also showed a change in the temperature slope in the deepest thermocouples when temperature reaches around 350–400 °C. This is the temperature range in which devolatilization starts. Therefore, as the local density of wood decreases, the particle is heated more easily. Otherwise, when the thermal conversion progresses and char is generated, the thermal conductivity decreases and heating slows down. This behaviour is noticeable in the deeper thermocouples since, in the superficial ones (1 mm and 4 mm), it occurs when the heating is very abrupt. A similar but softer trend seems to happen in the experimental

data at slightly higher temperatures.

3.4. Particle shrinkage

The shrinkage produced by the particle after 10 min of radiation exposure can be visualized using an isosurface with a minimum value of 0.1 for the solid fraction, and this can be compared with the initial particle. Fig. 10 shows this isosurface representation for the simulated particle and images of the pine particles used by Grønli [45] in his experiments before and after radiation exposure. The colours of the simulation images show the areas with wood or char. Significant shrinkage is visible in the experiment with a high radiation flux but not in the one with low radiation. The global longitudinal shrinkage is similar to that in the experimental images. However, radial shrinkage is only noticeable in the higher and lower regions and not in the middle of the particle. This is a consequence of the shrinkage algorithm which smooths the corners. In the middle of the pellet, the model also works, however the empty cells are filled with mass of the adjacent cells in the sides. This is possible since the mass movements happen in the direction

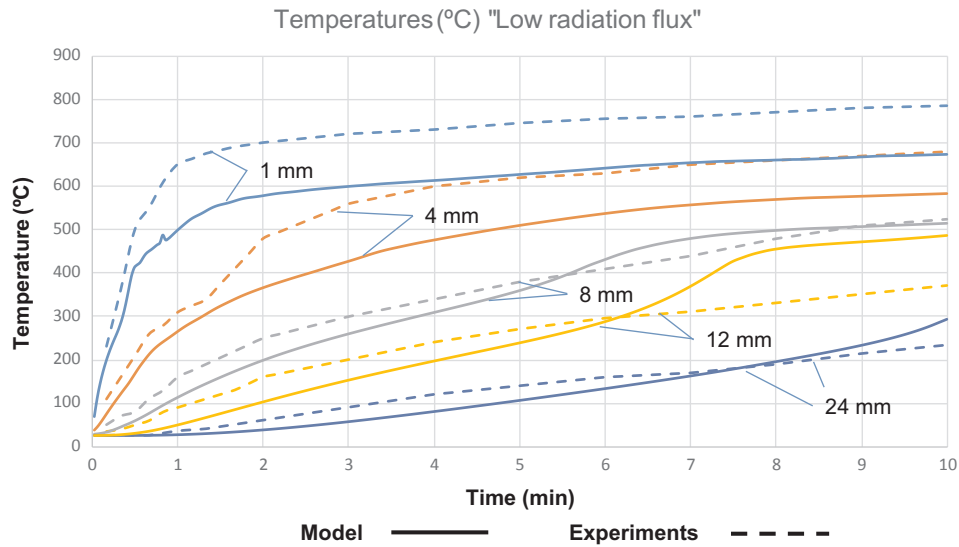


Fig. 9. Comparison of model predictions and experimental temperatures for pine wood irradiated with a low radiation flux.

of the vector pointing from each cell to the mass centre of the particle and a fraction of the cell mass can fill the middle cells in every compaction movement. This is a weakness of the model which is highly unrealistic in the middle of the pellet. The model still needs some development to solve this aspect. In addition, the model may work more appropriately if the various parameters involved, such as the specific

densities or the threshold solid fractions, are studied in detail. Regardless, there was a reasonably good approximation to the global shrinkage in large pieces of biomass.

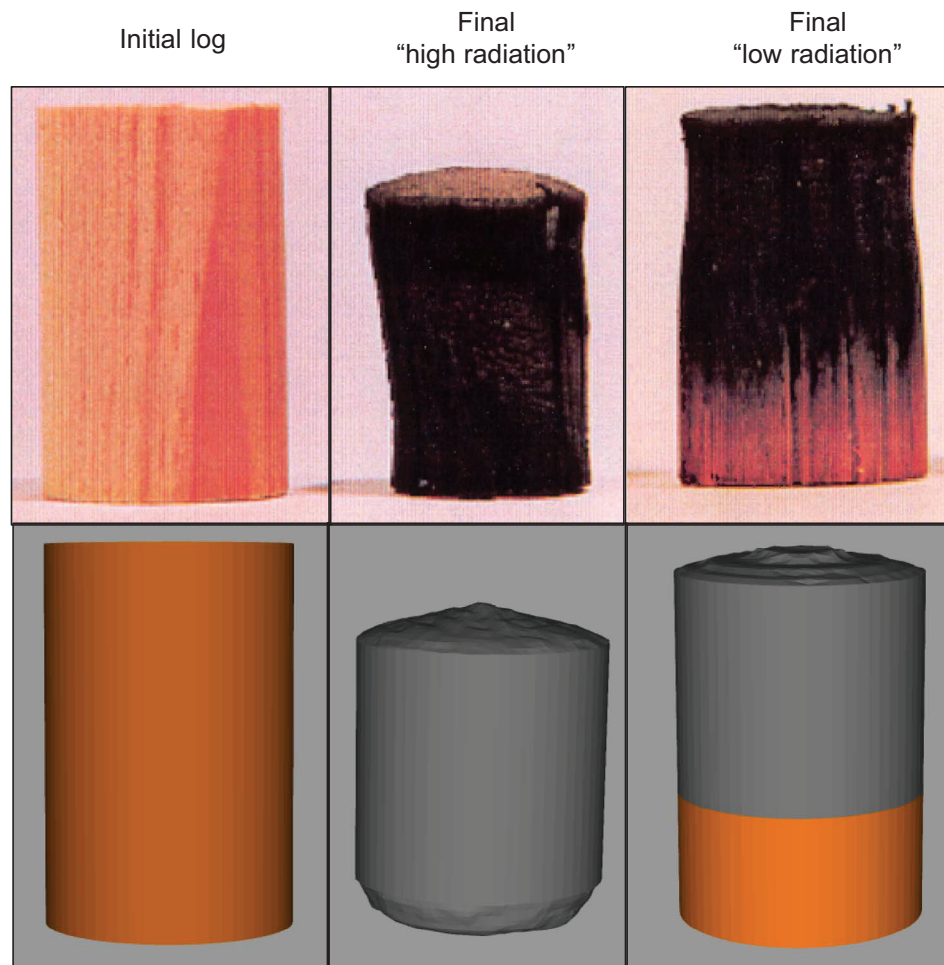


Fig. 10. Comparison of experimental particle images and isosurfaces of the solid fraction predicted by the model at the end of the tests.

4. Conclusions

This paper presents a comprehensive model for the simulation of the thermal conversion of large pieces of biomass. The model implements several variables that represent the state of the solid biomass in a CFD environment. Several submodels for heat transfer, reaction and particle shrinkage represent the physical phenomena that occur during biomass combustion. An experimental reactor, in which a biomass particle is irradiated with a xenon lamp, was simulated to test the conversion model. Two tests of ten minutes of exposure to different radiation intensities were simulated for pine wood. The main variables in the model allow analysis of the devolatilization front, the reaction temperatures and the gaseous emissions. The results of the simulations were compared with experimental measurements to evaluate the temperatures predicted by the model. A reasonably similar behaviour was found for the temperature evolution, considering uncertainties in the conditions, biomass composition and properties. In addition, a visualization of the global particle shrinkage after the tests was analysed and exhibited a relatively similar behaviour to that of the experiments. Some similarities between the model results and experiments were found; however, the model still needs to be developed and adjusted to achieve results that are more accurate.

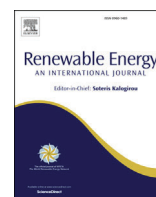
The model presented in this work can contribute to previous works through accurate three-dimensional predictions in a whole reactor, particle and gas. In addition, other submodels such as directional radiation in the whole computational domain, ash content consideration, interaction between particle with an accurate convective exchange, even under turbulent conditions, and a complete shrinkage model, at local (cell) and global (particle) scales complete a detailed comprehensive model.

Acknowledgements

The authors acknowledge financial support from Project ENE2015-67439-R of the Ministry of the Economy of Spain.

References

- Porteiro J, Granada E, Collazo J, Patiño D, Morán JC. Numerical modeling of a biomass pellet domestic boiler. *Energy Fuel* 2009;23:1067–75.
- Shin D, Choi S. The combustion of simulated waste particles in a fixed bed. *Combust Flame* 2000;121:167–80.
- Collazo J, Porteiro J, Míguez JL, Granada E, Gómez MA. Numerical simulation of a small-scale biomass boiler. *Energy Convers Manage* 2012;64:87–96.
- Thunman H, Leckner B. Modelling of the combustion front in a counter current fuel converter. *Proc Combust Inst* 2002;29:511–8.
- Gómez MA, Comesaña R, Álvarez Feijoo MA, Eguía P. Simulation of the effect of water temperature on domestic biomass boiler performance. *Energies* 2012;5:1044–61.
- Yin C, Rosendahl L, Kær SK, Clausen S, Hvid SL, Hiller T. Mathematical modeling and experimental study of biomass combustion in a thermal 108 MW grate-fired boiler. *Energy Fuel* 2008;22:1380–90.
- Zhou H, Jensen AD, Glarborg P, Jensen PA, Kavaliuskas A. Numerical modeling of straw combustion in a fixed bed. *Fuel* 2005;84:389–403.
- Kær SK. Numerical modelling of a straw-fired grate boiler. *Fuel* 2004;83:1183–90.
- van der Lans RP, Pedersen LT, Jensen A, Glarborg P, Dam-Johansen K. Modelling and experiments of straw combustion in a grate furnace. *Biomass Bioenergy* 2000;19:199–208.
- Yang YB, Sharifi VN, Swithenbank J. Numerical simulation of the burning characteristics of thermally-thick biomass fuels in packed beds, *Trans IChemE Part B. Process Saf Environ Prot* 2005;83:1–11.
- Collazo J, Porteiro J, Patiño D, Granada E. Numerical modeling of the combustion of densified wood under fixed-bed conditions. *Fuel* 2012;93:149–59.
- Gómez MA, Porteiro J, Patiño D, Míguez JL. CFD modelling of thermal conversion and packed bed compaction in biomass combustion. *Fuel* 2014;117:716–32.
- Karim MR, Naser J. Numerical study of the ignition front propagation of different pelletized biomass in a packed bed furnace. *Appl Therm Eng* 2018;128:772–84.
- Karim MR, Naser J. Progress in numerical modelling of packed bed biomass combustion. In: 19th Australasian fluid mechanics conference Melbourne, Australia; 2014.
- Karim MR, Bhuiyan AA, Naser J. Modeling of solid and bio-fuel combustion technologies, thermofluid modeling for energy efficiency applications 1. Elsevier Publications; 2016. 259–309.
- Mehrabian R, Zahirovic S, Scharler R, Obernberger I, Kleditzsch S, Wirtz S, et al. A CFD model for thermal conversion of thermally thick biomass particles. *Fuel Process Technol* 2012;95:96–108.
- Ström H, Thunman H. CFD simulations of biofuel bed conversion: a submodel for the drying and devolatilization of thermally thick wood particles. *Combust Flame* 2013;160:417–31.
- Gómez MA, Porteiro J, Patiño D, Míguez JL. Fast-solving thermally thick model of biomass particles embedded in a CFD code for the simulation of fixed-bed burners. *Energy Convers Manage* 2015;105:30–44.
- Gómez MA, Porteiro J, De la Cuesta D, Patiño D, Míguez JL. Dynamic Simulation of a Biomass Domestic Boiler Under Thermally Thick Considerations. *Energy Convers Manage* 2017;140:260–72.
- Mahmoudi AM, Besseron X, Hoffmann F, Markovic M, Peters B. Modelling of the biomass combustion on a forward acting grate using XDEM. *Chem Eng Sci* 2016;142:32–41.
- Wiese J, Wissing F, Höhner D, Wirtz S, Scherer V, Ley U, et al. DEM/CFD Modelling of the fuel conversion in a pellet stove. *Fuel Process Technol* 2016;152:223–39.
- Porteiro J, Granada E, Collazo J, Patiño D, Morán JC. A Model for the Combustion of Large Particles of Densified Wood. *Energy Fuel* 2007;21:3151–9.
- Babu BV, Chaurasia AS. Heat transfer and kinetics in the pyrolysis of shrinking biomass particle. *Chem Eng Sci* 2004;59:1999–2012.
- Carnahan B, Luther HA, James OW. *Applied Numerical Methods*. New York: Wiley; 1969.
- Lu H, Robert W, Peirce G, Ripa B, Baxter LL. Comprehensive study of biomass particle combustion. *Energy Fuel* 2008;22:2826–39.
- Thunman H, Leckner B, Niklasson F, Johnsson F. Combustion of wood particles – a particle model for Eulerian calculations. *Combust Flame* 2002;129:30–46.
- Gronli MG, Melaen MC. Mathematical model for wood pyrolysis - comparison of experimental measurements with model predictions. *Energy Fuel* 2000;14:791–800.
- Shi X, Ronsse F, Pieters JG. Finite element modeling of intraparticle heterogeneous tar conversion during pyrolysis of woody biomass particles. *Fuel Process Technol* 2016;148:302–16.
- Okekunle PO, Pattanotai T, Watanabe H, Okazaki K. Numerical and experimental investigation of intra-particle heat transfer and tar decomposition during pyrolysis of wood biomass. *J Therm Sci Technol* 2011;6:360–75.
- Soria J, Zeng K, Asensio D, Gauthier D, Flamant G, Mazza G. Comprehensive CFD modelling of solar fast pyrolysis of beech wood pellets. *Fuel Process Technol* 2017;158:226–37.
- Gómez MA, Porteiro J, Patiño D, Míguez JL. Eulerian CFD modelling for biomass combustion. Transient simulation of an underfeed pellet boiler. *Energy Convers Manage* 2015;101:666–80.
- Di Blasi C. Modeling wood gasification in a countercurrent fixed-bed reactor. *AIChE J*. 2004;50:2306–19.
- Zobel N, Anca-Couce A. Slow pyrolysis of wood particles: characterization of volatiles by Laser-Induced Fluorescence. *Proc Combust Inst* 2013;34:2355–62.
- Wagenaar BM, Prins W, Swaaij van WPM. Flash pyrolysis kinetics of pine wood. *Fuel Process Technol* 1993;36:291–8.
- Gómez MA, Porteiro J, De la Cuesta D, Patiño D, Míguez JL. Numerical simulation of the combustion process of a pellet-drop-feed boiler. *Fuel* 2016;184:987–99.
- Hagge M, Bryden K. Modeling the impact of shrinkage on the pyrolysis of dry biomass. *Chem Eng Sci* 2002;57:2811–23.
- Bryden KM, Ragland KW. Modeling of a deep, fixed bed combustor. *Energy Fuel* 1996;10:269–75.
- Rashidian B, Al-Abdeli YM, Yeoh GH, Guzzomi FG. Effect of freeboard deflectors on the temperature distribution in packed beds. *Appl Therm Eng* 2015;89:134–43.
- Alganash B, Paul MC, Watson IA. Numerical investigation of the heterogeneous combustion processes of solid fuels. *Fuel* 2015;141:236–49.
- Casal JM, Porteiro J, Míguez JL, Vázquez A. New methodology for CFD three-dimensional simulation of a walking beam type reheating furnace in steady state. *Appl Therm Eng* 2015;86:69–80.
- Bhuiyan AA, Naser J. Computational modelling of co-firing of biomass with coal under oxy-fuel condition in a small scale furnace. *Fuel* 2015;143:455–66.
- Bhuiyan AA, Naser J. Numerical modelling of oxy fuel combustion, the effect of radiative and convective heat transfer and burnout. *Fuel* 2015;139:268–84.
- Mikulčić H, Von Berg E, Vujanović M, Duić N. Numerical study of co-firing pulverized coal and biomass inside a cement calciner. *Waste Manage Res* 2014;32:661–9.
- Rebola A, Azevedo JLT. Modelling coal combustion with air and wet recycled flue gas as comburent in a 2.5 MWth furnace. *Appl Therm Eng* 2015;86:168–77.
- Gronli MG. A Theoretical and experimental study of the thermal degradation of biomass [Ph.D. thesis]. The Norwegian University of Science and Technology.
- Thunman H, Niklasson F, Johnsson F, Leckner B. Composition of volatile gases and thermochemical properties of wood for modeling of fixed or fluidized beds. *Energy Fuel* 2001;15:1488–97.
- Gómez MA, Patiño D, Comesaña R, Porteiro J, Álvarez Feijoo MA, Míguez JL. CFD simulation of a solar radiation absorber. *Int J Heat Mass Transfer* 2013;57:231–40.
- Versteeg HK, Malalasekera W. An introduction to computational fluid dynamics. 2nd ed. The finite volume method Pearson; 1995.
- Blondeau J, Jeanmart H. Biomass pyrolysis at high temperatures: prediction of gaseous species yields from an anisotropic particle. *Biomass Bioenergy* 2012;41:107–21.
- Purnomo D, Aerts J, Ragland KW. Pressurized downdraft combustion of woodchips twenty-third symposium (International) on combustion/The combustion institute;1990. p. 1025–32.



Numerical analysis of wood biomass packing factor in a fixed-bed gasification process

William A. González ^a, Juan F. Pérez ^{a,*}, Sergio Chapela ^b, Jacobo Porteiro ^b

^a Grupo de Manejo Eficiente de la Energía (GIMEL), Departamento de ingeniería Mecánica, Facultad de ingeniería, Universidad de Antioquia, Calle 67 No. 53-108, Medellín, Colombia

^b E.T.S. Ingenieros Industriales, Universidad de Vigo, Rúa Maxwell s/n, Campus Lagoas-Marcosende, 36310 Vigo, Pontevedra, Spain



ARTICLE INFO

Article history:

Available online 18 January 2018

Keywords:

Biomass
Packing factor
Fixed bed gasification
CFD
Numerical analysis
Heat transfer

ABSTRACT

The biomass gasification process in fixed bed was studied by means of computational fluid dynamics (CFD) numerical analysis. The aim was to evaluate the effect of the biomass packing factor on the thermochemical process. The fuel-wood used was *Jacaranda Copaia* in various shapes: chips, cylinders, and cubes with packing factors (PF) of 0.38, 0.48, and 0.59, respectively. The mathematical model is a transient 2D CFD model, which was developed through the implementation of User Defined Functions in ANSYS-Fluent. The model was extended to simulate the gasification process by expanding the chemical kinetic mechanism and by adapting the stages of pyrolysis, oxidation, and reduction. The model was validated with experimental data. The average relative error between experimental and numerical data was 5.45%. By means of the sensitivity analysis, it was found that with an increase in the packing factor from 0.38 to 0.59, the absorption of radiative heat transfer increases by 27% leading to increase the solid temperature in the reaction front, but due to a lower penetration of radiation, the drying and pyrolysis reaction rates decrease. But nevertheless, the higher solid temperature with packing factor favors the convective solid-gas heat transfer in the drying stage.

© 2018 Elsevier Ltd. All rights reserved.

1. Introduction

Biomass is a renewable energy source and its energy use in fixed bed gasifiers is an important process for power generation and cooking systems [1]. The comprehension of thermal, physical, and chemical phenomena involved in the biomass to gas (BTG) transformation enables improved reactor efficiency and reduced pollutant emissions [2]. The gasification process includes mass transfer mechanisms associated with drying, pyrolysis, oxidation, and reduction stages, and energy transfer mechanisms, such as convection and radiation. Therefore, acquisition of experimental data with complex parameters during the experimental stage is challenging [3]. Modeling helps to describe system behavior, enabling identification of complex phenomena, such as incident radiation, solid-gas heat transfer, diffusive parameters, and the kinetic interaction of particles in solid-gas reactions [4,5].

There is an ongoing line of work in the scientific community that study the conversion of biomass in fixed beds by means of CFD

models using commercial software. The CFD models require a phenomenological description of the biomass conversion to gaseous fuels. This interaction between the solid and gas phases has been implemented through User Defined Functions (UDFs), where sub models created in C++ were adapted; these sub-models are embedded into the code and therefore are also solved by the CFD software [2,6,7].

CFD models of biomass combustion and/or gasification in fixed beds have been used to study the phenomenology involved during thermochemical conversion, various important operation parameters of the process, and chemical kinetic mechanisms, and physical properties of biomass have been analyzed. Several authors developed dimensional models for both combustion [2,3,8] and gasification [9,10] in fixed beds, with their work aiming to study the influence of the heterogeneous properties of the bed during combustion, and to compare temperature fields and gaseous concentrations in the two-dimensional domain during gasification. Other authors used numerical models for validating such parameters as combustion time, furnace temperature, combustion gases emissions (including NO_x), carbon content in the ashes, and combustion total efficiency [11]. Regarding fixed bed combustion, several

* Corresponding author.

E-mail address: juanpb@udea.edu.co (J.F. Pérez).

studies experimentally measured flame front velocity, process speed movement (which is dependent on the air supply velocity), biomass heating value, and particle size in order to obtain a transient behavior of the local temperature, oxygen consumption rate, and heat transfer phenomena using model predictions [12]. Other authors have also validated gas composition for different air flows in downdraft gasification, as well as the temporal and spatial evolution of temperature, comparing model results with experimental ones available in the literature [13]. For downdraft gasifiers, the Lagrangian model to predict the temperature field inside the reactor, and comparing the theoretical temperature distribution with experimental data has been proposed by Janajreh et al. [14]. Other studies have focused on the analysis of the effect of the geometry and configuration of the combustion chamber over combustion efficiency, emissions and process temperature [6]. Regarding biomass shape and size, there are thermochemical conversion models used to predict the intra-particle temperature gradient, mass loss rate, particle size and density [7]. Physicochemical and geometrical properties of biomass have also been studied during the operation of reactors and burners, with several authors presenting numerical models where two types of geometries can be evaluated, including cylindrical particles (horizontal and upright) and spherical ones [7]. Other authors have focused on the analysis of the biomass gasification process through the evaluation of different types of biomass with several particle geometries, considering physicochemical properties, such as density, void fraction, sphericity, surface/volume ratio [13] and particle diameter [6].

The literature also presents the characterization and analysis of the flame front and process velocity movement as functions of the input experimental settings, such as air mass flow, biomass heating value and particle size. Those studies analyze the transient evolution of the reaction front for all solid to gas conversion stages [13], studying mass and heat transfer phenomena (including radiation, convection, and conduction phenomena) [12].

In general, CFD numerical models enable the prediction of the reactor/plant behavior to the variation of several operating conditions [11], where the analyses of the channeling generated in the bed is highlighted. Channeling has been blamed of generating higher concentrations of nitrous oxides and unburned products under combustion regimes [8]. This work presents a fixed bed biomass combustion model that has been extended to tackle gasification conditions. The effect of the packing factor on the gasification process behavior was evaluated. The validating parameters are temperature fields, flame front velocity, biomass consumption rate, syngas volumetric flow, low heating gas, equivalence ratio, cold gas efficiency, and producer gas composition. Afterwards, a sensitivity analysis of convection and radiation heat transfer mechanisms was performed in function of biomass packing factor, enabling a better description of the phenomenology involved in the process with different physical properties of wood biomass. The model used in this work allows to study different types of biomass, such as energy crops, forest, agricultural waste, and others, as renewable feedstock for thermochemical processes. These solid biofuels are characterized by different densities (bulk and particle) [15]. The packing factor (PF) quantifies the relationship between these two parameters of significant importance for the biomass gasification process in fixed bed [16].

2. Materials and methods

According to the state of the art, the numerical analyses of the effect of biomass packing factor ($PF = \text{Average bulk density}/\text{Particle density}$) on fixed bed gasification/combustion by means of models

or experimental tests are scarce. The PF parameter is a fundamental variable that affects gasification performance due to the random packing of biomass in a fixed bed [17]. Therefore, the packing factor is the process parameter (the operating condition as a function of biomass physical properties) considered in this study. Three values for the PF were studied and selected to perform the sensitivity analysis. The three geometries of wood biomass are chips, cylinders and cubes, with a PF of 0.38, 0.48 and 0.59, respectively.

The performance of the biomass gasification process as a function of PF has been evaluated in this work by analyzing its effect on heat transfer mechanisms of the reaction front (solid-gas convective heat transfer and radiative heat transfer in solid phase) among other key variables, such as solid temperature field, flame front velocity, biomass consumption rate, gas velocity, and fuel/air equivalence ratio. These parameters are the results obtained from the CFD model.

The experimental setup shown in Fig. 1 was designed and built for determining the process propagation velocity during biomass gasification in a batch type gasifier [18]. This reactor is known as a top-lit updraft reactor, or reverse downdraft fixed-bed reactor; the experimental setup is described in section 2.1. The experimental results were taken from a previous work presented by Lenis et al. [1] and were used to validate the CFD model as described in Section 3.

The model accuracy can be quantified through the root mean square error (RMSE) (see Eq. (1)). Other authors have used this parameter to determine the errors of gasification models with regard to the experimental data [19,20].

$$RMSE = \sqrt{\frac{\sum_{i=1}^n (X_{\text{reference},i} - X_{\text{model},i})^2}{n}} \quad (1)$$

2.1. Fuel physical and chemical characterization

The biomass used in the experimental tests considered as reference to validate the CFD model under gasification conditions is *Jacaranda Copaia* wood, this is a fast-growing wood native from Latin America, which reaches yields between 25 and 35 m³/ha/year with harvested time around 15 years [1]. Table 1 shows the biomass physical and chemical characterization for different shapes of wood fuels. Moreover, the volumetric airflow that has been setting in each experimental test is presented. The complete experimental study is shown in detail by Lenis et al. [1].

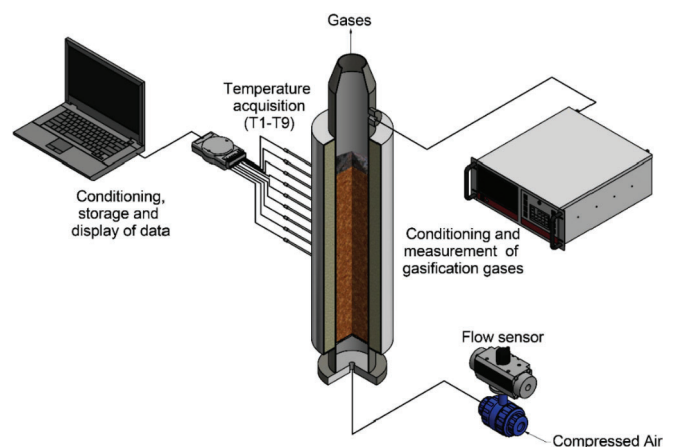





Fig. 1. Experimental setup.

Table 1
Physical and chemical characterization of *Jacaranda Copaia* woods (\pm standard deviation).

Properties	Wood biomass shape		
	Chips	Cylinders	Cubes
			
Air flow [slpm]	40.93 \pm 0.67	40.68 \pm 0.71	40.83 \pm 0.69
Dimensions [mm \pm 0.1 mm]	6–13	\varnothing 10 \times L8	10 \times 10 \times 8
Average bulk density [kg/m ³]	130.07 \pm 0.57	209.61 \pm 2.38	198.59 \pm 1.55
Particle density [kg/m ³]	344.21 \pm 16.01	434.43 \pm 15.92	338.52 \pm 11.19
Particle average hardness [Shore D]	33.75 \pm 3.08	43.75 \pm 2.41	33.82 \pm 3.62
Packing factor [–]	0.38 \pm 0.02	0.48 \pm 0.02	0.59 \pm 0.02
Equivalent radius [mm]	5.65 \pm 4.2	6.35 \pm 4.4	6.8 \pm 2.3
Sphericity [–]	0.76 \pm 0.11	0.85 \pm 0.09	0.79 \pm 0.02
Moisture [%]	5.4 \pm 0.02	9.4 \pm 0.1	9.4 \pm 0.1
Surface area/volume [mm ⁻¹]	0.69 \pm 0.02	0.55 \pm 0.01	0.56 \pm 0.01
Proximate analysis [% wt. d.b.]			
Volatile matter	89.92		
Fixed carbon	8.67		
Ash	1.41		
Ultimate analysis [%wt. d.a.f.]			
C	49.88		
H	7.35		
O	41.08		
N	1.52		
S	0.17		
Substitution formula [d.a.f]	CH _{1.769} O _{0.617} N _{0.026} S _{0.001}		
LHV _{db} [kJ/kg]	18212.95		

2.2. Experimental setup

The experimental setup used for validating the data obtained by simulation consists of a laboratory autothermal fixed bed gasifier that operates under atmospheric pressure and temperatures between 800 °C and 1000 °C under statistical repeatability conditions [17]. The main dimensions of the reactor are 102 mm internal diameter, 185 mm external diameter, and a bed length of 400 mm. The gasifying agent during the process is air, obtained from the lab's compressed air line, which is controlled by pressure regulators and valves, and measured by a Honeywell AWM500 flow meter. The gasifier gas outlet has a conditioning unit (drying and filtering) to measure the syngas composition (O₂, N₂, CO₂, CO, H₂ and CH₄) using Agilent 3000 Micro GC gas chromatography.

The gasifier is fed with biomass of different shapes, and it is lit from the top; this reactor is also known as an inverse reactor or top-lit up-draft (TLUD) reactor. The gasifying agent (air) is supplied from the bottom, causing a downward propagating reaction front. The temperature profile is measured by nine K type thermocouples with a separation between each one of 30 mm; these are inserted up to the center of the reactor as the fuel is fed. Fig. 1 shows a scheme of the experimental setup. Characteristic variables, such as the flame front progress from top to bottom, are measured. It is possible to assert that tests are conducted under unsteady state. This is because the gasifier walls are heated as the flame front advances [17]. A full description of this experimental configuration and the parameters derived thereof are described in detail in Refs. [4,21,22].

3. Model description

The fixed bed biomass gasification approach was developed by

considering separately the solid and gaseous phases. The model presented in this work is an extended version of the model developed for biomass combustion in fixed beds. All the solid parameters are formulated as Eulerian scalars that are embedded into the code by User Defined Scalars (UDS). The interaction between phases is modelled as sources in the corresponding transport equations, which are introduced in the code by User Defined Functions (UDFs) [2,3,6,7]. The solid fuel transformation in a gaseous fuel considers the main stages involved in the gasification

Table 2
Solid phase conservation equations.

$$\text{Solid phase energy conservation} \\ \frac{\partial(\epsilon \rho_p C_p T_s)}{\partial t} = \nabla \cdot (k_{s,\text{eff}} \cdot \nabla T_s) + S_s \quad (2)$$

$$\text{Solid fraction} \\ \frac{\partial \epsilon}{\partial t} = -\frac{\dot{\omega}_{\text{char}}'''}{\rho_p} \epsilon \quad (3)$$

$$\text{Moisture density} \\ \frac{\partial(\epsilon \rho_{\text{moist}})}{\partial t} = -\dot{\omega}_{\text{moist}}'''\epsilon \quad (4)$$

$$\text{Dry wood density} \\ \frac{\partial(\epsilon \rho_{\text{wood}})}{\partial t} = -\dot{\omega}_{\text{wood}}'''\epsilon \quad (5)$$

$$\text{Char density} \\ \frac{\partial(\epsilon \rho_{\text{char}})}{\partial t} = (\dot{\omega}_{\text{G,char}}'' - \dot{\omega}_{\text{C,char}}''')\epsilon \quad (6)$$

$$\text{Solid energy Source} \\ S_s = S_s^{\text{reac}} + S_{\text{char}}^{\text{reac}} + S_s^{\text{conv}} + S_s^{\text{rad}} + S_s^{\text{loss}} \quad (7)$$

process, such as drying, pyrolysis, oxidation, and reduction [4]. The species of solid phase (biomass) are solid fraction, moisture density, dry biomass density, char density and solid phase temperature [2]. The geometry of solid biomass is also considered to estimate the parameters involved in the solid-gas mass and heat transfer mechanisms. The model has been developed under the following hypothesis:

- 1) The bed is considered fixed during the time-step, i.e., any movement of the solid due to the feeding process or due to compaction of the bed, takes place at the end of the time-step and before the next one.
- 2) Biomass particles are considered thermally thin [4,23].
- 3) The volume of biomass does not vary during the drying and pyrolysis processes (shrinking density regime) [3,4].

Table 3
Energy source terms.

$$S_s^{\text{react}} = -\dot{\omega}'_{\text{mois}} e \text{ LH}_{\text{moist}} - \dot{\omega}'_{\text{wood}} f_{\text{gas}} e \text{ H}_{\text{dev}} + S_{\text{char}}^{\text{react}} e \quad (8)$$

$$S_{\text{char}}^{\text{react}} = \left(k_{\text{glob}}^{\text{ox}} A_v C_{\text{O}_2} M_C [(2\phi - 1)\Delta H_{\text{CO}_2} + 2(1 - \phi)\Delta H_{\text{CO}}] + k_{\text{glob}}^{\text{g1}} A_v C_{\text{CO}_2} M_C \Delta H_{\text{g1}} + k_{\text{glob}}^{\text{g2}} A_v C_{\text{H}_2\text{O}} M_C \Delta H_{\text{g2}} \right) k_{\text{s/g}} \quad (9)$$

$$S_s^{\text{conv}} = -S_g^{\text{conv}} = hA_v (T_g - T_s) \quad (10)$$

$$S_s^{\text{rad}} = \int_0^{4\pi} \left(\alpha_s I(r, s) - \frac{\alpha_s n^2 \sigma T_s^4}{\pi} \right) d\Omega \quad (11)$$

$$S_s^{\text{loss}} = \left(\dot{\omega}'_{\text{mois}} + \dot{\omega}'_{\text{wood}} f_{\text{gas}} + \dot{\omega}'_{\text{char}} \right) \varepsilon (C_p T_s)^{t-\Delta t} \quad (12)$$

Table 4
Chemical reactions.

Process	Chemical reaction
Drying	$R_m : \text{H}_2\text{O}_l \xrightarrow{k_m} \text{H}_2\text{O}_v \quad (13)$
Pyrolysis	$R_{p1} - R_{p3} : \text{Biomass} = \begin{cases} \xrightarrow{k_{p1}} \text{gas} \\ \xrightarrow{k_{p2}} \text{tars} \\ \xrightarrow{k_{p3}} \text{char} \end{cases} \quad (14)$
Heterogeneous char reactions	$R_{\text{ox}} : \text{C} + \phi \text{O}_2 \xrightarrow{k_{\text{ox}}} 2(1 - \phi)\text{CO} + (2\phi - 1)\text{CO}_2 \quad (15)$
	$R_{\text{g1}} : \text{C} + \text{CO}_2 \xrightarrow{k_{\text{g1}}} 2\text{CO} \quad (16)$
	$R_{\text{g2}} : \text{C} + \text{H}_2\text{O} \xrightarrow{k_{\text{g2}}} \text{CO} + \text{H}_2 \quad (17)$
Homogeneous reactions	$R_{\text{c1}} : \text{C}_6\text{H}_6 + 4.5\text{O}_2 \xrightarrow{k_{\text{c1}}} 6\text{CO} + 3\text{H}_2\text{O} \quad (18)$
	$R_{\text{c2}} : \text{CH}_4 + 1.5\text{O}_2 \xrightarrow{k_{\text{c2}}} \text{CO} + 2\text{H}_2\text{O} \quad (19)$
	$R_{\text{c3}} : 2\text{CO} + \text{O}_2 \xrightarrow{k_{\text{c3}}} 2\text{CO}_2 \quad (20)$
	$R_{\text{c4}} : 2\text{H}_2 + \text{O}_2 \xrightarrow{k_{\text{c4}}} 2\text{H}_2\text{O} \quad (21)$
	$R_{\text{g3}} : \text{CH}_4 + \text{H}_2\text{O} \xrightarrow{k_{\text{g3}}} \text{CO} + 3\text{H}_2 \quad (22)$
	$R_{\text{wg}} : \text{CO} + \text{H}_2\text{O} \xrightarrow{k_{\text{wg}}} \text{CO}_2 + \text{H}_2 \quad (23)$

- 4) The volume (particle size) of the biomass particle is affected by the oxidation and reduction reactions according to the shrinking core regime [24].
- 5) The moisture evaporation temperature is 100 °C and the process is thermally controlled [3,24].
- 6) The gases are considered as an ideal gas mixture [4,24].
- 7) Immediate outflow, i.e., there is no diffusion limitation for the gases from the interior of the particles to their surface.
- 8) The solid-gas reaction (oxidation and reduction) starts after the devolatilization process ends [3].

The CFD model presented in this work uses the SIMPLE algorithm for the governing equations [3,8]. The momentum and energy special discretization were solved through a second order upwind method, while radiation and pressure discretization were solved using PRESTO [25]. The radiation heat transfer was modelled using a modification of the Discrete Ordinate Model (DOM) where the solid phase is included [2,3]. The turbulence was modelled by the k-epsilon model with Enhanced Wall Treatment (EWT).

The model presents a conservative equation for each scalar variable of the solid phase. Table 2 shows the conservative equations used by the model (Eqs. (2)–(6)). The energy conservation of the solid phase is described by Eq. (2). This is a two dimensional and unsteady differential equation. The mass conservation of solid fraction, moisture density, dry wood density, and char density were modelled by Eqs. (3)–(6). The source term of the energy balance for the solid phase is presented in Eq. (7). These energy sources involve the energy consumed by drying, pyrolysis, and reduction, and the energy released by oxidation. Moreover, the convective and radiative heat transfer mechanisms, and the heat losses are considered in this energy source. The complete description of the model was presented in detail by Gómez et al. and Collazo et al. [2,3].

Table 3 shows the different source terms of the energy equation in solid phase (Eq. (7)). Eq. (8) is the absorbed energy during the drying and devolatilization processes, S_{char}^{react} term is represented in Eq. (9). This source term accounts for the energy released or consumed due to char reactions (oxidation and reduction). The convective heat exchange is opposite to the gas phase energy source (Eq. (10)). Through this parameter the convective solid-gas heat transfer is calculated. Eq. (11) is the approach to the radiation source term in the solid phase. The calculated energy loss due to the loss of solid mass in a cell over time is expressed in Eq. (12).

The chemical reactions of the previous model, biomass combustion under fixed bed conditions, considers the drying, pyrolysis, oxidation of char, tar, methane, hydrogen, and carbon monoxide dissociation [2,3]. However, the kinetic rates of these reactions had been adapted looking that the model estimate the producer gases composition with good accuracy, the kinetic rates of the reaction mechanism considered in this model are presented in Tables 5 and 7. To extend the model for simulating the biomass gasification process under fixed bed conditions, the kinetic mechanism was extended to include the reduction of steam, carbon dioxide, and hydrogen with char in the heterogeneous reactions (see Eqs (14)–(16)). Moreover, the methane reforming and the water gas shift reaction have been included in the homogeneous reaction mechanism, see Eqs. (17)–(22). The new kinetic mechanism was adapted to model the different sub-processes involved in the fixed bed gasification process [4].

The moisture evaporation temperature is 100 °C, but the model considers that in the already dried external layers, heating continues. Consequently, when the biomass particle starts to dry, a portion of the heat gained is used for drying the inner layers while the rest is invested in the overheating of the outer layers. This effect modelled by Eq. (24), in which only part of the heat gained by the

particle ($\tau = 0.5$) is employed for moisture evaporation. The pyrolysis is considered a conversion of the dry biomass into gas, tar, and char. The kinetic reaction of this process is modelled by three Arrhenius rates (Eq. (25) and Table 5).

$$\dot{\omega}_{moist}''' = \tau \frac{\rho_p C_p}{LH_{moist}} \frac{\partial T_s}{\partial t}, T_s \geq T_{evap} \quad (24)$$

Table 5
Kinetics of pyrolysis reactions.

k_i	A_i	Units of A_i	E_i [J·mol ⁻¹]	Ref.
k_{p1}	$1.44 \cdot 10^4$	s ⁻¹	88000	[26]
k_{p2}	$4.13 \cdot 10^6$	s ⁻¹	112700	[26]
k_{p3}	$7.38 \cdot 10^5$	s ⁻¹	106500	[26]

Table 6
Kinetics of heterogeneous char reactions.

k_i	A_i	Units of A_i	E_i [J·mol ⁻¹]	Ref.
k_{ox}	$1.7 \cdot T_s$	m·s ⁻¹	74830	[27,28]
k_{g1}	$3.42 \cdot T_s$	m·s ⁻¹	129700	[27,28]
k_{g2}	$5.7114 \cdot T_s$	m·s ⁻¹	129700	[28]

Table 7
Volumetric source terms in the solid-gas reactions.

$$S_{H_2O,moist} = \dot{\omega}_{moist}''' \epsilon \quad (29)$$

$$S_{i,vol} = \gamma_i (\dot{\omega}_{wood}''' - \dot{\omega}_{g,char}''') \epsilon \quad (30)$$

$$S_{CO_2,char} = ((2\phi - 1)k_{glob}^{ox} A_v C_{CO_2} M_{CO} - k_{glob}^{g1} A_v C_{CO_2} M_{CO_2}) \epsilon \quad (31)$$

$$S_{CO_2,char} = ((2\phi - 1)k_{glob}^{ox} A_v C_{CO_2} M_{CO} + 2k_{glob}^{g1} A_v C_{CO_2} M_{CO} + k_{glob}^{g2} A_v C_{H_2O} M_{CO}) \epsilon \quad (32)$$

$$S_{H_2O,char} = -k_{glob}^{g2} A_v C_{H_2O} M_{H_2O} \epsilon \quad (33)$$

$$S_{H_2,char} = k_{glob}^{g2} A_v C_{H_2O} M_{H_2} \epsilon \quad (34)$$

$$S_{O_2,char} = -\phi k_{glob}^{ox} A_v C_{O_2} M_{O_2} \quad (35)$$

Table 8
Kinetic rate of homogeneous reactions.

Reaction	Kinetic rate [kmol/m ³ /s]	Ref.
R_{c1}	$\dot{\omega}_{c1}''' = 1.3496 \cdot 10^9 \exp\left(\frac{1.256 \cdot 10^8}{R_i T}\right) C_{C_6H_6}^{-0.1} C_{CO_2}^{1.85}$	[2]
R_{c2}	$\dot{\omega}_{c2}''' = 2.9093 \cdot 10^8 \exp\left(\frac{8.023 \cdot 10^7}{R_i T}\right) T_g C_{CH_4}^{0.5} C_{CO_2}$	[29]
R_{c3}	$\dot{\omega}_{c3}''' = 7.0795 \cdot 10^{19} \exp\left(\frac{1.6628 \cdot 10^8}{R_i T}\right) C_{CO} C_{O_2}^{0.25} C_{H_2O}^{0.5}$	[29]
R_{c4}	$\dot{\omega}_{c4}''' = 1 \cdot 10^{14} \exp\left(\frac{4.2 \cdot 10^7}{R_i T}\right) C_{H_2} C_{CO_2}$	[29]
R_{g3}	$\dot{\omega}_{g3}''' = 3.015 \cdot 10^6 \exp\left(\frac{1.2552 \cdot 10^8}{R_i T}\right) C_{CH_4} C_{H_2O}$	[30]
R_{wg}	$\dot{\omega}_{wg}''' = 2780 \exp\left(\frac{1.26 \cdot 10^7}{R_i T}\right) C_{CO} C_{H_2O}$	[2]

$$\dot{\omega}_p''' = -\rho_{\text{wood}} \sum_{i=1}^3 A_i \exp\left(-\frac{E_i}{R_u T}\right) \quad (25)$$

The char consumption reaction was modelled through three heterogeneous reactions (Eq. (26) and Table 4). The global constants of heterogeneous reactions are described in Eq. (27). The parameter ϕ is considered as the char oxidation parameter (Eq. (28)). Kinetics reaction rates of the char oxidation are expressed in Table 6.

$$\dot{\omega}_c''' = k_{\text{ox}}^{\text{glob}} A_v \text{CO}_2 M_C + k_{\text{g1}}^{\text{glob}} A_v \text{CCO}_2 M_C + k_{\text{g2}}^{\text{glob}} A_v \text{CH}_2\text{O} M_C \quad (26)$$

$$k_1^{\text{glob}} = \frac{1}{\frac{1}{k_i} + \frac{1}{k_i^m}} \quad (27)$$

$$\phi = \frac{2 + 4.3 \exp(-3390/T)}{2(1 + 4.3 \exp(-3390/T))} \quad (28)$$

The volumetric source terms in the solid-gas conversion are shown in Table 7. Eq. (29) represents the H₂O source in the drying process. The source of volatile species in the devolatilization is expressed by Eq. (30). Eqs. (31)–(35) show sources terms of the different species involved in the adapted heterogeneous reactions.

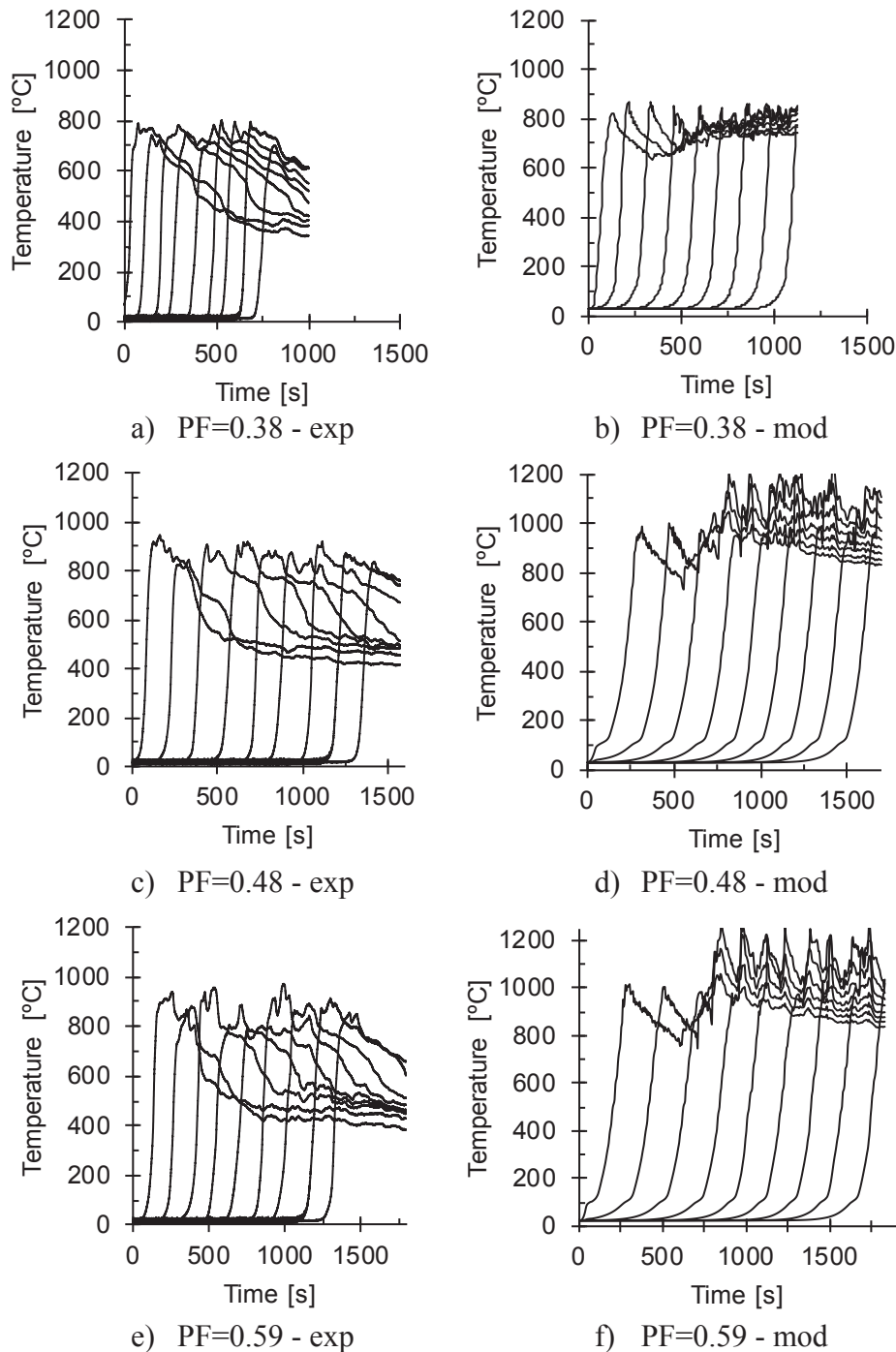


Fig. 2. Temperature fields.

The kinetic rates of the homogeneous reactions are shown in Table 8. The reaction constants behave on the Arrhenius form. The turbulence and kinetic interaction in the gaseous phase are calculated by the Finite-rate/Eddy-dissipation (FR-ED) model [3].

4. Results and discussion

The aim of this work is twofold. First, to extend the CFD model initially developed for simulating combustion in a fixed bed to simulate the gasification process. Therefore, in this section, a detailed model validation is presented. Second, to take advantage of the model versatility and power calculation, this study evaluated the effect of the packing factor of wood biomass on the fixed bed gasification process.

4.1. CFD model validation

4.1.1. Temperature field

Fig. 2 shows the comparison of temperature profiles obtained experimentally (coded with the suffix - exp), see Fig. 2 a, c, and e, against those calculated by numerical simulation (coded with the suffix - mod), see Fig. 2 b, d, and f.

The slight overestimation of the maximum temperature calculated by the model, shown in Fig. 2, is probably due to the bridging formation (channeling) taken by the air in some places inside the bed. The air channels favor small combustion zones, therefore, the temperature is increased [8,22]. Nevertheless, the model proved versatile and produced results similar to the experimental results. Numerical results in agreement to those reported for fixed bed biomass combustion are highlighted [12,13].

If we compare the experimental and model temperature profiles as functions of time, and we measure the elapsed time between the rise of thermocouple #1 and #9, the average discrepancy is 13%. This is a demonstration of the good agreement between the empirical and simulated values of some key parameters such as flame front velocity, the maximum temperature inside the bed, among others (see section 4.1.3.).

Analyzing the calculated temperature fields for the three PFs (Fig. 2 b, d and f), a higher separation in the first three thermocouples is observed. This finding is due to the model stabilization after ignition. In addition, the model results show two positive slopes in the solid temperature (Fig. 2 b, d and f); this behavior was not detected through the experimental temperature measurement inside the bed (Fig. 2 a, c and e). The first stage occurs approximately between room temperature and up to about 150 °C, whose average slope is 30 °C/min. This sub-process corresponds to the biomass drying stage. While the second stage that occurs between 150 and 200 °C and up to the maximum stage (with a slope of around 440 °C/min). This energy released by the exothermic reactions increases the process temperature. This phase has been identified in this kind of reactor under gasification conditions by other authors, and it is named the pyrocombustion stage [4,29], and refers to a situation where the volatile species is rapidly oxidized by the oxygen available around the particles. Therefore, according to the good agreement between the temperature fields, it is demonstrated that the CFD model can simulate the gasification process in fixed bed reactors with good accuracy.

4.1.2. Producer gas composition

Fig. 3 shows the experimental gas composition versus the one numerically estimated. For the PFs 0.48 and 0.59, the dimensional proximity of the model with the CO and H₂ composition is evident, while for chips (PF = 0.38) these two species are overestimated by the model. CH₄ is underestimated for all the biomass geometries, while the CO₂ is overestimated by the model during the three

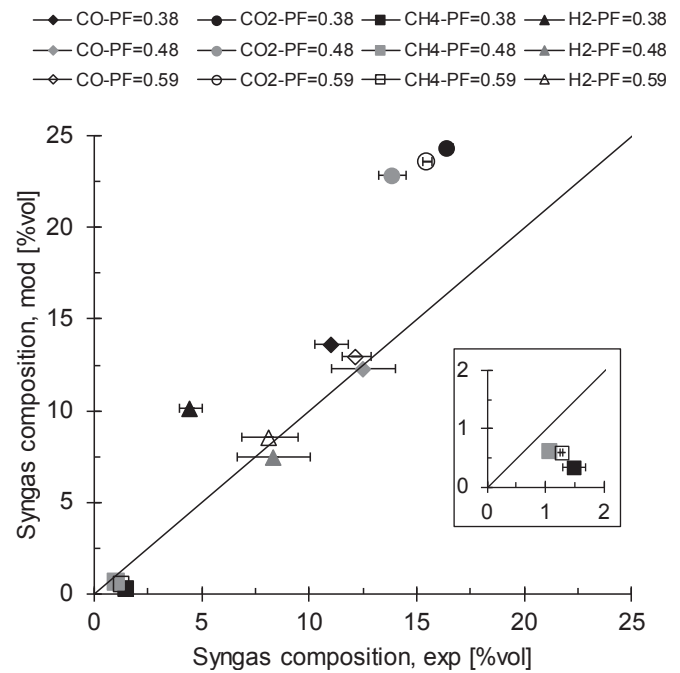


Fig. 3. Syngas composition-linear adjustment.

simulation cases. The CO₂ overestimation in the model is related to the carbon mass balance and generation of some preferential air paths, giving rise to small combustion zones. The CH₄ underestimation is due to the kinetic reaction selected for it, where some fraction of CH₄ can react with steam to produce H₂ through the reactor length (see Eq. (21)). The syngas composition has been presented by other authors with good dimensional proximity [13,14]. However, the produced gas composition depends on the kinetic mechanisms of the reaction and the kinetic rates used to simulate the thermochemical process. This finding explains why the produced gas composition is difficult to be estimated by modeling [4,31]. In this work, the good accuracy of the model regarding the producer gas composition is highlighted because the average root mean square error varies between ±0.76%vol to ±8.33%vol for the gaseous species (see Table 9).

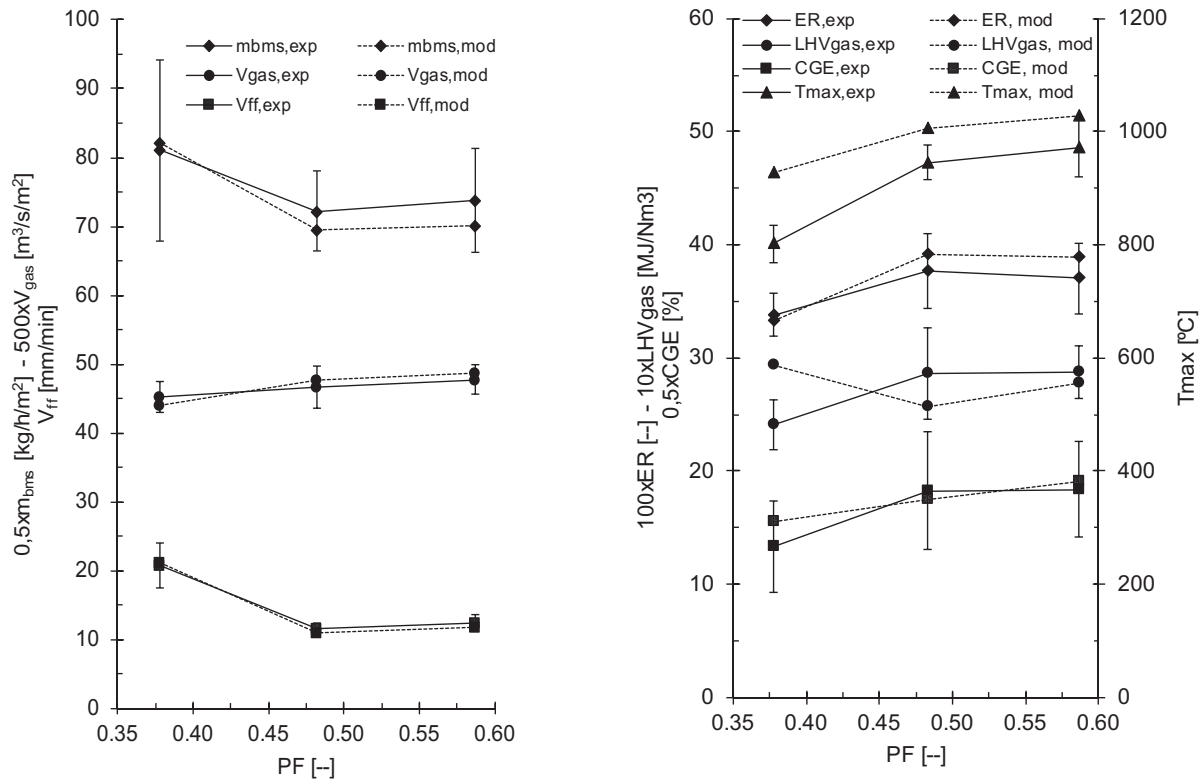
4.1.3. Process parameters

The model validation as a function of experimental (exp) and theoretical (mod) flame front velocity (V_{ff}) is presented in Fig. 4 a. The model tends to follow the experimental results, where the flame front velocity decreases if PF increases from 0.38 to 0.59. For

Table 9

Root mean square error of the CFD model vs Experimental results.

Validation parameter	Root mean square error [units]			
	PF = 0.38	PF = 0.48	PF = 0.59	Average
Syngas composition				
CO [%vol]	2.64	0.27	0.79	1.23
CO ₂ [%vol]	7.93	8.95	8.10	8.33
CH ₄ [%vol]	1.16	0.44	0.67	0.76
H ₂ [%vol]	5.65	0.93	0.40	2.33
V_{ff} [mm/min]	0.29	0.44	0.61	0.45
m_{bms} [kg/h/m ²]	2.30	5.59	7.24	5.04
V_{gas} [m ³ /s/m ²]	2.51×10^{-3}	2.22×10^{-3}	1.75×10^{-3}	2.16×10^{-3}
LHV _{gas} [MJ/Nm ³]	0.53	0.29	0.10	0.31
ER [-]	4.70×10^{-3}	1.51×10^{-2}	1.91×10^{-2}	1.30×10^{-2}
CGE [%]	4.50	1.58	1.26	2.45



a) Biomass consumption rate, gas generation rate and flame front velocity

b) Maximum temperature, equivalence ratio, syngas calorific value and cold efficiency of the process

Fig. 4. Process parameters as a function of PF.

PF = 0.38 the model tends to overestimate the propagation velocity, while for the two others PFs (0.48 and 0.59) the model slightly underestimates this parameter in regard to the experimental results. Nevertheless, the average relative error of the model regarding this parameter is 3.39%, which indicates the proper accuracy of the model for simulating the flame front propagation over the raw biomass under fix bed gasification conditions. The flame front velocity is higher for chips (PF = 0.38) because the surface-volume relation of this particle is 21% higher than for cubes and cylinders (see Table 1). Moreover, the low PF of chips (high bed void fraction) favors radiation penetration, which leads to increased amounts of biomass involved in the process [20]. The biomass consumption rate presents a similar trend to the one obtained from flame front velocity (see Fig. 4 a). This behavior is due to the fact that the biomass consumption rate is a function of this parameter [18].

The syngas volumetric flow (V_{gas}) results are also contrasted in Fig. 4 a. The model provides a good prediction of the gas production because it shows a trend where the gas flow increases if PF increases too. The response variables of the model are within the standard deviation of the experiments and indicate that the adapted model appropriately predicts these results.

Regarding the heating value of the syngas, the model slightly overestimates this parameter (LHV_{gas}) for PF = 0.38, due to the theoretical overestimation of CO and H_2 (see Fig. 4 b). For PFs of 0.48 and 0.59, following the trends of gaseous fuels (Fig. 3), the LHV_{gas} is slightly underestimated by the model. Although the CO and H_2 are well predicted by the model, it underestimates the

amount of CH_4 .

The Equivalence Ratio (ER) is a parameter that depends on the packing factor. Fig. 4 b shows that ER increases if PF rises, this is due to the lower flame front velocity caused by the high packing of the bed which reduces the biomass consumption rate [20]. For cylinders (PF = 0.48), it is highlighted that the model predicts the highest ER, which suggest that the mathematical approach predicts coherently the effect of the particle and bulk densities on the flame front velocity and biomass consumption rate.

Similarly, the maximum process temperature increases if PF increases. This is due to the fact the absorption of radiation by the solid phase is more intense when the bed void fraction is lower; therefore, as the penetration of radiative heat transfer decreases and leads to higher energy concentration in the reaction front that favors the increase of the temperature. This trend corresponds coherently with the behavior of ER, where, biomass consumption decreases from PF = 0.38 to PF = 0.59; therefore, the equivalence air-to-biomass ratio increases, thus, the process temperature increases [13,16].

The cold gas efficiency reaches higher values when PF increases. This can be seen in Fig. 4 b. A good relationship between the experimental and theoretical parameters is highlighted. The CGE increases due to the lower biomass consumption (low flame front velocity) that leads to decreased biomass energy fed to the thermochemical process for the low radiation penetration in the solid phase.

Regarding the model accuracy, it is possible to state that the model appropriately simulates the physicochemical processes of

biomass under gasification conditions in a fixed bed. This is stated according to low range variation of the model with regard to the experimental data calculated through the RMSE. This calculated error is shown in Table 9. The model can predict the trend of the response variables as a function of PF with a low relative error for the global parameters of the process, the average relative error of the model is 5.45%.

4.2. Sensitivity analysis

Once the model has been validated, it can be used as a computational tool to perform a sensitivity analysis, which may explain and describe some of the phenomena that cannot be seen or measured during the experimental phase. Hence, in this section

different phenomena that were affected by the biomass packing factor in a fixed bed are analyzed under gasification conditions. This study complements the previous work developed in an experimental setup, where empirical results were analyzed based on conceptual criteria of the process [1], while in this work, those parameters are quantified.

The effect of the three packing conditions has been analyzed for a fixed time of 500 s. To study the flame front through the reactor length, $x = 0.5$ m represents the top of the reactor, and $x = 0$ m represents the gasifier bottom (grate). Herein, the solid-gas convective heat transfer mechanism, absorption of radiative heat transfer in solid phase, and the distribution of solid temperature as a function of PF is discussed. These parameters define the flame front propagation under gasification conditions and quantify differences in the process for several characteristics [32].

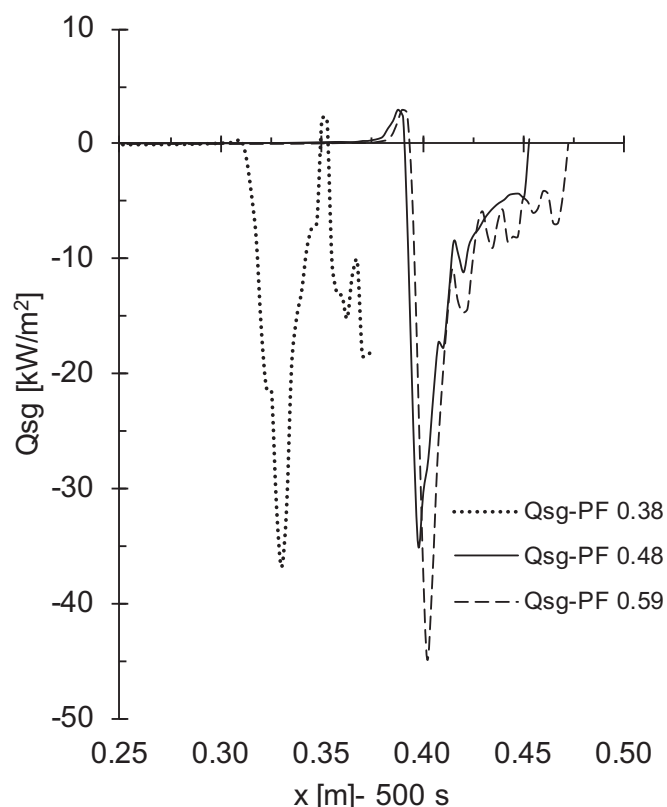


Fig. 5. Solid-gas heating transfer as a function of PF.

4.2.1. Convective solid-gas heat transfer

The convective solid-gas heat transfer between solid and gas as a function of PF is presented in Fig. 5. In all three cases of PF, solid transfers the highest energy to the gas in the drying zones, while in the pyro-combustion stage the heat is transferred from gas to solid phase [32]. Although for $PF = 0.38$ (chips) there is a small stage in the oxidation zone (near to $x = 0.36$ m) where solid transfers to gas. This phenomenon for wood chips is attributed to the formation of preferential paths which favor the highest temperatures in some zones of the flame front, and can produce a higher solid temperature that leads to transfer of heat from solid phase to gaseous phase at a specific point during the pyro-combustion stage [8].

The solid-gas heat transfer in the drying zone for the case of chips ($PF = 0.38$) is lower than the other two geometries (cubes and cylinders). This is because chips have a higher bed void fraction, as can be seen in the radiative heat transfer (see Section 4.2.2), which favors the penetration of radiation in the solid phase favoring high reaction rates due to high thickness of the flame front. This high penetration of radiative heat in the solid phase leads to low temperatures in the reaction front, and hence the heat transfer in the drying phase decreases. The convergence of a high radiative penetration in solid phase with high particle surface area/volume ratio and with low PF favors the activation of drying and pyrolysis reactions. This effect causes the flame front to advance faster for chips than for the other two PFs. The highest flame front velocity for chips is shown in Fig. 5, where the flame front is ahead in the case $PF = 0.38$ (chips), located in $x = 0.33$ m, while for cylinders and cubes, the reaction front is placed behind, between 0.4 and 0.42 m. In the pyro-combustion zone, the solid-gas heat transfer increases around 20% if PF increases from $PF = 0.38$ to $PF = 0.59$; while for

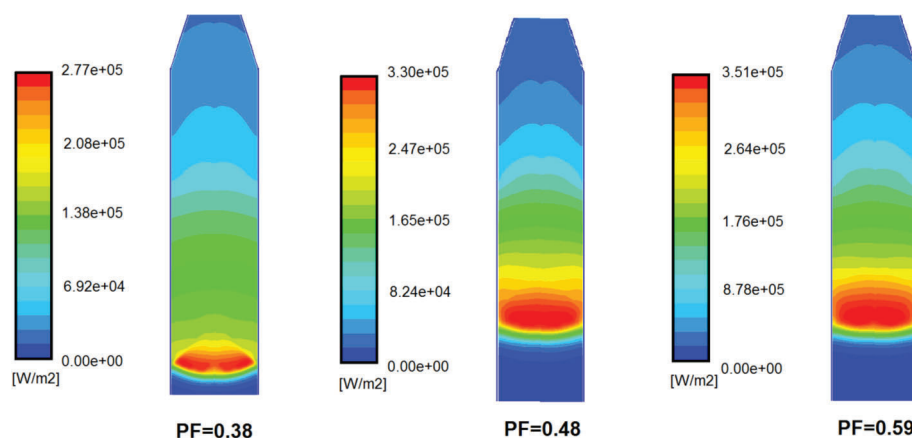


Fig. 6. Radiation absorption heat (W/m^2) – $t = 500$ s.

PF = 0.48, the lowest heating transfer rates are obtained during pyro-combustion due to the high bulk density, particle density and biomass hardness of cylinder shape, as can be seen in Fig. 5.

4.2.2. Radiative heat transfer

The absorption of radiative heat quantifies the amount of radiative energy absorbed by the solid phase; its calculation model is represented by Eq. (11). Fig. 6 shows how the radiative heat absorption increases if PF increases. This is because the low bed void fraction avoids the penetration of radiation in the bed causing that energy concentration increases in the flame front, which leads to an elevated temperature of the bed (see the 2D distribution of solid temperature in Fig. 7). The absorbed radiation in the solid phase increases with the PF. The relative increase with regard to the chips (PF = 0.38), is 18.77% for the cylindrical geometry (PF = 0.48), and 26.71% for cubes (PF = 0.59). The highest power absorbed by cubes (PF = 0.59) is due to the lower bed void fraction which favors a low radiation penetration [12], leading to low reaction front velocity and biomass consumption rate (as discussed in section 4.1.2.). The effects on fixed bed gasification when PF increases can be summarized as follows: the absorption of radiative heat transfer increases, leading to low reaction rates of drying and pyrolysis; however, the temperature in the reaction front increases favoring the production of gaseous fuels in the producer gas (H_2 , CO, and CH_4); therefore, the CGE increases. Similar trends based on the empirical observations were reported by Lenis et al. [1].

Fig. 7 presents the 2D distribution of solid temperature; this parameter is a useful datum to design gasifiers [33]. For the PF = 0.38 case, the flame front advances faster towards the raw biomass, hence, the maximum temperature in the reaction front decreases, because stages of drying and devolatilization are favored. In function of the 2D numerical results, it can be seen a high concavity of the solid temperature for PF = 0.38, explaining the high propagation velocity of the process due to the higher bed void fraction of biomass in the bed.

5. Conclusions

The adaptation of the model to gasification conditions required modification of the chemical kinetics of pyrolysis, oxidation, and reduction processes using the adequate kinetic mechanism of the reactions for gasification. The numerical simulation of biomass gasification has a dimensional prediction because the average relative error of all the thermodynamic variables that were validated (flame front velocity, biomass consumption rate, volumetric gas flow, gas heating value, equivalence ratio, and cold efficiency) are below 6%. Thereby, the model can be used as computational tool for predicting or diagnosing different systems under gasification conditions with air as the gasifying agent. It is highlighted that the

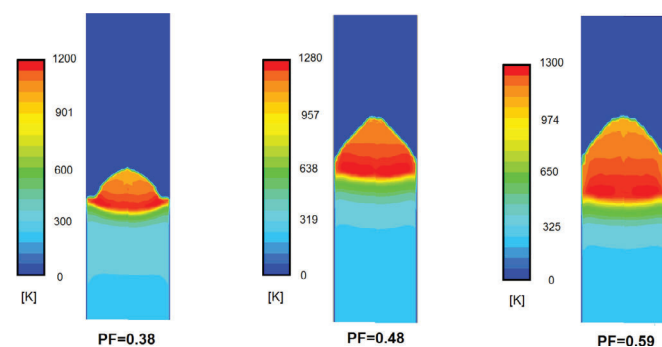


Fig. 7. Solid temperature (K) – $t = 500$ s.

biomass gasification 2D CFD model generates results within the experimental standard deviation of each validated variable, considering that the model predicts the trends of those parameters.

The effect of biomass PF increase (from 0.38 to 0.59) on fixed bed gasification can be summarized as follows: the absorption of radiative heat increases 26.71%, leading to low reaction rates of drying and pyrolysis. Thus, the flame front velocity decreases from 21.06 mm/min to 11.76 mm/min; whereas, the maximum temperature in the reaction front increases (from 927 °C to 1027 °C) favoring the production of gaseous fuels in the producer gas (H_2 , CO, and CH_4), and increasing the CGE from 31% to 38%.

The CFD model, which was adapted to gasification conditions, allows study of the phenomenology involved during the thermo-chemical transformation of biomass to a combustible gas. This fact allows making dimensional analyses of operational parameters, gases concentrations and heat transfer mechanisms studies. Due to these facts, this model can be used to simulate several types of fixed bed reactors with different fuels and geometries.

Acknowledgments

The authors acknowledge the financial support of Universidad de Antioquia through the project “Sostenibilidad 2017–2018.” In addition, this work was financially supported by project ENE2015-67439-R of the Ministry of Economy and Competitiveness and the work of Sergio Chapela López has been supported by the grant BES-2016-076785 of the Ministry of Economy, Industry and Competitiveness (Spain).

Nomenclature

A_i	Pre-exponential factor
A_v	Area-volume ratio (m^{-1})
C_i	Molar concentration ($kmol \cdot m^{-3}$)
C_p	Specific heat ($J \cdot kg^{-1} K^{-1}$)
D_i	Diffusivity of the specie i ($m^2 s^{-1}$)
d_{eq}	Equivalent diameter (m)
E_i	Activation energy
h	Convection coefficient ($W \cdot m^{-2} K^{-1}$)
H_i	Enthalpy of formation of the specie i ($J \cdot kg^{-1}$)
I	Irradiation intensity ($W \cdot m^{-2} sr$)
k	Thermal conductivity ($W \cdot m^{-1} K^{-1}$)
k_i	Kinetic constant of the reaction i
k_i^m	Mass transfer coefficient ($m \cdot s^{-1}$)
$k_{s/g}$	Constant of solid/gas distribution of the char reaction energy
LH	Latent heat ($J \cdot kg^{-1}$)
M_i	Molecular weight ($kg \cdot kmol^{-1}$)
n	Refractive index (–)
Nu	Nusselt number (–)
Pr	Prandtl number (–)
r	Position vector (m)
Re	Reynolds number (–)
R_u	Ideal gas constant
s	Direction vector (m)
S	Source term ($W \cdot m^{-3}$)
Sc	Schmidt number (–)
Sh	Sherwood number (–)
$S_{i,j}$	Source of the specie i from the component j ($kg \cdot m^{-3} s^{-1}$)
t	Time (s)
T	Temperature (K)

Greek symbols

α	Absorption coefficient (m^{-1})
----------	-------------------------------------

ε	Solid fraction (–)
ρ	Density ($\text{kg}\cdot\text{m}^{-3}$)
σ	Stefan-Boltzmann coefficient ($\text{W}\cdot\text{m}^{-2}\text{K}^{-4}$)
φ	Char oxidation parameter (–)
$\dot{\omega}_i'''$	Generation or consumption rates ($\text{kg}\cdot\text{m}^{-3}\text{s}^{-1}$)
Ω	Solid angle (sr)

Subscripts

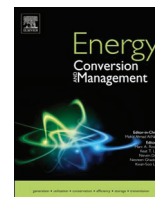
C	Consumption
char	Char
dev	Devolatilization
eff	Effective
evap	Evaporation
g	Gas
G	Generation
glob	Global
moist	Moisture
p	Particle
s	Solid
wood	Wood

Superscripts

conv	Convection
loss	Losses
reac	Reaction
rad	Radiation

References

- [1] Y.A. Lenis, J.F. Pérez, A. Melgar, Fixed bed gasification of Jacaranda Copaia wood: effect of packing factor and oxygen enriched air, *Ind. Crop. Prod.* 84 (2016) 166–175.
- [2] M.A. Gómez, J. Porteiro, D. Patiño, J.L. Míguez, CFD modelling of thermal conversion and packed bed compaction in biomass combustion, *Fuel* 117 (2014) 716–732.
- [3] J. Collazo, J. Porteiro, D. Patiño, E. Granada, Numerical modeling of the combustion of densified wood under fixed-bed conditions, *Fuel* 93 (2012) 149–159.
- [4] J.F. Pérez, A. Melgar, F. V. Tinaut, Modeling of fixed bed downdraft biomass gasification: application on lab-scale and industrial reactors, *Int. J. Energy Res.* (2014) 319–338.
- [5] D. Baruah, D.C. Baruah, Modeling of biomass gasification: a review, *Renew. Sustain. Energy Rev.* 39 (2014) 806–815.
- [6] H. Khodaei, Y.M. Al-Abdeli, F. Guzzomi, G.H. Yeoh, An overview of processes and considerations in the modelling of fixed-bed biomass combustion, *Energy* 88 (2015) 946–972.
- [7] R. Mehrabian, S. Zahirovic, R. Scharler, I. Obernberger, S. Kleditzsch, S. Wirtz, V. Scherer, H. Lu, L.L. Baxter, A CFD model for thermal conversion of thermally thick biomass particles, *Fuel Process. Technol.* 95 (2012) 96–108.
- [8] S. Hermansson, H. Thunman, CFD modelling of bed shrinkage and channelling in fixed-bed combustion, *Combust. Flame* 158 (2011) 988–999.
- [9] A.K. Olaleye, K.J. Adedayo, C. Wu, M.A. Nahil, M. Wang, P.T. Williams, Experimental study, dynamic modelling, validation and analysis of hydrogen production from biomass pyrolysis/gasification of biomass in a two-stage fixed bed reaction system, *Fuel* 137 (2014) 364–374.
- [10] M.A. Masmoudi, M. Sahraoui, N. Grioui, K. Halouani, 2-D Modeling of thermo-kinetics coupled with heat and mass transfer in the reduction zone of a fixed bed downdraft biomass gasifier, *Renew. Energy* 66 (2014) 288–298.
- [11] Y. Bin Yang, R. Newman, V. Sharifi, J. Swithenbank, J. Ariss, Mathematical modelling of straw combustion in a 38 MWe power plant furnace and effect of operating conditions, *Fuel* 86 (2007) 129–142.
- [12] D. Shin, S. Choi, The combustion of simulated waste particles in a fixed bed, *Combust. Flame* 180 (2000) 167–180.
- [13] S. Mahapatra, S. Kumar, S. Dasappa, Gasification of wood particles in a co-current packed bed: experiments and model analysis, *Fuel Process. Technol.* 145 (2016) 76–89.
- [14] I. Janajreh, M. Al Shrah, Numerical and experimental investigation of downdraft gasification of wood chips, *Energy Convers. Manag.* 65 (2013) 783–792.
- [15] J. Cai, Y. He, X. Yu, S.W. Banks, Y. Yang, X. Zhang, Y. Yu, R. Liu, A.V. Bridgwater, Review of physicochemical properties and analytical characterization of lignocellulosic biomass, *Renew. Sustain. Energy Rev.* 76 (2017) 309–322.
- [16] S. Mahapatra, S. Dasappa, Experiments and analysis of propagation front under gasification regimes in a packed bed, *Fuel Process. Technol.* 121 (2014) 83–90.
- [17] Y.A. Lenis, A.F. Agudelo, J.F. Pérez, Analysis of statistical repeatability of a fixed bed downdraft biomass gasification facility, *Appl. Therm. Eng.* 51 (2013) 1006–1016.
- [18] J.F. Pérez, A. Melgar, P. Nel, Effect of operating and design parameters on the gasification/combustion process of waste biomass in fixed bed downdraft reactors: an experimental study, *Fuel* 96 (2012) 487–496.
- [19] M. Vaezi, M. Passandideh-fard, M. Moghiman, M. Charmchi, On a methodology for selecting biomass materials for gasification purposes, *Fuel Process. Technol.* 98 (2012) 74–81.
- [20] J.F. Pérez, P.N. Benjumea, A. Melgar, Sensitivity analysis of a biomass gasification model in fixed bed downdraft reactors: effect of model and process parameters on reaction front, *Biomass Bioenergy* 83 (2015).
- [21] Y.A. Lenis, L.F. Osorio, Effects fixed bed gasification of wood species with potential as energy crops in Colombia: the effect of the physicochemical properties, *Energy Sources* (2013) 37–41.
- [22] Y.A. Lenis, J.F. Pérez, Gasification of sawdust and wood chips in a fixed bed under autothermal and stable conditions, *Energy Sources* (2015) 37–41.
- [23] Y. Bin, C. Ryu, A. Khor, N.E. Yates, V.N. Sharifi, J. Swithenbank, Effect of fuel properties on biomass combustion. Part II. Modelling approach — identification of the controlling factors, *Fuel* 84 (2005) 2116–2130.
- [24] M.A. Gómez, J. Porteiro, D. Patiño, J.L. Míguez, Fast-solving thermally thick model of biomass particles embedded in a CFD code for the simulation of fixed-bed burners, *Energy Convers. Manag.* 105 (2015) 30–44.
- [25] M.A. Gómez, D. Patiño, R. Comesaña, J. Porteiro, M.A. Álvarez Feijoo, J.L. Míguez, CFD simulation of a solar radiation absorber, *Int. J. Heat Mass Tran.* 57 (2013) 231–240.
- [26] K.M. Bryden, K.W. Ragland, C.J. Rutland, Modeling thermally thick pyrolysis of wood, *Biomass Bioenergy* 22 (2002) 41–53.
- [27] H. Thunman, B. Leckner, F. Niklasson, F. Johnsson, Combustion of Wood Particles — a Particle Model for Eulerian Calculations, 2180, 2002, pp. 30–46.
- [28] K.M. Bryden, K.W. Ragland, Numerical modeling of a deep, fixed bed combustor, *Energy Fuels* 10 (1996) 269–275.
- [29] C. Di Blasi, Dynamic behaviour of stratified downdraft gasifiers, *Chem. Eng. Sci.* 55 (2000) 2931–2944.
- [30] H. Liu, B.M. Gibbs, Modeling NH₃ and HCN emissions from biomass circulating fluidized bed gasifiers, *Fuel* 82 (2003) 1591–1604.
- [31] R. Johansson, H. Thunman, B. Leckner, Sensitivity analysis of a fixed bed combustion model, *Energy Fuels* (2007) 1493–1503.
- [32] F. V. Tinaut, A. Melgar, J.F. Pérez, A. Horrillo, Effect of biomass particle size and air superficial velocity on the gasification process in a downdraft fixed bed gasifier. An experimental and modelling study, *Fuel Process. Technol.* 89 (2008) 1076–1089.
- [33] K. Jaojaruek, Mathematical model to predict temperature profile and air – fuel equivalence ratio of a downdraft gasification process, *Energy Convers. Manag.* 83 (2014) 223–231.



Steady CFD combustion modeling for biomass boilers: An application to the study of the exhaust gas recirculation performance

M.A. Gómez^{a,*}, R. Martín^b, S. Chapela^b, J. Porteiro^b

^a Defense University Center, Spanish Naval Academy, Plaza de España s/n, 36900 Marín, Spain

^b Industrial Engineering School, University of Vigo, Lagoas-Marcosende s/n, 36310 Vigo, Spain

ARTICLE INFO

Keywords:

Biomass combustion
CFD modeling
EGR
Thermal performance

ABSTRACT

This work presents an efficient model to simulate the steady operation of biomass boilers and to analyze the thermal behavior of the system in different working scenarios. The model is based on the implementation of calculations on the thermal conversion of biomass in a computational fluid dynamics (CFD) environment to solve the gas phase. The mass, energy and species balances and reactions that take place in the biomass packed bed are introduced in a porous region inside the computational domain of the boiler. The biomass thermal conversion is combined with other submodels, such as radiation transport, gas transport and chemical reactions, to solve the complex combustion phenomena with relatively little computational effort. The model is tested by comparing two different simulations with their respective experimental tests. Parameters relative to the boiler thermal performance and contaminant emissions are compared with reasonably good results. The potential of the model to analyze different operation conditions of a boiler is applied to the theoretical study of the effect of the exhaust gas recirculation (EGR) on the boiler performance and the gas contaminant emissions. For this study, several simulations of a boiler fed with pure oxygen are performed by changing the EGR fraction and the oxygen excess. The results of the study show that the EGR effect can increase the boiler thermal performance, especially for low oxygen excess values. This effect also reduces the NO_x emissions for low oxygen excess values. EGR does not seem to have any significant effect on CO emissions.

1. Introduction

The pressing global necessity of reducing the use of fossil fuels is leading humanity to find a responsible source of energy that is both renewable and less polluting. To that end, biomass appears to be a solution as it is a solid fuel created from the waste of other industries, thus providing a form of recycling and creating a renewable energy source. Biomass is exploited through combustion. Therefore, an understanding of both its combustion process and the architecture of an appropriate combustion system designed to allow for an efficient energy conversion embodies a challenge of capital importance for humanity going forward.

In the task of understanding biomass combustion and geometrically designing an efficient boiler, recent computational developments have enabled the creation of simulation models. These simulation models can then be implemented in CFD packages to address the main goals of analyzing, understanding, developing and optimizing biomass combustion systems.

CFD codes are widely developed for the simulation of gaseous

combustion [1–3]. However, the combustion process of biomass starts in the solid phase by the production of different gases from the pellets that are produced by means of different phenomena, such as drying, pyrolysis and char heterogeneous reactions [4]. The conversion of solid biomass into gases is still a field in development, not only at a physical level but also in terms of how to implement it in a CFD package. As a result, the bed is the critical zone in modeling biomass combustion systems.

The simplest approach is to model the gases leaving the bed towards the freeboard as a boundary condition, where a certain composition of the gas is specified in terms of the species. That given gas composition for this inlet can be set using experimental data [5], or calculated using mass and energy balances that try to predict the products generated in the combustion process of biomass [6–9]. Porteiro et al. [6] modeled each incoming particle in the packed bed and, as a result of the thermal conversion, introduced the resulting fluxes the mass and energy in the gas phase domain. Other works [7–9] used the “walking column approach” to model the advance and combustion of the fuel along a grate through discrete columns and the properties and composition of each

* Corresponding author.

E-mail addresses: miguelgr@uvigo.es (M.A. Gómez), rubencmartinares@gmail.com (R. Martín), schapela@uvigo.es (S. Chapela), porteiro@uvigo.es (J. Porteiro).

<https://doi.org/10.1016/j.enconman.2018.10.052>

Received 7 August 2018; Received in revised form 29 September 2018; Accepted 16 October 2018

Available online 25 October 2018

0196-8904/ © 2018 Elsevier Ltd. All rights reserved.

Nomenclature

Ab	surface absorptivity of the particles [-]	T_s	solid phase temperature [K]
A_p	particle surface [m ²]	v_∞	gas velocity [m·s ⁻¹]
A_v	area-volume ratio [m ⁻¹]	V_p	particle volume [m ³]
d_{eq}	equivalent diameter [m]	Y_j	mass fraction of the j th gaseous species [-]
D_{cyl}	diameter of the cylindrical particle [m]	Y_c	char mass fraction [-]
D_j	diffusivity of the j th gaseous species in the mixture [m ² ·s ⁻¹]	Y_m	moisture mass fraction [-]
h	convection coefficient [W·m ⁻² ·K ⁻¹]	Y_v	volatiles mass fraction [-]
h_s	solid phase enthalpy [J·kg ⁻¹]	<i>Greek symbols</i>	
h_f^0	reaction enthalpy [J·kg ⁻¹]	α_s	absorption coefficient of solid phase [m ⁻¹]
I	irradiation intensity [W·m ⁻² ·sr]	α_g	absorption coefficient of gas phase [m ⁻¹]
k_g	thermal conductivity of the gas phase [W·m ⁻¹ ·K ⁻¹]	β	extinction coefficient [m ⁻¹]
k_s	thermal conductivity of the solid phase [W·m ⁻¹ ·K ⁻¹]	γ_k	mass fraction of the k th volatile species generated in the bed [-]
K^{ox}	kinetic constant for char direct oxidation reaction [m·s ⁻¹]	ε	solid fraction [-]
$K^{g,1}$	kinetic constant for char first gasification reaction [m·s ⁻¹]	ψ	fraction of char that reacts for oxidation or gasification reactions [-]
$K^{g,2}$	kinetic constant for char second gasification reaction [m·s ⁻¹]	λ	oxygen excess ratio [-]
K_m^{ox}	mass transfer constant for char direct oxidation reaction [m·s ⁻¹]	μ	viscosity [kg·m ⁻¹ ·s ⁻¹]
$K_m^{g,1}$	mass transfer constant for char first gasification reaction [m·s ⁻¹]	σ	Stefan-Boltzmann coefficient = 5.670373·10 ⁻⁸ [W·m ⁻² ·K ⁻⁴]
$K_m^{g,2}$	mass transfer constant for char second gasification reaction [m·s ⁻¹]	σ_s^{scat}	scattering coefficient of solid phase [m ⁻¹]
K_{glob}^{ox}	global constant for char direct oxidation reaction [m·s ⁻¹]	σ_g^{scat}	scattering coefficient of gas phase [m ⁻¹]
$K_{glob}^{g,1}$	global constant for char first gasification reaction [m·s ⁻¹]	Γ_k	stoichiometric coefficient of the pellet consumption for the specie k [-]
$K_{glob}^{g,2}$	global constant for char second gasification reaction [m·s ⁻¹]	Y	inertial resistance factor [m ⁻¹]
LHV	low heating value [J·kg ⁻¹]	η	permeability [m ²]
L_{cyl}	length of the cylindrical particle [m]	ρ_g	gas density [kg·m ⁻³]
M_k	molecular weight of the specie k [-]	ρ_p	particle density [kg·m ⁻³]
Nu	Nusselt number [-]	φ	char oxidation parameter [-]
n	refractive index [-]	Φ	scattering function [-]
Re	Reynolds number [-]	κ	sphericity [-]
\vec{r}	Position vector [m]	$\dot{\omega}_i$	specific rate of generation or consumption of gaseous species in the bed [kg·m ⁻³ ·s ⁻¹]
\vec{s}^i	scattering direction vector [-]	$\dot{\omega}_{H_2O,m}$	specific rate of generation or consumption of vapor in the bed [kg·m ⁻³ ·s ⁻¹]
Pr	Prandtl number [-]	$\dot{\omega}_f$	specific rate of generation or consumption of fuel in the bed [kg·m ⁻³ ·s ⁻¹]
Sh	Sherwood number [-]	$\dot{\omega}_{k,v}$	specific rate of generation or consumption of volatile species in the bed [kg·m ⁻³ ·s ⁻¹]
Sc	Schmidt number [-]	$\dot{\omega}_{k,c}$	specific rate of generation or consumption of char in the bed [kg·m ⁻³ ·s ⁻¹]
S	source term [W·m ⁻³]	$\dot{\omega}_{CO}$	Specific rate of generation or consumption of carbon monoxide in the bed [kg·m ⁻³ ·s ⁻¹]
S_{mom}	source term in the gas phase momentum equation [N·m ⁻³]	$\dot{\omega}_{CO_2}$	specific rate of generation or consumption of carbon dioxide in the bed [kg·m ⁻³ ·s ⁻¹]
t	time [s]	Ω	solid angle [sr]
T	temperature [K]		
T_g	gas phase temperature [K]		

column is updated with the position.

A limitation of these works is that all the calculations concerning the packed bed are external to the computational domain and the results are introduced in the domain as boundary conditions.

A more advanced approach is to model the packed bed as a part of the computational domain and use the different properties in the bed to calculate a local conversion of the biomass. As these models are applied individually to each computational cell, they require the use of a custom user defined function (UDF) to allow the user to expand the physical capabilities of the CFD solver and calculate new variables. Cooper and Hallet [10] and Thunman and Leckner [11] modeled the advance of char along a one-dimensional packed bed and calculated the interaction of particles with the gas phase in terms of chemical reactions, heat transfer, bed shrinkage and ash motion. Yang et al. [12] meshed the packed bed and applied the governing equations of several variables to solve the behavior of both solid and gas phases in the bed.

Collazo et al. [13] and Gómez et al. [14] implemented several variables representing the solid phase of a bed to account for the combustion stages and heat and mass exchanges. They tested these three-dimensional models with an experimental burner that analyzes the advance of combustion fronts.

A higher level of complexity is reached in works that model the particles with a thermally thick treatment, in which the thermal and composition gradients inside the biomass particle itself are considered. Yang et al. [15] studied a two-dimensional steady packed bed in which wood particles were discretized allowing to calculate internal variations of composition and temperature. Thunman et al. [16] divided the particles in several layers that represent the stages of combustion. The divisions of the layers move towards the center of the particle as the combustion advance.

This idea can be coupled with a three-dimensional solved packed bed, in which the different bed conditions are used as different input for

the particle model created. This approach was applied in several works, i.g., Mehrabian et al. [17,18] and Ström and Thunman [19]. These models usually need a high computational cost due to the high number of variables involved in the particle discretization. Gómez et al. [20] applied finite volume techniques to solve the particle internal subgrids of temperatures and layer volumes through linear equation systems that solve the variables in one step. This model allows to calculate large packed beds in reasonably short times. The same approach was adapted to operate in a domestic boiler [21]. Karim and Naser [22] also applied a three-dimensional model for packed beds to study different types of biomass fuels. Recently, they applied this three-dimensional model to simulate a moving grate boiler [23].

Other works focused the strategy in the particle modeling and the packed bed was considered as a large set of particles. Peters and Bruch [24] calculated the particle dynamics and conversion to build a packed bed through a discrete phase model (DPM). Wiese et al. [25] separately calculated the particle dynamics through a discrete element model (DEM) and introduced the results in a CFD computational domain to calculate the gas phase dynamics.

The use of these models in CFD solvers facilitates reducing the cost of empirical experimentation and expedites environmentally friendly development, as not every new component needs to be empirically tested, subsequently contributing to the overall acceleration of the biomass combustion systems. They also permit testing boilers in a wide variety of operating conditions. For example, a field of growing interest is the study of biomass combustion with enriched air. It is used to increase the efficiency in high temperature processes. There are only a few studies that simulated biomass combustion in this condition [26,27]. CFD was also applied to the study of EGR [28,29]. Bhuiyan et al. [28] studied the effect of recycled gases and oxygen enrichment on radiative and convective performance in a furnace. Karim et al. [29] applied their three-dimensional model [22] to simulate a packed bed furnace under oxy-fuel conditions with the software AVL Fire. Rajh et al. [30,31] used a one-dimensional bed model for the conversion of the waste wood of a grate, implemented in a 3D CFD model of a boiler to study the effect of recycled flue gases on the performance.

In the pursuit of expanding this understanding, the authors present a fast solving methodology with a reasonably high accuracy, and apply it to the study of a 30 [kW] boiler operating in different conditions. First, the model proposed is validated through a comparison to experimental results for the boiler operating at different levels of the oxygen excess ratio, for which a fairly good agreement to empirical data is obtained. Then, once the methodology is acceptably usable for representing a biomass combustion system, it is employed to study the impact of EGR and the air excess ratio on the performance and emissions of the boiler.

2. Experimental installation and simulation experiments

2.1. Experimental setup: Boiler

To show the capabilities of the proposed model, in this work, the study of a low power domestic biomass boiler has been approached. Specifically, it is a 35 [kW] model that is commercially available from KWB.

The boiler consists of two main differentiated parts, the freeboard and the heat exchanger. In the freeboard, the boiler features a single feed of fuel and a dual air feed, i.e., primary and secondary air intakes. The fuel is fed from the bottom of the bed into an inverse-conical shaped plate, which in general, causes the bed to grow faster in the middle and crumble radially as the combustion progresses. The described plate features a set of small holes which constitutes the primary air intake directly through the bed itself. The second air intake is arranged in a ring a few tens of millimeters over the average height of the bed. This ring is perimetrically fed with air from a single pipe, and features a group of nozzles that are oriented in such a way that the air

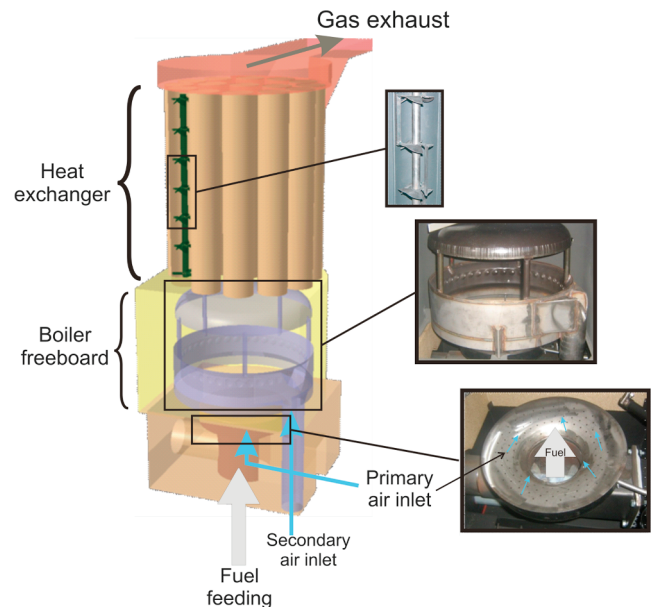


Fig. 1. Sketch of the boiler layout [32].

jets produce a swirl movement, enhancing turbulence and mixing preparation. On top of that, mechanically designed to be integrated as a sole part, a dome prevents the scenario of the flame reaching the boiler tubes. However, if this scenario occurs, the flame would undergo a flame quenching process, which would have negative consequences for both the performance and emissions of the boiler. The aforementioned tubes are part of a set of 15 tubes that constitute the heat exchanger of the boiler, and each of them are fitted with a praise in the gas side to induce (swirl movement) and improve the heat transfer to the water-cooled walls. Fig. 1 shows a sketch of the described boiler.

2.2. Fuel used

In this work, pinewood pellet is used as fuel, which was experimentally studied to determine the parameters that would influence its behavior in the boiler. To obtain such information, one of the tools used was a proximate analysis of the fuel as received (i.e., wet basis). A proximate analysis provides information about the content of the pellet in terms of water fraction, ash fraction, volatile fraction and combustible fraction of the pellet.

The data of the proximate analysis and the main particle properties are shown in Table 1. Experimental tests performed with the fuel showed a shape distribution of particles that follows a Rosin-Rammler distribution, as shown in Fig. 2.

2.3. Simulation experiments

In this work, the influence of two mixture preparation coefficients is studied, namely, the oxygen excess ratio and EGR fraction. The

Table 1
Proximate analysis and properties of the fuel employed.

Proximate analysis	Fuel parameters		
Moisture as received [wt%]	6.8	Equivalent formulation	$\text{CH}_{1.57}\text{O}_{0.74}\text{N}_{0.0025}$
Ash as received [wt%]	0.3	Density [kg·m ⁻³]	1200
Fixed carbon as received [wt%]	24.4	Cylindrical diameter [mm]	6.5
Volatile matter as received [wt%]	68.5	Average length [mm]	10.8
LHV as received [MJ/kg]	16.17	Solid fraction [-]	0.54

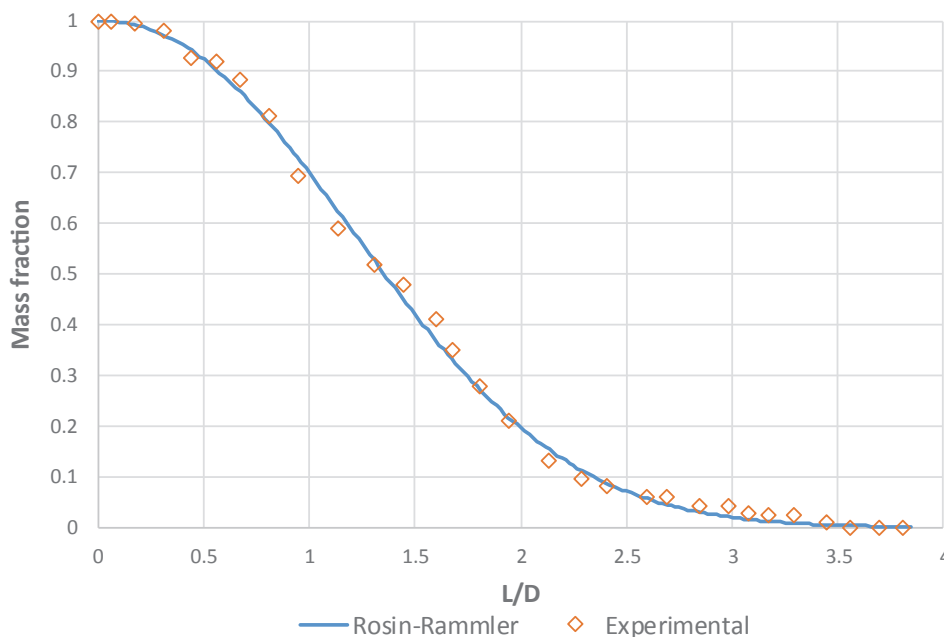


Fig. 2. Distribution of the mass of fuel vs the ratio L/D.

different simulation setups are configured in such a way that for a certain oxygen excess ratio, the influence of EGR is presented, and for a given EGR level, the influence of the oxygen excess ratio is studied. This constitutes a matrix of experiments in which the oxygen excess ratio ranges from 1 to 1.5, and EGR ranges from a 0% to a 50% level. Therefore, a total of 36 simulations were needed to describe the proposed study using an author-developed code implemented in ANSYS Fluent by means of a UDF.

The virtual experiments proposed are shown in Table 2, and the nomenclature introduced in this table is used in the experiments in the following sections. The model is first validated by the experiments corresponding to E1 and E2 in Table 5, in terms of the power generated, fume temperatures and gaseous emissions, see Section 4. The rest of the experiments are shown as a further capability of the model to include a certain EGR level, see Section 5. The highlighting done on this table corresponds to the simulation results shown in Section 5. SIM 02, 20 and 32 are used to understand the effect of EGR for a fixed air excess ratio. SIM 31, 33 and 36 are used to show the effect of the air excess ratio for a given EGR fraction.

3. Model description

The solver motor used in this work is the commercial CFD package ANSYS Fluent, which, on top of its default solvers, allows the user to program (C++) and build his own routines that couple with the already existing capabilities of the software.

CFD codes are highly developed to simulate gas phase phenomena,

but these models are not prepared to simulate the thermal conversion processes that occur during biomass combustion. Most of the content of this paper focuses on modeling the combustion of solid biomass and its interaction with gas. The paper describes several submodels in the combustion stages and the reactions of solid biomass, mass transfer from the packed bed to the gas phase, the heat exchanged between the bed and gas and the gas phase homogenous reactions. All these models are implemented in a CFD environment to integrate a comprehensive method that simulates the overall operation of a boiler.

The proposed model embodies a fast-solving procedure to solve biomass boilers in a steady state condition. It is composed of three different parts that interact with each other, i.e., solid phase (bed), gas phase (freeboard) and heat transfer.

3.1. Solid phase

The bed is included as part of the CFD domain in its totality, not having to rely on boundary conditions to model the gas emitted by the pellet particles in the bed. In contrast, each particle in the bed is in fact subjected to different conditions of temperature and composition, depending on how primary air flows through it. Based on this process, the decomposition of biomass into its constituent gases is calculated, which are then introduced as volumetric sources.

3.1.1. Solid energy equation and biomass decomposition

Subjecting the bed to different conditions, for example, temperature, is possible by defining the bed domain as porous media. This

Table 2
Matrix of virtual experiments simulated.

$\lambda \backslash$ EGR	0	0.1	0.2	0.3	0.4	0.5
1	SIM 01	SIM 07	SIM 13	SIM 19	SIM 25	SIM 31
1.1	SIM 02	SIM 08	SIM 14	SIM 20	SIM 26	SIM 32
1.2	SIM 03	SIM 09	SIM 15	SIM 21	SIM 27	SIM 33
1.3	SIM 04	SIM 10	SIM 16	SIM 22	SIM 28	SIM 34
1.4	SIM 05	SIM 11	SIM 17	SIM 23	SIM 29	SIM 35
1.5	SIM 06	SIM 12	SIM 18	SIM 24	SIM 30	SIM 36

allows the air to flow through it and to introduce a solid phase energy equation by transporting a new variable called solid enthalpy (Eq. (1)).

$$\frac{\partial(\varepsilon\rho_p h_s)}{\partial t} = \nabla(k_s \cdot \nabla T_s) + S_{h_s} \quad (1)$$

The importance of this new variable is crucial for capturing the first principle of thermodynamics, i.e., biomass contains a certain amount of releasable energy, which is being released in the form of gases at a certain temperature and pressure; therefore, it has a certain gas enthalpy. These gases cannot simply be introduced in the gas phase in these conditions without removing this releasable energy from the solid phase. As a result, a solid energy source has to be introduced to model the transfer of energy from the solid phase to the gas phase (Eq. (2)).

$$S_{h_s} = \dot{\omega}_f \left(LHV - \sum_j Y_j h_j^R \right) \quad (2)$$

The biomass decomposition means that the moisture contained in the pellets is going to dry and become part of the freeboard gases. In addition, the volatile content is going to leave the pellet as it heats up on the bed. Finally, the products of the char heterogeneous reactions are introduced in the gas phase of the bed.

This decomposition is modeled as a rate of conversion of the three different main constituents, i.e., moisture, volatile species and char. Eqs. (3)–(5). The fuel consumption rate is measured to be 0.00226 [kg/s] (8.14 [kg/h]), and with the fuel data in Section 2, the rates of generation of the gaseous species can thus be determined. Depending on the fuel composition, its proximate analysis and pyrolysis reactions modify the parameters Y_m , Y_v and Y_c .

$$\dot{\omega}_{H_2O,m} = \dot{\omega}_f Y_m \quad (3)$$

$$\dot{\omega}_{k,v} = \dot{\omega}_f Y_v \gamma_k \quad (4)$$

$$\dot{\omega}_{k,c} = \dot{\omega}_f Y_c \Gamma_k \quad (5)$$

These equations must be studied carefully as they contain considerable information regarding how the model is working and how the equations are related to their equivalent source term in the different transport equations for each species.

Eq. (3) is the simplest one and states that the water vapor generated is proportional to the moisture fraction. However, this only accounts for the amount of free water, and it is not inclusive of the water released during the pyrolysis.

Eq. (4) summarizes a group of 7 equations, one per of the volatile species considered in the proposed model, i.e., C_6H_6 , CH_4 , H_2 , CO , CO_2 , H_2O and NH_3 . All of them are generated during the pyrolysis. The fraction of fuel that is devolatilized is calculated through the kinetics of pyrolysis reactions (R.1)–(R.3), shown in Table 3. These reactions are

modeled through the kinetics proposed by Wagenaar et al. [33]. The parameters Y_v and Y_c are calculated as the ratios of pyrolysis reactions, as shown in Eqs. (9) and (10).

The char combustion is modeled as a direct char oxidation and two gasification equations, (the first with CO_2 and the second with H_2O), which capture the competition between the CO and CO_2 formation. These reactions (R.4)–(R.6), are also shown in Table 3 with their correspondent kinetics. Eq. (5) considers this set of char chemical reactions, and it is referring to a further group of 3 equations, one for each species involved in the three char reactions, i.e., H_2 , CO , and CO_2 . There is a slight difference in the way Eqs. (4) and (5) work. In Eq. (4), γ_k represents the mass fraction of each one of the volatile species, and it is known beforehand by its calculation following the methodology given in [34]. In the case of Eq. (5), Γ_k is determined through the kinetics of the three competitive reactions, mass fractions and the presence of reagents. The fraction of char in the cell correspondent to each reaction is given by the factors ψ_{ox} , $\psi_{g,1}$ and $\psi_{g,2}$, calculated as shown in Eqs. (14)–(16). These fractions are combined with the stoichiometry of the reactions (Eqs. (11)–(13)) to determine the mass flux of each specie k released in char reactions. This parameter (ψ_k) is modeled with a global rate of reaction (K_{glob}^k) that considers both reactions kinetics and reagents mass transfer. The char oxidation CO/CO_2 ratio is governed by the char oxidation parameter, Eq. (17).

$$Y_v = \frac{K^{gas} + K^{tar}}{K^{gas} + K^{tar} + K^{char}} \quad (9)$$

$$Y_c = \frac{K^{char}}{K^{gas} + K^{tar} + K^{char}} \quad (10)$$

$$\Gamma_{CO} = [2(1 - \varphi)\psi_{ox} + 2\psi_{g,1} + 1\psi_{g,2}] \frac{M_{CO}}{M_C} \quad (11)$$

$$\Gamma_{CO_2} = [(2\varphi - 1)\psi_{ox} - 1\psi_{g,1}] \frac{M_{CO_2}}{M_C} \quad (12)$$

$$\Gamma_{H_2} = \psi_{g,2} \frac{M_{H_2}}{M_C} \quad (13)$$

$$\psi_{ox} = \frac{K_{glob}^{ox} [O_2]}{K_{glob}^{ox} [O_2] + K_{glob}^{g,1} [CO_2] + K_{glob}^{g,2} [H_2O]} \quad (14)$$

$$\psi_{g,1} = \frac{K_{glob}^{g,1} [CO_2]}{K_{glob}^{ox} [O_2] + K_{glob}^{g,1} [CO_2] + K_{glob}^{g,2} [H_2O]} \quad (15)$$

$$\psi_{g,2} = \frac{K_{glob}^{g,2} [H_2O]}{K_{glob}^{ox} [O_2] + K_{glob}^{g,1} [CO_2] + K_{glob}^{g,2} [H_2O]} \quad (16)$$

Table 3
Pyrolysis and char reactions with their correspondent kinetics.

Pyrolysis reactions		Kinetics
Drywood \rightarrow Gas	(R.1)	$K^{gas} = 111 \cdot 10^9 \exp\left(-\frac{177 \cdot 10^3}{RT_s}\right)$
Drywood \rightarrow Tar	(R.2)	$K^{tar} = 9.28 \cdot 10^9 \exp\left(-\frac{149 \cdot 10^3}{RT_s}\right)$
Drywood \rightarrow Char	(R.3)	$K^{char} = 30.5 \cdot 10^9 \exp\left(-\frac{125 \cdot 10^3}{RT_s}\right)$
Heterogeneous char reactions		Kinetics
ox	$C + \varphi O_2 \rightarrow 2(1 - \varphi)CO + (2\varphi - 1)CO_2$	(R.4) $K^{ox} = 1.715 \cdot T_s \cdot \exp\left(-\frac{9000}{T_s}\right)$
g,1	$C + CO_2 \rightarrow 2CO$	(R.5) $K^{g,1} = 3.42 \cdot T_s \cdot \exp\left(-\frac{1.56 \cdot 10^4}{T_s}\right)$
g,2	$C + H_2O \rightarrow CO + H_2$	(R.6) $K^{g,2} = 5.7114 \cdot T_s \cdot \exp\left(-\frac{1.56 \cdot 10^4}{T_s}\right)$

Table 4
Composition of volatile species released in the devolatilization process.

Volatile specie (k)	Fraction (γ_k)
C ₆ H ₆	0.113
CH ₄	0.025
H ₂	0.038
CO	0.156
CO ₂	0.414
H ₂ O	0.251
NH ₃	0.0022

$$\varphi = \frac{2 + 4.3 \exp\left(\frac{-3390}{T_s}\right)}{2 \left[1 + 4.3 \exp\left(\frac{-3390}{T_s}\right) \right]} \quad (17)$$

3.1.2. Mass transfer

The set of equations described in the previous section refers to the chemical processes involved in the reaction of the freeboard gases with the solid phase (pellets), but the amount of freeboard gases arriving at the surface of the solid to react needs to be known. This mass transfer process is dominated by a mass transfer constant that is obtained in an analogous way as the convection coefficient is in Section 3.3.1, Eqs. (18) and (19). Note the similarity with Eqs. (30) and (31), shown below. The index j refers to each of the gaseous species reacting with the solid phase, i.e., O₂, H₂O and CO₂. The equivalent diameter considered in Eq. (18) refers to the diameter that a hypothetical pellet would have if it had a spherical shape of the same volume as the original pellet with the irregular shape. Its value is given in Table 1.

$$K_m^j = \frac{Sh \cdot D_j}{d_{eq}} \quad (18)$$

$$Sh = 2 + 1.1 \cdot Re^{0.6} \cdot Sc^{1/3} \quad (19)$$

Therefore, since char reactions are controlled both thermally and by the reactants diffusion, it means that these two physical processes will limit the global rate of reaction of each of the gaseous species reacting with the char. This statement finds its formulation in Eqs. (20)–(22) for each gaseous species.

$$K_{glob}^{ox} = \frac{1}{\frac{1}{K^{ox}} + \frac{1}{K_m^{ox}}} \quad (20)$$

$$K_{glob}^{g,1} = \frac{1}{\frac{1}{K^{g,1}} + \frac{1}{K_m^{g,1}}} \quad (21)$$

$$K_{glob}^{g,2} = \frac{1}{\frac{1}{K^{g,2}} + \frac{1}{K_m^{g,2}}} \quad (22)$$

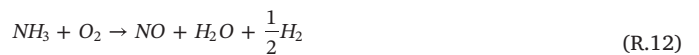
It might be argued that the diffusivity phenomenon of the species to reach the solid surface is taken into account twice: once by the diffusive term in the transport equation for each specie and twice in this mass transfer process. It must be noted that this has to be modeled this way since the mass transfer process takes place inside the cell itself. If the cells were small enough, the cell to cell diffusive term would be able to accurately limit the reaction speed, and this subtlety would not be necessary. The limitation comes from the fact that as the reactant species are consumed, more of them need to be fed to the reaction area to keep consuming the solid phase. However, since infinitely refined meshes are not feasible, diffusivity is taken into account in this fashion, artificially slowing down the reaction rate due to reactants not being present.

3.2. Gas phase

The gas products resulting from the ongoing char combustion in the solid phase are introduced in the gas phase of the packed bed for their combustion. The species composition of this resulting gas is conditioned by the biomass combustion rates in the solid phase, according to the bed state and expressed by the aforementioned equations, Eqs. (3)–(5). These species are water vapor (from the drying process, Eq. (3)), the volatile species (from wood devolatilization, Eq. (4)) and CO, CO₂ and H₂O (from char heterogeneous reactions (R.4)–(R.6)).

The volatile species are numerous and varied; however, with regard to hydrocarbons, they can be grouped under two main categories: heavy hydrocarbons (or tars, represented by benzene, C₆H₆) and light hydrocarbons (represented by methane, CH₄). They also feature CO, CO₂, H₂ and H₂O. The relative quantity of each of these species is defined according to the balance proposed by Thunman et al. [34]. In this work, a pyrolysis temperature of 1000 K was used to obtain the composition since the equations system returned positive values for all species. This ensures the mass and species balance is fulfilled. However, the energy balance is not fulfilled if the bed temperature is different. This is corrected through the energy source introduced (Eq. (2)), which compensates for the difference between the energy contained in the fuel and the energy of the species generated (volatiles and char). Table 4 shows the volatile species fractions released.

The authors have already published a set of chemical equations to describe the overall gas phase combustion in previous papers [14,20,32]. It is composed of the partial oxidation of the different hydrocarbons (C₆H₆ and CH₄), (R.7) and (R.8), the complete oxidation of hydrogen (H₂), (R.9), into carbon monoxide and water, which will then finish its combustion process by two mechanisms; first, its oxidation into carbon dioxide, (R.10); and second, a two-way reaction with water, (R.11). This second process will achieve an equilibrium status dependent not only on the forward and backward reaction rates but also on the hydrogen rate of oxidation. It must be noted that this two-way reaction must be introduced in the CFD package by means of two different reactions, i.e., the forwards and backwards reactions. The reaction scheme is completed by the NH₃ conversion into nitrogen, water and hydrogen by using a pair of equations that use NO as an intermediate species, as used by Brink [35], (R.12) and (R.13).



3.2.1. Momentum source

The fact that gas flows through the bed demands a special consideration on the momentum equation in the bed domain. Since the gas flow will worsen across porous media, a source term is needed to capture the momentum loss. It is expressed by Eq. (23) [36]. It takes into account the effect of three important magnitudes, namely, permeability, inertial losses and porosity, whereas Eqs. (24)–(27) account for permeability, inertial losses, sphericity and the equivalent diameter of the pellets, respectively. The equivalent diameter, calculated with

the average parameters of the fuel given in Table 1, is 8.8 mm, and the sphericity is 0.85.

$$S_{mom} = -\left(\frac{\mu}{\eta}v_{\infty} + Y\frac{1}{2}\rho_g v_{\infty}^2\right) \quad (23)$$

$$\eta = \frac{\kappa^2 d_{eq}^2 (1 - \varepsilon)^3}{150 \varepsilon^2} \quad (24)$$

$$Y = \frac{3.5 \varepsilon}{\kappa d_{eq} (1 - \varepsilon)^3} \quad (25)$$

$$\kappa = \frac{\pi^{1/3} (6V_p)^{2/3}}{A_p} \quad (26)$$

$$d_{eq} = D_{cyl} \left(\frac{3L_{cyl}}{2D_{cyl}}\right)^{1/3} \quad (27)$$

3.3. Heat transfer

Heat transfer plays an important role in the accuracy of a biomass combustion simulation. It takes place in very different ways, i.e., conduction, convection and radiation.

3.3.1. Conduction and convection

Conduction occurs in the gas phase between the different species in the freeboard and in the solid phase through the packed bed. This is a diffusive process that is modeled by using a thermal conductivity coefficient. This coefficient is determined experimentally for the solid phase, being 0.17 for a bed of wood particles and 0.12 for a bed of char particles. The homonymous magnitude for the gas phase is calculated through a mass weighted average of the different species, following Eq. (28).

$$k_g = \sum_i x_i k_{g_i} \quad (28)$$

The heat exchange between the solid and gas is a convective process, which is modeled by a source term in the energy equations of both the solid and gas phase. Since the heat rejected by one phase is received by the other phase, Eq. (29) applies to the description of the physical exchange, where the convective coefficient is calculated as per Eq. (30), which is the Nusselt number estimated by the correlation proposed by Wakao and Kagueli [37], Eq. (31).

$$S_s^{conv} = -S_g^{conv} = hA_v(T_g - T_s) \quad (29)$$

$$h = \frac{Nu \cdot k_g}{d_{eq}} \quad (30)$$

$$Nu = 2 + 1.1 \cdot Re^{0.6} \cdot Pr^{1/3} \quad (31)$$

3.3.2. Radiation

Because a biomass boiler is a high temperature system, radiation is the most important mechanism of heat transfer. It takes place mainly between the packed bed and the flame in the gas phase as well as between the solid particles inside the bed.

In this work, the radiation model used was already presented by the authors in [38]. It is a modification of the discrete ordinates model (DOM), which enables it to take into account both the solid and gas phase participation inside the packed bed.

The default radiative transfer equation (RTE), Eq. (32), is modified so that absorption, emission and scattering terms consider the contribution of the gas phase and solid phase. In addition, two source terms have to be included in the energy equations: one in the solid phase energy equation, Eq. (33), and the second one in the gas phase energy equation, Eq. (34).

A schematic of the modified DOM is presented in Fig. 3.

$$\nabla I(\mathbf{r}, \mathbf{s}) + (\alpha_s + \alpha_g + \sigma_g^{scat} + \sigma_s^{scat})I(\mathbf{r}, \mathbf{s}) = \frac{\alpha_s n^2 \sigma T_s^4}{\pi} + \frac{\alpha_g n^2 \sigma T_g^4}{\pi} + \frac{\sigma_g^{scat} + \sigma_s^{scat}}{4\pi} \int_0^{4\pi} I(\mathbf{r}, \mathbf{s}') \Phi(\mathbf{s}, \mathbf{s}') d\Omega \quad (32)$$

$$S_s^{rad} = \int_0^{4\pi} \left(\alpha_s I(\mathbf{r}, \mathbf{s}) - \frac{\alpha_s n^2 \sigma T_s^4}{\pi} \right) d\Omega \quad (33)$$

$$S_g^{rad} = \int_0^{4\pi} \left(\alpha_g I(\mathbf{r}, \mathbf{s}) - \frac{\alpha_g n^2 \sigma T_g^4}{\pi} \right) d\Omega \quad (34)$$

The approach of this method is treating the porous region as semitransparent media, using absorption and scattering coefficients to characterize the bed. An extinction coefficient for a bed of particles can be calculated as a function of the particle diameter and the porosity of the medium, using the formulation in [39], Eq. (35). The absorption and scattering coefficients can be related to the extinction coefficient through the surface absorptivity of the particles and the hypothesis of diffuse reflectivity, Eqs. (36) and (37), respectively. In the freeboard

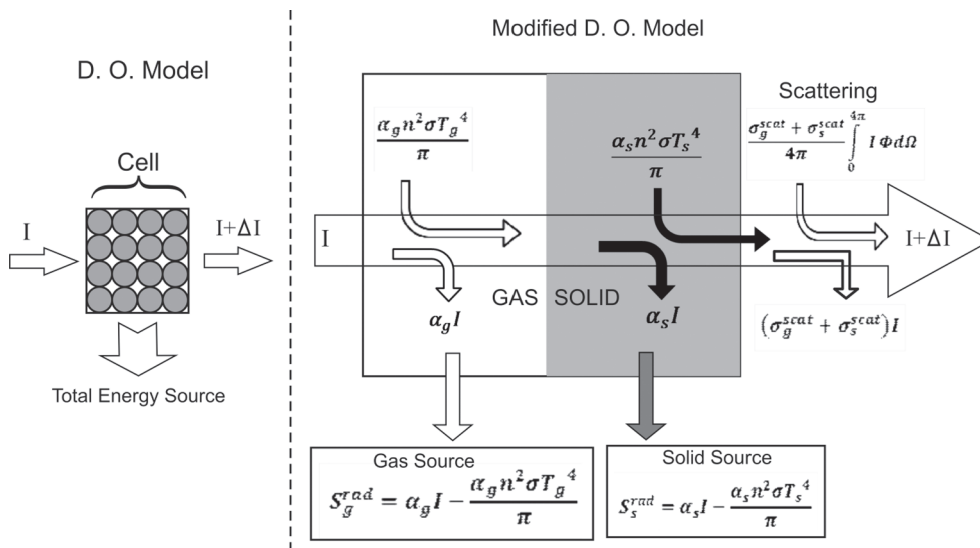


Fig. 3. Schematic explanation of the modified DOM [38].

region (outside of the bed), the absorption coefficient is calculated through the weighted sum of gray gases model (WSGGM), and the scattering coefficient of a common gas is negligible in comparison with the absorption coefficient.

Radiative heat transfer is relevant in the bed since this has a high absorption coefficient. Therefore, most of the incident radiation from the flame is extinguished in a depth of only a few millimeters. Therefore, most radiation is absorbed by the first two layers of particles. This heating contributes to heat the bed and keep the pyrolysis active. On the other hand, the bed has a high emissivity which causes a high heat emission to the boiler freeboard. Both processes, absorption and emission, play an important role in the packed bed energy balance and contribute to the combustion stability.

$$\beta_s = -\frac{1}{d_{eq}} \ln(1 - \epsilon) \tag{35}$$

$$\alpha_s = Ab \cdot \beta_s \tag{36}$$

$$\beta_s = \alpha_s + \sigma_s^{scat} \tag{37}$$

3.4. General models, mesh details and boundary conditions

The models previously described are implemented in a CFD environment and work in conjunction with other models integrated in the code. Second-order upwind methods are used to solve the spatial discretization of all equations except the turbulence since the first order scheme achieves a better convergence. The pressure is solved with PRESTO. The radiation transport is solved with a modification of the discrete ordinate model (DOM) (explained above) in the porous bed and through the original DOM in the rest of the domains. Turbulence was modeled through the realizable k-ε model. The chemical reactions are solved with Eddy Dissipation Concept (EDC). Particle drag was not considered in this work. Therefore, the whole solid fuel content is considered to react in the bed domain.

Several meshes were tested for the boiler geometry and to analyze the results' convergence on parameters such as heat transferred, gas emissions and the temperature fields inside the furnace. No significant changes were observed for grids with elements smaller than 10 mm on a side. The final grid used was a polyhedral mesh of approximately 1.5

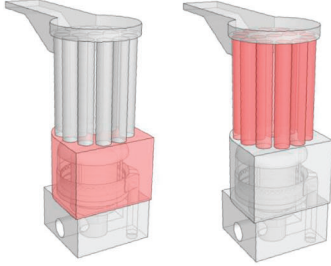
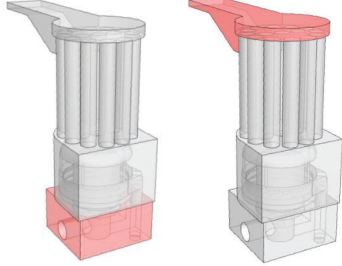
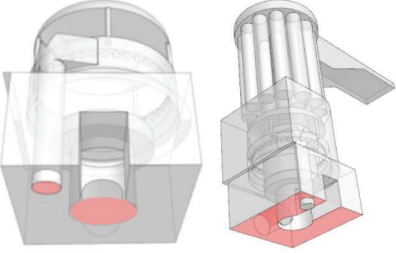
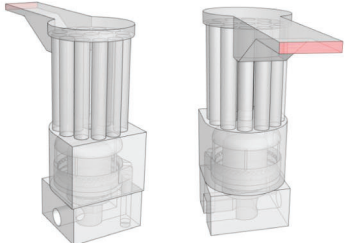
<p>Heat exchanger</p> <p>Walls cooled by water. Heat used by the heating system</p>	<p>Convection coefficient $h = 2500 \text{ W/m}^2\text{K}$ Water temperature $70 \text{ }^\circ\text{C}$ Steel thickness 3 mm</p>	
<p>Air cooled walls</p> <p>Convection coefficient $h = 15 \text{ W/m}^2\text{K}$ Air temperature $20 \text{ }^\circ\text{C}$ Steel thickness 3 mm</p>	<p>Convection coefficient $h = 15 \text{ W/m}^2\text{K}$ Air temperature $20 \text{ }^\circ\text{C}$ Steel thickness 3 mm</p>	
<p>Inlets</p> <p>Primary and secondary air inlets and infiltrations at the bottom of the boiler</p>	<p>Variable mass fluxes and ratios of oxygen, nitrogen and flue gases for simulated cases</p>	
<p>Flue gases outlet</p> <p>Measurements of gas emissions located in this boundary surface</p>	<p>Pressure outlet at atmospheric conditions</p>	

Fig. 4. Main boundary conditions of the boiler.

million elements, which offers an accurate spatial resolution without an excessively high computational cost. The average length of the cells is approximately 6 mm. For the regions close to the heat exchanger, the packed bed and the flame region were refined to ensure a higher accuracy of the key parameters such as heat transfer and chemical reactions. These zones are the bed region, especially near the small holes of the air injection, the cells close to the heat exchanger and the flame zone in which important temperature and species gradients are expected. The average cell sizes of 3 mm and 5 mm were used in the bed and heat exchanger regions, respectively.

Fig. 4 shows the main boundary conditions of the boiler and their main parameters and coefficients.

4. Experimental contrast

The experimental boiler was tested through several experiments to analyze its performance and thermal behavior. Fig. 5 shows a sketch of the whole experimental setup where the boiler is located. The boiler is connected to a water circuit, which receives heat from the combustion in the boiler and transports the hot water to an air-cooled heat sink, which then cycles back the cold water into the boiler heat exchanger. Several flowmeters are installed in the water circuit, also in both primary and secondary air inlets and a last one in the exhaust. In addition, a gas analyzer is located in the exhaust tube to measure some parameters of the flue gases, such as temperature or gases concentrations.

Two experiments (E1 and E2) were performed in the described boiler with different rates of primary and secondary air flow since these air rates can affect the boiler behavior, especially gas emissions. For both experiments, the fuel rate introduced in the grate was equivalent to 36.6 [kW] and the water temperature was 70 [°C]. Table 5 shows the flow rates measured in the primary and secondary inlets. It also includes the air infiltrations, which are obtained as the flow rate difference between what goes in on the primary and secondary inlets and what goes out on the outlet. It must be noted that infiltrations should be assessed when the fuel is not burning so that balances are kept.

These measurements show that the flow rate of air infiltrations is relatively high. Air infiltrations are not usually an especially negative factor since they work as an extra contribution to the secondary air. In practice, air infiltrations are virtually unavoidable since this type of boiler works with negative pressure, and the air is filtered by any existing slot. They occur very commonly in the fuel feeding screws. In the boiler simulated in this work, most infiltrations are located in the lower region of the boiler. As the exact location of all infiltrations is impossible to determine, we modeled the infiltration inlet at the bottom of the boiler, as shown in Fig. 4.

In the experiments performed with the boiler, a steady state is reached to analyze the overall behavior. Parameters such as the heat exchanged, fume temperatures and emissions of CO₂, CO and NO_x are compared to those collected from the numerical simulations performed with the model. Fig. 6 shows the comparison of these parameters for both tests E1 and E2. The gas analyzer located in the boiler exhaust duct reports the measurements of CO, CO₂ and NO_x volumetric concentrations considering a regular 10% oxygen concentration. The simulation results are also expressed in a 10% oxygen base.

Since these measurements are collected far from the flame region, the flame prediction of the model cannot be validated, but it can be useful to predict the general behavior of the boiler and study how it affects performance and gas emissions.

Fig. 6 shows the comparison between simulation and experimental tests, with results being reasonably close for most of the parameters. Good predictions of net heat transferred and fume temperatures are observed, as the maximum discrepancy found is lower than 5%. The comparison of CO₂ emissions also achieves good predictions. This parameter depends on the carbon balance when the reactions can be considered to be completed. Since the CO emissions are relatively low, reactions can in fact be considered to be completed; therefore the slight

discrepancies in CO₂ emissions can be caused by a potential inaccuracy in the fuel composition data. A greater error can be observed in the prediction of CO and NO_x emissions; however, these results can be deemed reasonably good considering the simplicity of the CO and NO reaction mechanisms applied in the model.

5. Results and discussion

After contrasting the model with two experimental tests in which no gas recirculation was present, in this section, the results of several theoretical tests are shown as an extension of the model to understand the behavior of the boiler when a certain fraction of EGR is present. The results are presented in terms of 3D fields of the main variables inside the boiler and the gas emissions. A total of 36 tests were performed varying both the exhaust recirculation fraction (from 0 to 0.5) and the oxygen excess (from 1 to 1.5), following Table 2. It must be noted that these cases consider infiltrations to be zero and the boiler to be fed by pure oxygen in order to draw a fair conclusion for the theoretical study proposed. The boiler is always fed with an equivalent fuel flow rate so that the boiler produces a power of 36.6 [kW].

5.1. Effect of EGR

The effect of EGR in the boiler behavior can be visualized through the contours of the main variables affecting the combustion process. Some variables such as temperature and reacting species are shown below. Fig. 7 shows the temperature and the oxygen concentration fields on the boiler central plane for different EGR fractions with a fixed oxygen excess of 1.1. Thermally, the main effect of EGR is an increase in the temperature of the freeboard gases, especially in the flame. This is caused by the recirculation of hot gases that increases the gas inlet temperature. This way, the flame becomes more reactive, since a higher temperature favors the reaction kinetics. It is especially noticeable in the primary gas injection, just over the fuel grate, in which a high temperature concentration is visible. In the oxygen concentration field, the main difference is found in the primary and secondary air regions, in which the oxygen concentration decreases with the gas recirculation fraction. Inside the freeboard, no significant differences of oxygen concentration are found since the oxygen excess is the same for all of the cases. Fig. 8 shows the contours of light hydrocarbons (represented by CH₄), CO and NO, which help to visualize the combustion process and the effectiveness of reactions. The CH₄ concentration field shows that EGR improves the reactivity of hydrocarbons since the mole fraction is lower inside the flame, and the visible region of CH₄ looks shorter. A similar behavior is found in the CO profile, which reflects an increase of reactivity with the EGR. The NO profile shows a positive

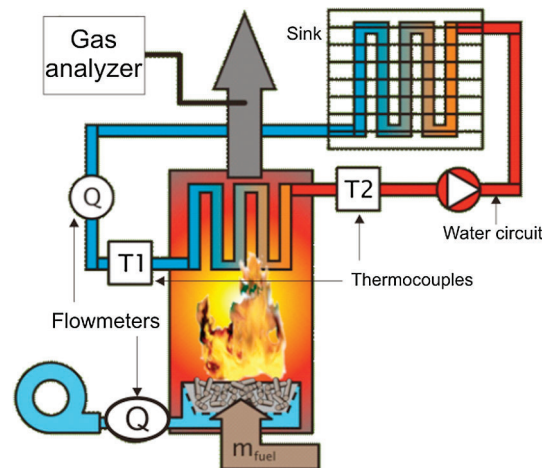


Fig. 5. Schematic of the experimental setup [32].

Table 5
Operating conditions for the experimental tests.

Test	Fuel Feeding Rate [g·s ⁻¹]	Primary Air Flow Rate [g·s ⁻¹]	Secondary Air Flow Rate [g·s ⁻¹]	Air Infiltration [g·s ⁻¹]
E1	2.26	4.7 (13%)	9.6 (27%)	20.6 (60%)
E2	2.26	7.3 (22%)	8.0 (24%)	17.6 (54%)

effect of EGR to reduce the contaminant emissions of NO_x due to the reduction of NO concentration beyond the flame region. This effect may be caused by the dilution of oxygen produced by the inert species present in the exhaust gases. A typical explanation for the reduction of NO_x emissions when EGR is applied on combustion engines is the temperature reduction of the mixture. In this case, the reduction of temperature does not occur in the freeboard, as the exhaust recirculation is done without any cooling process prior to reintroducing the hot gases. Therefore, the NO reduction effect can only be attributed to the oxygen dilution.

5.2. Effect of oxygen excess (λ)

The effect of oxygen excess was also studied for different recirculation fractions. The oxygen excess ratio was varied from 1 to 1.5, measured in the oxygen inlet. Nevertheless, the recirculation effect adds a certain fraction of oxygen in the primary and secondary gas injections. As a result, the effective oxygen excess ratio is increased by EGR. Figs. 9 and 10 show the field of the main variables inside the boiler for a fixed EGR fraction of 0.5 and different oxygen excess ratios in the inlets. In Fig. 9, the temperature and oxygen profiles show a great increase of the flame temperature due to the higher oxygen supply of the primary inlet, which allows for a faster reaction of char and the hydrocarbons released from the bed. Because of the higher quantity of air, more

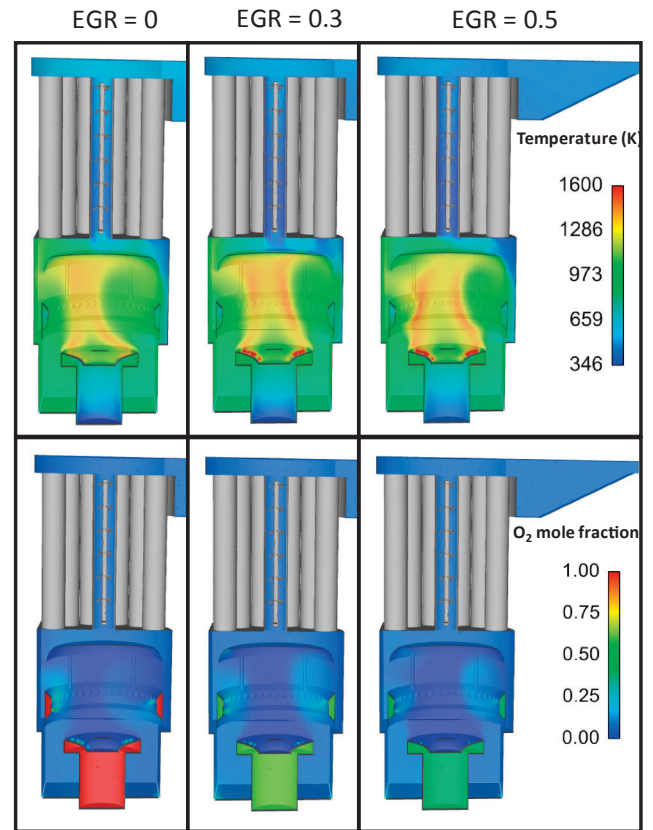


Fig. 7. Fields of temperature and O₂ fractions inside the boiler for EGR fractions 0, 0.3 and 0.5 and an oxygen excess $\lambda = 1.1$.

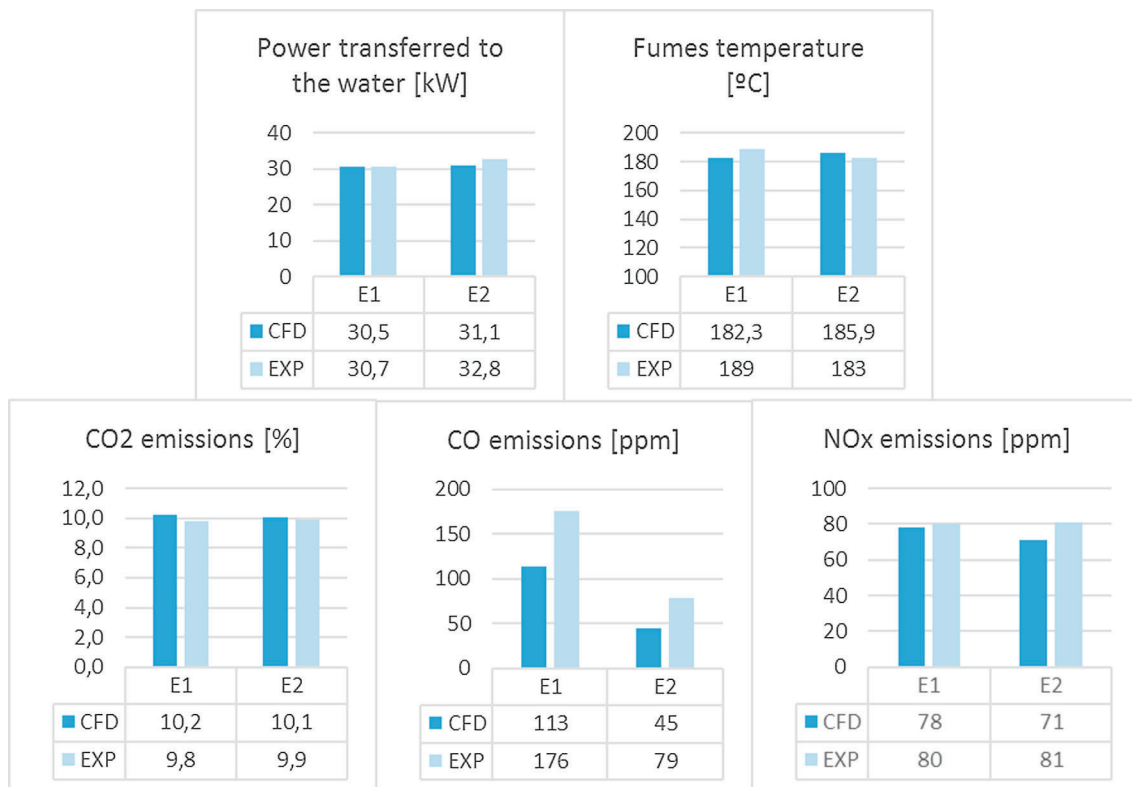


Fig. 6. Experimental results vs model prediction.

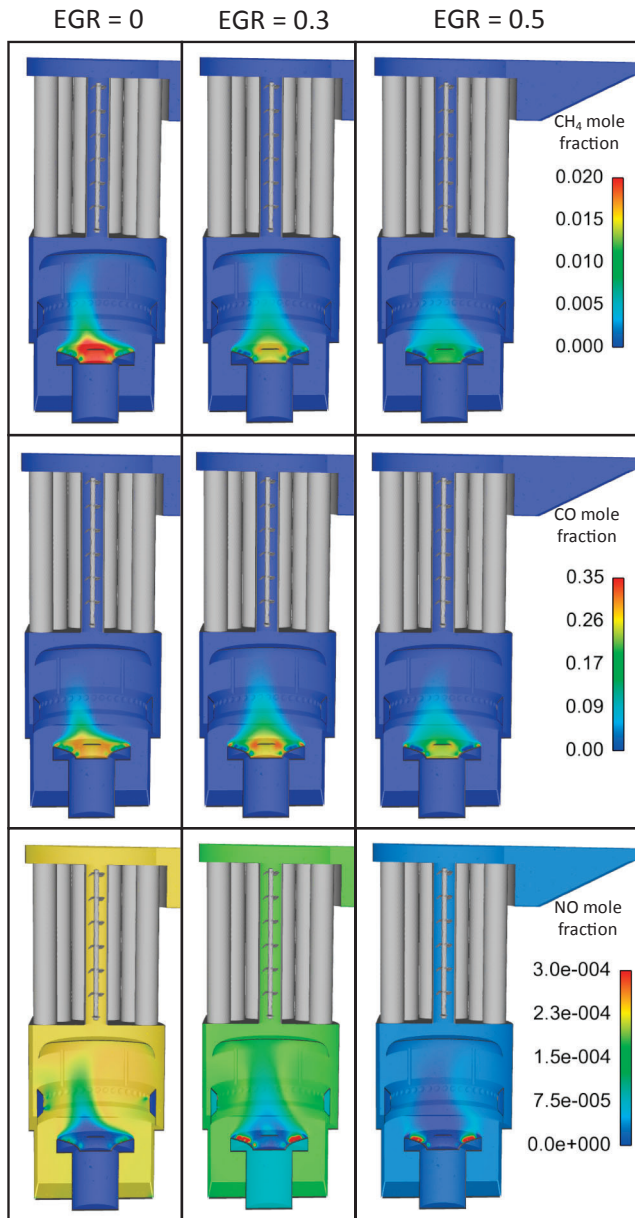


Fig. 8. Fields of CH_4 , CO and NO fractions inside the boiler for EGR fractions of 0, 0.3 and 0.5 and an oxygen excess ratio of $\lambda = 1.1$.

oxygen is available for reaction; therefore, char and volatiles emitted from the bed will react more readily and that is the reason why the flame is concentrated in that area. For the rest of the boiler freeboard, the temperature fields do not show significant differences. In Fig. 10, the profiles of CH_4 , CO and NO are shown. CH_4 and CO contours show a similar trend. High concentrations of these species are present in a larger region of the freeboard for low values of λ since the reactions are delayed due to the lack of oxygen. This difficulty to complete the reactions produces more unburnt species. Therefore, more contaminant emissions are expected when the boiler operates with a low value of λ . The field of the NO mole fraction shows a clear increase of NO concentration in the whole boiler when the oxygen excess ratio grows. This may be caused by the higher concentrations of oxygen, which is the same way that it happens when the EGR fraction decreases (Fig. 8). It can also be affected by the high temperature reached just over the grate where the higher concentrations of NO are found, especially when the value of λ is increased.

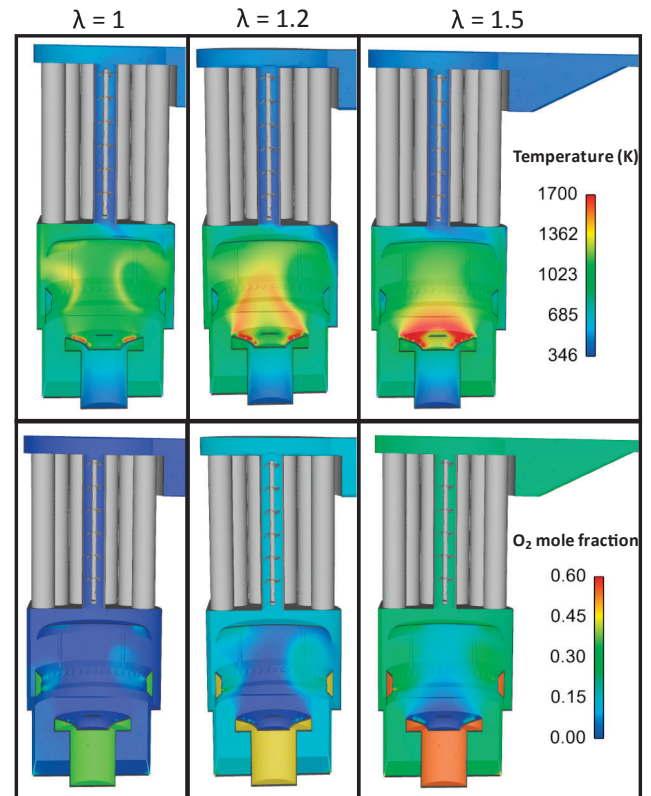


Fig. 9. Fields of temperature and O_2 fraction inside the boiler for oxygen excess ratios of 1, 1.2 and 1.5 for a fixed EGR of 0.5.

5.3. Boiler performance and exhaust emissions

In this section, the results of the whole set of simulations are compared to draw conclusions about the combined effect of EGR and λ on the heat transferred to the water and the boiler emissions. Fig. 11 shows the heat transferred from the hot gases to the water, i.e., the boiler useful energy. The graph shows, on one hand, that EGR increases the heat transferred, especially for low values of λ . In addition, on the other hand, a rise of λ decreases the heat transferred to the water. In this case, the increase of the flow of gases produces two opposite tendencies. On the one hand, the increase of gas velocity enhances the convective heat transfer. On the other hand, the increase of the flow of gases produces a higher thermal inertia of the gas stream. This gas stream is more difficult to cool, and it transports a higher sensible enthalpy to the exhaust. In this case, the simulation shows that the increase of thermal inertia has a higher influence than the enhancement of convective heat transfer. The same could be argued in the case of EGR, as the flow rate through the boiler is higher when recirculation is on. However, the exhaust mass flow rate is kept the same for a given λ , which means that no more heat quantity is rejected in the exhaust. Therefore, heat rejected in the exhaust is kept the same as the increase in flow rate is recirculated, i.e., the heat is not rejected; rather, it is recirculated. The reason why the heat transferred to the water is higher with EGR is that, as consequence of the higher mass flow rate through the boiler, the gas velocities are higher. This results in an improvement in the heat exchanger convection coefficients that boosts the amount of convective heat transferred to the water. The boiler transfers approximately 36 [kW] in the most favorable case of those simulated, which means that the boiler performance increases up to 98%.

The flue gases emissions are also analyzed. Fig. 12 shows the concentration of CO_2 in the flue gases relative to the 10% of O_2 volumetric concentration. This fact produces the increase of CO_2 concentration with λ . EGR does not produce any visible effect since the CO_2

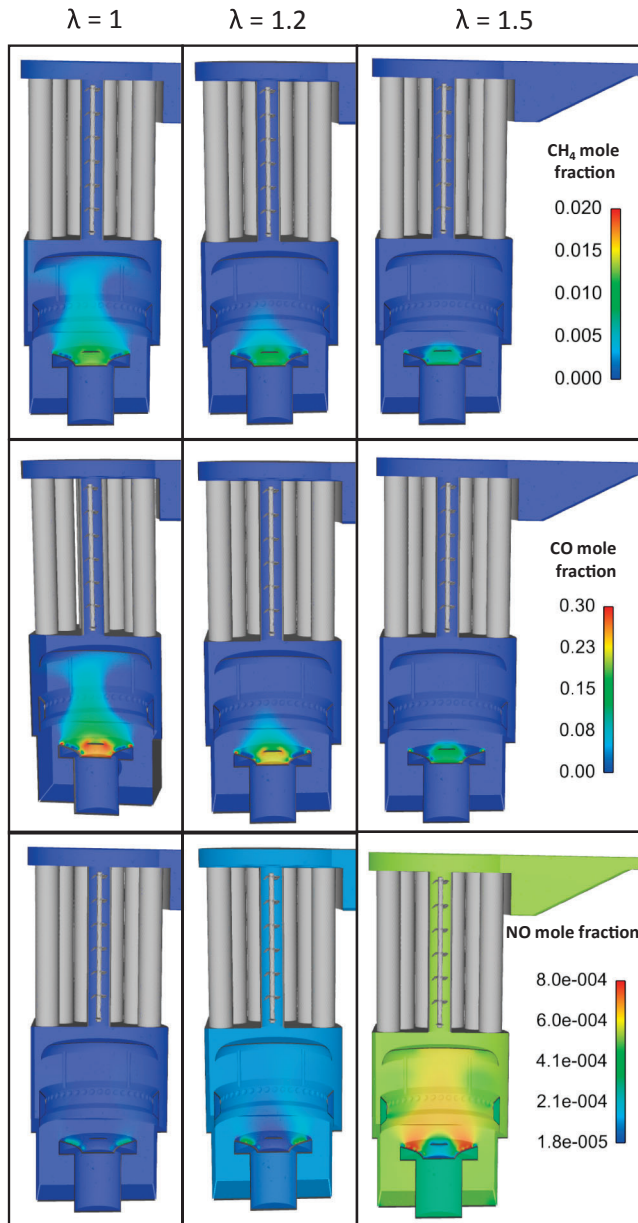


Fig. 10. Fields of CH₄, CO and NO fractions inside the boiler for oxygen excess ratios of 1, 1.2 and 1.5 for a fixed EGR of 0.5.

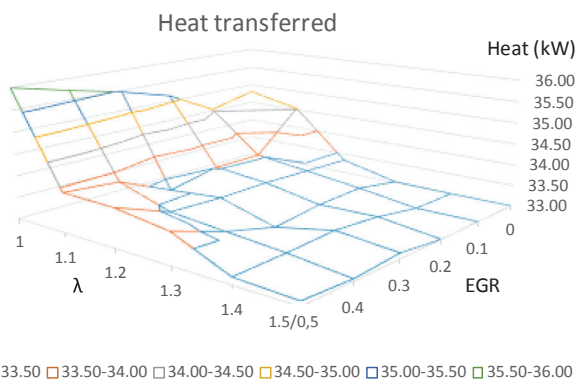


Fig. 11. Combined effect of EGR and λ on the heat transferred by the boiler.

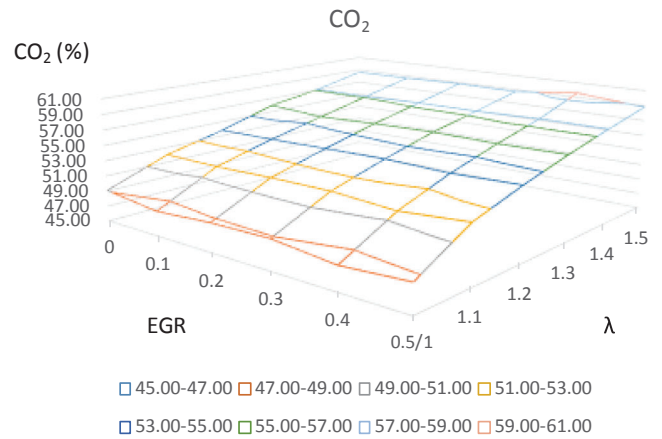


Fig. 12. Combined effect of EGR and λ on CO₂ concentration in flue gases.

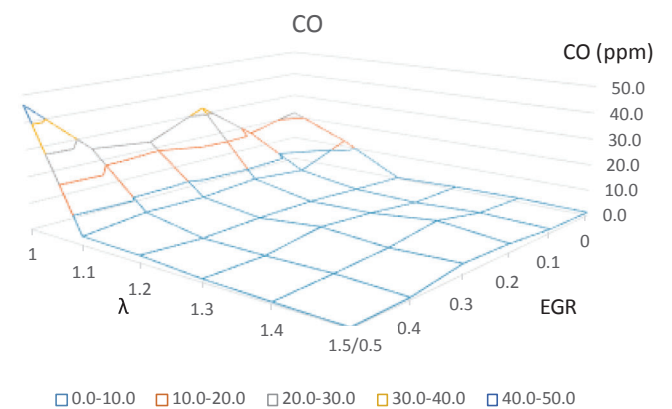


Fig. 13. Combined effect of EGR and λ on CO concentration in flue gases.

concentration only depends on the fuel mass balance and the inlet flow. Therefore, for the same value of λ , the CO₂ concentration must remain constant, as long as the reactions are completed. The CO₂ concentrations shown in this figure reach values close to 60%. These high values are caused because a nearly pure oxygen flow is introduced at the inlets. Therefore, the concentration of CO₂ and H₂O is high when the reactions are complete. Fig. 13 shows that the concentration of CO is also relative to the 10% of O₂ in the exhaust gases. This boiler has a good behavior to avoid high CO emissions due to the aforementioned design that avoids the flame quenching. This good behavior was already seen in experimental tests, and the effect of feeding more oxygen is a further improvement on this, as the CO emissions are virtually null for most of the operation points simulated. The only visible effect is the increase of emissions for low values of λ , which was expected because the oxygen provided is just enough to complete the reactions, and some CO leaves the boiler without reacting. In the same way it occurred with CO₂, no noticeable effect is produced by EGR on CO either.

The effect of EGR and oxygen excess ratio on NO emissions, (which eventually means NO_x), is shown in Fig. 14. The oxygen excess ratio clearly increases the NO production, especially when increasing EGR as well, due to the high temperatures reached by the flame. The effect of EGR is more complex. There is an area in which NO emissions creep up as the EGR fraction is increasing, but it reaches a point (at approximately the EGR fraction of 0.4 in the case studied) at which two different effects take place. For higher air excess ratios, the NO emissions keep increasing from this point on, with a higher slope. However, for slightly lean stoichiometries, i.e., lower air excess ratios, the effect is the opposite, with NO emissions decreasing from that point on. This may occur because EGR boosts the oxygen excess, which increases the NO production if λ is high, but the boost of λ is negligible if λ is low.

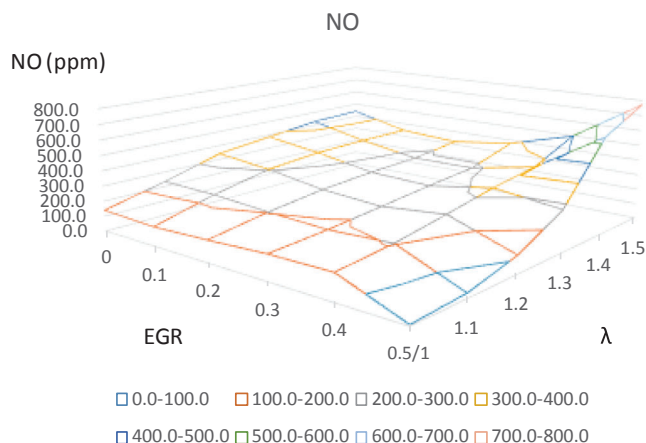


Fig. 14. Combined effect of EGR and λ on NO concentration in flue gases.

6. Conclusions

In this paper, a theoretical study on the influence of EGR and oxygen excess ratio (λ) in a biomass boiler fed with pure oxygen is performed. For this purpose, an efficient numerical model for the simulation of biomass combustion is proposed through additional in-built routines on a CFD commercial code. The model implements several submodels of thermal conversion of solid biomass as well as heat and mass transfer, chemical reactions and radiation transport to solve the behavior of a boiler in a steady state situation with a relatively low computational cost.

The model is applied to the simulation of several experimental tests in a domestic boiler. The agreement was assessed on some parameters such as the net heat transferred, the fume temperatures and the gas emissions, with the simulated results showing a reasonably good correlation to the experimental data. Even CO and NO_x predictions are reasonably good considering the simplicity of the CO and NO mechanisms. These predictions could be improved by considering other mechanisms such as the NO destruction in presence of char and CO since these species play an important role in the balance formation-destruction of NO.

To carry out the study, a set of 36 simulations were performed and the results were analyzed. Parameters such as the flame temperature and gas concentrations inside the boiler freeboard were studied through the 3D fields of the variables. The combined effect of EGR and oxygen excess ratio on boiler performance and contaminant emissions was studied for the ranges of 0–0.5 for the EGR fraction and of 1–1.5 for the oxygen excess ratio.

The results showed a noticeable increase of heat transferred when EGR increases and the oxygen excess is low. EGR reduces NO emissions at low values of the oxygen excess ratio but the emissions increase significantly when oxygen is abundant. No significant effect of EGR was found on CO emissions. Therefore, EGR can be positive for thermal performance and contaminant emissions at moderately low values of the oxygen excess ($\lambda = 1.1$ – 1.2).

Acknowledgments

The authors acknowledge financial support from Project ENE2015-67439-R of the Ministry of the Economy of Spain.

References

- Chen J, Song W, Xu D. Optimal combustor dimensions for the catalytic combustion of methane-air mixtures in micro-channels. *Energy Convers Manage* 2017;134:197–207.
- Guo C, et al. Effect of fuel injection characteristics on the performance of a free-piston diesel engine linear generator: CFD simulation and experimental results. *Energy Convers Manage* 2018;160:302–12.
- Shu J, et al. Experimental and computational study on the effects of injection timing on thermodynamics, combustion and emission characteristics of a natural gas (NG)-diesel dual fuel engine at low speed and low load. *Energy Convers Manage* 2018;160:426–38.
- Karim MR, Naser J. Progress in numerical modelling of packed bed biomass combustion. Proceedings of the 19th Australasian fluid mechanics conference, AFMC 2014. 2014.
- Eskilsson D, et al. Optimisation of efficiency and emissions in pellet burners. *Biomass Bioenergy* 2004;27(6):541–6.
- Porteiro J, et al. Numerical modeling of a biomass pellet domestic boiler. *Energy Fuels* 2009;23(2):1067–75.
- Kær SK. Numerical modelling of a straw-fired grate boiler. *Fuel* 2004;83(9):1183–90.
- Yin C, et al. Mathematical modeling and experimental study of biomass combustion in a thermal 108 MW grate-fired boiler. *Energy Fuels* 2008;22(2):1380–90.
- Zhou H, et al. Numerical modeling of straw combustion in a fixed bed. *Fuel* 2005;84(4):389–403.
- Cooper J, Hallett WLH. A numerical model for packed-bed combustion of char particles. *Chem Eng Sci* 2000;55(20):4451–60.
- Thunman H, Leckner B. Co-current and counter-current fixed bed combustion of biofuel – a comparison. *Fuel* 2003;82(3):275–83.
- Yang YB, et al. Mathematical modelling of MSW incineration on a travelling bed. *Waste Manage (Oxford)* 2002;22(4):369–80.
- Collazo J, et al. Numerical modeling of the combustion of densified wood under fixed-bed conditions. *Fuel* 2012;93:149–59.
- Gómez MA, et al. CFD modelling of thermal conversion and packed bed compaction in biomass combustion. *Fuel* 2014;117(PART A):716–32.
- Yang YB, et al. Fuel size effect on pinewood combustion in a packed bed. *Fuel* 2005;84(16):2026–38.
- Thunman H, et al. Combustion of wood particles – a particle model for Eulerian calculations. *Combust Flame* 2002;129(1–2):30–46.
- Mehrabian R, et al. A CFD model for thermal conversion of thermally thick biomass particles. *Fuel Process Technol* 2012;95:96–108.
- Mehrabian R, Scharler R, Obernberger I. Effects of pyrolysis conditions on the heating rate in biomass particles and applicability of TGA kinetic parameters in particle thermal conversion modelling. *Fuel* 2012;93:567–75.
- Ström H, Thunman H. CFD simulations of biofuel bed conversion: a submodel for the drying and devolatilization of thermally thick wood particles. *Combust Flame* 2013;160(2):417–31.
- Gómez MA, et al. Fast-solving thermally thick model of biomass particles embedded in a CFD code for the simulation of fixed-bed burners. *Energy Convers Manage* 2015;105:30–44.
- Gómez MA, et al. Dynamic simulation of a biomass domestic boiler under thermally thick considerations. *Energy Convers Manage* 2017;140:260–72.
- Karim MR, Naser J. Numerical study of the ignition front propagation of different pelletised biomass in a packed bed furnace. *Appl Therm Eng* 2018;128:772–84.
- Karim MR, Naser J. CFD modelling of combustion and associated emission of wet woody biomass in a 4 MW moving grate boiler. *Fuel* 2018;222:656–74.
- Peters B, Bruch C. Drying and pyrolysis of wood particles: experiments and simulation. *J Anal Appl Pyroly* 2003;70(2):233–50.
- Wiese J, et al. DEM/CFD modeling of the fuel conversion in a pellet stove. *Fuel Process Technol* 2016;152:223–39.
- Yu Z, Ma X, Liao Y. Mathematical modeling of combustion in a grate-fired boiler burning straw and effect of operating conditions under air- and oxygen-enriched atmospheres. *Renew Energy* 2010;35(5):895–903.
- Nimmo W, Daood SS, Gibbs BM. The effect of O₂ enrichment on NO_x formation in biomass co-fired pulverised coal combustion. *Fuel* 2010;89(10):2945–52.
- Bhuiyan AA, Naser J. Numerical modelling of oxy fuel combustion, the effect of radiative and convective heat transfer and burnout. *Fuel* 2015;139:268–84.
- Karim MR, Bhuiyan AA, Naser J. Effect of recycled flue gas ratios for pellet type biomass combustion in a packed bed furnace. *Int J Heat Mass Transf* 2018;120:1031–43.
- Rajh B, et al. Advanced modelling and testing of a 13 MWth waste wood-fired grate boiler with recycled flue gas. *Energy Convers Manage* 2016;125:230–41.
- Rajh B, et al. Advanced CFD modelling of air and recycled flue gas staging in a waste wood-fired grate boiler for higher combustion efficiency and greater environmental benefits. *J Environ Manage* 2018;218:200–8.
- Gómez MA, et al. Eulerian CFD modelling for biomass combustion. Transient simulation of an underfeed pellet boiler. *Energy Convers Manage* 2015;101:666–80.
- Wagenaar BM, Prins W, van Swaaij WPM. Flash pyrolysis kinetics of pine wood. *Fuel Process Technol* 1993;36(1–3):291–8.
- Thunman H, et al. Composition of volatile gases and thermochemical properties of wood for modeling of fixed or fluidized beds. *Energy Fuels* 2001;15(6):1488–97.
- Brink A, Kilpinen P, Hupa M. A simplified kinetic rate expression for describing the oxidation of volatile fuel-N in biomass combustion. *Energy Fuels* 2001;15(5):1094–9.
- Ergun S. Fluid flow through packed columns. *Chem Eng Prog* 1952;48(2):89–94.
- Wakao N, Kagueli S, Funazkri T. Effect of fluid dispersion coefficients on particle-to-fluid heat transfer coefficients in packed beds. Correlation of Nusselt numbers. *Chem Eng Sci* 1979;34(3):325–36.
- Gómez MA, et al. CFD simulation of a solar radiation absorber. *Int J Heat Mass Transf* 2013;57(1):231–40.
- Shin D, Choi S. The combustion of simulated waste particles in a fixed bed. *Combust Flame* 2000;121(1–2):167–80.

Improving Bed Movement Physics in Biomass Computational Fluid Dynamics Combustion Simulations

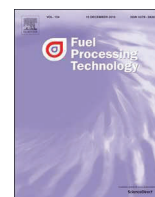
Luis González Varela Cesar Álvarez Bermúdez Sergio Chapela Jacobo Porteiro José L. Míguez Tabarés

To cite this article: Varela, L.G., Bermúdez, C.Á., Chapela, S., Porteiro, J. and Tabarés, J.L.M. (2019), Improving Bed Movement Physics in Biomass Computational Fluid Dynamics Combustion Simulations. Chem. Eng. Technol., 42: 2556-2564. doi:[10.1002/ceat.201800674](https://doi.org/10.1002/ceat.201800674)

The final authenticated version is available online at: <https://doi.org/10.1002/ceat.201800674>

Abstract:

A detailed description of the first functional new approach to simulate the bed physics in biomass boilers in a Eulerian mathematical framework is presented. In particular, the analysis of the context of the collapse due to gravitational forces, the design of an automated algorithm that is responsible for its simulation under ANSYS-Fluent, the concrete implementation of this algorithm, and its test with experimental contrasted data are described. The proposed solution can replicate the angle of repose of different fuels in biomass combustion boilers by implementing a series of geometric mechanisms applied to the mesh. The selected approach mainly responds to a computational efficiency requirement; both memory management and execution speed are relevant.



Research article

Three-dimensional CFD simulation of a large-scale grate-fired biomass furnace



César A. Bermúdez, Jacobo Porteiro*, Luis G. Varela, Sergio Chapela, David Patiño

Industrial Engineering School, University of Vigo, Lagoas-Marcosende s/n, Vigo, Spain

ARTICLE INFO

Keywords:

CFD
Biomass
Combustion
Grate-fired
Eulerian

ABSTRACT

Moving grate boilers are widely used in the combustion of solid biomass at industrial scale for heat and power production. This type of systems allows to use wide range of fuels, including those with a high moisture and ash content. However, biomass boilers present several associated problems, such as e pollutant missions or ageing phenomena that can reduce the efficiency of the boilers or damage them such as fouling, slagging or corrosion. CFD tools can be used to study biomass combustion systems providing information useful to optimize the operation and design of the boilers. In this work, an Eulerian fixed-bed biomass combustion model coupled with the CFD commercial code ANSYS-Fluent will be used to carry out the simulation of a large-scale moving grate biomass furnace. New procedures have to be developed to adapt the model operation to the characteristics of this case. The numerical results are compared with experimental data from literature. The new procedures provide a solution of the bed morphology, which is validated against the experimental data.

1. Introduction

The global energy demand is set to grow more than 25% to 2040. The concern about global warming and the need for new energy supplies have led to an increase in the share of renewables energies in the global power mix, rising from 25% to above 40% by 2040 [1].

Biomass is a renewable energy source that can be found worldwide in many different forms and types and from different origins such as agriculture, forestry, by-products, residues and wastes or even algae [2]. Its availability and its diversity, alongside its versatility to be converted into solid, liquid and gaseous fuels, have placed biomass as the fourth largest energy source after coal, oil and natural gas, representing between 10% and 14% of the global energy supply [3,4].

Biomass can be obtained from existing biomass stocks, which are usually residues, or dedicated energy feedstocks [5]. The latter tend to be high-yielding energy crops which are commonly used to produce liquid biofuels such as bioethanol and biodiesel [6–9]. However, there have been debates about the sustainability of this model due to the risk of using farmland and crops for biofuels production instead of food supply and the increase of greenhouse gas emissions associated with land clearing and cultivation [1,3]. Because of this, the called second-generation feedstocks, which mainly include lignocellulosic biomass, residues and crops that do not interfere with food production, are more attractive from an environmental and sustainable point of view [10,11].

It is possible to obtain high quality biofuels, as those produced from the dedicated energy crops, from these feedstocks with much lower environmental impact by various processes such as gasification, fermentation or pyrolysis [12–16].

In developed countries these high quality biofuels are mainly used as motor fuel and woody biomass is used for heat and power production and residential heating, being alternatives to fossil fuels [3,17]. Biomass can be a key factor for developing nations which do not have access to or cannot afford other energy sources, especially for rural areas where solid biomass is already the most important source of energy [3,5].

The most common methods to obtain energy from solid biomass are direct combustion, gasification and pyrolysis, which are thermochemical processes [4,5]. The biomass combustion is a widely used method for heat and power production due to its versatility and adaptability. The fuels used are very diverse and can be pre-treated by methods like densification, torrefaction or drying, which improve their qualities [18–22]. Also, biomass combustion has a broad application range, going from small-scale boilers to industrial furnaces dedicated to heat and/or power production [5,18,22–24].

To fulfil the requirements of each specific application and to allow the use of different fuels, several methods of combustion of solid biomass and boiler designs are used. The most common systems of solid biomass combustion are fixed bed combustors, bubbling and circulating

* Corresponding author.

E-mail address: porteiro@uvigo.es (J. Porteiro).

<https://doi.org/10.1016/j.fuproc.2019.106219>

Received 1 March 2019; Received in revised form 31 July 2019; Accepted 15 September 2019

Available online 24 October 2019

0378-3820/ © 2019 Elsevier B.V. All rights reserved.

fluidized bed combustors and suspension combustors. Pile burners and grate-fired boilers are the two typical types of fixed bed combustors [5]. Grate-fired boilers can burn almost any solid fuel, even low-grade ones, and are relatively cheap to produce and very robust. Also, the grate usually presents movement mechanisms to distribute the fuel bed and to collect the ash, which allows the continuous operating of the boiler. These characteristics have made grate-firing the most used technology for the combustion of solid biomass for large-scale boilers [5,23,25].

However, the combustion of biomass presents some associated problems. Gases and particulate matter, which are harmful to human health, are emitted during the biomass combustion [26–29]. Also, phenomena such as fouling, slagging and corrosion, that reduce the thermal efficiency of the boiler and can cause damage to it, are present mainly due to the alkalis content of the biomass [30–32].

For these reasons, it is necessary to study the combustion of biomass to improve the efficiency and performance of the combustion systems and to reduce the pollutant emission. Computational Fluid Dynamics (CFD) are widely used in the study of biomass combustion systems [33–43]. CFD codes are useful in the study of the combustion behaviour and adaptability of different fuels in biomass combustion systems [33,34]. Ash deposition and fouling can also be analysed using these techniques, to have a better understanding of these phenomena and minimize their negative effects [35,36]. Also, the CFD simulations allow to test different boiler operating conditions and to improve their design [37,38].

CFD commercial codes can be used to calculate the gas phase but submodels are necessary to model the solid bed and the thermal processes that occur in it. The gas and the bed interact with each other so it is necessary to couple the CFD code with the bed submodels. In some works, the bed is externally modelled through empirical correlations on an external solver and the solution is introduced through an inlet with specific boundary conditions [34,39,42]. In others, the effect of the bed is modelled by energy and species sinks and sources acting over a predefined cell zone, where the bed is expected to be located. This approach has already been successfully used to simulate grate-fired boilers [37]. However, these methods do not contemplate many of the phenomena that occur in the bed, especially the bed movements and its consequences. To carry out more comprehensive simulations, it is necessary to use models that reflect the evolution of each fuel particle and their effect on the boiler gas flow. Discrete Element Method models are used to model the physical phenomena of solid particles. Coupling CFD and DEM allows to simulate fluid systems with solid particles able to move and to interact with the gas [40,41]. Nonetheless, this method has a high computational cost associated and can increase simulation times excessively, especially in large-scale cases where there are a large number of particles moving over a wide area, which is the case of grate-fired boilers [40]. Eulerian models are a more balanced approach to take into account the solid fuel bed behaviour with enough precision but lower computational requirements than DEM methods [41].

Since 2005, Porteiro et al. have been developing an Eulerian model for the simulation of the combustion/gasification of biomass fully integrated into the commercial CFD code ANSYS-Fluent, which is able to simulate fixed bed biomass boilers [42–46]. In the early stages, the model was zero-dimensional and consisted of a stand-alone code which was calculated in an external solver. In the CFD simulation, the bed was modelled as an inlet boundary. The radiation incident in this inlet was computed and passed to the solver which returned the gas temperature, species, velocities and particles as inputs for the bed inlet [42]. Later, this code was fully integrated into the CFD simulation domain, defining the bed cell zone as a porous medium and the energy and mass sources that model the bed reaction, by a User Defined Function programmed in C/C++ [43]. The next step was to introduce solid phase variables into the UDF. The solution of the transport equations of each scalar will model the transient evolution of the solid bed, achieving a more realistic approach. These Eulerian solid bed variables are introduced as User Defined Scalars [44,45]. Also, other submodels and mechanisms

such as heat and mass transfer, particle shrinkage, bed compaction and fuel feeding, using Lagrangian trajectories or advective flux terms in the transport equations, have been developed and implemented in the code during this time [44–46]. New procedures and improvements are still being done and the development is open to collaborations. The results of the CFD simulations carried out during these works have been compared to experimental data, showing a good approximation between the CFD results and the reality and therefore validating the model.

In this work, a CFD three-dimensional transient simulation of a 4 MW grate-fired biomass furnace will be carried out using ANSYS-Fluent and the aforementioned bed model. This will be the first time that this model is used to simulate a grate-fired boiler. Some new procedures have to be developed to adequate the model operation to this type of boiler. The results will be compared to experimental measures taken in the real furnace. This will serve to check if the model is suitable to accurately simulate large-scale grate-fired boilers.

2. Model

The CFD code ANSYS-Fluent will provide the solution of the gas phase while the bed model will carry out the solution of the solid phase physical and chemical phenomena and the coupling between both phases. The simulation domain can be divided into two zones: the bed and the freeboard. The bed is modelled as a porous zone where the aforementioned UDS's characterise the solid phase. In the freeboard only the gas phase is defined and therefore only homogeneous reactions happen there.

In this section, the model main characteristics and submodels, alongside the new developments, are presented. Further details on the model's procedures and characteristics can be found in previous works [44–46].

2.1. Solid phase

The cell zone where the solid fuel bed is located is modelled as a porous disperse medium. The solid properties are characterised by UDS's which represent local volume-averaged values for each computational cell. This method allows to work with meshes of different cell sizes, greater or less than the size of the fuel particles since each cell does not represent a single particle, but a volume-averaged specific region of the bed.

The scalars which characterise the solid bed in each cell are: solid fraction ($m_{\text{solid}}^3/m_{\text{cell}}^3$), solid temperature (K), moisture density ($\text{kg}/m_{\text{solid}}^3$), dry wood density ($\text{kg}/m_{\text{solid}}^3$), char density ($\text{kg}/m_{\text{solid}}^3$), solid ash density ($\text{kg}/m_{\text{solid}}^3$) and third power of the particle average diameter (m^3).

The solid fraction represents the portion of the cell that is occupied by solid while the densities determine the composition of this solid volume. The third power of the particle average diameter characterizes the size of the theoretical particle (or particles) that is represented by the solid bed located at the cell.

Since the model considers the particles to be thermally thin, the temperature is assumed to be constant through all the solid volume of each cell and is defined by the solid temperature scalar. The thermally thin hypothesis is one of the strongest assumptions made in the model and it will have an impact on the results. Studies applying a subgrid thermally thick treatment to the particles have been made, showing more precise results than the thermally thin assumption [47]. However, the computational cost is too high to be used in this case.

The evolution of the scalars is governed by transport equations (Eqs. (1)–(8)). These equations include a transient term which represents the temporal variation of each scalar. The transport equation of the solid temperature scalar does not control the evolution of the scalar directly but the variation of the solid phase enthalpy (Eq. (1)), from which the solid temperature is calculated. The solid enthalpy transport equation

includes a diffusive term, which is not present in the other transport equations because there is no mass diffusion between the solids. The right-hand terms of Eqs. (1)–(8) represent the consumptions and generation (only for the char) for each scalar. Eqs. (4)–(6) reflect the solid densities variations produced during drying, wood pyrolysis and char reactions. Wood pyrolysis and char reactions modify the solid fraction and the particle diameter as seen in Eqs. (2) and (3). The ash is considered non-reactive but can be compacted by the bed movements. When the porosity of cell drops below a specified limit, the solid fuel can collapse causing the compaction of the bed [41].

$$\frac{\partial(\varepsilon\rho_p h_s)}{\partial t} = \nabla(k_{s,eff} \cdot \nabla T_s) + S_{h_s} \quad (1)$$

$$\frac{\partial\varepsilon}{\partial t} = \left(\frac{\dot{\omega}_{wood}'''}{\rho_{wood}^s} + \frac{\dot{\omega}_{G,char}'''}{\rho_{char}^s} - \dot{\omega}_{C,char}''' \right) \varepsilon \quad (2)$$

$$\frac{\partial d_{eq}^3}{\partial t} = \left(\frac{-\dot{\omega}_{wood}'''}{\rho_{wood}^s} + \frac{\dot{\omega}_{G,char}'''}{\rho_{char}^s} - \dot{\omega}_{C,char}''' \right) d_{eq}^3 \quad (3)$$

$$\frac{\partial(\varepsilon\rho_{moisture})}{\partial t} = -\omega_{moisture}''' \cdot \varepsilon \quad (4)$$

$$\frac{\partial(\varepsilon\rho_{wood})}{\partial t} = -\omega_{wood}''' \cdot \varepsilon \quad (5)$$

$$\frac{\partial(\varepsilon\rho_{char})}{\partial t} = (\omega_{G,char}''' - \omega_{C,char}''') \cdot \varepsilon \quad (6)$$

$$\frac{\partial(\varepsilon\rho_{ash})}{\partial t} = 0 \quad (7)$$

The total density of the particle is calculated as the sum of the other solid densities as seen in Eq. (8). The thermal conductivity of the particles is also calculated by a mass-weighted average in function of the particle components [44].

$$\rho_p = \rho_{moisture} + \rho_{wood} + \rho_{char} + \rho_{ash} \quad (8)$$

Drying will occur at temperatures equal or greater than evaporation temperature (373.15 K). Once the moisture has evaporated and enough temperature is reached, the dry wood will start to be consumed producing gas, tar and char due to pyrolysis. These pyrolysis reactions are modelled by three Arrhenius equations [48,49]. The char will be consumed by three heterogeneous reactions: oxidation, gasification by carbon dioxide and gasification by water vapour [50].

2.2. Gas phase

CFD codes can solve the gas phase along the combustion reactions and other chemical reactions that occur in it and have been widely used to simulate biomass grate-fired boilers [37,51,52]. ANSYS-Fluent includes several models to solve the different variables and phenomena that occur in the gas phase for this type of systems, where combustion is present [53,54]. Mass, momentum, energy, turbulence and species transport conservation equations are solved to achieve a solution.

The realizable k- ε model, which has been already used satisfactorily in biomass combustion simulations, was chosen as turbulence model [37,41,51,52]. Enhanced wall treatment option is used. The radiation is modelled by the discrete ordinates model, which was modified to enable its interaction with the solid phase [55]. To model the interaction between turbulence and chemistry, the FR-ED model is used. This model combines the Finite Rate and Eddy Dissipation Concept models, allowing a better control of the reactants consumption rate [56].

The gases produced during the solid fuel drying, devolatilization and pyrolysis of the wood and the char reactions, are introduced into the gas phase by a mass source for each specie. Drying will produce water vapour. The char oxidation and the two gasification reactions will generate carbon monoxide, carbon dioxide and hydrogen [50].

During the pyrolysis, methane, benzene, carbon monoxide, carbon dioxide, hydrogen and water vapour are released [57,58]. These species can react between them and with other species present in the gas phase according to a set of chemical reactions and their kinetics. These reactions are: partial oxidation of methane and benzene to carbon monoxide, oxidation of hydrogen, oxidation of carbon monoxide, water-gas shift reaction and methane steam reforming reaction [59,60].

2.3. New feeding methodology

The feeding procedures already available in the model were not well suited for boilers with lateral feeding, like the one studied in this work. For this reason, a new procedure able to recreate the behaviour of this type of feeding was developed. The so-called *saturation feeding* method is divided in two steps:

First, the amount of mass to be introduced is calculated. This value can be set by a mass flow ratio or calculated in function of the desired thermal power output and the fuel thermal properties. Then, the fresh fuel is introduced in a group of cells which is designated as inlet. The amount introduced in each cell is weighted in function of each cell volume and the total volume of all the inlet cells. The scalars of the inlet cells are recalculated to take into account the changes due to the new mass (m_{feed}) entering the cells.

Eqs. (9)–(12) are used to recalculate the values of the scalars in the inlet cells.

$$\varepsilon = \varepsilon + \frac{m_{feed}}{\rho_p^0 \cdot V_{cell}} \quad (9)$$

$$\rho_i = \frac{\rho_i \cdot \varepsilon \cdot V_{cell} + m_{feed} \cdot Y_i^0}{\varepsilon \cdot V_{cell} + \frac{m_{feed}}{\rho_p^0}} \quad (10)$$

$$d_{eq}^3 = \frac{d_{eq}^3 \cdot \varepsilon \cdot V_{cell} + d_{eq}^3 \cdot \frac{m_{feed}}{\rho_p^0}}{\varepsilon \cdot V_{cell} + \frac{m_{feed}}{\rho_p^0}} \quad (11)$$

$$T_s = \frac{T_s \cdot \varepsilon \cdot V_{cell} \cdot \sum_i (\rho_i \cdot C_{p,i}) + T_s^0 \cdot \frac{m_{feed}}{\rho_p^0} \cdot \sum_i (\rho_i^0 \cdot C_{p,i})}{\left(\varepsilon \cdot V_{cell} + \frac{m_{feed}}{\rho_p^0} \right) \cdot \left(\sum_i (\rho_i \cdot C_{p,i}) + \sum_i (\rho_i^0 \cdot C_{p,i}) \right)} \quad (12)$$

The volume of the cells may be not enough to receive the incoming fuel because the solid volume fed is higher than the volume of the inlet cells or because the cells are already filled with fuel. In these cases, the solid fraction in the inlet cells will be higher than the maximum limit of compaction of the solid fuel. In this case, these cells are considered as oversaturated and therefore marked for further readjustment.

The second step is to desaturate those cells. For this purpose, a geometrical has been developed. The objective of this method is to simulate the effect of the screw conveyors which are typically used in grate-fired boilers to introduce the fuel into the bed. These systems push the fresh fuel into the boiler. If the fuel inlet is close to the grate surface, the fuel tends to pile up at the end of the screws and the new fuel pushes the heap of fuel forward. The saturated cells are considered as the effect of the new fuel entering the bed and trying to push the fuel pile forward.

The procedure developed works as follows: A unit vector, called *push-vector*, with the direction of the main thrust of the feeding system has been pre-established by the user. The procedure will loop over the bed cells looking for the oversaturated cells. Once an oversaturated cell is located, a loop over all the faces of the cell is carried out. The scalar product of the face vector (outgoing unit vector normal to the face) and the push vector is calculated. Of all the faces, the one whose dot product is higher is taken. The cell that shares this face with the oversaturated cell is the neighbour cell better located in the direction of the push vector. This neighbour cell is designated as the receiver cell and it will

receive the excess of solid volume (V_s) of the oversaturated cell.

Eqs. (13)–(16) are used to recalculate the values of the scalars in the receiver cell. The procedure is repeated until there are no more bed cells with a value of solid fraction above the limit.

$$\varepsilon = \varepsilon + \frac{V_s}{V_{cell}} \quad (13)$$

$$\rho_i = \frac{\rho_i \cdot \varepsilon \cdot V_{cell} + V_s \cdot \rho_{i,sat}}{\varepsilon \cdot V_{cell} + V_s} \quad (14)$$

$$d_{eq}^3 = \frac{d_{eq}^3 \cdot \varepsilon \cdot V_{cell} + d_{eq,sat}^3 \cdot V_s}{\varepsilon \cdot V_{cell} + V_s} \quad (15)$$

$$T_s = \frac{T_s \cdot \varepsilon \cdot V_{cell} \cdot \sum_i (\rho_i \cdot C_{P i}) + T_{s,sat} \cdot V_s \cdot \sum_i (\rho_{i,sat} \cdot C_{P i})}{(\varepsilon \cdot V_{cell} + V_s) \cdot (\sum_i (\rho_i \cdot C_{P i}) + \sum_i (\rho_{i,sat} \cdot C_{P i}))} \quad (16)$$

3. Methodology

The validation of the model operation in a large-scale grate-fired boiler will be carried out by simulating the furnace operating in the same conditions as presented by Razmjoo et al. in [61].

3.1. Boiler description

The system studied is a 4 MW grate-fired biomass boiler. The boiler consists of a furnace and a heat exchanger located at the outlet of the furnace. The heat exchanger has not been included in the simulation and only the furnace will be studied. The reciprocating grate is formed of 11 rows of grate bars which are mobile. The grate has a width of 1.7 m and a length of 5 m. The rows movement pushes the fuel forward and mixes it. The primary air is distributed under three air chambers located under the grate. The air enters the bed through slots between the grate bars. The secondary air enters the hearth by several nozzles located at the side walls above the bed. In the upper part of the furnace, above the dome that covers the hearth, there is a burnout zone. In this zone, the tertiary air is inserted through several ports to complete the oxidation of the gases.

Based on the furnace description and schematic views presented in

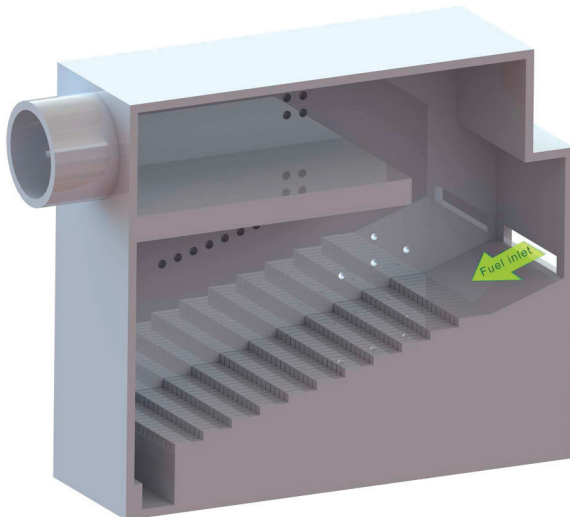


Fig. 1. CAD of the furnace without lateral wall.

Table 1
Boiler operating parameters [61].

Operating parameters	
Boiler load (MW)	3.9
Fuel feeding rate (kg/s)	0.485
Primary air, chamber 1 (kg/s)	0.313
Primary air, chamber 2 (kg/s)	0.300
Primary air, chamber 3 (kg/s)	0.204
Secondary air (kg/s)	0.288
Tertiary air (kg/s)	0.506

Table 2
Proximate analysis of the fuel as received [61].

Proximate analysis as received	
Moisture (wt%)	52.9
Volatile (wt%)	37.4
Fixed carbon (wt%)	9.3
Ash (wt%)	0.4
LHV (MJ/kg)	9.924

Table 3
Ultimate analysis of the fuel [61].

Ultimate analysis in dry basis	
Carbon (%)	52.4
Hydrogen (%)	5.9
Oxygen (%)	40.6
Nitrogen (%)	0.19
Sulfur (%)	0.0022

Table 4
Fuel physical properties [61,62].

Physical properties	
Density (kg/m ³)	687
Equivalent diameter (m)	0.02
Sphericity (-)	0.3
Packing (-)	0.3

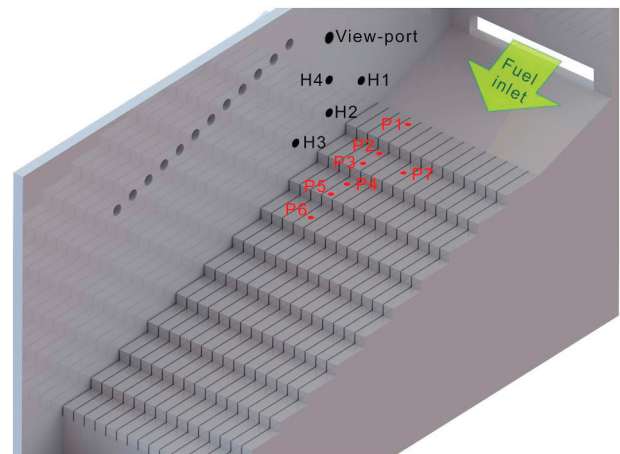


Fig. 2. View of the grate and the side wall with the virtual measuring ports and points locations.

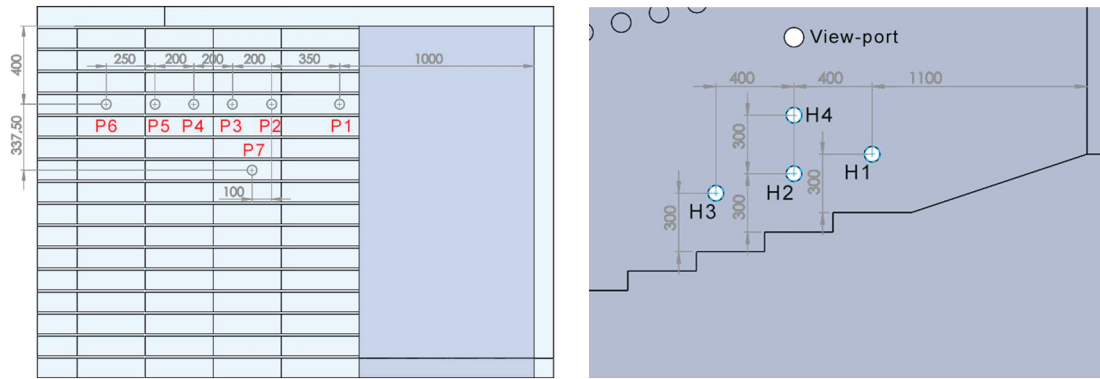


Fig. 3. Top and lateral view of the upper part of the grate with the measurement points locations dimensions.

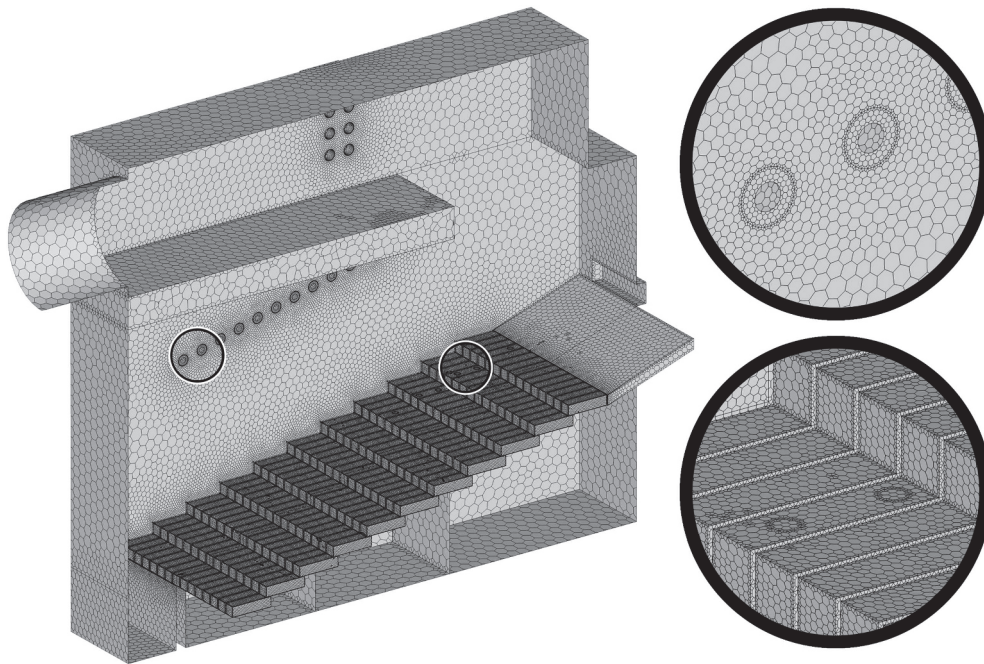


Fig. 4. Mid cut of the surface mesh with details of the secondary air nozzles and the grate.

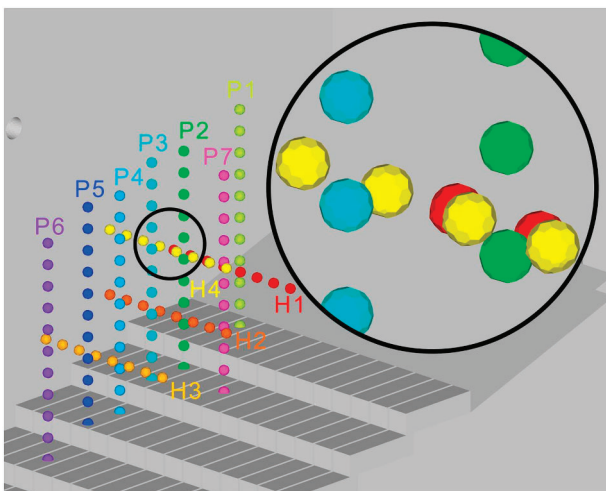


Fig. 5. Measurement spheres locations and detail of the spheres.

the work previously mentioned [61], a CAD of the boiler has been made. In Fig. 1, the furnace CAD can be seen. Some assumptions and simplifications have to be made. Since the exact number and location of the secondary and tertiary air nozzles and the shape of the grate bars are not detailed, they have been placed based on the images and descriptions provided in [61], but their real position might differ from the one used in the model.

3.2. Operating conditions and fuel

The boiler can operate at different loads by adjusting its operating parameters. Razmjoo et al. have presented data corresponding to 3 different operating conditions. The measurements of temperature profiles along the bed height have been taken with the boiler working at a load of 3.9 MW [61]. Because of this, the simulation will be carried out using the operating parameters that correspond to a thermal load of 3.9 MW, which are presented in Table 1 [61].

The fuel used in the experimental work is a mixture of woody residues (woodchips, bark, and sawdust) with a high moisture content. The results of the fuel proximate and ultimate analysis are shown in Tables 2 and 3 [61].

The only data available about the physical properties of the fuel is that it is composed by a mixture of woodchips, bark and sawdust with

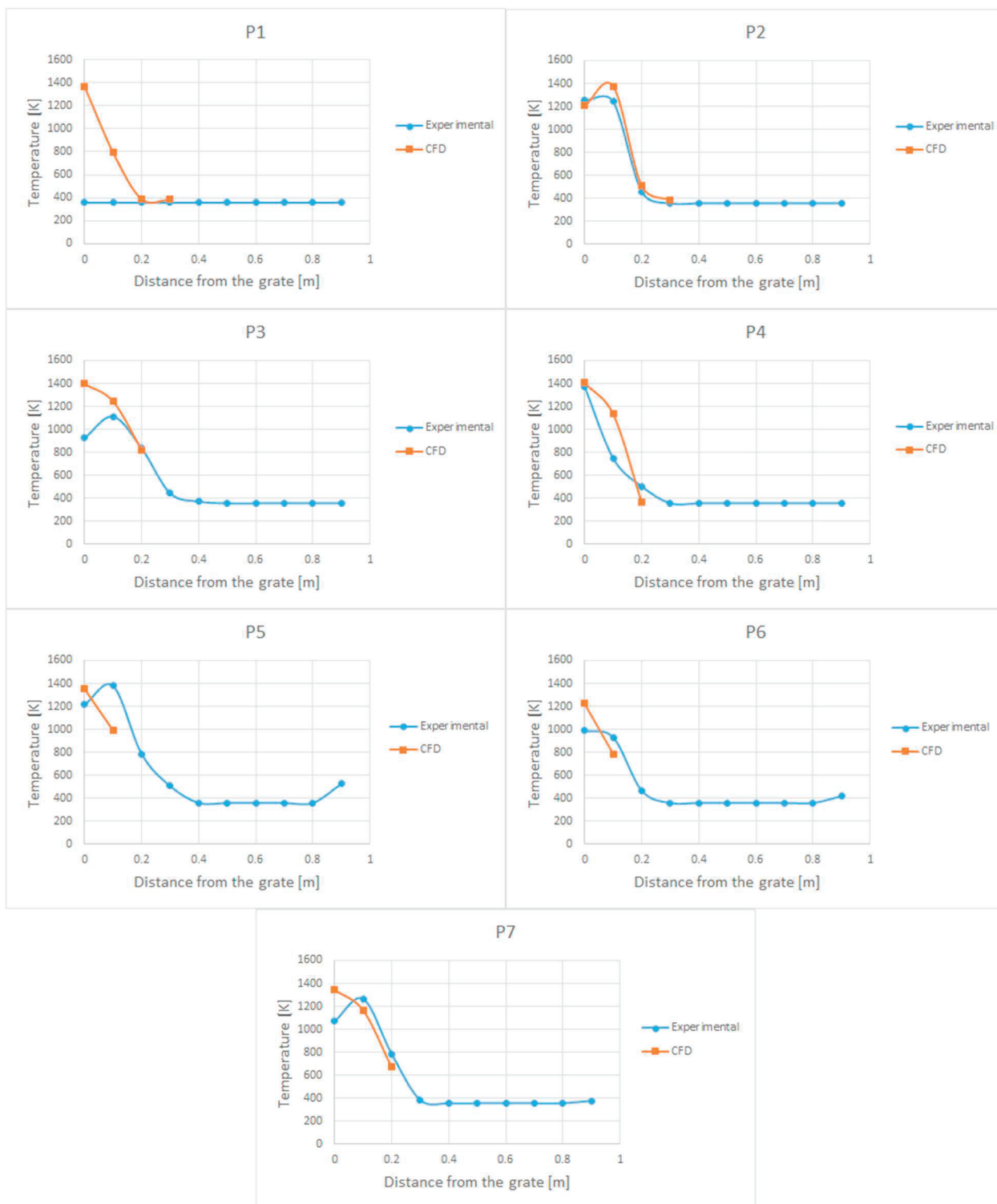


Fig. 6. Bed temperature profiles along the height of the bed at positions P1–P7.

an average particle size of about 20 mm [61]. From this information, it has been assumed that the fuel is mainly composed of woodchips, so the other physical parameters needed (density, sphericity and packing factor) are taken from data corresponding to pine chip [62]. The particle density is recalculated to take into account the different moisture content of the fuel of this case. The physical parameters are shown in Table 4. This assumption will not affect the chemical properties of the fuel since the proximate and ultimate analysis data presented in the experimental work is used.

3.3. Measurements

Razmjoo et al. obtained the experimental measures inserting probes inside the boiler during its operation. The probes were introduced through several ports located on a side wall. Vertical measures of the bed temperature were taken starting at the grate surface at the positions P1–P7, which location can be seen in Figs. 2 and 3, and increasing the height in 0.1 m intervals until reaching the bed surface (around 1 m) [61].

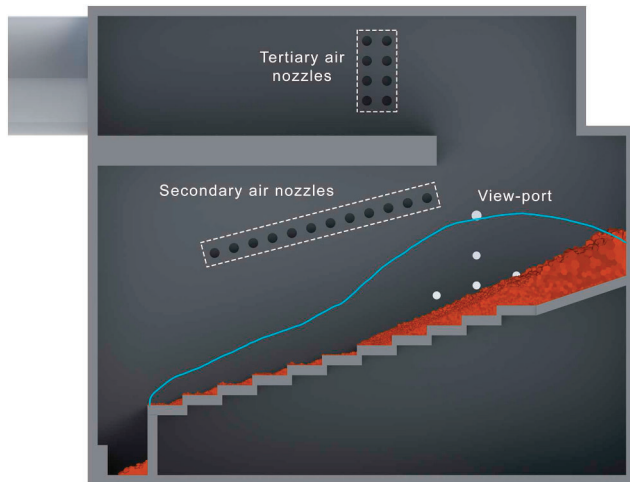


Fig. 7. Side view of the boiler with comparison between the numerical solid fuel bed (brown) and the rough distribution of the experimental fuel bed (blue line) [61]. (For interpretation of the references to colour in this figure legend, the reader is referred to the web version of this article.)

Horizontal measures of the gas temperature were taken through the ports H1-H4, which location can be seen in Figs. 2 and 3. The port H1 is located above the first grate step, the H2 above the second step and H3 above the third step, all of them at a height of 0.3 m above their respective step. The port H4 is located 0.3 m above the port H2. The dimensions of these positions can be seen in Fig. 3. The measures were taken horizontally, starting from the ports, in intervals of 0.1 m towards the centre of the furnace.

3.4. Discretization and boundary conditions

The surface mesh is composed of trias from which, the three-dimensional tetrahedra are created. The tetrahedra are then converted to polyhedra to reduce the number of elements. Also, the bed model movements have shown a better response in polyhedra meshes compared with tetrahedra or hexahedra meshes since with higher number of faces the probability of finding cells well aligned with the push-vector is higher.

The mesh is more refined near the walls and where higher gradients are expected, as in the bed region near the grate or in the secondary and tertiary air nozzles as can be seen in Fig. 4, where the elements have an average edge length of 5 mm. The tridimensional cells grow towards the centre of the volumes, with a ratio of 1.1, to reduce the number of elements.

In the points where measures will be taken, 50 mm diameter spheres have been created. The surfaces of the spheres have been discretized by 15 mm trias and their volumes in tetrahedra, which are then converted to polyhedra. This results in spheres with an average of 75 volumetric elements. It has been chosen to create 50 mm spheres because it is half the distance of separation between measuring points. Using bigger spheres would result in little space between spheres and less precision in measuring the temperature of the point. On the other hand, decreasing the size of the spheres would require to use smaller elements to discretize the spheres, resulting in an increase in the number of elements of the mesh without achieving higher precision. These spheres can be seen in Fig. 5.

The temperature of each measuring point will be the volume-weighted average value of the cells of its correspondent sphere. This is done instead of taking the values of the cells located at the coordinates of the measurement points to reduce any possible error produced by taking punctual values.

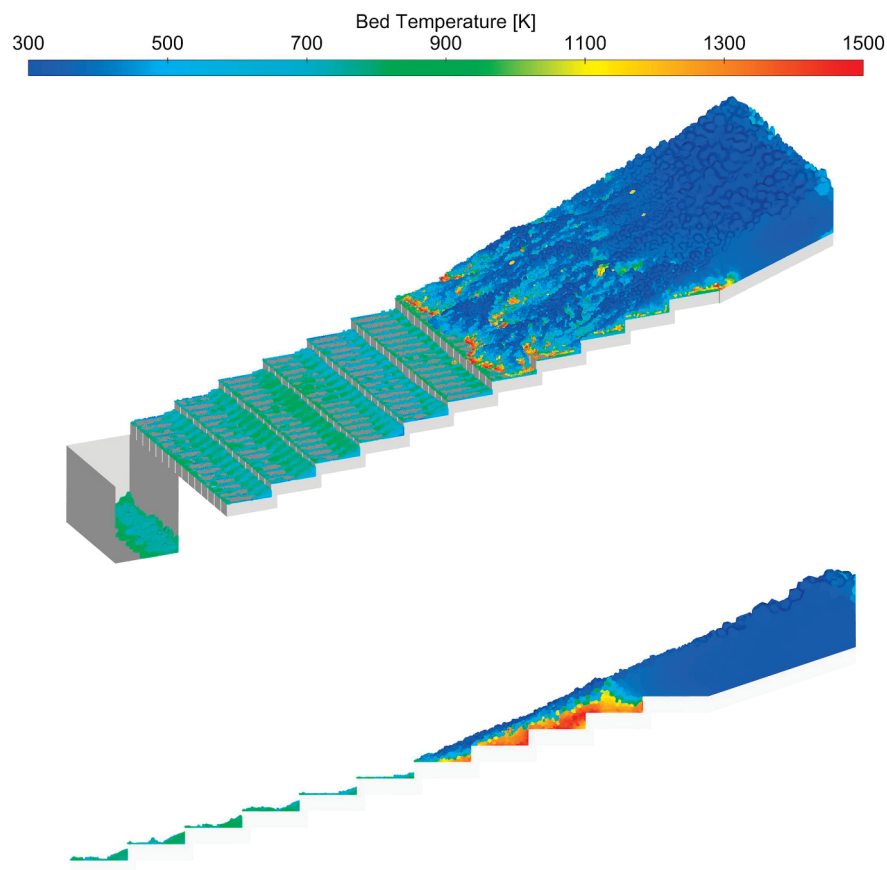


Fig. 8. Contours of bed temperature of the full bed (above) and mid-plane cut view (below).

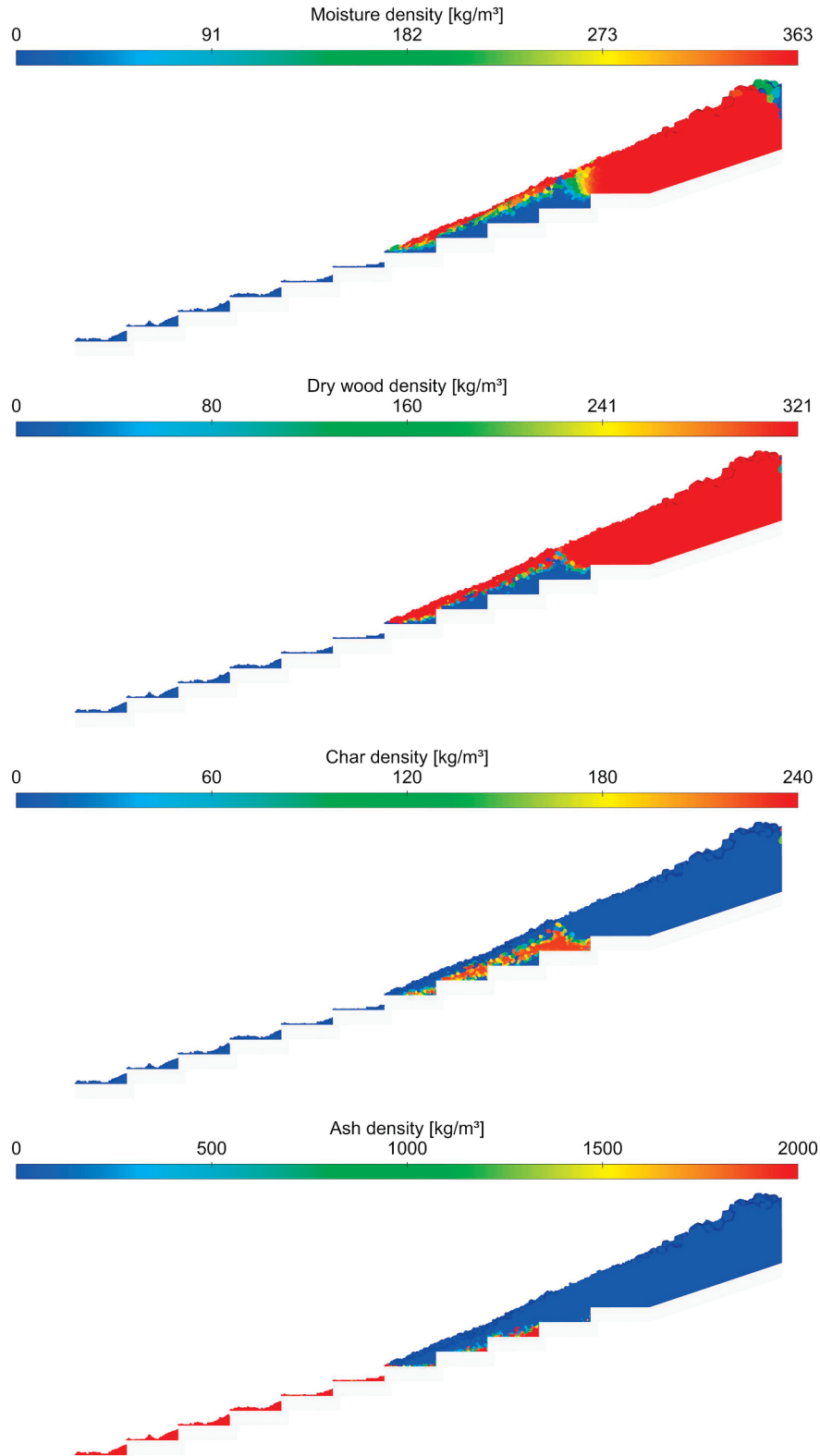


Fig. 9. Mid-plane cuts of the bed showing the different solid bed densities contours.

Mesh-independence runs have been carried out proving that reducing more the average element size will not provide a significant improvement in the accuracy of the solution but it would increase the simulation times excessively. The final mesh is formed of more than 1.5 million polyhedral elements.

Several boundaries are set as mass-flow inlets introducing the air-

flow ratios specified in Table 1. One air inlet is defined for each primary air chamber and four more for the secondary and tertiary air supplies (one for each one in both sides of the furnace). The air, like the fuel, is introduced at a temperature of 300 K. The fuel is introduced in the upper part of the grate, in a cell zone designated as fuel inlet, by the method described in Section 2.3.

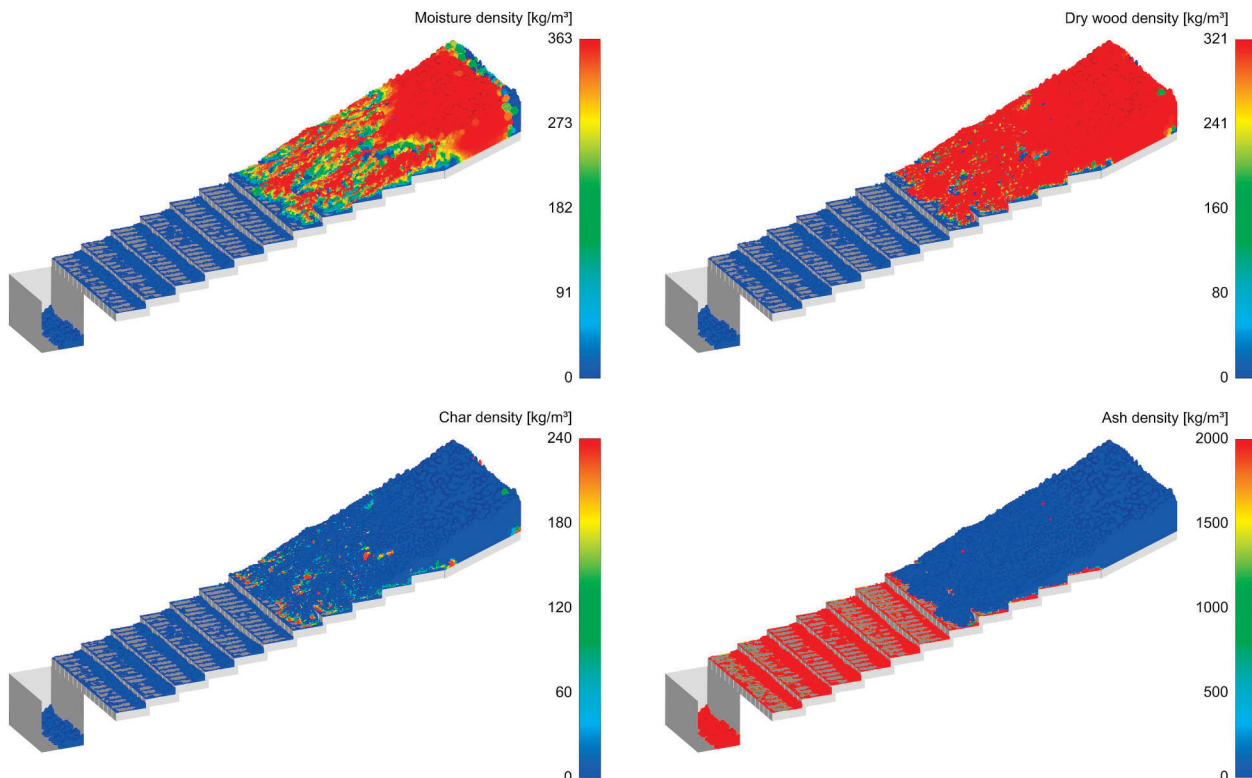


Fig. 10. Contours of the solid bed densities.

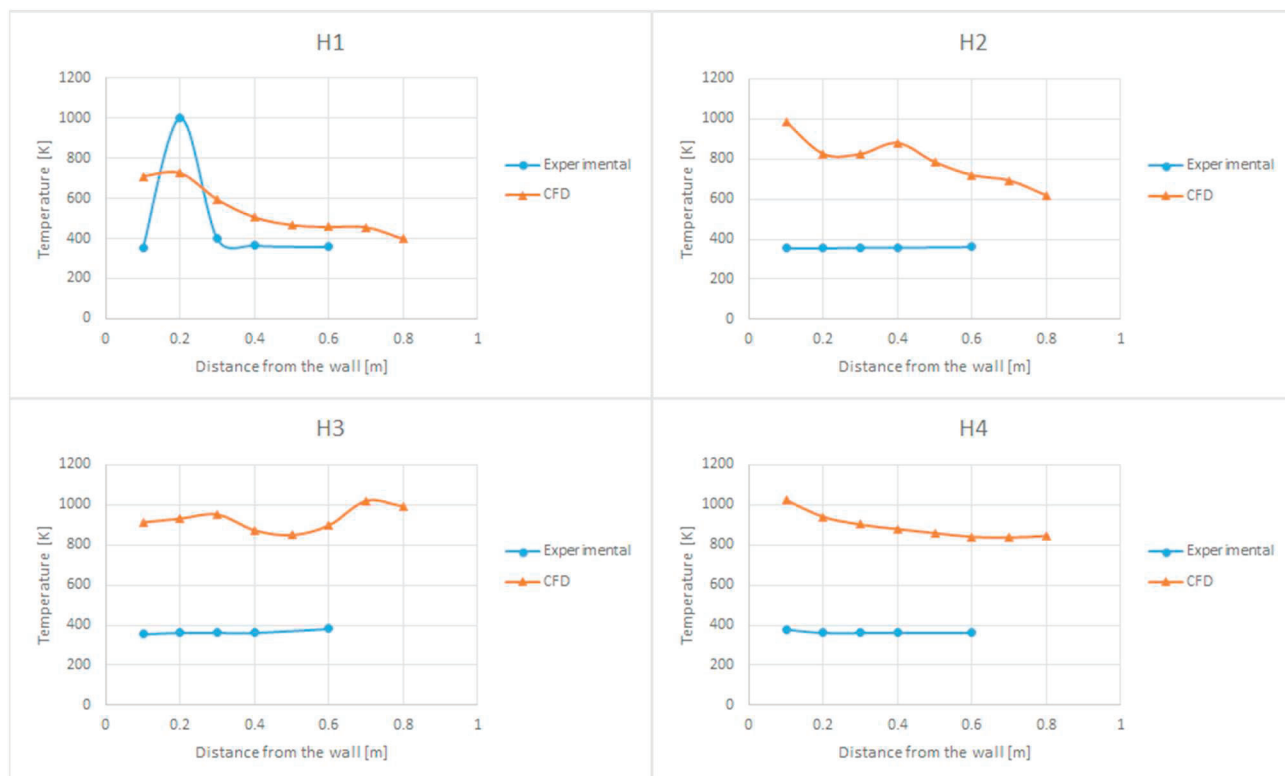


Fig. 11. Gas temperature profiles at the positions H1–H4 starting at the side wall and advancing towards the centre.

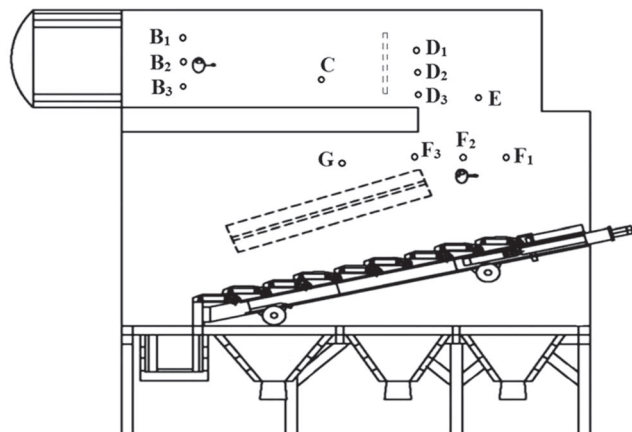


Fig. 12. Schematic view of the furnace with the locations of gas temperature measurement points B1–B3, C, D1–D3, E, F1–F3 and G [64].

Since there is no clear information regarding the materials the boiler is made of, it has been assumed that the dome and the walls around the bed are made of fire-bricks and the other walls and grate are built in steel. The width of the walls is set to 100 mm for the fire-bricks and 5 mm for the steel walls, assuming convective heat transfer to still air in the outside with a coefficient of 12 W/m²·K. In the inside, the emissivity of the walls is set to 0.8, due to the fouling over the surfaces [44].

4. Results and discussion

After 5000 s of flow-time, the different monitors are stable showing no variations or oscillating periodically ranging between the same values. For this, it is considered that the simulation has reached a pseudo-steady state and it is converged. Then, the bed and gas temperatures in the measurement spheres are monitored and the simulation is executed during 750 more seconds to obtain averaged values. In this section, these values are presented and compared with the experimental data presented by Razmjoo et al. [61]. Also, contours of temperatures, bed solid densities and species will be shown to analyse the model operation.

The bed temperature profiles measured at the positions P1–P7 are presented in Fig. 6. The experimental data is compared with the CFD results. The numerical data at the measurement points that the solid fuel bed does not reach is excluded from the graphs of Fig. 6, as there are not solid temperature values for those positions. Because of this, it can be deduced that bed height in the simulation is lower than in the experimental tests. In Fig. 7, a comparison between the numerical solid fuel bed and the experimental bed height is shown, demonstrating the previous deduction. There is a clear difference in the fuel bed height between the experimental and the CFD, which may be caused by various reasons. In the experimental work, it is declared that the fuel bed is intentionally kept thick to achieve a higher pressure drop, having a bed thickness of about 1 m at the upper part of the grate [61]. However, the method used to increase the bed height is not specified. Because of this, a fuel feeding ratio that provides the nominal power indicated for operating conditions (a) has been set. Probably, it would have been necessary to increase this feeding ratio at some point to increase the bed thickness. However, due to the lack of information about this, it has been decided to not vary the fuel feeding ratio, although this is considered one of the main reasons of the difference in the results. Other factor that can influence the bed thickness is the thermally thin assumption. This results in faster heating rates for the solid bed, which lead to thinner bed layers. Additionally, the Eulerian model does not take into account the physical shape of the particles in the bed for the compaction procedure, resulting in a bed with lower height. These considerations and assumptions are probably the main reasons of the

differences in the bed height between the experimental and the simulation.

The shape of the bed and its temperatures can be seen in Figs. 6 and 7. The height of the bed is above 0.3 m over the first step (P1), around 0.2–0.3 m over the second (P2, P3 and P7), between 0.1 and 0.2 m over the third (P4 and P5) and around 0.2 m over the fourth (P6).

Despite the difference in the bed thickness between the model and the experiments, the temperature profiles show a good correlation at the heights where the numerical solid fuel bed exists. P1 measures show higher temperatures in the numerical results in comparison with the experimental ones at the heights of 0 and 0.1 m (Fig. 6). In the temperature contour of the full bed in Fig. 8 it can be seen that there is combustion over the first step of the grate, however, in the mid-plane cut view, it can be seen that in the middle of this first row the bed is cold. This indicates that the fuel is not burning all over the row, and just in some zones near the side walls. Because of this, although the P1 graph shows a noticeable difference between the numerical and experimental profiles, the state of the bed over the first grate step is quite similar to the experimental, especially in the centre of the grate. At the 0.2 and 0.3 m heights, the results are practically identical, as, in both cases, there is wet bed at a temperature around 360 K in that zone.

Measurement points P2, P3 and P7 are located over the second grate step. The graphs (Fig. 6) show that higher temperatures are reached closer to the grate, at heights of 0 and 0.1 m. In this zone, the temperature varies approximately between 1200 and 1400 K. At 0.2 m, the temperature drops in all cases. In P2, which is closer to the fresh bed inlet, the temperature drops to around 450 K for experimental and to around 500 K in the CFD simulation. However, for P7 and P3, which are located in the middle and close to the border of the second step respectively, the temperature drops to around 800 K in P3 and to 700 K in P7 at a height of 0.2 m. This difference can be appreciated in Fig. 8 mid-plane cut view, where it can be seen that over the second grate row, the bed is colder in the zone closer to the first row, where P2 is located, and hotter towards the border of the row, where P7 and P3 are located. The fresh fuel pushing from the inlet causes this effect. At 0.3 m, there are no solid fuel bed for the points P3 and P7 but there is bed around 380 K at P2 being dried.

The temperature profiles of these 3 points give valuable information about the different combustion zones and bed layers. In base of the measured temperatures a combustion pattern can be established. Between 0 and 0.15 m above the grate surface the temperature ranges between 1000 and 1400 K. This indicates that this is the zone where the combustion of the char takes place, near the grate surface. Between 0.15 and 0.25 m, the temperatures are in the 400–900 K range, being the zone where the wood is completely dried and then pyrolysed producing char and gases. Finally, the bed fuel at heights higher than 0.25 m, is fresh fuel being dried at temperatures around 380 K. These results are in accordance with the combustion pattern presented by Razmjoo et al., with the exception of the raw fuel layer thickness [61].

At the third and fourth rows, the height of the bed and the thickness of the different combustion layers decrease. Measuring points P4 and P5 are located at the third row, with P4 being closer to the inlet and P5 to the border of the step and P6 is located at the fourth row. It can be seen in Fig. 7 that the height of the bed decreases as it advances down the grate. At P4, the bed reaches a height over 0.2 m but in P5 and P6 the bed height is lower than 0.2 m. In Fig. 6 it can be seen that in the three points, the higher temperature is recorded at the grate level, being around 1400 K for P4 and P5 and 1200 K for P6. At 0.1 m, the temperature drops 400 degrees at P5 and P6 and around 300 degrees for P4. At P4, there is fresh fuel below 400 K at a height of 0.2 m but in the positions P5 and P6, the raw fuel layer is not thick enough to reach the 0.2 m measurement point. These simulation values have an acceptable correlation with the experimental data in the zones where the fuel bed exists with the difference of not having the thicker raw fuel layer.

In cross-current flow furnace the combustion tends to start at the surface of the bed and to advance towards the grate. However, it has

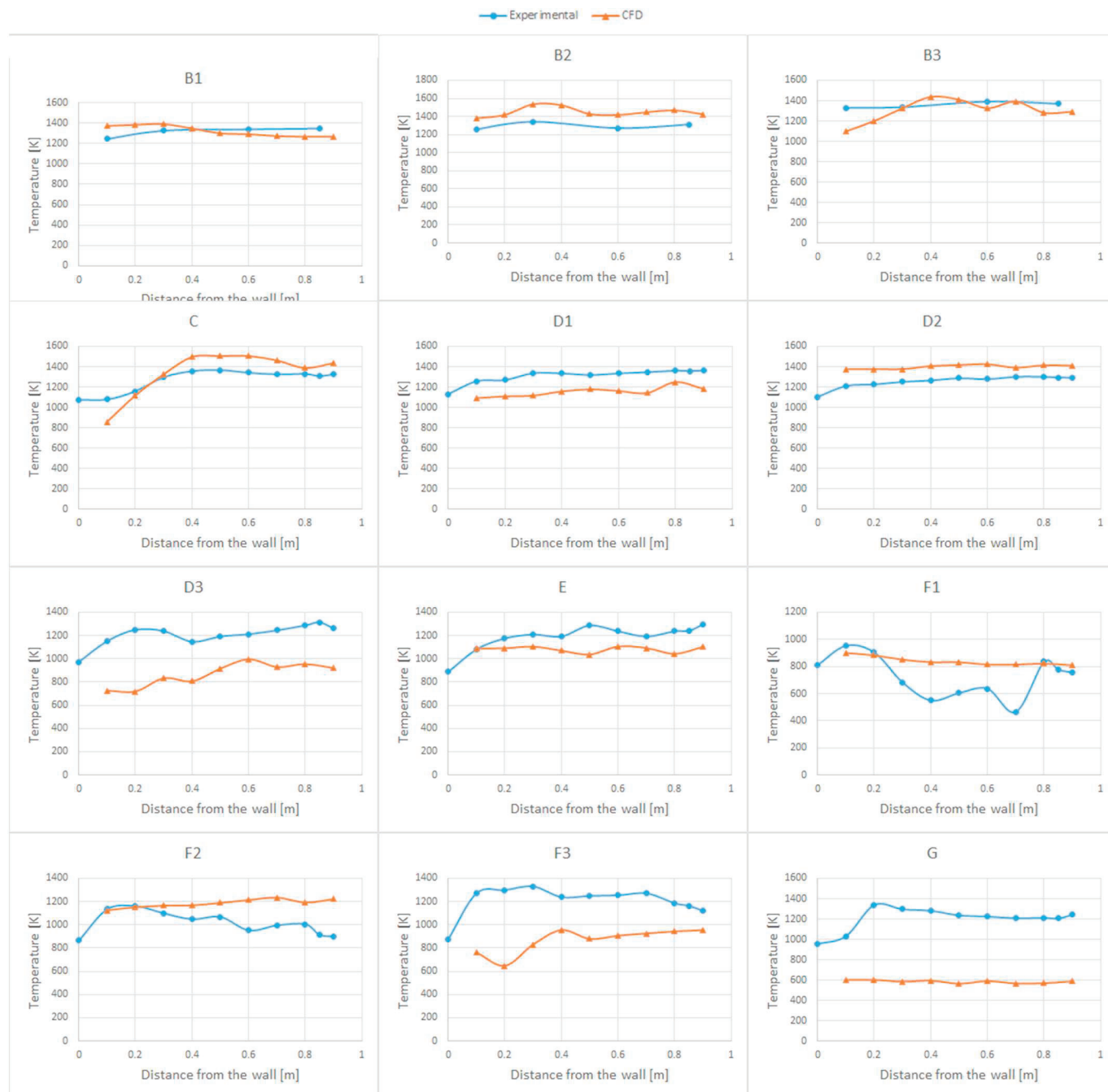


Fig. 13. Gas temperature profiles at the positions B1–B3, C, D1–D3, E, F1–F3 and G starting at the side wall and advancing towards the centre.

been proven that in cases of fuel with a high moisture content, like the one used in this case, the combustion takes place near the grate with the ignition front propagating towards the surface, as the results obtained in this work [63]. In Fig. 9 the solid densities of the bed are shown. The different layers are clearly appreciable and it can be seen how, starting from the grate, there is a first layer of the remaining ash, followed by the char layer which is covered by the wood, which is being dried from below. Three-dimensional views of the contours of the solid bed densities can be seen in Fig. 10. In these figures it can be appreciated how the fuel is distributed over the grate, having the wet wood as the top layer and the char layer almost completely covered by it.

In Fig. 11, the numerical and experimental profiles of gas temperature measured at the positions H1–H4 are presented. The gas measuring ports H1–H3 are located at 0.3 m above the grate and the H4 at 0.6 m. As it has been seen, the numerical bed heights measured are

lower than 0.3 m, with the exception of the position P1. The H1 measurement points are located over the first grate step, where the height of the bed is around 0.3 m. Because of this, the measuring points of H1 are covered by fresh fuel but the H2–H4 points are located above the bed. However, in the experimental work the raw fuel layer, which has a quite homogeneous temperature, covers all the horizontal measuring points, resulting in flat temperature profiles, with the exception of a peak value at 0.2 m in H1. This causes some differences in the gas temperatures profiles between the CFD and the experimental data which can be seen in Fig. 11. The H1 profiles are the most similar due having wet fuel at that height in both cases. However, in the CFD case the average temperature is a bit higher because the raw fuel layer is thinner and at a slightly higher temperature. In the other measurement points the differences are notable, since the oxidation of the gases produced by the pyrolysis and the char gasification takes places above

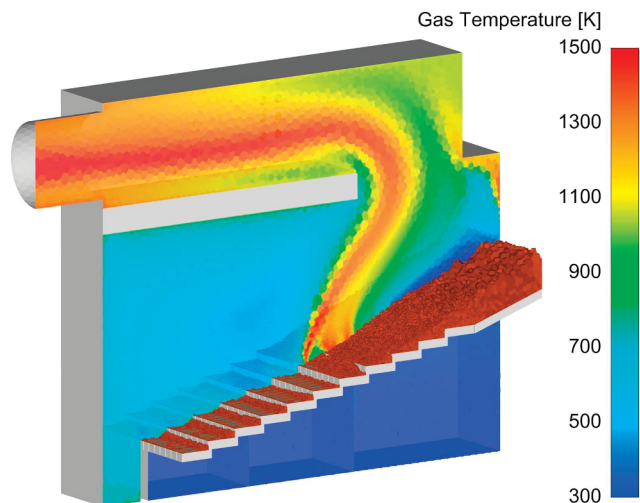


Fig. 14. Gas temperature contours in the mid-plane of the furnace.

the bed surface. Since the bed surface in the CFD simulation is lower, the combustion takes place at lower heights, causing the gas temperatures to be between 400 and 600 degrees higher than in the experimental measures. The numerical gas temperature profiles show a general trend with the higher temperatures closer to the wall and decreasing towards the centre of the furnace. However, the H3 profile shows an increasing tendency with a peak temperature value of 1000 K in the centre of the furnace, at 0.7 m from the wall. The position of H3 is close to the main streak of gases leaving the bed, which explains this peak value and different tendency.

Since the data of these points are very conditioned by the bed raw fuel layer thickness, which is the main difference between the numerical and experimental results, it has been considered interesting to analyse the gas temperature at other locations outside the bed region. Razmjoo et al. have characterised the hot gas during the furnace operation in a previous work [64].

Fig. 12 shows the locations of the measurement ports, from where the gas temperature measurements were taken, in a schematic view of the furnace [64]. In Fig. 13, the experimental and numerical gas temperatures profiles are compared. It can be seen that in the points located after the tertiary air injections (B1–B3 and C) the temperatures obtained by the simulation are in the same ranges that the experimental values. This indicates that the overall operation of the boiler has been simulated with enough precision, besides the differences detected closer to the solid fuel bed due to the thinner raw fuel layer, since the thermal power output of the CFD simulation corresponds with the experimental one. At the points situated at the entrance of the combustion chamber (D1–D3 and E) the predictions of the numerical simulation are also close to the experimental measurements, with the exception of D3, which shows lower temperatures in the simulation. This can be explained because in the simulation results, there is no combustion taking place in the lower half of the grate, so the primary air that enters by the third air chamber along with the secondary air that enters above this zone, will reach the combustion chamber at a lower temperature than the gas flowing above the upper part of the bed. This effect can be appreciated in Fig. 14, which shows the contours of the gas temperature in the mid-section of the furnace. The CFD measures at D3 are affected by this colder gas stream entering the combustion chamber. The measurements at the points situated at the upper part of the hearth, above the bed, show some discrepancies. At F1 and F2 the temperature profiles show an acceptable prediction of the simulation, however, at F3 and, especially, at G. In these points, the effect of not having bed burning over the lower half of the grate causes that the numerical values are lower than the experimental measurements. This effect is more notorious at G because it is located above the nozzles of the secondary

air. This indicates that the difference in the height and distribution of the solid fuel bed has a strong impact on the results. However, due to the number and level of uncertainties involved in the experimental tests and on the modelling, it is probable that there are other factors involved in the differences between the experimental and the numerical gas temperatures, although it is not possible to determine which processes collectively contributed to the differences observed.

The contours of the different gaseous species concentrations can be seen in Fig. 15. There is a high concentration of water vapour due to the high moisture content of the fuel, especially above the first grate steps, where a large volume of bed is being dried. Over the next steps there is a high production rate of methane, carbon monoxide and hydrogen. The oxidation of this species causes the high gas temperatures seen in Fig. 14. As it has been said, in the lower half of the grate, there is not combustion taking place, as there is only ash. Because of this the oxygen that enters by the third primary air chamber is not being consumed. However, even with this oxygen excess, the combustion of the gases is not complete, having a notable concentration of species such as benzene, methane, carbon monoxide or hydrogen at the outlet. It can be seen how the gas flow in this zone is stratified, with the fresh air flowing by the bottom of the combustion chamber and the unburnt gases flowing in the upper part.

5. Conclusions

In this work, a three-dimensional CFD simulation of 4 MW grate-fired furnace using wet woody biomass as fuel has been carried out. An Eulerian thermally-thin fixed bed model was used in combination with the commercial CFD code ANSYS-Fluent to simulate the biomass solid fuel bed and its interaction with the gas phase. A new procedure to recreate the effect of the lateral feeding system has been successfully developed to adequate the model functioning to the characteristics of this case. Once the simulation is converged, the solid bed and gas temperatures are recorded in the measurement points during 750 s of flow-time to obtain time-averaged values. The numerical data is compared with experimental data from literature to validate the bed model functioning.

Bed temperature profiles are obtained and compared with the experimental temperature profiles presented by Razmjoo et al. [61]. The combustion pattern of the fuel bed is identified, showing a behaviour typically found in cross current grate-fired boilers using fuels with a high moisture content. In these cases, the combustion layer is located near the grate with the ignition front propagating towards the surface of the bed [63]. The data show that the maximum bed temperatures, around 1400 K, are reached in the char combustion layer, located between the grate surface and a height of 0.15 m approximately. Between 0.15 and 0.25 m, the temperatures are in the range of 400–900 K. In this layer, the wood is completely dried and pyrolyzes into char and gas. Above 0.25 m the bed is formed by raw fuel which is starting to dry. Here, the most notorious difference between the numerical and experimental results is found because the thickness of the raw fuel layer in the experimental furnace is significantly higher than in the CFD simulation. However, this is probably caused by the fact that in the operation of the furnace the bed is intentionally kept thick, and this has not been taken into account in the simulation. This also caused a discrepancy in the gas temperature measurements comparison between CFD and experimental. In the measurement points which are located inside the bed in both cases, the results show a strong correlation. Regarding the gas temperature measurements, the points, which are located near the solid fuel bed surface, or even inside the raw fuel layer, have shown a greater deviation between experimental and numerical results than the points which are located more distanced from the bed. The latter have shown a good approximation between the simulation and the experimental tests.

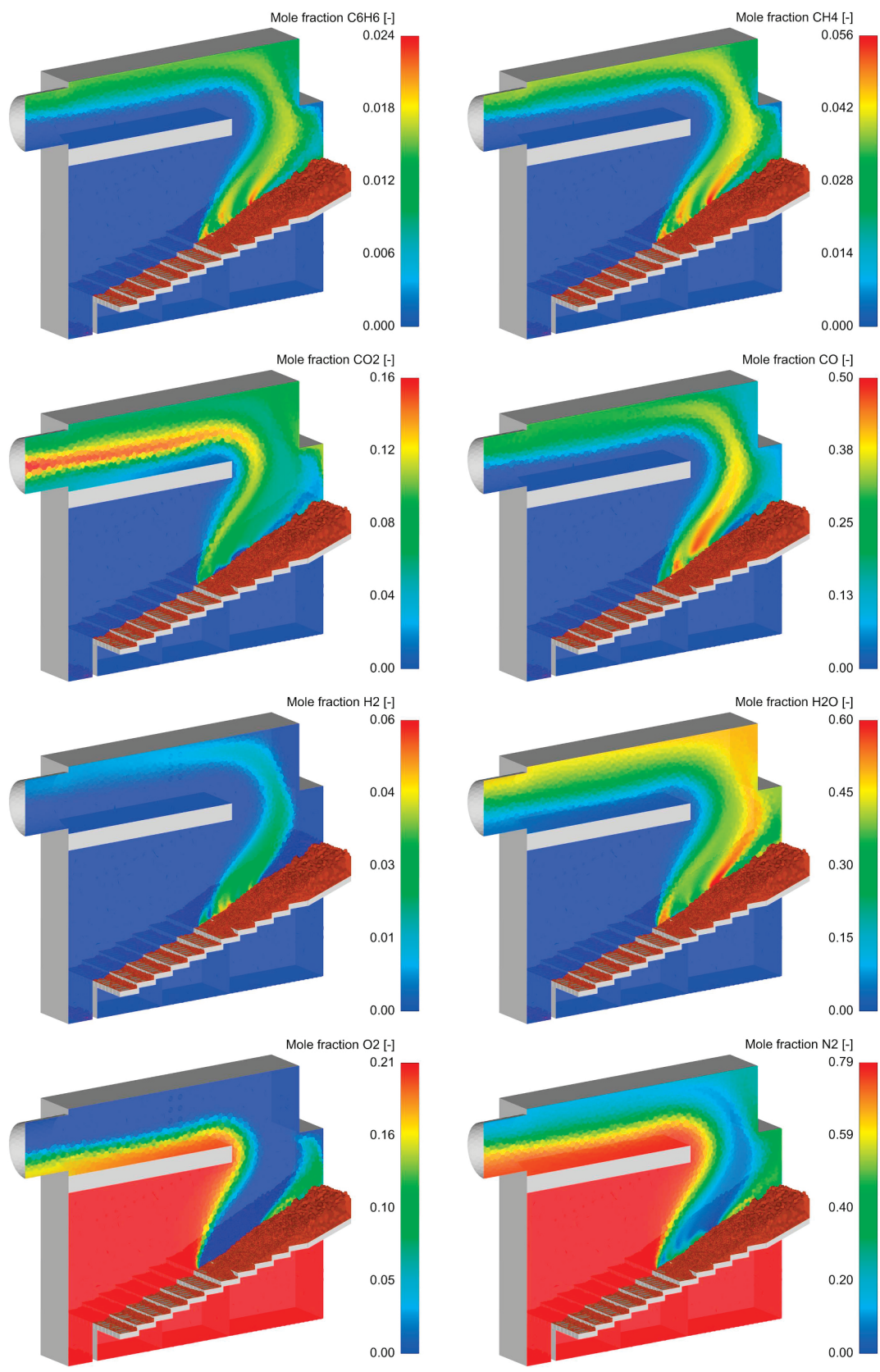


Fig. 15. Contours of species mole fractions in the mid-plane of the furnace.

Nomenclature

Acronyms

CFD	Computational Fluid Dynamics
DEM	Discrete Element Method
DPM	Discrete phase model
FR-ED	Finite Rate - Eddy Dissipation
LHV	Lower heating value
UDF	User Defined Function
UDS	User Defined Scalar

Latin symbols

C_p	specific heat, [J/kg·K]
d_{eq}	particle equivalent diameter, [m]
h	enthalpy, [J/kg]
k	thermal conductivity, [W/m·K]
m	mass, [kg]
S	source term, [W/m ³]
T	temperature, [K]
t	time, [s]
V	volume, [m ³]
Y_i	mass fraction of the component i , [–]

Greek symbols

ϵ	solid fraction, [–]
ρ	density, [kg/m ³]
$\dot{\omega}_i'''$	consumption or generation rate of the i component, [kg/m ³ ·s]

Subscripts

ash	ash
C	consumption
char	char
eff	effective
G	generation
i	wood components (moisture, dry wood, char and ash)
moisture	moisture
p	particle
s	solid
sat	property of the saturated cell
wood	dry wood

Superscripts

0	initial/fresh fuel
S	specific

Acknowledgements

The authors acknowledge the financial support from the European Union's Horizon 2020 - Research and Innovation Framework Programme under grant agreement no. 760551. The work of Sergio Chapela López was supported by grant BES-2016-076785 of the Ministry of Economy, Industry and Competitiveness (Spain).

References

- [1] International Energy Agency, World Energy Outlook 2018, <https://www.iea.org/weo2018/>, (2018), Accessed date: 13 November 2018.
- [2] Javier Sánchez, María Dolores Curt, Nicolas Robert, Jesús Fernández, Chapter two – biomass resources, in: Carmen Lago, Natalia Caldés, Yolanda Lechón (Eds.), The Role of Bioenergy in the Emerging Bioeconomy, Resources, Technologies, Sustainability and Policy, 2019, pp. 25–111, <https://doi.org/10.1016/B978-0-12-813056-8.00002-9>.
- [3] World Energy Council, Bioenergy, World Energy Resources 2016, 2016 https://www.worldenergy.org/wp-content/uploads/2017/03/WERResources_Bioenergy_2016.pdf (accessed 13 November 2018).
- [4] Jorge Islas, Fabio Manzini, Omar Maserá, Viridiana Vargas, Chapter four – solid biomass to heat and power, in: Carmen Lago, Natalia Caldés, Yolanda Lechón (Eds.), The Role of Bioenergy in the Emerging Bioeconomy, Resources, Technologies, Sustainability and Policy, 2019, pp. 145–177, <https://doi.org/10.1016/B978-0-12-813056-8.00004-2>.
- [5] Richard L. Bain, Ralph P. Overend, Kevin R. Craig, Biomass-fired power generation, Fuel Process. Technol. 54 (1998) 1–16, [https://doi.org/10.1016/S0378-3820\(97\)00058-1](https://doi.org/10.1016/S0378-3820(97)00058-1).
- [6] Mercedes Ballesteros, Paloma Manzanares, Chapter three – liquid biofuels, in: Carmen Lago, Natalia Caldés, Yolanda Lechón (Eds.), The Role of Bioenergy in the Emerging Bioeconomy, Resources, Technologies, Sustainability and Policy, 2019, pp. 113–144, <https://doi.org/10.1016/B978-0-12-813056-8.00003-0>.
- [7] A.A. Apostolakou, I.K. Kookos, C. Marazioti, K.C. Angelopoulos, Techno-economic analysis of a biodiesel production process from vegetable oils, Fuel Process. Technol. 90 (2009) 1023–1031, <https://doi.org/10.1016/j.fuproc.2009.04.017>.
- [8] Fabiana P. de Sousa, Claudia C. Cardoso, Vânia M.D. Pasa, Producing hydrocarbons for green diesel and jet fuel formulation from palm kernel fat over Pd/C, Fuel Process. Technol. 143 (2016) 35–42, <https://doi.org/10.1016/j.fuproc.2015.10.024>.
- [9] Ulf Neuling, Martin Kaltschmitt, Techno-economic and environmental analysis of aviation biofuels, Fuel Process. Technol. 171 (2018) 54–69, <https://doi.org/10.1016/j.fuproc.2017.09.022>.
- [10] Lydia Stougie, Georgios A. Tsalidis, Hedzer J. van der Kooij, Gijbert Korevaar, Environmental and exergetic sustainability assessment of power generation from biomass, Renew. Energy 128 (Part B) (2018) 520–528, <https://doi.org/10.1016/j.renene.2017.06.046>.
- [11] Vaibhav Dhyani, Thallada Bhaskar, A comprehensive review on the pyrolysis of lignocellulosic biomass, Renew. Energy 129 (Part B) (2018) 695–716, <https://doi.org/10.1016/j.renene.2017.04.035>.
- [12] Carlos A. Estrada, Andrés Melgar, Juan F. Pérez, Performance prediction of a decentralized power plant (120 kWe) using a multi-particle model of a downdraft biomass gasification process, Energy Convers. Manag. 181 (2019) 258–271, <https://doi.org/10.1016/j.enconman.2018.12.002>.
- [13] K. Anastasakis, I. Kitsiou, W. de Jong, Fast devolatilization characteristics of 'low cost' biomass fuels, wood and reed. Potential feedstock for gasification, Fuel Process. Technol. 142 (2016) 157–166, <https://doi.org/10.1016/j.fuproc.2015.10.018>.
- [14] Ayesha Tariq Sipra, Ningbo Gao, Haris Sarwar, Municipal solid waste (MSW) pyrolysis for bio-fuel production: a review of effects of MSW components and catalysts, Fuel Process. Technol. 175 (2018) 131–147, <https://doi.org/10.1016/j.fuproc.2018.02.012>.
- [15] Ashutosh Agarwal, Masud Rana, Jeong-Hun Park, Advancement in technologies for the depolymerisation of lignin, Fuel Process. Technol. 181 (2018) 115–132, <https://doi.org/10.1016/j.fuproc.2018.09.017>.
- [16] Gianluca Caposciutti, Hernán Almuina-Villar, Alba Dieguez-Alonso, Thomas Gruber, Joachim Kelz, Umberto Desideri, Christoph Hochenauer, Robert Scharler, Andrés Anca-Couce, Experimental investigation on biomass shrinking and swelling behaviour: particles pyrolysis and wood logs combustion, Biomass Bioenergy 123 (2019) 1–13, <https://doi.org/10.1016/j.biombioe.2019.01.044>.
- [17] Derek W. Bunn, Jorge Redondo-Martín, José I. Muñoz-Hernández, Pablo Diaz-Cachinero, Analysis of coal conversion to biomass as a transitional technology, Renew. Energy 132 (2019) 752–760, <https://doi.org/10.1016/j.renene.2018.08.045>.
- [18] Svetlana Proskurina, Jussi Heinimö, Fabian Schipfer, Esa Vakkilainen, Biomass for industrial applications: the role of torrefaction, Renew. Energy 111 (2017) 265–274, <https://doi.org/10.1016/j.renene.2017.04.015>.
- [19] Priyabrata Pradhan, Sanjay M. Mahanaji, Amit Arora, Production and utilization of fuel pellets from biomass: a review, Fuel Process. Technol. 181 (2018) 215–232. doi:<https://doi.org/10.1016/j.fuproc.2018.09.021>.
- [20] Hasti Hosseinizand, Shahab Sokhansanj, C. Jim Lim, Co-pelletization of microalgae Chlorella vulgaris and pine sawdust to produce solid fuels, Fuel Process. Technol. 177 (2018) 129–139, <https://doi.org/10.1016/j.fuproc.2018.04.015>.
- [21] Ana Álvarez, Dositeo Nogueiro, Consuelo Pizarro, María Matos, Julio L. Bueno, Non-oxidative torrefaction of biomass to enhance its fuel properties, Energy 158 (2018) 1–8, <https://doi.org/10.1016/j.energy.2018.06.009>.
- [22] D. Patiño, J. Moran, J. Porteiro, J. Collazo, E. Granada, J.L. Miguez, Improving the cofiring process of wood pellet and refuse derived fuel in a small-scale boiler plant, Energy Fuel 22 (2008) 2121–2128, <https://doi.org/10.1021/ef800093c>.
- [23] Suzan Abdelhady, Domenico Borello, Ahmed Shaban, Techno-economic assessment of biomass power plant fed with rice straw: sensitivity and parametric analysis of the performance and the LCOE, Renew. Energy 115 (2018) 1026–1034, <https://doi.org/10.1016/j.renene.2017.09.040>.
- [24] Kui Wang, Yonatan Zhang, Gasper Sekelj, Philip K. Hopke, Economic analysis of a field monitored residential wood pellet boiler heating system in New York State, Renew. Energy 133 (2019) 500–511, <https://doi.org/10.1016/j.renene.2018.10.026>.
- [25] Esa Kari Vakkilainen, 9 – direct and grate firing of biomass, in: Esa Kari Vakkilainen (Author), Steam Generation From Biomass, Construction and Design of Large Boilers (2017) 203–210. doi:<https://doi.org/10.1016/B978-0-12-804389-9.00009-5>.
- [26] E.J.S. Mitchell, A.R. Lea-Langton, J.M. Jones, A. Williams, P. Layden, R. Johnson,

- The impact of fuel properties on the emissions from the combustion of biomass and other solid fuels in a fixed bed domestic stove, *Fuel Process. Technol.* 142 (2016) 115–123, <https://doi.org/10.1016/j.fuproc.2015.09.031>.
- [27] Zhongfa Hu, Xuebin Wang, Adewale Adeosun, Renhui Ruan, Houzhang Tan, Aggravated fine particulate matter emissions from heating-upgraded biomass and biochar combustion: the effect of pretreatment temperature, *Fuel Process. Technol.* 171 (2018) 1–9, <https://doi.org/10.1016/j.fuproc.2017.11.002>.
- [28] Guillaume Schmidt, Gwenaëlle Trouvé, Gontrand Leyssens, Cornelius Schönnenbeck, Paul Genevray, Fabrice Cazier, Dorothée Dewaele, Coralie Vandenbilcke, Elodie Faivre, Yann Denance, Céline Le Dreff-Lorimier, Wood washing: influence on gaseous and particulate emissions during wood combustion in a domestic pellet stove, *Fuel Process. Technol.* 174 (2018) 104–117, <https://doi.org/10.1016/j.fuproc.2018.02.020>.
- [29] David Patiño, Raquel Pérez-Orozco, Jacobo Porteiro, Magín Lapuerta, Characterization of biomass PM emissions using thermophoretic sampling: composition and morphological description of the carbonaceous residues, *J. Aerosol Sci.* 127 (2019) 49–62, <https://doi.org/10.1016/j.jaerosci.2018.10.005>.
- [30] Araceli Regueiro, David Patiño, Enrique Granada, Jacobo Porteiro, Experimental study on the fouling behaviour of an underfeed fixed-bed biomass combustor, *Appl. Therm. Eng.* 112 (2017) 523–533, <https://doi.org/10.1016/j.applthermaleng.2016.10.105>.
- [31] Manoj Paneru, Selahattin Babat, Jörg Maier, Günter Scheffknecht, Role of potassium in deposit formation during wood pellets combustion, *Fuel Process. Technol.* 141 (Part 2) (2016) 266–275, <https://doi.org/10.1016/j.fuproc.2015.10.008>.
- [32] Joaquín Capablo, Formation of alkali salt deposits in biomass combustion, *Fuel Process. Technol.* 153 (2016) 58–73, <https://doi.org/10.1016/j.fuproc.2016.07.025>.
- [33] M.A. Gómez, J. Porteiro, S. Chapela, J.L. Míguez, An Eulerian model for the simulation of the thermal conversion of a single large biomass particle, *Fuel* 220 (2018) 671–681, <https://doi.org/10.1016/j.fuel.2018.02.063>.
- [34] Nesiadis Athanasios, Nikolopoulos Nikolaos, Margaritis Nikolaos, Grammelis Panagiotis, Emmanuel Kakaras, Optimization of a log wood boiler through CFD simulation methods, *Fuel Process. Technol.* 137 (2015) 75–92, <https://doi.org/10.1016/j.fuproc.2015.04.010>.
- [35] S. Chapela, J. Porteiro, M.A. Gómez, D. Patiño, J.L. Míguez, Comprehensive CFD modeling of the ash deposition in a biomass packed bed burner, *Fuel* 234 (2018) 1099–1122, <https://doi.org/10.1016/j.fuel.2018.07.121>.
- [36] S. Chapela, J. Porteiro, M. Garabatos, D. Patiño, M.A. Gómez, J.L. Míguez, CFD study of fouling phenomena in small-scale biomass boilers: experimental validation with two different boilers, *Renew. Energy* 140 (2019), <https://doi.org/10.1016/j.renene.2019.03.081>.
- [37] Adeline Rezeau, Luis I. Díez, Javier Royo, Maryori Díaz-Ramírez, Efficient diagnosis of grate-fired biomass boilers by a simplified CFD-based approach, *Fuel Process. Technol.* 171 (2018) 318–329, <https://doi.org/10.1016/j.fuproc.2017.11.024>.
- [38] Anqi Zhou, Hongpeng Xu, Yaojie Tu, Feiyang Zhao, Zhiming Zheng, Wenming Yang, Numerical investigation of the effect of air supply and oxygen enrichment on the biomass combustion in the grate boiler, *Appl. Therm. Eng.* 156 (2019) 550–561, <https://doi.org/10.1016/j.applthermaleng.2019.04.053>.
- [39] Ali Shiehnejadhesar, Robert Scharler, Ramin Mehrabian, Ingwald Obernberger, Development and validation of CFD models for gas phase reactions in biomass grate furnaces considering gas streak formation above the packed bed, *Fuel Process. Technol.* 139 (2015) 142–158, <https://doi.org/10.1016/j.fuproc.2015.07.029>.
- [40] E. Simsek, B. Brosch, S. Wirtz, V. Scherer, F. Krüll, Numerical simulation of grate firing systems using a coupled CFD/discrete element method (DEM), *Powder Technol.* 193 (2009) 266–273, <https://doi.org/10.1016/j.powtec.2009.03.011>.
- [41] Jens Wiese, Frank Wissing, Dominik Höhner, Siegmund Wirtz, Viktor Scherer, Ursula Ley, Hans Martin Behr, DEM/CFD modeling of the fuel conversion in a pellet stove, *Fuel Process. Technol.* 152 (2016) 223–239, <https://doi.org/10.1016/j.fuproc.2016.06.005>.
- [42] Jacobo Porteiro, Joaquín Collazo, David Patiño, Enrique Granada, Jorge Carlos Moran Gonzalez, José Luis Míguez, Numerical modeling of a biomass pellet domestic boiler, *Energy Fuel* 23 (2009) 1067–1075, <https://doi.org/10.1021/ef8008458>.
- [43] J. Collazo, J. Porteiro, J.L. Míguez, E. Granada, M.A. Gómez, Numerical simulation of a small-scale biomass boiler, *Energy Convers. Manag.* 64 (2012) 87–96, <https://doi.org/10.1016/j.enconman.2012.05.020>.
- [44] M.A. Gómez, J. Porteiro, D. Patiño, J.L. Míguez, CFD modelling of thermal conversion and packed bed compaction in biomass combustion, *Fuel* 117 (Part A) (2014) 716–732, <https://doi.org/10.1016/j.fuel.2013.08.078>.
- [45] M.A. Gómez, J. Porteiro, D. Patiño, J.L. Míguez, Eulerian CFD modelling for biomass combustion. Transient simulation of an underfeed pellet boiler, *Energy Convers. Manag.* 101 (2015) 666–680, <https://doi.org/10.1016/j.enconman.2015.06.003>.
- [46] M.A. Gómez, J. Porteiro, D. de la Cuesta, D. Patiño, J.L. Míguez, Numerical simulation of the combustion process of a pellet-drop-feed boiler, *Fuel* 184 (2016) 987–999, <https://doi.org/10.1016/j.fuel.2015.11.082>.
- [47] M.A. Gómez, J. Porteiro, D. Patiño, J.L. Míguez, Fast-solving thermally thick model of biomass particles embedded in a CFD code for the simulation of fixed-bed burners, *Energy Convers. Manag.* 105 (2015) 30–44, <https://doi.org/10.1016/j.enconman.2015.07.059>.
- [48] B.M. Wagenaar, W. Prins, W.P.M. van Swaaij, Flash pyrolysis kinetics of pine wood, *Fuel Process. Technol.* 36 (1993) 291–298, [https://doi.org/10.1016/0378-3820\(93\)90039-7](https://doi.org/10.1016/0378-3820(93)90039-7).
- [49] Nelson Sousa, João L.T. Azevedo, Model simplifications on biomass particle combustion, *Fuel* 184 (2016) 948–956, <https://doi.org/10.1016/j.fuel.2016.03.106>.
- [50] H. Thunman, B. Leckner, F. Niklasson, F. Johnsson, Combustion of wood particles—a particle model for eulerian calculations, *Combustion and Flame* 129 (2002) 30–46, [https://doi.org/10.1016/S0010-2180\(01\)00371-6](https://doi.org/10.1016/S0010-2180(01)00371-6).
- [51] Hartmut Mätzing, Hans-Joachim Gehrman, Helmut Seifert, Dieter Stapf, Modelling grate combustion of biomass and low rank fuels with CFD application, *Waste Manag.* 78 (2018) 686–697, <https://doi.org/10.1016/j.wasman.2018.05.008>.
- [52] Mohammadreza Farokhi, Madjid Birouk, Modeling of the gas-phase combustion of a grate-firing biomass furnace using an extended approach of Eddy Dissipation Concept, *Fuel* 227 (2018) 412–423, <https://doi.org/10.1016/j.fuel.2018.04.102>.
- [53] ANSYS Fluent Theory Guide 17.2, (2016).
- [54] J. Collazo, J. Porteiro, D. Patiño, J.L. Míguez, E. Granada, J. Moran, Simulation and experimental validation of a methanol burner, *Fuel* 88 (2009) 326–334, <https://doi.org/10.1016/j.fuel.2008.09.003>.
- [55] M.A. Gómez, D. Patiño, R. Comesaña, J. Porteiro, M.A. Álvarez Feijoo, J.L. Míguez, CFD simulation of a solar radiation absorber, *Int. J. Heat Mass Transf.* 57 (2013) 231–240, <https://doi.org/10.1016/j.ijheatmasstransfer.2012.09.061>.
- [56] S. Chapela, J. Porteiro, M. Costa, Effect of the turbulence – chemistry interaction in packed-bed biomass combustion, *Energy Fuel* 31 (2017) 9967–9982, <https://doi.org/10.1021/acs.energyfuels.7b00516>.
- [57] Henrik Thunman, Fredrik Niklasson, Filip Johnsson, Bo Leckner, Composition of volatile gases and thermochemical properties of wood for modeling of fixed or fluidized beds, *Energy Fuel* 15 (2001) 1488–1497, <https://doi.org/10.1021/ef010097q>.
- [58] Daniel Neves, Henrik Thunman, Arlindo Matos, Luís Tarelho, Alberto Gómez-Barea, Characterization and prediction of biomass pyrolysis products, *Prog. Energy Combust. Sci.* 37 (2011) 611–630, <https://doi.org/10.1016/j.peccs.2011.01.001>.
- [59] W.P. Jones, R.P. Lindstedt, Global reaction schemes for hydrocarbon combustion, *Combustion and Flame* 73 (1988) 233–249, [https://doi.org/10.1016/0010-2180\(88\)90021-1](https://doi.org/10.1016/0010-2180(88)90021-1).
- [60] Jimmy Andersen, Peter Arendt Jensen, Knud Erik Meyer, Søren Lovmand Hvid, Peter Glarborg, Experimental and numerical investigation of gas-phase freeboard combustion. Part 1: main combustion process, *Energy Fuel* 23 (2009) 5773–5782, <https://doi.org/10.1021/ef900752a>.
- [61] Narges Razmjoo, Hamid Sefidari, Michael Strand, Measurements of temperature and gas composition within the burning bed of wet woody residues in a 4 MW moving grate boiler, *Fuel Process. Technol.* 152 (2016) 438–445, <https://doi.org/10.1016/j.fuproc.2016.07.011>.
- [62] J. Porteiro, D. Patiño, J. Collazo, E. Granada, J. Moran, J.L. Míguez, Experimental analysis of the ignition front propagation of several biomass fuels in a fixed-bed combustor, *Fuel* 89 (2010) 26–35, <https://doi.org/10.1016/j.fuel.2009.01.024>.
- [63] H. Thunman, B. Leckner, Ignition front propagation of a reaction front in cross-current bed combustion of wet biofuels, *Fuel* 80 (2001) 473–481, [https://doi.org/10.1016/S0010-2361\(00\)00127-7](https://doi.org/10.1016/S0010-2361(00)00127-7).
- [64] Narges Razmjoo, Hamid Sefidari, Michael Strand, Characterization of hot gas in a 4 MW reciprocating grate boiler, *Fuel Process. Technol.* 124 (2014) 21–27, <https://doi.org/10.1016/j.fuproc.2014.02.011>.

1
2
3
4 *CFD-based coupled multiphase modeling of biochar production using*
5 *a large-scale pyrolysis plant*
6
7
8
9

10 Hassan Khodaei ^{a,b*}, Luis Gonzalez ^c, Sergio Chapela ^c, Jacobo Porteiro ^c, Petr Nikrityuk ^a, Chris Olson ^{b*}

11
12 a: Department of Chemical and Materials Engineering, Donadeo Innovation Centre for Engineering
13
14 University of Alberta, Edmonton, AB, T6G 1H9, Canada

15
16 b: Innovative Reduction Strategies Inc. (IRSI), 6415 75 Street NW, Edmonton, AB, T6E 0T3, Canada

17
18 c: Industrial Engineering School, University of Vigo, Lagoas-Marcosende s/n, 36310 Vigo, Spain
19
20
21
22
23

24 (*) corresponding authors:

25
26 Email address: hkhodaei@ualberta.ca; Hassan.k@irstrategies.org; Tel: +1(587) 936 3977,

27
28 Email address: Chris Olson c.olson@irstrategies.org; Chris Olson c.olson@irsi-inc.com,

29
30 Tel: +1(780) 394 6173

31
32 Address: Innovative Reduction Strategies Inc. (IRSI), 6415 75 Street NW, Edmonton, AB, T6E 0T3,
33
34 Canada; <http://irsi-inc.com/>
35
36
37
38
39
40
41
42
43
44
45
46
47
48
49
50
51
52
53
54
55
56
57
58
59
60
61
62
63
64
65

1
2
3
4
5
6
7
8
9
10
11
12
13
14
15
16
17
18
19
20
21
22
23
24
25
26
27
28
29
30
31
32
33
34
35
36
37
38
39
40
41
42
43
44
45
46
47
48
49
50
51
52
53
54
55
56
57
58
59
60
61
62
63
64
65

Highlights

- Coupled multiphase modelling of biochar production
- Higher efficient co-combustion of air/wood volatile and non-premixed air/propane
- Higher efficient thermal conversion with lower moisture and uniform heat flux

UNDER REVIEW

1
2
3
4
5
6
7
8
9
10
11
12
13
14
15
16
17
18
19
20
21
22
23
24
25
26
27
28
29
30
31
32
33
34
35
36
37
38
39
40
41
42
43
44
45
46
47
48
49
50
51
52
53
54
55
56
57
58
59
60
61
62
63
64
65

CFD-based coupled multiphase modeling of biochar production using a large-scale pyrolysis plant

Abstract

This paper presents a combined CFD simulation of the thermal conversion of biomass to biochar and the co-combustion of air and biomass volatiles with non-premixed swirl air and volatiles in an industrial pyrolysis plant. The main objective of this study is to investigate thermal conversion process in indirect industrial biochar plants taking into accounts the main challenges associated with biochar production. A set of variables are implemented to model the solid phase and utilized with the Ansys-Fluent gas phase. Several sub-models have been introduced to simulate the thermal conversion of biomass to biochar, taking into consideration heat and mass transfer, drying, pyrolysis, density, and volume shrinkage. A non-uniform heat flux obtained by simulating the non-premixed co-combustion of the swirl propane burner and the wood volatile gas has been implemented as an inlet boundary condition in the pyrolysis section. The feasibility of the self-ignition of wood volatiles has been investigated and the heat transfer rate between the thermal oxidizer and the pyrolysis section in the indirect biochar plant is analyzed considering two typical wood moisture contents. The contribution of the wood moisture content and the non-uniformity of the heat transfer rate in the indirect biochar reactor results in a dramatic increase in the necessary residence time for the thermal conversion and consequently requires additional capital and operational expenses.

Key words: Thermal conversion, Biomass, Pyrolysis, Biochar, Co-combustion.

Nomenclature

A_i	Pre-exponential factor (S^{-1})	α	Absorption coefficient (m^{-1})
A_p	Particle area (m^2)	β	Extinction coefficient (m^{-1})
A_b	Bed material absorptance (-)	γ	Devolatilization fraction (-)
A_v	Area to volume ratio (m^{-1})	ε	Solid fraction (-)
b	Model constant (-)	ξ_i	Equivalent heating value of species i
C_p	Specific heat ($J.kg^{-1}K^{-1}$)	η	Permeability (m^2)
D_{cil}	Cylindrical diameter (m)	κ	Equivalent heating value
d_{eq}	Equivalent diameter (m)	λ_s	Geometrical parameter
D_{i_i}	Diffusivity of species I in the mixture ($m^2.s^{-1}$)	μ	Gas viscosity ($kg.m^{-1}s^{-1}$)
E_m	Emissivity (-)	ρ	Density ($kg.m^{-3}$)
f_v	Porosity (-)	σ	Stefan-Boltzmann coefficient ($W.m^{-2}K^{-4}$)
h	Convection coefficient ($W.m^{-2}.k^{-1}$)	τ	Fraction of heat received by the particle employed in drying (-)
I	Irradiation intensity ($W.m^{-2} sr$)	Υ	Inertial loss (m^{-1})
k	Thermal conductivity ($W.m^{-1}k^{-1}$)	φ	Char oxidation parameter (-)
L_{cil}	Cylindrical length (m)	ϕ	Scattering function (m^{-1})
LH	Latent heat ($J.kg^{-1}$)	ψ	Sphericity (-)
M	Molecular weight ($kg kmol^{-1}$)	$\dot{\omega}'''$	Generation or consumption of wood components ($kg.m^{-3}s^{-1}$)
Nu	Nusselt number (-)	Ω	Solid angle (sr)
Pr	Prandtl number (-)	<i>Sub/Superscripts</i>	
Re	Reynolds number (-)	p	particle
K	Ideal gas constant ($J.K^{-1}mol^{-1}$)	s	solid
$S_{i,j}$	Surface of species i from component j ($kg.m^{-3}S^{-1}$)	g	gas
Sh	Sherwood number (-)	eff	effective
Sc	Schmidt number (-)	c	consumption
S	Source term ($W.m^{-3}$)	G	Generation
S_g^{rad}	Gas term radiation energy source ($W.m^{-3}$)	$moist$	moisture
T	Temperature (K)	$wood$	Dry wood
V_p	Volume (m^3)	$char$	Char
v_α	Gas velocity ($m.s^{-1}$)	ash	Ash
Y_i	Fraction of component i (-)	$evap$	evaporation
		dev	devolatilization
		rad	radiation

Introduction

Biochar, an environmentally friendly product resulting from the thermochemical processing of biomass, has gained a lot of attention recently due to its great capacity to produce various valuable products such as activated carbon in addition to the material's application as an agricultural soil amendment, a water treatment filtration medium, an additive to energy storage systems, and a fuel source for direct combustion and co-firing [1]. Different carbonization methods are utilized to produce biochar depending on the characteristics of the wood material used as a feedstock and the desired characteristics of the resulting biochar, as well as its accompanying pyrolysis gasses. These technologies could be summarized as: slow pyrolysis, fast pyrolysis [2], flash pyrolysis [3], intermediate pyrolysis [4] and vacuum pyrolysis [5]. The residence time, heating rate, particle size and temperature are the most influential parameters to produce high-quality biochar [6, 7]. Slow pyrolysis is known as the most conventional carbonization method. It occurs at a slow heating rate in the absence of oxygen at a temperature range of 500–950 [K], a heating rate of 0.1–1 [K/s], a particle size of 5–50 [mm] and a residence time of 450–550 [s] [3, 7, 8]

Biomass decomposition begins when water evaporates from the biomass feedstock (physical process). A few seconds after the drying, the second stage of the process (devolatilization) takes place, which corresponds to the main pyrolysis process and leads to the production of pyrolysis gases, in turn causing the production of charcoal or biochar [9]. If the objective is a high char yield, a low temperature and low heating rate are chosen. However, if the purpose is to maximize the yield of fuel gas resulting from pyrolysis, a higher temperature and a low heating rate with a long residence time are preferred [9]. It is obvious that the residence time is always directly influenced by other parameters such as the temperature and heating rate. In recent decades, the production of biochar from forest biomass has been explored, in part thanks to new, efficient indirect heat transfer technologies such as retort augers [10, 11], moving bed conveyor systems [12] and rotary kiln biochar reactors [13]. However, there are a lot of challenges associated with continuous and batch industrial-scale plants which have not been resolved yet. Some of these challenges include the non-efficient heat recovery system for pyrolysis gas, the non-uniform heat transfer between the pyrolysis and combustion chamber, the deformation of materials due to high temperatures, and non-efficient supply air and volatile suction mechanisms intended to prevent combustion in the pyrolysis section. The first objective of this study is to introduce an efficient pattern of non-premixed volatile combustion that coincides with a non-premixed swirl propane burner, and to investigate the influence of heat transfer between the combustion chamber and pyrolysis section.

In industrial biochar plants ranging between 50–5000 kg/hour as addressed in Table 1, a propane, natural gas burner or electrical heater is utilized to reach the desired temperature in the pyrolysis section. Once the desired temperature is achieved, the volatile gases produced in the pyrolysis section are premixed with additional air (or not premixed) and then directed into the combustion zone to generate the main portion of thermal energy required for the pyrolysis process to carry forward. This creates a closed loop once a temperature is reached that eliminates any need for additional input energy. The thermal energy generated from the combustion of the volatile gases is transferred indirectly through the intersection wall between the combustion chamber and the pyrolysis section.

In some technologies, such as retort augers or rotary kiln reactors, self-igniting biomass volatiles could compensate for the heat deficit and provide the heating rate and pyrolysis temperature required to produce biochar during the stable time [12]. Different parameters are associated with the self-ignition of biomass volatiles, such as a lower moisture content, the quality of the wood (high volatile content), the thermal oxidizer having a geometrical shape, or appropriate excess air. However, in the industrial fixed-bed or moving-grate system with a feeding rate over 1000 kg/hour (the current plant), the smaller surface area (the interface) between the thermal oxidizer and pyrolysis section and lower feedstock agitation lead to

poor heat transfer and a low temperature in pyrolysis section. Therefore, the injection of biomass volatiles should coincide with the combustion of auxiliary propane or natural gas in order to provide the heat required to produce biochar. Table 1 shows a comparison between different biochar technologies in terms of throughput capacities, feedstock type and size, moisture content and laboratory and industrial scales.

Table 1: Biomass specifications for different pyrolysis reactors

Characteristics	Fixed bed	Fluidized bed	Circulating bed	Rotary drum	Moving bed	Retort auger
Max. capacity (t/day)	500	200	100	200	84–120	50
Particle shape	Logs	Fine particles Pellets	Fine particles Pellets	Fine particles, pellets, chips, chops	Fine particles, pellets, chips, chops	Fine particles, pellets, chips, chops
Particle size	1–2m long, 3–10cm diameter	< 2mm	< 2mm	1–50 mm long	1–50 mm long	1–50 mm long
Moisture content (%)	10–50%	< 10%	< 10%	< 10%	10–20% (current case)	< 10%
Laboratory/pilot scale	[14]	[15]	[16]	[17]	[18]	[15]
Industrial scale	[12]	[12]	[12]	FEECO International, Inc.	Ulysses (I) (current case)	PYREG

Note: The data addressed in the table are based on San Miguel et al.[19], Garcia-Perez et al.[12], PYREG, FEECO International Inc, Innovative Reduction Strategies Inc.

In this regard, the CFD simulation of biomass volatile combustion in the thermal oxidizer is of principal importance and is a valuable method to improve thermal efficiency in the indirect biochar plant. This improvement could have an indirect impact on the residence time during the feedstocks' thermal conversion and can be classified into the following categories: 1) the position of the burner and volatile gas nozzles from the intersection plate 2) adequate mixing of volatile gas and excess air 3) the geometrical configuration of the thermal oxidizer. Chander and Ray [20] provide an overview of flame impingement heat transfer taking into account the flame shapes, stabilization, total heat flux, operating conditions and burner geometry in different experimental configurations as well as various models and computations of the flame impingement heat transfer process. Baltasar et al. [21] conducted a comprehensive study on the combustion of propane in a swirl propane burner for the purpose of investigating turbulence, overall emissions, and the temperature near the burner region for different representative operating conditions. Except for the NO_x concentration in the combustion products, the mathematical model is validated by experimental measurement, particularly in the area close to the nozzle injection zone. The effect of Flow Gas Recirculation (FGR) or vitiated air in the propane combustion have been investigated and the results indicate that low percentages of CO₂ are present in the preheated inlet air, which inhibits the production of radicals and leads to a reduction in the peak flame speed [22]. It should be noted that a significant number of biomass volatiles are CO₂. Yilmaz et al. [23] investigated the influence of turbulence and radiation models on combustion characteristics in a swirl propane-hydrogen diffusion process, taking into account the renormalization group (RNG), the Reynolds stress model, P1,

1
2
3
4 and discrete transfer radiation models in which the velocity, CO₂, CO, and temperature gradient agree
5 reasonably well with the earlier experimental findings aggregated by Baltasar et al. [21]. The efficiency
6 and emissions of a domestic gas burner with a swirl flame was investigated by Hou et al. [24], showing
7 that the swirl burner yields a higher thermal efficiency and emits only a slightly higher CO concentration
8 than the conventional radial flow burner. A numerical investigation of swirl flow and non-swirl flow of a
9 premixed methane-air mixture [25] demonstrated that recirculating the hot combustion product,
10 particularly in the center of the recirculation zone, increases the upper and lower flame stability and
11 enhances the performance of the combustion compared to the non-swirl flow. Co-flow injection in non-
12 premixed combustion has been investigated by Hall and Pitz [26] taking into account the flame shape and
13 temperature. Erete et al. [27] studied the effect of different CO₂ dilution ratios in non-premixed
14 air/methane combustion. The results of this study indicate that a higher CO₂ dilution ratio leads to a
15 reduction in the flame length and temperature as well as a lower NO concentration. The homogenous
16 reaction of biomass volatile gases in the freeboard area above the bed has been studied by Gomez et al. [28,
17 29] by introducing a semi-global reaction of volatiles, using a realizable $k-\epsilon$ model with enhanced wall
18 treatment for turbulence and finite-rate/eddy dissipation modeling for biomass species reactions. The
19 composition of the volatiles in their study was chosen based on the comprehensive studies on the
20 characterization of pyrolysis in different biomasses conducted by Thunman et al. [30, 31]. Gomez et
21 al. [32] investigate how to improve the performance of biomass combustion through exhaust gas
22 recirculation, implementing a combined CFD simulation of the solid phase thermal conversion and gas
23 phase combustion in the freeboard area above a boiler. Danon et al. [33] use a commercial CFD code
24 considering Eddy Dissipation Concept (EDC) turbulence-chemistry reaction with the realizable model. It
25 was found that the preheated air temperature, the distance of the burner from the stack, the burner
26 patterns, and the recirculation zones are important to minimize CO emissions. Mehrabian et al. [34] used
27 10 species as wood volatile components to simulate the homogenous reaction of wood volatiles in a
28 packed-bed biomass combustion system. It should be noted that most studies are related to the direct
29 combustion of biomass with the final ash product; however, in indirect biochar technology, combustion
30 does not occur in the freeboard area above the bed, so the sub-process of volatile combustion should be
31 modelled separately. In the recent study, Khodaei et al. [35] investigate the axial injection of biomass
32 volatiles premixed with air in a large-scale biochar reactor (the current plant). The injection of biomass
33 volatiles coincides with additional propane, which significantly increases the heat transfer rate between
34 the combustion chamber and the pyrolysis section. However, the premixed high-temperature volatile gas
35 (around 500 K) when introduced to air may cause partial explosion in the system, particularly, when the
36 size of volatiles nozzle is small. Overcoming this barrier is possible through implementation of a large
37 Venturi duct system, which creates enough suction and premixed air and volatiles without any partial
38 combustion; however, this technology is not thermally efficient, so the non-premixed injection of
39 volatiles and air coinciding with the non-premixed injection of propane in a swirl burner is proposed as
40 the best solution to ensure that safety precautions are followed and guarantee the efficient combustion of
41 biomass volatiles.

42
43
44
45
46
47
48
49
50
51 Over the last few decades, many efforts have been devoted to developing a comprehensive model for the
52 thermochemical degradation of woody biomass, taking into consideration different sub-processes of
53 biomass thermal conversion such as drying, devolatilization and char conversion. These models are
54 categorized by the dimensionality of the models and the level of discretization with respect to
55 implementation in the numerical simulation [36, 37]. The prediction of the species, temperature and
56 ignition rate is investigated by modelling zero- or one-dimensional bed model [38, 39], two-dimensional
57 counter-current moving bed combustion is investigated by van der Lans et al. [40] by dividing the bed into
58 different subdomains, and by Yang et al. [41] using two different numerical domains for the bed and the
59
60
61
62
63
64
65

1
2
3
4 freeboard area above the bed. There have also been studies that have assessed the effect of moisture in the
5 direct thermal conversion of biomass [42]. The particle-resolved modelling approach, deployed on a 2D
6 platform, considering a combination of a finite number of particles and a 1D transient model, has been
7 deployed to solve the mass and energy balance for every individual particle, while the interaction between
8 the solid particle and the gas phase is then introduced by a porous media domain [43]. Anisotropy and the
9 highly varied boundary conditions require the model to be extended dimensionally; however, 3D models
10 do not necessarily result in significantly higher accuracy compared to 2D models [37]. Collazo et al. [44]
11 proposed a 3D model employing cell-by-cell solid particle modelling using a disperse porous media
12 approach. The dense discrete phase model (DDPM) is used by Mehrabian et al. [45, 46]. In this approach,
13 particle trajectories are computed in a Lagrangian frame to create a three-dimensional bed of particles,
14 and the thermal conversion of each solid particle is coupled with the gas phase. The bed density and mass
15 shrinkage during the pyrolysis process with constant porosity have been studied by Bryden et al. [47] and
16 de-Blasi et al. [48]. Volume shrinkage during char conversion has been investigated by Hermansson and
17 Thunman [49]. Gomez et al. [29] proposed a comprehensive CFD commercial code (Ansys-Fluent)
18 simulation of the transient combustion of packed-bed biomass. The porous medium approach is used, and
19 a set of transport equations introduced to represent the solid phase variables and interaction between the
20 solid and gas phases, taking into consideration an enhanced radiation and bed compaction models.
21 Notably, in indirect biochar production technology, the main objective is to produce biochar through
22 indirect heat transfer in the absence of oxygen. Therefore, the sub-process of char consumption should not
23 be considered. Although considerable research has been devoted to modelling the thermal conversion of
24 biomass and waste materials into energy and ash products (combustion), less attention has been paid to
25 the conversion of biomass to biofuel and biochar products. Yao et al. [50] have investigated the co-
26 production of biochar and syngas in a small-scale upper-feed biomass gasifier with lateral air injection. A
27 1D model was developed to describe the entire bed and the Repetitive Particle Model (RPM [51]) is used
28 to resolve the solid phase. The mixing behavior of biomass and biochar in a bubbling fluidized bed has
29 been studied by Sharma et al. [52]. The Euler–Euler (EE) approach [53], which treats the gas phase and
30 the biomass and biochar particles as interpenetrating continua, has also been investigated. It should be
31 noted that this approach is appropriate only if the parameters of a single particle (e.g. particle size,
32 temperature and species concentration gradient inside the particle) which influence the gasification
33 performance are negligible, meaning that intra-particle phenomenon can be considered to increase the
34 accuracy of gasification models. Aramideh et al. [15] performed a numerical simulation of fast pyrolysis
35 in an auger reactor. Similarly, to the previous investigation, they used interpenetrating continua
36 considering the movement of particles in a rotational reference framework. A comprehensive review of a
37 detailed pyrolysis mechanism in a single biomass particle is addressed by Di-Blasi [54] considering
38 multi-step mechanisms of cellulose pyrolysis, intra-particle heat transfer and particle shrinkage and
39 emphasizing the need to implement the single-particle models in CFD reactor models. Neves et al. [31]
40 performed an extensive review of the pyrolytic characteristics of different biomasses in an inert
41 atmosphere and a temperature range of 200–1000 °C. The composition of pyrolytic volatiles is described
42 by means of a relevant number of species: H₂O, tar, CO₂, CO, H₂, CH₄ and other light hydrocarbons. It
43 was shown that operating parameters other than the temperature (e.g. classification of heating rate, fuel
44 properties) influence the yield of char. Biomass characterization and the main kinetic feature of biomass
45 pyrolysis, devolatilization and primary and secondary species reactions have been investigated by Ranzi
46 et al. [55] taking into account the characterization of the degradation steps, their characteristic times, and
47 the prediction of product distributions. In this study, the devolatilization of dry wood is modeled using a
48 three-step mechanism that is extensively employed in biomass combustion models considering the
49 competition of three Arrhenius rates corresponding to each conversion process [29].
50
51
52
53
54
55
56
57
58
59
60
61
62
63
64
65

1
2
3
4
5
6
7
8
9
10
11
12
13
14
15
16
17
18
19
20
21
22
23
24
25
26
27
28
29
30
31
32
33
34
35
36
37
38
39
40
41
42
43
44
45
46
47
48
49
50
51
52
53
54
55
56
57
58
59
60
61
62
63
64
65

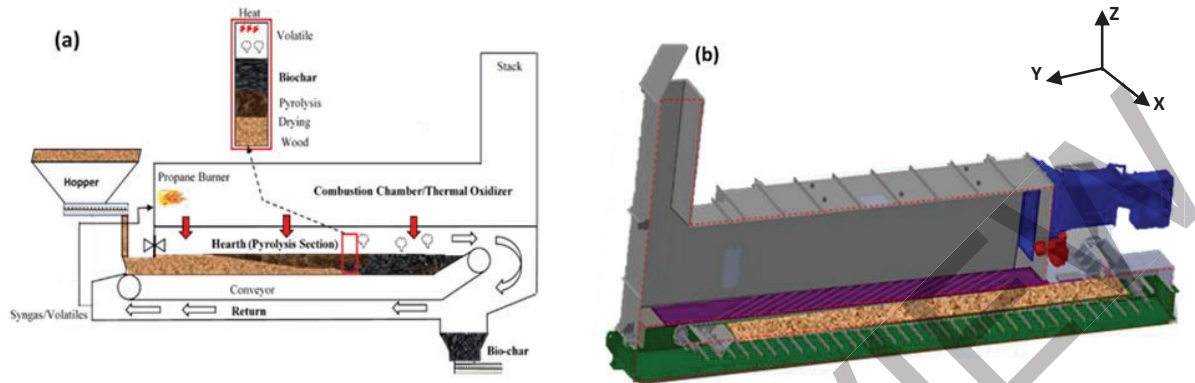
Despite the existence of excellent numerical studies on numerous aspects of biomass combustion, there is a need in the research for modelling slow pyrolysis techniques with the explicit objective of producing raw biochar or activated carbon materials in industrial packed beds. In addition, the indirect production of biochar in slow pyrolysis systems has always faced several challenges, such as the non-uniformity of the heat transfer rate between the combustion and pyrolysis sections and the resulting effect on the residence time in different sub-processes of thermal conversion. This challenge results in low-quality biochar material (excess of torrefied wood or ash content in biochar), which is a common issue in most industrial biochar plants. Moreover, increasing the thermal efficiency and performance of the plants by introducing a highly efficient volatile injection system to make use of the co-combustion of volatiles and propane is highly recommended. Understanding the above-mentioned barriers during the operation of industrial biochar plants will lead to a combined CFD simulation of the pyrolysis plant enabling the troubleshooting of the reactor's limitations and will result in appropriate solutions for the current industrial biochar plant. This will inform future iterations of the current technology. Detailed process specification of the Ulysses plant is addressed in the following section.

The main novelties of this study are the emphasis on the importance of coupling CFD simulation to overcome the issues of low-quality biochar production in indirect pyrolysis plants, low-efficiency volatile combustion in the thermal oxidizer and mutual indirect relationships between pyrolytic volatile combustion and biochar thermal conversion. Furthermore, volatile self-ignition in the current plant and the moisture content have been analyzed, and the effect of a non-uniform heat transfer profile on the thermal conversion process and the resulting biochar yield has been investigated comprehensively.

2.1 Ulysses (I) specifications

The specifications of the Ulysses unit (I) and the technical challenges associated with the low quality of the biochar produced by this pyrolysis plant are addressed in this section. The Ulysses pyrolysis unit is designed to process 3,000 kg/h of wood planer shavings. This re-locatable unit can theoretically process 5,000 kg/h of such shavings. Figure 1(a) shows a schematic of the indirect biochar plant. This pyrolysis unit contains a pyrolysis hearth (green), a volatile gas recovery section (blue) and a combustion chamber or thermal oxidizer (gray), as shown in Figure 1 (b). Biochar is produced in this reactor under slow pyrolysis conditions and using indirect heat transfer technology which has the capability to produce biochar in a continuous process [12]. Wood planer shavings are used as the feed material. The swirl propane burner (red in Figure 1(b) provides the initial heat required for the start-up of the pyrolysis process and will supply the heat demanded during thermal conversion to sustain a sufficient heat flux for the pyrolysis section. The burner includes a ring with a 45° surface, and 40 propane injection holes (5mm x 4mm) are projected on the ring surface. The swirl air diffuser is surrounded by these holes in order to provide the propane with stoichiometric air (See Figure 2(i)). Notably, the desired temperature in slow pyrolysis reactors is 500–773 K and to reach this range, it is advised to pre-heat the system up to 573 K [56]. A syngas ejector (blue in Figure 1(b) is utilized to create suction with a centrifugal fan and a supply of premixed hot volatile gas blended with stoichiometric air for combustion. Notably, on the left side of the pyrolysis section, there is a duct which connects the pyrolysis section to the combustion chamber and directs the volatile gases into the combustion chamber using the blue ejector as shown in Figure 1(a). The intersection of the 304 stainless steel plate is an interface between the thermal oxidizer and the pyrolysis section with the purpose of facilitating the indirect transfer of heat from the combustion zone to the pyrolysis section as illustrated in purple in Figure 1(b). The flue gas temperature in the biochar reactor is measured continuously by two thermocouples (Type K) in the thermal oxidizer (gray) located in the right-side wall of the combustion chamber (X=2, 5m from the propane burner tip). The aim is to monitor the temperature in the combustion chamber and three thermocouples (Type K) placed in the right-side wall of

1
2
3
4 pyrolysis section in the freeboard area above the bed close to the inlet, middle and discharge of the
5 pyrolysis chamber, ensuring there is a stable temperature range up to 1373 K.
6
7
8
9



23 Figure 1. (a): A schematic of the continuous slow pyrolysis reactor (Ulysses I [35]); (b): Cross-sectional
24 view of 3D CAD drawing of the reactor. Gray, green, red, blue and purple represent the combustion
25 chamber, pyrolysis section, swirl propane burner, volatile duct side and intersection plate, respectively.
26 The shaded area in the interior of pyrolysis section illustrates the wood planer shavings covering the chain
27 conveyor
28
29

30 2.2 Troubleshooting the reactor

31
32 The reactor was operated several times for approximately 5–8 hours including the start-up time. The
33 operational results show that the quality of biochar did meet the Class 1 designation for biochar as stated
34 by the International Biochar Initiative guidelines [57, 58]. However, the primary assessment of heat
35 transfer in the Ulysses (I) unit confirms that only a small portion of the heat produced in the combustion
36 chamber was absorbed by the pyrolysis section [59]. Figure 2 (a) shows the side-duct system used in this
37 reactor to inject premixed air and the volatile gas into the combustion chamber. In fact, sustaining the
38 desired temperature range (673–773 K) in the pyrolysis section (hearth) to produce biochar is a common
39 challenge. The main contributors to the lower temperature in the combustion chamber are the size of the
40 duct used to inject the volatile gas into the combustion chamber, the non-uniform distribution of air and
41 volatiles in the combustion chamber, the low velocity of the premixed air, and the volatiles in the inlet
42 duct. Moreover, premixing high-temperature volatiles with excess air sometimes creates partial
43 explosions in the duct system and results in low combustion efficiency. To increase the performance of
44 the reactor and resolve the technical issues, a 10 cm excess air nozzle surrounded by 10 (10 mm) nozzles
45 is proposed at a low distance (40 cm) beneath the center of the swirl propane burner. These volatile
46 nozzles axially inject the volatile gas produced in the pyrolysis section and the stoichiometric air is
47 provided by a centrifugal fan through a 10 cm nozzle. Figure 2(b) (i), (ii) shows the swirl propane burner
48 and non-premixed volatile injection system, respectively. Previous investigations with this reactor have
49 demonstrated that co-injection of premixed air/wood volatile gases is the most efficient method for
50 increasing the performance of the reactor compared to side duct premixed injection (the current case).
51 This value is chosen based on the reactor process design, the primary simulation of thermal conversion in
52 pyrolysis section, and the proximate and ultimate analysis of feeding materials. The operational
53 parameters used in this study have been addressed in Table 2.
54
55
56
57
58
59
60
61
62
63
64
65

The feedstock used in the Ulysses I reactor was wood planer shavings. Table 3 summarizes the physical and chemical properties of the wood planer shavings, including the bulk density, proximate analysis (content of volatile matter (VM), fixed carbon (FC) and ash), ultimate analysis (elemental content) based on the document issued by Inno-Tec Alberta [59]. Moreover, the composition of the wood planer shavings' volatile gas (with 20% and 5% moisture) and the stoichiometric air supplied for combustion have been calculated based on data from the Biomass Exchange [60] and addressed in Table 4. This information is used as the inlet boundary condition for the volatile gas in the combustion chamber.

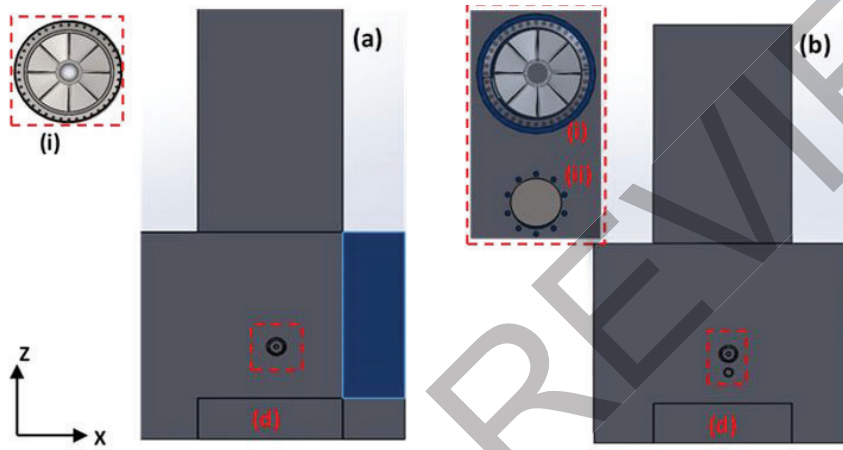


Figure 2: The configuration of the current reactor (a) and the proposed scenario (b); (a)-(i): Swirl propane burner; (a, b)-(d): pyrolysis section; (b)-(i, ii): swirl propane burner and non-premixed volatile and air nozzles

Table 2: Different cases utilized to analyze wood volatile combustion in the combustion chamber

Cases	Swirl propane burner	Non-premixed volatiles	Swirl propane burner				Non-premixed volatiles and air			
			m_p [kg/s]	V_p [m/s]	m_a [m/s]	V_a [m/s]	$m_{volatile}$ [kg/s]	$V_{volatile}$ [m/s]	m_{air} [kg/s]	V_{air} [m/s]
Start-up	√	√	0.015	7	0.57	22.75	N/A	N/A	N/A	N/A
Steady	√	√	0.015	7	0.57	22.75	0.026	48	0.12	16

Note: λ denotes the excess air ratio (actual/stoichiometric air: fuel ratio)

Table 3: Characteristics of wood planer shavings required for CFD simulation [59]

Proximate analysis on a wet basis [%]	Volatile matter	0.67	0.78
	Ash	0.027	0.03
	Fixed carbon	0.127	0.13
	Moisture content	0.2	0.05
Ultimate analysis on a dry basis [%]	Carbon	49.01	
	Hydrogen	6.13	
	Nitrogen	<0.1	
	Sulphur	<0.1	
	Oxygen	44.36	
Wood density [kg/m ³]	89 (untapped)	150 (tapped)	
Sphericity [61]	[-]		0.1
Equivalent diameter [m]	0.005		[62]
LHV (d.b) [J/kg]	19.5e ⁶		
K _{wood} (d.b) [63]	[59] [W/m.K]		0.087
C _{p,wood} (d.b) [J/kg.K]	1760		[64]

Table 4: Wood volatile mass fractions used as an inlet boundary condition in the non-premixed volatile nozzle

Wood volatile components	Mass fraction [-] non-premixed	
	5% moisture	20% moisture
CO [%]	0.087	0.19
CO ₂ [%]	0.262	0.57
CH ₄ [%]	0.0176	0.038
H ₂ O [%]	0.092	0.2
Air and/or volatiles	500 (Volatiles)	
Temperature [K]	370 (Air)	
Area of inlet volatile and (or) excess air nozzles [m ²]		
0.0051 (Air and volatiles)		
0.007 (Air)		
10*(0.01m) volatiles		

3. Model Description

The reactor can run as a continuously moving grate or in a semi-continuous or batch process. Generally, in the slat-chain biochar plant, the moving of the grate should be adjusted based on the residence time required for making fully charred material. The conveyor speed should be adjusted by a PLC controller in order to provide enough residence time for the thermal conversion process. Therefore, the movement of the bed can be set by adjusting the On/Off ratio to control the system output. It should be clarified that a

batch process does not mean shutting down the system after each running period in the slat-chain biochar plant. In fact, the conveyor runs a certain amount of material into the system and then stops. This process is described as a partially continuous system. After the thermal conversion finishes, the material is discharged into the quench cooling system while the conveyor feeds in the new materials. Experimental testing with the Ulysses system shows that the system could work in these conditions. The most important thing, and an aspect which requires appropriate attention, is that the heat flux and temperature across the pyrolysis section should be distributed uniformly. Another reason for utilizing the batch condition in this investigation is the model's limitation. In fact, the model developed by GTE group at the University of Vigo imposes a restriction on numerical simulation, for this case. Although they have improved the physics recently such as improving bed movement physics [65] and three-dimensional CFD simulation of a large-scale grate-fired biomass furnace [66], this model does not have a specific movement to simulate a chain conveyor displacement at present. Therefore, during this study, the solid bed continuous movement will not be considered so that, a batch condition will be used in this investigation. Table 5 shows a review of some past research performed by GTE group utilizing different scale of the biomass thermal conversion model.

Table 5: A review of some investigations employed thermal conversion model developed by GTE group

	Scale	Feedstocks	Feature	Year	Reference
1	Lab-scale	Wood pellet	Investigate the behavior of bed and its interaction with the freeboard area above the bed.	2012	[44]
2	Lab-scale	Wood pellet	Fixed bed thermal conversion, Bed compaction and local bed shrinkage	2014	[29]
3	Lab-scale	Wood pellet	Development of thermally thick model to utilize in biomass combustion models	2015	[67]
4	Commercial pellet drop boiler	Wood pellet	Fully embedded transient bed model and Lagrangian-Eulerian conversion are implemented for particle drop feeding system	2016	[28]
5	Commercial biomass domestic boiler	Wood pellet	A developed sub grid thermally thick model was used to divide particle into several grid points and utilized in the biomass boiler considering constant and variable feeding rate.	2017	[68]
6	laboratory autothermal fixed bed gasifier	Wood (Chips, cylinder, cube)	Effect of biomass packing factor on the drying, pyrolysis and bed temperature in fixed bed gasification process	2018	[69]
7	Underfeed grate boiler	Pine wood pellet	The combined effect of EGR (Exhaust Gas Recirculation), oxygen excess ratio on boiler performance and contaminant emissions in the freeboard area taking into accounts several sub-model of biomass combustions	2019	[32]
8	4MW grate fired boiler	Wood chips, bark and saw dust	Eulerian fixed-bed biomass combustion model coupled with the CFD commercial code to perform the simulation of a large-scale moving grate biomass furnace	2020	[66]

1
2
3
4 In a continuous system, the chain conveyor is assumed to move with a constant axial velocity. In these
5 conditions, each segment of the conveyor from the beginning to the end is exposed to a different heat
6 flux; according to experimental observation, the process of thermal conversion normally starts in
7 approximately the middle of the conveyor. On the other hand, a low concentration of volatile gases
8 produced in the pyrolysis section, which are then combusted in the thermal oxidizer section, results in the
9 heat transfer rate between the thermal oxidizer and the pyrolysis section being lower than the values
10 addressed in this study. Assuming that the conveyor is fully covered with fresh wood in the batch (or in
11 partially continuous conditions), this results in a higher char production and consequently leads to the
12 maximum heat generated in the combustion chamber, which is more appropriate considering that the
13 main objective of this study is to increase the heat production by combusting a higher amount of volatiles
14 and consequently providing the heat required for thermal conversion through indirect heat transfer
15 between the pyrolysis and thermal oxidizer sections. Therefore, batch conditions are considered in this
16 study and can be implemented as the plant's maximum volatile production capacity in continuous
17 conditions.
18
19
20

21
22 The wood planer shavings are modelled as a porous zone and the solid phase variables are introduced in
23 the CFD code via the User-Defined Functions platform, which enables the coupling of the C++,
24 programmed cell-based sub-models that are numerically solved in conjunction with the CFD model. The
25 pyrolysis section is divided into two regions: the area covered with wood planer shavings (porous
26 domain) which is where the solid and gas phases interact, and the freeboard area above the bed, which is
27 defined as a gas phase. In the case of a heat flux on a rectangular 6mm intersection plate (in purple in
28 Figure 1(b)), heat gradually transfers into the gas phase and then the solid phase (porous domain). Six
29 scalar variables are defined to characterize the solid phase. These variables are (1) the temperature, (2) the
30 solid fraction, (3) moisture density, (4) the dry biomass density, (5) the char density, and (6) the volume
31 of particle represented by the mean of the third power of its diameter (d_p). A detailed methodology of the
32 bed domain is addressed in several publications performed by the GTE group at the University of Vigo
33 [29, 44, 67, 68]. Table 6 shows the equations utilized to model the thermal conversion in this
34 investigation, and the combustion of the propane and wood volatile gases were modelled using a semi-
35 global homogenous reaction (R1-R6) and the kinetics of a solid phase heterogenous reaction as shown in
36 Table 7. The reactions are computed using the Arrhenius expression. The drying rate is modelled using an
37 evaporation process when the temperature reaches a value of 373.15 K (heat sink model; Eq.1). The
38 devolatilization process is affected by several factors, such as solid temperatures, heating rates and the
39 thicknesses of the particle reaction layers [70]. The devolatilization of dry wood is modeled using a
40 three-step mechanism that is extensively employed in biomass combustion models, considering the
41 competition of three Arrhenius rates that correspond to each conversion process (Table 6 Eq.2, Table 7
42 (I))[29].
43
44
45
46
47

48 The following assumptions are used when modelling wood carbonization in the indirect pyrolysis unit:

- 49 • The porous medium is modelled as a disperse medium with local volume average properties
50 within each computational cell
- 51 • Thermally thin spherical-equivalent particles are assumed in the bed
- 52 • The solid density varies during drying, devolatilization and the char reaction
- 53 • Drying is assumed to occur at a specific temperature and to be thermally controlled
- 54 • Three-step mechanisms are employed for devolatilizing dry wood
- 55 • The product gases generated inside the particles are released instantaneously into their gas phase,
56 which results in an immediate outflow condition
- 57
- 58
- 59
- 60
- 61
- 62
- 63
- 64
- 65

- The gas-solid heat exchange is performed by convection and radiation, and the solids exchange heat by conduction and radiation
- The gases emitted into the gas phase through the solid phase are the same temperature as the solids
- An incompressible ideal gas is assumed in the mixture
- The thermal conversion process in the pyrolysis section is assumed to have occurred in the absence of oxygen in the pyrolysis section. Notably, this assumption is valid for indirect biochar reactors.
- Even though the char reaction was allowed during the modeling, the lower temperature in the indirect pyrolysis plant and local conditions led to a negligible char reactivity, hence the char reaction will be omitted from the analysis

Table 6: Equations of solid consumption rates and phase variables

Drying rate	$\dot{\omega}'''_{moist} = \tau \frac{\rho_p C_p}{LH_{moist}} \frac{\partial T_s}{\partial t}, T_s \geq T_{evap}$	(1)
Devolatilization rate	$\dot{\omega}'''_{wood} = \rho_{wood} \sum_{i=1}^3 A_i \exp\left(-\frac{E_i}{RT_s}\right)$	(2)
Char generation rate	$\dot{\omega}'''_{G,char} = \rho_{wood} A_i \exp\left(-\frac{E_i}{RT_s}\right)$	(3)
Solid temperature	$\frac{\partial(\varepsilon \rho_p C_p T_s)}{\partial t} = \nabla(k_{s,eff} \cdot \nabla T_s) + S_s$	(4)
Solid fraction	$\frac{\partial \varepsilon}{\partial t} = -\frac{\dot{\omega}'''_{c,char}}{\rho_p} \varepsilon$	(5)
Third power of particle diameter	$\frac{\lambda d_{p3}}{dt} = -\frac{\dot{\omega}'''_{c,char}}{\rho_p} d_{p3}$	(6)
Moisture density	$\frac{\partial(\varepsilon \rho_m)}{\partial t} = -\dot{\omega}'''_{moist} \varepsilon$	(7)
Dry wood density	$\frac{\partial(\varepsilon \rho_w)}{\partial t} = -\dot{\omega}'''_{wood} \varepsilon$	(8)
Char density	$\frac{\lambda(\varepsilon \rho_c)}{\lambda t} = -(\dot{\omega}'''_{G,char} - \dot{\omega}'''_{c,char})$	(9)
Total particle density	$\rho_p = \rho_{moist} + \rho_{wood} + \rho_{char}$	(10)
Energy equation source	$S_s = S_s^{reac} + S_s^{conv} + S_s^{rad} + S_s^{loss}$	(11)
Reaction source terms	$S_s^{reac} = -\dot{\omega}'''_{moist} \varepsilon \cdot LH_{moist} - \dot{\omega}'''_{wood} \varepsilon \cdot f_{gas} \cdot LH_{dev} + S_{char}^{reac}$	(12)
Mass loss source terms	$S_s^{loss} = (\dot{\omega}'''_{moist} + \dot{\omega}'''_{wood} + \dot{\omega}'''_{char}) \cdot \varepsilon \cdot (C_p T_s)^{t-\Delta t}$	(13)
Convection source term	$S_s^{conv} = -S_g^{conv} = h A_v (T_g - T_s)$	(14)
	$h = \frac{Nu \cdot k_g}{d_{eq}}; k_m^i = \frac{Sh \cdot D_{i1}}{d_{eq}}$	(15.16)
	$Nu = 2 + 1.1 \cdot Re^{0.6} \cdot Pr^{1/3}$	(17.18)
	$Sh = 2 + 1.1 \cdot Re^{0.6} \cdot Sc^{1/3}$	
Momentum	$S_{mom} = -\left(\frac{\mu}{\eta} v_\infty + \gamma \frac{1}{2} \rho_g v^2\right)$	(19)
	$\eta = \frac{\psi^2 d_{eq}^2}{150 (1-f_v)^2}; \gamma = \frac{3.5 (1-f_v)}{\psi d_{eq} f_v^3}$	(20)
	$\psi = \frac{\pi^{1/3} (6V_p)^{2/3}}{A_p}; d_{eq} = D_{cil} \left(\frac{3L_{cil}}{2D_{cil}}\right)^{1/3}$	(21)

$$S_s^{rad} = \int_0^{4\pi} \left(\alpha_s I(r, s) - \frac{\alpha_s n^2 \sigma T_s^4}{\pi} \right) d\Omega \quad (22)$$

$$S_g^{rad} = \int_0^{4\pi} \left(\alpha_g I(r, s) - \frac{\alpha_g n^2 \sigma T_s^4}{\pi} \right) d\Omega \quad (23)$$

$$S_g^{rad-} = \int_0^{4\pi} \left((\alpha_g + \alpha_s) I(r, s) - \frac{(\alpha_g + \alpha_s) n^2 \sigma T_s^4}{\pi} \right) d\Omega \quad (24)$$

$$S_{comp} = \int_0^{4\pi} \left(\alpha_g I(r, s) - \frac{\alpha_g n^2 \sigma T_s^4}{\pi} \right) d\Omega \quad (25)$$

$$S_g^{rad} = S_g^{rad-} + S_{comp} \quad (26)$$

Table 7: Chemical reaction of wood volatiles and propane used in this study; (I): Three Arrhenius rates in pyrolysis reaction.

Reactions	Kinetics	Unit	Ref.
R1 $H_2 + \frac{1}{2}O_2 \rightarrow H_2O$	$9.87 \times 10^8 \exp\left(-\frac{3.1 e+07}{RT}\right)[H_2][O_2]$	[J/kg mol]	[29]
R2 $CO + \frac{1}{2}O_2 \rightarrow CO_2$	$2.239 \times 10^{12} \exp\left(-\frac{1.702 e+08}{RT}\right)[CO][O_2]^{0.25}[H_2O]^{0.5}$	[J/kg mol]	[29]
R3 $CO_2 + H_2 \rightarrow H_2O + CO$	$1.00 \times 10^8 \exp\left(-\frac{6.28 e+07}{RT}\right)[CO_2][H_2O]$	[J/kg mol]	[71]
R4 $C_3H_8 + \frac{3}{2}O_2 \rightarrow 3CO + 4H_2O$	$4 \times 10^{15} \exp\left(-\frac{7.067 e+07}{RT}\right)[C_3H_8][O_2]$	[J/kg mol]	[71]
R5 $H_2O + CO \rightarrow CO_2 + H_2$	$2.78 \exp\left(-\frac{1.225 e+07}{RT}\right)[H_2O][CO]$	[J/kg mol]	[29]
R6 $CH_4 + \frac{3}{2}O_2 \rightarrow CO + 2H_2O$	$5.012 \times 10^{11} \exp\left(-\frac{2.0 e+08}{RT}\right)[CH_4]^{0.7}[O_2]^{0.8}$	[J/kg mol]	[29]
(I): Kinetics of the solid heterogenous reactions			
Pyrolysis reactions	Kinetics	Unit	Ref.
Dry wood \rightarrow Gas	$A_1 = 111 \times 10^9 (s^{-1}), E_1 = 177 \times 10^3$	[J.mol ⁻¹]	[29]
Dry wood \rightarrow Tar	$A_2 = 9.28 \times 10^9 (s^{-1}), E_2 = 149 \times 10^3$	[J.mol ⁻¹]	[29]
Dry wood \rightarrow Char	$A_3 = 30.5 \times 10^9 (s^{-1}), E_3 = 125 \times 10^3$	[J.mol ⁻¹]	[29]

4. Numeric and Validation

4.1. Numeric

The reactor is represented by a 3D domain in commercial CFD software [53]. A non-structured grid is made in the area of the swirl air diffuser, the propane tubular nozzle, the front nozzle area of the propane, the non-premixed excess air, and the wood volatile nozzles. A structured grid is used for the rest of the geometry to avoid excess mesh in the domain. The total number of elements is based on the inlet boundary condition in the geometries as follow 3,000,000 (start-up condition), 3,687,971 (proposed case), 5,861,607 (current case). The highest grid resolution is chosen for the current case, which supplies the premixed volatiles and the excess air through a large volatile side duct (1.8 m x 2.4 m). The minimum non-structured grid size is 0.4 mm in the propane inlet holes. To check the mesh independently, a grid analysis was performed from 740,000 to 2,700,000 elements in the area in front of the nozzles and the non-realistic velocity magnitude is observed in the vicinity of the diffuser blades with 740,000 elements; meanwhile, the two other mesh topologies were totally independent of the simulation results. In this study the minimum number of non-structured elements used in the air diffuser, propane ring and non-premixed volatile nozzles was 2,100,000 elements. Polyhedral and mixed poly-structured mesh have been analyzed; however, high continuity residual was observed in polyhedral and mixed poly-structured grids. Therefore,

a combined non-structured and structured mesh is chosen as the best grid domain for the combustion chamber in different cases. Figure 3 (a) illustrates the mixed grid domain for the thermal oxidizer (combustion chamber). The injection zone with a higher resolution is addressed in Figure 3 ((a)– (i, ii).

In the pyrolysis section, however, analyzing the morphology of different grids (quad and polyhedral), it was found that there are some problems associated with structured quad grids, particularly in the inflated area between the bed surface and the freeboard zone above the bed. It should be noted that the simulation results for three different polyhedral grid sizes (0.01, 0.015, 0.02 m) indicate that the results of the simulations are almost independent of the mesh size. Therefore, polyhedral mesh with a minimum grid size of 0.01 m and a total element number of 2,100,000 was chosen, as illustrated in Figure 3(b).

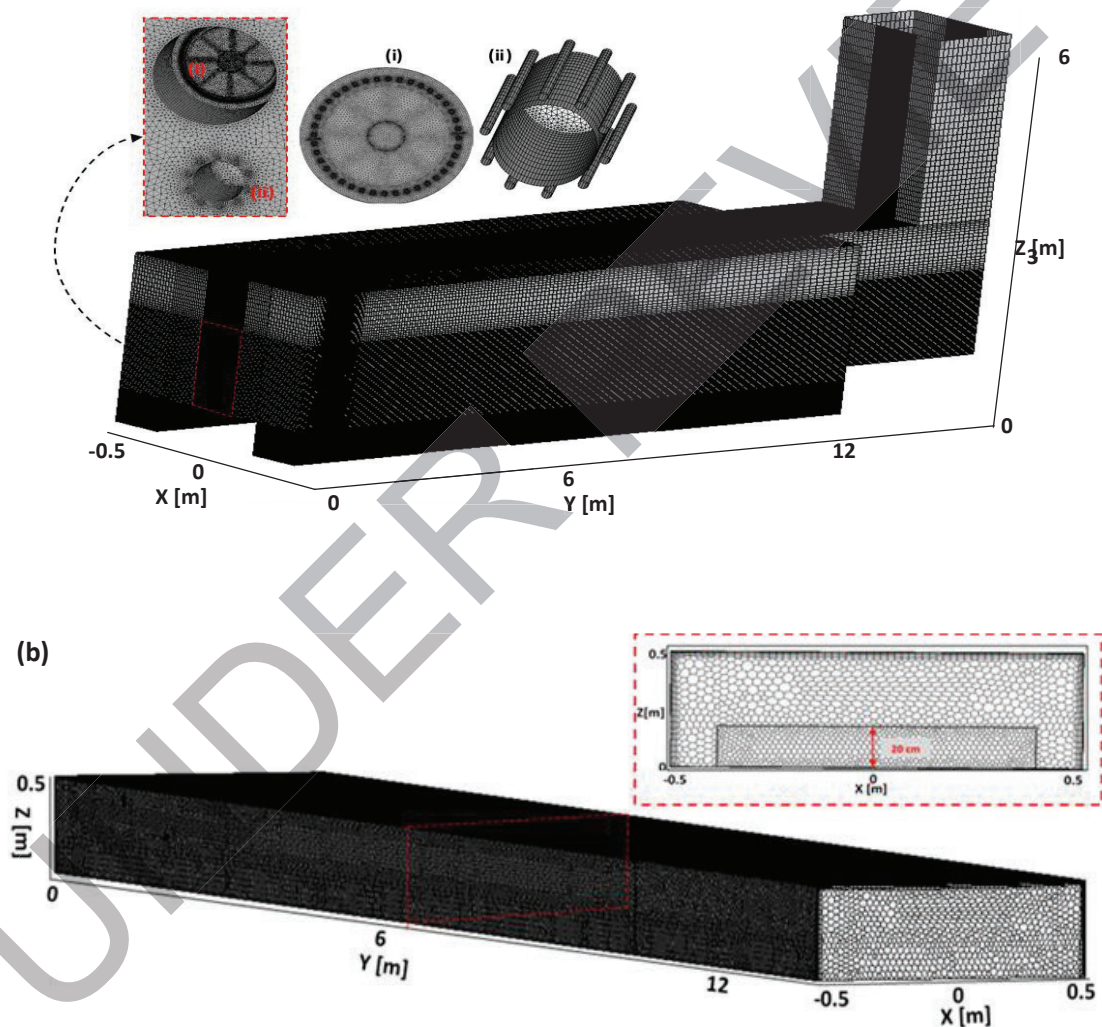


Figure 3(a) Mixed structured and non-structured grids proposed for the plants' thermal oxidizer: (i): higher resolution of swirl air/propane injection zone; (ii): 10 volatile and air injection nozzles ; (b): polyhedral grids for solid and gas phase domains in the pyrolysis section and the middle Y plane.

1
2
3
4 In the present work, the commercial software Ansys-Fluent is employed to perform the simulations using
5 the species model [53]. A finite-rate model with full multi-component and thermal diffusion and the Eddy
6 Dissipation concept is applied for the experimental validation and the finite-rate model/Eddy Dissipation
7 model is chosen in the other numerical analysis. After comparing the simulation results with the
8 experimental and CFD simulations addressed in Section 4, it was found that the finite-rate/eddy
9 dissipation model can be brought into closer agreement with the results of the experimental measurement
10 and published CFD works [21, 23]. In Fluent, the pressure-velocity coupling scheme used is SIMPLE and
11 the least square cell-based approach is used to calculate the gradients required for constructing the values
12 of scalars at cell faces and computing secondary diffusion terms and velocity derivatives. The pressure
13 interpolation scheme used is standard and the second-order upwind scheme is used for the momentum, the
14 turbulent kinetic energy, the turbulent dissipation rate, the species and the energy, respectively. The
15 viscous models Realizable K-epsilon with standard wall function, RNG with swirl-dominated flow and
16 K- ω SST have been examined as addressed in the present study [35]. The Realizable K-epsilon model is
17 in good agreement with the experimental measurements and the standard average CO₂ range for Power
18 Flame propane swirl burners [72]. Furthermore, a high continuity residual problem is reported in RNG
19 with a swirl-dominated flow; therefore, the realizable K-epsilon model is chosen as the main model. The
20 P1 radiation model is used to account for the radiation heat transfer and the WSGGM-cell-based method
21 is employed to calculate the absorption coefficient. In the solid thermal conversion model, a modified
22 discrete ordinates model (DOM) proposed by Gomez et al.[29] is utilized to consider both solid and gas
23 temperatures and resolve the unexpected energy imbalance associated with the standard DO model
24 (Eqs. 22–26). The convective heat transfer coefficient in the intersection plate surface is chosen based on
25 a primarily transient simulation of the mixture of volatile gas in the pyrolysis section with an average heat
26 flux of 14,500 W/m² (the reactor-designed heat flux) and the value is 18 W/m²K.
27
28
29
30
31
32

33 4.2. Validations

34 In this study, five different sets of validations have been performed. Five thermocouples have been placed
35 in the pyrolysis and thermal oxidizer section in order to measure the temperature during the process. Due
36 to the industrial application of the plant, it was impossible to install more thermocouples. Three K-type
37 thermocouples were placed at a distance of 20 cm from the right-hand wall of the pyrolysis section,
38 located at Y=1.7, 5.8, 11.98m from the feeding system. Two K-type thermocouples were placed at a
39 distance of 20 cm from the right-hand wall of the thermal oxidizer. In the pyrolysis section, the
40 thermocouples' probes are perpendicular to the lateral side of the bed and the distance between the
41 thermocouples' tips and the bed is X=0.05 m. The transient thermal conversion model is utilized to
42 simulate the thermal conversion of the solid phase and the non-uniform heat flux derived from the
43 combustion of volatiles in the current reactor is used as the inlet boundary condition (see Figure 2(a)).
44
45
46

47 The first validation is performed assuming that there is a 20% wood moisture content in the bed. The
48 temperature is measured after the transient (start-up) condition after two different time steps (500, 1400 s)
49 for at least 15 tests from January to March 2016, with the average ambient temperature being 267, 270,
50 275 K in the Edmonton area. The first time step chosen is 500 seconds after start-up. The total reactor
51 running time was approximately 5 hours and the start-up time is approximately 40 minutes. Close
52 agreement between experimental measurement and CFD simulation was reported in the thermocouple
53 closer to the hot spot zone in the intersection plate due to the stronger heat flux, and reasonable agreement
54 is observed between the pyrolysis outlet thermocouple and the numerical results. After 1500 seconds,
55 close agreement is observed with the middle thermocouple and the numerical results, which could be due
56 to the diffusion of moisture and volatile matter in the freeboard area. In this reactor, the outlet gases do
57 not escape into the atmosphere but are directed to the return chamber below the pyrolysis section.
58
59
60
61
62
63
64
65

1
2
3
4 Therefore, the measured temperature in the outlet is higher than the temperature reported in the CFD
5 simulation. Notably, the return chamber is not considered in the CFD simulation due to the extensive
6 numerical cost, and a temperature of 300 K is used as the outlet boundary condition. Figure 4(a)
7 represents the temperatures measured by three thermocouples in the freeboard area in the corresponding
8 time slot and temperature profile in the CFD simulation. It should be noted that the first objective of this
9 investigation is to overcome the issue of thermal efficiency and produce high-quality biochar by
10 introducing the most efficient scenario. As additional components such as cyclone separators and CO₂/
11 O₂ sensors will be added in the future development of the biochar plants, the measurement of the combustion
12 products is not considered in this study; however, the model was implemented and validated in numerous
13 published investigations prior to its adjustment in this study [29, 44, 67, 68].
14
15

16
17 To validate the non-premixed swirl air/propane combustion (the second validation), the analysis of CO₂
18 mass fraction measurement shows that the standard level of CO₂ in front of the Power Flame propane
19 burner is 0.12. The simulation results show that the volume of the CO₂ mass fraction at start-up is 0.137,
20 which is similar to the standard level of the CO₂ mass fraction reported for the Power Flame burner. It
21 should be noted that the reported CO₂ mass fraction in the swirl propane burner is valid in different
22 combustion chambers if the burner installation instructions are fully implemented, and the swirl burner
23 has been properly adjusted [33].
24
25

26 The simulation results were validated against experimental measurements of the temperature in the
27 reactor during start-up (the third validation). The temperature profile along the combustion chamber was
28 measured continuously via two K-type thermocouples placed at a distance of 20 cm from the reactor's
29 right-hand wall, at an axial distance of 2.5 meters from the propane nozzle tip. Close agreement was
30 obtained between the observed temperature (which is recorded continuously during start-up) and the
31 predicted temperature of the swirl propane CFD simulation. This is addressed in Figure 4(b).
32
33

34 In order to validate the semi-global reaction of propane in the swirl propane burner (fourth validation), the
35 2D axisymmetric simulation of a laboratory-scale swirl nozzle addressed in the literature [21, 23] was
36 used and the simulation results were validated by experimentally investigating the temperature and
37 emission measurements in the laboratory-scale swirl propane nozzle [21, 23]. There was reasonable
38 agreement of the CO₂ and temperature profile in the front nozzle area obtained using the finite-rate model
39 and the semi-global reaction addressed in Table 7 (R1-R5). Figure 4(d) illustrates the CO₂ validation of
40 the semi-global reaction of propane in the front nozzle area, validated against the experimental
41 measurement and the corresponding numerical model [21]. The contour of the temperature in front of the
42 swirl nozzle is addressed in Figure 4(e).
43
44

45 The biochar samples produced in several experimental tests with the same feedstocks represent the same
46 volume shrinkage with the results of CFD simulation (fifth validation). The volume shrinkage value
47 reported in these experimental tests is around 50% of the total feedstock volume, which is very close to
48 the numerical values (53–57%). A comparison between the experimental and CFD volume shrinkage is
49 addressed in Section 5.2, Figure 10 (e) and Table 9.
50
51
52
53
54
55
56
57
58
59
60
61
62
63
64
65

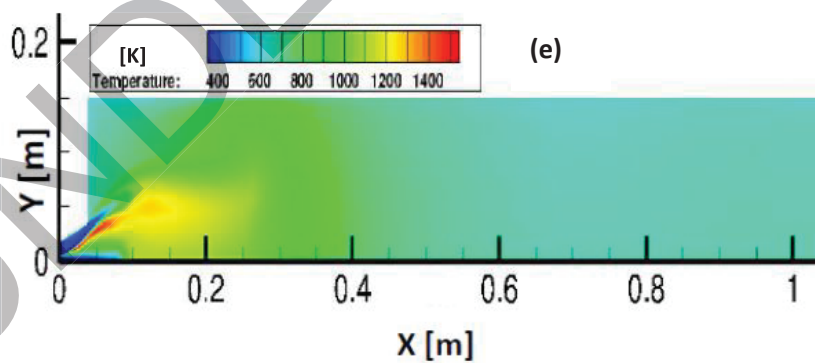
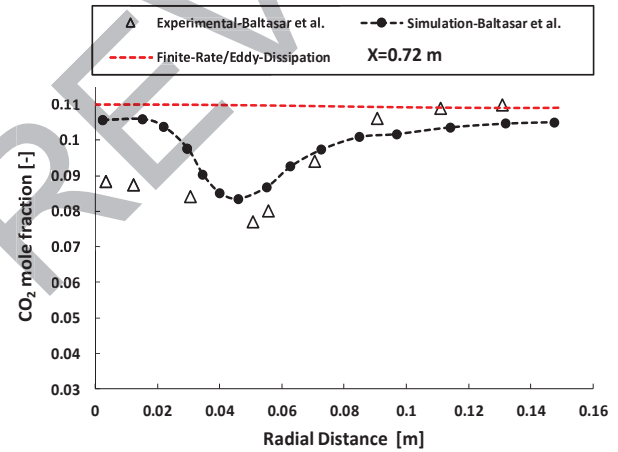
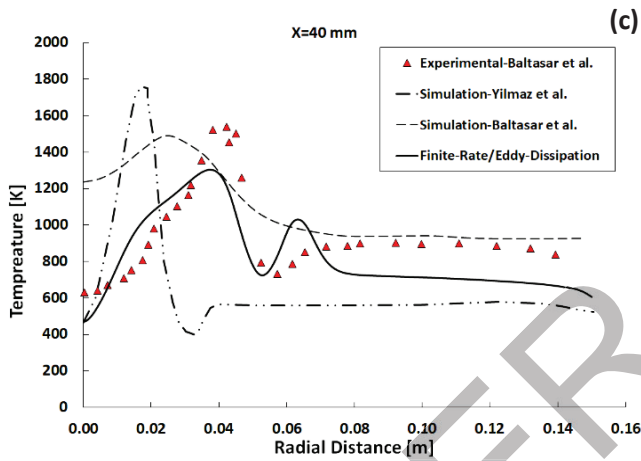
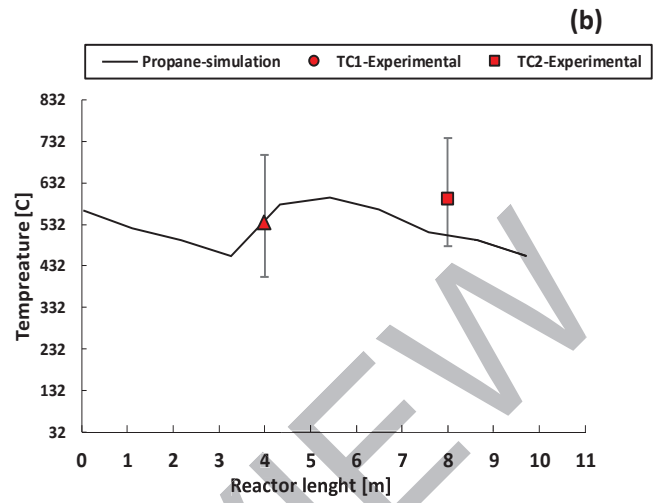
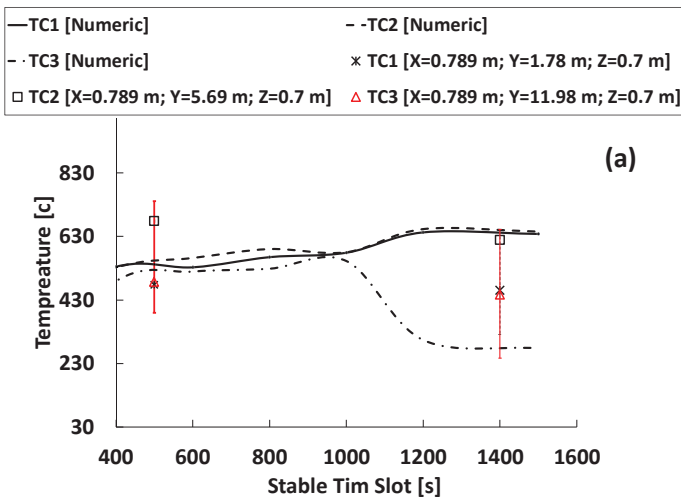


Figure 4 (a): Temperature validation in reactor pyrolysis section during thermal conversion process; (b): temperature measurement and numerical validation of combustion in thermal oxidizer (steady state condition); (c), (d): numerical validation of the experimental and CFD simulations of the swirl propane burner; (e): contour of temperature in front of the swirl nozzle [21, 23]

5. Results and Discussion

5.1. Co-combustion of wood volatiles and propane

This section analyzes the self-ignition of non-premixed air/wood pyrolytic gases during the stable time and the co-combustion of non-premixed air/wood volatiles and non-premixed swirl air/propane.

Self-ignition of volatiles: Knowing that premixing high-temperature volatile gases with air may cause a partial explosion in the combustion chamber, as reported in the current reactor, the improvement of a non-premixed configuration should be pursued. In this regard, preheating excess air before injection into the combustion chamber and utilizing the swirl air diffuser, similarly to the swirl propane burner, could be the best way to enhance thermal efficiency in the non-premixed volatile gas configuration. Increasing the number of non-premixed volatile gas nozzles and the smaller volatile flow diameters may also help improve the overall combustion efficiency by reducing the size of the primary combustion zone in the flame. Therefore, as an alternative, the self-ignition of pyrolytic volatiles is analyzed based on two different cases. The first case is a simple pattern of non-premixed injection of volatiles, and the second is an advanced swirl burner. The mass flow rate of the volatiles is 75% of the maximum load of the plant in order to compensate for the lack of propane. The simple non-premixed volatile simulation was not successful, and the flame pattern did not form during the simulation due to the less efficient premixing of volatiles and the lower temperature in the combustion chamber. However, in the advanced non-premixed air/volatile swirl burner, the volatiles ignite and the simulation results show that the main combustion indices improve significantly compared to the simple pattern. Figure 5 (a, b) illustrates the boundary heat flux and temperature distribution in the intersection wall, respectively; however, the average heat flux and temperature in the intersection wall are not enough to compensate for the heat required for biochar production due to the higher moisture content and CO₂ concentration and low hydrocarbon content in the feedstock and the small interface area between the thermal oxidizer and pyrolysis section. These issues are addressed in the introduction as the main challenges associated with the self-ignition of volatiles in industrial fixed and moving-grate biochar plants. Moreover, utilizing an advance swirl volatile nozzle requires extra capital and operating costs which are not economically viable. Therefore, the non-premixed co-injection of air/propane with a simple air/volatile pattern (Figure 2 (b)–(ii)) is considered in this study.

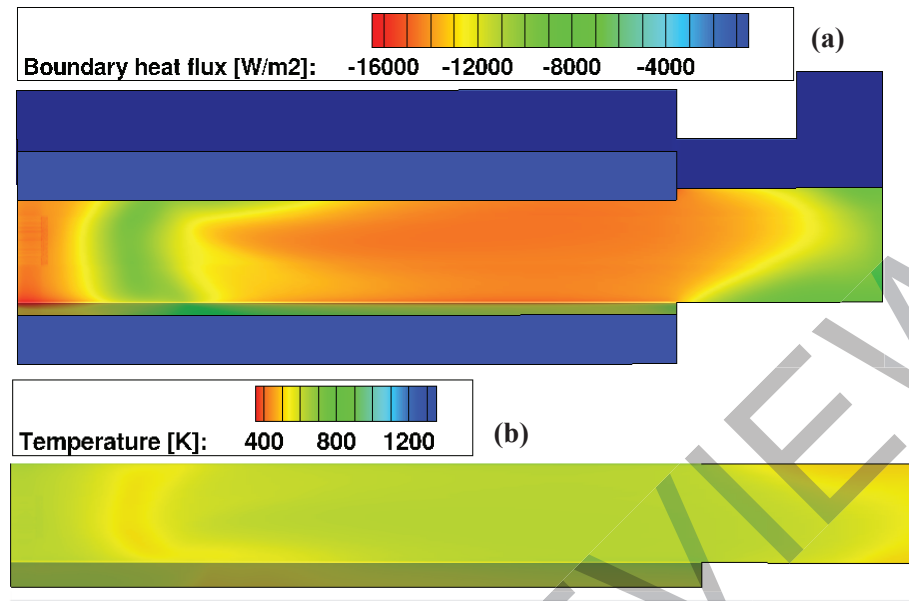


Figure 5: Self ignition of wood volatiles: (a): heat flux distribution in the intersection wall; (b): distribution of temperature in the intersection wall

Knowing that premixing high-temperature volatile gases with air may cause a partial explosion in the combustion chamber, as is reported in the current reactor, supports the notion that the improvement of a non-premixed configuration should be pursued. The following results are from the combustion simulation of non-premixed volatile gases and air, which coincide with non-premixed swirl air and propane combustion. The main objective of this section is to find the average heat flux and non-uniform distribution of heat flux in the intersection plate located between the thermal oxidizer and the pyrolysis section. This heat flux is then introduced as a boundary condition in Part B in order to simulate the thermal conversion of biomass into biochar. The flame pattern in the swirl propane burner is influenced significantly by the swirl excess air diffuser in the propane burner, which causes the effective mixing of air and propane. This means that the flame's primary combustion zone in the swirl propane burner is shorter than that in the volatile gas nozzles and the fully developed flame is formed at a shorter diffusion length in the swirl propane burner compared to the non-premixed volatile gas injection configuration. Figure 6(a) shows the contour of the temperature in the middle plane (i), the path line of the temperature in front of the injection zone (iii) and the corresponding heat flux distributed in the intersection plate (a, b-(ii)). Due to the angular injection of propane and the swirl air diffuser, the effective mixing of propane and air occurred, which resulted in the high production of CO_2 and H_2O in front of the swirl burner as illustrated in the contours of CO_2 and H_2O in Figures 7 (b and c), respectively. The uniform injection of volatile gases via the ten (10 mm) nozzles, the appropriate oxygen levels and the higher temperature of the volatile matter in non-premixed states demonstrates that reactions 2, 5 and 6 (Table 7) have a greater impact on volatile combustion. Since a significant portion of wood volatiles are CO_2 , H_2O and CO , it is incorrect to evaluate the combustion performance only based on emission indices. In fact, heat transfer analysis is strongly advised in indirect biochar reactors. Due to the cost of the auxiliary propane, the potential to reduce the propane consumption is high, which strengthens the importance of utilizing a non-premixed volatile injection configuration in indirect biochar reactors.

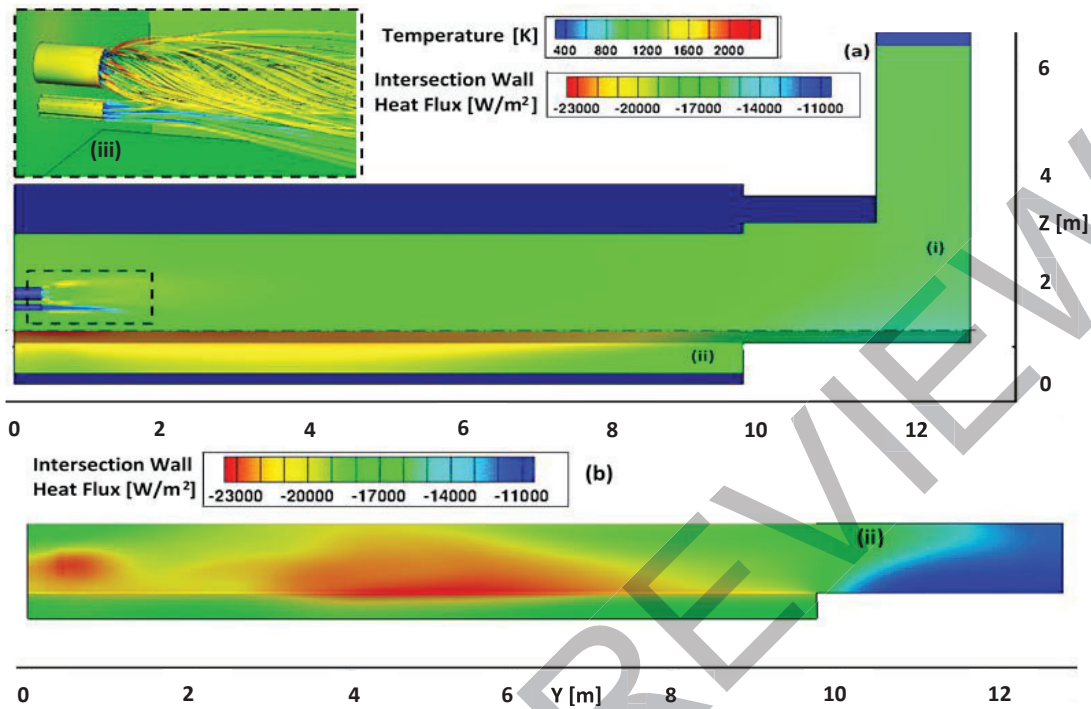


Figure 6 (a-(i)): 3D temperature profile and middle cross-sectional plane of the non-premixed combustion of biomass volatiles/air and swirl propane/air; (a-(ii)): the non-uniform heat flux distribution on the intersection wall; (a-(iii)): the flame path line in the front nozzle area; (b-(ii)): the non-uniform heat flux distributed on the intersection wall

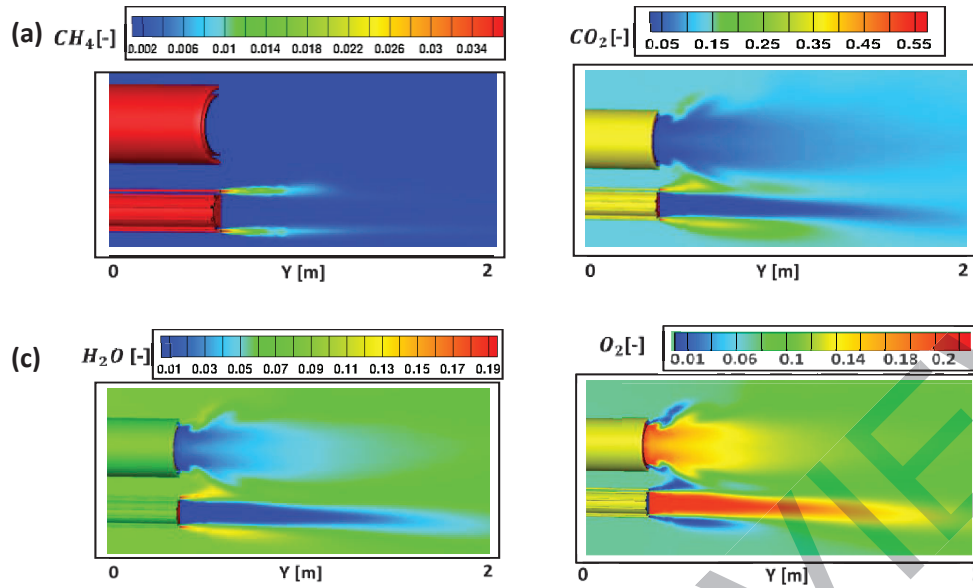


Figure 7: Contours of co-combustion of non-premixed volatiles/air and non-premixed swirl propane for CH_4 :(a); CO_2 (b); H_2O :(c); O_2 :(d)
 Note: the middle section plane is assumed to be at a distance of 2m in front of the nozzles

5.2. Indirect slow pyrolysis biochar thermal conversion

In this biochar reactor, wood planer shavings with a 20% moisture content were used as the feedstock for biochar production. However, due to the high residence time and poor biochar quality, a lower moisture content is considered in this investigation, to decrease the residence time of biochar production. A shorter residence time could be a good reason for pretreating feeding materials using additional dryers, preheating the materials using a Flow Gas Recirculation (FGR) system or other heat recovery technologies. The non-uniform distribution of heat flux derived from Part A is introduced as an inlet boundary condition for the intersection wall thanks to the Fluent profile interface. To compare the effect of uniformity and non-uniformity of the heat flux distribution on the surface of the intersection wall, which is located between the combustion chamber and the pyrolysis section, the average heat flux distribution in the intersection wall is calculated in Fluent and utilized in Cases 1, 3 as an inlet boundary condition. The reason for using the average heat flux is to demonstrate that it is advisable to use a certain number of smaller burners with small uniform volatile injection systems instead of a large central burner with a main non-premixed volatile injection system. Table 8 shows the different states of the simulation performed in this investigation.

Table 8: Four proposed cases to simulate the thermal conversion of biomass to form biochar

Case	Moisture content [%]	Uniform heat flux [W/m^2]	Non-uniform heat flux [W/m^2]
1	5	18500	N/A
2	5	-	Non-uniform flux distribution profile is added
3	20	18500	N/A
4	20	-	Non-uniform flux distribution profile is added

1
2
3
4
5
6
7
8 Figure 8: illustrates the simulation results at 280 seconds for 5% moisture (Cases 1, 2) and 800 seconds
9 for 20% moisture contents (Cases 3, 4) in the middle Y plane. The evolution of the wood planer shavings
10 during thermal conversion is addressed in this illustration, addressing the major parameters such as the
11 density of moisture, dry wood and biochar in the domain as well as the diffusion of the pyrolytic gases
12 during the process. Comparing these parameters in different cases could help the reader to understand the
13 difference between a uniform and non-uniform heat transfer rate in the pyrolysis section, as well as how
14 the moisture content affects the residence time during biochar formation. Case 2-(III) shows that the
15 formation of biochar is not uniform when there is a non-uniform heat flux distribution on the intersection
16 wall between the thermal oxidizer and pyrolysis section, unlike Case 1-(III), which is the uniform heat
17 flux condition. The contour of moisture and dry wood density in Case 2-(I, II) demonstrate the effect of a
18 non-uniform heat flux on the evaporation and pyrolysis rate compared to Case 1-(I, II). Furthermore, the
19 diffusion pattern of species contours (CH_4 , H_2O and CO_2) in Case 1-(IV-VI) is almost symmetrical
20 compared to Case 2-(IV-VI). It should be noted that in the selected time steps, more than 60 percent of
21 volatiles were released. Interestingly, this non-uniformity does not occur when a 20% moisture content is
22 analyzed under two intersection boundary conditions (Cases 3, 4). Except for the H_2O contours (Case 3
23 (IV)), there is not too much difference between a uniform and non-uniform flux distribution as addressed
24 in Case 3 (I-III, V) compared to Case 4 (I-III, V). In fact, a higher moisture content (20%) requires more
25 energy to evaporate the moisture content inside the wood, which results in a higher residence time (800
26 seconds). This longer time allows the system to be stabilized thermodynamically; the freeboard
27 temperature profile in these configurations experiences a gently inclined slope during thermal conversion,
28 which could be a reason for the similarity between Cases 3 and 4, as illustrated in Figure 9 (a, b). On the
29 other hand, the effect of a non-uniform heat flux on the formation of biochar in lower moisture feedstocks
30 is significantly greater than in higher moisture feedstocks. Figure 9 (a) shows that in two non-uniform
31 states (Cases 2, 4), the average convective heat transfer coefficient experiences higher fluctuation,
32 particularly in Case 2 (5% moisture) with a maximum convective heat transfer coefficient of $24 \text{ W/m}^2\text{K}$.
33 This is another reason for the influence of a non-uniform heat transfer rate on thermal conversion in the
34 lower moisture content feedstocks. The fluctuation rate of volatiles released from the biomass material
35 may cause problems, particularly when the co-combustion of volatile gases in indirect pyrolysis
36 technology is considered. In fact, it is difficult to thermally control the system and provide a stable
37 pyrolysis temperature and heating rate when non-steady volatile gases are injected into the combustion
38 chamber at a high flow rate. It should be noted that a higher moisture content not only increases the
39 residence time in the pyrolysis section, but also plays a negative role in the combustion of volatiles in the
40 thermal oxidizer. This is particularly important when the plant is designed to cause self-ignition of the
41 volatiles, for example in a rotary kiln or retort auger (for the recommended level of moisture content for a
42 rotary kiln and retort auger, see Table 1).
43
44
45
46
47
48
49
50
51
52
53
54
55
56
57
58
59
60
61
62
63
64
65

1
2
3
4
5
6
7
8
9
10
11
12
13
14
15
16
17
18
19
20
21
22
23
24
25
26
27
28
29
30
31
32
33
34
35
36
37
38
39
40
41
42
43
44
45
46
47
48
49
50
51
52
53
54
55
56
57
58
59
60
61
62
63
64
65

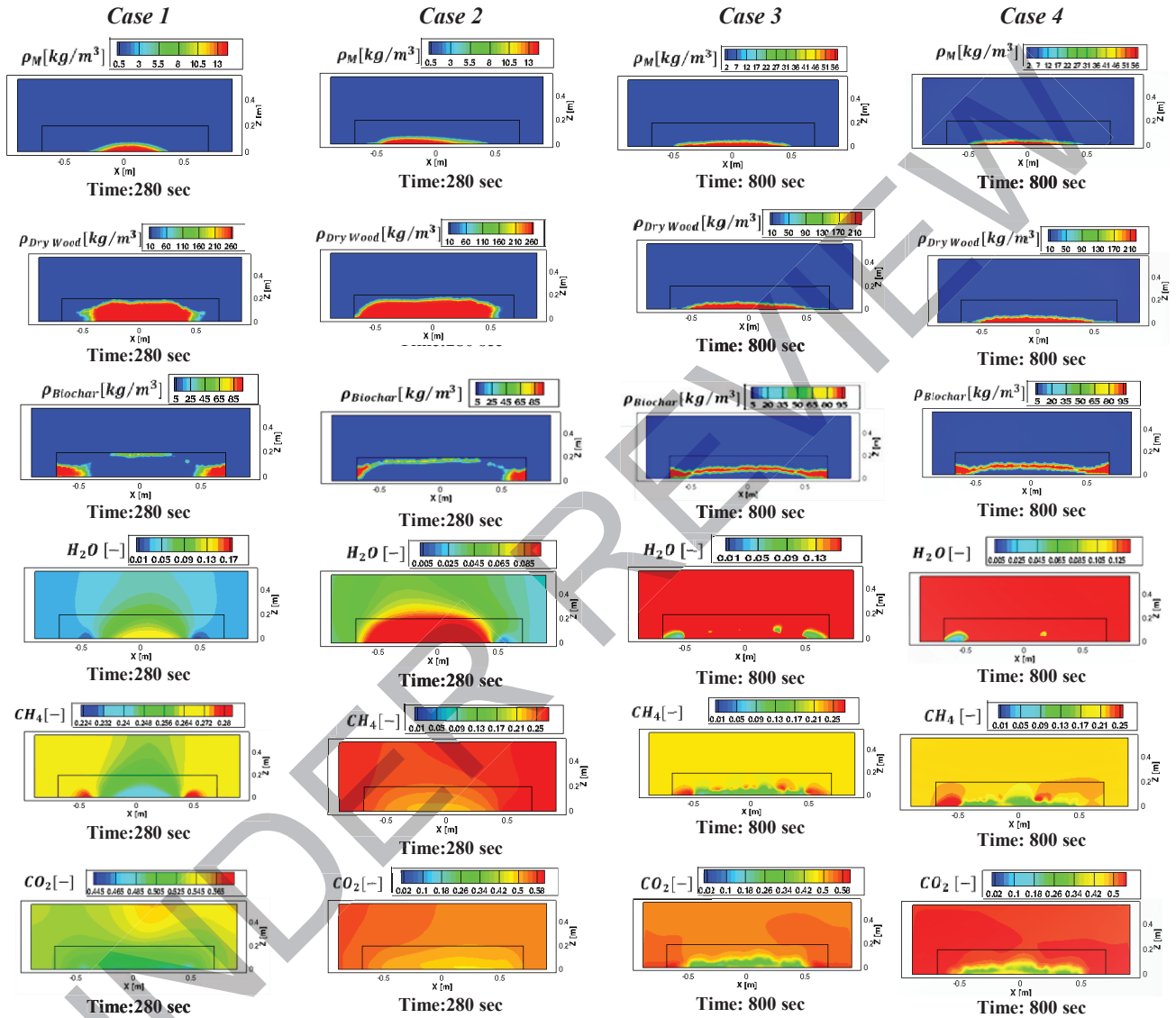


Figure 8: A comparison of different cases in the middle section plane (Y) at the selected time steps.

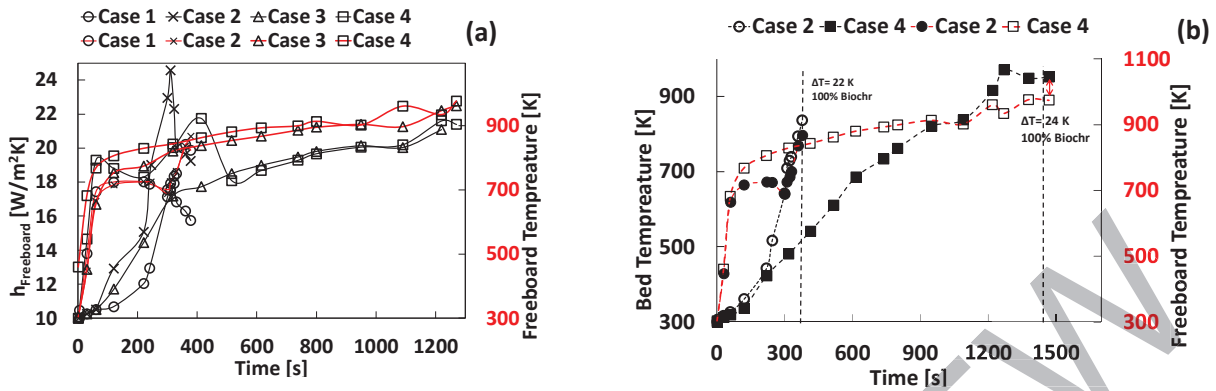


Figure 9 (a): Volume average of convective heat transfer coefficient in the freeboard area above the bed versus freeboard temperature; (b): Average bed temperature versus freeboard temperature. Note: the dashed lines represent the temperature difference between the bed and freeboard area during and after biochar formation.

Figure 10 (a, e) illustrates the final production of biochar in different states. It should be noted that the time step is chosen based on the following assumptions: 1) zero moisture and volatile content in the domains; 2) no further change in the biochar density contour in subsequent time steps. The volume shrinkage in four cases is almost the same as the real volume shrinkage of wood planer shavings reported in several biochar sample tests in the current reactor and other batch rotary kiln pilot units designed and fabricated by IRSI. The volume shrinkage value reported in these experimental tests is around 50% of the total feedstock volume. A comparison between experimental and CFD volume shrinkage is addressed in Figure 10(e) and Table 9. The residence time required to produce 100% biochar in Case 4 (non-uniform heat flux with 20% moisture) is 0.19 higher than Case 3 (uniform heat flux with 20% moisture); however, the residence time for Cases 1 and 2 (5% moisture) is almost the same. Figure 9(b) compares the formation of biochar in Cases 2 and 4 and demonstrates that while the difference between the bed and the temperature of the freeboard above the bed is greater than 100 °C ($\Delta T \geq 100$), the domain is not fully covered by biochar, whereas, in $\Delta T \leq 25$, fully developed biochar density appears in the domain which coincides with zero moisture and minimum volatile contents in the bed. The contours of Cases 1-4 (III) in Figure 8 confirm the above statement. When the temperature of the high-quality biochar in the reactor discharge is measured, along with the exhaust gas temperature measured by the thermocouple placed in the side wall of pyrolysis section (in the freeboard area) and the biochar external surface temperature measured by the infra-red gun thermometer, this shows that the lower difference between the discharge biochar temperature and the freeboard gas results in higher-quality biochar. In fact, this is a practical method to make sure that the production meets the standard quality of biochar.

Although the non-uniform distribution of the heat flux during the evaporation time does not have a significant effect, increasing the moisture content (in Cases 3,4) leads the evaporation time to increase to around 3.5 times higher than Cases 1,2 (see Figure 11 (a)). The average mass fractions of volatile components in two non-uniform cases (2, 4) are depicted in Figure 11 (d). It was shown that a fast diffusion rate in a short time step occurs when the feedstock has a 5% moisture content, rather than 20%. In fact, controlling the heat transfer rate between the thermal oxidizer and pyrolysis section to supply the threshold temperature for biochar production is a challenge with the shorter residence times.

1
2
3
4 Table 9 sets out the characteristics of the biochar produced by Ulysses I and compares the biochar with
5 the feedstock (wood planer shavings). The quality of the biochar produced by the plant is classified as
6 Class 1 according to the International Biochar Initiative (IBI). Class 1 is equal to or greater than 60%
7 carbon content (wt. % on a dry basis) [59]. A high value of fixed carbon indicates a high grade of biochar,
8 and a low value of volatile matter in the biochar means just the opposite. The volatile content in the
9 biochar is slightly high (17.85% on a dry basis) compared with a typical biochar (average 8.5% on dry
10 basis). Notably, in our model, a zero-volume average of volatiles in the domain and a minimal
11 temperature difference between the porous domain (biochar) and the freeboard area are the criteria to
12 finish the simulation in different cases. The residence time predicted by the model is almost like the
13 residence time required in the experimental biochar production. The total residence time to convert the
14 feedstock to biochar according to the experimental measurement is 1410 s for a non-uniform flux and
15 20% moisture content. In this case, the simulation indicates that the residence time is 1470 s. The
16 prediction of the biochar density is also confirmed by the proximate and ultimate analysis of biochar and
17 density addressed in Table 9. In Case 4, the highest biochar yield occurs at 950K, as shown in Figure 11
18 (c); however, the volatile gases' temperature measured in the freeboard area in the pyrolysis section was
19 873 K (TC2 at Figure 4(a)) when the biochar materials were fully discharged from the system. It should
20 be noted that this temperature is for the feedstocks with 20% moisture contents.

21
22
23
24
25
26 The remaining volatiles in the proximate analysis of the sample's report (bolded number in Table 9) is
27 due to complexity of the wood structure (the content of volatiles in different structure of the wood such as
28 cellulose, hemicellulose and lignin) and a sophisticated pyrolysis model is needed to predict the exact
29 amount of volatiles in the biochar product. The post-processing of biochar under a chemical or physical
30 activation process results in a zero concentration of wood volatiles in the products. Generally, these high-
31 quality materials are known as activated carbon. The mass fraction of ash in the feedstock is introduced
32 into the model as the solid part of the wood and is considered non-reactive; thus, no consumption rate is
33 considered. In addition, the model could not predict the ash contents, the metal contents, the other
34 morphological characteristics of the biochar or the surface area.

35
36
37 A deep understanding of the bed's behavior during thermal conversion requires an analysis of the average
38 thermal conductivity and specific heat capacity of the bed during the process. Figure 11 (e) illustrates
39 these parameters against the bed temperature in different cases. In Case 1, $k_{s,eff}$ experiences a plateau
40 between 200 to 300 seconds corresponding to a peak time for volatile and moisture diffusion in the
41 freeboard area above the bed, as indicated by the red elliptic dash line in this figure. However, this trend
42 does not appear in Case 2. Due to the stronger heat flux in the area close to the central nozzles (Figure
43 6(a, b)), faster thermal conversion and volatile diffusion happened in this area in a shorter time frame,
44 creating a non-plateauing, more steeply inclined line in this case (See $k_{s,eff}$ for Case 2 in Figure 11(e).
45 however, it seems that average $k_{s,eff}$ in Case 3 is higher than $k_{s,eff}$ in Case 4 (non-uniform heat flux)
46 particularly during evaporation and pyrolysis (200–1200 s). It should be noted that the longest biochar
47 residence time (1512s) occurs in Case 4 and that since the pyrolysis chamber has an opening area, there is
48 enough time for most of the volatile content to escape at the end of process, which could be a reason for
49 sharp drop in $k_{s,eff}$, C_p in Case 4, as addressed in Figure 11(e). In the two non-uniform cases (Cases 2,
50 4), the average C_p is almost below the uniform states (Cases 1, 3) during drying and devolatilization with
51 a moderately gentle slope unlike the non-uniform states (Cases 1, 4).

52
53
54
55
56 Overall, the influence of the moisture content is greater than that of the non-uniform heat flux in the
57 indirect biochar reactor. However, in a continuous system with a lower retention time, the temperature
58 distribution in the system is of great significance, particularly in the area far from the central burners.
59 Therefore, a uniform heat distribution with multiple small-scale propane burners, combined with the co-
60
61
62
63
64
65

axial injection of volatiles in a continuous reactor, is strongly recommended even in the batch reactors which use feedstocks with lower moisture contents.

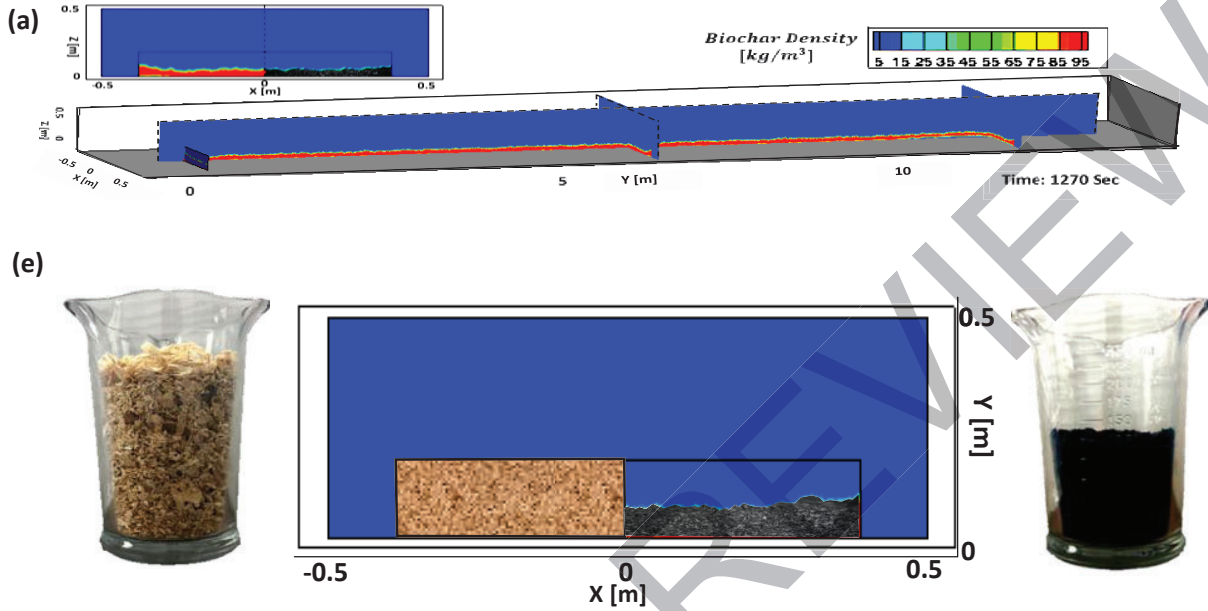




Figure 10: (a-d): Final biochar contours in different cases in the middle section plans X, Y; (e): volume shrinkage of feedstock in Case 2

Table 9: Wood planer shavings and biochar characteristics produced by Ulysses I

Characteristics		Wood planer shavings (feedstock)	Biochar (product)
Appearance			
Bulk density [kg/m ³]	Untapped	Wet basis [kg/m ³] 82	Dry basis 94
		Dry basis [kg/m ³] 94	[kg/m ³]
	Tapped	Wet basis [kg/m ³] 129	Dry basis 131
		Dry basis [kg/m ³] 149	[kg/m ³]
Proximate analysis on a dry basis [%]	Volatile matter	85.18%	17.85%
	Ash	0.3%	1.43%
	Fixed carbon	15.11%	83.46%
Ultimate analysis on a dry basis [%]	Carbon	49.01%	81.86%
	Hydrogen	6.13%	2.92%
	Nitrogen	<0.1%	0.14%
	Sulphur	<0.1%	0.1%
Heating value on a dry basis	Oxygen	44.36%	13.55%
		19.5 [MJ/kg] 5.41 [kW/kg]	30.1 [MJ/kg] 8.37 [kW/kg]

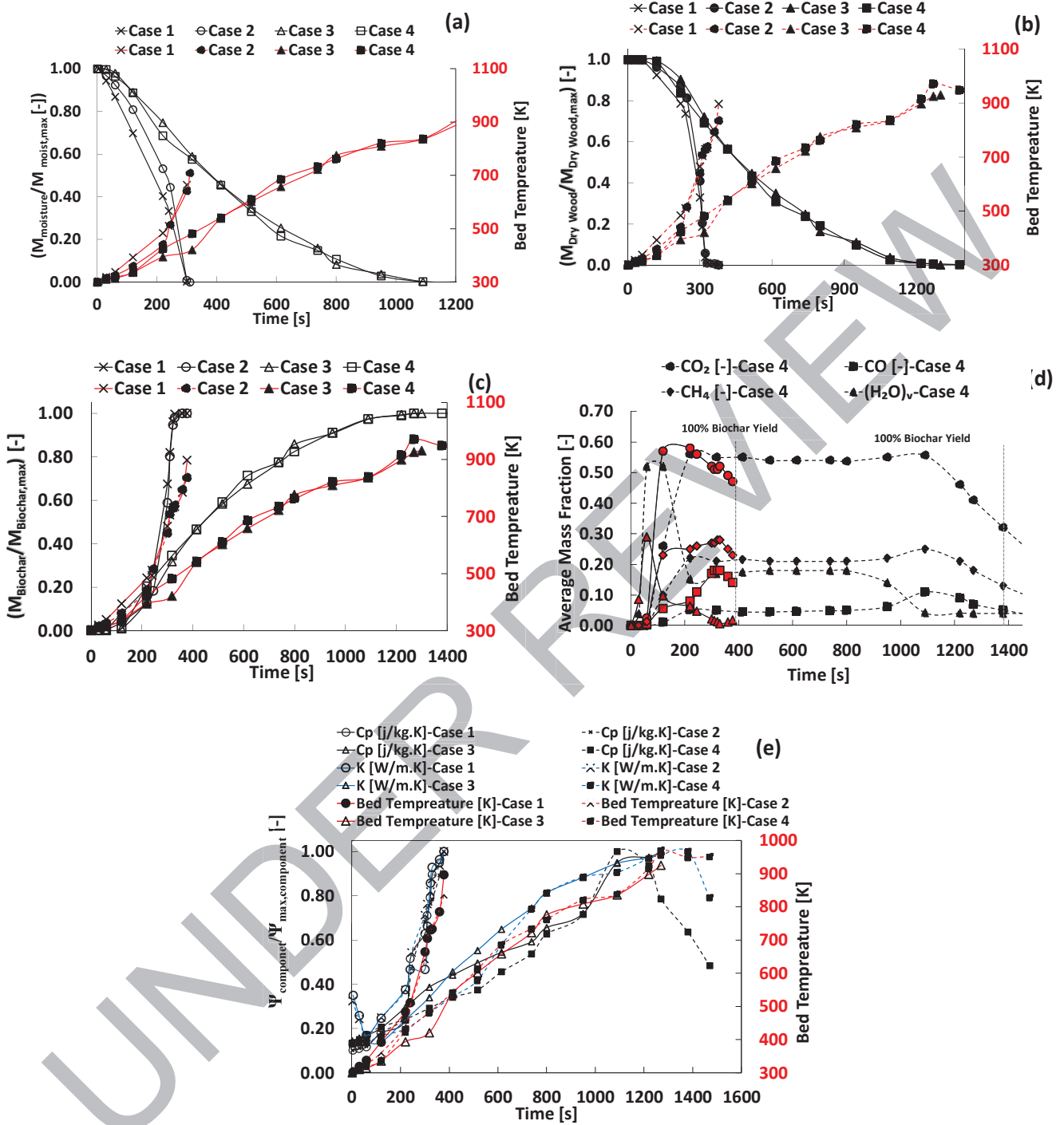


Figure 11 Evaluation of different characteristics during thermal conversion process for different cases.

6. Conclusion

The co-combustion of biomass volatile propane can increase the thermal efficiency of the combustion and thermal conversion process in indirect pyrolysis reactors by increasing the temperature and heat

1
2
3
4 transfer rate between the thermal oxidizer and pyrolysis section in the indirect biochar plant and
5 consequently reducing the residence time of biochar production. Validation against experimental data
6 published in the literature and measured in the system demonstrates reasonable agreements. The co-
7 axial injection of non-premixed biomass volatiles and air combined with swirl auxiliary burners
8 increases thermal efficiency in indirect pyrolysis plants. The role played by the moisture content in
9 increasing the residence time for biochar production is significant. A higher moisture content (20%)
10 increases the residence time 3.5 times compared with lower moisture content feedstocks (5%) and
11 leads to higher capital and operating costs. The non-uniform distribution of the heat flux in the
12 indirect biochar reactor does not have a notable influence on the thermal conversion process when the
13 moisture content in the feedstock is high. Conversely, it has a significant effect on the thermal
14 conversion process with a lower level moisture content in the feedstock; moreover, this non-
15 uniformity creates low-quality biochar in the continuous moving-grate reactor as material relocates
16 from the higher heat flux zone to the lower heat flux zone. In the lower moisture content feedstock,
17 thermal conversion took place very fast, making it a considerable challenge to control and utilize
18 volatile matter in the combustion process in the thermal oxidizer chamber.
19
20
21
22

23 A lower temperature difference between the discharged biochar and the freeboard temperature is a
24 good criterion to check the quality of biochar. The shrinkage value of biochar produced from wood
25 planer shavings during thermal conversion is remarkable based on the experimental sample
26 measurements and CFD simulation (approximately 50%), therefore, volume shrinkage during drying
27 and pyrolysis should be considered during the thermal conversion modelling of small-sized biomass
28 feedstocks such as wood planer shavings, saw dust, etc. The self-ignition of volatile matter during the
29 stable time is only possible when there is an adequate geometrical design with the maximum interface
30 surface area between the thermal oxidizer and pyrolysis section, and a high-quality volatile content
31 and minimum moisture content in the feedstocks.
32
33

34 The following recommendations could be considered for any future developments in indirect pyrolysis
35 plant:
36

- 37 • Utilize a small-scale symmetrical burner and volatile injection systems instead of a central burner
38 and volatile injection systems
- 39 • The swirl injection of volatiles enhances the diffusion effect in the non-premixed system and
40 leads to more efficient combustion
- 41 • A metal with high thermal conductivity is strongly advised to create a uniform temperature
42 distribution in the intersection wall between the hearth and thermal oxidizer
- 43 • Solid particulate matter and NO_x analysis should be considered in any future CFD development
44 of thermal conversion in the pyrolysis section
- 45 • The role played by solid particulates in the co-combustion of volatiles should be considered
46 unless a separation cyclone is utilized between the pyrolysis and combustion sections.
47
48
49
50
51

52 *Acknowledgments:*

- 53 • The Mitacs Accelerate Postdoctoral Scholarship program is greatly appreciated for providing this
54 project with financial support.
- 55 • The researchers from the University of Vigo would like to acknowledge the financial support
56 from the project 'Modelado de la expulsión de materia particulada en lechos fijos de biomasa.
57 desarrollo de submodelos y validación experimental' (RTI2018-100765-B-I00). The work of
58
59
60
61
62
63
64
65

1
2
3
4 Sergio Chapela López was supported by grant BES-2016-076785 of the Ministry of Economy,
5 Industry and Competitiveness (Spain).
6

- 7 • The Ansys Startup Program proposed by the Simu Tec Group is gratefully acknowledged for
8 supporting the computational fluid dynamic work performed by Innovative Reduction Strategies
9 Inc. (IRSI)
- 10 • Mr. Qinghai (Jerry) Jin is greatly acknowledged for the IRSI CAD and engineering models and
11 drawing of the plant.
12
13
14
15

16 *References*

- 17 1. Cha, J., Park, SH, Jung, SC, Ryu, C, Jeon, JK, Shin, MC, Park, YK, Production and utilization of
18 biochar: a review. *Journal of Industrial and Engineering Chemistry*, 2016. 40: p. 1-15.
- 19 2. Scott, D.S., et al., A second look at fast pyrolysis of biomass—the RTI process. *Journal of*
20 *Analytical and Applied Pyrolysis*, 1999. 51(1): p. 23-37.
- 21 3. Laird, D., Brown, RC, Amonette, JE, Lehmann, J, Review of the pyrolysis platform for
22 coproducing bio- oil and biochar. *Biofuels, Bioproducts and Biorefining*, 2009. 3(5): p. 547-562.
- 23 4. Kebelmann, K., Hornung, A, Karsten, U, Griffiths, G, Intermediate pyrolysis and product
24 identification by TGA and Py-GC/MS of green microalgae and their extracted protein and lipid
25 components. *Biomass and bioenergy*, 2013. 49: p. 38-48.
- 26 5. Britt, B., Buchanan, AC, Cooney, MJ, Martineau, DR, Flash vacuum pyrolysis of methoxy-
27 substituted lignin model compounds. *The Journal of organic chemistry*, 2000. 65(5): p. 1376-
28 1389.
- 29 6. Bridgwater, T., *Pyrolysis of Biomass. IEA Bioenergy: Task 34. Bioenergy Research Group,*
30 *Aston University, Birmingham, UK, 2007.*
- 31 7. Jahiril, M.I., Rasul, M.G, Chowdhury, A, Ashwath, N, Biofuels production through biomass
32 pyrolysis—a technological review. *Energies*, 2012. 5(12): p. 4952-5001.
- 33 8. Balat, M., Balat, Me, Kırtay, E, Balat, H, Main routes for the thermo-conversion of biomass into
34 fuels and chemicals. Part 1: Pyrolysis systems. *Energy Conversion and Management*, 2009.
35 50(12): p. 3147-3157.
- 36 9. Demirbas, A., Arin, G, An overview of biomass pyrolysis. *Energy sources*, 2002. 24(5): p. 471-
37 482.
- 38 10. Kelkar, S., Saffron, CM, Chai, L, Bovee, J, Stuecken, TR, Garedew, M, Li, Z, Kriegel, RM,
39 *Pyrolysis of spent coffee grounds using a screw-conveyor reactor. Fuel Processing Technology,*
40 2015. 137: p. 170-178.
- 41 11. Choi, G., Oh, S.J, Kim, J.S, Clean pyrolysis oil from a continuous two-stage pyrolysis of scrap
42 tires using in-situ and ex-situ desulfurization. *Energy*, 2017. 141: p. 2234-2241.
- 43 12. Garcia-Perez, M., Lewis, T, Kruger, CE, Methods for producing biochar and advanced biofuels in
44 Washington State, (Part1,3), in Washington State University, Pullman, WA. 2012: USA. p.
45 67,137.
- 46 13. Kern, S., Halwachs, M, Kampichler, G, Pfeifer, C, Pröll, T, Hofbauer, H, Rotary kiln pyrolysis of
47 straw and fermentation residues in a 3 MW pilot plant—Influence of pyrolysis temperature on
48 pyrolysis product performance. *Journal of analytical and applied pyrolysis*, 2012. 97: p. 1-10.
- 49 14. Yue, Y., et al., Characteristics and potential values of bio-oil, syngas and biochar derived from
50 Salsola collina Pall. in a fixed bed slow pyrolysis system. *Bioresource technology*, 2016. 220: p.
51 378-383.
- 52 15. Aramideh, S., Xiong, Q, Kong, S.C, Brown, R.C, Numerical simulation of biomass fast pyrolysis
53 in an auger reactor. *Fuel*, 2015. 156: p. 234-242.
54
55
56
57
58
59
60
61
62
63
64
65

16. Hansen, V., Müller-Stöver, D, Ahrenfeldt, J, Holm, J.K, Henriksen, U.B, Hauggaard-Nielsen, H, Gasification biochar as a valuable by-product for carbon sequestration and soil amendment. *Biomass and Bioenergy*, 2015. 72: p. 300-308.
17. Babler, M.U., Phounglamcheik, A, Amovic, M, Ljunggren, R, Engvall, K, Modeling and pilot plant runs of slow biomass pyrolysis in a rotary kiln. *Applied Energy*, 2017. 207: p. 123-133.
18. Denyesa, M.J., Matovicb, D, Zeeba, B.A, Rutterc, A, Report on the Production and Characterization of Biochar Produced at Burt's Greenhouses (Odessa, ON). 2013, Department of Chemistry and Chemical Engineering, Royal Military College Canada, Kingston, ON, Canada K7K 7B4.
19. San Miguel G, M.J., Fernandez-Akarregi AR, Conversion of Wood into Liquid Fuels: A review of the science and technology behind the fast pyrolysis of biomass. 2011. 7.
20. Chander, S., Ray, A, Flame impingement heat transfer: a review. *Energy conversion and Management*, 2005. 46(18-19): p. 2803-2837.
21. Baltasar, J., Carvalho, M, Coelho, P, Costa, M, Flue gas recirculation in a gas-fired laboratory furnace: measurements and modelling. *Fuel*, 1997. 76(10): p. 919-929.
22. Gokulakrishnan, P., Fuller, C, Klassen, MS, Joklik, RG, Kochar, YN, Vaden, SN, Lieuwen, TC, Seitzman, JM, Experiments and modeling of propane combustion with vitiation. *Combustion and Flame*, 2014. 161(8): p. 2038-2053.
23. Yılmaz, İ., Taştan, M, İlbaş, M, Tarhan, C, Effect of turbulence and radiation models on combustion characteristics in propane-hydrogen diffusion flames. *Energy conversion and management*, 2013. 72: p. 179-186.
24. Hou, S., Lee, C, Lin, T, Efficiency and emissions of a new domestic gas burner with a swirling flame. *Energy Conversion and Management*, 2007. 48(5): p. 1401-1410.
25. Sahota, G., Khandelwal, B, Kumar, S, Experimental investigations on a new active swirl based microcombustor for an integrated micro-reformer system. *Energy conversion and management*, 2011. 52(10): p. 3206-3213.
26. Hall, C.A., Pitz, RW, Experimental and numerical study of H₂-air non-premixed cellular tubular flames. *Proceedings of the Combustion Institute*, 2017. 36(1): p. 1595-1602.
27. Erete, J., Hughes, K, Ma, L, Fairweather, M, Pourkashanian, M, Williams, A, Effect of CO₂ dilution on the structure and emissions from turbulent, non-premixed methane-air jet flames. *Journal of the Energy Institute*, 2017. 90(2): p. 191-200.
28. Gómez, M., Porteiro, J, De la Cuesta, D, Patiño, D, Míguez, JL, Numerical simulation of the combustion process of a pellet-drop-feed boiler. *Fuel*, 2016. 184: p. 987-999.
29. Gómez, M., Porteiro J, Patiño D, Míguez J.L., CFD modelling of thermal conversion and packed bed compaction in biomass combustion. *Fuel*, 2014. 117: p. 716-732.
30. Thunman, H., Niklasson, F, Johnsson, F, Leckner, B, Composition of volatile gases and thermochemical properties of wood for modeling of fixed or fluidized beds. *Energy & Fuels*, 2001. 15(6): p. 1488-1497.
31. Neves, D., Thunman, H, Matos, A, Tarelho, L, Gómez-Barea, A, Characterization and prediction of biomass pyrolysis products. *Progress in Energy and Combustion Science*, 2011. 37(5): p. 611-630.
32. Gómez, M., Martín, R, Chapela, S, Porteiro, J, Steady CFD combustion modeling for biomass boilers: An application to the study of the exhaust gas recirculation performance. *Energy Conversion and Management*, 2019. 179: p. 91-103.
33. Danon, B., Cho, E.S, De Jong, W, Roekaerts, DJEM, Numerical investigation of burner positioning effects in a multi-burner flameless combustion furnace. *Applied thermal engineering*, 2011. 31(17-18): p. 3885-3896.
34. Mehrabian, R., Shiehnejadhesar, A, Scharler, R, Obernberger, I, Multi-physics modelling of packed bed biomass combustion. *Fuel*, 2014. 122: p. 164-178.

- 1
 - 2
 - 3
 - 4
 - 5
 - 6
 - 7
 - 8
 - 9
 - 10
 - 11
 - 12
 - 13
 - 14
 - 15
 - 16
 - 17
 - 18
 - 19
 - 20
 - 21
 - 22
 - 23
 - 24
 - 25
 - 26
 - 27
 - 28
 - 29
 - 30
 - 31
 - 32
 - 33
 - 34
 - 35
 - 36
 - 37
 - 38
 - 39
 - 40
 - 41
 - 42
 - 43
 - 44
 - 45
 - 46
 - 47
 - 48
 - 49
 - 50
 - 51
 - 52
 - 53
 - 54
 - 55
 - 56
 - 57
 - 58
 - 59
 - 60
 - 61
 - 62
 - 63
 - 64
 - 65
35. Khodaei, H., Olson, C, Nikrityuk, P, Numerical investigations of the impact of inflow conditions on characteristics of a large-scale pyrolysis unit. *Energy*, 2019. 169: p. 1101-1111.
36. Khodaei, H., Al-Abdeli YA, Guzzomi F and Yeoh GH., An overview of processes and considerations in the modelling of fixed-bed biomass combustion. *Energy*, 2015. 88: p. 946-972.
37. Haberle, I., Skreiberg, Ø, Lazar, J, Haugen, NL, Numerical models for thermochemical degradation of thermally thick woody biomass, and their application in domestic wood heating appliances and grate furnaces. *Progress in Energy and Combustion Science*, 2017. 63: p. 204-252.
38. Yang, Y., Ryu C, Khor A, Sharifi V.N, Swithenbank J., Fuel size effect on pinewood combustion in a packed bed. *Fuel*, 2005. 84(16): p. 2026-2038.
39. Zhou, H., Jensen A.D, Glarborg P, Jensen P.A, Kavaliauskas A., Numerical modelling of straw combustion in a fixed bed. *fuel*, 2005. 84: p. 389-403.
40. van der Lans, R., Pedersen L.T, Jensen A, Glarborg P, Johansen D., Modelling and experiments of straw combustion in a grate furnace. *Biomass and Bioenergy*, 2000. 19: p. 199-208.
41. Yang, Y., Newman R, Sharifi V.N, Swithenbank J, Ariss J., Mathematical modelling of straw combustion in a 38 MWe power plant furnace and effect of operating conditions. *Fuel*, 2007. 86: p. 129-142.
42. Yang, Y.B., Yamauchi, H., Sharifi, V. N, and Swithenbank, J., Effect of moisture on the combustion of biomass and simulated solis waste in a packed bed *J Inst Energy*, 2003. 76: p. 105-15.
43. Peters, B., Schröder E, Bruch C, Nussbaumer T., Measurements and particle resolved modelling of heat-up and drying of a packed bed. *Biomass and Bioenergy*, 2002. 23(4): p. 291-306.
44. Collazo, J., Porteiro J, Patiño D, Granada E., Numerical modeling of the combustion of densified wood under fixed-bed conditions. *Fuel*, 2012. 93: p. 149-159.
45. Mehrabian, R., Zahirovic, S, Scharler, R, Obernberger, I, Kleditzsch, S, Wirtz, S, Scherer, V, Lu, H, Baxter, L.L, A CFD model for thermal conversion of thermally thick biomass particles. *Fuel Processing Technology*, 2012. 95: p. 96-108.
46. Mehrabian, R., Shiehnejadhesar A, Scharler R, Obernberger I., Multi-physics modelling of packed-bed biomass combustion. *Fuel*, 2014. 122: p. 164-178.
47. Bryden, K., Ragland K.W., Numerical modeling of a deep, fixed bed combustor. *Energy and Fuels*, 1996: p. 269-275.
48. Di Blasi, C., Heat, momentum and mass transport through a shrinking biomass particle exposed to thermal radiation. *Chemical engineering science*, 1996. 51(7): p. 1121-1132.
49. Hermansson, S., Thunman H., CFD modelling of bed shrinkage and channelling in fixed-bed combustion. *Combustion and Flame*, 2011. 158(5): p. 988-999.
50. Yao, Z., You, S, Ge, T, Wang, C, Biomass gasification for syngas and biochar co-production: Energy application and economic evaluation. *Applied Energy*, 2018. 209: p. 43-55.
51. Gupta, P., Sadhukhan, A, Saha, R, Analysis of the combustion reaction of carbon and lignite char with ignition and extinction phenomena: Shrinking sphere model. *International Journal of Chemical Kinetics*, 2007. 39(6): p. 307-319.
52. Sharma, A., Wang, S, Pareek, V, Yang, H, Zhang, D, CFD modeling of mixing/segregation behavior of biomass and biochar particles in a bubbling fluidized bed. *Chemical Engineering Science*, 2014. 106: p. 264-274.
53. Ansys-Fluent 2019. Theory guide. 2019, Ansys inc: USA.
54. Di Blasi, C., Modeling chemical and physical processes of wood and biomass pyrolysis. *Progress in Energy and Combustion Science*, 2008. 34(1): p. 47-90.
55. Ranzi, E., Cuoci, A, Faravelli, T, Frassoldati, A, Migliavacca, G, Pierucci, S, Sommariva, S, Chemical kinetics of biomass pyrolysis. *Energy & Fuels*, 2008. 22(6): p. 4292-4300.
56. Chen, D., Yin, L, Wang, He, P, Pyrolysis technologies for municipal solid waste: a review. *Waste management*, 2014. 34(12): p. 2466-2486.
57. Initiative, I.B., Standardized product definition and product testing guidelines for biochar that is used in soil. *IBI biochar standards*, 2012.

- 1
- 2
- 3
- 4 58. Riley, J.T., Routine coal and coke analysis: collection, interpretation, and use of analytical data. 2007: ASTM International.
- 5
- 6 59. Tak J, H.D., Anderson T, Tymchak A, Ulysses Design Report. 2015, Innovative Reduction
- 7 Strategies Inc.: InnoTec Alberta, Edmonton, Canada. p. 27.
- 8
- 9 60. MBioEX. Biomass Exchange Data File. 2018.
- 10 61. Horttanainen, M., Saastamoinen J, Sarkomaa P., Operational limits of ignition front propagation
- 11 against airflow in packed beds of different wood fuels. Energy & Fuels, 2002. 16: p. 676-686.
- 12 62. Rezaei, H., Physical and thermal characterization of ground wood chip and ground wood pellet
- 13 particles. 2017, University of British Columbia.
- 14 63. Bederina, M., Marmoret, L, Mezreb, K, Khenfer, MM, Bali, A, Quéneudec, M, Effect of the
- 15 addition of wood shavings on thermal conductivity of sand concretes: experimental study and
- 16 modelling. Construction and Building Materials, 2007. 21(3): p. 662-668.
- 17 64. Ahn, H., Sauer, TJ, Richard, TL, Glanville, Thomas D, Determination of thermal properties of
- 18 composting bulking materials. Bioresource technology, 2009. 100(17): p. 3974-3981.
- 19 65. Varela, L.G., Bermúdez, C.Á, Chapela, S, Porteiro, J, Tabarés, J.L M, Improving Bed Movement
- 20 Physics in Biomass Computational Fluid Dynamics Combustion Simulations. Chemical
- 21 Engineering & Technology, 2019. 42(12): p. 2556-2564.
- 22 66. Bermúdez, C.A., Porteiro, J, Varela, L.G, Chapela, S, Patiño, D, Three-dimensional CFD
- 23 simulation of a large-scale grate-fired biomass furnace. Fuel Processing Technology, 2020. 198:
- 24 p. 106219.
- 25 67. Gómez, M., Porteiro, J, Patiño, D, Míguez, JL, Fast-solving thermally thick model of biomass
- 26 particles embedded in a CFD code for the simulation of fixed-bed burners. Energy Conversion
- 27 and Management, 2015. 105: p. 30-44.
- 28 68. Gómez, M., Porteiro, J, De la Cuesta, D, Patiño, D, Míguez, JL, Dynamic simulation of a biomass
- 29 domestic boiler under thermally thick considerations. Energy Conversion and Management, 2017.
- 30 140: p. 260-272.
- 31 69. González, W.A., Pérez, J.F, Chapela, S, Porteiro, J, Numerical analysis of wood biomass packing
- 32 factor in a fixed-bed gasification process. Renewable energy, 2018. 121: p. 579-589.
- 33 70. Di Blasi, C., Modeling wood gasification in a countercurrent fixed- bed reactor. AIChE Journal,
- 34 2004. 50(9): p. 2306-2319.
- 35 71. Kestel, M., Nikrityuk, P, Hennig, O, Hasse, Ch, Numerical study of the partial oxidation of a coal
- 36 particle in steam and dry air atmospheres. IMA Journal of Applied Mathematics, 2012. 77(1): p.
- 37 32-46.
- 38 72. Incorporated, P.F., Power flame incorporated has installation and operation manual. 2017, Power
- 39 Flame Incorporate: USA. p. 48.
- 40
- 41
- 42
- 43
- 44
- 45
- 46
- 47
- 48
- 49
- 50
- 51
- 52
- 53
- 54
- 55
- 56
- 57
- 58
- 59
- 60
- 61
- 62
- 63
- 64
- 65

Tables and Figures

Table 1: Biomass specifications for different pyrolysis reactors

Characteristics	Fixed bed	Fluidized bed	Circulating bed	Rotary drum	Moving bed	Retort auger
Max. capacity (t/day)	500	200	100	200	84–120	50
Particle shape	Logs	Fine particles Pellets	Fine particles Pellets	Fine particles, pellets, chips, chops	Fine particles, pellets, chips, chops	Fine particles, pellets, chips, chops
Particle size	1–2m long, 3–10cm diameter	< 2mm	< 2mm	1–50 mm long	1–50 mm long	1–50 mm long
Moisture content (%)	10–50%	< 10%	< 10%	< 10%	10–20% (current case)	< 10%
Laboratory/pilot scale	[14]	[15]	[16]	[17]	[18]	[15]
Industrial scale	[12]	[12]	[12]	FEECO International, Inc.	Ulysses (I) (current case)	PYREG

Note: The data addressed in the table are based on San Miguel et al.[19], Garcia-Perez et al.[12], PYREG, FEECO International Inc, Innovative Reduction Strategies Inc.

Table 2: Different cases utilized to analyze wood volatile combustion in the combustion chamber

Cases	Swirl propane burner	Non-premixed volatiles	Swirl propane burner				Non-premixed volatiles and air			
			m_p [kg/s]	V_p [m/s]	m_a [m/s]	V_a [m/s]	$m_{volatile}$ [kg/s]	$V_{volatile}$ [m/s]	m_{air} [kg/s]	V_{air} [m/s]
Start-up	√	√	0.015	7	0.57	22.75	N/A	N/A	N/A	N/A
Steady	√	√	0.015	7	0.57	22.75	0.026	48	0.12	16

Note: λ denotes the excess air ratio (actual/stoichiometric air: fuel ratio)

Table 3: Characteristics of wood planer shavings required for CFD simulation [59]

	Volatile matter	0.67	0.78
Proximate analysis on a wet basis [%]	Ash	0.027	0.03
	Fixed carbon	0.127	0.13
	Moisture content	0.2	0.05
Ultimate analysis on a dry basis [%]	Carbon	49.01	
	Hydrogen	6.13	
	Nitrogen	<0.1	
	Sulphur	<0.1	
	Oxygen	44.36	
Wood density [kg/m ³]	89 (untapped)	150 (tapped)	
Sphericity [61]	[-]		0.1
Equivalent diameter [m]	0.005		[62]
LHV (d.b) [J/kg]	19.5e ⁶		
K _{wood} (d.b) [63]	[59] [W/m.K]		0.087
C _{p,wood} (d.b) [J/kg.K]	1760		[64]

Table 4: Wood volatile mass fractions used as an inlet boundary condition in the non-premixed volatile nozzle

Wood volatile components	Mass fraction [-] non-premixed	
	5% moisture	20% moisture
CO [%]	0.087	0.19
CO ₂ [%]	0.262	0.57
CH ₄ [%]	0.0176	0.038
H ₂ O [%]	0.092	0.2
Air and/or volatiles Temperature [K]	500 (Volatiles) 370 (Air)	
Area of inlet volatile and (or) excess air nozzles [m ²]	0.0051 (Air and volatiles) 0.007 (Air) 10*(0.01m) volatiles	

Table 5: A review of some investigations employed thermal conversion model developed by GTE group

	Scale	Feedstocks	Feature	Year	Reference
1	Lab-scale	Wood pellet	Investigate the behavior of bed and its interaction with the freeboard area above the bed.	2012	[44]
2	Lab-scale	Wood pellet	Fixed bed thermal conversion, Bed compaction and local bed shrinkage	2014	[29]
3	Lab-scale	Wood pellet	Development of thermally thick model to utilize in biomass combustion models	2015	[67]
4	Commercial pellet drop boiler	Wood pellet	Fully embedded transient bed model and Lagrangian-Eulerian conversion are implemented for particle drop feeding system	2016	[28]
5	Commercial biomass domestic boiler	Wood pellet	A developed sub grid thermally thick model was used to divide particle into several grid points and utilized in the biomass boiler considering constant and variable feeding rate.	2017	[68]
6	laboratory autothermal fixed bed gasifier	Wood (Chips, cylinder, cube)	Effect of biomass packing factor on the drying, pyrolysis and bed temperature in fixed bed gasification process	2018	[69]
7	Underfeed grate boiler	Pine wood pellet	The combined effect of EGR (Exhaust Gas Recirculation), oxygen excess ratio on boiler performance and contaminant emissions in the freeboard area taking into accounts several sub-model of biomass combustions	2019	[32]
8	4MW grate fired boiler	Wood chips, bark and saw dust	Eulerian fixed-bed biomass combustion model coupled with the CFD commercial code to perform the simulation of a large-scale moving grate biomass furnace	2020	[66]

Table 6: Equations of solid consumption rates and phase variables

Drying rate	$\dot{\omega}'''_{moist} = \tau \frac{\rho_p C_p}{LH_{moist}} \frac{\partial T_s}{\partial t}, T_s \geq T_{evap}$	(1)
Devolatilization rate	$\dot{\omega}'''_{wood} = \rho_{wood} \sum_{i=1}^3 A_i \exp\left(-\frac{E_i}{RT_s}\right)$	(2)
Char generation rate	$\dot{\omega}'''_{G,char} = \rho_{wood} A_i \exp\left(-\frac{E_i}{RT_s}\right)$	(3)
Solid temperature	$\frac{\partial(\varepsilon \rho_p C_p T_s)}{\partial t} = \nabla(k_{s,eff} \cdot \nabla T_s) + S_s$	(4)
Solid fraction	$\frac{\partial \varepsilon}{\partial t} = -\frac{\dot{\omega}'''_{c,char}}{\rho_p} \varepsilon$	(5)
Third power of particle diameter	$\frac{\lambda d_{p3}}{dt} = -\frac{\dot{\omega}'''_{c,char}}{\rho_p} d_{p3}$	(6)
Moisture density	$\frac{\partial(\varepsilon \rho_m)}{\partial t} = -\dot{\omega}'''_{moist} \varepsilon$	(7)
Dry wood density	$\frac{\partial(\varepsilon \rho_w)}{\partial t} = -\dot{\omega}'''_{wood} \varepsilon$	(8)
Char density	$\frac{\lambda(\varepsilon \rho_c)}{\lambda t} = -(\dot{\omega}'''_{G,char} - \dot{\omega}'''_{c,char})$	(9)
Total particle density	$\rho_p = \rho_{moist} + \rho_{wood} + \rho_{char}$	(10)
Energy equation source	$S_s = S_s^{reac} + S_s^{conv} + S_s^{rad} + S_s^{loss}$	(11)
Reaction source terms	$S_s^{reac} = -\dot{\omega}'''_{moist} \varepsilon \cdot LH_{moist} - \dot{\omega}'''_{wood} \varepsilon \cdot f_{gas} \cdot LH_{dev} + S_{char}^{reac}$	(12)
Mass loss source terms	$S_s^{loss} = (\dot{\omega}'''_{moist} + \dot{\omega}'''_{wood} + \dot{\omega}'''_{char}) \cdot \varepsilon \cdot (C_p T_s)^{t-\Delta t}$	(13)
Convection source term	$S_s^{conv} = -S_g^{conv} = h A_v (T_g - T_s)$	(14)
	$h = \frac{Nu \cdot k_g}{d_{eq}}; k_m^i = \frac{Sh \cdot D_{i1}}{d_{eq}}$	(15.16)
	$Nu = 2 + 1.1 \cdot Re^{0.6} \cdot Pr^{1/3}$	(17.18)
	$Sh = 2 + 1.1 \cdot Re^{0.6} \cdot Sc^{1/3}$	
Momentum	$S_{mom} = -\left(\frac{\mu}{\eta} v_{\infty} + \gamma \frac{1}{2} \rho_g v^2\right)$	(19)
	$\eta = \frac{\psi^2 d_{eq}^2 f_p^3}{150 (1-f_v)^2}; \gamma = \frac{3.5 (1-f_v)}{\psi d_{eq} f_v^3}$	(20)
	$\psi = \frac{\pi^{1/3} (6V_p)^{2/3}}{A_p}; d_{eq} = D_{cil} \left(\frac{3L_{cil}}{2D_{cil}}\right)^{1/3}$	(21)
		(22)
Radiation	$S_s^{rad} = \int_0^{4\pi} \left(\alpha_s I(r, s) - \frac{\alpha_s n^2 \sigma T_s^4}{\pi}\right) d\Omega$	(23)
	$S_g^{rad} = \int_0^{4\pi} \left(\alpha_g I(r, s) - \frac{\alpha_g n^2 \sigma T_s^4}{\pi}\right) d\Omega$	(24)
	$S_g^{rad-} = \int_0^{4\pi} \left((\alpha_g + \alpha_s) I(r, s) - \frac{(\alpha_g + \alpha_s) n^2 \sigma T_s^4}{\pi}\right) d\Omega$	(25)
	$S_{comp} = \int_0^{4\pi} \left(\alpha_g I(r, s) - \frac{\alpha_g n^2 \sigma T_s^4}{\pi}\right) d\Omega$	(26)
	$S_g^{rad} = S_g^{rad-} + S_{comp}$	



Table 7: Chemical reaction of wood volatiles and propane used in this study; (I): Three Arrhenius rates in pyrolysis reaction.

Reactions	Kinetics	Unit	Ref.
R1 $H_2 + \frac{1}{2}O_2 \rightarrow H_2O$	$9.87 \times 10^8 \exp(-\frac{3.1 e+07}{RT})[H_2][O_2]$	[J/kg mol]	[29]
R2 $CO + \frac{1}{2}O_2 \rightarrow CO_2$	$2.239 \times 10^{12} \exp(-\frac{1.702 e+08}{RT})[CO][O_2]^{0.25}[H_2O]^{0.5}$	[J/kg mol]	[29]
R3 $CO_2 + H_2 \rightarrow H_2O + CO$	$1.00 \times 10^8 \exp(-\frac{6.28 e+07}{RT})[CO_2][H_2O]$	[J/kg mol]	[71]
R4 $C_3H_8 + \frac{3}{2}O_2 \rightarrow 3CO + 4H_2O$	$4 \times 10^{15} \exp(-\frac{7.067 e+07}{RT})[C_3H_8][O_2]$	[J/kg mol]	[71]
R5 $H_2O + CO \rightarrow CO_2 + H_2$	$2.78 \exp(-\frac{1.225 e+07}{RT})[H_2O][CO]$	[J/kg mol]	[29]
R6 $CH_4 + \frac{3}{2}O_2 \rightarrow CO + 2H_2O$	$5.012 \times 10^{11} \exp(-\frac{2.0 e+08}{RT})[CH_4]^{0.7}[O_2]^{0.8}$	[J/kg mol]	[29]
(I): Kinetics of the solid heterogenous reactions			
Pyrolysis reactions	Kinetics	Unit	Ref.
<i>Dry wood</i> \rightarrow <i>Gas</i>	$A_1 = 111 \times 10^9 (s^{-1}), E_1 = 177 \times 10^3$	[J.mol ⁻¹]	[29]
<i>Dry wood</i> \rightarrow <i>Tar</i>	$A_2 = 9.28 \times 10^9 (s^{-1}), E_2 = 149 \times 10^3$	[J.mol ⁻¹]	[29]
<i>Dry wood</i> \rightarrow <i>Char</i>	$A_3 = 30.5 \times 10^9 (s^{-1}), E_3 = 125 \times 10^3$	[J.mol ⁻¹]	[29]

Table 8: Four proposed cases to simulate the thermal conversion of biomass to form biochar

Case	Moisture content [%]	Uniform heat flux [W/m ²]	Non-uniform heat flux [W/m ²]
1	5	18500	N/A
2	5	-	Non-uniform flux distribution profile is added
3	20	18500	N/A
4	20	-	Non-uniform flux distribution profile is added

Table 9: Wood planer shavings and biochar characteristics produced by Ulysses I

Characteristics	Wood planer shavings (feedstock)	Biochar (product)	
Appearance			
Bulk density [kg/m ³]	Untapped	Wet basis [kg/m ³] 82	Dry basis] 94
		Dry basis [kg/m ³] 94	[kg/m ³]
	Tapped	Wet basis [kg/m ³] 129	Dry basis 131
		Dry basis [kg/m ³] 149	[kg/m ³]
Proximate analysis on a dry basis [%]	Volatile matter	85.18%	17.85%
	Ash	0.3%	1.43%
	Fixed carbon	15.11%	83.46%
Ultimate analysis on a dry basis [%]	Carbon	49.01%	81.86%
	Hydrogen	6.13%	2.92%
	Nitrogen	<0.1%	0.14%
	Sulphur	<0.1%	0.1%
Heating value on a dry basis	Oxygen	44.36%	13.55%
		19.5 [MJ/kg] 5.41 [kW/kg]	30.1 [MJ/kg] 8.37 [kW/kg]

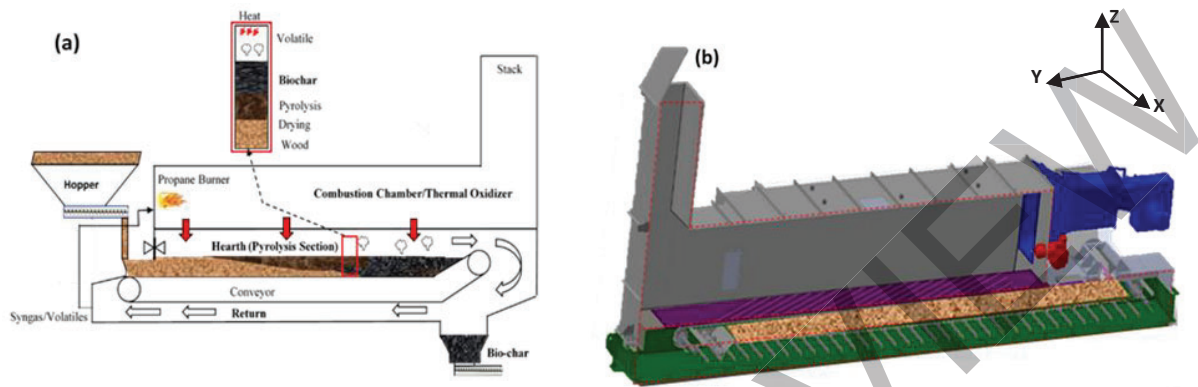


Figure 1. (a): A schematic of the continuous slow pyrolysis reactor (Ulysses I [35]); (b): Cross-sectional view of 3D CAD drawing of the reactor. Gray, green, red, blue and purple represent the combustion chamber, pyrolysis section, swirl propane burner, volatile duct side and intersection plate, respectively. The shaded area in the interior of pyrolysis section illustrates the wood planer shavings covering the chain conveyor

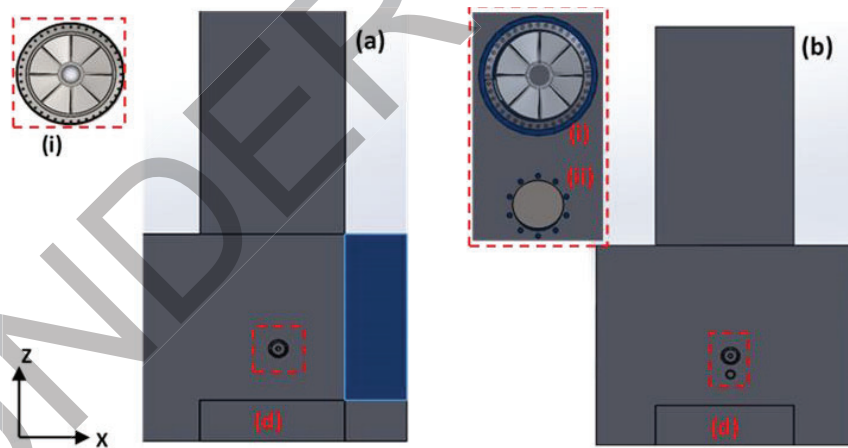


Figure 2: The configuration of the current reactor (a) and the proposed scenario (b); (a)-(i): Swirl propane burner; (a, b)-(d): pyrolysis section; (b)-(i, ii): swirl propane burner and non-premixed volatile and air nozzles

1
2
3
4
5
6
7
8
9
10
11
12
13
14
15
16
17
18
19
20
21
22
23
24
25
26
27
28
29
30
31
32
33
34
35
36
37
38
39
40
41
42
43
44
45
46
47
48
49
50
51
52
53
54
55
56
57
58
59
60
61
62
63
64
65

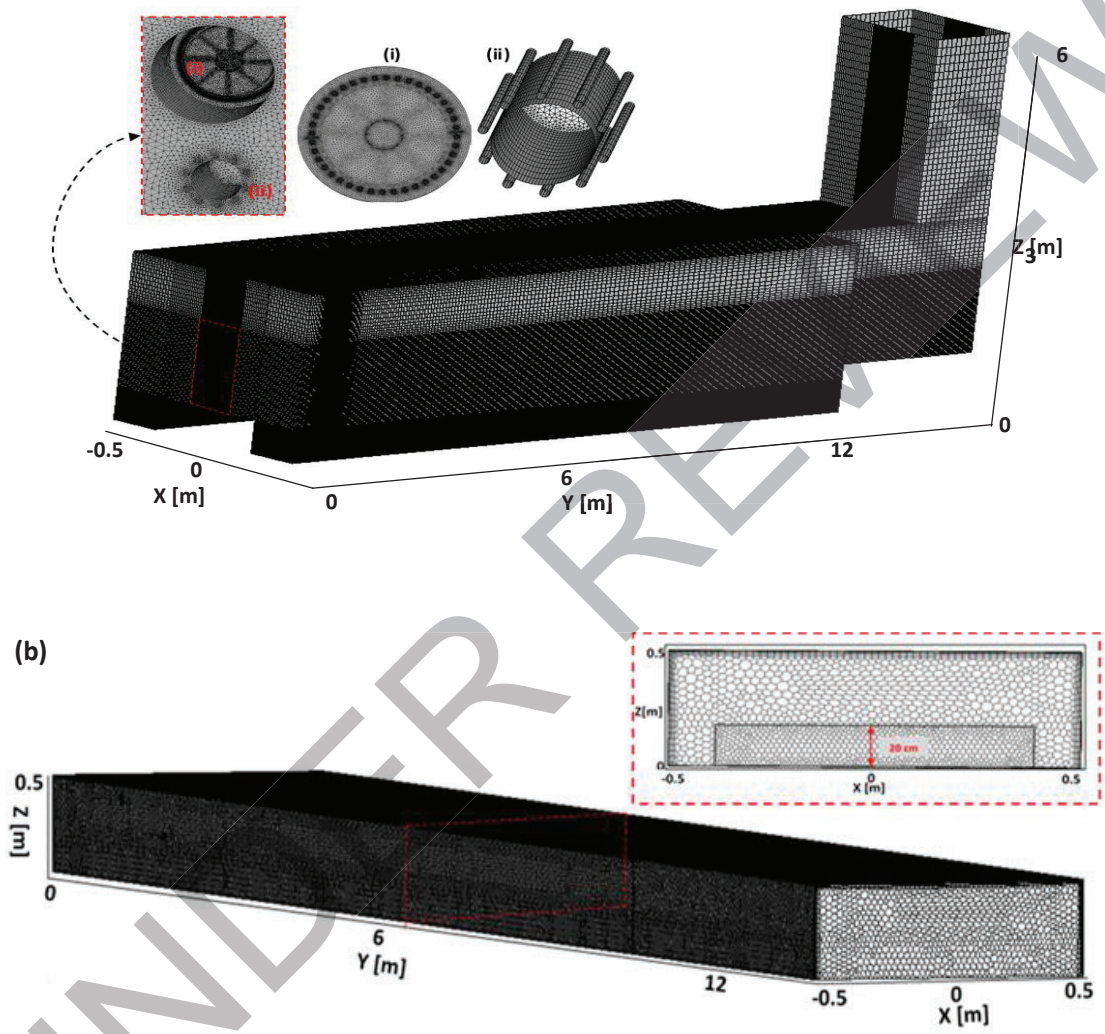
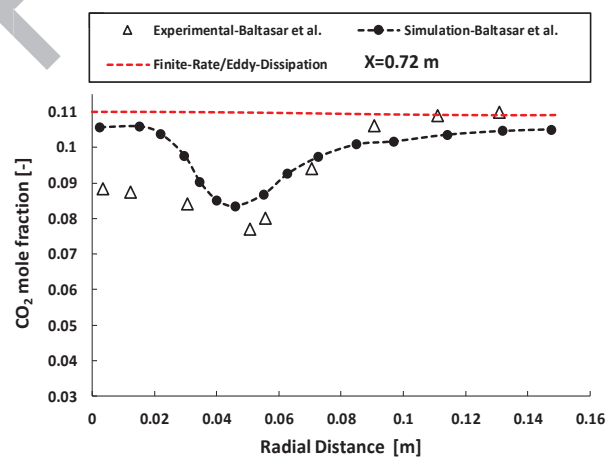
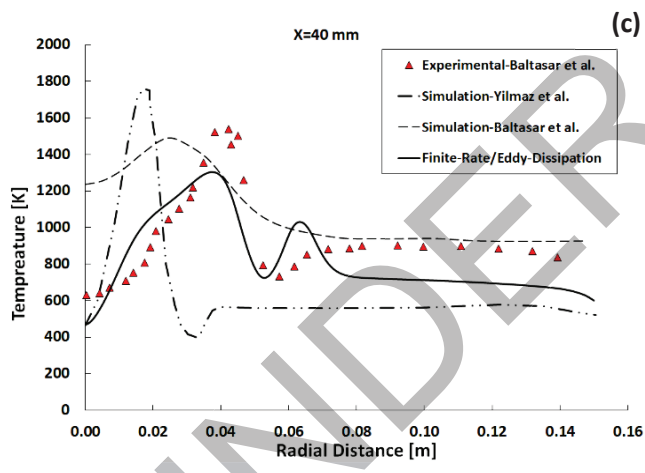
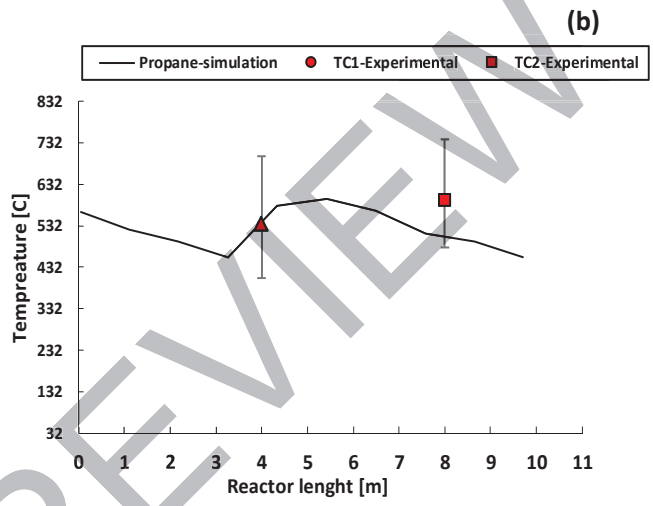
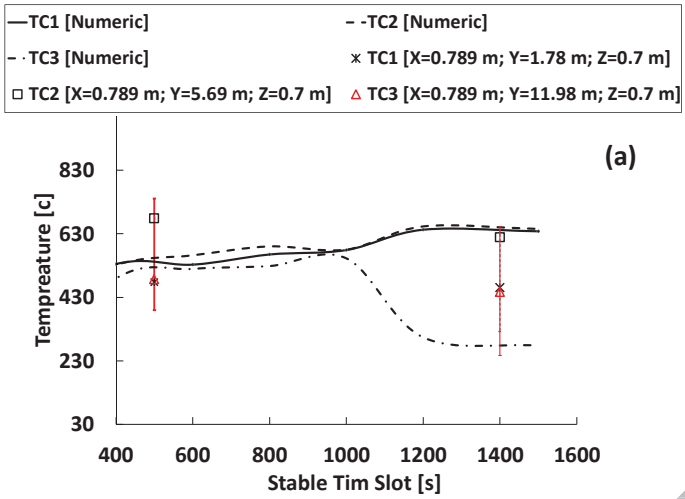


Figure 3(a) Mixed structured and non-structured grids proposed for the plants' thermal oxidizer: (i): higher resolution of swirl air/propane injection zone; (ii): 10 volatile and air injection nozzles ; (b): polyhedral grids for solid and gas phase domains in the pyrolysis section and the middle Y plane.

1
2
3
4
5
6
7
8
9
10
11
12
13
14
15
16
17
18
19
20
21
22
23
24
25
26
27
28
29
30
31
32
33
34
35
36
37
38
39
40
41
42
43
44
45
46
47
48
49
50
51
52
53
54
55
56
57
58
59
60
61
62
63
64
65



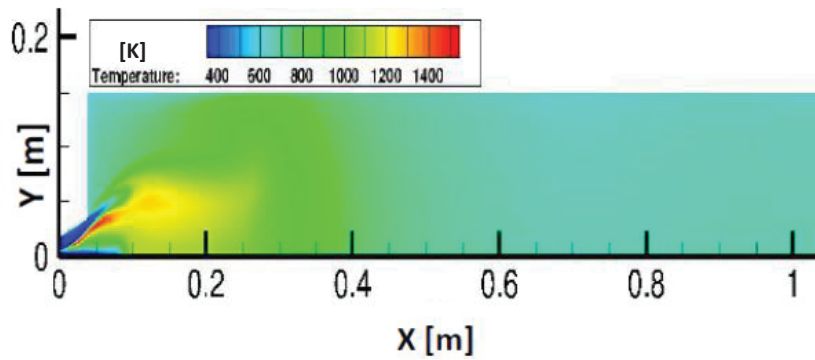


Figure 4 (a): Temperature validation in reactor pyrolysis section during thermal conversion process; (b): temperature measurement and numerical validation of combustion in thermal oxidizer (steady state condition); (c), (d): numerical validation of the experimental and CFD simulations of the swirl propane burner; (e): contour of temperature in front of the swirl nozzle [21, 23]

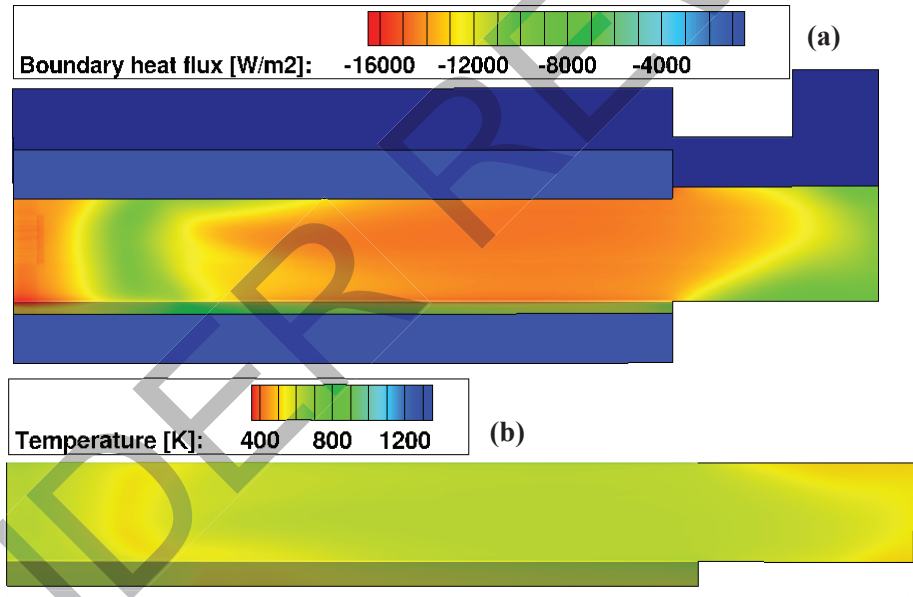


Figure 5: Self ignition of wood volatiles: (a): heat flux distribution in the intersection wall; (b): distribution of temperature in the intersection wall

1
2
3
4
5
6
7
8
9
10
11
12
13
14
15
16
17
18
19
20
21
22
23
24
25
26
27
28
29
30
31
32
33
34
35
36
37
38
39
40
41
42
43
44
45
46
47
48
49
50
51
52
53
54
55
56
57
58
59
60
61
62
63
64
65

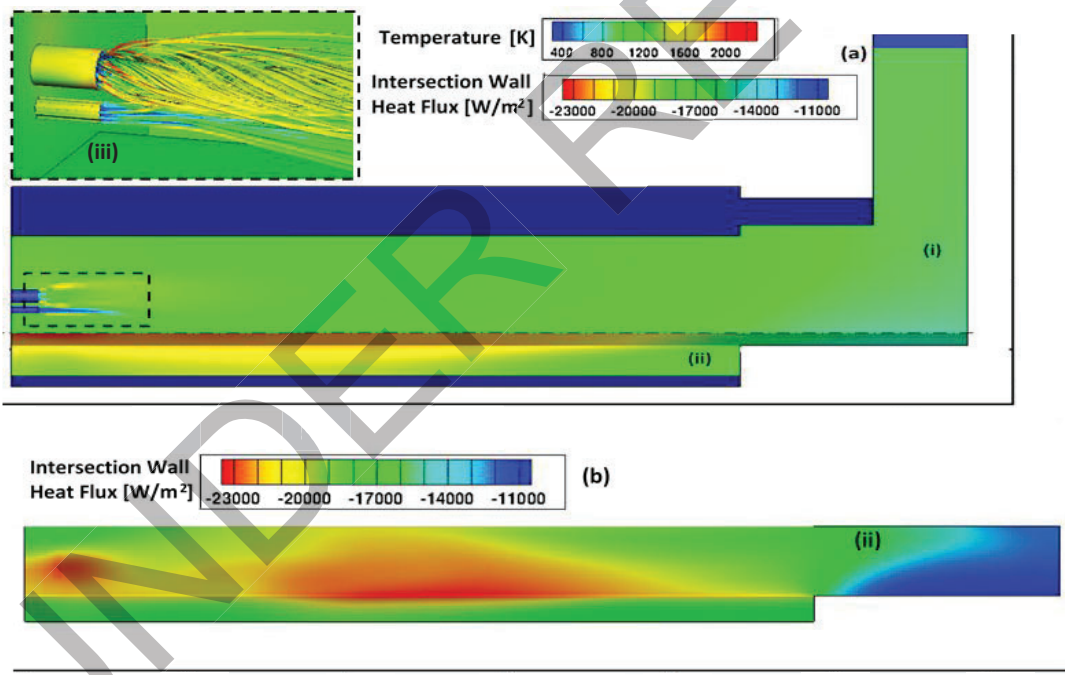


Figure 6 (a-(i)): 3D temperature profile and middle cross-sectional plane of the non-premixed combustion of biomass volatiles/air and swirl propane/air; (a-(ii)): the non-uniform heat flux distribution on the intersection wall; (a-(iii)): the flame path line in the front nozzle area; (b-(ii)): the non-uniform heat flux distributed on the intersection wall

1
2
3
4
5
6
7
8
9
10
11
12
13
14
15
16
17
18
19
20
21
22
23
24
25
26
27
28
29
30
31
32
33
34
35
36
37
38
39
40
41
42
43
44
45
46
47
48
49
50
51
52
53
54
55
56
57
58
59
60
61
62
63
64
65

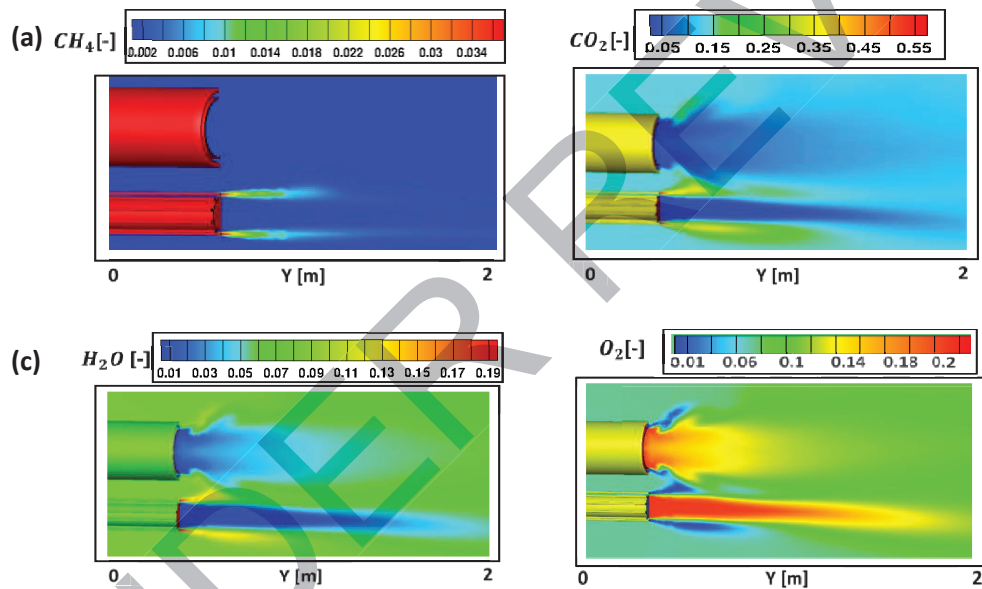
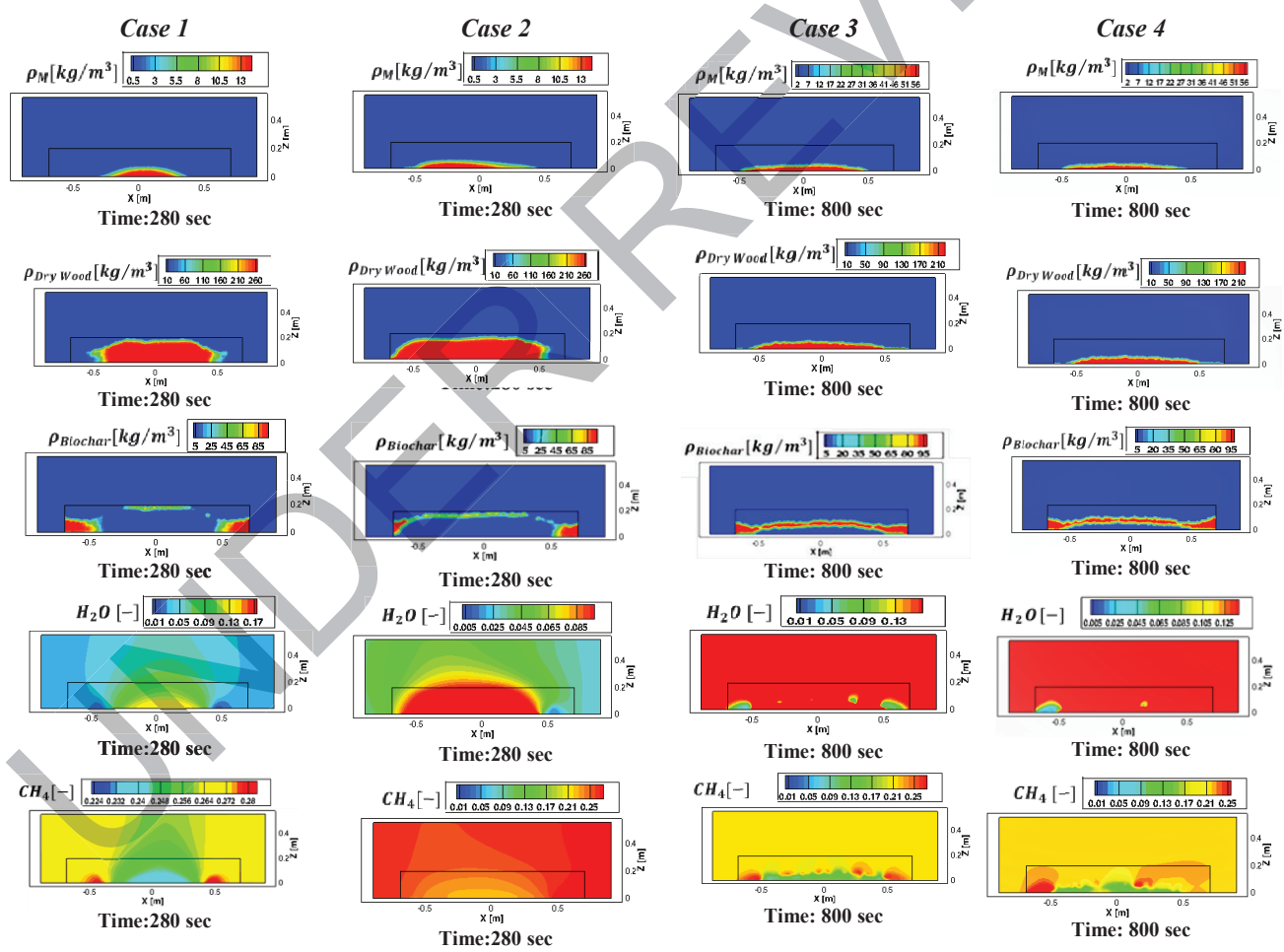


Figure 7: Contours of co-combustion of non-premixed volatiles/air and non-premixed swirl propane for CH_4 :(a); CO_2 (b); H_2O :(c); O_2 :(d)

Note: the middle section plane is assumed to be at a distance of 2m in front of the nozzles

1
2
3
4
5
6
7
8
9
10
11
12
13
14
15
16
17
18
19
20
21
22
23
24
25
26
27
28
29
30
31
32
33
34
35
36
37
38
39
40
41
42
43
44
45
46
47
48
49
50
51
52
53
54
55
56
57
58
59
60
61
62
63
64
65



VI

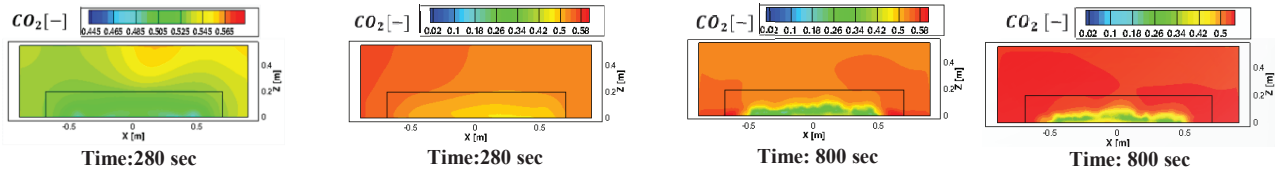


Figure 8: A comparison of different cases in the middle section plane (Y) at the selected time steps.

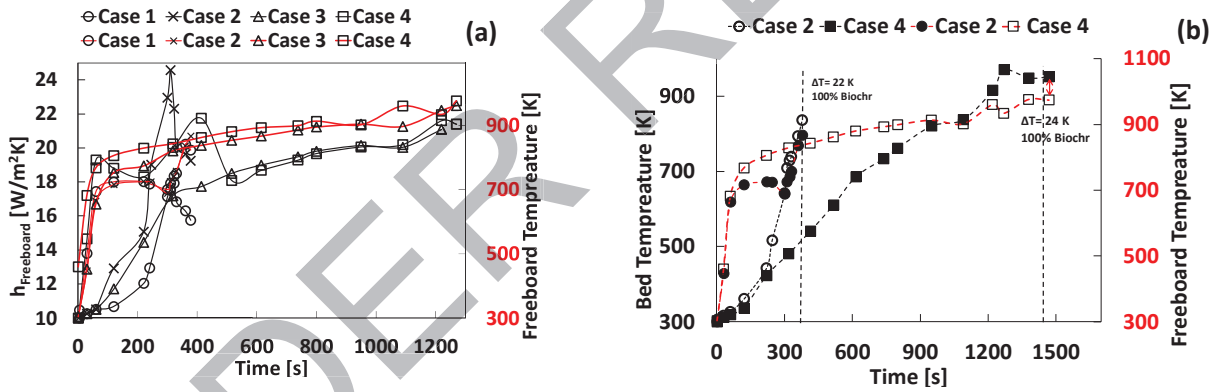
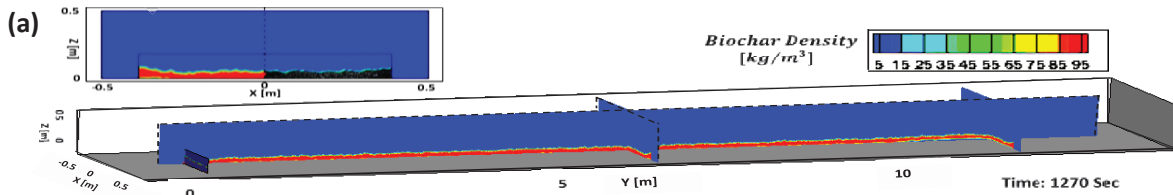


Figure 9 (a): Volume average of convective heat transfer coefficient in the freeboard area above the bed versus freeboard temperature; (b): Average bed temperature versus freeboard temperature. Note: the dashed lines represent the temperature difference between the bed and freeboard area during and after biochar formation.



(e)

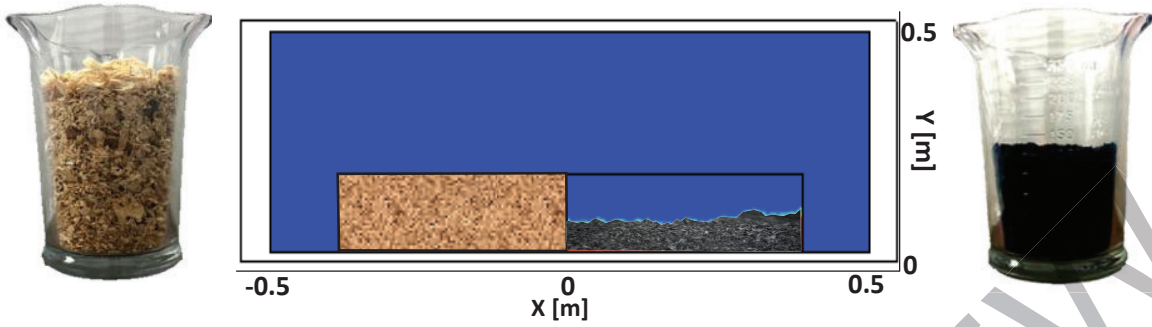
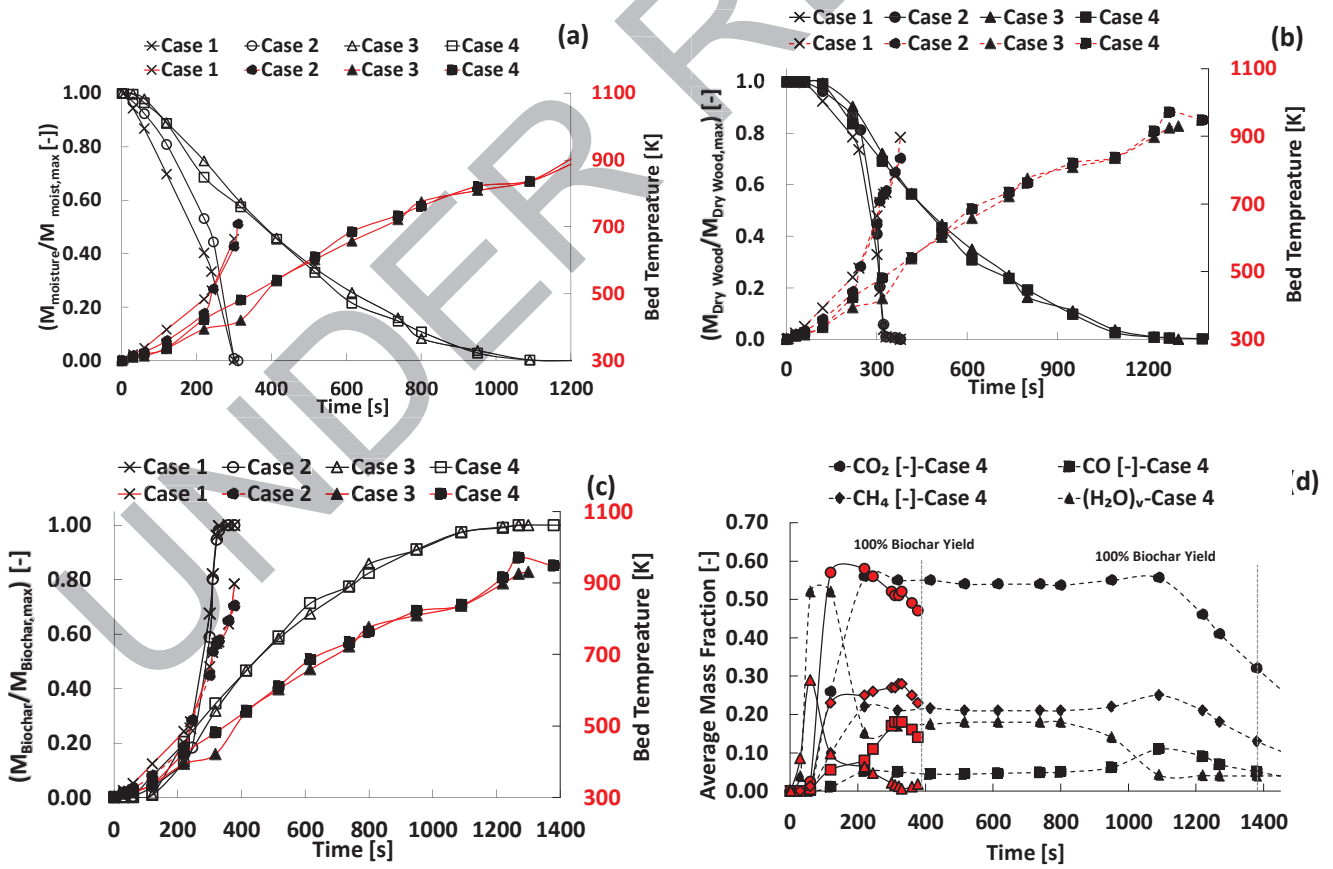


Figure 10: (a-d): Final biochar contours in different cases in the middle section plans X, Y; (e); volume shrinkage of feedstock in Case 2



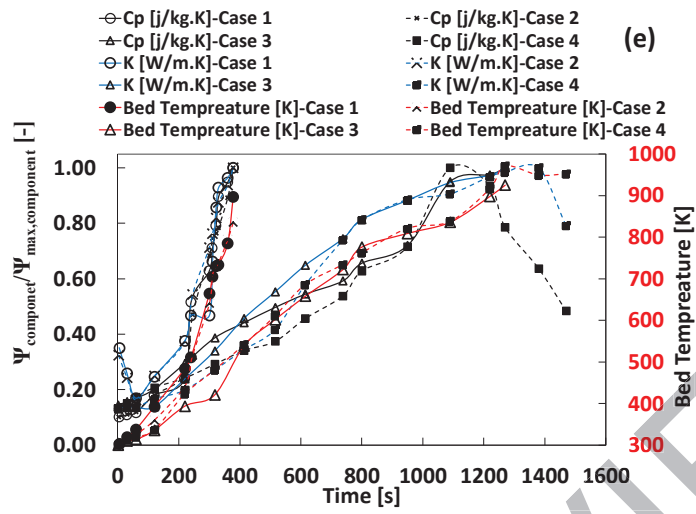


Figure 11 Evaluation of different characteristics during thermal conversion process for different cases.

ANEXO D.

Ejemplo de código perteneciente a
la interfaz gráfica de usuario


```

7282 -----DEFINICION DE LOS ELEMENTOS GRAFICOS-----
7283
7284 (lambda ATIS
7285 (let (not-pane_bed_model)
7286 (let (panel_bed_model (cx-create-panel "UV100 Thermally-This Bed Model v0.5 (for research use)" 'update-callback update-zb 'apply-callback apply-cb)
7287 (setf coeff_frame_adv (cx-create-table panel_bed_model "" 'border #f below 0)
7288 (setf advanced_to_button (cx-create-toggle-button coeff_frame_adv "Advanced" 'activate-callback apply-toggle 'state #f 'col 5)
7289 (cx-create-text coeff_frame_adv
7290 (setf file_address_text (cx-create-text-entry coeff_frame_adv "" 'col 2 'width 20))
7291 (cx-create-button coeff_frame_adv "write all" 'panel-button #f 'col 3 'activate-callback apply-write)
7292 (cx-create-button coeff_frame_adv "write fuel" 'panel-button #f 'col 4 'activate-callback apply-write-fuel)
7293 (cx-create-button coeff_frame_adv "read" 'panel-button #f 'col 5 'activate-callback apply-read)
7294
7295 (setf tab_frame (cx-create-frame-tabbed-panel bed_model "tab" 'border #f 'below coeff_frame_adv 'right-of 0)
7296 (setf tab_initial_parameters (cx-create-tab tab_frame "Initial Parameters")
7297 (setf coeff_frame_models (cx-create-frame tab_initial_parameters "Select:" 'border #f)
7298 (setf list_model (cx-create-drop-down-list coeff_frame_models "Feeding Method"
7299 (cx-create-item "Feed" 'feed)
7300 (cx-create-item "Feed + Ignition" 'feed_ignition)
7301 (cx-create-item "Feed + Ignition + Conversion" 'feed_ignition_conversion)
7302 (cx-set-list-items list_model (list 'constant 'wako & kaguri 'j-collburn 'chilton))
7303 (setf list_thun (cx-create-drop-down-list coeff_frame_models "Composition of emitted gases during devolatilization" 'editable #f 'width 30 'multiple-selections #f 'below list_model 'activate-callback apply-thun))
7304 (cx-set-list-items list_thun (list 'temperature 'constant))
7305
7306 (setf (cx-show-item list_thun #f)
7307 (setf temp_suspensido_entry (cx-create-text-entry coeff_frame_start "Ignition concentration" 'border #f 'below coeff_frame_models)
7308 (setf tiempo_ensendido_entry (cx-create-text-entry coeff_frame_start "Ignition time (s)" 'width 34)
7309 (setf altura_ensendido_entry (cx-create-text-entry coeff_frame_start "Bed height from which ignition is performed (m)" 'width 34 'below tiempo_ensendido_entry)
7310 (setf coeff_frame_non_parameters (cx-create-frame tab_initial_parameters "Boiler Parameters" 'border #f 'below altura_ensendido_entry)
7311 (setf temp_boiler_entry (cx-create-text-entry coeff_frame_non_parameters "Boiler temperature (K)" 'width 34)
7312 (setf temp_boiler_min_entry (cx-create-text-entry coeff_frame_non_parameters "Boiler minimum temperature (K)" 'width 34)
7313 (setf temp_boiler_max_entry (cx-create-text-entry coeff_frame_non_parameters "Boiler maximum temperature (K)" 'width 34)
7314 (setf performance_entry (cx-create-text-entry table non_parameters "Ignited Efficiency (-)" 'width 34 'row 0 'col 0)
7315 (cx-show-item coeff_frame_start #f)
7316
7317 (setf coeff_feed_parameters (cx-create-frame tab_initial_parameters "Substrate Feeding Configuration" 'border #f 'right-of coeff_frame_models)
7318 (setf table_feed_parameters (cx-create-table coeff_feed_parameters "" 'border #f 'below continuous_feeding)
7319 (setf feed_cyl_diam_entry (cx-create-text-entry table_feed_parameters "Feeding Cyl. Dia. (m)" 'row 1 'width 35)
7320 (setf feed_multipler_entry (cx-create-text-entry table_feed_parameters "Feeding Multiplier (-)" 'row 2 'width 35)
7321 (setf feed_cycle_entry (cx-create-text-entry table_feed_parameters "Feeding Cycle (s)" 'row 3 'width 35)
7322 (setf feed_on_interval_entry (cx-create-text-entry table_feed_parameters "Feeding system ON time in each cycle (s)" 'row 4 'width 35)
7323 (setf allim_text_frame (cx-create-text-table table_feed_parameters "" 'width 34 'row 0 'col 0)
7324 (setf list_dpm_feed (cx-create-drop-down-list coeff_dpm_parameters "DPM Feeding Configuration" 'border #f 'right-of coeff_frame_models)
7325 (cx-set-list-items list_dpm_feed (list 'constant 'g/s))
7326 (setf feed_rate_dpm (cx-create-text-entry coeff_dpm_parameters "Feeding rate (if constant) (g/s)" 'below list_dpm_feed 'width 30)
7327 (setf feed_avg_rate_dpm (cx-create-text-entry coeff_dpm_parameters "Time-averaged feeding rate (if random) (g/s)" 'below feed_rate_dpm 'width 30)
7328 (setf dpm_iterations_entry (cx-create-integer-entry coeff_dpm_parameters "Number of iterations per time-step" 'below feed_avg_rate_dpm 'width 30)
7329 (setf dpm_injection_entry (cx-create-text-entry coeff_dpm_parameters "DPM injection name" 'below dpm_iterations_entry 'width 30)
7330 (setf frame_initial_advanced (cx-create-frame tab_initial_parameters "Boiler" 'border #f 'right-of coeff_frame_models)
7331 (cx-show-item coeff_frame_initial_advanced #f)
7332 (cx-show-item coeff_frame_non_parameters #f)
7333 (cx-show-item allim_text_frame #f)
7334 (cx-show-item feed_on_interval_entry #f)
7335
7336 (setf tab_bed (cx-create-tab tab_frame "Bed")
7337 (setf coeff_frame_densities (cx-create-frame tab_bed "Densities" 'border #f)
7338 (setf table_densities (cx-create-table coeff_frame_densities "" 'border #f)
7339 (setf ref_density_fresh_bed_entry (cx-create-text-entry table_densities "Initial density of the fresh particle(s) a.r. (kg/m3_solid)" 'row 0 'width 30))
7340
7341 (setf sp_density_ash_entry (cx-create-text-entry table_densities "Specific density of ash (kg-char/m3-ash)" 'row 1)
7342 (setf sp_density_ash_entry (cx-create-text-entry table_densities "Specific density of char (kg-sh/m3-ash)" 'row 0)
7343 (setf coeff_frame_parameters (cx-create-frame tab_bed "Physical Parameters" 'border #f 'right-of coeff_frame_densities)
7344 (setf table_parameters (cx-create-table coeff_frame_parameters "" 'border #f)
7345
7346 ; Creación de la pestaña Bed
7347 ; Creación del frame que contendrá los wal
7348 ; Tabla para codernar las entradas de texto
7349 ; Entradas de texto
7350 ; Entradas de texto para la densidad
7351 ; Entradas de texto para la densidad
7352 ; Creación del frame que conti
7353 ; Tabla para codernar las entradas de texto
7354

```

ANEXO E.

Imágenes de la interfaz gráfica de
usuario para un caso concreto

